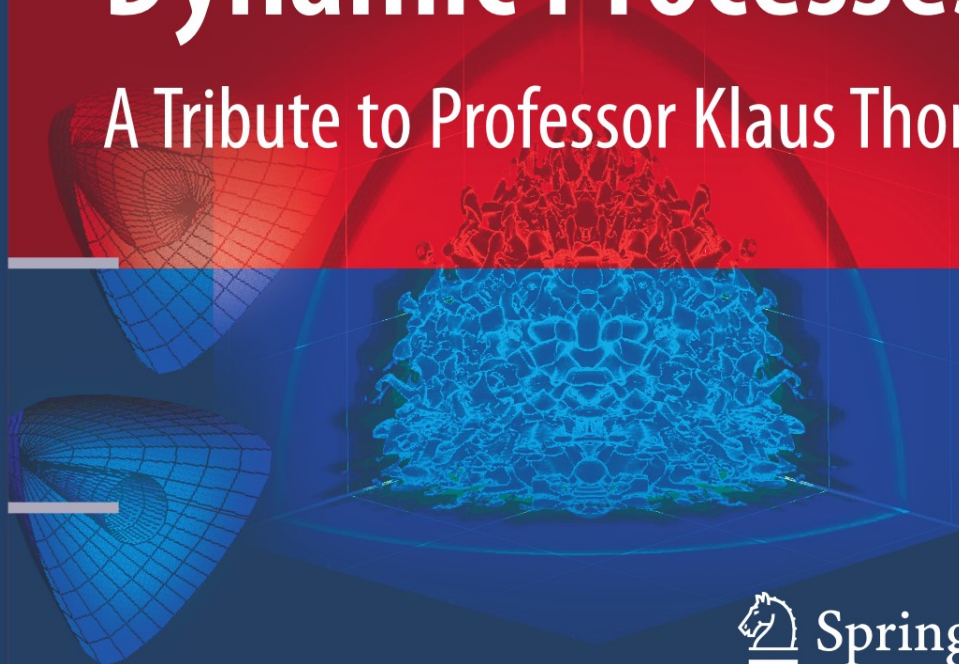


Stefan Hiermaier
Editor

Predictive Modeling of Dynamic Processes

A Tribute to Professor Klaus Thoma



 Springer

Predictive Modeling of Dynamic Processes

Stefan Hiermaier
Editor

Predictive Modeling of Dynamic Processes

A Tribute to Professor Klaus Thoma

 Springer

Editor

Stefan Hiermaier
Fraunhofer Institut für Kurzzeitdynamik
Ernst-Mach-Institut
Eckerstr. 4
79104 Freiburg
Germany
hiermaier@emi.fhg.de

ISBN 978-1-4419-0726-4 e-ISBN 978-1-4419-0727-1

DOI 10.1007/978-1-4419-0727-1

Springer Dordrecht Heidelberg London New York

Library of Congress Control Number: 2009930384

© Springer Science+Business Media, LLC 2009

All rights reserved. This work may not be translated or copied in whole or in part without the written permission of the publisher (Springer Science+Business Media, LLC, 233 Spring Street, New York, NY 10013, USA), except for brief excerpts in connection with reviews or scholarly analysis. Use in connection with any form of information storage and retrieval, electronic adaptation, computer software, or by similar or dissimilar methodology now known or hereafter developed is forbidden.

The use in this publication of trade names, trademarks, service marks, and similar terms, even if they are not identified as such, is not to be taken as an expression of opinion as to whether or not they are subject to proprietary rights.

Printed on acid-free paper

Springer is part of Springer Science+Business Media (www.springer.com)

Preface

Scientist, innovator and entrepreneur – these qualities are attributed to Joseph von Fraunhofer and are nowadays demanded of executive managers in Fraunhofer Gesellschaft. And all three attributes apply fully to Professor Dr. Klaus Thoma, director of the Fraunhofer-Institut für Kurzzeitdynamik, Ernst-Mach-Institut, and professor at the University of the German Armed Forces in Munich.

This festschrift is dedicated to Klaus Thoma on the occasion of his 60th birthday in August 2009. His manifold activities in the scientific and industrial community encompass the entire spectrum of dynamic applications. With Klaus Thoma's worldwide recognition there were many authors, familiar with him personally and professionally, who had the desire to contribute to this work.

Klaus Thoma graduated from the Technical University Munich in Physics and earned his PhD at the same university in 1978. The following nine years he made his career in the research and development division of Messerschmitt-Bölkow-Blohm (MBB), now EADS. His deep understanding of physics combined with his early understanding of the potential of numerical solution methodologies provided the direction for his becoming a leader in his field. Computer based investigations of automotive crash or military impact scenarios were anything but common in the early 1980's. However, Klaus Thoma, with his innovative foresight, was already expert in this area. His advanced knowledge and expertise led him to make close contacts to the most prestigious research laboratories and software houses in the United States. The detailed insight in the theoretical basics and the potential he recognized in the combination of experiments and numerical simulation fascinated him so much that it has been a guiding principal throughout his professional life.

Already head of a development department at MBB he decided to found his own company CONDAT together with Josef Kiermeir in 1987. This was a manifestation of the innate entrepreneurial talent of Klaus Thoma. Successfully they managed to establish the company in the limited German market. Success was guaranteed again

by his detailed understanding of physics and the implementation and application through numerical methods.

Seven years later Klaus Thoma became professor at the University of the German Armed Forces in Munich, but only for a short period of less than two years. A bigger challenge was waiting for him in Freiburg. The Fraunhofer-Institut für Kurzzeitdynamik needed a new director and after a rigorous search process he was selected. No other institute could be closer to Thoma's expertise than the high-dynamic experimental laboratories at Ernst-Mach-Institut. But not content with the status quo, his appointment also meant some fundamental changes to the institute. For example, automotive crash was never a topic before at EMI. Moreover, the creation of a new department concerned with numerical simulation and material testing allowed for an important re-orientation of the research performed at EMI. At the same time the traditional research topics at EMI were not only maintained but expanded where possible, resulting in an overall growth in project activity.

Through Klaus Thoma's leadership and vision the Ernst-Mach-Institut has become synonymous with the most advanced and highest quality applied research in dynamics. Be it material research for safer cars, invention of computer-tomocinematography, electric armour or the development of protective shielding systems for the International Space Station – Ernst-Mach is involved and at the forefront. And not one to stand still, Klaus Thoma has continuing, new ambitions for his institute. Public safety and security in times of asymmetric threats to mention only one new area.

In 2007, as a further recognition of Klaus Thoma's many contributions, he was awarded the Bundesverdienstkreuz for his exceptional achievements in the sciences and the transfer of technologies. The contributors to this book and the many colleagues that have been fortunate to know him, both personally and professionally, fully expect that his fine work will continue into the future. Klaus Thoma with his unique and powerful blend of scientist, innovator, entrepreneur and strong personal character will clearly continue to provide vision, leadership, and friendship to the international research community.

Oakland,
April 2009

Naury K. Birnbaum
Vice President
ANSYS, Inc.

Contents

Introduction	1
Stefan Hiermaier	
Part I Simulation of Automotive Crash Processes	
1 Simulation of Recoverable Foams under Impact Loading	9
Stefan Kolling, Andre Werner, Tobias Erhart and Paul A. Du Bois	
1.1 Introduction	10
1.2 Current Implementation According to Fu Chang	11
1.2.1 Theoretical Framework	11
1.2.2 Validation Tests	13
1.2.3 Application: Leg Impact	17
1.3 Addition of a Damage Model	19
1.3.1 Theoretical Framework	19
1.3.2 Examples	22
References	24
2 The Numerical Simulation of Foam – An Example of Inter-Industrial Synergy	27
Paul A. Du Bois	
2.1 Introduction	27
2.2 Foams – Physical Nature and Numerical Modeling	28
2.3 Numerical Modeling of Foams in Automotive Crash	30
2.4 Impacted Foam – The Columbia Accident	35
2.5 Summary and Conclusion	41
References	42
3 Influence of Hardening Relations on Forming Limit Curves Predicted by the Theory of Marciniak, Kuczyński, and Pokora	43
Heinrich Werner	
3.1 Introduction	43
3.2 Theoretical Model	45

3.2.1	Constitutive Equations	47
3.2.2	Derivation of Evolution Equations for the Onset of Instability	48
3.3	Numerical Solution Method	51
3.4	Initial Conditions	53
3.5	Validation	55
3.6	Convergence Properties	57
3.7	Influence of Different Hardening Relations on the FLCs	58
3.7.1	Effect of Various Quasi-Static Hardening Relations on Forming Limit Curves	59
3.7.2	Effect of Various Strain Rate Formulations on the Forming Limit Curves	61
3.8	Summary	63
	References	64
4	The Challenge to Predict Material Failure in Crashworthiness	
	Applications: Simulation of Producibility to Serviceability	67
	André Haufe, Markus Feucht and Frieder Neukamm	
4.1	Introduction	68
4.2	The Process Chain of Sheet Metal Part Manufacturing	68
4.3	Some Ideas for Failure Modelling in Forming and Crashworthiness Simulations	70
4.3.1	The Barlat Constitutive Model for Forming Simulations .	71
4.3.2	Constitutive Models for Crashworthiness Applications ..	72
4.3.3	A Hybrid Approach to Estimate the Void Volume Fraction in Forming Simulations	73
4.3.4	A Generalized Scalar Damage Model for Forming and Crashworthiness Simulations	75
4.4	Path-Dependent Localization	77
4.4.1	Stress and Strain Measures	77
4.4.2	Linear Accumulation of the Instability Criterion	79
4.4.3	Nonlinear Accumulation of the Instability Criterion	80
4.5	Post Critical Behaviour	81
4.5.1	Damage-Dependent Yield Stress	82
4.5.2	Energy Dissipation and Fadeout	83
4.6	Application of a Demonstrator Part	84
4.7	Conclusions	85
	References	87
5	Cohesive Zone Modeling for Adhesives	89
	Matthias Nossek and Stephan Marzi	
5.1	Introduction	90
5.2	Characterization Procedure	90
5.2.1	Bulk Tensile Tests	91
5.2.2	Coupon Tests	92
5.2.3	Fracture Mechanical Tests	93

- 5.3 Cohesive Zone Model 94
- 5.4 Validation 99
- 5.5 Application 101
- 5.6 Summary 104
- References 104
- 6 Modeling the Plasticity of Various Material Classes with a Single Quadratic Yield Function 107**
Markus Wicklein
- 6.1 Introduction 107
- 6.2 A Quadratic Yield Function 109
- 6.3 Parameter Identification for Foams 112
- 6.4 Application to Honeycombs 114
- 6.5 Application to Carbon Fiber-Reinforced Plastics 117
- 6.6 Outlook 118
- References 119
- 7 On the Computation of a Generalised Dynamic J-Integral and its Application to the Durability of Steel Structures 121**
Ingbert Mangerig and Stefan Kolling
- 7.1 Introduction 121
- 7.2 Basic Equations 123
- 7.3 Theory of Configurational Forces 124
- 7.4 Finite Element Formulation 126
- 7.5 Fatigue, Stress Intensity Factor and Crack Growth Rate 127
- 7.6 Application to Durability Analysis 128
- 7.7 Summary 130
- References 131

Part II Numerical Modeling of Blast and Impact Phenomena

- 8 The MAX-Analysis: New Computational and Post-Processing Procedures for Vehicle Safety Analysis 135**
David Vinckier
- 8.1 Introduction 135
- 8.2 Prediction Capabilities for Vehicle Mine and IED Blast Simulations 136
- 8.3 The MAX-Analysis: Unification of the Computational Results ... 138
- 8.4 Summary 140
- 9 10 Years RHT: A Review of Concrete Modelling and Hydrocode Applications 143**
Werner Riedel
- 9.1 Introduction: Dynamic Measurements and Model Development .. 143
 - 9.1.1 The Starting Point of the Developments 143
 - 9.1.2 Equation of State for a Large-Scale Heterogeneous Composite 146

9.1.3	Combining Civil Engineering Knowledge and Shock Physics	148
9.2	Applications in Impact Analysis	150
9.2.1	Extended Validation and Sensitivity Analysis	150
9.2.2	Deformable Projectiles and Coupling with Explosions ...	154
9.3	Protecting Critical Infrastructure against Explosion Effects	155
9.3.1	Comparison to Engineering Models and Empirical Formula	158
9.3.2	From Power Plant Security to Future High-Rise-Buildings	159
9.4	Summary and Outlook	163
	References	163
10	Numerical Simulations of the Penetration of Glass Using Two Pressure-Dependent Constitutive Models	167
	Sidney Chocron and Charles E. Anderson Jr.	
10.1	Introduction	167
10.2	Materials	168
10.3	Experimental Techniques for Material Characterization	168
10.3.1	'Bomb' Technique	168
10.3.2	'Sleeve' Technique	170
10.4	Constitutive Model Interpretations	171
10.4.1	Drucker-Prager Model	171
10.4.2	Mohr-Coulomb Model	173
10.5	Numerical Simulation of Penetration	175
10.5.1	Drucker-Prager Model	176
10.5.2	Mohr-Coulomb Model	180
10.6	Summary and Conclusions	182
	Appendix	184
	References	186
11	On the main mechanisms in ballistic perforation of steel plates at sub-ordnance impact velocities	189
	Tore Børvik, Sumita Dey, Odd Sture Hopperstad and Magnus Langseth	
11.1	Introduction	190
11.2	Experimental Studies	191
11.2.1	Experimental Set-Up	191
11.2.2	Projectiles and Targets	192
11.2.3	Experimental Programs	193
11.3	Experimental Results	194
11.3.1	Effect of Projectile Impact Velocity	194
11.3.2	Effect of Target Thickness	195
11.3.3	Effect of Projectile Nose-Shape	196
11.3.4	Effect of Target Strength	199
11.3.5	Effect of Target Layering	201
11.3.6	Summary of Experimental Data	203

11.4	Material Modelling, Material Tests and Identification of Material	
	Constants	206
11.4.1	Constitutive Relation and Fracture Criteria	206
11.4.2	Material Data and Model Calibration	209
11.5	Numerical Studies	211
11.5.1	Numerical Models	212
11.5.2	Some Numerical Results	213
11.6	Concluding Remarks	216
	References	217
12	Dimensioning of concrete walls against small calibre impact including models for deformable penetrators and the scattering of experimental results	221
	Norbert Gebbeken, Tobias Linse, Thomas Hartmann, Martien Teich and Achim Pietzsch	
12.1	Introduction	221
12.2	Penetration and perforation of concrete walls with non-deformable penetrators	223
12.3	Deformable projectiles	226
12.3.1	Jacketed projectiles	226
12.3.2	Homogenous deformable projectiles	229
12.4	Scattering of experimental data	232
12.5	The new software-tool PenSim	235
	References	236
13	Numerical Analysis of Fluiddynamic Instabilities and Pressure Fluctuations in the Near Field of a Detonation	239
	Arno Klomfass	
13.1	Introduction	239
13.2	Physical Models	243
13.3	Numerical Methods	245
13.4	Computational Methodology	247
13.5	Results 1D, 2D and 3D Free Field	248
13.6	Results 2D Above-Ground Detonation	250
13.7	Conclusions	251
	References	251
14	Numerical Simulation of Muzzle Exit and Separation Process for Sabot-Guided Projectiles at $M > 1$	261
	Jörn van Keuk and Arno Klomfass	
14.1	Introduction	261
14.2	Technical Specifications / Experimental Setup	262
14.3	Numerical Solution Method	263
14.4	Simulation Results / Comparison with Experiments	264
14.5	Conclusions / Future Work	268
	References	269

15 Numerical Analysis of the Supercavitating Flow about blunt Bodies . 271
 Arno Klomfass and Manfred Salk

- 15.1 Introduction 271
- 15.2 Physical Models 273
 - 15.2.1 Conservation Equations 273
 - 15.2.2 Equation of State 273
- 15.3 Numerical Method 275
- 15.4 Steady State Flow Fields 276
- 15.5 Summary 277
- References 278

16 Numerical Analysis Method for the RC Structures Subjected to Aircraft Impact and HE Detonation 281
 Masahide Katayama and Masaharu Itoh

- 16.1 Introduction 281
- 16.2 Analytical Method 282
 - 16.2.1 Analysis Code 282
 - 16.2.2 Material Models 283
- 16.3 Numerical Analyses 287
 - 16.3.1 Missile Impact on RC Structure (2D) 287
 - 16.3.2 HE Detonations On and Near the RC Slab (2D & 3D) . . . 290
 - 16.3.3 F-4 Phantom Crashing on a RC Wall (3D) 296
 - 16.3.4 Boeing 747 Jet Impacting on Thick Concrete Walls (3D) . 302
 - 16.3.5 HE Detonation in Tunnel Structure with Inner Steel Liner (3D) 307
- 16.4 Conclusions 311
- References 311

17 Groundshock Displacements – Experiment and Simulation 315
 Eliahu Racah

- 17.1 Introduction 316
- 17.2 Experiment 316
 - 17.2.1 Experimental Setup 316
 - 17.2.2 Experimental results 317
- 17.3 MSC.DYTRAN DYMMAT14 Material Model 319
 - 17.3.1 Deviatoric Behavior 319
 - 17.3.2 Hydrostatic Behavior 321
- 17.4 Soil Data 321
 - 17.4.1 Density 322
 - 17.4.2 Refraction Survey and Elastic Moduli 323
 - 17.4.3 Pressiometer Tests and Volumetric Crush 324
 - 17.4.4 Direct Shear Tests and Yield Surface 325
- 17.5 Simulation 326
 - 17.5.1 Simulation Setup 326
 - 17.5.2 Simulation Results and Discussion 327
- 17.6 Conclusion 330

References 330

Part III Numerical Simulation of Hypervelocity Impact Effects

18 Hypervelocity Impact Induced Shock Waves and Related Equations of State 333

Stefan Hiermaier

18.1 Introduction 333

18.2 Shock Wave Formation and the Necessity of Adequate Equations of State 334

18.2.1 Wave Dispersion due to Nonlinear Compressive Material Characteristics 334

18.2.2 Requirements to an EoS with Respect to Shock Formation 336

18.3 Equations of State for the Simulations of Shock Processes 337

18.3.1 Complete versus Incomplete Equations of State 337

18.3.2 Mie-Grüneisen Shock EoS 339

18.3.3 Equations of State for Porous Materials 340

References 347

19 Artificial Viscosity Methods for Modelling Shock Wave Propagation . 349

James Campbell and Rade Vignjevic

19.1 Introduction 349

19.2 The Von Neumann - Richtmyer viscosity 350

19.2.1 Demonstration 352

19.2.2 Wall Heating 356

19.3 Test problems for shock viscosity formulations 356

19.3.1 Sod shock tube 356

19.3.2 Noh generic constant velocity shock 358

19.3.3 Saltzman piston 359

19.4 Alternative forms of artificial viscosity 361

19.4.1 Edge centred viscosity 362

19.4.2 Tensor viscosity 363

19.5 Summary 364

References 364

20 Review of Development of the Smooth Particle Hydrodynamics (SPH) Method 367

Rade Vignjevic and James Campbell

20.1 Introduction 367

20.2 Basic Formulation 372

20.3 Conservation Equations 373

20.4 Kernel Function 377

20.5 Variable Smoothing Length 378

20.6 Neighbour Search 379

20.7 SPH Shortcomings 380

20.7.1 Consistency 380

20.7.2	Tensile Instability	384
20.7.3	Zero-Energy Modes	389
20.8	Summary	391
	References	392
21	Assessing the Resiliency of Composite Structural Systems and Materials Used in Earth-Orbiting Spacecraft to Hypervelocity Projectile Impact	397
	William P. Schonberg	
21.1	Introduction	397
21.2	Historical Overview	400
21.3	Composite Material Panels	401
21.3.1	HVI Response Characterization	401
21.3.2	Use in MOD Protection Systems	403
21.4	Honeycomb Sandwich Panels	406
21.4.1	Early Work – The 1960s and 70s	406
21.4.2	The 1980s and 90s	407
21.4.3	Recent Work	409
21.5	Conclusions	410
	References	411
22	Numerical Simulation in Micrometeoroid and Orbital Debris Risk Assessment	417
	Shannon Ryan	
22.1	Introduction	417
22.2	Ballistic Limit Simulation of a Representative Satellite Structure Wall	423
22.2.1	Target Definition	424
22.2.2	Experimental Validation of the Numerical Simulation	424
22.2.3	Simulation Results	426
22.3	Simulation of Hypervelocity Impact on a Representative Satellite Structure Wall Causing Penetration and Fragment Ejection	428
22.3.1	Target Definition	430
22.3.2	Experimental Validation of the Numerical Simulation	430
22.3.3	Simulation Results	434
22.4	Numerical Simulation of Impact Induced Disturbances in Satellite Structures	435
22.4.1	Target Definition	436
22.4.2	Experimental Validation of the Numerical Simulation	436
22.4.3	Simulation Results	439
22.5	Discussion and Summary	444
	References	445

23 Numerical Modeling of Crater Formation by Meteorite Impact and Nuclear Explosion 447
Charles L. Mader
23.1 The NOBEL Code 447
23.2 Modeling the Arizona Meteor Crater 449
23.3 Modeling the SEDAN Crater Created by a Nuclear Explosion 452
23.4 Conclusions 455
References 457

Index 459

List of Contributors

Charles E. Anderson Jr.

Engineering Dynamics Department, Southwest Research Institute, San Antonio, TX 78250, USA, e-mail: canderson@swri.edu

Tore Børvik

Structural Impact Laboratory (SIMLab), Centre for Research-based Innovation (CRI), Norwegian University of Science and Technology, NO-7491 Trondheim, Norway and Norwegian Defence Estates Agency, Research & Development Department, NO-0103 Oslo, Norway e-mail: tore.Børvik@ntnu.no

James Campbell

Cranfield University, School of Engineering - Applied Mechanics, Cranfield, Bedford, UK e-mail: J.Campbell@cranfield.ac.uk

Sidney Chocron

Engineering Dynamics Department, Southwest Research Institute, San Antonio, TX 78250, USA, e-mail: sidney.chocron@swri.org

Sumita Dey

Structural Impact Laboratory (SIMLab), Centre for Research-based Innovation (CRI), Norwegian University of Science and Technology, NO-7491 Trondheim, Norway and Norwegian Defence Estates Agency, Research & Development Department, NO-0103 Oslo, Norway e-mail: sumita.dey@forsvarsbygg.no

Paul A. Du Bois

Consulting Engineer, Freiligrathstr. 6, 63071 Offenbach, Germany e-mail: paul.dubois@gmx.net

Tobias Erhart

Dynamore GmbH, Industriestr. 2, D- 70565 Stuttgart, Germany e-mail: tobias.erhart@dynamore.de

Markus Feucht

Daimler AG, EP/SPB, W059/HPC X271, 71059 Sindelfingen, Germany e-mail:
markus.feucht@daimler.com

Norbert Gebbeken

Institute of Engineering Mechanics and Structural Mechanics, University of the
German Armed Forces Munich, Werner-Heisenberg-Weg 39, 85577 Neubiberg,
Germany e-mail: norbert.gebbeken@unibw.de

André Haufe

DYNAmore GmbH, Industriestrasse 2, D-70565 Stuttgart, Germany, e-mail:
andre.haufe@dynamore.de

Stefan Hiermaier

Fraunhofer-Institute für Kurzzeitdynamik, Ernst-Mach-Institute, Eckerstr. 4, 79104,
Freiburg, Germany e-mail: hiermaier@emi.fraunhofer.de

Odd Sture Hopperstad

Structural Impact Laboratory (SIMLab), Centre for Research-based Innovation
(CRI) and Department of Structural Engineering, Norwegian University of Science
and Technology, Rich. Birkelands vei 1A, NO-7491 Trondheim, Norway e-mail:
odd.hopperstad@ntnu.no

Masaharu Itoh

Impact Dynamics Team, ITOCHU Techno-Solutions, 2-5, Kasumigaseki 3-chome,
Chiyoda-ku, Tokyo 100-6080, Japan e-mail: masaharu.itoh@ctc-g.co.jp

Masahide Katayama

Impact Dynamics Team, ITOCHU Techno-Solutions, 2-5, Kasumigaseki 3-chome,
Chiyoda-ku, Tokyo 100-6080, Japan e-mail: masahide.katayama@ctc-g.co.jp

Jörn van Keuk

Ernst-Mach-Institute, Eckerstr. 4, 79104 Freiburg, Germany, e-mail:
keuk@emi.fhg.de

Arno Klomfass

Fraunhofer Institute for High Speed Dynamics, Ernst-Mach-Institute, Eckerstr. 4,
79104 Freiburg, Germany e-mail: klomfass@emi.fraunhofer.de

Stefan Kolling

Giessen University of Applied Sciences, Laboratory of Mechanics, Wiesenstr. 14,
35390 Giessen, Germany, e-mail: name@email.address

Magnus Langseth

Structural Impact Laboratory (SIMLab), Centre for Research-based Innovation
(CRI) and Department of Structural Engineering, Norwegian University of Science
and Technology, Rich. Birkelands vei 1A, NO-7491 Trondheim, Norway e-mail:
magnus.langseth@ntnu.no

Tobias Linse

Institute of Engineering Mechanics and Structural Mechanics, University of the

German Armed Forces Munich, Werner-Heisenberg-Weg 39, 85577 Neubiberg, Germany e-mail: tobias.linse@unibw.de

Charles L. Mader
Mader Consulting Co., Honolulu, HI, 96825-2860, USA e-mail: mccoeh@aol.com

Ingbert Mangerig
Bundeswehr University Munich, Chair in Steel Structures, Werner-Heisenberg-Weg 39, 85577 Neubiberg, Germany e-mail: Ingbert.Mangerig@unibw.de

Stephan Marzi
Fraunhofer Institut für Fertigungstechnik und Angewandte Materialforschung (IFAM), Wiener Str. 12, D-28359 Bremen, Germany e-mail: Stephan.Marzi@ifam.fraunhofer.de

Frieder Neukamm
Daimler AG, EP/SPB, W059/HPC X271, 71059 Sindelfingen, Germany e-mail: frieder.neukamm@daimler.com

Matthias Nossek
Fraunhofer Institut für Kurzzeitdynamik, Ernst-Mach-Institut (EMI), Eckerstr. 4, 79104 Freiburg, Germany e-mail: Matthias.Nossek@emi.fraunhofer.de

Eliahu Racah
RAFAEL Advanced Defense Systems, MANOR Advanced Defense Technologies Division, P.O. Box 2250 (770), Haifa 31021, Israel e-mail: racahe@rafael.co.il

Werner Riedel
Fraunhofer-Institute für Kurzzeitdynamik, Ernst-Mach-Institute (EMI), Eckerstr. 4, 79104, Freiburg, Germany e-mail: riedel@emi.fraunhofer.de

Shannon Ryan
USRA Lunar and Planetary Institute / NASA Johnson Space Center, USA e-mail: shannon.j.ryan@nasa.gov

William P. Schonberg
Civil, Architectural, and Environmental Engineering Department Missouri University of Science & Technology, Rolla, Missouri 65409, USA e-mail: wschon@mst.edu

Rade Vignjevic
Cranfield University, School of Engineering - Applied Mechanics, Cranfield, Bedford, UK e-mail: v.rade@cranfield.ac.uk

David Vinckier
CONDAT Projekt GmbH, Maximilianstrae 28, 85298 Scheyern-Fernhag, Germany, e-mail: david.vinckier@condat-scheyern.de

Andre Werner
Northeastern University, Department of Structural Engineering, Boston, MA 02115, USA e-mail: A_W_e_r_n_e_r@web.de

Heinrich Werner

BMW Group, Knorrstrasse 147, 80788 Munich, Germany e-mail: heinrich.werner@bmw.de

Markus Wicklein

Fraunhofer Institute for High-Speed-Dynamics, Ernst-Mach-Institut, EMI, Eckerstr. 4, 79104 Freiburg, Germany e-mail: Markus.Wicklein@emi.fraunhofer.de

Introduction

Stefan Hiermaier

Festschrift for Klaus Thoma

It is the excellency of the group of distinguished authors contributing to this festschrift that makes it exceptional and, hence, appropriate for the natural aim of a festschrift. Another unique point of this book is the wide spectrum of *physics of dynamic processes* that is covered in three parts. And exactly as such the festschrift reflects the spectrum of scientific interests and experiences that are characteristic for the person it is dedicated to, *Klaus Thoma*.

Alone the term *dynamic processes*, in the sense of rapid load cases applied to materials and structures, stands for a whole diversity of physical phenomena and related applications. The meaning of the term ranges from crash analyses for automotive safety over military impact and blast scenarios to the so-called hypervelocity impact of space debris and meteorites on space vehicles and planets. It is the intention of this book to give an overview on the state-of-the-art numerical methodologies for predictive simulations of these processes. Therefore, the whole book is organised in three parts, each dealing with the various simulation aspects of the individual regime of dynamic processes.

It would lead beyond the scope of this book to describe the whole spectrum of physical and mathematical basics that enable a predictive simulation of the dynamic processes addressed in the various contributions. For such a purpose, the reader is kindly referred to the manifold literature existing already. In this brief introduction, an idea of the commonalities as well as of the differences between the individual levels of dynamic processes shall be provided.

Stefan Hiermaier

Fraunhofer-Institute für Kurzzeitdynamik, Ernst-Mach-Institute, Eckerstr. 4, 79104, Freiburg, Germany e-mail: hiermaier@emi.fraunhofer.de

Dynamic Processes – Physical Phenomena and Modelling Aspects

The characteristic difference between quasi-static, low-dynamic and high-dynamic problems, respectively, is the increasing predominance of wave effects on the material and structural behaviour. Therefore, to distinguish the dynamic processes covered here from cyclic load problems or eigenfrequency analyses, the term *transient processes* would seem to be better suited. However, *dynamic* is the established keyword and it is not the intention of this book to redefine terminologies.

What makes the transient character of dynamic processes so important for the comprehension of the observed physical phenomena and for the predictive quality of numerical methods modelling these processes?

Basically, the propagation of pressure and release waves inside solid structures is the vehicle by which equilibrium between acting forces and a material dependent deformation state is communicated. Even a quasi-static load, albeit applied as tardily as possible, introduces stress waves to the material. These waves propagate at the material's sound speed. What we observe, however, is that the rate of change of the applied load level influences the mechanical material behaviour. Dynamic load application means high rates of changes in deformation and, as a consequence, the propagated waves evoke increasing local strain rates and gradients. Directly related are inertia effects on the microscopic level of the material, viscosity effects and, hence, a strain rate dependent material behaviour is observed. The combination of high rates of change in the load with high pressure amplitudes even leads to specific wave types that are potentially catastrophic for structural integrity. These so-called shock waves result from superimposed wave components, each of them travelling at different sound speeds. Shock waves are characterized by extremely short pressure rise times. Under quasi-static and low-dynamic loads, repeated propagation and reflection of acoustic waves lead to a final deformation state that may or may not lead to failure. High-dynamic processes are characterized by wave propagations where each individual wave can cause fundamental changes in the material state, e.g. local failure or phase changes.

Thus, rate effects are generally present in dynamic processes. However, the related phenomena can range from strain rate dependent plasticity to material phase changes. The strain rates in the low-dynamic regime are predominantly influencing the strength properties of materials and, therefore, described in the deviatoric stress space. Extremely high dynamics, on the other side, may lead to hydrostatic pressures that exceed the strength thresholds of materials by orders of magnitude. That is why we see the same types of code, i.e. the so-called hydrocodes, applied for automotive crash analyses as well as for the simulation of nuclear explosions. In order to apply the potential of the codes properly, it is important to separate the strain rate spectrum into regimes and to formulate mathematical descriptions accordingly.

Regimes of Dynamic Loading

Strain rate, i.e. the time rate of change of strain tensor components, has turned out to be the measure of choice for the level of dynamic loading conditions. Accordingly, we can separate the spectrum of dynamics into three distinct regimes:

Low Dynamics

Here, the dependency of a material's mechanical behaviour on strain rates is observed in its plastic and failure thresholds, typically formulated as surfaces in the deviatoric stress space. Occasionally also the elastic properties of materials. The regime is characterized by strain rates up to $500 [s^{-1}]$. Relevant applications are automotive crash or deep drawing processes.

Moderate Dynamics

At strain rates between 500 and $10^5 [s^{-1}]$ both material strength effects and shock wave phenomena are observed. The formulation of a non-linear, though incomplete Equation of State (EoS) (see chapter 18) is necessary to describe the existence and propagation of shock waves. Representative applications are military impact and blast loads.

High Dynamics

Strain rates of $10^6 [s^{-1}]$ and beyond are present when debris particles impact space vehicles or under planetary impact conditions. For the latter, shock waves lead to pressures of 10 to $100 [GPa]$ and have a duration in the order of seconds. The long shock durations demand for a complete EoS since now heat conduction takes place at these extreme conditions.

With respect to the numerical simulation of processes in the above mentioned regimes of dynamic loading conditions we find two main branches demanding for attention:

- An adequate discretization of the problem in space and time
- and a mathematical description of material behaviour.

Hydrocodes – Numerical Simulation of Dynamic Processes

Hydrocodes, also called *wave-propagation-codes*, are the typical class of numerical tool for the simulation of crash and impact and at the same time not linked to a specific kind of discretization. Developed in the early 1950's to simulate the physical effects of nuclear weapons, a fluid dynamic approach solving the conservation equations for mass, momentum and energy was chosen. Landmarks in hydrocode development have been set by the Los Alamos National Laboratory (LANL) and

the Lawrence Livermore National Laboratory (LLNL). Nowadays available commercial codes for crash and impact simulation all have at least parts of their roots in these codes. The primary application at the time first hydrocodes were developed did not demand for a constitutive equation of shear stresses nor for related failure criteria since the prevailing hydrostatic pressures exceeded the shear strengths by orders of magnitude. Only for later applications for detonation and impact induced shock wave simulations in fluids and structures including structural deformations, deviatoric stress components have been implemented. Over decades models for more and more physical phenomena found implementation into hydrocodes. Therefore, by the nature of their applications and their origins, hydrocodes are also an ideal platform for coupled and adaptive discretizations. Typical representatives of hydrocodes, to name but a few, are ABAQUS, AUTODYN, CTH, DYTRAN, EPIC, HEMP, HULL, LS-DYNA, OURANOS, PAM-SHOCK and RADIOS.

Characteristic elements employed in a hydrocodes are:

- Solution of the conservation equations for mass, momentum and energy.
- Decoupled treatment of the stress tensor in terms of deviatoric and hydrostatic components.
- Formulation of a nonlinear equation of state accounting for shock wave formation and propagation.
- Constitutive equations for elastic and inelastic, rate-dependent material behaviour including damage, failure and post-failure behaviour.
- Arbitrary spatial and explicit time integration.
- A numerical methodology to capture shock waves, e.g. artificial viscosity or Godunov methods.

The strain rate dependent finite deformation of structures is described by kinematic and constitutive equations. A solution of the related partial differential equations with the aim of investigating dynamic deformation and energy dissipation needs to include a time resolved description of the process including wave propagation effects. Thus, these equations are to be solved and hence discretized both in space and time. Since analytical or closed form solutions for the complex processes are not at hand, numerical methods have been and are being developed to find approximative solutions. Part of the approximation and core philosophy of numerical methods is the so-called *discretization* of the governing equations, i.e. their selective solution at a finite number of spatial locations and instants of time within the investigated domain. From the particular solutions at discrete locations a subsequent overall continuous solution is reconstructed.

Spatial discretizations of the basic equations may be achieved by various kinds of finite methods to be described in the following chapters. Finite elements (FEM), finite differences (FDM), finite volumes (FVM) or mesh-free methods (MFM) are general categories of numerical methods developed to several different sub-branches for specific applications each. Formulated in Lagrangean or Eulerian kinematics the resulting individual methods are often specifically derived for certain structural components or loading conditions. Examples are finite elements which can be formulated as generally as a numerical method can be or as specific as e.g. plate or shell elements for thin walled structures with two-dimensional stress states.

Concerning *time discretization*, explicit and implicit schemes based on finite difference approximations exist to account for the time dependence of the basic equations. Whereas the explicit formulations are of less computational costs compared to implicit ones, their stability and precision is limited by the time step size. Implicit methods are capable of larger time steps at the same or higher accuracy and its precision can easily be controlled. However, for most dynamic processes under crash or impact conditions an explicit integration scheme is still preferable since a resolution of wave propagation effects demands for extremely short time steps in the order of micro- or nano-seconds which is, thus, eliminating the advantage of implicit methods.

Marching solutions in time, i.e. stepping forward along the discrete instants in time at which solutions are provided, solve the set of equations at each time step in a specific order. Typically, solutions of the time dependent equation in hydrocodes are organized in the following, or a similar, manner:

- A Define the initial conditions for the whole system at a start time $t = t_0$.
- B Evaluate the maximum size for a stable time step, i.e. without losing information or over-predicting propagation speeds.
- C Solve the set of discretized equations according to a procedure equal or similar to what is illustrated in Figure 1.
- D Use the results of C to provide new initial conditions for the next time step and continue with B until a predefined end-time is reached.

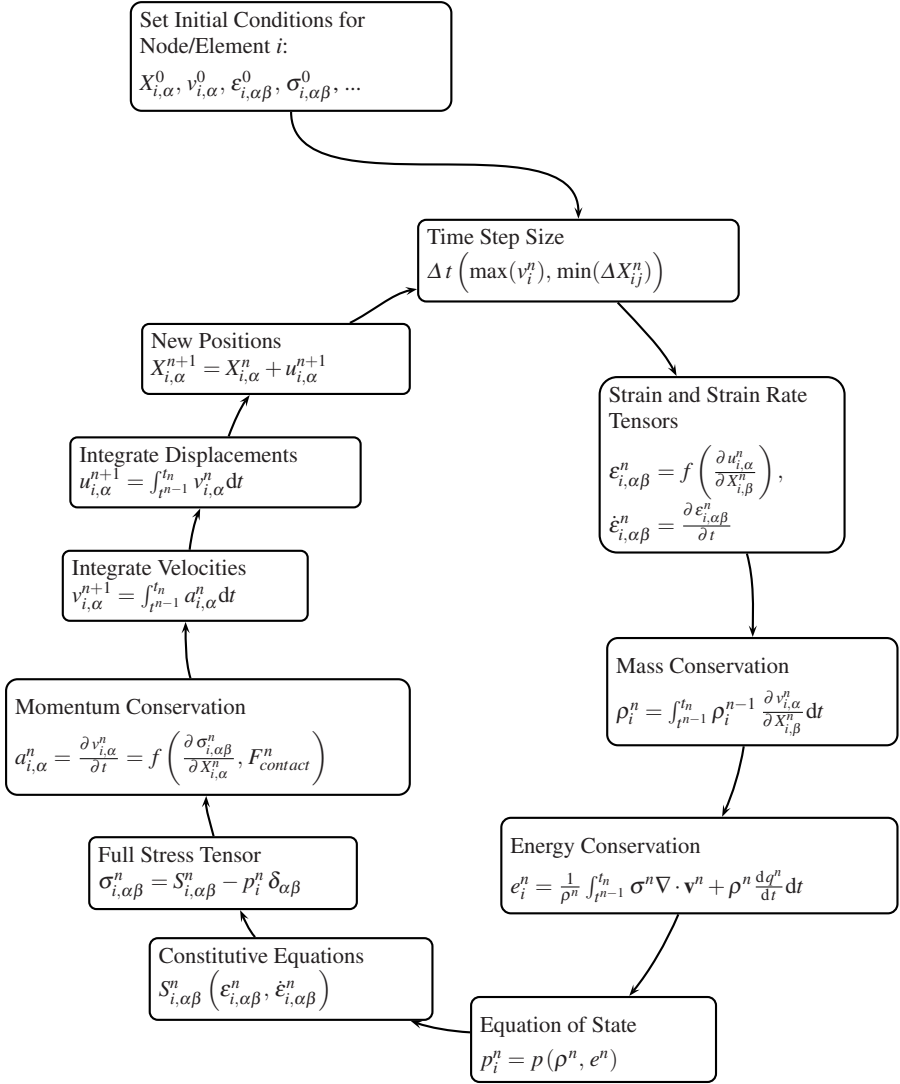


Fig. 1 Consecutive solution of equations as to be solved at each discretizing entity i within each time step n .

Part I
Simulation of Automotive Crash Processes

Chapter 1

Simulation of Recoverable Foams under Impact Loading

Stefan Kolling, Andre Werner, Tobias Erhart and Paul A. Du Bois

Abstract Simulation of recoverable foams is usually based on hyperelasticity. Since foams are always strain-rate dependent, the viscosity of the material has to be considered additionally in the material model. One disadvantage of a viscous description is the time-consuming parameter identification associated with the determination of the damping constants. An alternative is given by tabulated formulations where stress-strain relations based on uniaxial static and dynamic tensile tests at different strain rates are used directly as input. This approach is implemented in the material law no. 83 (Fu-Chang-Foam) in LS-DYNA, see [1] and [2]. We briefly show the theoretical background and the algorithmic setup of the tabulated Fu-Chang model and demonstrate the applicability of the model to non-uniaxial loading. Major problems occur in the simulation of unloading processes. These difficulties are due to the identification of unloading by the product of strain and strain rate as implemented in material law no. 83 so far. If the strain rate oscillates strongly, a unique identification of loading and unloading is no longer possible. Therefore, an extension of the model with elastic damage is presented that is capable of identifying unloading in a natural way, i.e. by a decrease of the stored hyperelastic energy of the system. With our model, hysteresis effects can be simulated and energy is dissipated. The model is formulated in a user-friendly way by a tabulated description of damage.

Stefan Kolling
Giessen University of Applied Sciences, Laboratory of Mechanics, Wiesenstr. 14, 35390 Giessen, Germany, e-mail: stefan.kolling@mmew.fh-giessen.de

Andre Werner
Northeastern University, Department of Structural Engineering, Boston, MA 02115, USA e-mail: A.W.e.r.n.e.r@web.de

Tobias Erhart
Dynamore GmbH, Industriestr. 2, D- 70565 Stuttgart, Germany e-mail: tobias.erhart@dynamore.de

Paul A. Du Bois
Consulting Engineer, Freiligrathstr. 6, 63071 Offenbach, Germany e-mail: paul.dubois@gmx.net

1.1 Introduction

Simulation of soft foams is an important topic in engineering practice and the formulation of the proper deformation mechanism represents an interesting field in academic research, too. The exciting thing (for a numericist) is that foams are not continua but they are open- or closed cell structures. The mechanical properties thus depend upon the geometric structure of the foam (i.e. size and shape of the cells) and the intrinsic properties of the cell wall material. Deformation mechanisms include cell wall bending up to elastic buckling followed by a "plastification" phase. This behavior is reversible in soft polymer foams, hence the notation "recoverable foam". The range of application goes from door and pillar paddings, dummy components, seat cushions, bumpers to mattresses. In open cell structures, the property of the contained fluid has an effect on the mechanical response [4]. For the numerical treatment of such foams, see [5] and [6].

In this paper, we describe the material behavior in a phenomenological way by hyperelasticity and size effects are thus neglected. The chosen approach considers the foam as a continuum and the foam's macroscopic behavior is reproduced. This method has been successfully used in many applications [7], [8], [9]. If strain-rate dependency has to be considered, viscous dampers also have to be taken into account in the material model. A disadvantage of such a description is time-consuming parameter identification associated with the damping constants. In the LS-DYNA implementation according to Fu Chang [10], a tabulated formulation is used which allows a fast generation of the input data based on uniaxial static and dynamic tensile tests at different strain rates. In an extension of this material law, we use an elastic damage formulation for the modeling of the unloading behavior, i.e. forming of a hysteresis during cyclic loading, see [11] for the theoretical background. The model is likewise formulated in a user-friendly way by a tabulated description of the damage curve as shown in [12] and [13]. We show the basic equations and algorithmic setup of our model which has been implemented in LS-DYNA 971.

The results presented in this paper has already been published in [3] and [7] for the most parts and are developed hand in hand with the experimental performance of the Ernst Mach Institute in Freiburg. In this context the authors express their thanks to Hartwig Nahme and Frank Huberth from EMI for their experimental support and we seize the opportunity to dedicate this paper to the occasion of Prof. Dr. Klaus Thoma's birthday.

1.2 Current Implementation According to Fu Chang

1.2.1 Theoretical Framework

The numerical simulation of foam materials is based on a tabulated approach of hyperelasticity formulated in the principal (true) stress space. In LS_DYNA the case for a material with uncoupled principal engineering stresses (foam) is covered in MAT_083 or MAT_FU_CHANG_FOAM. For clarity the algorithm will be briefly summarized. We limit this to the case where the stress-strain curve covers both the compressive and the tensile region (TFLAG=1) and the computation of stresses consequently makes no distinction between tension or compression. A slightly simplified formulation with linear stress-strain relationship in tension (TFLAG=0) is also available in the code but not treated here. The algorithm under consideration then proceeds as follows:

1. Compute the square of the left stretch tensor V from the deformation gradient F

$$\mathbf{V}^2 = \mathbf{F}\mathbf{F}^T \quad (1.1)$$

2. Diagonalize the left stretch tensor by computing the eigenvectors arranged in the matrix Φ and compute the principal stretch ratios λ_i

$$\lambda^2 = \Phi^T \mathbf{V}^2 \Phi = \begin{pmatrix} \lambda_1^2 & 0 & 0 \\ 0 & \lambda_2^2 & 0 \\ 0 & 0 & \lambda_3^2 \end{pmatrix} \Rightarrow \lambda = \begin{pmatrix} \lambda_1 & 0 & 0 \\ 0 & \lambda_2 & 0 \\ 0 & 0 & \lambda_3 \end{pmatrix} \quad (1.2)$$

3. Compute the strain rates via velocity gradient L in the principal directions of the left stretch tensor

$$\dot{\epsilon} = \frac{1}{2} (\mathbf{L} + \mathbf{L}^T), \quad \dot{\lambda} = \Phi^T \dot{\epsilon} \Phi = \begin{pmatrix} \dot{\lambda}_1 & 0 & 0 \\ 0 & \dot{\lambda}_2 & 0 \\ 0 & 0 & \dot{\lambda}_3 \end{pmatrix} \quad (1.3)$$

4. Filter the principal strain rate values. Here we use a simple or running 12point averaging scheme (SRAF=1/0):

$$\begin{aligned} \lambda_i^{ns} &= \sum_{m=n-11}^n \frac{\lambda_i^m}{12} & \text{if } \text{SRAF} = 1 \\ \lambda_i^{nr} &= \frac{\lambda_i^n}{12} + \sum_{m=n-11}^{n-1} \frac{\lambda_i^{mr}}{11} & \text{if } \text{SRAF} = 0 \end{aligned} \quad (1.4)$$

5. Compute principal engineering strains taking into account that the tabulated stress-strain values are positive in compression and negative in tension

$$\epsilon_{0i} = 1 - \lambda_i \quad (1.5)$$

6. Convert strain rates to engineering strain rates if needed ($SFLAG=0/1$). Set strain rate value to zero in a principal direction if we have unloading:

$$\begin{aligned} \dot{\varepsilon}_i &= \begin{cases} |\dot{\lambda}_i| & \text{if } \dot{\lambda}_i \varepsilon_{0i} < 0 \\ 0 & \text{if } \dot{\lambda}_i \varepsilon_{0i} > 0 \end{cases} \\ \dot{\varepsilon}_i &= \dot{\varepsilon}_i (1 - \varepsilon_{0i} * SFLAG) \end{aligned} \quad (1.6)$$

7. Compute principal engineering stresses by a table lookup. The table lookup uses strain and strain rate in each principal direction ($RFLAG=1$). Then compute principal true stresses that are positive in tension.

$$\sigma_i = - \frac{\sigma_{0i}(\varepsilon_{0i}, \dot{\varepsilon}_i)}{\lambda_j \lambda_k} \quad (1.7)$$

8. Compute Cauchy stresses in the global system using the fact that in a hyperelastic material the eigenvectors of the true stress tensor and the left stretch tensor are identical

$$\sigma = \Phi \begin{pmatrix} \sigma_1 & 0 & 0 \\ 0 & \sigma_2 & 0 \\ 0 & 0 & \sigma_3 \end{pmatrix} \Phi^T \quad (1.8)$$

This summarizes the approach followed in most foam material laws implemented in LS-DYNA and in the popular MAT_083 or MAT_FU_CHANG_FOAM in particular. It has proven to be a valid and useful tool for the simulation of foam structures under dynamic loading in countless applications. More detail about some of the alternative formulations that were made available can be found in [10].

It has to be emphasized, however, that this formulation considers not the real viscosity of the material. The formulation is referred to as "strain-rate-dependent-hyperelasticity" (a nomenclature that is a contradiction in terms) that wangles viscosity in a numerical way.

A further weak point of this material model was recently shown to be the unloading response. The unloading algorithm is incorporated in step 6 above. If the signs of strain and strain rate are opposite the strain rate value is set to zero and the computed stresses are automatically on the lowest curve of the tabulated input data. The approach is in principle numerically stable but the unloading response is rate-independent. In practical applications though, the oscillatory response which is intrinsically linked to elastic behavior causes non-zero strain rate values to be computed during the unloading phase. This will cause too high stress values to be evaluated and rebound velocities of impactors are accordingly overestimated.

In the present study an alternative unloading model is proposed based on a damage formulation. One of the advantages of this formulation is that the unloading response of the material can be rate dependent.

1.2.2 Validation Tests

In daily engineering practice, experimental data is available for compression and (if any) tensile tests only. This is, of course, sufficient to validate a material card for MAT_83. In this section, we show additionally the accuracy of the Fu Chang model for non-uniaxial loads like shear and torsion.

The results are taken from [15]. In a first example, we simulate a compression test as it is shown in Figure 1.1. The technical stress-strain relation obtained from this can be used directly in MAT_83. As can be seen in Figure 1.1, the material shows a Poisson coefficient close to zero. This is only the case for low density foams, roughly below 200g/l. High density structural foams ($> 200\text{g/l}$) cannot be treated by MAT_83 since they exhibit a non-negligible Poisson effect.

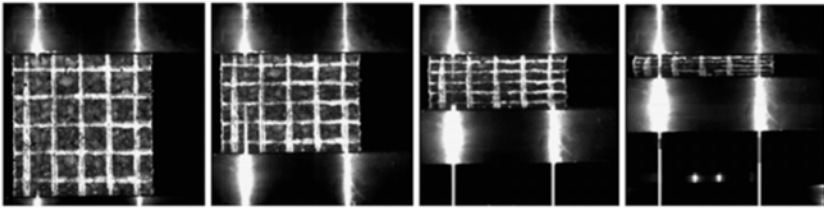


Fig. 1.1 Experimental performance of a compression test.

For EPP RG30 (RG denotes the density in g/l) the compression test has been simulated with LS-DYNA. The results of the computation and the corresponding FE-model are given in Figure 1.2. The loading path can be fitted exactly with MAT_83. Furthermore, the influence of the viscous coefficient DAMP is shown whereas it can be seen that utilizing a DAMP constant of 0.5% leads to a slightly overestimation of the stress level during the loading phase. However, the unloading path cannot be simulated sufficiently. As one can see, in the unloading range the obtained stresses deviate highly from the test results which are caused by the detection algorithm deployed in the material model MAT_83.

In Figure 1.3 the strain rates and node velocities are shown. Looking at the picture clarifies the problem since one can clearly observe the varying positive and negative strain rates which in turn lead simultaneously occurring loading and unloading areas.

In the next example, a tensile test for EPP RG40 is shown. The specimen and the results for two different strain rates are given in Figure 1.4. The simulations show a good agreement with the experiment given the fact that the results were computed by using input data from different experimental tests. However, the obtained stress

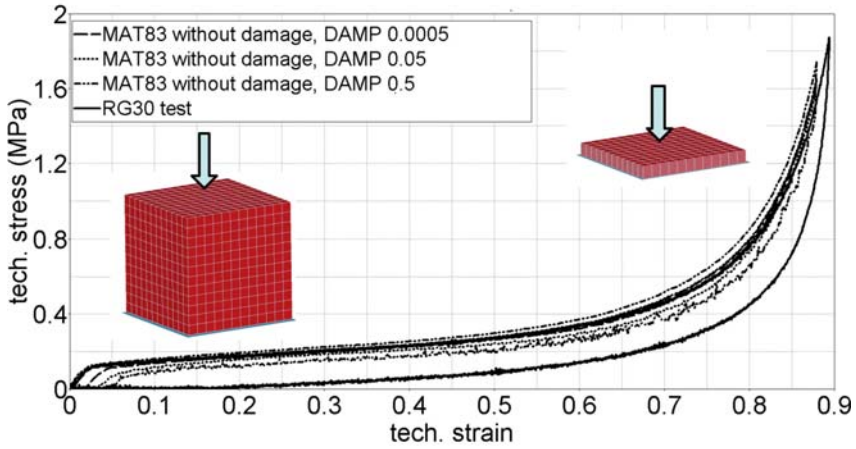


Fig. 1.2 Simulation of a compression test.

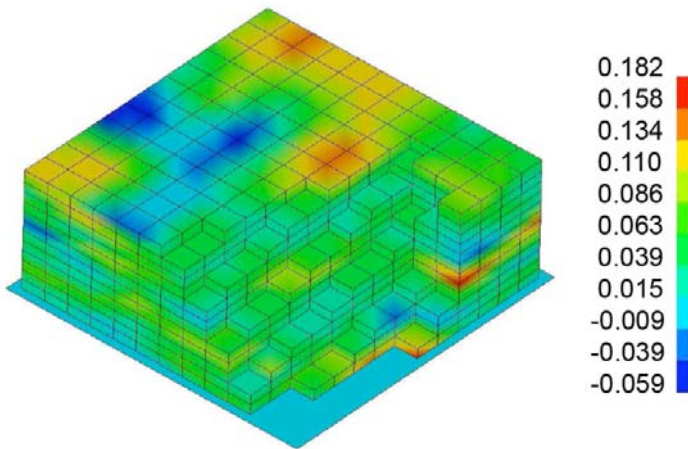


Fig. 1.3 Strain rates compression test unloading phase.

strain characteristic is close to the experimental test results. This fact and looking at the loading path results of the compression test simulation where updated experimental test data were used let us reasonable assume that if updated input data would have been utilized the simulation results would have matched the experimental tests very close.

Another imported fact should be emphasized namely that EPP shows a non-negligible Poisson effect under tension, see corresponding experimental perfor-

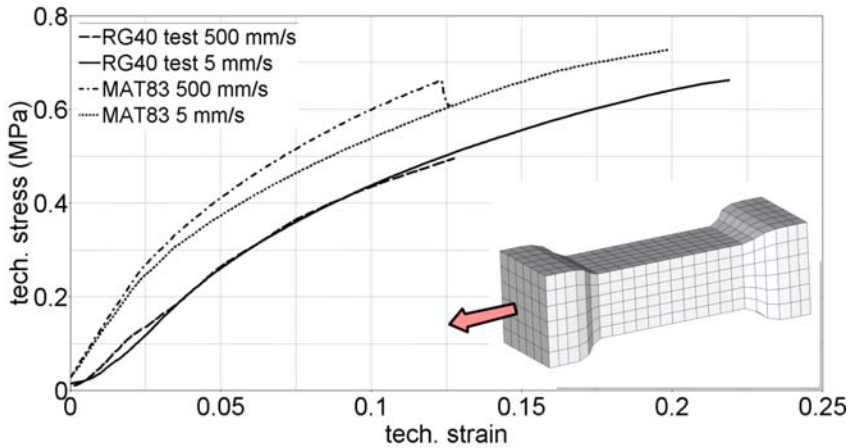


Fig. 1.4 Tensile test.

mance in [19], [20] and [17]. However, tensile stress plays fortunately a secondary role in real structures made from EPP-foam.

Now we test the input data some non-uniaxial tests. First we consider a simple shear test as it is shown in Figure 1.5. The experimental setup consists of two shear test specimens glued with three steel plates. The lower and the upper steel plates are fixed on the right hand side and a prescribed displacement is applied to the middle plate. Thus a simple shear situation is forced.

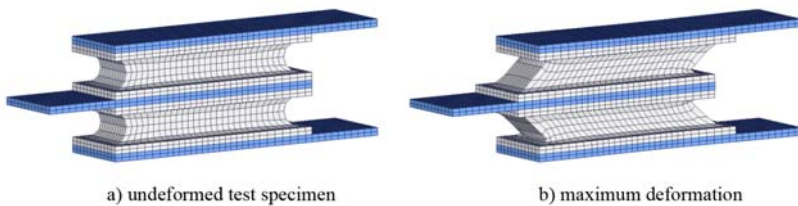


Fig. 1.5 Shear test simulation.

The results of the simulation and the experimental data taken from [17] are given in Figure 1.6. Up to 10mm the simulation is very close to the experiment whereas deviation in initial stiffness can be observed. Furthermore for larger deformation, a softening behavior caused by onset of failure of the tested material can be detected that cannot be simulated with Fu-Chang’s foam.

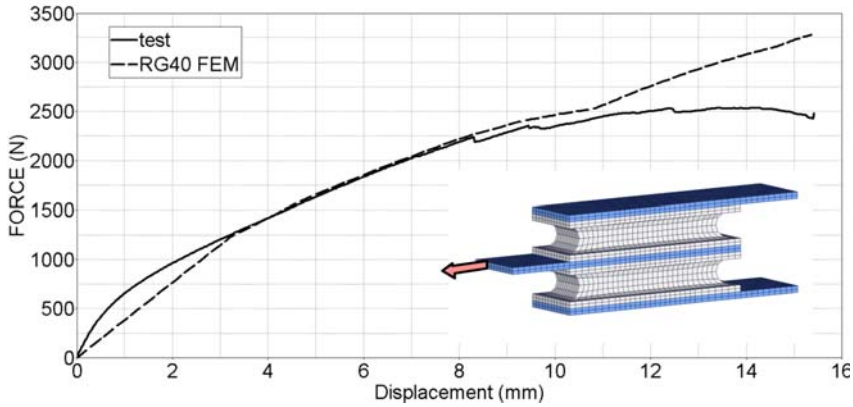


Fig. 1.6 Simple shear test.

As a last example, we simulate a torsion test presented by Schlimmer in [20]. Here, a cylindrical foam specimen is glued between two cylinders made from steel, see Figure 1.7 and Figure 1.8. With this setup, a wide range of mixed mode loading can be applied. Here a torsion test has been performed where one of the steel cylinders is fixed and the other one performs a rotational motion whereas the longitudinal translational degree of freedom is free. The simulations were conducted incorporating the viscous hourglass formulation available in LS-DYNA. Figure 1.7 shows the temporal evolution of the torsion test.

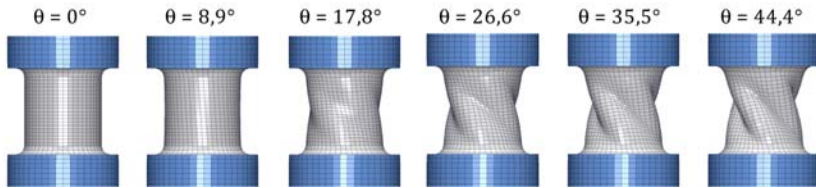


Fig. 1.7 Simulation of a torsion test at different torsion angles.

In the experiment, global shear stress and strain as well as the longitudinal strain have been measured. Despite the fact that here a complex state of stress were simulated using a constitutive law based on compression and tensile test data as well as neglecting the Poisson effect results show a very good agreement to the experimental data. The small variation in both obtained result quantities are within a reasonable range and the global behavior of the tested specimen can be modeled sufficiently.

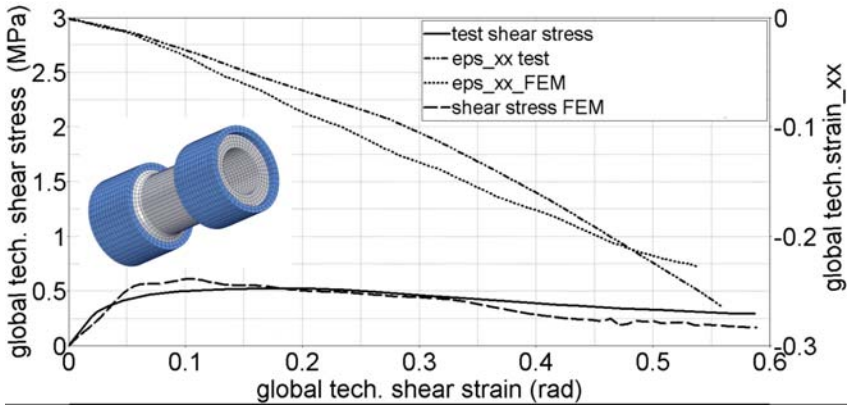


Fig. 1.8 Torsion test.

To sum up it can be said that the current implementation of MAT.83 leads to pretty good results in comparison to experiments. It shows the applicability of Fu Chang’s foam model for the simulation of structural parts made from soft foam even for more complex stress states. The unloading path due to the hyperelastic model remains the biggest stumbling block. In the next section, we show an extension of the current formulation using elastic damage for unloading simulation.

1.2.3 Application: Leg Impact

The following example is taken from [7]. It shows a typical application of Chang’s foam model. The legform impactor consists of two metal tubes with an outer diameter of 70mm representing the tibia and the femur. Physical properties such as mass, moments of inertia and center of gravity are specified in the EEVC-WG17 report. for both femur and tibia, a layer of Confor foam (CF-45 1; thickness 25mm) is used to model the flesh.

The impactor is covered by a 6 mm thick neoprene skin. For extended validation a specific test configuration was designed, see Figure 1.9. This target has a wooden solid block with three pieces of foam material attached to it. The position, depth and stiffness of the foam blocks are variable. These parameters were adjusted to meet a reasonable range for all recorded signals (bending angle, tibia acceleration and shear displacement).

Calibration of the foam material was completed by performing pre-tests with a steel cylinder hitting the foam. In the validation test procedure several configura-

tions were analyzed: tests at different speeds (40, 35 kph), variations of vertical position of the legform impactor relative to the target and angular tests (up to 15). A typical result of the validation procedure is shown in Figure 1.9. The main focus is an overall satisfying correlation of test and simulation.

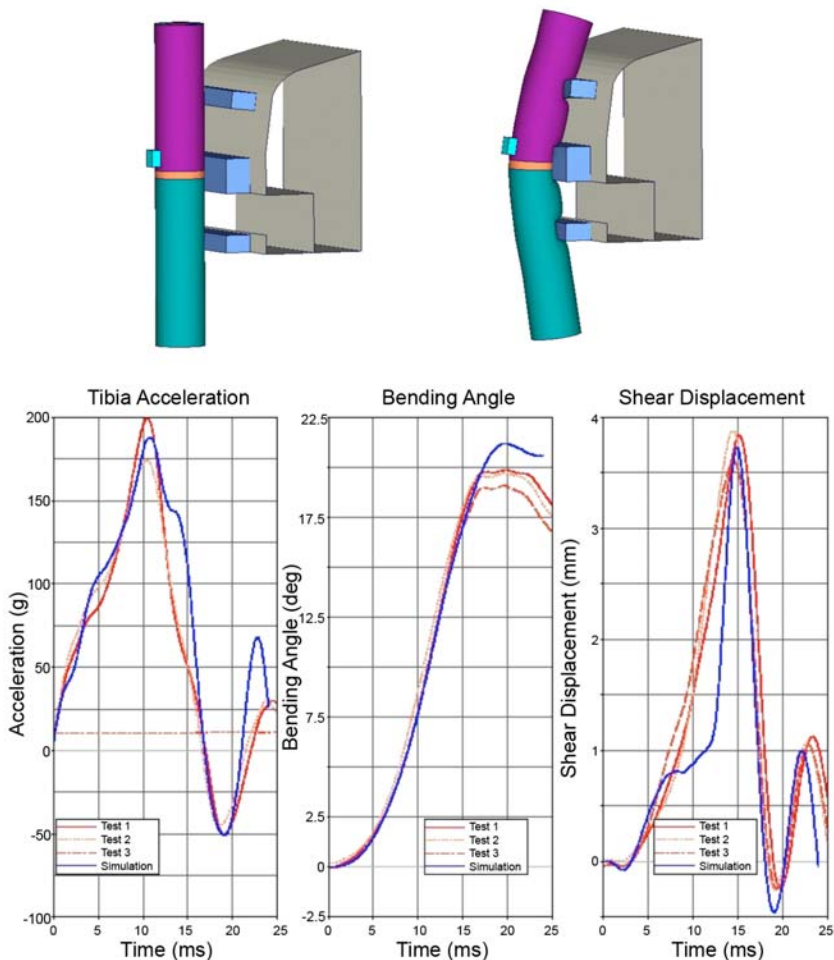


Fig. 1.9 Leg impact test configuration and results of the validation.

1.3 Addition of a Damage Model

1.3.1 Theoretical Framework

First one must realize that the current formulation of our foam material law is nothing else than a tabulated generalization of a hyperelastic material law based on the Hill functional [14]. Hill gives the energy per unit undeformed volume of the material as

$$W = \sum_{i=1}^3 \sum_{j=1}^m \frac{\mu_j}{\alpha_j} (\lambda_i^{\alpha_j} - 1) + \frac{1}{n} \sum_{j=1}^m \frac{\mu_j}{\alpha_j} (J^{-n\alpha_j} - 1) \quad (1.9)$$

The corresponding expression for the true stress is easily obtained by differentiation:

$$\sigma_i = \frac{1}{\lambda_k \lambda_j} \frac{\partial W}{\partial \lambda_i} = \sum_{j=1}^m \frac{\mu_j}{J} [\lambda_i^{\alpha_j} - J^{-n\alpha_j}] \quad (1.10)$$

The case of a foam material corresponds to setting $n=0$ meaning the material has a zero Poisson coefficient, for the engineering stress we then obtain:

$$\sigma_{0i} = \frac{\partial W}{\partial \lambda_i} = \sum_{j=1}^m \frac{\mu_j}{\lambda_i} [\lambda_i^{\alpha_j} - 1] \quad (1.11)$$

Which is a fully uncoupled expression: any principal engineering stress component in a foam depends solely on the value of the stretch ratio in the corresponding principal direction. The polynomial expression can then be replaced by any continuous tabulated function which can be directly obtained from the test:

$$\sigma_{0i} = \sigma_{0i}(\epsilon_{0i}) = \sigma_{0i}(1 - \lambda_i) \quad (1.12)$$

Here we have defined the engineering strain to be positive in compression as is usually done for foams. Rate effects are then considered by replacing the single load curve data by a table of load curves corresponding to experiments at different strain rates:

$$\sigma_{0i} = \sigma_{0i}(\epsilon_{0i}, \dot{\epsilon}_{0i}) \quad (1.13)$$

In the damage model we will need to evaluate the hyperelastic energy as well as the true stress in the material, expressing Hill's functional for $n = 0$ shows that the energy per unit undeformed volume is also uncoupled in terms of the principal stretch ratios:

$$\begin{aligned}
\lim_{n \rightarrow 0} W &= \sum_{i=1}^3 \sum_{j=1}^m \frac{\mu_j}{\alpha_j} \left(\lambda_i^{\alpha_j} - 1 \right) + \lim_{n \rightarrow 0} \frac{1}{n} \sum_{j=1}^m \frac{\mu_j}{\alpha_j} \left(J^{-n\alpha_j} - 1 \right) \\
&= \sum_{i=1}^3 \left[\sum_{j=1}^m \frac{\mu_j}{\alpha_j} \left(\lambda_i^{\alpha_j} - 1 \right) - \sum_{j=1}^m \mu_j \ln \lambda_i \right].
\end{aligned} \tag{1.14}$$

Consequently the energy can also be generalized to a sum of 3 tabulated functions of the principal stretch ratios:

$$W = \sum_{i=1}^3 W_u(\lambda_i) \tag{1.15}$$

So in a foam, the energy per unit undeformed volume is uncoupled in the principal directions. It is easily seen that the function corresponds to the energy absorption under uniaxial loading. Indeed uniaxial loading in a foam corresponds to:

$$\lambda_i \neq 1, \lambda_j = \lambda_k = 1 \tag{1.16}$$

And thus

$$\begin{aligned}
W_u(\lambda_i) &= \sum_{i=1}^3 \left[\sum_{j=1}^m \frac{\mu_j}{\alpha_j} \left(\lambda_i^{\alpha_j} - 1 \right) - \sum_{j=1}^m \mu_j \ln \lambda_i \right] \\
&= \sum_{j=1}^m \frac{\mu_j}{\alpha_j} \left(\lambda_i^{\alpha_j} - 1 \right) - \sum_{j=1}^m \mu_j \ln \lambda_i
\end{aligned} \tag{1.17}$$

Consequently, in the generalized case the function W_u is obtained by integration of the engineering stress curve measured in a uniaxial tension/compression test:

$$W_u(\lambda_i) = \int_0^{\lambda_i} \sigma_0(\varepsilon_0) d\varepsilon_0 \tag{1.18}$$

The damage model will now be defined from a quasistatic experiment where loading and unloading path are carefully measured. Tensile and compressive tests should be performed ideally.

To each stress strain point on the loading curve corresponds a value of the uniaxial energy obtained by integration. Maximum tensile and compressive deformation correspond to maximum values of the energy in tension and compression: $W_{\max t}$ and $W_{\max c}$. A damage value is then attributed as a function of the current of maximum energy ratios:

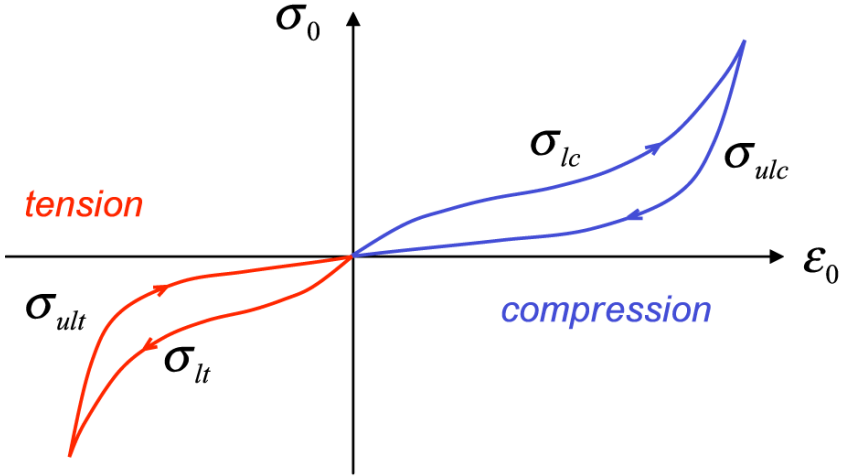


Fig. 1.10 Loading and unloading curves.

$$d = \begin{cases} d\left(\frac{W}{W_{\max c}}\right) = 1 - \frac{\sigma_{ulc}}{\sigma_{lc}} & \text{if } \epsilon_0 > 0 \\ d\left(-\frac{W}{W_{\max t}}\right) = 1 - \frac{\sigma_{ult}}{\sigma_{lt}} & \text{if } \epsilon_0 < 0 \end{cases} \quad (1.19)$$

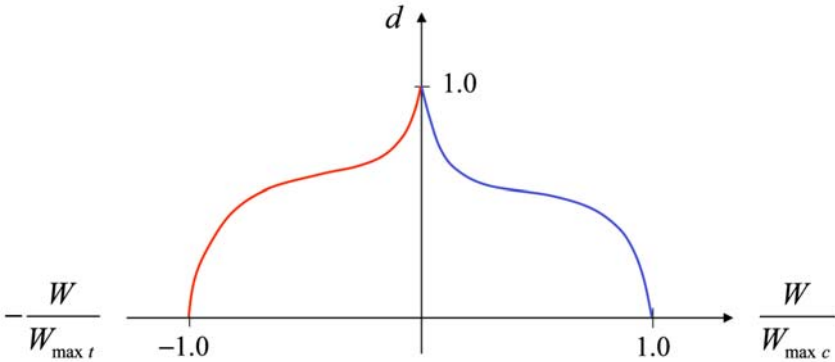


Fig. 1.11 Damage as function of energy ratio (qualitative sketch).

It should be noticed that the energy is set to a negative value in case of tension. This has the advantage that only one damage function will be necessary for the whole range of compression and tension.

Consequently from the usual tabulated data $\sigma_{0i} = \sigma_{0i}(\varepsilon_{0i}, \dot{\varepsilon}_{0i})$ we will internally derive and store two additional load curves: the uniaxial hyperelastic energy $W_u(\varepsilon_{0i})$ and the damage function $d(W/W_{\max})$.

With these additional data available the damage algorithm becomes very efficient and the modifications to the basic algorithm presented earlier are minor. An additional step is created.

5b. Compute quasistatic principal engineering stresses, check if we are in tension or in compression and compute the damage:

$$\begin{aligned}
 \sigma_{0i} &= \sigma_{0i}(\varepsilon_{0i}, 0) \\
 W &= W_u(\lambda_1) + W_u(\lambda_2) + W_u(\lambda_3) \\
 W_{\max} &= \max(W, W_{\max}) \\
 J &= \lambda_1 \lambda_2 \lambda_3 \\
 J \leq 1 &\Rightarrow d = d\left(\frac{W}{W_{\max}}\right) \\
 J > 1 &\Rightarrow d = d\left(-\frac{W}{W_{\max}}\right)
 \end{aligned} \tag{1.20}$$

Steps 6 and 7 are then modified as follows:

$$\begin{aligned}
 \varepsilon_{0i} &= 1 - \lambda_i \\
 \dot{\varepsilon}_i &= \left| \dot{\lambda}_i \right| \\
 \dot{\varepsilon}_i &= \dot{\varepsilon}_i (1 - \varepsilon_{0i} * SFLAG) \\
 \sigma_i &= -(1 - d) \frac{\sigma_{0i}(\varepsilon_{0i}, \dot{\varepsilon}_i)}{\lambda_j \lambda_k}
 \end{aligned} \tag{1.21}$$

Showing that rate effects are now applied also during unloading and hysteresis is a consequence of the damage mechanism rather than the viscosity. For this model the quasistatic unloading and loading paths should be the first two curves in the table corresponding to very low values of the strain rate. They will then determine the hysteresis and hardly have any influence on the viscosity of the material. For good functioning of the model, it is essential that these two curves form a closed loop, i.e. begin- and endpoint should be identical for both curves.

1.3.2 Examples

1.3.2.1 Cyclic Loading

At first the effect of the new damage formulation will be shown in a single element test, where compressive uniaxial loading is applied with prescribed motion. Loading and unloading curves are given in tabulated form as closed loop with maximum

strain $\epsilon_{\max} = 0.47$ (see dashed line in Figure 1.12).

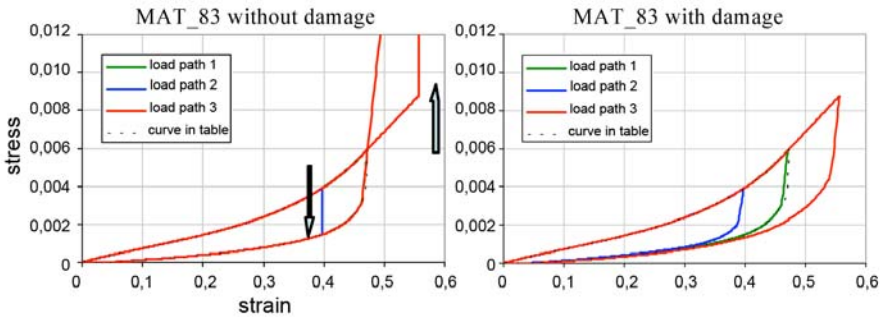


Fig. 1.12 Simulation of cyclic loading with and without damage.

As expected, loading can be reproduced exactly with and without the new damage formulation. On the other hand, clear differences are present in case of unloading. Without the damage formulation, strain rate is set to zero if the unloading criterion is met. This results in a sudden jump of the stress path from loading curve to unloading curve. In case of load path 1 with $\epsilon_{\max} = 0.47$, which exactly matches the prescribed curves, this seems to be no problem. But in case of load path 2 with less deformation ($\epsilon_{\max} = 0.40$) an unphysical abrupt stress drop can be observed. Load path 3 with higher compression $\epsilon_{\max} = 0.55$ is even worse, since the jump from loading to unloading curve leads to an increase in stress, which is physical nonsense. With the new damage formulation, we obtain the exact curve as given in the input data again for load path 1. For load paths 2 and 3, the unloading behavior is affine to the prescribed unloading and therefore appears to be reasonable from an engineering point of view.

1.3.2.2 Impact test

In this experiment, a rigid sphere (mass 10kg, diameter 135mm) centrally hits a rectangular foam block (RG110, 200x200x40 mm) with an initial velocity of 5.22m/s. After a maximum of penetration is reached, the ball bounces back in the opposite direction.

Comparing the force over time curves in Figure 1.13, it gets obvious that the loading phase is well captured with the old and the new formulation. Apparently this is not the case during the rebound phase, which is governed by unloading of the

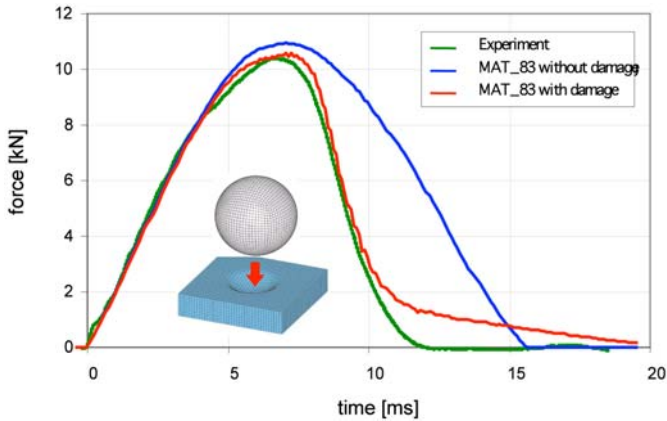


Fig. 1.13 Impact test – experiment vs. simulation with and without damage.

foam material. With the new damage formulation, an enhancement of the simulation result is evident.

References

1. LS-DYNA User Manual and Theoretical Manual, Livermore Software Technology Corporation.
2. Du Bois, P.A. (2004): Crashworthiness Engineering Course Notes, Livermore Software Technology Corporation.
3. Kolling, S.; Werner, A.; Erhart, T.; Du Bois, P.A. (2007): An elastic damage model for the simulation of recoverable polymeric foams, Proceedings of the 6th LS-DYNA Forum, Frankenthal, Germany, B-II: 31–42.
4. Mills, N.J.; Gilchrist, A. (2000): The high strain extension of open cell foams. *Journal of Engineering Materials and Technology – Transactions of the ASME* 122: 67–73.
5. Ehlers, W. (2002): Foundations of multiphasic and porous materials. In: Ehlers, W., Bluhm, J. (eds.) *Porous Media: Theory, Experiments and Numerical Applications*, pp. 3–86. Springer-Verlag, Berlin.
6. Markert, B. (2005): Porous Media Viscoelasticity with Application to Polymeric Foams, Dissertation, Report No. II-12 of the Institute of Applied Mechanics (CE), Universitt Stuttgart, Germany.
7. Du Bois, P.A.; Kolling, S.; Koesters, M.; Frank, T. (2006): Material behaviour of polymers under impact loading. *International Journal of Impact Engineering* 32: 725–740.
8. M. Schrodtt, G. Benderoth, A. Kuehhorn, G. Silber (2005): Hyperelastic description of polymer soft foams at finite deformations. *Technische Mechanik* 25 (3-4): 162–173.
9. Feng, W.W. (2003): On constitutive equations for elastomers and foams. 4th European LS-DYNA Users Conference, pp. D-II-15/28.
10. Chang, Fu S.; Song, Y; Lu, D.X.; DeSilva, C.N. (1998): Unified constitutive equations for foam materials. *Journal of Engineering Materials and Technology – Transactions of the ASME* 120 (3): 212–217.
11. Miehe, C. (1995): Discontinuous and Continuous Damage Evolution in Ogden-Type Large Strain Elastic Materials, *European Journal of Mechanics, A/Solids* 14: 697–720.

12. Kolling, S.; Benson, D.J.; Du Bois, P.A. (2005): A simplified rubber model with damage. 4th LS-DYNA Forum, Bamberg, 2005, Conference Proceedings, pp. B-II-01/10.
13. Kolling, S.; Du Bois, P.A.; Benson, D.J.; Feng, W.W. (2007): A tabulated formulation of hyperelasticity with rate effects and damage. *Computational Mechanics* 40 (5): 885–899.
14. Hill, R. (1978): Aspects of invariance in solid mechanics, *Adv. Appl. Mech.* 18: 1–75.
15. A. Werner (2006): Zur Simulation reversibler EPP-Schäume unter mehrachsiger und stoartiger Beanspruchung. Diplomarbeit BTU Cottbus.
16. Mills, N.J.; Zhu, H. (1999): The high strain compression of closed-cell polymer foams. *Journal of the Mechanics and Physics of Solids*, 47:669–695.
17. Fremgen, C.M.; Huber, U.; Maier, M. (2005): Experimental investigation of polypropylen foams as base for numerical simulation. *Cellular Metals and Polymers*, Eds.: R. F. Singer et al., Trans Tech Publications, Zrich, Schweiz.
18. Mills, N.J.; Gilchrist, A. (1999): Shear and Compressive Impact of Polypropylene Bead Foam. *Cellular Polymers*, 18(3): 157–174.
19. Huber, U.; Maier, M. (2005): Experimentelle Untersuchung von Polypropylen-Schaum als Basis für die numerische Simulation. Workshop 'Simulation von Schaumstoffen mit stark nichtlinearem Verhalten', Hohenwart, Germany.
20. Münch, M.; Rohde, S.; Schlimmer, M. (2005): Mehrachsige Beanspruchung von thermoplastischen Konstruktionsschaumstoffen. Workshop 'Simulation von Schaumstoffen mit stark nichtlinearem Verhalten', Hohenwart, Germany.

Chapter 2

The Numerical Simulation of Foam – An Example of Inter-Industrial Synergy

Paul A. Du Bois

Abstract Low density foams made by some expansion process of polymeric materials are widely used in industry. Their main mechanical characteristic is the high compressibility expressed by the near zero value of the Poisson's ratio. The numerical simulation of these materials remained secondary and enigmatic throughout the 1980's. It was the automotive safety related CAE work that prompted systematic research into a methodology for the reliable and predictive simulation of foam materials in the 1990's. This research program was carried out by an FAT working group and would last 12 years. Complementary work preliminary with respect to high velocity impact, sever shear deformation and tensile fracture was performed by NASA during the Columbia accident investigation and the results of this development work have in turn benefited the automotive industry. The article reviews the history of the foam simulation related R& D work during the last 2 decades.

2.1 Introduction

Throughout history the defence industry has acted as an engine for technological innovation. It suffices to realize that most of Archimedes' inventions were motivated by the defence needs of Syracuse and that Newton and his contemporaries unravelled the mystery of gravity while working on very down to earth problems of ballistics [1]. Similarly, the ultimate discontinuity in humanity's technological evolution : world war 2, has given us radar technology, electrical computing, nuclear energy, jet engines and space flight amongst many other innovations. Industry as a whole has profited traditionally from the investments made in defence research through a continuous technological transfer.

Paul A. Du Bois
Consulting Engineer, Freiligrathstr. 6, 63071 Offenbach, Germany e-mail: paul.dubois@gmx.net

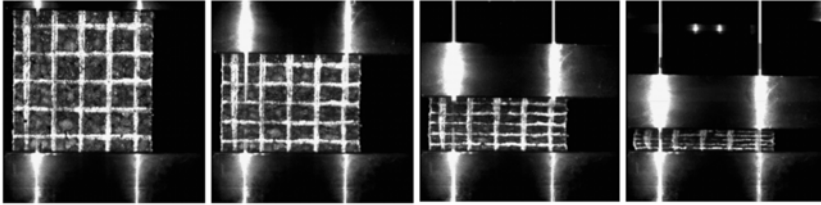


Fig. 2.1 Compression test on a low density foam.

Numerical simulation has not been an exception to this general rule, the roots of modern simulation techniques go back to the war years at Los Alamos where John von Neumann and Robert Richtmeyer supported the design of the implosion device that would render the plutonium bomb possible. Up to the 1960's publications on simulation work [2] show mainly applications originating in the defence community. The simulation of foam materials on the other hand originated, at least to the best of knowledge of this author, entirely in the automotive world but its evolution was not less diverse nor inter-disciplinary and somewhat remarkable. The purpose of this article is to review this interesting story.

2.2 Foams – Physical Nature and Numerical Modeling

From the viewpoint of a material scientist, any material that is manufactured by an expansion process is considered a foam. The base material is thereby irrelevant and can be polymeric, metallic or other. Foams are of course used in every industry ranging from furniture to building isolation products but the need for simulation originally arose in the automotive world. In automobiles foams are needed for comfort (seats), safety (bumpers and paddings) and stiffness (so called structural foams).

To a numericist the intuitive notion of a foam has little to do with the art of manufacturing and a material is said to be foam-like if it exhibits no lateral deformation under a uniaxial compressive load (see Figure 2.1). Most foam materials are also elastic in the sense that they recover to their undeformed configuration after some period of time. The numerical simulation of foams is based on the observation of Storakers [3] that Hill's energy functional of hyperelasticity can be used to describe the simple special case of foams where principal engineering stresses are uncoupled, i.e. depend only upon the stretch ratio in the corresponding principal direction. To see this we start from the expression for Hill's energy functional

$$W = \sum_{m=1}^k \frac{\mu_m}{\alpha_m} \left(\lambda_1^{\alpha_m} + \lambda_2^{\alpha_m} + \lambda_3^{\alpha_m} - 3 + \frac{1}{n} (J^{-\alpha_m n} - 1) \right) \quad (2.1)$$



Fig. 2.2 Member Companies of the FAT AK27 Working Group Foam.

and set $n=0$:

$$W = \sum_{m=1}^k \frac{\mu_m}{\alpha_m} (\lambda_1^{\alpha_m} + \lambda_2^{\alpha_m} + \lambda_3^{\alpha_m} - 3) \tag{2.2}$$

We then obtain the expression for engineering and true principal stresses in the usual way of hyperelasticity :

$$\lambda_i \lambda_k \sigma_i = \tau_i = \frac{\partial W}{\partial \lambda_i} \tag{2.3}$$

$$\tau_i = \frac{1}{\lambda_i} \sum_{m=1}^k \mu_m (\lambda_i^{\alpha_m} - 1) \tag{2.4}$$

The decisive step for practical applications is then made by observing that a tabulated generalisation is trivial due to the uncoupled nature of the equations. Consequently the results of uniaxial tensile and compressive tests in terms of engineering stress and engineering strain can be used directly as input to the material model for use in an engineering software such as LS-DYNA.([6] and [7]).

However, the way from a theoretical model to industrial application usually proves to be a long and tedious path. The number of practical problems to be solved is important to say the least. We are confronted with the physics of foams that show viscosity causing such phenomena as damping, rate dependency, hysteresis, stress relaxation and creep. All these phenomena cannot be described by simple hyperelasticity and imply that the solution of the problem in terms of computing stresses from strains and strain rates no longer has a unique solution. Then there is the problem of numerical stability, accuracy and efficiency. The efficiency aspect when dealing

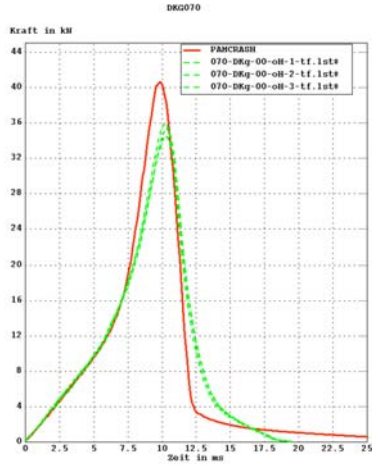


Fig. 2.3 Comparison test/Simulation results for a sphere impact on Bayfill RG70.

with explicit integration codes that are used in crash simulations and dynamic simulations of all kinds is strongly depending on the stable timestep of the simulation. Foams are highly compressible and small dimensions of the compressed finite elements will inevitably lead to small timesteps and correspondingly high computing times.

2.3 Numerical Modeling of Foams in Automotive Crash

Due to the necessity of simulating foam response during an automotive crash event and the lack of fast, reliable solution algorithms as well as material data a working group foams ('Arbeitsgruppe Schaum') was founded by the German FAT (Forschungsgemeinschaftautomobiltechnik) in the autumn of 1996. Participating members of the working group were most of the German automotive companies (Volkswagen, AUDI, Mercedes-Benz, Opel, Ford and Porsche) and a number of supplier companies (JCI, Keiper, Karmann, BAYER, BASF and Autoliv). (See Figure 2.2) Speaker of the working group was dr. Christian Stender from Volkswagen during the entire research effort. The project would consist of a large combined numerical/experimental program where the author would perform numerical simulations with 3 widely use softwares (LS-DYNA, Pamcrash and Radioss) and the experimental data would be produced by a team around Dr. Hartwig Nahme at EMI (Ernst Mach Institute) in Freiburg. The total effort would extend over a period of roughly 12 years and was completed recently towards the end of 2008. The project was divided into two phases. The first phase or methodology phase ran from 1996

till 2002. Four classes of low density foams were selected : seatfoam, PU-bumper foam, padding foam and EPP-bumper foam. For each of these materials a suitable simulation technology able to accommodate the dynamic response under impact loading was developed. This was done based on the example of a single material for each class of foams with a selected density of around 50 g/l. In the second phase of the project databases were created for all 4 classes of foams at different densities, varying between 30 g/l and 200 g/l.

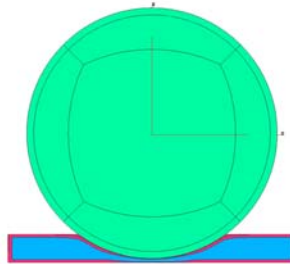


Fig. 2.4 Simulation model for a large sphere impact on a Foam Block, deformed shape.

Realizing that only a massive approach can lead to a reliable simulation tool, the FAT project involved many thousands of experiments and corresponding numerical simulations. Indeed maybe the most challenging aspect of numerical simulation is to define what can be reasonably expected from a simulation result. In other words : how close to the test result can we get, how predictive can we possibly be. The answer to this question lies in a good understanding of experimental spread and model limitations. In the case of foams the problem seems somewhat frightening at first sight. Indeed a foam is not a continuum but a structure consisting of open and/or closed cells. The mechanical properties are a function of the intrinsic material properties of the cell wall material but also of the geometry of the structure : the size and shape of the cells. The numerical model is based on solid finite elements and uses continuum theory. It consequently cannot account for microstructural effects and can only be valid as long as the element size exceeds the cell size by some factor (preferably at least 10). Due to the small cell size in automotive foams this is usually uncritical (with the exception of certain thin structures such as roof covers) but other problems arise at the macroscopic level.

Density variations are the main problem in foam parts. Global density variations can occur in individual batches due to the manufacturing process. Local density variations showing a density gradient from the surface to the inner of the part are an inevitable consequence of skin formation that occurs in the cold forming process of PU foams and during the pressure bonding of EPF (Expanded particle foams). These local density variations depend (amongst other factors) upon the part geometry and

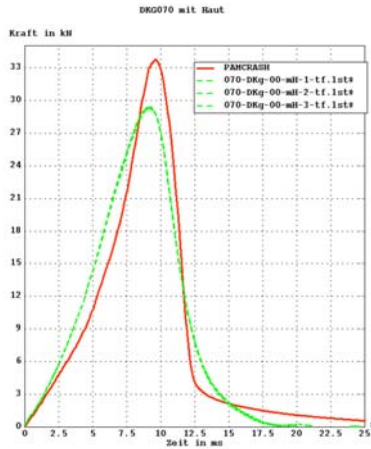


Fig. 2.5 Comparison test/Simulation results for a sphere impact on Bayfill RG70 Kernel density assumed 70g/l.

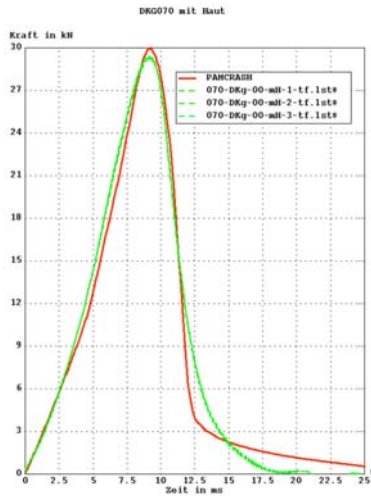


Fig. 2.6 Comparison test/Simulation results for a sphere impact on Bayfill RG70 Kernel density assumed 76g/l.

are impossible to account for in an exact way in a numerical model. An approximate way is to lump the skin effect or the higher density part of the foam component in a single layer of solid elements at the surface of the part. Only practical and massive experience can determine the confidence level that may be attributed to such an approach. In [4] an example is shown of the influence of a density variation in the

kernel of a PU bumperfoam upon the maximum force measured during the impact of a 30kg aluminium sphere on a foam block with and without skin layer. Figure 2.4 shows the test setup. In Figure 2.3 the comparison between test and simulation results is shown for the foam block without skin (a so-called cut sample) and a density of 70 g/l. The correspondence is good in particular where the initial slope of the force-time curve is concerned. The high intrusions later on lead to rupture in the foam block which was not simulated and thus leads to a divergence between test and numerical results. However these differences are explainable. next a cold formed part was examined. The intention was to manufacture a cold formed part with a kernel density of 70 g/l. The resulting global and thus measurable density was 85 g/l due to the higher density in the skin layer. In Figures 5 and 6 we again compare test and simulation results. In Figure 5 the numerical model assumed a kernel density of 70g/l (resulting in a rather bad comparison to test) and in Figure 6 the kernel density was assumed to be 76 g/l. The variation of less then 10% in kernel density could very well occur in real manufacturing circumstances. The conclusions from studies like these are very important for the industrial analyst:

- Repeated tests are essential to get an idea of the scatter in test results
- Different kinds of tests are essential to deal with unknown parameters such as the density distribution in the part
- There are always outlayers
- Much time could otherwise be wasted fitting models to single test results
- Kernel density is decisive rather than the nominal density
- Damage (and failure) modeling is desirable (but was not assessed by the working group at this point in time)

The first phase of the FAT project resulted in numerous improvements of the foam material laws in all 3 participating softwares. A user friendly setup based on input of directly measurable engineering stress-strain curves under uniaxial compression and uniaxial tension was at the base of the methodology. Further improvements with regard to numerical stability included optimized estimates of the stable timestep as well as stiffness proportional damping and strain rate filtering. Under-integrated solid elements were usually employed in order to accommodate the huge aspect ratios that can occur due to the high compression (up to 98%) that is sometimes locally observed in foams.

Engineering stress-strain curves can be defined for loading and unloading regimes at different strain rates. Suitable experimental techniques were developed by EMI, in particular the need for dynamic testing at constant velocity (constant engineering strain rate) was clearly established. An example of static and dynamic input curves for a PU62IF70 foam with a density of 70 g/l is shown in Figure 2.8. Maybe the most important aspect of the data preparation for foam material laws is the need to extrapolate the experimental data at high compressions. Foam plateau stresses are very low (less then 1. MegaPascal) compared to the yield strength of the surrounding metallic structures. Experimental data are at best available to 20 times the level of the plateau stress and thus still an order of magnitude below the stresses that can

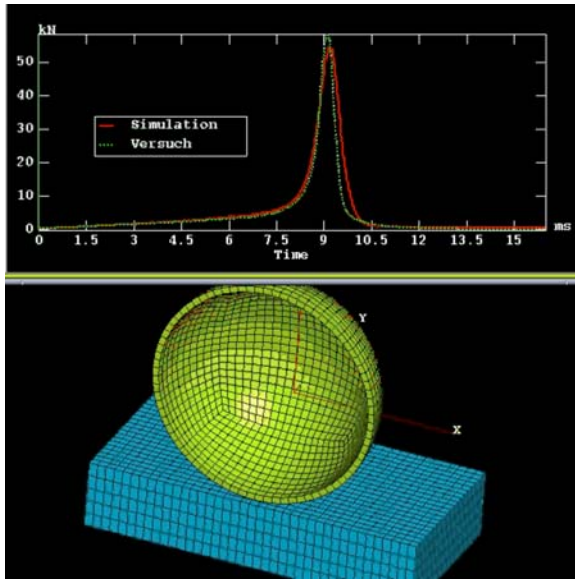


Fig. 2.7 Simulation model and results comparison for a Foam validation test.

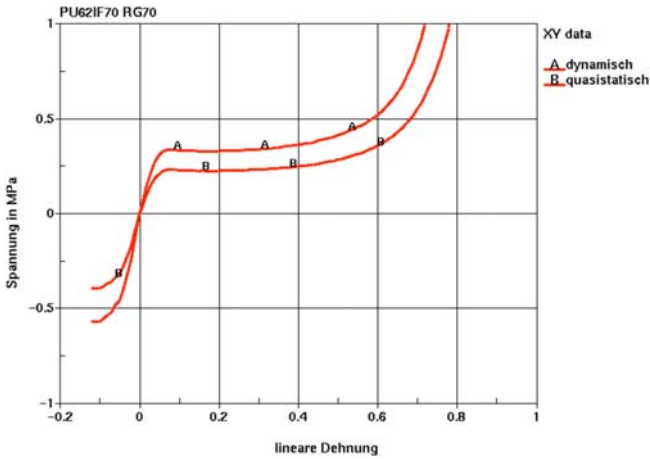


Fig. 2.8 Static and dynamic stress-strain curves for Bayfill RG70.

occur during a crash event when the metallic parts are plastified. The extrapolation of experimental data is always to some degree arbitrary. We have consistently used a higher order hyperbolic function with good practical results and an example of our extrapolation procedure is shown in Figures 2.9 till 2.11.

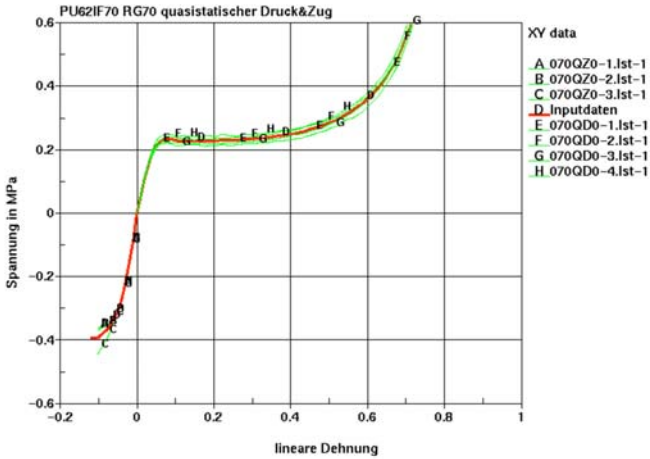


Fig. 2.9 Quasistatic stress-strain curves for Bayfill RG70 test results versus material model input-data up to 0.6MPa.

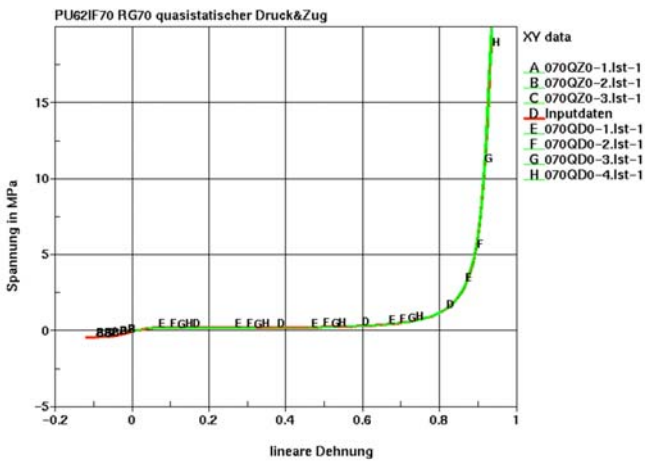


Fig. 2.10 quasistatic stress-strain curves for Bayfill RG70 test results versus material model input-data up to 20.0MPa.

2.4 Impacted Foam – The Columbia Accident

Such was the situation when on January 16 2003, Columbia’s leading edge was impacted by a chunk of foam suspected to have separated from the external tank bipod ramp at 81 seconds into its launch. Columbia was traveling at Mach 2.46, at an altitude of 65,860 feet. The foam was calculated to have hit the orbiter at 700 – 800 feet

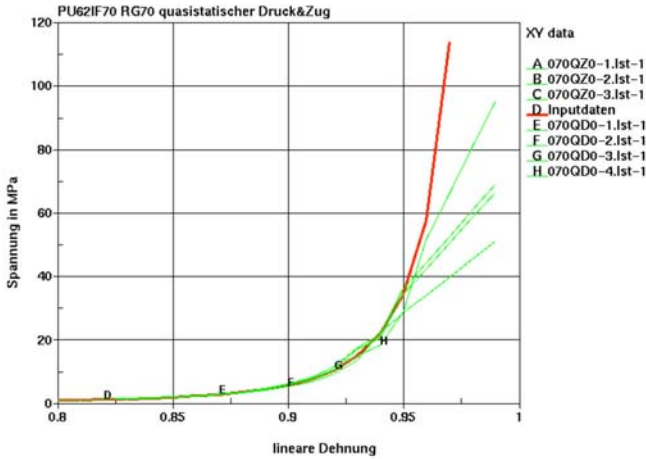


Fig. 2.11 quasistatic stress-strain curves for Bayfill RG70 test results versus material model input-data up to 120.MPa.

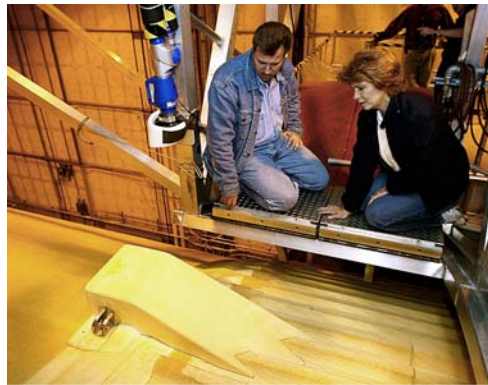


Fig. 2.12 BX250 foam block like the one that separated from the bipod ramp.

per second. A similar chunk of foam is shown in Figure 2.12. The object was suspected to have hit the Reinforced Carbon-Carbon (RCC) Panels Protect the Leading Edges of the Orbiter (Figure 2.13 and 2.14). The GRC (Glenn research Center) Impact Lab was Requested to Assist in the Columbia Accident Investigation based on its extensive expertise in impact testing and analysis. Most of GRC's previous work had been in jet engine debris containment. Now they were asked to provide simulation and testing work in support of the full scale impact test that would be performed in San Antonio Texas by SWRI. The first part of the job was to do Impact Testing to

Characterize ET Foam and RCC and constitute adequate material models for both materials.

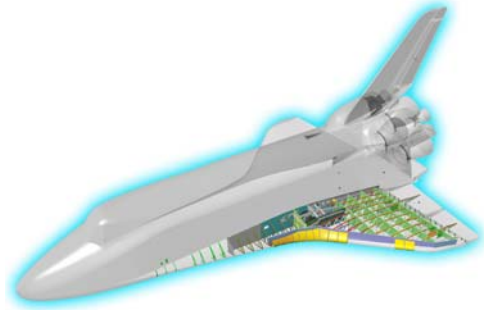


Fig. 2.13 Reinforced Carbon-Carbon Panels Protect the Leading Edges of the Orbiter.



Fig. 2.14 RCC Leading Edge with T-Seal.

The analysis work was performed with the LS-DYNA code by a team around dr. Kelly Carney from GRC. Through literature and personal contacts with the author the results of the FAT investigations were available to this group but they soon realized that the circumstances of the Columbia accident called for extensive additional research. In particular it became necessary to investigate the response of the foam at very high strain rates and assess the response in vacuum. It was also proven important to simulate the tensile failure of the material upon impact.

In addition to the traditional quasistatic testing of the BX250 ET foam dynamic testing was performed to evaluate the projectile performance of the material model. The test originally employed to verify the MAT83 model was performed at

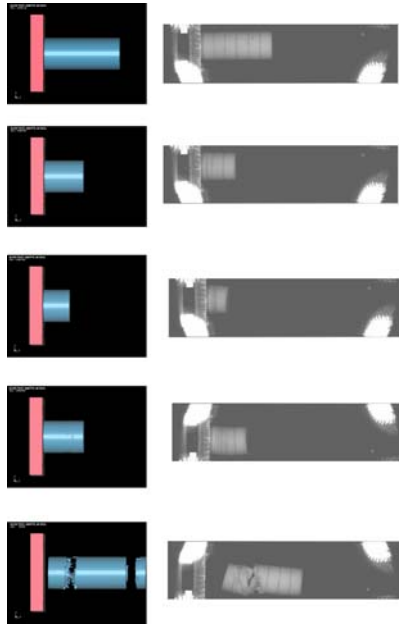


Fig. 2.15 90 degree impact simulation and test.

NASA/GRC, consisting of a foam projectile impacting a comparatively rigid plate. Load cells were mounted at the corners of the plate and high speed video was also employed. The test set-up was modeled employing LS-DYNA and results were processed based on the output of the analytical load cells and visual data available via LSPREPOST. A freeze frame video clip for both analysis and test may be seen compared in Figures 2.19 and 2.20, for 90 and 23 degree impacts respectively. The dynamic impact tests required a specially built 2 inch vacuum gun. BX250 ET foam specimens were shot at angles of 10, 15, 23, and 90 degrees on load cells at 700 and 800 ft/sec to evaluate foam projectile response at 1 psi and atmospheric pressures.

The strain rate testing was limited to less than 500 sec^{-1} due to equipment operation limits. The actual strain rate experienced at a point mid way in the specimen has been solved for analytically and were seen to be far in excess of anything tested before. However, the effect of strain rates within the limited testing performed indicated that the strain rate dependence of the stress strain relationship becomes constant above the existing 429/s curve.

The simulation boundary forces were summed in the plate normal direction and compared to the summed plate normal load cell responses as shown in Figures 2.21 and 2.15 for 90 and 23 degree impacts respectively. As can be seen in these figures, the model conservatively replicates the loading events from the projectile as

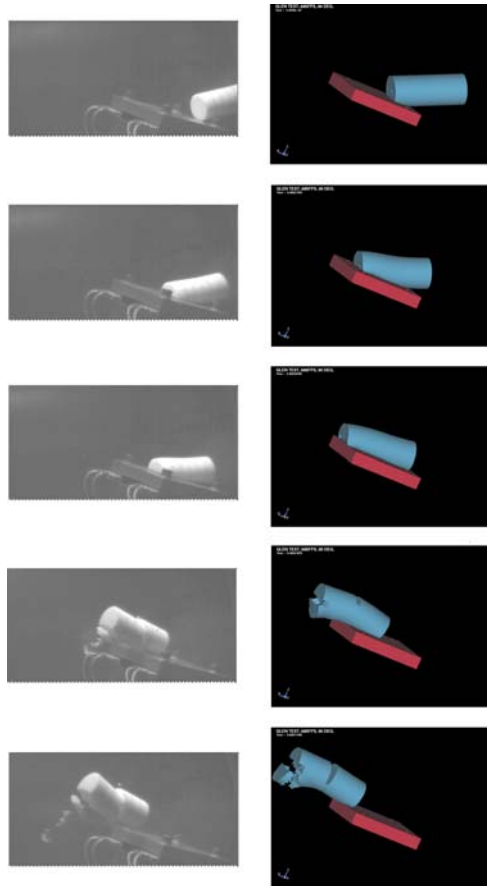


Fig. 2.16 23 degree impact simulation and test.

predicted from test. These experimental data were at the base of the analysis foam model. The high strain rate and failure response of the material was reverse engineered by comparison of numerical and test results.

In a second phase of the investigation foam samples were shot at RCC coupons and the response was used to evaluate the RCC numerical model. Finally different impact scenarios were investigated with foam blocks impacting RCC leading edge panels at different angles and velocities. For this purpose a numerical model of the RCC panel was built with 43000 shell elements and the foam block was modeled with 147000 solid elements. Figure 2.16 shows the numerical model used in the simulation of the critical panel 8 impact event. The LS-DYNA predictions corre-

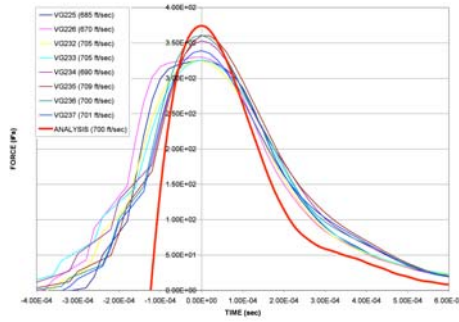


Fig. 2.17 Simulation vs Test Plate Normal Boundary Forces (90 deg.).

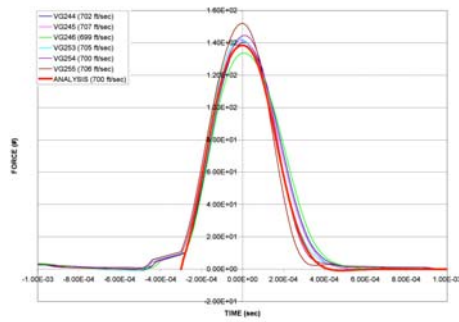


Fig. 2.18 Simulation vs Test Plate Normal Boundary Forces (23 deg.).

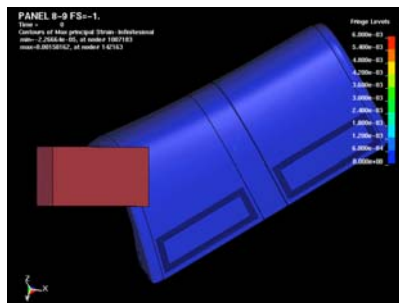


Fig. 2.19 Simulation model for impact of Foam Block on Orbiter Leading Edge Mock-Up.

lated well with the full scale test that was ultimately performed in San Antonio. (See Figures 2.17 and 2.18).

The external tank foam test and simulation program had thereby been completed. It was demonstrated full scale tests at SWRI at atmosphere would be representative



Fig. 2.20 Ballistic impact test results.

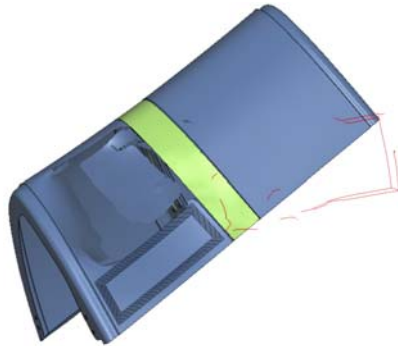


Fig. 2.21 LS-DYNA Simulation result.

of actual impact event in vacuum and a validated foam model for computer analysis predictions had been developed. In particular the numerical model for the foam included a tensile rupture criterion allowing the foam block to separate into multiply connected parts after impact.

2.5 Summary and Conclusion

In the Columbia accident investigation NASA had added a capability to simulate extreme conditions to the foam material models. This became relevant to the automotive industry in the 21st century with the implementation of pedestrian protection legislation and the subsequent use of very low density (30 g/l) foams in bumpers leading to extreme deformations and occasional rupture during lower leg impact test events. The next step in the simulation of these high deformation phenomena could be the introduction of meshless or particle methods such as EFG (element free Galerkin) which allow to push the simulation beyond the point where classical Lagrangean elements can go. In conclusion, it can be said that the industrial appli-

cation pushes the simulation techniques forward as more challenging problems are assessed. Specific problems and the subsequent research and progress in simulation technology occurs in many different fields but most of the resulting methods turn out to be amazingly general and useful in a broad range of industries. The value of a continued exchange of information can therefore not be overstated.

References

1. Cohen IB, (1987), *The birth of a new physics*, Penguin Books Ltd., Harmondsworth, UK
2. Kulak RF and Schwer LE, Eds., (1991), *Computational Aspects of Contact, Impact and Penetration*, Elmepress International, Lausanne, Switzerland
3. Storakers B, (1986), On the material representation and constitutive branching in finite compressible elasticity, *Journal of the Mechanics and Physics of Solids* 34, 125 – 145
4. Du Bois PA, (2005), Numerical simulation of foam materials under impact loads, *Proceedings EuroPam*, Potsdam
5. Carney K, Melis M, Fasanella EL, Lyle KH, Gabrys J, (2004) *Material Modeling of Space Shuttle Leading Edge and External Tank Materials For Use in the Columbia Accident Investigation*, *Proceedings from 8th International LS-DYNA Users Conference*, Dearborn MI
6. N N, (2003), *LS-DYNA Keyword Users Manual Version 970*, Livermore Software Technology Corporation
7. Chang FS, (1995), *Constitutive Equation Development of Foam Materials*, Ph.D. Dissertation, Wayne State University, Detroit, Michigan

Chapter 3

Influence of Hardening Relations on Forming Limit Curves Predicted by the Theory of Marciniak, Kuczyński, and Pokora

Heinrich Werner

Abstract The forming limit curve (FLC) is one of the tools to predict the maximum permissible strains of thin metallic sheets which are loaded in the membrane plane in different states of stress. It may be used to assess forming operations in the press shops as well as unintentional deformations, such as vehicle, aircraft, or train crashes. In the present work, the FLC theory of Marciniak, Kuczyński and Pokora, originally written for a Swift type hardening relation and a power law type strain rate dependence, is formulated in detail for generalized hardening relations $\bar{\sigma} = g(\bar{\varepsilon}, \dot{\bar{\varepsilon}})$. The derivation is restricted to the tension-tension quadrant of the FLC and neglects inertia effects. Special attention is paid to the initial conditions of the numerical integration of the resulting two evolution equations. By applying different formulations to the quasi-static and later to the strain rate dependent hardening relation of a particular material, the substantial influence of this aspect of the constitutive material model on the calculated FLC is demonstrated. The results underscore the necessity for highly accurate experimental input data to avoid extrapolation of the hardening relation. This is of particular importance over the large strain region; as well as for the entire anticipated strain rate interval.

3.1 Introduction

Historically the interest in predicting process limits in the plastic deformation of thin metallic sheets has its roots in the press shops. There are however, many situations where thin sheets are subjected to unintentional deformations up to fracture, such as in vehicle, aircraft, or train crashes. The importance of predicting the maximum permissible strains in different states of stress – experimentally as well as theoretically – is undisputed. This is reflected in the multitude of papers written since Keeler and Backofen [19] and Goodwin [8] introduced the concept of forming limit diagrams

Heinrich Werner, BMW Group, Knorrstrasse 147, 80788 Munich, Germany e-mail: heinrich.werner@bmw.de

in the 1960s.

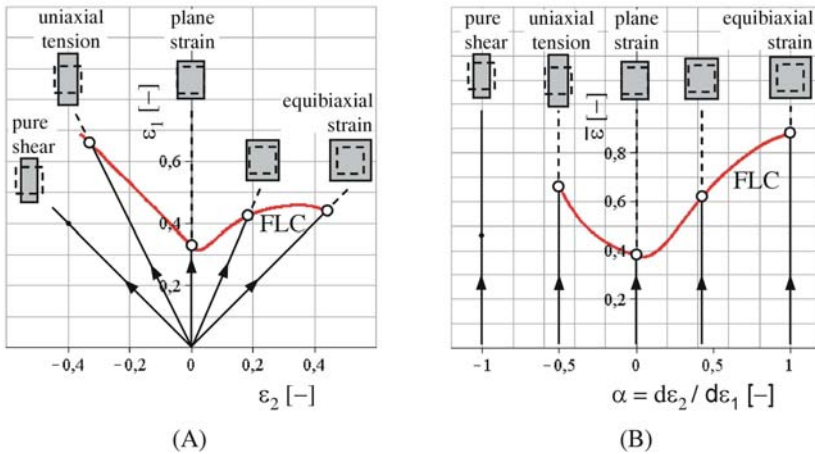


Fig. 3.1 The Forming Limit Curve (FLC) is defined as the connection of all points which mark the onset of instability for a sequence of strain paths. Dashed rectangles indicate sheet size at start of deformation; grey shaded rectangles indicate their shape at onset of instability. (A): Representation in principal strain space (classical FLC), (B): Equivalent strain as a function of the ratio of principal strain increments.

As indicated in Figure 3.1, the thin sheet is subjected to a sequence of membrane strain states. For each individual strain path, which is characterised by the ratio of minor to major strain increment, the strain state at which the local necking (through the sheet thickness) becomes unstable is recorded. Major and minor strains at the onset of instability provide the individual data points (the forming limit) in principal strain space, indicated by a circle in Figure 3.1-(A). Connecting the forming limits for a sequence of strain states establishes the forming limit curve (FLC). The value of the alternative graph of Figure 3.1-(B) is to display the data in a clearer manner for cases in which successive forming operations are to be displayed on the same diagram.

In experimental practice the detection and definition of the onset of instability is a topic of considerable complexity, see Hotz and Timm [16], Hora and Tong [14] as well as the standards ISO 12004 [17] and ASTM E2218 [1].

Regarding the theoretical prediction of FLCs, the work of Marciniak and co-workers [23, 24] represents an outstanding contribution. Subsequent work in this field has focused on refining constitutive material models and on taking non-proportional strain paths into account, see Ghosh [7] and Graf and Hosford [9, 10],

to name just a few. At present three approaches are prevalent in the theoretical prediction of FLC. First, there are models based on the Marciniak theory, i.e. the CRACH algorithm of Gese and Dell [6] containing a sophisticated constitutive model; or those of Banabic et al. focusing on improved yield criteria [2] and effects of stresses normal to the plane of the sheet [3]. Second there are the models of Hora and Tong [14, 15] based on the enhanced modified maximum force criterion (eMMFC), and third, the finite element based approaches where a domain similar to that of Figure 3.2 is discretized. The benchmark test BM1 of Numisheet 2008 provides a good overview of the capabilities of these various models; see Volk et al. [30, 31].

In order not to miss the broader picture of failure modelling it should be pointed out that the onset of instability – which is generally expressed in FLCs – is but one process, ultimately leading to fracture. Since fracture depends on such a multitude of influencing factors, any comprehensive numerical model must include more than one FLC-based failure criterion, see for instance Hooputra et al. [13], Kessler et al. [20] and the models compared in a survey of Wierzbicki et al. [32]. Hiermaiers book [11] and an extensive book chapter authored by El-Magd [4] provide a rich source of information on failure modelling.

In the present work, the theory of Marciniak, Kuczyński and Pokora [24], originally written for a Swift type hardening relation and a power law type strain rate dependence, is formulated in detail for generalized hardening relations $\bar{\sigma} = g(\bar{\epsilon}, \dot{\bar{\epsilon}})$. The derivation is restricted to the tension-tension quadrant of the FLC (positive minor principal strain, $\epsilon_2 \geq 0$) and neglects inertia effects. Special attention is paid to the initial conditions of the numerical integration of the resulting two evolution equations. By applying different formulations to the quasi-static and later to the strain rate dependent hardening relation of a particular material, the substantial influence of this aspect of the constitutive material model on the FLC is demonstrated. The results underscore the necessity for highly accurate experimental input data, particularly over the large strain region; as well as for the entire anticipated strain rate interval.

3.2 Theoretical Model

Figure 3.2 shows part of a sheet subject to a membrane loading by the principal stresses σ_{1A} and σ_{2A} acting at some distance from the small initial imperfection, the neck. σ_{1A} , the major principal stress acts perpendicular to the neck axis. In regions A and B the material properties are identical. The initial imperfection is characterised by the inhomogeneity parameter¹ f_i , which is defined by the differences in initial

¹ To predict forming limit curves for a given sheet material f_i must be determined from at least one experimental strain path ($\alpha = const.$) in order to determine the sheets specific properties.

sheet thickness of regions A and B:

$$f_i = 1 - \frac{t_{0B}}{t_{0A}} \tag{3.1}$$

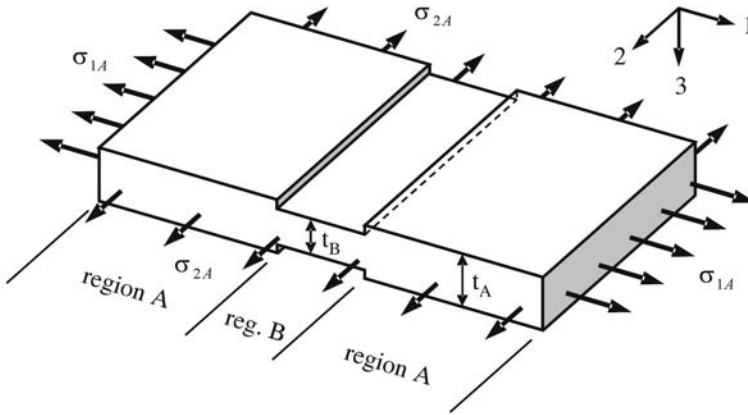


Fig. 3.2 Schematic representation of the initial imperfection in the sheet.

According to the time history of the applied stresses, the strains at some distance from the neck will evolve. This strain path, which is actually prescribed in a numerical solution method need not necessarily be constant during the deformation process. It may adequately be defined by the ratio of the principal plastic strain increments in region A:

$$\frac{d\varepsilon_{2A}}{d\varepsilon_{1A}} = \alpha \tag{3.2}$$

During the deformation process, there will suddenly be a stronger increase in effective plastic strain in region B as compared to region A; indicating the onset of plastic instability. Therefore, the ratio:

$$\frac{d\bar{\varepsilon}_A}{d\bar{\varepsilon}_B} = \beta \tag{3.3}$$

will be used as the indicator of plastic instability². Solving the evolution equations for β is the central task of the theory, and will be covered in more detail in the following sections.

² In the examples shown later, the criterion for onset of instability is $d\bar{\varepsilon}_A/d\bar{\varepsilon}_B \leq 1/25$.

3.2.1 Constitutive Equations

Consistent with Marciniak and Kuczyński's approach [23], it will be assumed that the elastic strain components are negligible relative to the plastic components. Therefore, the Lévy - von Mises flow rule [21, 25] is applicable. In order to model this rigid-plastic material behaviour, the flow rule of Hill [12] is applied. For a planar isotropic material³ which is characterised by a time independent average R-value

$$\bar{R} = \frac{R_0 + 2R_{45} + R_{90}}{4} \quad (3.4)$$

the increments of plastic strain are given by:

$$d\varepsilon_1 = \left(\sigma_1 - \frac{\bar{R}}{1+\bar{R}}\sigma_2 \right) \frac{d\bar{\varepsilon}}{\bar{\sigma}} \quad (3.5)$$

$$d\varepsilon_2 = \left(-\frac{\bar{R}}{1+\bar{R}}\sigma_1 + \sigma_2 \right) \frac{d\bar{\varepsilon}}{\bar{\sigma}} \quad (3.6)$$

$$d\varepsilon_3 = -d\varepsilon_1 - d\varepsilon_2 = -\frac{\sigma_1 + \sigma_2}{1+\bar{R}} \frac{d\bar{\varepsilon}}{\bar{\sigma}} \quad (3.7)$$

Based on the hypothesis of equivalent plastic work

$$\sigma_1 d\varepsilon_1 + \sigma_2 d\varepsilon_2 + \sigma_3 d\varepsilon_3 = \bar{\sigma} d\bar{\varepsilon} \quad , \quad (3.8)$$

the increment of equivalent plastic strain $d\bar{\varepsilon}$ becomes:

$$d\bar{\varepsilon} = \sqrt{\frac{1+\bar{R}}{1+2\bar{R}}} \sqrt{(1+\bar{R})(d\varepsilon_1^2 + d\varepsilon_2^2) + 2\bar{R}d\varepsilon_1 d\varepsilon_2} \quad (3.9)$$

and the related equivalent stress $\bar{\sigma}$ is given by:

$$\bar{\sigma} = \sqrt{\sigma_1^2 - \left(\frac{2\bar{R}}{1+\bar{R}} \right) \sigma_1 \sigma_2 + \sigma_2^2} \quad (3.10)$$

Any reasonably well-defined function may be used to define a unique hardening relation as a function of equivalent plastic strain and strain rate:

$$\bar{\sigma} = g(\bar{\varepsilon}, \dot{\bar{\varepsilon}}) \quad (3.11)$$

Examples of this function are (3.38) and the relations in Tables 3.3 and 3.4.

³ In the plane of the sheet the material properties are identical in all directions whereas through the thickness they are different. Thus, a state of *planar isotropy* and *normal anisotropy* is assumed.

3.2.2 Derivation of Evolution Equations for the Onset of Instability

Given the inhomogeneity parameter, the initial sheet thickness in region B is given by:

$$t_{0B} = (1 - f_i) t_{0A} \quad (3.12)$$

The sheet thicknesses are related to the strains in thickness direction by:

$$t_A = t_{0A} \exp(\varepsilon_{3A}) \quad (3.13)$$

$$t_B = t_{0B} \exp(\varepsilon_{3B}) \quad (3.14)$$

The force equilibrium in 1-direction requires that:

$$\sigma_{1A} t_A = \sigma_{1B} t_B \quad (3.15)$$

A relation for the stress and strain components in region A as a function of α and \bar{R} is obtained as follows: equations (3.2), (3.5), (3.6) and (3.9) are written for region A and solved for the unknowns σ_{1A} , σ_{2A} , $d\varepsilon_{1A}$ and $d\varepsilon_{2A}$. The result is:

$$\frac{\sigma_{1A}}{\bar{\sigma}_A} = \sqrt{\frac{1 + \bar{R}}{1 + 2\bar{R}}} \frac{[1 + \bar{R}(1 + \alpha)]}{\sqrt{1 + \alpha^2 + \bar{R}(1 + \alpha)^2}} \quad (3.16)$$

$$\frac{\sigma_{2A}}{\bar{\sigma}_A} = \sqrt{\frac{1 + \bar{R}}{1 + 2\bar{R}}} \frac{[\alpha + \bar{R}(1 + \alpha)]}{\sqrt{1 + \alpha^2 + \bar{R}(1 + \alpha)^2}} \quad (3.17)$$

The major principal stress σ_{1A} is positive if the condition $\alpha > -(1 + \bar{R})/\bar{R}$ is fulfilled. From (3.16) and (3.17) the ratio of the principal stress components follows as:

$$\frac{\sigma_{2A}}{\sigma_{1A}} = \frac{\alpha + \bar{R}(1 + \alpha)}{1 + \bar{R}(1 + \alpha)} \quad (3.18)$$

Table 3.1 shows the ratio of the stress components for three important strain paths, valid for region A as well as for region B.

The increment of the principal strain parallel to the necking axis becomes:

$$\frac{d\varepsilon_{2A}}{d\varepsilon_A} = \alpha \sqrt{\frac{1 + 2\bar{R}}{1 + \bar{R}}} \frac{1}{\sqrt{1 + \alpha^2 + \bar{R}(1 + \alpha)^2}} \quad (3.19)$$

Applying the constant volume assumption,

$$d\varepsilon_{1A} + d\varepsilon_{2A} + d\varepsilon_{3A} = 0 \quad (3.20)$$

as well as equations (3.2) and (3.19), the strain increment through the thickness in region A becomes:

Table 3.1 Ratios of stress components for three strain paths (plane stress, $\sigma_3 = 0$).

–	Uniaxial Tension	Plane Strain	Equibiaxial Strain
–	$\alpha = -\frac{\bar{R}}{1+\bar{R}}$	$\alpha = 0$	$\alpha = 1$
$\frac{\sigma_1}{\bar{\sigma}}$	1	$\frac{1+\bar{R}}{\sqrt{1+2\bar{R}}}$	$\sqrt{\frac{1+\bar{R}}{2}}$
$\frac{\sigma_2}{\bar{\sigma}}$	0	$\frac{\bar{R}}{\sqrt{1+2\bar{R}}}$	$\sqrt{\frac{1+\bar{R}}{2}}$
$\frac{\sigma_2}{\sigma_1}$	0	$\frac{\bar{R}}{1+\bar{R}}$	1

$$\frac{d\varepsilon_{3A}}{d\bar{\varepsilon}_A} = -\sqrt{\frac{1+2\bar{R}}{1+\bar{R}}} \frac{(1+\alpha)}{\sqrt{1+\alpha^2+\bar{R}(1+\alpha)^2}} \quad (3.21)$$

Table 3.2 Ratios of strain components for three strain paths (plane stress, $\sigma_3 = 0$).

–	Uniaxial Tension	Plane Strain	Equibiaxial Strain
–	$\alpha = -\frac{\bar{R}}{1+\bar{R}}$	$\alpha = 0$	$\alpha = 1$
$\frac{d\varepsilon_1}{d\bar{\varepsilon}}$	1	$\frac{\sqrt{1+2\bar{R}}}{1+\bar{R}}$	$\frac{1}{\sqrt{2(1+\bar{R})}}$
$\frac{d\varepsilon_2}{d\bar{\varepsilon}}$	$-\frac{\bar{R}}{1+\bar{R}}$	0	$\frac{1}{\sqrt{2(1+\bar{R})}}$
$\frac{d\varepsilon_3}{d\bar{\varepsilon}}$	$-\frac{1}{1+\bar{R}}$	$-\frac{\sqrt{1+2\bar{R}}}{1+\bar{R}}$	$-\sqrt{\frac{2}{1+\bar{R}}}$

The derivation of the corresponding relations for region B begins with the strain increment $d\varepsilon_{2B}$. The equivalent stress in region B according to (3.10) becomes:

$$\bar{\sigma}_B = \sqrt{\sigma_{1B}^2 - \left(\frac{2\bar{R}}{1+\bar{R}}\right) \sigma_{1B} \sigma_{2B} + \sigma_{2B}^2} \quad (3.22)$$

Taking (3.6) into account, the strain component $d\epsilon_{2B}$ is:

$$d\epsilon_{2B} = \left(-\frac{\bar{R}}{1+\bar{R}}\sigma_{1B} + \sigma_{2B} \right) \frac{d\bar{\epsilon}_B}{\bar{\sigma}_B} \quad (3.23)$$

By inserting (3.22), the strain increment in region B parallel to the axis of the neck follows as:

$$\frac{d\epsilon_{2B}}{d\bar{\epsilon}_B} = \text{signum}(\alpha) \sqrt{1 - \frac{(1+2\bar{R})}{(1+\bar{R})^2} \left(\frac{\sigma_{1B}}{\bar{\sigma}_B} \right)^2} \quad (3.24)$$

Solving the three equations (3.19), (3.23) and the following compatibility relation

$$d\epsilon_{2A} = d\epsilon_{2B} \quad (3.25)$$

for the unknowns σ_{1B} , $d\epsilon_{2A}$ and $d\epsilon_{2B}$, the ratio $\sigma_{1B}/\bar{\sigma}_B$ results in the relation:

$$\frac{\sigma_{1B}}{\bar{\sigma}_B} = \sqrt{\frac{(1+\bar{R})^2}{1+2\bar{R}} - \frac{(1+\bar{R})\alpha^2}{1+\alpha^2+\bar{R}(1+\alpha)^2} \left(\frac{d\bar{\epsilon}_A}{d\bar{\epsilon}_B} \right)^2} \quad (3.26)$$

To ensure a strictly positive argument of the square root in (3.26) – especially in cases of nonproportional loading histories ($\alpha \neq \text{const.}$) –, the condition

$$\left| \frac{d\bar{\epsilon}_A}{d\bar{\epsilon}_B} \right| < \sqrt{\frac{(1+\bar{R}) [1 + \alpha^2 + \bar{R}(1+\alpha)^2]}{\alpha^2(1+2\bar{R})}} \quad (3.27)$$

must be verified.

The strain increment in the thickness direction in region B results from solving (3.23) and (3.7) as applied to region B

$$d\epsilon_{3B} = -\frac{\sigma_{1B} + \sigma_{2B}}{1+\bar{R}} \frac{d\bar{\epsilon}_B}{\bar{\sigma}_B} \quad (3.28)$$

Solving for σ_{2B} and $d\epsilon_{3B}$ results in:

$$\frac{d\epsilon_{3B}}{d\bar{\epsilon}_B} = -\frac{1}{(1+\bar{R})} \frac{d\epsilon_{2B}}{d\bar{\epsilon}_B} - \frac{(1+2\bar{R})}{(1+\bar{R})^2} \left(\frac{\sigma_{1B}}{\bar{\sigma}_B} \right) \quad (3.29)$$

By introducing (3.24) and (3.26) into (3.29), the first evolution equation is found:

$$\begin{aligned} \frac{d\epsilon_{3B}}{d\bar{\epsilon}_B} = & -\frac{\sqrt{1+2\bar{R}}}{(1+\bar{R})} \left[\text{signum}(\alpha) \sqrt{\frac{\alpha^2}{(1+\bar{R}) [1 + \alpha^2 + \bar{R}(1+\alpha)^2]} \left(\frac{d\bar{\epsilon}_A}{d\bar{\epsilon}_B} \right)} \right. \\ & \left. + \sqrt{1 - \frac{(1+2\bar{R})\alpha^2}{(1+\bar{R}) [1 + \alpha^2 + \bar{R}(1+\alpha)^2]} \left(\frac{d\bar{\epsilon}_A}{d\bar{\epsilon}_B} \right)^2} \right] \end{aligned} \quad (3.30)$$

The second fundamental equation used to determine the onset of instability follows from the force equilibrium relation (3.15):

$$\bar{\sigma}_A t_A \left(\frac{\sigma_{1A}}{\bar{\sigma}_A} \right) = \bar{\sigma}_B t_B \left(\frac{\sigma_{1B}}{\bar{\sigma}_B} \right)$$

Introducing (3.12) to (3.14) yields

$$\frac{\left(\frac{\sigma_{1A}}{\bar{\sigma}_A} \right)}{\left(\frac{\sigma_{1B}}{\bar{\sigma}_B} \right)} = (1 - f_i) \frac{\bar{\sigma}_B}{\bar{\sigma}_A} \exp(\epsilon_{3B} - \epsilon_{3A}) \quad (3.31)$$

and the final form is achieved by introducing (3.16) and (3.26) into (3.31):

$$\frac{1 + \bar{R}(1 + \alpha)}{\sqrt{(1 + \bar{R}) [1 + \alpha^2 + \bar{R}(1 + \alpha)^2] - (1 + 2\bar{R}) \alpha^2 \left(\frac{d\bar{\epsilon}_A}{d\bar{\epsilon}_B} \right)^2}} - (1 - f_i) \frac{\bar{\sigma}_B(\bar{\epsilon}_B, \dot{\bar{\epsilon}}_B)}{\bar{\sigma}_A(\bar{\epsilon}_A, \dot{\bar{\epsilon}}_A)} \exp(\epsilon_{3B} - \epsilon_{3A}) = 0 \quad (3.32)$$

It should be emphasised that the strain rate within the neck $\dot{\bar{\epsilon}}_B$ is coupled to the strain rate in region A. From

$$\frac{\dot{\bar{\epsilon}}_B}{\dot{\bar{\epsilon}}_A} = \frac{d\bar{\epsilon}_B}{dt} \frac{dt}{d\bar{\epsilon}_A}$$

the strain rate in region B follows as:

$$\dot{\bar{\epsilon}}_B = \frac{1}{\beta} \dot{\bar{\epsilon}}_A \quad (3.33)$$

Consequently, the strain rate within the neck is approximately one order of magnitude greater than that of region A in the final stage of the neck development (see footnote 2). For materials exhibiting a positive strain rate sensitivity, a significant delay in the onset of the instability may result, see sections 3.5 and 3.7.2. Therefore, the inclusion of strain rate effects in the FLC calculation should be mandatory. Relations (3.30) and (3.32) together with the hardening relation (3.11) form the basis of a numerical integration scheme which uses the ratio $\beta = d\bar{\epsilon}_A/d\bar{\epsilon}_B$ as its primary unknown. The initial conditions for this system are described in section 3.4.

3.3 Numerical Solution Method

The numerical determination of the onset of instability is accomplished by using an implicit integration method to solve equations (3.30) and (3.32). The primary unknown $\beta = d\bar{\epsilon}_A/d\bar{\epsilon}_B$ is determined as a function of the equivalent plastic strain in the area of the neck (region B). By defining a constant step size $d\bar{\epsilon}_B$, typically on the order of $2 \cdot 10^{-4}$, the solution is advanced in steps from $n = 0, 1, 2, \dots, N$:

$$\bar{\epsilon}_B|_{n+1} = \bar{\epsilon}_B|_n + d\bar{\epsilon}_B \quad (3.34)$$

The equivalent plastic strain at some distance from the neck (region A) follows from:

$$\bar{\epsilon}_A|_{n+1} = \bar{\epsilon}_A|_n + \underbrace{\frac{d\bar{\epsilon}_A}{d\bar{\epsilon}_B}}_{\beta_{n+1/2}} d\bar{\epsilon}_B \quad (3.35)$$

Figure 3.3 illustrates the arithmetic averaging of the gradient β between steps n and $n + 1$. It results in a method whose discretization error approaches zero as $d\bar{\epsilon}_B \rightarrow 0$, like $c \cdot d\bar{\epsilon}_B$ for some constant c (see section 3.6 for an example of its convergence properties).

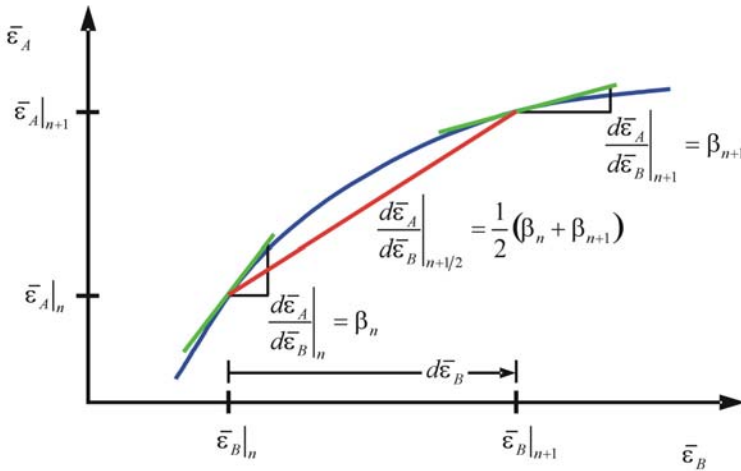


Fig. 3.3 Integration scheme to determine the increment in plastic strain $d\bar{\epsilon}_A$.

In order to determine β_{n+1} for each integration step, an iterative solution procedure is applied. It guarantees that (3.32) is fulfilled within machine tolerance at step $n + 1$. During the iteration, outlined in Figure 3.4, β is varied from 1 to 0 in steps of 0.01. A change in sign of the left hand side of (3.32) signals a successful bracketing of the solution space for β . The final solution β_{n+1} is subsequently determined by a secant method, which makes use of the same set of equations as shown in Figure 3.4. Details of the secant method may be found in Press et al. [26].

The numerical integration is continued until $\beta_{n+1} < 1/25$. The equivalent plastic strain in region A at this instant is defined as the onset of plastic instability $\bar{\epsilon}_A^*$.

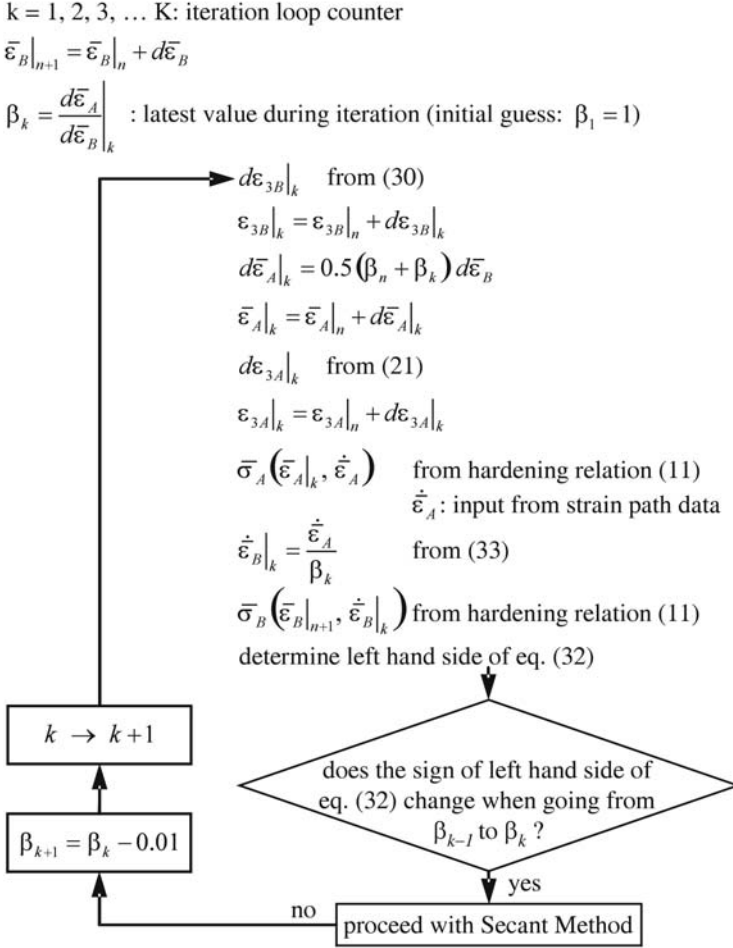


Fig. 3.4 Basic algorithm for an iterative determination of $\bar{\varepsilon}_B|_{n+1}$, β_{n+1} , $\varepsilon_{3B}|_{n+1}$, $\bar{\varepsilon}_A|_{n+1}$ and $\varepsilon_{3A}|_{n+1}$ during one integration step from n to $n + 1$.

3.4 Initial Conditions

To start the integration algorithm outlined in section 3.3, five entities must be prescribed: $\bar{\varepsilon}_A|_0$, $\varepsilon_{3A}|_0$, $\bar{\varepsilon}_B|_0$, $\varepsilon_{3B}|_0$, $d\bar{\varepsilon}_A/d\bar{\varepsilon}_B|_0 = \beta_0$. It will be assumed that the stresses in region A are just about to induce plastic flow:

$$\bar{\varepsilon}_A|_0 = 0 \quad (3.36)$$

$$\varepsilon_{3A}|_0 = 0 \quad (3.37)$$

A very small positive value is assigned to the equivalent plastic strain in region A in actual computations. This helps to avoid convergence problems encountered in certain kinds of hardening relations. For instance, the Hollomon formulation $\bar{\sigma} = C_1 \bar{\epsilon}^n$ shows an infinite gradient $d\bar{\sigma}/d\bar{\epsilon}$ for $\bar{\epsilon} \rightarrow 0$ and $0 < n < 1$.

The remaining three values are determined iteratively. As illustrated in Figure 3.5, for two values $\bar{\epsilon}_A|_0 = 10^{-12}$ and $\bar{\epsilon}_A|_1 = 10^{-4}$ the strains in region B are determined in complete analogy to the basic algorithm of Figure 3.4. This allows β_0 to be found from a finite difference approximation of the gradient $d\bar{\epsilon}_A/d\bar{\epsilon}_B$ as illustrated in Figure 3.5.

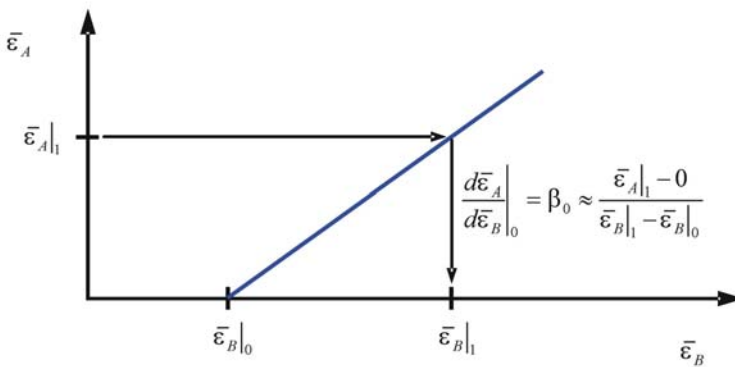


Fig. 3.5 Numerical approximation of the initial value β_0 .

This comparatively complex process ensures that a mathematically consistent set of initial values is determined. The differences between using the process described above and a much simpler process which uses $\beta_0 = 1$ as an approximate initial value are shown in Figure 3.6 for a specific example.

Figure 3.6 indicates that the final result is hardly different when $\beta_0 = 1$ is used. Although it may be tempting to use the simpler initial conditions in practical computations, the present author is not aware of guidelines for determining under which circumstances a proper solution will result⁴. Tests have revealed that the amplitude of the oscillation decreases with decreasing values of the inhomogeneity parameter f_i .

⁴ The investigations of Lorenz [22] in the field of meteorology are one prominent example that the solutions of even small systems of ordinary nonlinear equations may seriously be affected by small changes in initial conditions.

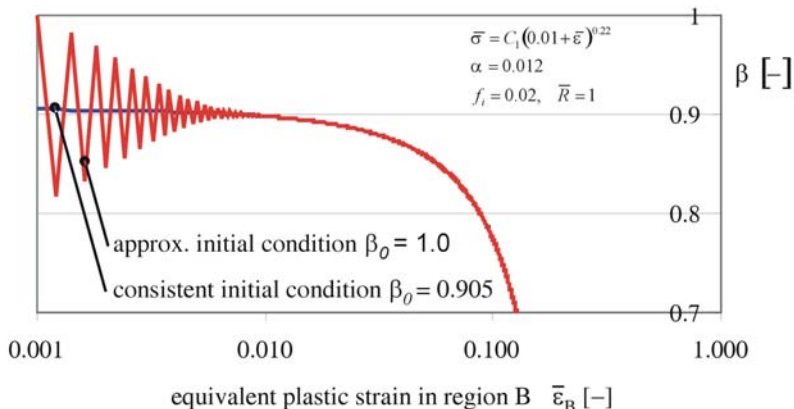


Fig. 3.6 A consistent set of initial conditions leads to a smooth function whereas the approximate initial condition $\beta_0 = 1$ leads to a damped oscillation. For $d\bar{\epsilon}_B > 0.01$ both solutions are nearly identical.

3.5 Validation

Marciniak, Kuczyński and Pokora published detailed results in their Figure 3.2 of [24] for a hardening relation as a function of equivalent strain and strain rate:

$$\bar{\sigma} = C_1 (0.01 + \bar{\epsilon})^{0.22} \dot{\bar{\epsilon}}^m \quad (3.38)$$

The exponent m , representing the strain rate sensitivity of the material, had been varied whereas the parameters $\alpha = 1$ (equibiaxial strain path), $\bar{R} = 1$ (isotropic material behaviour) and $f_i = 0.02$ were kept constant. Constant C_1 does not influence the results in any way and may therefore be chosen in a numerically convenient manner. Figure 3.7 shows a comparison of the results of Marciniak et al.[24] and those of the present work. For four values of the exponent m , the equivalent strain in region A $\bar{\epsilon}_A$ is shown as a function of the equivalent strain in region B $\bar{\epsilon}_B$. The agreement with respect to the functional dependence as well as the equivalent strain $\bar{\epsilon}_A^*$ marking the onset of instability is excellent.

Figure 3.8 shows the accompanying development of the gradient $\beta = d\bar{\epsilon}_A/d\bar{\epsilon}_B$ as a function of the equivalent strain in the neck $\bar{\epsilon}_B$. Special emphasis is given to the initial values of β .

By comparing the forming limit curves for proportional loading conditions ($\alpha = \text{const.}$) in Figure 3.9, the significant influence of strain rate effects on the onset of instability becomes evident, especially near plane strain conditions ($\epsilon_2 \rightarrow 0$).

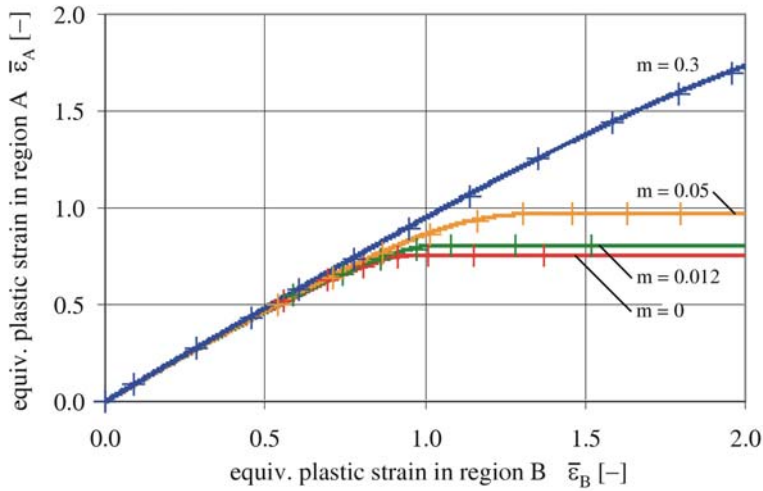


Fig. 3.7 Development of equivalent plastic strain in region A as a function of the equivalent plastic strain in the neck (region B) for four values of the strain rate exponent m . Crosses mark the results of Marciniak et al. ([24], Fig. 2); the full lines were computed with the algorithm of sections 3.3 and 3.4. Results for equibiaxial strain path $\alpha = 1$.

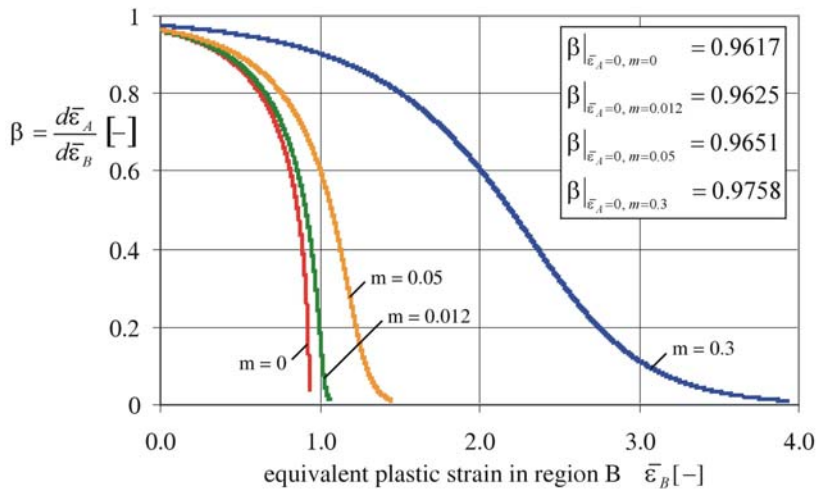


Fig. 3.8 Development of the gradient β as a function of the equivalent plastic strain in the neck (region B) for four values of the strain rate exponent m . Results for equibiaxial strain path $\alpha = 1$.

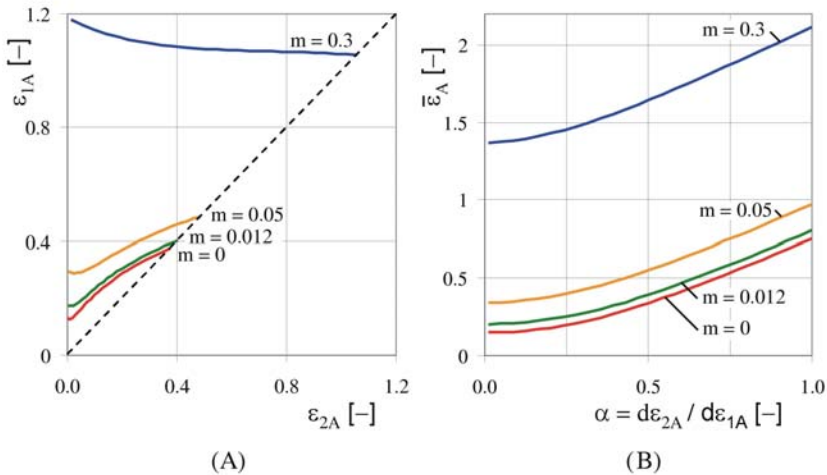


Fig. 3.9 Forming limit curves for the test case of Marciniak et al. [24] emphasising the influence of strain rate effects on the onset of instability. (A): major vs. minor principal strain. (B): equivalent strain vs. α .

A final comment on the parameters m and f_i may be necessary. For ferritic steel grades, the maximum m -values are around 0.025 while the typical inhomogeneity parameters f_i are approximately one order of magnitude lower than in the test example above, see the Participants Information of Gese in Volk et al. ([31], p 25). Comparing the forming limit in plane strain conditions⁵ for a value of $m = 0$ with those of $m = 0.025$ shows an increase of 104% in the major principal strain at the onset of instability! Therefore, the strain rate behaviour of the material in question must be reflected in the computation of forming limit curves.

3.6 Convergence Properties

In order to demonstrate that the integration schemes discretization error approaches zero with decreasing step size $d\bar{\epsilon}_B$, an example from section 3.5 is used in which $\alpha = 1$, $\bar{R} = 1$, $m = 0.05$, $f_i = 0.02$. For a sequence of nine step sizes, $d\bar{\epsilon}_B = 2^k \cdot 10^{-4}$, $k = 0, 1, 2, \dots, 8$ the onset of instability $\bar{\epsilon}_A^*$ is determined⁶. As shown in Figure 3.10, the solution tends towards a limiting value. By halving the step size the absolute error is reduced by approximately the same factor. This can be seen by comparing for instance, errors e_7 and e_8 as shown below. It should be remarked that

⁵ The hardening relation (3.38) was used in combination with $f_i = 0.001$.

⁶ The computations were carried out on a PC in DOUBLE PRECISION resulting in a floating point precision of $2.2 \cdot 10^{-16}$ according to the definition of eps in Press et al. ([26], section 20.1).

a further reduction in step size, to below $1 \cdot 10^{-4}$ is unnecessary and may very well be counterproductive as the solution is diverging due to round-off errors.

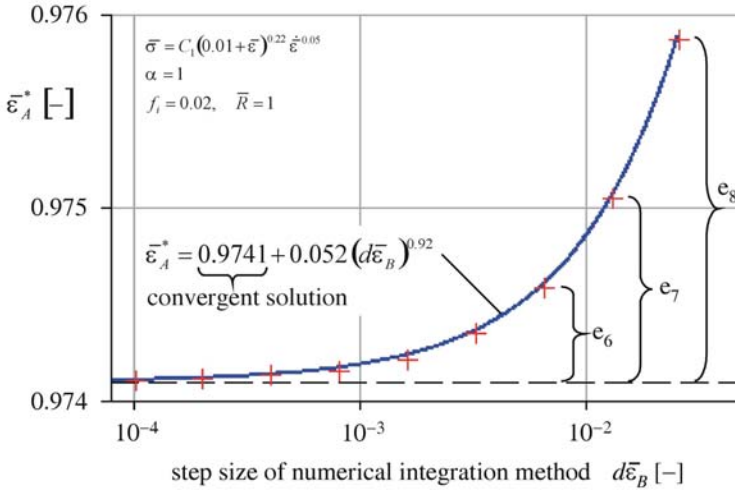


Fig. 3.10 Convergence of the numerical solution with decreasing step size. Convergence is towards the limiting value $\bar{\epsilon}_A^* = 0.9741$, which indicates the onset of instability.

3.7 Influence of Different Hardening Relations on the FLCs

The results of theoretically determined FLCs depend crucially on the constitutive model of the material behaviour employed. In this section the influences of the hardening relation on the forming limit curve will be examined. The equally important shape of the yield locus will not be treated in this paper. Neglecting the yield locus, a quantitative comparison of the theoretical FLCs with the experimentally determined FLC does not make sense and is therefore left out of this discussion. Graf and Hosford [9] have shown the pronounced influence of the yield locus onto the shape of the forming limit curve.

A TRIP steel has been chosen as the object of investigation. Detailed data has been determined for this material within a transnational research project [28]. Section 3.7.1 will focus on the effect of different approximations of the quasi-static hardening relation only; while in section 3.7.2, the main emphasis will be on strain rate effects.

3.7.1 Effect of Various Quasi-Static Hardening Relations on Forming Limit Curves

Within the research project [28], tensile tests had been carried out over strain rates from 0.004 s^{-1} (quasi-static) to 200 s^{-1} . Bulge tests at the quasi-static strain rate provided additional important information in the higher ranges of equivalent strain, which cannot be generated from pure tensile tests.

Often, however, the numerical analyst is faced with the problem that only data from tensile tests is available; which is generally far too limited for the computation of a FLC. Extrapolation of the hardening curve becomes thus inevitable, raising the frequently asked question for the "best" extrapolation function. Table 3.3 contains an undoubtedly subjective choice of four hardening relations which were fitted to the test data using various strategies. Function 1, abbreviated as $g_1(\bar{\epsilon})$, serves as the reference since it utilizes both tensile and bulge test data. The constants of the remaining functions were fitted using only the available tensile test data. The behaviour of function 4 for higher values of equivalent strain is governed by the linear term $1055.8\bar{\epsilon}$. Its gradient, 1055.8 has been determined directly from the last two measured points, see arrows in Figure 3.11. Upon initial inspection of Figure 3.11, all four functions provide a very satisfactory material description in the range of the tensile test data. Beyond an equivalent strain of 0.18, however, the hardening behaviour is clearly different, raising questions about its effect on the resulting forming limit curves.

Table 3.3 Hardening relations used to approximate experimental data of a TRIP steel for a quasi-static strain rate of 0.004 s^{-1} . Stress in [MPa].

No.	Hardening Relation	Strategy to fit constants
1	$\bar{\sigma} = \underbrace{502.6 + 250.4\bar{\epsilon} + 527.7 [1 - \exp(-\bar{\epsilon}/0.135)]^{0.6}}_{g_1(\bar{\epsilon})}$	tensile and bulge test data.
2	$\bar{\sigma} = 1037 - (1037 - 559.5) \exp(-12\bar{\epsilon})$	tensile data.
3	$\bar{\sigma} = 1435.2 (0.011 + \bar{\epsilon})^{0.22}$	tensile data.
4	$\bar{\sigma} = 478.8 + 1055.8\bar{\epsilon} + 345.4\sqrt{1 - \exp(-\bar{\epsilon}/0.072)}$	tensile data. Gradient extrapolation, see text.

Figure 3.12 shows the resulting FLCs for the hardening relations of Table 3.3. An inhomogeneity parameter $f_i = 0.0011$, isotropic material behaviour $\bar{R} = 1$, and constant strain paths $\alpha = \text{const.}$ are the basis of these results. Since the gradient of the hardening relation $d\bar{\sigma}/d\bar{\epsilon}$ is of dominating influence, it is clear that relation No.

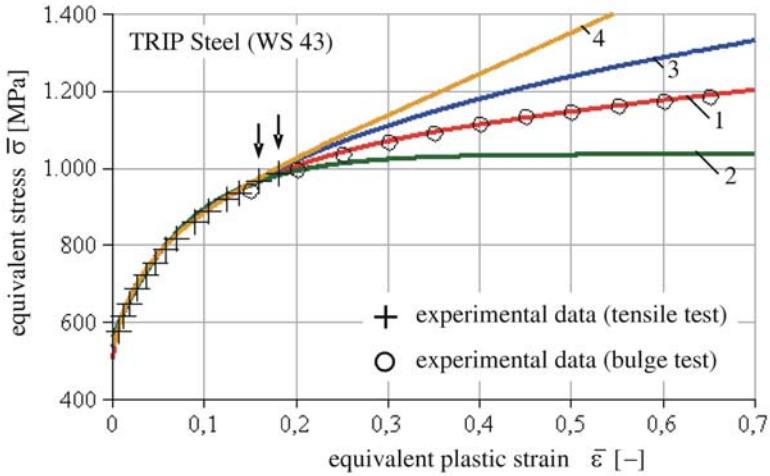


Fig. 3.11 Comparison of the hardening relations for a TRIP steel according to Table 3.3 with experimentally determined data. Arrows mark points used for extrapolation by last known gradient in function 4.

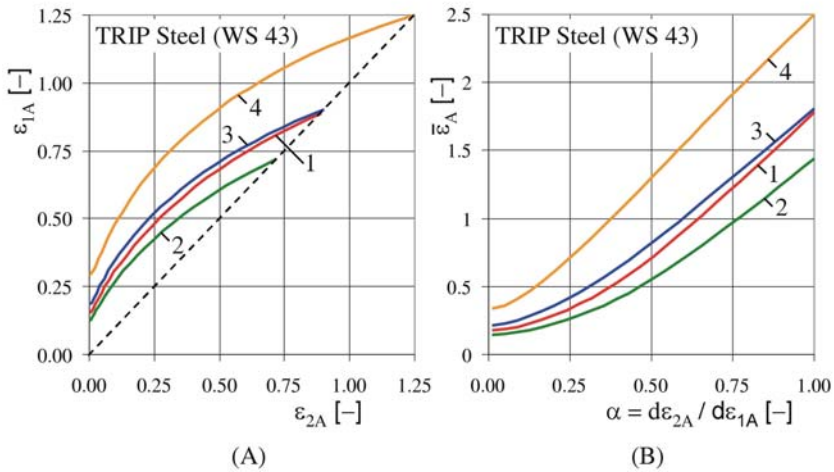


Fig. 3.12 Theoretical forming limit curves for the hardening functions of Table 3.3, approximating the TRIP steel to various degrees of accuracy in the high strain region. (A): major principal strain vs. minor principal strain. (B): equivalent strain vs. α .

4 will lead to the highest forming limits. The difference between these four results is predominantly visible near plane strain $\alpha \rightarrow 0$ and therefore of considerable prac-

tical importance. With reference to hardening relation 1, relation 2 provides a limit strain which is 17% lower, see Figure 3.12 (B). Relation 3 results in a 22% higher value and relation 4 shows a striking 92% increase! The essential message to be derived from this comparison is to avoid any extrapolation of hardening relations. Measurements of high quality stress strain curves at equivalent strain levels far beyond those of standard tensile tests are the essential basis of theoretically determined forming limit curves.

3.7.2 Effect of Various Strain Rate Formulations on the Forming Limit Curves

Since the hardening properties of many materials depend on strain rate, influences on the forming limit curve are to be expected – an effect clearly shown by Marciniak et al. [24] more than three decades ago. Similar to the choice of suitable functions for the approximation of quasistatic hardening relations, strain rate dependencies may be formulated in a multitude of ways. Additive or multiplicative terms, which extend pure quasi-static approximations, are among the most popular formulations. Three different approximations of this type are applied to the TRIP steel data investigated in [28]. Since only tensile test data is available at higher strain rates, extrapolation beyond an equivalent strain of 0.18 is even more demanding; see the comments at the end of section 3.7.2. Table 3.4 lists the functions, which were used in combination with the quasi-static approximation $g_1(\bar{\epsilon})$ of Table 3.3.

Table 3.4 Strain rate dependent hardening relations used to approximate experimental data of a TRIP steel for $0.004 s^{-1} \leq \dot{\bar{\epsilon}} \leq 200 s^{-1}$. Stress in [MPa].

No.	Hardening Relation	Author
1a	$\bar{\sigma} = g_1(\bar{\epsilon}) \cdot (\dot{\bar{\epsilon}}/0.004)^{0.01}$	Cowper-Symonds [29]
1a	$\bar{\sigma} = g_1(\bar{\epsilon}) \cdot [1 + 0.0105 \ln(\dot{\bar{\epsilon}}/0.004)]$	Johnson-Cook [18]
1b	$\bar{\sigma} = g_1(\bar{\epsilon}) + 45.8 (\dot{\bar{\epsilon}}^{0.2} - 0.004^{0.2})$	El-Magd [5]
1c	$\bar{\sigma} = g_1(\bar{\epsilon}) + \left[1.39 + \frac{2180}{1+55\bar{\epsilon}} \left(\frac{0.004}{\dot{\bar{\epsilon}}} \right)^{0.6} + (5461\bar{\epsilon} - 228) \left(\frac{0.004}{\dot{\bar{\epsilon}}} \right)^{0.55} \right] (\dot{\bar{\epsilon}} - 0.004)^{0.7}$	Werner

Denoting both, the Cowper-Symonds and Johnson-Cook formulation by 1a is justified because the differences are negligible in the region of interest. The rate dependence 1b developed by El-Magd is based on a microstructural model, whereas

the present author's purely empirical function 1c sought to provide a well-behaved optimum fit of the data points. Figure 3.13 illustrates these hardening relations together with experimental data points.

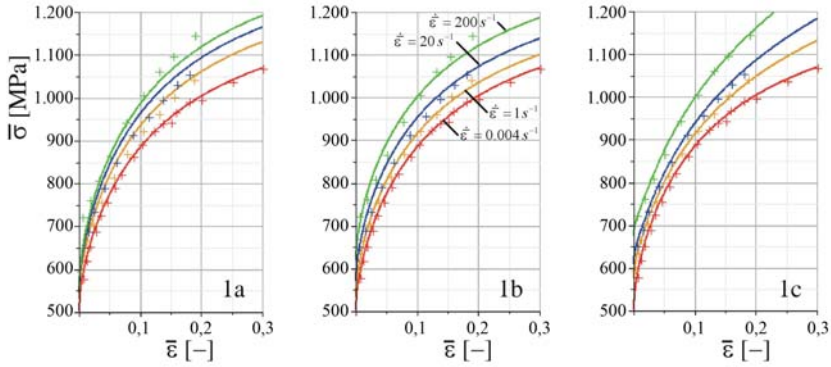


Fig. 3.13 Comparison of the strain rate dependent hardening relations for a TRIP steel according to Table 3.4 with experimentally determined data (crosses).

The forming limit curves resulting from the hardening relations of Table 3.4 are shown in Figure 3.14 for proportional strain paths $\alpha = const.$ and two strain rates applied in region A at some distance from the neck. Even in forming operations, local strain rates of $10 s^{-1}$ are not uncommon, whereas in automotive crash situations $10 s^{-1}$ represents the lower end of observable strain rates in areas undergoing severe deformations.

At first glance, Figure 3.14 reveals major differences in the vicinity of plane strain, $\epsilon_{2A} \rightarrow 0$. Whereas the rate formulations 1a and 1b do not display such pronounced influences, approximation 1c, fitting the experimental data the "best", shows a substantial strain rate effect. The reason for putting the word best in quotation marks becomes obvious when considering the degree of extrapolation of the rate-dependent experimental data. In case of plane strain, $\epsilon_{2A} = 0$ in Figure 3.14 (B), the equivalent strain at onset of instability for approximation 1c is 0.43. Looking at Figure 3.13 the measured rate-dependent data points end at an equivalent strain of 0.18. This means that an extrapolation of $0.43/0.18 = 2.4$ was required to generate the data. Nonetheless, this ends up constituting the best result! For the equibiaxial strain path $\epsilon_{2A} = \epsilon_{1A}$, the onset of instability takes place at an equivalent strain of 2.49, resulting in an extrapolation factor of nearly 14! In this situation, it would be unreasonable to claim such an empirical fit to be adequate.

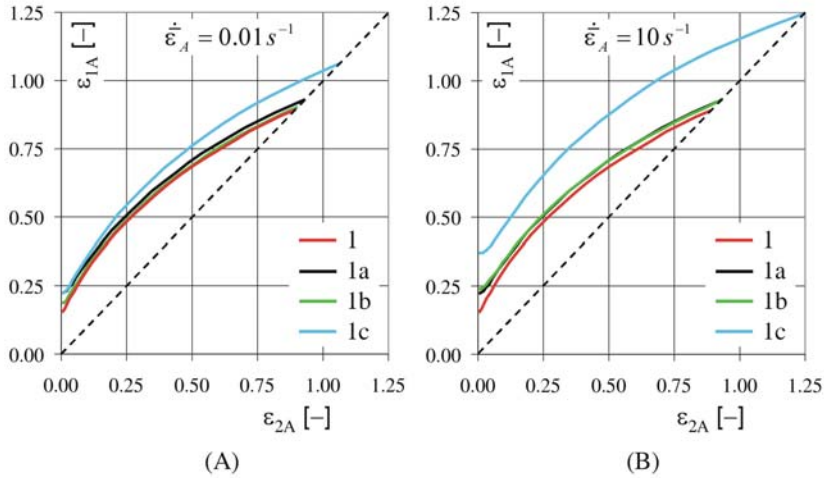


Fig. 3.14 Theoretical forming limit curves resulting from the strain rate dependent hardening functions of Table 3.4. For reference, curve 1 of Figure 3.12 is included. (A): Deformation in region A proceeds at a constant strain rate of 0.01 s^{-1} . (B): Deformation proceeds at constant strain rate of 10 s^{-1} .

3.8 Summary

Predicting the structural failure of thin sheet components in complex forming and crash situations remains a demanding task. The forming limit curve (FLC) is one of several tools which are routinely applied in project work at BMW using the finite element analysis software Abaqus [27] in order to evaluate the likeliness of failure in bodies in white subjected to various crash load cases.

The present work provides a detailed derivation and validation of the theoretical method of Marciniak et al. [24] used to determine the FLC of thin sheets. Because of its critical importance in crash situations, the main focus is on applying generalized relations which describe the hardening of a material as a function of strain and strain rate. By comparing FLCs, resulting from various approximations for the rate dependent hardening relation of one particular steel, the following conclusions may be drawn:

1. The results clearly indicate that the theoretical prediction of a FLC makes great demands on the quality and the comprehensiveness of the experimental input data used as the basis for the constitutive model. Differences of 20% to 90% may result from improperly chosen extrapolations of the hardening relation!
2. The FLC computation is particularly sensitive to the constitutive model used. Therefore, in order to maximize the benefit of this theory, yield locus, flow rule

and rate dependent hardening relations must be based on carefully measured data – not on extrapolated or even assumed data.

Provided that these requirements are fulfilled, the Marciniak theory and its descendants greatly help to improve the prediction of failure in thin sheets– in forming as well as in crash analyses.

Acknowledgements The author greatly appreciates the kind and competent assistance of Christian Suci in improving the phrasing of this article.

References

1. ASTM Standard E2218-02(2008) Standard Test Method for Determining Forming Limit Curves. ASTM International, West Conshohocken, PA
2. Banabic D, Aretz H, Paraianu L, Jurco P (2005) Application of various FLD modelling approaches. *Modelling Simul Mater Sci Eng* 13:759-769
3. Banabic D, Soare S (2008) On the effect of the normal pressure upon the forming limit strains. *Numisheet 2008, Part A*:199-204, Interlaken, Switzerland
4. El-Magd E (2003) Modeling and simulation of mechanical behavior. In: Totten G E, Xie L, Funatani K (eds) *Modeling and simulation for material selection and mechanical design*, pp 195-300. Marcel-Dekker, New York
5. El-Magd E (2006) Beschreibung des Fließverhaltens und der Versagensgrenzen. *Tagung Werkstoffprüfung 2006*, Bad Neuenahr, Germany
6. Gese H, Dell H (2006) Numerical prediction of FLC with the program CRACH. *Proceedings of the FLC Zurich 2006, IVP, ETH Zurich, Switzerland*
7. Ghosh A K (1978) Plastic flow properties in relation to localized necking in sheets. In: Koistinen D P, Wang N-M (eds) *Mechanics of sheet metal forming*, pp 287-312, Plenum Press, New York
8. Goodwin G M (1968) Application of strain analysis to sheet metal forming problems in press shop. *SAE paper No 680093:380-387*
9. Graf A, Hosford W F (1990) Calculations of forming limit diagrams. *Metallurgical Transactions A* 21:87-94
10. Graf A, Hosford W (1994) The influence of strain-path changes on forming limit diagrams of Al 6111 T4. *Int J mech Sci* 36:897-910
11. Hiermaier S (2008) *Structures under crash and impact. Continuum mechanics, discretization and experimental characterization*. Springer, New York
12. Hill R (1948) A theory of the yielding and plastic flow of anisotropic metals. *Proc Roy Soc London A* 193:281-297
13. Hooputra H, Gese H, Dell H, Werner H (2004) A comprehensive failure model for crashworthiness simulation of aluminium extrusions. *International Journal of Crashworthiness* 9:449-463
14. Hora P, Tong L (2006) Prediction of forming limits in virtual sheet metal forming – yesterday, today and tomorrow. *Proceedings of the FLC Zurich 2006, IVP, ETH Zurich, Switzerland*
15. Hora P, Tong L (2008) Theoretical prediction of the influence of curvature and thickness on the FLC by the enhanced Modified Maximum Force Criterion. *Numisheet 2008, Part A*:205-210, Interlaken, Switzerland
16. Hotz W, Timm J (2008) Experimental determination of forming limit curves (FLC). *Numisheet 2008, Part A*:271-278, Interlaken, Switzerland

17. International Organization for Standardization ISO 12004-1:2008 Metallic materials – Sheet and strip – Determination of forming-limit curves – Part 1: Measurement and application of forming-limit curves in the press shop
18. Johnson G R Cook W H (1985) Fracture characteristics of three metals subjected to various strains, strain rates, temperatures and pressures. *Engineering Fracture Mechanics* 21:31-48
19. Keeler S P, Backofen W A (1963) Plastic instability and fracture in sheets stretched over rigid punches. *Trans ASM* 56:25-48
20. Kessler L, Gese H, Metzmacher G, Werner H (2008) An approach to model sheet failure after onset of localized necking in industrial high strength steel stamping and crash simulations. SAE 2008 World Congress, SAE Technical Paper Series 2008-01-0503, Detroit, Michigan
21. Lévy M (1870) Mémoire sur les équations générales des mouvements intérieurs des corps solides ductiles au delà des limites où l'élasticité pourrait les ramener à leur premier état. *Comptes rendus hebdomadaires des séances de l'Académie des Sciences* 70:1323-1325
22. Lorenz E N (1960) Maximum simplification of the dynamic equations. *Tellus* 12:243-254
23. Marciniak Z, Kuczyński K (1967): Limit strains in the processes of stretch-forming sheet metal. *Int J mech Sci* 9:609-620
24. Marciniak Z, Kuczyński K, Pokora T (1973): Influence of the plastic properties of a material on the forming limit diagram for sheet metal in tension. *Int J mech Sci* 15:789-805
25. Mises R von (1913) *Mechanik der festen Körper im plastisch-deformablen Zustand*. Nachr Königl Ges Wiss Göttingen, Math-phys Kl 582-592
26. Press W H, Teukolsky S A, Vetterling W T, Flannery B P (1992) *Numerical Recipes in FORTRAN. The art of Scientific Computing*. Cambridge University Press, Cambridge
27. SIMULIA (2008) *Abaqus Analysis User's Manual*. 166 Valley Street, Providence, RI 02909, USA
28. Steinbeck G, Bleck W, El-Magd E, Bork C-P, Sonsino C, Masendorf R, Evertz T, Menne M (eds) (2007) *Ermittlung des Werkstoffverhaltens und des Beschichtungseinflusses durch rechnerische Methoden zur Verkürzung der Entwicklungszeiten im Fahrzeugbau mit Stahl*. Forschungsvereinigung Stahlanwendung e.V., Projekt 603, Düsseldorf, Germany
29. Symonds P S (1967) *Survey of methods of analysis for plastic deformation of structures under dynamic loading*. Brown Univ, Div of Eng Report BU/NSRDC/1-67
30. Volk W, Illig R, Kupfer H, Wahlen A, Hora P, Kessler L, Hotz, W (2008) Benchmark 1 – Virtual forming limit curves. Part A: Physical tryout report. *Numisheet 2008, Part B:3-9*, Interlaken, Switzerland
31. Volk W, Wahlen A, Hora P, Kessler L, Hotz, W (2008) Benchmark 1 – Virtual forming limit curves. Part B: Benchmark analysis. *Numisheet 2008, Part B:11-19, Part C:21-42*, Interlaken, Switzerland
32. Wierzbicki T, Bao Y, Lee Y-W, Bai Y (2005) Calibration and evaluation of seven fracture models. *Int J mech Sci* 47:719-743

Chapter 4

The Challenge to Predict Material Failure in Crashworthiness Applications: Simulation of Producibility to Serviceability

André Haufe, Markus Feucht and Frieder Neukamm

Abstract In recent years, the requirements on passive safety of cars have grown to high standards, leading to a permanent demand on an increase in simulation accuracy. Additionally, demands on fuel efficiency and CO₂ – reduction are confronting the car body designers with the need of substantial weight reduction. Here the increasing use of high and ultrahigh strength steel grades for bodies in white can be identified as major trend. At the same time simulation techniques are urged to predict formability and crashworthiness performance better and better. The present contribution will focus on one of the most urging challenges in sheet metal forming and crashworthiness simulation for high strength steels, namely alternative or enhanced constitutive formulations to predict failure and cracking of the blank and furthermore the inclusion of forming results in crashworthiness finite element models in order to predict material failure in such numerical investigations. In a broader view this simulation process chain may be termed as 'producibility to serviceability' since the driving force behind forming simulations used to be the question if a certain part can be produced on certain press equipment with a defined number of forming stages from a specific material of given initial thickness. Carrying over the forming results to other simulation disciplines like crashworthiness or NVH, where the serviceability of the designed structure is investigated further, will eventually give more insight into the effects of pre-straining and possible pre-damaging emerging from production processes on the target discipline. The whole topic is rather demanding since nowadays the crashworthiness of bodies in white is assessed to a major extend

André Haufe

DYNAmore GmbH, Industriestrasse 2, D-70565 Stuttgart, Germany, e-mail: andre.haufe@dynamore.de

Markus Feucht

Daimler AG, EP/SPB, W059/HPC X271, 71059 Sindelfingen, Germany e-mail: markus.feucht@daimler.com

Frieder Neukamm

Daimler AG, EP/SPB, W059/HPC X271, 71059 Sindelfingen, Germany e-mail: frieder.neukamm@daimler.com

by finite element simulations without taking the production history into account. In this context, high strength steel qualities are known to be more problematic. The present contribution discusses two possible engineering driven approaches to close the constitutive gap between the forming and crashworthiness world.

4.1 Introduction

As mentioned earlier the production history may have an enormous effect on part performance in crashworthiness applications. The present contribution will focus on parts made of high strength steel and will disregard similar problems that may arise for polymers and plastics in occupant safety simulation. It is clear though, that the process chain of sheet metal manufacturing not only starts at sheet metal forming but instead the blank has already some history of production before it is actually formed into some automotive part. Great effort is being put into the theory and application of numerical models that are able to predict constitutive properties of every single stage during sheet metal production. One of the projects that focuses on the earlier stages of production history is present in section 2, while section 3 will discuss some of the new models that may become more popular in future. Section 4 discusses path dependent localization in the context of a newly proposed damage mode. Section 5 focuses on the post critical behaviour while section 6 will present first results gained with a demonstrator part.

4.2 The Process Chain of Sheet Metal Part Manufacturing

The individual process steps of sheet metal production are illustrated in Fig. 4.1 together with the principal properties a descriptive model should take into account in order to enable predictive numerical studies. Within a research project supported by funds of 'WING' by the German Federal Ministry of Education and Research (BMBF), grant # 03X0501E, most of the simulation problems along the process chain were solved. So a newly developed data transfer structure that includes the various results of a previous simulation step are passed on to the corresponding following step. Hereby, the data is meaningfully reduced. This procedure also allows feedback to the preceding step, i.e. from cold-rolling or heat treating to the material design or crashworthiness to forming simulation and thus allows purposeful material optimization by e.g. the steel manufacturer. Moreover, the software solution developed within the project provides a precise description of the steel characteristics which can be passed on also to customers of the steel manufacturer, i.e. the automotive industry.

Within the WING project the process chain simulation is exemplified by a dual phase steel that is being newly developed. In addition the individual process steps like cold-rolling, annealing, skin-pass-rolling, forming, spring back, and the crash-worthiness simulation are illustrated with the help of continuum-mechanical and micromechanical material models.

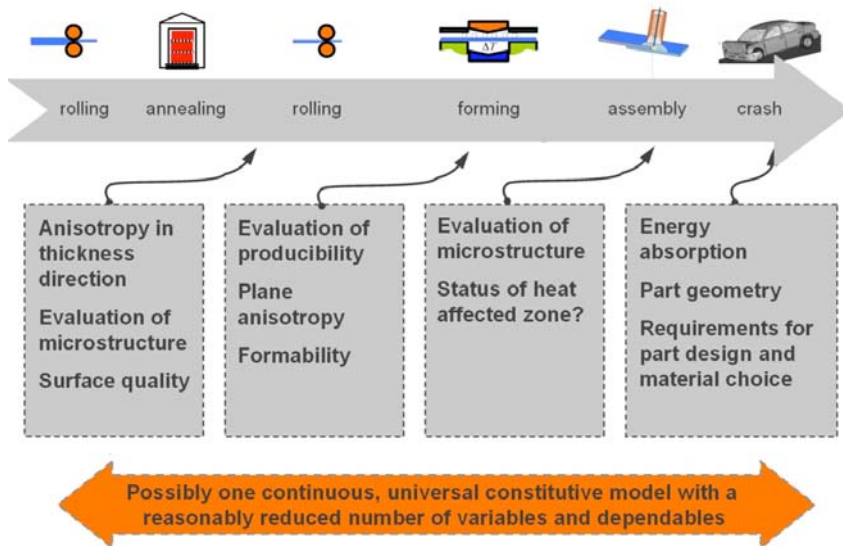


Fig. 4.1 Process chain modeling: Principle work- and data-flow.

For a continuous process chain simulation where macroscopic properties are considered, micro-structure, texture and damage parameters of existing simulation tools based on a continuum mechanical approach and physically based models are to be unified on the so called meso-scale. In addition these models need to be adapted to common simulation tools. This applies particularly to models of texture simulation. In order to be able to compute all parameters of the individually scaled and applied models along the process chain (e.g. micro-, meso- & macro-scale models), the aforementioned data management structure needs to be able to unify all different demands and characteristics of the individual mechanical models that are applied. For the description of texture and yield locus of forming simulations Taylor-based models, finite element based polycrystalline models and self-consistent models are available, which shall also be able to capture the behaviour of multi-phase steel. For the description of the micro-structure development during annealing and possible welding new thermodynamic-kinetic models describing nucleus formation and growth of all phases of the matrix are being used for the

first time. For the characterisation of deformation boundaries during rolling and forming damage-mechanical models are adapted to the corresponding process conditions.

Along the process chain predominantly the finite element method is being used. Micro-structural characteristics are modelled by local variables, whose evolution is described by internal equations. Experimental methods like tension test, tension-compression tests or biaxial tests of sheet metal are used to gain necessary macroscopic parameters for the applied plasticity models on forming and crashworthiness level. However usually different constitutive models – though usually based on classical plasticity theory – are used in forming and crashworthiness simulations. Hence in order to unify the approach and enable the usage of history data from forming simulations in crashworthiness applications new or updated constitutive models need to be developed.

4.3 Some Ideas for Failure Modelling in Forming and Crashworthiness Simulations

On behalf of improvements for crashworthiness simulations, great effort has been done throughout the past years regarding the treatment of crack formation and propagation. Current state of the art here is the use of failure models that accumulate damage on an incremental basis. Most models are based on the observations of Bridgman [1], who found that failure strain in metallic materials depends on the hydrostatic pressure. Examples of models in use are the Gurson model with extensions by Tvergaard and Needleman [2], and the failure model of Johnson and Cook [3]. As a shortcoming, the mechanical properties of sheet metal parts for crashworthiness calculations are usually assumed to be as in a maiden-like material delivery state. This disregards the changes in constitutive properties resulting from previous treatment in the process chain of sheet metal part manufacturing, including i.e. deep-drawing. In the easiest case, a local increase of the yield stress due to work hardening can be expected which may play an important role for low-speed impact cases. Since plastic pre-straining also results in a reduction of the remaining strain up to failure, the effect of pre-damaging should be phenomenologically taken into account in crashworthiness simulations. This in turn leads to the fact that not only plastic strains but also the damage state evolved during forming simulations should be modelled.

For crashworthiness computations, the constitutive models used are usually isotropic and based on the von Mises flow rule or the Gurson, Tvergaard & Needleman approach (see Fig 4.2(b)). For forming simulations, a more sophisticated and anisotropic description of yield loci - often based on the Hill-criterion - is considered important (see Fig 4.2(a)), which makes it necessary to use different constitu-

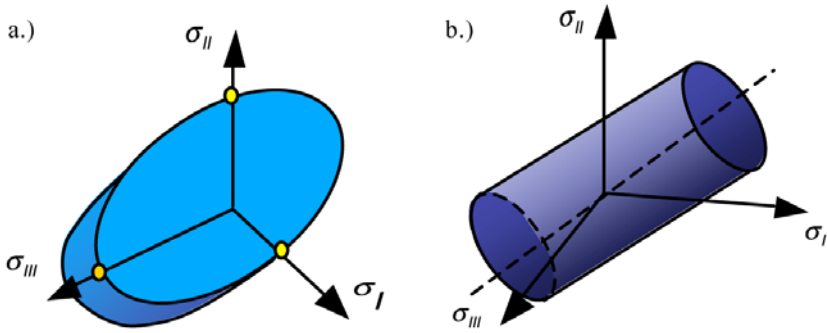


Fig. 4.2 Process chain modeling: Principle work- and data-flow.

tive models for both parts of the process chain. A damage model suitable to be used for both disciplines therefore has to be able to correctly predict damage regardless of the details of the constitutive model formulation.

4.3.1 The Barlat Constitutive Model for Forming Simulations

The constitutive model used in the actual approach for the forming simulation is the anisotropic yield locus by Barlat, Lege and Brem 1991 [4], which is used to allow for a consideration of anisotropic yield loci in crashworthiness calculations also. The model is based on the assumption of isochoric plastic behaviour, thus by definition yielding a volumetric strain rate $\dot{\epsilon}_p^{pl}$ equal to zero.

For the plane stress case (implemented in LS-DYNA as Mat.036), the yield function is defined as

$$\Phi = a|K_1 + K_2|^M + a|K_1 - K_2|^M + c|2K_2|^M = 2\sigma_Y^M \quad (4.1)$$

with

$$K_1 = \frac{\sigma_x + h\sigma_y}{2} \quad (4.2)$$

$$K_2 = \sqrt{\left(\frac{\sigma_x - h\sigma_y}{2}\right)^2 + p^2\tau_{xy}^2}$$

Here, σ_y is the actual yield stress; a, c, h and p are anisotropy parameters usually calculated from planar r-values.

4.3.2 Constitutive Models for Crashworthiness Applications

The Gurson-model with extension by Tvergaard and Needleman [2] is based on a micromechanical model describing growth and nucleation of spheroid voids in rigid-perfectly plastic material. It offers a complete description of ductile material behaviour, including softening and failure. The yield function is dependent on hydrostatic pressure and the effective void volume fraction f :

$$\Phi = \frac{q^2}{\sigma_M^2} + 2q_1 f^* \cosh\left(\frac{-3q_2 p}{2\sigma_M}\right) - 1 - (q_1 f^*)^2 = 0 \quad (4.3)$$

With

σ_M : actual flow stress in matrix material

p : hydrostatic pressure

q : equivalent (von Mises) stress

f^* : effective void volume fraction

Damage evolution is defined in a cumulative way:

$$\Delta f = \underbrace{(1-f)\Delta\varepsilon_p^{pl}}_{\text{void growth}} + \underbrace{A\Delta\varepsilon_M^{pl}}_{\text{void nucleation}} \quad (4.4)$$

with

$$A = \frac{f_N}{s_N \sqrt{2\pi}} e^{-\frac{1}{2} \left(\frac{\varepsilon_M^{pl} - \varepsilon_N}{s_N \sqrt{2\pi}} \right)^2} \quad (4.5)$$

As can be seen from equation 4.4, damage evolution consists of void growth due to volumetric plastic straining, and the nucleation of voids due to deviatoric plastic straining. Usually, void growth is considered the dominating mechanism of material deterioration under tensile loading. This implies the volumetric part of the plastic strain rate $\dot{\varepsilon}_p^{pl}$ being different from zero as long as the void volume fraction f – and therefore the damage – is growing. This will happen under arbitrary loading conditions of tensile nature, i.e. positive mean stress. Although based on the von Mises plastic potential, the Gurson model violates by its definition the assumption of isochoric plastic flow, which is common in classical plasticity theory. In terms of practical use, this is shown by a plastic Poisson's ratio being different from 0.5.

$$\nu_p = -\frac{\varepsilon_{p,yy}}{\varepsilon_{p,xx}} \quad (4.6)$$

Hence, the volume increase during loading is caused by a growing void volume fraction f .

4.3.3 A Hybrid Approach to Estimate the Void Volume Fraction in Forming Simulations

As mentioned above, the GTN model is constructed by two internal variables: namely the equivalent plastics strain and the void volume fraction f . While the plastic stain is a common history variable also for standard forming constitutive models, the void volume fraction is specific to the GTN model. Hence, when the GTN model shall be applied in combination with a forming simulation, the void volume fraction f is needed for initialization. One approach to gain this necessary parameter is to use the evolution equations of the GTN model hybridly during the forming simulation to estimate the void volume fraction (see Fig 4.3).

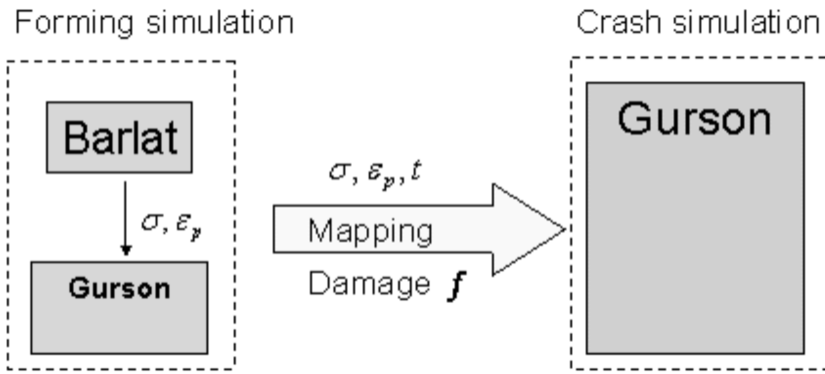


Fig. 4.3 Combination of Gurson and Barlat models by the hybrid Gurson approach in forming simulations.

The difference in volumetric plastic straining is the reason for the fact that the Gurson model cannot be coupled to an isochoric material model by simply transferring the calculated stress and strain tensors. To calculate the corresponding pore volume fraction from an isochoric constitutive model, the volumetric strain rate of the Gurson model has to be estimated from the existing strain rate tensor. For this purpose, the compatibility equation and the flow rule of the GTN model are used:

The associated flow rule

$$\Delta \varepsilon_{ij}^p = \Delta \lambda \frac{\partial \Phi}{\partial \sigma_{ij}} \tag{4.7}$$

is separated into a volumetric and deviatoric part

$$\left. \begin{aligned} \Delta \varepsilon_{kk}^p &= \Delta \varepsilon_p = \Delta \lambda \frac{\partial \Phi}{\partial p} \\ \Delta \varepsilon_{eq}^p &= \Delta \varepsilon_q = \Delta \lambda \frac{\partial \Phi}{\partial q} \end{aligned} \right\} \Delta \varepsilon_p \frac{\partial \Phi}{\partial q} + \Delta \varepsilon_q \frac{\partial \Phi}{\partial p} = 0 \tag{4.8}$$

$$\rightarrow \Delta \varepsilon_p = -\Delta \varepsilon_q \frac{\frac{\partial \Phi}{\partial p}}{\frac{\partial \Phi}{\partial q}} \quad (4.9)$$

Employing the respective derivatives of the flow rule $\Phi(\sigma_{ij})$, and approximating using a Taylor series expansion, leads to the following relation for the volumetric strain increment as a function of the deviatoric strain increment:

$$\Delta \varepsilon_p = -\Delta \varepsilon_q \frac{-3q_2 q_1 \sigma_M f^*}{2q} \sinh\left(\frac{-3q_2 p}{2\sigma_M}\right) \quad (4.10)$$

By using this relation, the adjacent volumetric strain increment of the GTN model can be estimated from an isochoric model like e.g. the Barlat model.

The differences in mechanical behaviour between the two models are yet not cured. Since the GTN model would lead to a volume increase, which the Barlat model does not, different strains will be computed during forming. This leads to incorrect values of damage when compared to a pure GTN model, getting worse the higher the void volume fraction, and therefore the change in volume is. This is a principal problem of the two material models, which can be considered fundamentally incompatible. A simulation using the GTN model, simply leads to different results in terms of strains compared to e.g. the Barlat model.

To solve this problem, a correction term to the Gurson damage evolution is considered. Based on the known relation of two principal plastic strains, for incompressible models like Barlat in uniaxial tension ($-\varepsilon_1 = 2\varepsilon_2$), and the relation for arbitrary Poisson's ratio ($-\nu\varepsilon_1 = \varepsilon_2$), a correction term was derived:

$$\Delta f = c \left[(1-f) \Delta \varepsilon_q \frac{3q_2 q_1 \sigma_M f^*}{2q} \sinh\left(\frac{-3q_2 \eta p}{2\sigma_M}\right) + A \Delta \varepsilon_q \right] \quad (4.11)$$

with

$$c = \frac{4}{4 + 3q_2^2 q_1 f^* \eta} dx \quad (4.12)$$

The relation derived as equation 4.11 associates isochoric strain increments of the Barlat model to an increment of void volume fraction of the Gurson model. For the uniaxial tension case, the correction term is exact for the known appearance of the strain rate tensors of both models. For different load cases such as equibiaxial tension, this relation has to be set up separately, as no closed formulation of the correction term for arbitrary values of triaxiality η can be found. As a workaround, a correction factor S was introduced based on phenomenological findings. The correction term now reads as follows:

$$c = \frac{4}{4 + q_2^2 q_1 f^* S} \quad (4.13)$$

Using simple numerical tests of characteristic load cases, a table of correction factors S can be defined, to get a satisfactory fit of damage evolution for arbitrary values of triaxiality η . While this approach is unusual from continuum mechanics point of view, it has been implemented and tested with good results within a master thesis supervised DYNAmore and Daimler. The interested reader is referred to [10].

4.3.4 A Generalized Scalar Damage Model for Forming and Crashworthiness Simulations

In the following, the damage model GISSMO (Generalized Incremental Stress-State dependent damage MOdel), which is currently under development at Daimler will be presented. The main issues of the model are a combination of the proven features of a failure description provided by damage models for crashworthiness calculations, together with an incremental formulation for the description of material instability and localization. Yet, a user-friendly and simplified input of material parameters is intended, which will be achieved by a phenomenological formulation of ductile damage. Special attention is paid to considering the point of instability or localization, as this is a central issue in forming simulations. For crashworthiness simulations of ductile materials, the correct description of instability and localization can also greatly influence computation results.

In general, it can be expected that stress states will usually not be the same in a forming process compared to a following crash loading scenario. The model therefore includes not only the description of failure, but also functionality to provide an incremental and therefore path-dependent treatment of instability. This is needed to avoid a limitation of the traditional forming limit curve (FLC), which considers only the final state of deformation at the end of a forming process, and therefore does not take into account possible changes in strain path. Therefore the conventional FLC can not be used for multi-stage deformation processes, as which the two steps – forming and crash – of the sheet metal process chain can be considered.

In order to allow for the treatment of arbitrary strain paths in the prediction of localization and failure, incremental formulations were chosen for both. The concept is to independently accumulate a measure for forming intensity F , and a measure for damage D , respectively.

$$\Delta D = \frac{n}{\varepsilon_f} D \left(1 - \frac{1}{n}\right) \Delta \varepsilon_v \quad (4.14)$$

This equation represents a generalization of the well-known linear accumulation rule for damage as proposed by Johnson and Cook [3]. In this equation, the

exponent n allows for a nonlinear accumulation of damage until failure. This introduces a possibility to fit the model to data of multi-stage material tests. The actual equivalent plastic strain increment is denominated as $\Delta \varepsilon_v$. The quantity ε_f represents the triaxiality-dependent failure strain, which is used as a weighting function in this relation. The input of this failure strain is realized as a load curve of failure strain values vs. triaxiality, which allows for an arbitrary definition of triaxiality-dependent failure strains. This is needed to ensure flexibility when used for a wide range of different metallic materials.

As soon as the forming intensity measure F reaches unity, a coupling of accumulated damage to the stress tensor using the effective stress concept proposed by Lemaitre is initiated. When – as an input for the accumulation of forming intensity F – a curve of triaxiality-dependent material instability is used this value represents the onset of material instability and therefore the end of mesh-size convergence of results.

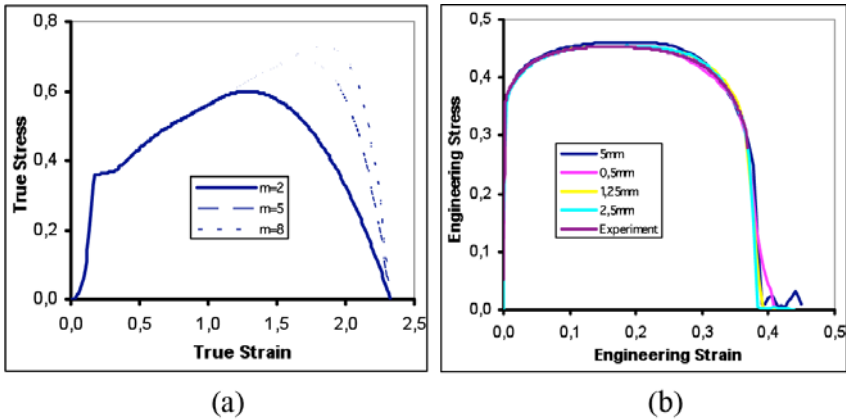


Fig. 4.4 (a) Influence of the fading Exponent m . (b) Regularization of tensile test simulations with different element sizes.

For the practical application of the model to finite element simulations with limited mesh sizes, this marks the beginning of the need for regularization of different mesh sizes. For the GISSMO model, the regularization treatment is combined with the damage model. The basic idea here is to regularize the amount of energy that is dissipated in the process of crack development and propagation. For a finite element model this results in a variation of the rate of stress reduction through element fade-out. It is achieved through a modification of Lemaitre's effective stress concept:

$$\sigma^* = \sigma \left(1 - \left(\frac{D - D_{crit}}{1 - D_{crit}} \right)^m \right) \quad (4.15)$$

for $D \geq D_{crit}$

This introduces an exponent m , which governs the rate of fading stress and can be defined depending on the actual element size.

4.4 Path-Dependent Localization

In the following methods of treating material instability or localized deformation as applied in the GISSMO model (see section 4.3.4) will be described. The basic idea is to determine the strains at the onset of localization from tests under constant stress state (proportional loading). For example, tensile tests with various notch radii, shear tests and biaxial tests can be used. The resulting forming limit curve is used as an input for the aforementioned constitutive model. Furthermore the curve is used as weighting function for the path-dependent accumulation of necking intensity up to the expected point of instability.

In general, the localization behaviour of materials in numerical simulations depends on yield locus and evolution of the yield stress. As a direct determination of yield curves from specimen tests is not possible for the post-critical range of deformation, stress extrapolation based on engineering assumptions (or models) is used. Due to this, and as a cause of the inherent mesh-dependency of results in the post-critical range, the used parameters of an extrapolation would determine the material properties in the post-critical range, and lead to mesh-dependent results. Therefore, a damage-based regularization for the post-critical range is proposed in the present contribution. A more comprehensive description of localization issues can be found in De Borst et al. [9].

A motivation for the treatment of instability is to determine the beginning of material softening, which is used as a damage threshold for the coupling of damage to the yield stress in crashworthiness applications. This will be described further in section 6.

4.4.1 Stress and Strain Measures

The traditional way of treating possible instabilities in sheet metal forming processes is the comparison of resulting strains in the final stage with a fixed curve of principal strain values (Forming Limit Curve - FLC). It is well known that the form-

ing limit curve does not take into account any changes in strain path as it considers only the final stage of deformation.

A practical approach for a strain-path dependent forming limit determination was made by Müschenborn and Sonne [5]. They proposed a transformation of the FLC from principal strain $(\varepsilon_1, \varepsilon_2)$ -space to a notation using the equivalent plastic strain ε_v :

$$\varepsilon_v = \frac{2}{\sqrt{3}} \sqrt{\varepsilon_1^2 + \varepsilon_2^2 + \varepsilon_1 \varepsilon_2} \quad (4.16)$$

The idea in treating non-proportional strain paths was to consider the FLC curve as the locus of equivalent strain to necking, depending on the respective strain state. The usual notation for crashworthiness purposes is a characterization of load state using the invariants of the stress tensor. This is sufficient for isotropic material models, since the invariant notation is independent of the respective material direction considered.

For the plane stress case, which is a common assumption for sheet metal problems, strain increments can be directly related to stress values. Therefore, the strain-based notation of the FLC can be transformed to a notation in invariants of the stress tensor. In crashworthiness computations the notation using the stress triaxiality η is common practice:

$$\eta = \frac{\sigma_m}{\sigma_v} \quad (4.17)$$

with σ_m (mean stress) being the first invariant of stress tensor here given for plane stress ($\sigma_3 = 0$):

$$\sigma_m = \frac{\sigma_1 + \sigma_2}{3} = -p \quad (4.18)$$

Furthermore σ_v is the equivalent or von Mises stress:

$$\sigma_v = \sqrt{\sigma_1^2 + \sigma_2^2 - \sigma_1 \sigma_2} \quad (4.19)$$

Using these quantities, the FLD can be directly transformed to this notation. It will be used in the following since the GISSMO model has been developed with respect to these quantities. Both strain- and stress-based notations are equivalent for the isotropic and plane stress case and proportional loading, therefore a determination of the necking locus could also be formulated in strain-based notation. Defining the ratio of principal strain increments

$$\rho = \frac{d\varepsilon_2}{d\varepsilon_1} \quad (4.20)$$

which is equal to the ratio of principal strains if proportional loading is assumed, and the ratio of principal stresses

$$\alpha = \frac{\sigma_2}{\sigma_1} = \frac{1 + 2\rho}{2 + \rho} \tag{4.21}$$

allow the expression of the triaxiality ratio η as a function of the principal strain ratio:

$$\eta = \frac{\alpha + 1}{3\sqrt{\alpha^2 - \alpha + 1}} \tag{4.22}$$

This relation is only valid for plane stress, isotropy and proportional loading. Similar transformations to a number of different notations can also be found in Bai and Wierzbicki [6]. Figure 4.5 depicts a FLC in principal strain coordinates transformed to the corresponding strain/triaxiality coordinates.

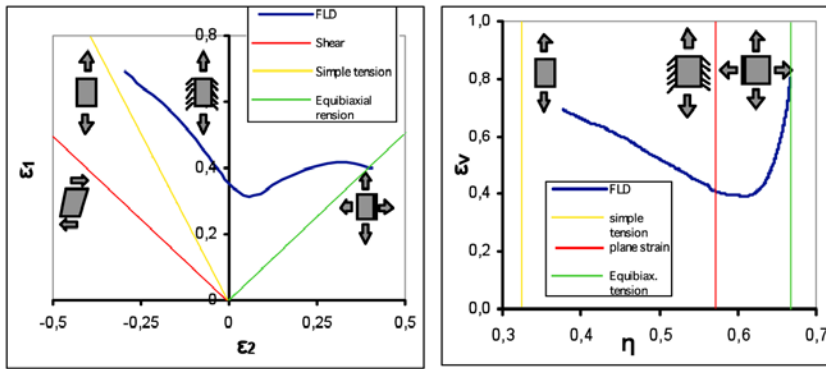


Fig. 4.5 FLC in principal strain coordinates and in strain/triaxiality coordinates.

The usual way would be to compare the actual value of accumulated equivalent plastic strain to the limit value for a respective triaxiality. This corresponds to using the principal strain notation and would inherently result in the same limitations as there is no consideration of strain path changes.

4.4.2 Linear Accumulation of the Instability Criterion

The implementation in the GISSMO model uses therefore the transformed FLC curve in coordinates of equivalent plastic strain and triaxiality as a weighting function for the accumulation of 'Forming Intensity', which, in this context, rather is a measure of the remaining formability. For this purpose the forming limit curve is introduced to the linear incremental formulation that was proposed by Johnson and

Cook [3] for the linear accumulation of damage to failure:

$$\Delta F = \frac{\Delta \varepsilon_v}{\varepsilon_{v,loc}} \quad (4.23)$$

Where $\varepsilon_{v,loc}$ is the equivalent plastic strain to localization, defined as a function of triaxiality η – see Figure 4.5. F is therefore accumulated linearly, while the function of equivalent plastic strain to necking represents a triaxiality-dependent weighting function. When F reaches unity, necking is expected to occur. Proportional loading is included as special case and leads to a necking strain that is the same as predicted by the standard FLC.

4.4.3 Nonlinear Accumulation of the Instability Criterion

Recent publications indicate a possible nonlinearity in the relation of damage and equivalent plastic strain, even for proportional strain paths. Weck et al. [7] performed measurements on a model material, that showed a rather exponential relation between strain and damage in form of void growth. It seems a reasonable assumption that the development of plastic strain up to necking also obeys a nonlinear relation, yet no method that would allow for a direct measurement of this quantity is known to the authors.

Despite this a nonlinear means of accumulation is introduced to the GISSMO model, using the same relation as for the accumulation of ductile damage to failure. An identification of parameters for this relation will hardly be possible from direct tests, rather by means of reverse engineering simulations of multi-stage forming processes. The introduction of an additional parameter n therefore allows to fit the model to existing test data.

The linear accumulation (eqn. 4.23) is replaced by

$$\Delta F = \frac{n}{\varepsilon_{v,loc}} F^{(1-1/n)} \Delta \varepsilon_v \quad (4.24)$$

introducing the accumulation exponent $n \geq 1$. For $n = 1$, eqn. 4.24 reduces to the linear form of eqn. 4.23. For proportional loading, or – in general – constant values of $\varepsilon_{v,loc}$, eqn. 4.24 can be integrated to yield a relation between the 'forming intensity' F and the equivalent plastic strain:

$$F = \left(\frac{\varepsilon_v}{\varepsilon_{v,loc}} \right)^n \quad \text{for } \varepsilon_{v,loc} = \text{const.} \quad (4.25)$$

For $n = 1$, eqn. 4.25 is a linear relation of current equivalent plastic strain and equivalent plastic strain to failure as depicted in Figure 4.6.

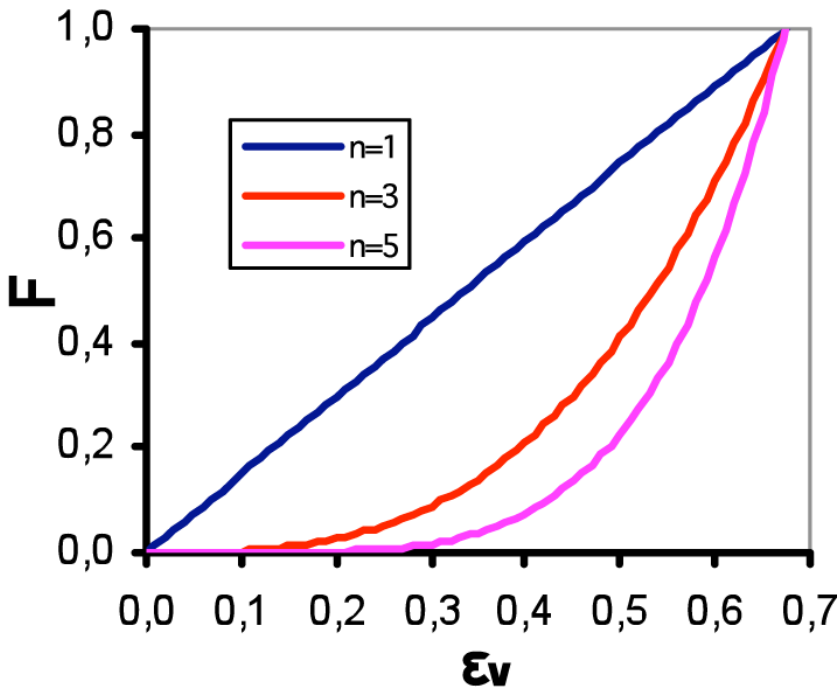


Fig. 4.6 Nonlinear accumulation $\epsilon_{v,loc} = 0.68$.

Using these relations, the forming intensity parameter F is accumulated the same way as the damage parameter D . The difference is limited to the use of a different weighting function, which is defined as a curve of limit strain depending on triaxiality for F , whereas for the failure parameter D the fracture strain as a function of triaxiality is input.

4.5 Post Critical Behaviour

The post-critical range of deformation usually is not of interest for forming simulations, since the occurrence of instability or necking phenomena are already considered as failure due to the fact that a part showing these effects will not pass quality assurance for production. However, for crashworthiness purposes it is important to

capture the post-critical behaviour of a material, since a maximum in energy absorption can be achieved only through a complete use of material ductility. The modelling of the post-critical behaviour of metals using the Finite Element Method always introduces an undesired mesh-size dependency on results. As soon as the instability develops, deformation reduces to a localized area and is no longer uniform. From this point on, no mesh convergence can be achieved. Through discretisation, an artificial length scale is introduced to the model, which will lead to unphysical results if no countermeasures are taken.

For the correct description of post-critical behaviour different flow curves for each mesh size considered would have to be used since the amount of energy that has to be dissipated in post-critical regime strongly depends on the mesh size. Instead of using this rather impractical approach the mesh-size regularization is realized through the damage formulation. Energy regularization is done through the definition of a mesh-size dependent failure strain and the coupling of damage to the stress tensor in post-critical deformation. The GISSMO model uses the effective stress concept which was proposed by Lemaitre [8].

4.5.1 Damage-Dependent Yield Stress

As was proposed by Lemaitre [8] the damage and stress tensor are related according to the effective stress concept:

$$\sigma^* = \sigma (1 - D) \quad (4.26)$$

In combination with the treatment of material instability as described above a damage threshold can be defined. As the damage parameter D reaches the damage threshold damage and flow stress will be coupled. The current implementation allows for to either entering a damage threshold as a fixed input parameter or for using the damage value corresponding to the instability point detected as described above. Either way as soon as the post-critical range of deformation is reached a value of critical damage D_{crit} is determined and used for the calculation of the effective stress tensor:

$$\sigma^* = \sigma \left(1 - \left(\frac{D - D_{crit}}{1 - D_{crit}} \right)^m \right) \quad (4.27)$$

for $D \geq D_{crit}$

Here a fading exponent m is introduced which will be further described below.

4.5.2 Energy Dissipation and Fadeout

In order to model the physical phenomena of failure, which include the formation of voids and micro-cracks, formation of a macroscopic crack, and crack propagation up to complete failure, it is necessary to take into account the amount of energy that is dissipated throughout the process. Also, for numerical reasons, it is not of help for model stability to simply delete elements which are still holding considerable amounts of stress.

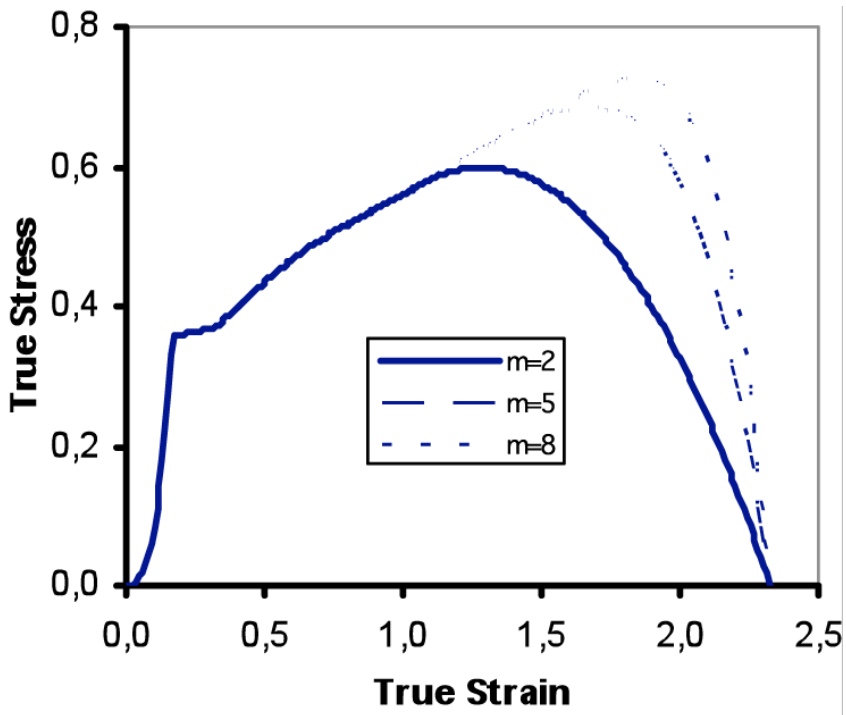


Fig. 4.7 Influence of the fading Exponent m .

The strategy followed in the GISSMO model is the definition of an element-size dependent fading exponent m , see equation (4.27). Using this coefficient, one can directly influence the amount of energy that is dissipated during element fade-out. In Figure 4.7 the effect of different values for m are shown by the area below the true stress-true strain curve.

This allows for a regularization not only of fracture strains, but also of the energy consumed during the post-critical deformation. Using this approach one can achieve

a reasonably good regularization of the resulting engineering stress-engineering strain curves in tensile tests with different mesh sizes, see figures 4.8 and 4.9.

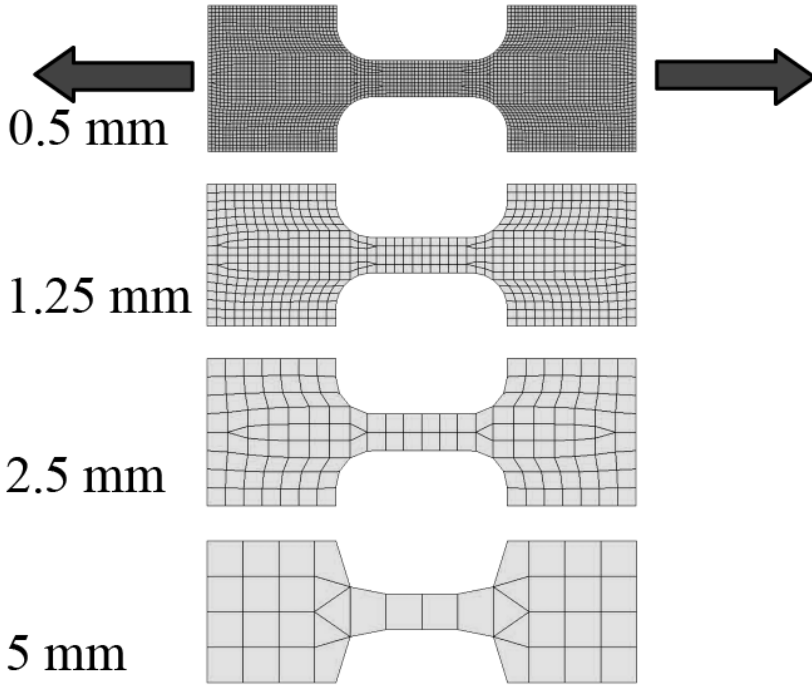


Fig. 4.8 Tensile test specimen modelled with different element sizes.

4.6 Application of a Demonstrator Part

As a demonstrator part the drawing process of a cross-die specimen is used. It provides a wide range of stress states during loading which in turn allows the control of failure predictions in wide domain that shows certain stress states. The following picture shows the computation results using artificial material parameters of dual phase steel:

In these regions, the coupling of damage and stress tensor according to equation 4.27 is used and localization develops. This leads eventually to fracture and rupture at a drawing depth of 50mm as depicted in Figure 4.11.

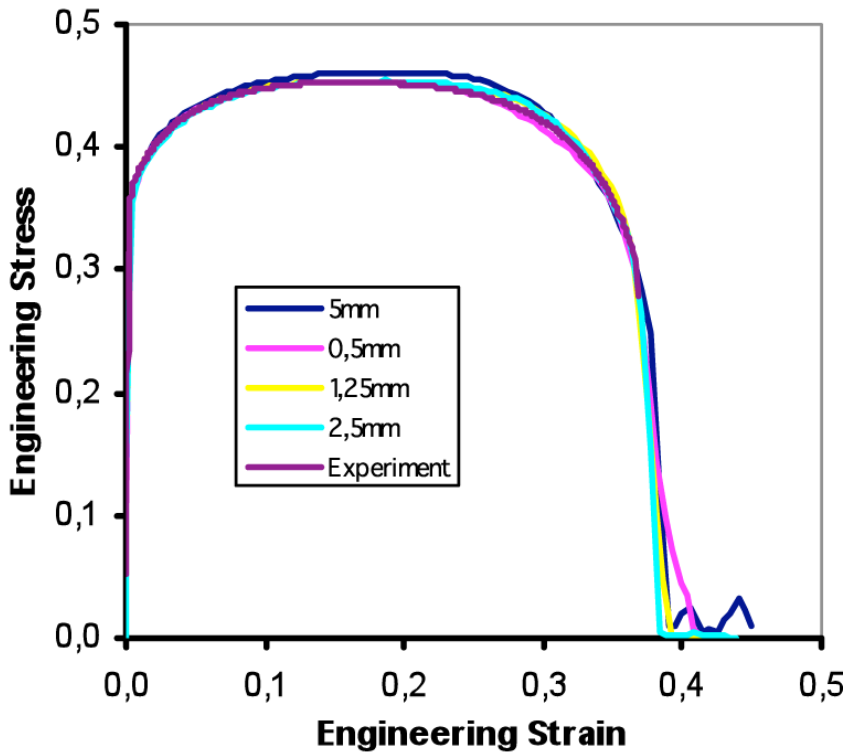


Fig. 4.9 Simulations of tensile tests using different mesh sizes compared to experimental curve.

The regions at the edge of the specimen at which the value of the damage parameter D are close to unity can be seen. The first failed elements are deleted at the front of the specimen.

4.7 Conclusions

In the present contribution the latest work on closing the constitutive gap between sheet metal forming simulations and crashworthiness have been shown. Clearly, there is much more work on the way in academia, at research institutes and other privately owned companies than shown in this paper. However, the main challenge of any model that may be applied successfully will be the ease of use and the compatibility with existing models. For many years companies spend a lot of money to calibrate material parameters of certain plasticity models by an enormous amount of test data – this holds for the forming as well as fro the crashworthiness world.

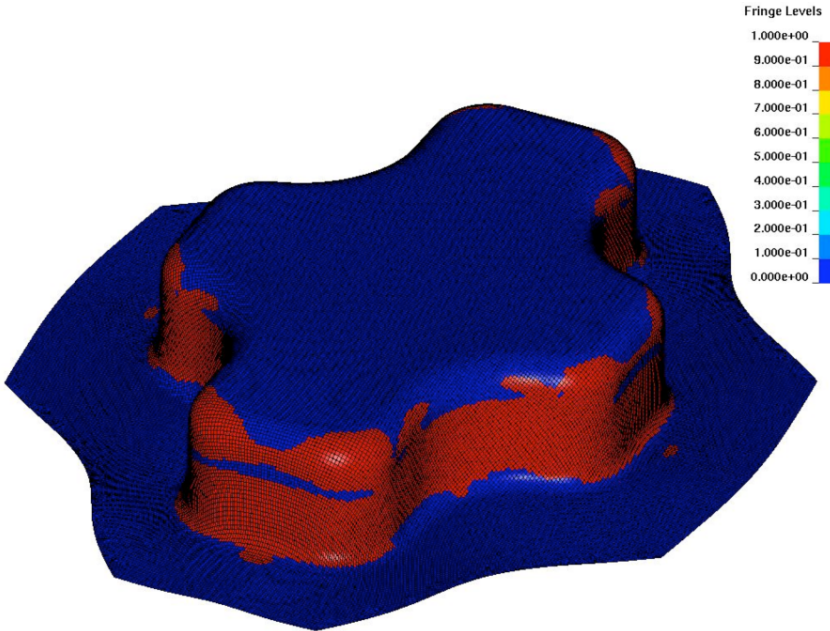


Fig. 4.10 Contour plot showing regions with beginning localisation ($F = 1$ at a drawing depth of 43mm).

Any new model must integrate this past efforts into its approach. Otherwise it will not be used simply for economical reasons.

In the present work a hybrid model has been discussed. Here the necessary data to initialize the Gurson, Tvergaard & Needleman models used in crashworthiness applications is gained by a damage formulation that mimics the evolution law of the GTN model within the forming simulation framework. While this idea is generally working, it has to be calibrated for each constitutive model that is to be used. So beside its applicability it might be too complicated to be implemented for every constitutive model in commercial finite element codes.

Alternatively a newly developed damage mode has been introduced. The present state of the GISSMO damage model as described above shows some promising potential when used for the simulation of tensile, shear and biaxial test specimen. Though phenomenologically based it introduces a number of features that might be suited to describe the physics of ductile damage and failure in a variety of stress states and for different materials. Yet, limitations in predictive performance result not only from deficiencies in material modelling, but also from coarse discretization especially in crashworthiness simulations. Further research has to be done to take modelling problems resulting from limited mesh sizes into account. Further work on

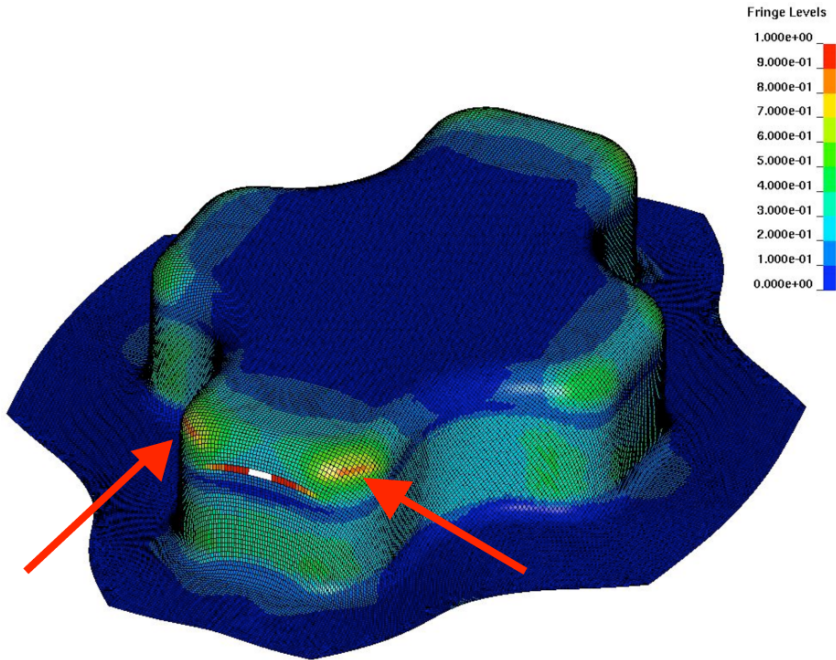


Fig. 4.11 Contour plot of damage D at the moment of crack initiation (Arrows). Drawing depth is 50mm.

the model is needed in order to extend the functionality, including a visco-plastic formulation that allows for a consideration of strain-rate effects on material behaviour. Further investigations and comparison with results from deep-drawn parts will have to be conducted to proof the practical relevance of the methods described above.

Depending on the materials, a greater number of different specimen tests will be needed to identify the parameters for the damage model. Methods of numerical optimization will have to be considered in order to allow for an effective preparation of material cards.

Acknowledgements Part of this work was supported by funds of the project 'WING' by the German Federal Ministry of Education and Research (BMBF), grant # 03X0501E.

References

1. Bridgman PW, (1952), Studies in Large Plastic Flow and Fracture, With Special Emphasis on the Effects of Hydrostatic Pressure, McGraw Hill Inc., New York.

2. Tvergaard V, Needleman A, (1984), Analysis of the Cup-Cone Fracture in a Round Tensile Bar. *Archive of Mechanics* 32, pp. 157–169.
3. Johnson GR, Cook WH, (1985), Fracture Characteristics of Three Metals Subjected to Various Strains, Strain Rates, Temperatures and Pressures. *Eng. Fracture Mechanics* 21, pp. 31–48.
4. Barlat F, Lege DJ, Brem JC, (1991), A Six-Component Yield Function for Anisotropic Materials, *Int. Journal of Plasticity* 7, pp. 693–712.
5. Müschenborn W, Sonne H-M, (1975), Influence of the Strain Path on the Forming Limits of Sheet Metal, *Arch. Eisenhüttenwesen* 46(9), pp. 597–602.
6. Bai Y, Wierzbicki T, (2008,) Forming Severity Concept for Predicting Sheet Necking Under Complex Loading Histories, *Int. Journal of Mechanical Sciences* 50, pp. 1012–1022.
7. Weck A, Wilkinson DS, Toda H, Maire E, (2006), 2D and 3D Visualization of Ductile Fracture, *Advanced Engineering Materials* 8 (6), pp. 469–472.
8. Lemaitre J, (1985), A Continuous Damage Mechanics Model for Ductile Fracture, *Journal of Engineering Materials and Technology* 107, pp. 83–89.
9. De Borst R, Sluys L J, Mühlhaus H-B, Pamin J, (1993), Fundamental Issues in Finite Element Analyses of Localization of Deformation, *Engineering Computations* 10, pp. 99–121.
10. Schmeing F, Haufe A, Feucht M, (2007), Forming and Crash Induced Damage Evolution and Failure Prediction. Part I: Extension of the Gurson Model to Forming Simulations, 6th German LS-DYNA Forum H-I-01.

Chapter 5

Cohesive Zone Modeling for Adhesives

Matthias Nossek and Stephan Marzi

Abstract Adhesives are very widely used in industry. In each application field, the adhesive that is used must fulfill specific requirements. Adhesive types can be classified for instance by their (thermo-) mechanical properties, their machining or their curing conditions. This paper describes, by way of example, the characterization criteria for structural and flexible adhesives with respect to differences in their mechanical properties under various test conditions such as loading rate or environmental temperature.

For further increased industrial application of adhesives, for example to improve the crash performance of cars, the ability to predict the mechanical behavior by numerical simulation is required. Cohesive Zone Models (CZMs) are well suited for modeling adhesives. In this paper a tri-linear, strain-rate dependent CZM is presented. This model is compared to the bi-linear, strain-rate independent model implemented in ABAQUSTM.

The parameters of these models are determined by direct testing of tensile bulk, tapered double cantilever beam, lap-shear and T-peel specimens. The model validation was carried out by comparing experiment results and simulations for a U-shaped specimen under different loading velocities. The application of these CZMs in offset crash test simulations is presented and compared to experimental data.

M. Nossek

Fraunhofer Institut für Kurzzeitdynamik, Ernst-Mach-Institut (EMI), Eckerstr. 4, D-79104 Freiburg, Germany, e-mail: Matthias.Nossek@emi.fraunhofer.de

S. Marzi

Fraunhofer Institut für Fertigungstechnik und Angewandte Materialforschung (IFAM), Wiener Str. 12, D-28359 Bremen, Germany, e-mail: Stephan.Marzi@ifam.fraunhofer.de

5.1 Introduction

The increasing use of bonded joints in the automotive industry requires the development of simulation tools, which are able to predict the mechanical behavior from initial elasticity up to failure. Typical adhesives used in car structures may differ in their mechanical properties as they have to fulfill various conditions depending on their particular function in the car structure.

The choice of the proper adhesive depends on various boundary conditions. For example, structural adhesives possess high stiffness and show elastic-plastic strain-rate dependent behavior. These adhesives are commonly applied in thin bond lines with an adhesive layer thickness below half a millimeter. In contrast, flexible adhesives may be used to fill larger gaps, where layer thicknesses of a few millimeters occur. Flexible adhesives can take high elastic strains up to several hundred percent, while their stiffness does not exceed values above a few MPa. Section 5.2 outlines the characterization procedure for two typical adhesives: the structural adhesive A and the flexible adhesive B. For the determination of material parameters, the following test types will be presented: tensile bulk, tapered double cantilever beam, lap-shear and T-peel tests. Effects of rate-dependency are considered for the structural adhesive, while the flexible adhesive is investigated at different environmental temperatures.

Cohesive zone models can be successfully used to model the fracture behavior of a bonded joint in a crash simulation. However, models available in commercial Finite-Element codes do not currently consider rate-dependencies which are observed in experimental results. Therefore a tri-linear, rate-dependent cohesive zone model is proposed in section 5.3. The model is applied for thin bond lines and the structural adhesive A.

The validation of the new model is presented in section 5.4 for a U-shaped specimen. The numerical results are compared to the experiments at different loading velocities. Furthermore, the proposed rate-dependent, tri-linear cohesive zone model is compared to the bi-linear formulation.

Finally, section 5.5 presents an application in a front car module. An offset crash test of the module is simulated using both the bi-linear and the tri-linear cohesive zone model and the results are compared with experimental observations.

5.2 Characterization Procedure

This chapter shows the mechanical characterization of two adhesives: the structural adhesive A and the flexible adhesive B. Corresponding to their field of application, the structural adhesive A is investigated for thin adhesive layers, $t_{adh} = 0.2 - 0.3 \text{ mm}$, while the flexible adhesive B is analyzed for applications consisting of thick adhesive layers, $t_{adh} = 5 \text{ mm}$. The characterization procedure used to identify the mechanical properties presented here can be separated into three groups of tests: bulk tests investigate the general mechanical properties of the adhesive,

coupon tests of adhesive joints consider the interaction with the adherend materials and fracture mechanical tests give information about the energy dissipated when a crack propagates through the adhesive layer. A typical bulk specimen which is used to determine the stiffness, Poisson's ratio, fracture strain and elastic-plastic behavior of a material is the tensile bulk specimen, which is standardized in EN ISO 527. The experimental results show significant differences in the mechanical behavior between the structural and flexible adhesive (section 5.2.1). Hence, the adhesives can first be classified by tensile bulk tests.

Besides the characterization of the pure bulk properties, the failure behavior of a bonded joint is of prime interest in a crash case. Coupon tests consider the influence of the adherends, the surface pretreatment and other manufacturing parameters on the mechanical failure behavior of the joint, as found in a real automotive structure. Since the loading of an adhesive joint can in general be separated into peel and shear, T-Peel tests characterize the peel behavior, while lap-shear samples are used to analyze the shear behavior of the joint (section 5.2.2).

The crack propagation inside the adhesive layer can be described by the critical energy release rate, which is measured in fracture mechanical tests for specific crack modes. For Mode-I this can be done with the (tapered) double cantilever beam test and for Mode-II with, for example, the end-notched flexure test or the end-loaded shear joint. Tapered double cantilever beam tests were carried out for the adhesive A and the results are given in section 5.2.3.

5.2.1 Bulk Tensile Tests

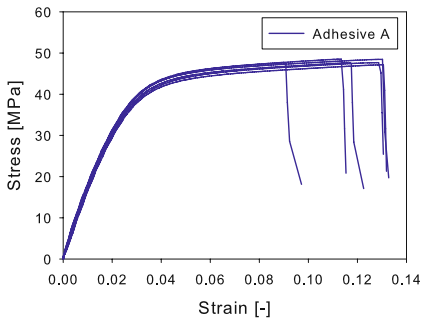


Fig. 5.1 Adhesive A: Stress-strain curves, strain rate $\dot{\epsilon} = 8.35 \text{ s}^{-1}$.

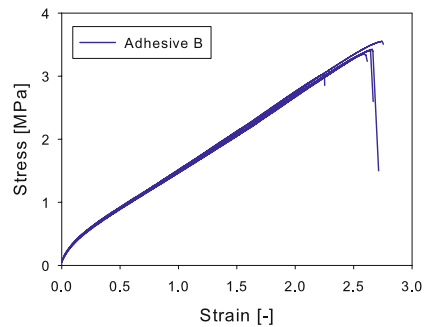


Fig. 5.2 Adhesive B: Stress-strain curves, strain rate $\dot{\epsilon} = 1.67 \text{ s}^{-1}$.

Figures 5.1 and 5.2 show strain-stress relationships for adhesive A and adhesive B obtained in tensile bulk tests under quasi-static loading conditions. The differences in the stress and strain behavior between the adhesives are clearly visi-

ble. Adhesive A behaves like a typical elastic-plastic material, with a maximum strain at failure below 15% and a yield stress above 40 MPa. The flexible adhesive B takes large elastic strains, $\epsilon_{max} \approx 250\%$, with low maximum stresses at failure, $\sigma_{max} < 4 MPa$.

5.2.2 Coupon Tests

Compared to bulk tests, specimen types such as T-Peel (Fig. 5.3) and lap-shear (Fig. 5.4) are closer to the application in automotive structures because joints with the adherend materials from the real structure are investigated. In T-Peel tests, the measured force increases until a peak load is reached and the adhesive layer starts to fail. During the failure, the force reaches some plateau value. Both peak and plateau load can be taken into account for characterization of the adhesive joint. Evaluating lap-shear tests, the maximum force which is reached is of greatest interest. After this maximum force is reached, the failure of the joint usually occurs quite fast, depending on the overlap length of the specimen.

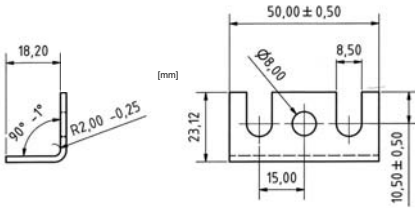


Fig. 5.3 Dimensions of a T-Peel adherend (half a specimen).

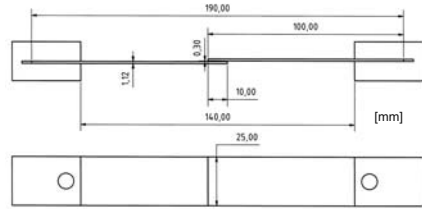


Fig. 5.4 Dimensions of the single lap-shear specimen.

For the adhesive A, T-Peel tests were carried out at two velocities, $v_{test} = 0.033 mm/s$ and $v_{test} = 2.5 mm/s$, while for the lap-shear tests the test velocities $v_{test} = 0.083 mm/s$ and $v_{test} = 7.0 mm/s$ were chosen. The coupon specimens fabricated with the flexible adhesive B were tested in a rotary impact device to obtain results at high deformation rates. The samples were conditioned at three different temperatures ($T = -30^\circ C, 23^\circ C$ and $80^\circ C$).

In the T-Peel tests, the data measured show a significant increase in the peel and the plateau force with increasing test velocity (Fig. 5.5). An increasing test velocity in lap-shear tests causes an increase in the obtained nominal shear strength (Fig. 5.6). However, the stiffness of both investigated specimen types does not depend on the test velocity.

Figures 5.7 and 5.8 show the results of the T-Peel and lap-shear tests with the adhesive B. It can be seen that the specimens conditioned at $-30^\circ C$ do not take large deformations. Comparing the samples conditioned at $23^\circ C$ and $80^\circ C$, no differences in the shape of the obtained results can be detected. The adhesive was applied on

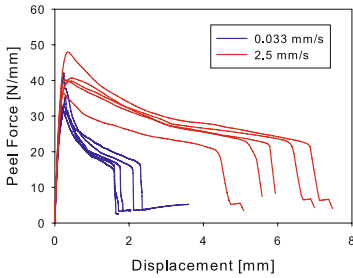


Fig. 5.5 Adhesive A: T-Peel test results.

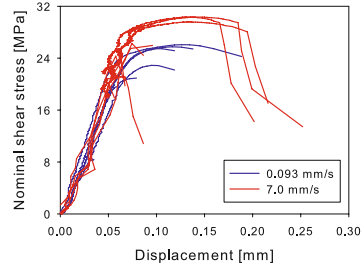


Fig. 5.6 Adhesive A: Single lap-shear test results.

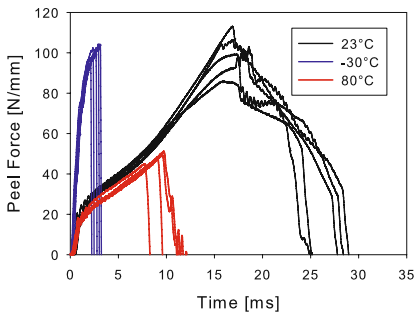


Fig. 5.7 Adhesive B: Results of dynamic T-Peel tests at different temperatures ($v_{test} = 5600\text{ mm/s}$.)

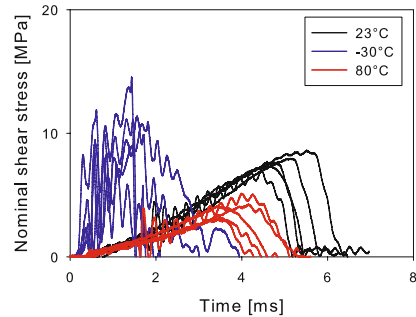


Fig. 5.8 Adhesive B: Results of dynamic single lap-shear tests at different temperatures ($v_{test} = 5600\text{ mm/s}$.)

varnished adherend surfaces. When testing specimens conditioned at 80°C , the failure occurs between the varnish and the adherend. Thus, an earlier failure is detected under hot conditions, but this failure is not caused by the adhesive properties.

5.2.3 Fracture Mechanical Tests

The critical energy release rate under Mode I loading, G_{IC} , is measured with a Tapered Double Cantilever Beam (TDCB) specimen (Fig. 5.9). The adherends consist of steel of width $w = 5\text{ mm}$.

The specimen (Fig. 5.9) is loaded until a crack starts to propagate through the adhesive layer. Then, this crack propagation is stopped by unloading the specimen and the crack area is measured on the fracture surface of the specimen after the test. G_{IC} is found by correlation of this measured crack area with the integrated force displacement curve (Fig. 5.10) as proposed in [1]. For the adhesive A, G_{IC} is somewhat insensitive to the load rate, $G_{IC} = 5.6 \pm 0.5\text{ N/mm}$ for quasi-static conditions

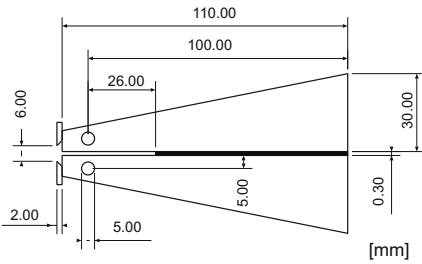


Fig. 5.9 Dimensions of TDCB specimen.

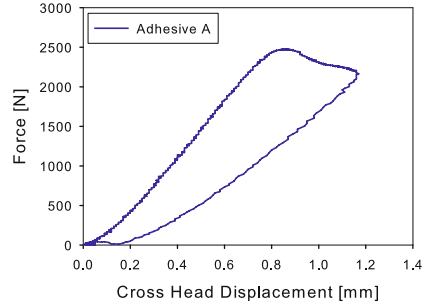


Fig. 5.10 Typical force-displacement curve obtained in a TDCB test.

and $G_{IC} = 5.0 \pm 0.3 \text{ N/mm}$ at fast test velocities. The evaluation of G_{IC} according to [1] assumes that the amount of energy additionally dissipated to form a plastic region at the crack tip prior to crack propagation is negligibly small. New investigations of Marzi et al. [2] found this assumption to be flawed when referring to the actual TDCB specimen dimensions. According to their results, the correct G_{IC} seems to be smaller, approx. 60 – 80% of the value given here.

The end-notched flexure (ENF) specimen is widely used to measure the critical energy release rate G_{IIC} under Mode-II loading. However, when investigating high strength, structural adhesives such as adhesive A, this specimen type seems to be inappropriate for several reasons. The adherends must deform purely elastically in an ENF test in order to evaluate G_{IIC} by an analytical solution. This theoretical requirement will not be satisfied when the investigated adhesives possess large fracture toughness, as expected for crash-optimized, structural adhesives. There are further disadvantages from a practical point of view. Ensuring a proper, constant adhesive thickness over the whole adhesive layer is quite difficult because of the large specimen dimensions, and the large specimen mass will cause testing problems at higher velocities. Hence, Marzi et al. [3] propose an end-loaded shear joint (ELSJ) specimen, which possesses many benefits compared to standard tests according to the state of the art. With this specimen, G_{IIC} can also be determined for high strength adhesives under both quasi-static and dynamic test conditions.

5.3 Cohesive Zone Model

From a macroscopic point of view the cohesive zone approach is well suited for modeling cohesive debonding. Finite element formulations based on this approach combine fracture mechanics with continuum damage formulations. In fracture mechanics, generally speaking, the initiation and growth of cracks is analyzed. Three types of crack modes are distinguished as shown on the right side of fig. 5.11.

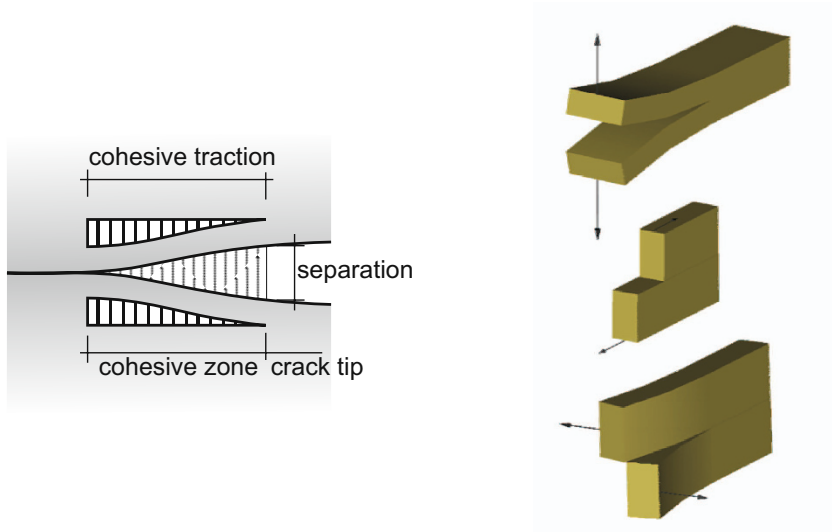


Fig. 5.11 Cohesive debonding and fracture mechanical crack modes.

In the cohesive zone model it is assumed that during crack growth a fracture process zone exists ahead of the crack tip. In that zone, micro-scale cracks or voids initiate, grow, and eventually coalesce with the main crack. All these microscopic processes dissipate energy. From a macroscopic point of view, this amount of energy is necessary to create new material surfaces. In the cohesive zone approach this energy dissipation is modeled using a relationship between cohesive traction and separation (see fig. 5.11, left). The integral of the cohesive traction over the separation until its final value δ^f determines the fracture energy or critical energy release rate (see eq. 5.1). An overview of various traction-separation relationships used in specific cohesive zone models can be found in [4].

$$G_C = \int_0^{\delta^f} \sigma d\delta \quad (5.1)$$

Cohesive zone models are suitable not only for crack modeling, but also for modeling the behavior of adhesive layers. In contrast to standard cohesive zone modeling, the approach has to be extended for adhesive modeling in order to take into account adhesive characteristics such as plasticity or strain-rate dependency. Such an extension is presented in the following sections. As a basis, the cohesive zone model of Camanho and Davila [5] implemented into AbaqusTM is used. Camanho and Davila use a bi-linear constitutive relationship between separation and cohesive traction. The interface is linear elastic until failure initiation, followed by a linear degradation for increasing separation (see Fig. 5.12). For adhesive modeling it is not necessary to distinguish between Mode-II and Mode-III. For every crack mode, three material parameters are used: stiffness ($K_i = E/t$), ultimate strength (σ_0) and

critical energy release rate (G_C). Due to the fact that negative Mode-I separation cannot cause debonding, the constitutive relationship for this type of load is purely elastic.

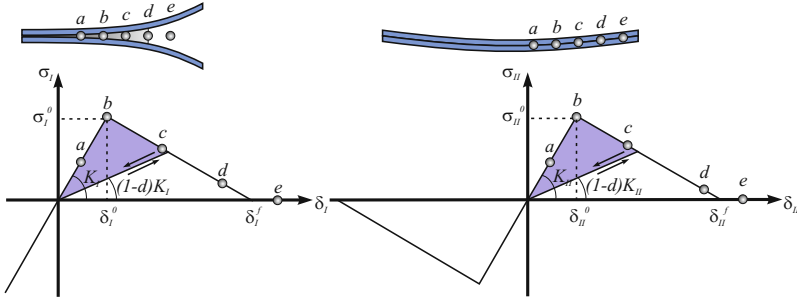


Fig. 5.12 Bi-linear constitutive relationship for crack Mode I (left) and II (right).

The points a-e in fig. 5.12 mark different states of the cohesive debonding process, from initially elastic (a) until complete failure (e). The closing and reopening of cracks before failure is modeled using cohesive tractions on line back to the origin. In the case of Mixed-Mode loading (consisting of contributions from Mode-I and Mode-II), interaction criteria for both damage initiation and crack-propagation are used. For the determination of Mixed-Mode states the quantities δ_m (Mixed-Mode separation) and β (Mixed-Mode ratio) of eq. 5.2 are used.

$$\delta_m = \sqrt{\{\delta_I\}^2 + \delta_{II}^2}, \quad 0 \leq \beta = \frac{\delta_{II}}{\{\delta_I\}} < \infty \quad (5.2)$$

$\beta = 0$ represents pure Mode-I loading, $\beta = \infty$ is pure Mode-II. In eq. 5.2, as in the following, the curly brackets denote Macaulay brackets, which take into account only positive values. For damage initiation, a normalized quadratic stress failure criterion (eq. 5.3) is used. σ_I^0 and σ_{II}^0 are material strength parameters for Mode-I and Mode-II respectively.

$$\left(\frac{\{\sigma_I\}}{\sigma_I^0}\right)^2 + \left(\frac{\sigma_{II}}{\sigma_{II}^0}\right)^2 = 1 \rightarrow \delta_m^0 = \begin{cases} \delta_I^0 \delta_{II}^0 \sqrt{\frac{1+\beta^2}{(\delta_I^0)^2 + (\beta \delta_{II}^0)^2}} & \delta_I^0 > 0 \\ \delta_{II}^0 & \delta_I^0 \leq 0 \end{cases} \quad (5.3)$$

For Mode-I, due to the Macaulay brackets, traction debonding under pressure does not occur. Based on the normalized quadratic stress interaction criterion and the initial linear elasticity, a Mixed-Mode damage initiation separation value δ_m^0 can be calculated for the current Mixed-Mode state.

After damage initiation the interaction during crack opening is modeled with the so-called Benzeggagh-Kenane (B-K) criterion [6] (eq. 5.4). The Mixed-Mode

energy release rate is always bounded by the Mode-I and Mode-II critical energy release rate. In eq. 5.4, η is the Mixed-Mode interaction coefficient.

$$G_{IC} + (G_{IIC} - G_{IC}) \left(\frac{G_{IIC}}{G_{IC} + G_{IIC}} \right)^\eta = G_C \quad (5.4)$$

Based on eq. 5.4 and the bi-linear constitutive relationship, the final Mixed-Mode separation can be calculated from eq. 5.5.

$$\delta_m^f = \begin{cases} \frac{2(1+\beta^2)}{\delta_m^0(K_I + \beta^2 K_{II})} \left[G_{IC} + (G_{IIC} - G_{IC}) \left(\frac{\beta^2 K_{II}}{K_I + \beta^2 K_{II}} \right)^\eta \right] & \delta_I > 0 \\ \delta_{II}^f & \delta_I \leq 0 \end{cases} \quad (5.5)$$

In continuum mechanical modelling, the isotropic damage model of eq. 5.6 is used.

$$\sigma_i = \left[(1-d) + \delta_{II} \frac{\{-\delta_3\}}{\delta_3} d \right] K_i \delta_i, i = I, II \quad (5.6)$$

The first summand within the square brackets controls the influence of plasticity and damage on the traction value. With the second summand this influence on the Mode-I traction is removed for negative Mode-I separation. Therefore the Macaulay bracket definition and the Kronecker-delta is used. d is the isotropic damage value. Thermodynamic consistency is assured by fulfilling eq. 5.7 which demands a non-decreasing damage value.

$$\dot{d} \geq 0 \quad (5.7)$$

For the bi-linear constitutive relationship and a current Mixed-Mode state, a trial damage value d^* is calculated from 5.8. If the trial damage value is higher than the current damage, the current damage is updated.

$$d^* = \begin{cases} 0 & \delta_m^0 > \delta_m \\ \frac{\delta_m^f (\delta_m - \delta_m^0)}{\delta_m (\delta_m^f - \delta_m^0)} & \delta_m^0 \leq \delta_m < \delta_m^f \\ 1 & \delta_m^f \geq \delta_m \end{cases} \quad (5.8)$$

With the bi-linear constitutive relationship, adhesive characteristics such as plasticity or strain-rate dependency cannot be adequately described. One possibility for phenomenological modeling of the plastic adhesive behavior is to use a tri-linear traction-separation relationship. In this simple manner, no irreversible strain components are taken into account, only their effects on the traction are modeled. Just

as in the bi-linear constitutive relationship, unloading and reloading processes are described by a line to the origin in the traction-separation diagram (Fig. 5.13).

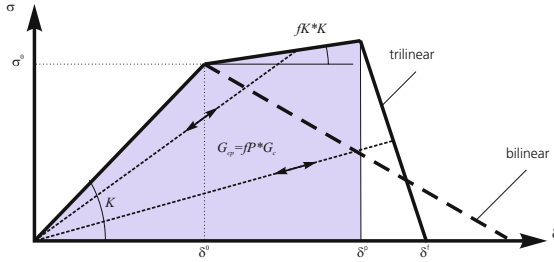


Fig. 5.13 Tri-linear constitutive traction-separation relationship.

For modeling the effects of plasticity within the tri-linear constitutive relationship, two additional parameters are used, fK and fP . Here, both are isotropic model parameters and cannot be chosen independently for every crack mode. Due to its relationship to the other material parameters (K , σ^0 and G_C), the size of the plateau region can strongly differ from Mode-I to Mode-II. In the plateau region the slope can be controlled by fK , for example using values greater than 0 for increasing stress under plastic deformation (hardening). The end of the plateau region is determined by fP . It defines the fraction of stored energy of the current separation state in relation to the critical energy release rate G_C . The strain-rate dependence on ultimate strength is modeled by a logarithmic dependency (see eq. 5.9), which is also used in other models, for example the Johnson-Cook model [7].

$$\sigma_0(\dot{\epsilon}) = \sigma_0^{qs} \left(1 + C \ln \frac{\dot{\epsilon}}{\dot{\epsilon}_0} \right) \tag{5.9}$$

The equations necessary to determine the trial damage values for the isotropic damage model in eq. 5.6 and the tri-linear constitutive relationship are given in eq. 5.10.

$$d^* = \begin{cases} 0 & \delta_m \leq \delta_m^0 \\ \frac{(\delta_m - \delta_m^0)(1 - fK)}{\delta_m} & \delta_m^0 < \delta_m \leq \delta_m^p \\ \frac{\delta_m^f(\delta_m - \delta_m^p) + (\delta_m^p - \delta_m^0)(\delta_m^f - \delta_m)(1 - fK)}{\delta_m(\delta_m^f - \delta_m^p)} & \delta_m^p < \delta_m < \delta_m^f \\ 1 & \delta_m^f \geq \delta_m \end{cases} \tag{5.10}$$

For the tri-linear constitutive relationship, fig. 5.14 shows possible states of critical traction as a limit surface over a plane of Mode-I and Mode-II separation. Along the axes, the constitutive behavior is pure Mode-I or Mode-II. In negative Mode-

I direction the limit surface extends to infinity; the response in this region is pure Mode-II.

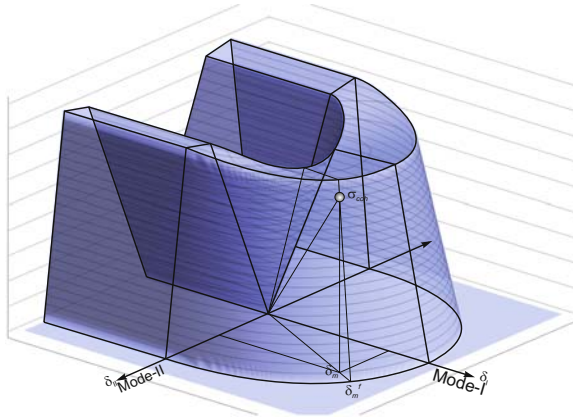


Fig. 5.14 Limit surface as traction over separation.

5.4 Validation

With respect to the application in full car simulations, the cohesive zone model is validated by a test case of intermediate complexity. The experimental setup and the numerical model are shown in fig. 5.15. In contrast to the experiments within the characterization procedure, in this test case, the states of Mixed-Mode and strain-rate in the adhesive change strongly.

The test specimen consists of a steel sheet bonded on a U-shaped steel frame. The steel sheet is loaded quasi-statically and dynamically by a hemispheric impactor. The displacement and force of the impactor were recorded. Furthermore, the behavior of the adhesive was observed by two high-speed cameras. One observed the adhesive behavior on the open front side of the cantilever, the other on the specimen side. The films are used for determining crack initiation and crack speed.

The simulations were performed with ABAQUSTM. Two different mesh sizes were investigated: an element length of 4 mm and a finer mesh of 2 mm element length. The U-shaped steel frame is modeled with reduced integrated solid elements (C3D8R), its support (see fig. 5.15, right) with shells (S4R). The material behavior of both these components is modeled as linear elastic. Reduced integrated shell elements (S4R) are also used for the steel sheet. The material of the steel sheet is modeled as elastic-plastic, strain-rate dependent and temperature dependent. For the adhesive, three-dimensional cohesive zone elements (COH3D8) are used. The constitutive adhesive behavior is modeled in two ways: Firstly with the standard bi-

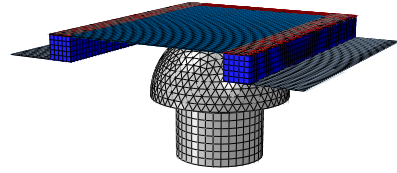
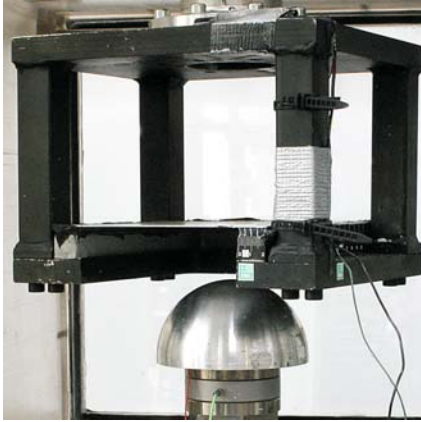


Fig. 5.15 Validation with *U-shaped* specimen: experimental setup and numerical model.

linear and strain-rate independent AbaqusTM model and secondly with the tri-linear strain-rate dependent model using a user subroutine. For the different loading velocities, independent material parameter sets were identified for the standard, strain-rate independent model from the characterization procedure.

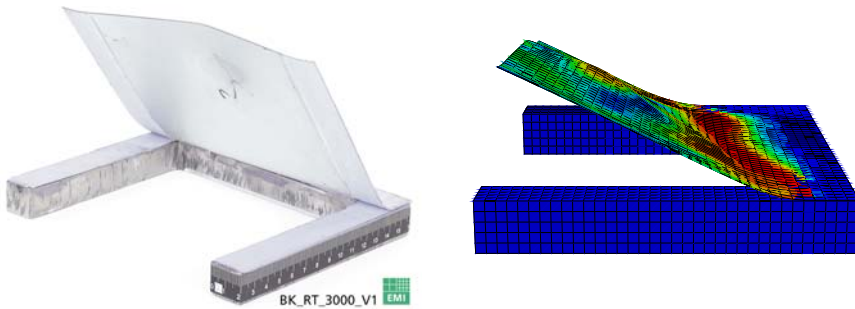


Fig. 5.16 Deformation of *U-shaped* specimen: final experimental state (left) and state during simulation.

Both experiments and simulations show crack initiation in the adhesive on the inner side of the open front of the specimen. The crack then grows slowly to the outer side. After full cracking over the cantilever width, the steel sheet is peeled from the frame and the impact force is considerably reduced. The final deformation state for an experiment is shown in fig. 5.16 (left). The right side of fig. 5.16 shows an intermediate state of deformation in the simulation. Due to the dynamic deformation process, the Mixed-Mode states and the strain-rate change strongly. The Mixed-Mode state is dominated by Mode-I on the inner side of the cantilever and changes to nearly pure Mode-II on the outer side.

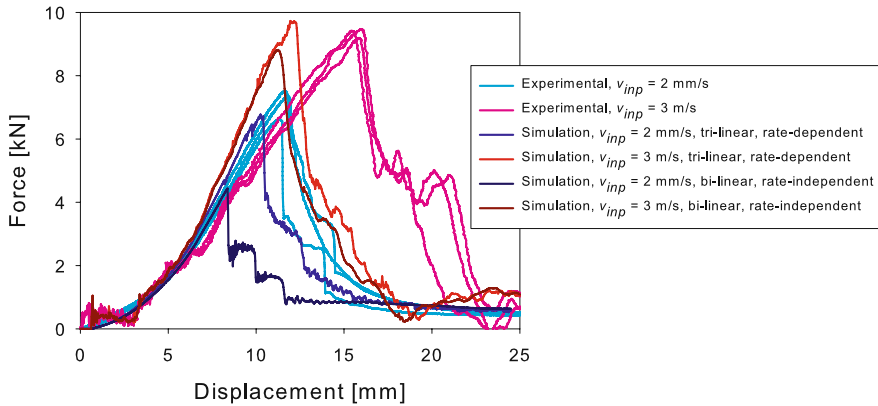


Fig. 5.17 Force-displacement diagram for experiments and simulations.

The experiments show loading-dependent maxima in the force (see fig. 5.17). It must be pointed out that at the higher loading speed there was a slight movement between frame and fixture in the experiments, resulting in a lower slope in the force-displacement diagram. The loading-speed dependent peak forces are replicated using with the tri-linear strain-rate dependent cohesive zone model. With the standard bi-linear, strain-rate independent cohesive zone model, the force maxima in the dynamic case are also predicted well, but for the quasi-static loading speed (using the quasi-static parameter set) the simulation underestimates the peak force. The reasons for this can be found in the strong local increase in the strain-rate in the adhesive just ahead of the crack tip. The resulting increase in adhesive strength cannot be modeled using the strain-rate independent model.

The global response of the specimen is quite independent of the mesh in the investigated range. Here, in general, we observed little mesh dependence in simulations with cohesive elements as long as the elements were smaller than the size of the damage process zone.

5.5 Application

The cohesive zone models presented here are used in actual crash simulation. Compared to real crash tests, the ability to make prognoses and the influence of the adhesive model are analyzed. This was done for a pre-development test car having - compared to a series production car - a high number of bond lines (shown in red in

fig. 5.18, right) and a reduced number of spot welds¹. Due to this reduction, the adhesive bond lines play a more important role in assuring the cohesion of assemblies. The test case is an offset crash, as shown in fig. 5.18.

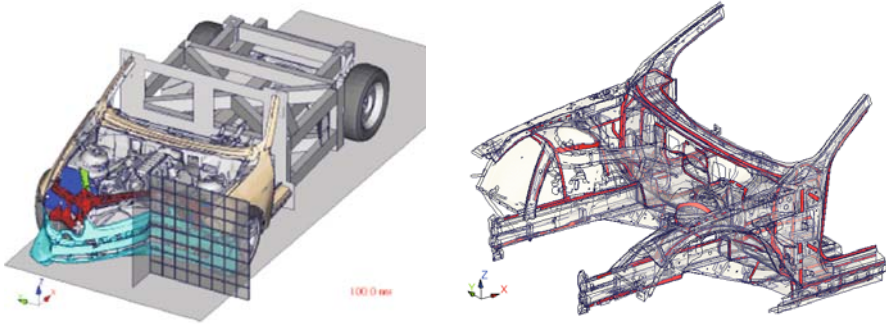


Fig. 5.18 Offset crash test of test car; Right: bond lines in test car (courtesy of BMW Group).

In the crash test, the force on the barrier and the acceleration of several points within the test car were recorded. In the simulations with ABAQUSTM, cohesive elements are used for the adhesive. Both the strain-rate independent cohesive zone model and the tri-linear strain-rate dependent cohesive zone model are used. Due to inaccuracies of the geometric model, the geometry of the cohesive layer cannot be taken from the geometric model. Instead, constant values for the adhesive thickness and width are used. This is in contrast to real production processes where, due to the joining process, small variations in thickness and width cannot be avoided. The simulation predicts the experimental force on the barrier very well, both in characteristics and maxima (see fig. 5.19, left). Comparison of the simulation results shows that the differences in the cohesive zone model (bi-linear and tri-linear) only lead to small differences in the full car test. This is evident for the force on the barrier as well as for the acceleration of gauge points in the test car.

Keeping in mind that the adhesive bond lines are essential in this pre-development test, these results show the applicability of the cohesive zone model in crash simulations. It has to be pointed out that the element size used in such a simulation is 3 to 4 mm, meaning that local deformations in flanges and the adhesive process zones can only be modeled approximately. However, the model seems to be robust enough to yield acceptable results in such cases as well. The small differences between the results for the two models show furthermore that the global solution is not very sensitive to details in the adhesive model. This is in contrast to the results obtained for the U-shaped specimen and can be explained by the limited influence of the adhesive on the global response of a full-size car. Whereas characterization tests or test

¹ The test has been performed solely for validating the crash simulation software ABAQUSTM and does not represent or suggest any actual BMW internal design criteria. The configuration tested does not represent the series production status.

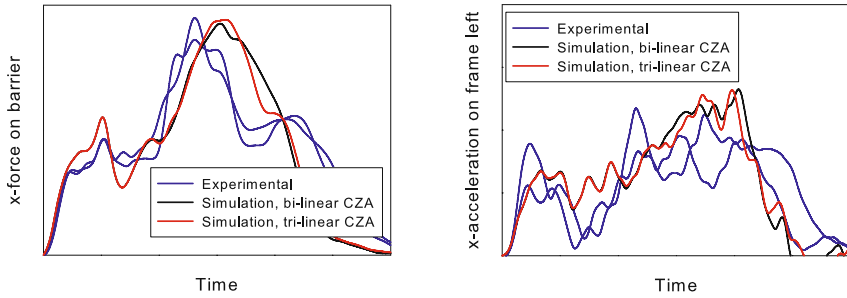


Fig. 5.19 Offset crash test: force on the barrier (left) and x-acceleration of the gauge point in the test car (courtesy of BMW Group).

cases like the U-shaped specimen are designed to be sensitive to the adhesive behavior, in large and more complex structures many other effects are also important and good results will be obtained if the cohesive zone model describes key features of the adhesive. This finding was also emphasized by a study on solution sensitivity carried out at the BMW Group. It showed a higher dependency on numerical parameters such as the type of shell element formulations or on simplifications in the geometrical modeling than on the details of the cohesive zone model, as long as two basic parameters, the critical energy release rate and the failure stress, are preserved.

The simulations can be used for predicting the high-loaded regions in the bond lines. This is shown in fig. 5.20. In this figure, intact elements are shown in green whilst failed elements are shown in red. Once again, the simulation with the tri-linear model produces similar results to the bi-linear model (not shown), with respect to the behavior of the bond lines.

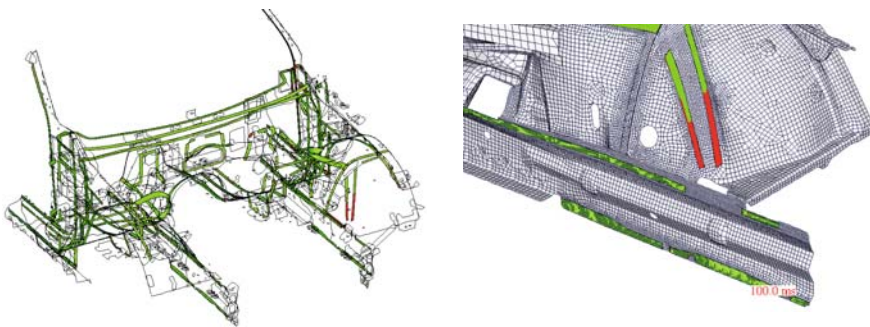


Fig. 5.20 Behavior of bond lines in a car offset crash¹; Right: detailed view on the wheelhouse and engine support (courtesy of BMW Group).

5.6 Summary

Compared to conventional joining techniques, adhesive bonds provide many advantages for industrial applications. The fields of applications range from structural adhesive joints with a bond thickness below 0.5 mm to flexible joints with a thickness of a few millimeters. Differences in the mechanical behavior of these adhesive classes were shown within the characterization. Bulk, coupon and fracture mechanical tests were carried out to investigate the influence of loading-rate, temperature or surface pretreatment on the test results. A new specimen type is described [3] for evaluating the critical energy release rate, G_{IIC} , under pure Mode-II loading of high-strength, structural adhesives.

Special numerical models are required to represent an adhesive joint within a crash simulation. The cohesive zone model is particularly well suited for modeling adhesive joints in large structures, since it provides a compromise between numerical accuracy and computational efficiency. However, as structural adhesives show elastic-plastic behavior, standard bi-linear traction-separation relationships are inadequate in some cases. A cohesive zone model with a phenomenological, tri-linear traction-separation law was presented. Additionally, the model contains strain-rate effects at the traction level.

The new cohesive zone model was validated by experiments on a U-shaped specimen, and the results were compared to results obtained with the bi-linear model. For this kind of specimen, the influence of the type of adhesive model was particularly evident from the results. Finally, both models were successfully applied in an offset crash test. Due to the minor influence of the adhesive layer on the global response, major differences do not arise. For this large structure with a high number of components, good results were obtained with both cohesive zone models. For cases where the behavior of the adhesive influences the global response more strongly, a detailed description including the effects of strain-rate and plasticity is now available.

Acknowledgements The authors acknowledge the contributions from H. Werner (BMW Group) to this paper. Furthermore we thank O. Hesebeck, O. Klapp (Fraunhofer IFAM) and M. Sauer (Fraunhofer EMI) for their support.

References

1. Brede M, Heise F-J (2008) Methodenentwicklung zur Berechnung von höherfesten Stahlklebverbindungen des Fahrzeugbaus unter Crashbelastung. FOSTA-project P676, Düsseldorf.
2. Marzi S, Hesebeck O, Brede M, and Kleiner F (2009) A rate-dependent cohesive zone model for adhesive layers loaded in mode I, J. Adh. Sc. Tech. 23:881–898
3. Marzi S, Hesebeck O, Brede M, and Kleiner F (2009) An end-loaded shear joint (ELSJ) specimen to measure the critical energy release rate of tough, structural adhesives in mode II, J. Adh. Sc. Tech., submitted for publication.
4. Alfano G (2006) On the influence of the shape of the interface law on the application of cohesive zone models, CST, 66:723–730.

5. Camanho PP and Davila CG (2002) Mixed-mode decohesion elements for the simulation of delamination in composite materials, NASA TM-2002-211739.
6. Benzeggagh ML and Kenane M (1996) Measurement of mixed-mode delamination fracture toughness of unidirectional glass/epoxy composites with mixed-mode bending apparatus, CST 56:439–449.
7. Johnson GR and Cook WH (1983) A constitutive model and data for metals subjected to large strains, high strain rates and high temperatures, Proceedings International Symposium on Ballistics.

Chapter 6

Modeling the Plasticity of Various Material Classes with a Single Quadratic Yield Function

Markus Wicklein

Abstract In this paper, a general quadratic yield function is discussed, which was originally proposed by Chen et al for fiber-reinforced composites [1]. Its applicability to plastically deformable foams, honeycombs, and CFRP (carbon fiberreinforced plastic) is shown. For isotropic elastic-plastic foams it is proven, that the ellipsoid model is a special case of Chen's quadratic yield function, and the according plasticity coefficients are determined analytically. The applicability to aluminum honeycombs is demonstrated by simulation of 4-point bending tests of sandwich structures. Both analytical and experimental procedures are utilized for the derivation of the plasticity coefficients of the honeycomb core. Hypervelocity impact tests on CFRP and numerical simulations are presented as validation of the modeling approach to this kind of material. Finally, suggestions are given for further developments of the plasticity model that could overcome existing limitations.

6.1 Introduction

Since Tresca's pioneering work in the 19th century, the importance of plasticity theory for understanding the deformation behavior of solid materials has continuously grown. With the establishment of the finite-element method and its realization on computer systems in the second half of the 20th century, plasticity modeling has become a standard for engineers to evaluate structures under mechanical loading. Today, the number of plasticity models available for constitutive modeling of materials under crash and impact is enormous and keeps increasing with new materials being developed almost every day. Therefore, it is worthwhile to consider theoretical yield functions, which offer general mathematical descriptions that allow to model different materials or even different classes of materials only by changing the

Markus Wicklein

Fraunhofer Institute for High-Speed-Dynamics, Ernst-Mach-Institut, EMI, Eckerstr. 4, 79104 Freiburg, Germany, e-mail: Markus.Wicklein@emi.fraunhofer.de

parameter sets. However, usually the number of material constants in a plasticity model increases with increasing flexibility and generality. Before applying such a model, all parameters must be determined – from theory, experiment, or numerical simulations. Hence, the generality of the model has to be traded off against the effort of parameter identification.

In this paper, a general quadratic yield function is discussed, which was originally proposed by Chen et al for fiber-reinforced composites [1]. Its applicability to plastically deformable foams, honeycombs, and CFRP (carbon fiber-reinforced plastic) is shown. Each of these materials is heterogeneous – only on different scales. For example, the cell size in a foam may be a few millimeters, while the diameter of a fiber in a composite can be as small as a few micrometers. Nevertheless, these materials can be considered as homogeneous continua if the spatial load distribution changes slowly, compared to the materials' characteristic lengths. This is true for the applications regarded in this paper. If this condition is not fulfilled, microscopic and mesoscopic approaches are necessary. There are many publications on such studies to be found.

Evaluating existing plasticity models, two important distinctions become obvious: the symmetry of the material (isotropic or anisotropic) and its plastic compressibility (constant or non-constant volume plasticity). If we combine these two criteria, a matrix of four different material classes can be established (Figure 6.1).

It is generally accepted that cast metals are isotropic and do not change their volume under purely plastic deformation, i. e. if no microporosity exists. Constant volume plasticity is also a good approximation for extruded metals and sheet metals. However, the material properties are anisotropic due to the extrusion or rolling process. Many different manufacturing routes are available for metal foams. Depending on the quality of the process, anisotropies can be induced in the foam. However, metal foams are usually considered as isotropic – especially, when compared to honeycombs, where the mechanical properties in the out-of-plane direction are radically different from those within the plane. Because of the cellular structure of foams and honeycombs, volume changes are possible under plastic deformation in contrast to non-porous metals.

In Figure 6.1 only one example is given for each of the four material classes. However, there are many other materials that are actually included in each class. Metallic materials were discussed above, but polymers can be considered as well. Although the physical processes on the atomistic scale are completely different in polymers compared to metals, the description of polymers through yield functions can be of advantage for many engineering applications.

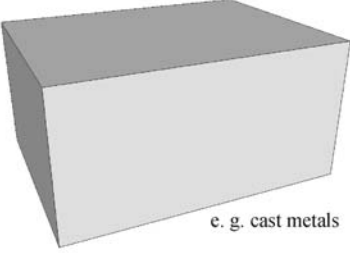
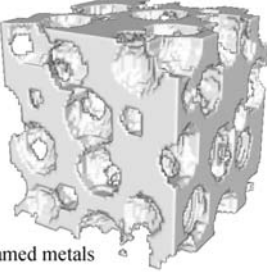
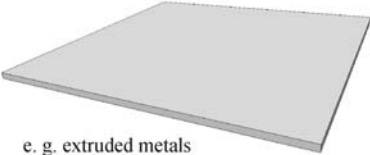
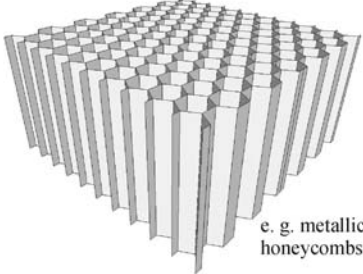
	Constant volume plasticity	Non-constant volume plasticity
Isotropic	 <p>e. g. cast metals</p>	 <p>e. g. foamed metals</p>
Anisotropic	 <p>e. g. extruded metals</p>	 <p>e. g. metallic honeycombs</p>

Fig. 6.1 Classification of plastically deformable materials. Examples are given for each combination of isotropic/anisotropic behavior and constant/non-constant volume plasticity, respectively.

6.2 A Quadratic Yield Function

The yield function proposed by Chen et al [1] is quadratic in the components of the stress tensor referring to the principal directions 1, 2, and 3 of an orthotropic material:

$$\begin{aligned}
 f(\sigma_{ij}) = & a_{11}\sigma_{11}^2 + a_{22}\sigma_{22}^2 + a_{33}\sigma_{33}^2 + \\
 & + 2a_{12}\sigma_{11}\sigma_{22} + 2a_{23}\sigma_{22}\sigma_{33} + 2a_{13}\sigma_{11}\sigma_{33} + \\
 & + 2a_{44}\sigma_{23}^2 + 2a_{55}\sigma_{31}^2 + 2a_{66}\sigma_{12}^2 = k
 \end{aligned}
 \tag{6.1}$$

It is defined by ten material parameters. The nine plasticity coefficients a_{11}, \dots, a_{66} determine the shape of the yield surface in stress space. Its size is given by the hardening parameter k . The plasticity coefficients are assumed to be constant. Thus, by changing the value of k , isotropic hardening or softening can be modeled.

With the assumption of an associated flow rule ($d\lambda$ is a non-negative scalar factor of proportionality)

$$d\epsilon_{ij}^p = d\lambda \frac{\partial f}{\partial \sigma_{ij}} \tag{6.2}$$

and insertion of the yield function (6.1), the increments of plastic strain can be calculated:

$$\begin{pmatrix} d\epsilon_{11}^p \\ d\epsilon_{22}^p \\ d\epsilon_{33}^p \\ d\epsilon_{23}^p \\ d\epsilon_{31}^p \\ d\epsilon_{12}^p \end{pmatrix} = \begin{pmatrix} a_{11}\sigma_{11} + a_{12}\sigma_{22} + a_{13}\sigma_{33} \\ a_{12}\sigma_{11} + a_{22}\sigma_{22} + a_{23}\sigma_{33} \\ a_{13}\sigma_{11} + a_{23}\sigma_{22} + a_{33}\sigma_{33} \\ 2a_{44}\sigma_{23} \\ 2a_{55}\sigma_{31} \\ 2a_{66}\sigma_{12} \end{pmatrix} \cdot 2d\lambda \tag{6.3}$$

As we consider isotropic hardening, the hardening process can be described by a single master curve using a function of the effective stress in terms of the effective plastic strain. These values are given for uniaxial tensile loading in the 1-direction of the material by

$$\bar{\sigma} \equiv \sqrt{\frac{3}{2}}f = \sqrt{\frac{3a_{11}}{2}}|\sigma_{11}| \tag{6.4}$$

and

$$\bar{\epsilon}^p = \sqrt{\frac{2}{3}}|\epsilon_{11}^p| \quad \text{with} \quad \epsilon_{11}^p = \epsilon_{11} - \frac{\sigma_{11}}{E_{11}}, \tag{6.5}$$

respectively. E_{11} is the corresponding Young's modulus of the material in 1-direction.

Chen et al [1] stated that the plasticity coefficients of the yield function (6.1) can be chosen in such a way that it reduces either to the criterion proposed by von Mises [9] or by Hill [6]. The first two columns of table 6.1 show the coefficients for these two plasticity models, which can be applied for example to cast metals and extruded metals, respectively.

Table 6.1 Specification of plasticity parameters of the general yield function for various materials.

	Cast metals	Extruded metals	Foamed metals honeycombs	Metallic CFRP	
	Ref. [9]	Ref. [6]	6.3	Ref. [8]	Ref. [10]
a_{11}	2/3	a_{11}	a_{11}	1	0.025
a_{22}	2/3	a_{22}	a_{11}	158	1
a_{33}	2/3	a_{33}	a_{11}	158	0.660
a_{12}	-1/3	$a_{33} - (a_{11} + a_{22} + a_{33})/2$	$a_{11} - 3/2$	0	-0.129
a_{23}	-1/3	$a_{11} - (a_{11} + a_{22} + a_{33})/2$	$a_{11} - 3/2$	0	-0.473
a_{13}	-1/3	$a_{22} - (a_{11} + a_{22} + a_{33})/2$	$a_{11} - 3/2$	0	0
a_{44}	1	a_{44}	3/2	50	3.157
a_{55}	1	a_{55}	3/2	3.1	2.128
a_{66}	1	a_{66}	3/2	0.5	0.061

Note that the hardening parameter k is not included in the table. It is treated as a free variable in this paper. For the von Mises model, all plasticity coefficients are quantitatively fixed, implying that the shape of the yield surface cannot be varied. Nevertheless, its size changes with k , which can be related to a uniaxial yield stress. As the von Mises criterion can be written as a function depending only on the second invariant of the stress deviator tensor, it is an isotropic plasticity model. Its plastic incompressibility can be shown by evaluating the plastic strain increments (6.3). The relative plastic volume change during deformation is given by [2]:

$$\frac{dV}{V} = d\epsilon_{ii}^p \tag{6.6}$$

Insertion of (6.3) into (6.6) yields

$$\frac{dV}{V} = [(a_{11} + a_{12} + a_{13})\sigma_{11} + (a_{12} + a_{22} + a_{23})\sigma_{22} + (a_{13} + a_{23} + a_{33})\sigma_{33}]2d\lambda \tag{6.7}$$

Using the plasticity coefficients of the von Mises model, the dilatation is zero for any stress state, and constant volume plasticity is proven.

In the case of Hill (see table 6.1), six independent plasticity coefficients are available, i. e. $a_{11}, a_{22}, a_{33}, a_{44}, a_{55},$ and a_{66} . The coupling coefficients $a_{12}, a_{23},$ and a_{13} are functions of these. It is obvious that the Hill model is generally anisotropic. The plastic incompressibility can be proven similarly as in von Mises' case.

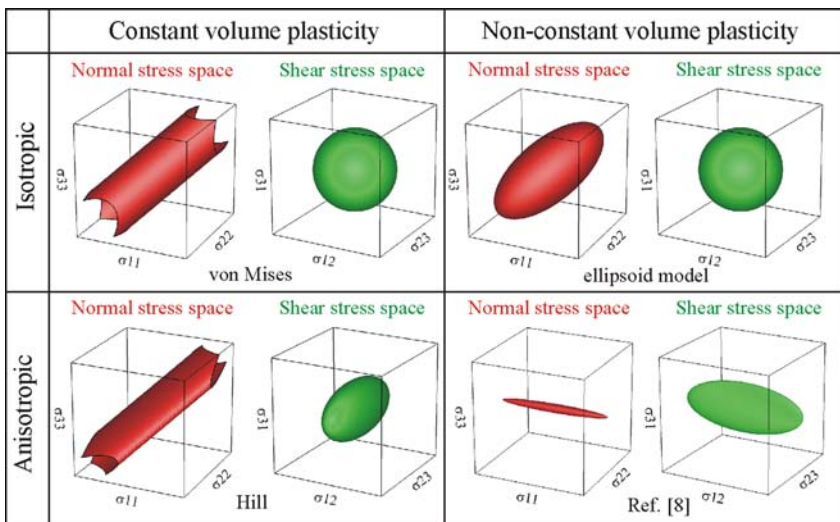


Fig. 6.2 Typical yield surfaces for the material classes defined in Fig. 1.1 in normal and shear stress space, respectively. For non-constant volume plasticity, the yield surfaces in normal stress space are closed.

The parameter set for foams in table 6.1 will be discussed in detail in section 6.3. The values for metallic honeycombs and CFRP were derived by Spinner and Wicklein [8] and Wicklein et al [10], respectively. Some of the results of those studies will be outlined in sections 6.4 and 6.5.

The yield functions of the different material classes correspond to yield surfaces in six-dimensional stress space, which are impossible to plot. Therefore, they are visualized in Fig. 6.2 by separate surfaces in normal stress space (shear stresses set to zero) and shear stress space (normal stresses set to zero). The von Mises yield surface in normal stress space is the famous hollow cylinder with the hydrostatic axis as center of its rotational symmetry. In shear stress space, we obtain the surface of a sphere centered at the origin of the coordinate system. The anisotropy of Hill's theory results in deformations of the von Mises yield surfaces in the different material directions.

6.3 Parameter Identification for Foams

The total elastic strain energy per unit volume W of a linear elastic, isotropic material is given by [2] :

$$W = \frac{1+\nu}{E} J_2 + \frac{1-2\nu}{6E} I_1^2 \quad (6.8)$$

Here, ν is the elastic Poisson number, E the Young's modulus, J_2 the second invariant of the stress deviator tensor, and I_1 the first invariant of the stress tensor. The first term is the distortional energy, while the second one describes the dilatational energy. For the modeling of isotropic materials, the von Mises equivalent stress σ_{vM} and the hydrostatic pressure p are more common quantities to be used than the invariants. They are defined as

$$\sigma_{vM} = \sqrt{3J_2} \quad (6.9)$$

and

$$p = \frac{I_1}{3} \quad (6.10)$$

Thus, equation (6.8) becomes

$$W = \frac{1+\nu}{3E} \sigma_{vM}^2 + \frac{3-6\nu}{2E} p^2 \quad (6.11)$$

If we assume that, in an isotropic material, plastic deformations occur, when W reaches a critical value, equation (6.11) can be interpreted as a yield function. And, because it takes into account both the distortional and the dilatational energy, it is a yield criterion for plastically compressible materials. Indeed, by rearranging (6.11),

the ellipsoid model for elastic-plastic foams, of which different versions were reviewed by Hanssen et al [5], is found

$$\left(\frac{\sigma_{vM}}{a}\right)^2 + \left(\frac{p}{b}\right)^2 = 1 \quad (6.12)$$

with the two material constants a and b . Note that the von Mises model can be derived likewise by neglecting the dilatational contribution. As Chen's yield function (6.1) and the ellipsoid model (6.12) are both quadratic functions of the stresses, it will be examined in the following whether or not the ellipsoid model is a special case of the general yield function (6.1). If this applies, it will be possible to determine the plasticity coefficients a_{ij} in terms of the material constants a and b . For the purpose of comparison and as the general yield function is given in [stress²], we rewrite (6.12):

$$\sigma_{vM}^2 + \left(\frac{a}{b}\right)^2 p^2 = a^2 \quad (6.13)$$

Using

$$\sigma_{vM}^2 = \frac{1}{2} \left[(\sigma_{11} - \sigma_{22})^2 + (\sigma_{22} - \sigma_{33})^2 + (\sigma_{33} - \sigma_{11})^2 \right] + 3\sigma_{12}^2 + 3\sigma_{23}^2 + 3\sigma_{31}^2 \quad (6.14)$$

which is identical to

$$\sigma_{vM}^2 = \sigma_{11}^2 + \sigma_{22}^2 + \sigma_{33}^2 - \sigma_{11}\sigma_{22} - \sigma_{22}\sigma_{33} - \sigma_{11}\sigma_{33} + 3\sigma_{12}^2 + 3\sigma_{23}^2 + 3\sigma_{31}^2 \quad (6.15)$$

and

$$p^2 = \frac{1}{9} (\sigma_{11}^2 + \sigma_{22}^2 + \sigma_{33}^2 + 2\sigma_{11}\sigma_{22} + 2\sigma_{22}\sigma_{33} + 2\sigma_{11}\sigma_{33}) \quad (6.16)$$

the ellipsoid model becomes

$$\begin{aligned} & \left(1 + \frac{1}{9} \left(\frac{a}{b}\right)^2\right) \sigma_{11}^2 + \left(1 + \frac{1}{9} \left(\frac{a}{b}\right)^2\right) \sigma_{22}^2 + \left(1 + \frac{1}{9} \left(\frac{a}{b}\right)^2\right) \sigma_{33}^2 + \\ & + \left(\frac{2}{9} \left(\frac{a}{b}\right)^2 - 1\right) \sigma_{11}\sigma_{22} + \left(\frac{2}{9} \left(\frac{a}{b}\right)^2 - 1\right) \sigma_{22}\sigma_{33} + \left(\frac{2}{9} \left(\frac{a}{b}\right)^2 - 1\right) \sigma_{11}\sigma_{33} + \\ & + 3\sigma_{23}^2 + 3\sigma_{31}^2 + 3\sigma_{12}^2 = a^2 \end{aligned} \quad (6.17)$$

A comparison of equations (6.17) and (6.1) shows that the ellipsoid model is a special case of the general yield function. The relations between the plasticity coefficients, the hardening parameter k , and the material constants a and b are:

$$a_{11} = a_{22} = a_{33} = 1 + \left(\frac{a}{3b}\right)^2 \quad (6.18)$$

$$a_{12} = a_{23} = a_{13} = \left(\frac{a}{3b}\right)^2 - \frac{1}{2} \quad (6.19)$$

$$a_{44} = a_{55} = a_{66} = \frac{3}{2} \quad (6.20)$$

$$k = a^2 \quad (6.21)$$

Insertion of (6.18) into (6.19) yields

$$a_{12} = a_{11} - \frac{3}{2} \quad (6.22)$$

as documented in table 6.1. Hence, when elastic-plastic foams are to be modeled with the yield function (6.1), a_{11} and k are the only free parameters. While a and b define the half axes of the ellipsoid (see Fig. 6.2, normal stress space), a_{11} and k determine its aspect ratio and size, respectively. The isotropy of the ellipsoid model is self-evident, because the derivation was based on the energy W of isotropic materials only. The relative plastic volume change (6.7) for this foam model is:

$$\frac{dV}{V} = 6d\lambda (a_{11} - 1) (\sigma_{11} + \sigma_{22} + \sigma_{33}) = 18d\lambda (a_{11} - 1)p \quad (6.23)$$

As a and b are positive, a_{11} is greater than 1 (see equation (6.18)). Therefore, the plastic volume change is unequal to zero, if the hydrostatic pressure and $d\lambda$ are unequal to zero.

6.4 Application to Honeycombs

The most complex material class of those presented in Fig. 6.1 is the combination of anisotropy and non-constant volume plasticity. Aluminum honeycombs are examples of this class. They are being used as core materials in sandwich structures, where high stiffness and low weight are necessary, e. g. in the aerospace industry. On the other hand, their plastic compressibility makes them attractive for applications where energy absorption is required. In the Apollo lunar module, for example, aluminum honeycombs were already used in the primary struts for energy absorption during landing [7]. In the automotive industry, their use as crash barriers is well established. Protection of buildings against blast waves is another promising application of aluminum honeycombs, see for example [3].

In [8] the applicability of the yield function (6.1) to regular aluminum honeycombs was shown, it will be shortly summarized in the following. The 1-axis of the material coordinate system was defined in the out-of-plane direction of the honeycombs. Compression tests in 1-direction were used to determine the master hardening curve. The coefficient a_{11} can be set to 1 without loss of generality, when the initial value of k is adjusted to the results of the compression tests. Choosing another value for a_{11} would also be possible, if the new value for k is chosen correspondingly. The initial effective stress of the master curve $\bar{\sigma}_{\#1}$ could be determined

from the compressive yield stress with equation (6.4). No experimental data was available in the 2-direction. Therefore, the analytical approximation by Gibson and Ashby [4] was applied. There, the yield stress in 2-direction of a honeycomb with double thickness vertical walls is given in terms of the cell wall thickness t , its length l , the characteristic angle θ , and the yield stress of the solid cell wall material σ_S^y .

$$\sigma_{22}^y = \left(\frac{t}{l}\right)^2 \frac{1}{2 \cos^2(\theta)} \sigma_S^y \quad (6.24)$$

For regular honeycombs $\theta = 30^\circ$. We can now calculate a_{22} from the fact that this initial yield stress must correspond to the initial effective stress of the master curve (see equation (6.4)).

$$\bar{\sigma}_{\#1} = \sqrt{\frac{3a_{22}}{2}} |\sigma_{22}^y| \quad (6.25)$$

For regular honeycombs, the plasticity coefficients a_{22} and a_{33} are identical. The coupling coefficients can be derived from the plastic Poisson numbers of the honeycomb. For example, let us consider a uniaxial compressive loading in 1-direction. Equation (6.3) becomes:

$$\begin{pmatrix} d\varepsilon_{11}^p \\ d\varepsilon_{22}^p \\ d\varepsilon_{33}^p \\ d\varepsilon_{23}^p \\ d\varepsilon_{31}^p \\ d\varepsilon_{12}^p \end{pmatrix} = \begin{pmatrix} a_{11}\sigma_{11} \\ a_{12}\sigma_{11} \\ a_{13}\sigma_{11} \\ 0 \\ 0 \\ 0 \end{pmatrix} \cdot 2d\lambda \quad (6.26)$$

For loading in 1-direction, plastic strains perpendicular to the loading direction can be neglected for aluminum honeycombs. Thus, a_{12} and a_{13} must be zero. The shear coefficients can be calculated following an approach similar to equation (6.25). The complete parameter set is included in table 6.1. The yield surface for the honeycombs in normal stress space (Fig. 6.2) is a very elongated ellipsoid aligned in the 11-direction. The elongation results from the high yield stress in the out-of-plane direction compared to all in-plane directions. The reasons for its orientation along the 11-axis are the vanishing plastic Poisson ratios and the assumption of an associated flow rule. For uniaxial loading, the direction of plastic flow (perpendicular to the yield surface) must not have components in any other direction.

The validation of the plasticity model was done by simulation of 4-point bending tests of sandwich structures with CFRP face sheets with different support distances. Details of the sandwich structures are described in [10]. Fig. 6.3 illustrates the deformations of a sandwich in both experiment and simulation with the finite-element code ANSYS[®] AUTODYN[®].

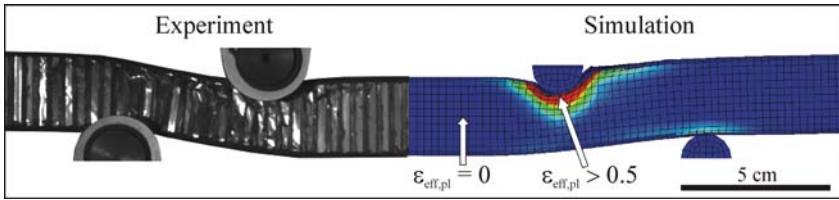


Fig. 6.3 4-point bending test of a sandwich structure with CFRP face sheets and aluminum honeycomb core. Contours of effective plastic strain are given in the simulation plot.

Compressive and shear loading dominate in the honeycomb core. Localization of the deformation can be observed in the contour plot of the simulation. The quantitative results are summarized in Fig. 6.4. The force diagram of the experiment (Fig. 6.4 a) shows an initial elastic regime followed by a peak and an almost constant plateau. The force peak which was also observed under uniaxial compression, cannot be modeled in the simulation, because the master curve in the applied FE-code can only reproduce continuously increasing yield stresses. The overall predicted force level of the simulation is satisfying. However, strong oscillations of the simulated force are visible. One explanation for this is the limited modeling of the CFRP face sheets for this loading scenario. In the experiment, the plates fail under in-plane compression, which was not modeled in [10]. For crash applications of aluminum honeycombs, it is important to predict the amount of absorbed energy correctly. Fig. 6.4 b) proves that this was achieved in the simulation.

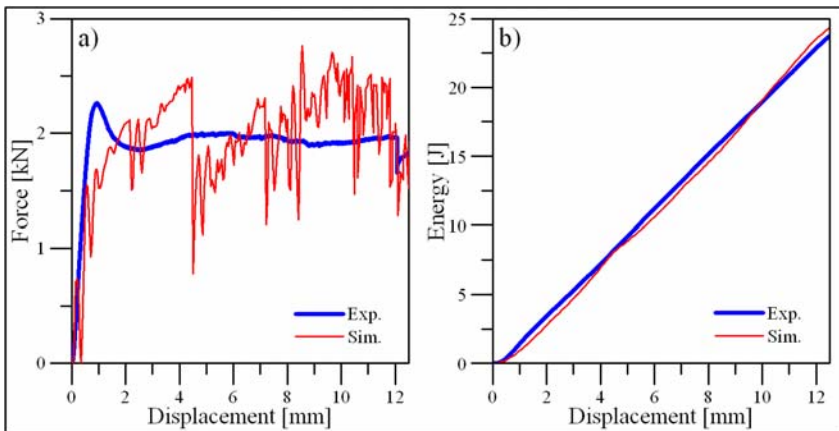


Fig. 6.4 Comparison of experimental and numerical results for the 4-point bending test from 6.3. a) Force-displacement diagram. b) Absorbed energy.

6.5 Application to Carbon Fiber-Reinforced Plastics

For modeling purposes, the mechanical behavior of CFRP is usually represented by a combination of elasticity, damage, and failure models. Nevertheless, in reality, irreversible plastic deformations can occur. They are usually much smaller than for the materials shown in Fig. 6.1. Sometimes it can be necessary to model these plastic deformations, e. g. when CFRP plates are loaded in out-of-plane direction under impact. The yield function (6.1) was originally developed for fiber-reinforced composites in general, not CFRP specifically. One motivation for the yield function was that fiber-reinforced composites can exhibit plastic compressibility [1]. Furthermore, as such materials are in general anisotropic, it is interesting to note that fiber-reinforced composites exist, which belong to the same material class in Fig. 6.1 as aluminum honeycombs (anisotropic, non-constant volume plasticity).

The general yield function (6.1) was applied to CFRP in a study funded by ESA/ESTEC under contract 18763/04/NL/SFe. Some results of that work are presented in [10]. The primary aim of the investigation was the numerical simulation of CFRP under hypervelocity impact, as it can occur when a satellite wall is hit by a space debris particle. A CFRP representative for satellite applications was chosen for the study. The laminate's lay-up was anisotropic with no fibers in the 2-direction of the material. Tension tests in this direction revealed plastic deformations which can be attributed to the epoxy resin matrix. In the numerical simulations, the individual layers of the laminate were not modeled explicitly. Instead, they were homogenized over the thickness in the sense of an orthotropic continuum approach. The hardening behavior in 2-direction was used for the master curve of the model. As for the honeycomb before, the corresponding plasticity coefficient was chosen as 1. The other coefficients were derived from an evaluation of the deformation and failure behavior of the CFRP under various states of stress. As an example, let us consider tensile loading in 1-direction, where no plasticity was observed before failure. For the determination of a_{11} , this was taken into account by ensuring that the failure stress corresponded to $\bar{\sigma}_{\#1}$, the first effective stress value of the master curve. Thus, for a loading in that direction, no plasticity will be predicted in the simulation before failure.

For the numerical simulations of the hypervelocity impact on CFRP, ANSYS[®] AUTODYN[®] was utilized. In order to capture the complete behavior of the composite under this highly dynamic loading, orthotropic elasticity, a polynomial equation of state, and a damage and failure description were combined with the plasticity model. Due to the extremely large deformations and fragmentation occurring under impact, the material close to the impact region was discretized using the meshfree SPH (smoothed particles hydrodynamics) method. Depending on the size of the projectile, up to 18 particles over the thickness were used for the 1.37 mm thick CFRP sheets. The material model was validated by simulations of planar plate impact and hypervelocity impact tests. Different projectile diameters, velocities, and impact angles were investigated for hypervelocity impact. Fig. 6.5 a) illustrates the debris

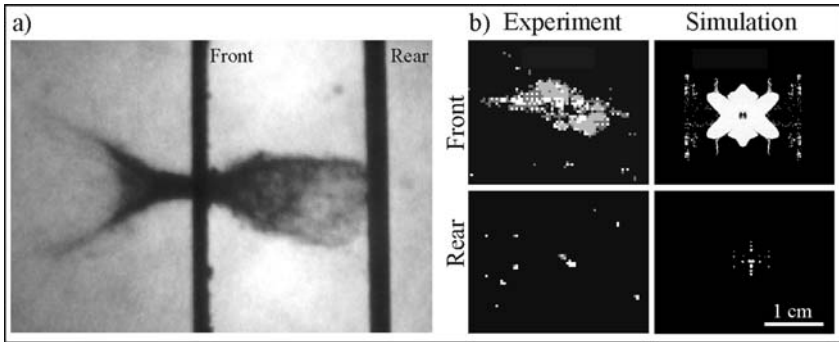


Fig. 6.5 Perpendicular hypervelocity impact (4.577 km/s) of an aluminum sphere (diameter 0.782 mm) on two CFRP plates. a) High-speed image. The projectile impacted from the right-hand side on the front plate. b) Comparison of delamination between experiment and simulation.

cloud during one test and Fig. 6.5 b) the resulting damage in the CFRP. The projectile perforates the front plate (Fig. 6.5 a), but not the rear plate. The delamination of the CFRP plates was determined from ultrasonic tests (Fig. 6.5 b), 'experiment'. Delamination is clearly visible in the front sheet, while the rear is almost undamaged.

In the simulation, the projectile also perforates only the front plate. In Fig. 6.5 b), the white areas in the simulation results represent material with an effective plastic strain of at least 0.155 % (A 3d truncated contour plot was used to visualize the plasticity within the plates as well). This was the largest value of plasticity found in the characterization tests before failure. Therefore, the plotted regions can be interpreted as minimum extensions of the damaged areas in the simulations. Comparison of experiment and simulation reveals that these plastic deformations within the plates correspond well with the delamination region in the test. Note that a value of 0.155 % of plastic deformation is still orders of magnitudes smaller than the values occurring in honeycomb modeling, for example.

6.6 Outlook

The applicability of the quadratic yield function (1) to plasticity modeling of different material classes has been demonstrated in the preceding sections. For foams, a parameter set for the ellipsoid model, which is often applied for isotropic cellular materials, has been derived. For honeycombs and CFRP, the predictive modeling capabilities were validated by comparison of experimental and numerical results. However, limitations exist in the plasticity model discussed in section 2, which should be overcome in future developments:

1. The yield function (6.1) does not distinguish between tension and compression for uniaxial normal loading due to its quadratic formulation. Introducing an offset tensor $\sigma_{ij,0}$ would shift the yield locus from the origin of stress space allowing for a tension/compression asymmetry.
2. Constant plasticity coefficients only permit to model isotropic hardening. However, the hardening behavior of the materials of the previous sections can vary dramatically for different stress states. A general hardening description is possible by substitution of the plasticity coefficients by plasticity functions of the effective plastic strain. In the same way, strain rate effects could also be included in these functions: $a_{ij} = a_{ij}(\bar{\epsilon}^p, \dot{\bar{\epsilon}})$. With such plasticity functions, deformation induced anisotropy of initially isotropic materials could be modeled as well. This type of behavior can occur in foams, for example.
3. Finally, a non-associated flow rule would provide a further degree of freedom in modeling.

Therefore, an enhanced yield function would be:

$$\begin{aligned}
 f(\sigma_{ij}, \sigma_{ij,0}, \bar{\epsilon}^p, \dot{\bar{\epsilon}}) &= a_{11}(\bar{\epsilon}^p, \dot{\bar{\epsilon}})(\sigma_{11} - \sigma_{11,0})^2 + a_{22}(\bar{\epsilon}^p, \dot{\bar{\epsilon}})(\sigma_{22} - \sigma_{22,0})^2 + \\
 &+ a_{33}(\bar{\epsilon}^p, \dot{\bar{\epsilon}})(\sigma_{33} - \sigma_{33,0})^2 + 2a_{12}(\bar{\epsilon}^p, \dot{\bar{\epsilon}})(\sigma_{11} - \sigma_{11,0})(\sigma_{22} - \sigma_{22,0}) + \\
 &+ 2a_{23}(\bar{\epsilon}^p, \dot{\bar{\epsilon}})(\sigma_{22} - \sigma_{22,0})(\sigma_{33} - \sigma_{33,0}) + 2a_{13}(\bar{\epsilon}^p, \dot{\bar{\epsilon}})(\sigma_{11} - \sigma_{11,0})(\sigma_{33} - \sigma_{33,0}) + \\
 &+ 2a_{44}(\bar{\epsilon}^p, \dot{\bar{\epsilon}})\sigma_{23}^2 + 2a_{55}(\bar{\epsilon}^p, \dot{\bar{\epsilon}})\sigma_{31}^2 + 2a_{66}(\bar{\epsilon}^p, \dot{\bar{\epsilon}})\sigma_{12}^2 = 1
 \end{aligned}
 \tag{6.27}$$

Note that the hardening parameter k is eliminated here, because the hardening is now modeled by the nine plasticity functions. Hence, the dimension of these functions is [stress^{−2}].

References

1. Chen JK, Allahdadi FA, Sun CT (1997) A quadratic yield function for fiber-reinforced composites. *J. Compos. Mater.* 31(8):788–811
2. Chen WF, Han DJ (1988) *Plasticity for structural engineers*. Springer, New York
3. Dharmasena KP, Wadley HNG, Xue Z, Hutchinson JW (2008) Mechanical response of metallic honeycomb sandwich panel structures to high-intensity dynamic loading. *Int. J. Impact Eng.* 35:1063–1074
4. Gibson LJ, Ashby MF (1997) *Cellular solids – Structure and properties – Second edition*. Cambridge University Press
5. Hanssen AG, Hopperstad OS, Langseth M, Ilstad H (2002) Validation of constitutive models applicable to aluminium foams. *Int. J. Mech. Sci.* 44: 359–406
6. Hill R (1950) *The mathematical theory of plasticity*. Oxford University Press, London
7. Rogers WF (1972) APOLLO Experience report – Lunar module landing gear subsystem, NASA TN D-6850
8. Spinner S, Wicklein M (2009) Kontinuumsmechanische Modellierung und Simulation von Sandwichstrukturen fr dynamische Belastungen (Modeling and simulation of sandwich struc-

- tures for dynamic loading). Proceedings of 4th Landshuter Leichtbau-Colloquium, February 26-27
9. von Mises R (1913) Mechanik der festen Krper im plastisch-deformablen Zustand (Mechanics of solids in the plastic-deformable state). Gttinger Nachrichten Math.-Phys. Klasse 1 582–592
 10. Wicklein M, Ryan S, White DM, Clegg RA (2008) Hypervelocity impact on CFRP: testing, material modelling, and numerical simulation. *Int. J. Impact Eng.* 35:1861–1869

Chapter 7

On the Computation of a Generalised Dynamic J-Integral and its Application to the Durability of Steel Structures

Ingbert Mangerig and Stefan Kolling

Abstract A theoretical description and a computational method are presented to calculate the J-integral in the context of the finite element method. In the derivation, we use the theory of configurational forces where the fully three-dimensional case and large deformations for non-linear elastic materials under dynamic loading are taken into account. Analogue to the local balance of momentum, the so-called Eshelby stress holds a configurational force balance, where configurational forces correspond to the volume forces in the physical space. A discretised finite element description is obtained by the weak form of the configurational force balance. Thus, the configurational forces acting on the finite element nodes may be computed as the physical boundary value problem is solved. For the static case and small deformations, the configurational force corresponds to the well known J-integral in fracture mechanics, though not restricted to the crack-mode I state. As a practical example, we show how the J-integral, combined with Paris' equation, can be used to predict the ultimate life time of a steel structure containing components with cracks.

7.1 Introduction

In many fields of industrial application, the mechanism and prediction of fracture processes play an important role. Such as in construction engineering where many of the bridges made from steel have been built fifty years ago or even earlier. The investigation of these bridges due to their durability is a great field of interests in civil engineering. In particular if so-called 'vital elements', i.e. parts of the structure

Ingbert Mangerig

Bundeswehr University Munich, Chair in Steel Structures, Werner-Heisenberg-Weg 39, 85577 Neubiberg, Germany e-mail: Ingbert.Mangerig@unibw.de

Stefan Kolling

Giessen University of Applied Sciences, Laboratory of Mechanics, Wiesenstr. 14, 35390 Giessen, Germany, e-mail: stefan.kolling@mmew.fh-giessen.de

which are responsible for load carrying capacity of the entire structure, are cracked. The basis for the treatment of structures with initial cracks is the energy release rate during a virtual displacement of the crack-tip: the so-called J-integral introduced by Rice [1]. In linear elastic fracture mechanics, the J-integral combined with Paris' equation, see Paris and Erdogan [2], results in an empirical concept to predict the durability due to fatigue of a structure. For a non-standard geometry, the J-integral has to be computed numerically, e.g. by the finite element method. Although many commercial FE-packages are able to calculate the J-integral, the results are usually restricted to simple cases like crack mode-I, small deformations and quasi-static loading. Most of the commercial finite element codes are not able to calculate the J-integral in the fully three-dimensional case and if dynamic effects has to be taken into account. In this paper, we present a numerical technique based on the theory of configurational forces, which is able to overcome this restrictions. The theory stands for a more general context and has been established as a useful tool to investigate the energy change of inhomogeneous continuum mechanical systems. Configurational forces allow the numerical simulation in a wide range of mechanics and material science.

The idea of calculating configurational forces with finite elements goes back to the work of Braun [3]. Especially with respect to fracture mechanics, this numerical technique has been applied in the papers by Steinmann [4], Steinmann, Ackermann and Barth [5] and Mueller, Kolling and Gross [6]. In the latter one it is shown additionally, how configurational forces can be used to improve discretization meshes. In a later work, Mueller and Maugin [7] demonstrate how configurational forces can be used to simulate mixed mode crack propagation.

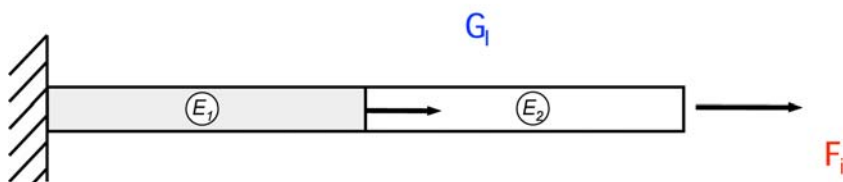


Fig. 7.1 Spatial and material forces on a two-phase bar.

In the static case, the change of the energy is given by the gradient of the total potential. The result is a generalised force, which is called the configurational (or material) force and was introduced by Eshelby in 1951 [8]. In Figure 7.1, we demonstrate the difference between spatial (Newtonian) forces F_i and material forces G_i on a two-phase bar consisting of two different materials with Young's moduli E_1 and E_2 : While spatial forces are generated by variations of the energy W relative to the ambient space at fixed position in the material, i.e.

$$\left. \frac{\partial W}{\partial x_i} \right|_{X_I} = F_i,$$

material forces are generated by variations relative to the ambient material at fixed position in space, i.e.

$$\left. \frac{\partial W}{\partial X_I} \right|_{x_i} = G_I.$$

With other words: material forces act on material inhomogeneities (the phase boundary that separates the two materials in Figure 7.1). The physical meaning of this force is given by the considered problem: direction of diffusing atoms, dislocation movement or crack propagation among others. In the dynamic case, the change of the energy is given by the gradient of the Lagrangian, i.e. the difference of kinetic and strain energy. This results in the so-called dynamic energy momentum tensor which, likewise, was introduced by Eshelby [9]. In the present paper, Eshelby's idea to derive a generalised (configurational) balance equation (balance of momentum for the material motion problem) is recast. A weak formulation of this balance equation is used to obtain the J-integral by finite elements very convenient without using the usual way of defining an integration path surrounding the crack tip. The focus is set to hyper-elastic materials. For an extension of the theory towards plasticity and visco-elasticity, see the books by Maugin [10], Gurtin [11] and Kienzler and Herrmann [12].

7.2 Basic Equations

Our subject under consideration is a homogeneous body B (density ρ_0) with body forces f_i . In our derivations following [3] and [13], Cartesian coordinates and the index notation are used for more clarity. The small indices (e.g. x_i) denote coordinates with respect to the actual (material) configuration and the capitals (e.g. X_J) refer to the reference configuration. In a hyper-elastic continuum, there exists a strain energy function $W = \hat{W}(F_{IJ})$ from which the stresses can be derived as

$$P_{IJ} = \frac{\partial W}{\partial F_{IJ}}. \quad (7.1)$$

Here, $F_{IJ} = \partial x_i / \partial X_J$ is the deformation gradient and P_{IJ} is the first Piola-Kirchhoff stress-tensor. With the stress-tensor in equation (7.1), the local form of the momentum balance can be written as

$$P_{IJ,J} + f_i = \rho_0 \dot{v}_i, \quad (7.2)$$

where v_i is the (local) velocity.

The second Piola-Kirchhoff (pseudo) stress $S_{IJ} = 2\partial W / \partial C_{IJ}$ is obtained by deriving the energy function with respect to the right Cauchy-Green strain tensor

$C_{IJ} = F_{kI}F_{kJ}$. First and second Piola-Kirchhoff stresses are related by $P_{iK} = F_{iL}S_{LK}$. The (true) Cauchy stress σ_{ij} can be obtained by forming

$$\sigma_{ij} = J^{-1}P_{iK}F_{jK} = J^{-1}F_{iL}S_{LK}F_{jK}, \quad (7.3)$$

where $J = \det F_{iJ}$ is the relative volume.

7.3 Theory of Configurational Forces

A number of different approaches exist of the meanwhile well known concept of configurational forces. Without going mathematically into detail, it is instructive to begin with a summary of some well-established approaches that can be found in the literature cited above.

Eshelby's Approach: *The force on a dislocation or point defect, as understood in solid-state physics, and the crack extension force of fracture mechanics are examples of quantities which measure the rate at which the total energy of a physical system varies as some kind of departure from uniformity within it changes its configuration.* In this statement, Eshelby considers the driving force on a material defect as the rate of energy associated with a virtual movement of the defect. Consequently, configurational forces can be derived from the gradient of the Lagrange function using standard analysis of the classical balance laws.

Gurtin's Approach: *...configurational forces should be viewed as basic primitive objects consistent with their own force balance, rather than as variational constructs.* Consequently, an independent system of configurational forces and their balance is assumed and the balance of configurational forces is elevated to the level of an autonomous law of nature, which is as fundamental as Newton's law of motion. This is in contrast to the original papers by Eshelby in which the constitutive assumptions of the bulk material play a central role in the derivation of the form of the configurational force.

Maugin's Approach: *Balance of configurational forces is the pull-back of the standard balance to the material manifold, configurational forces are secondary quantities.* Starting point is the balance of forces in the deformed configuration written in terms of quantities defined with respect to the undeformed configuration. Multiplying by the transposed deformation gradient from left leads, after some simplifications, to the balance of standard linear momentum and the balance of configurational (material) linear momentum. This procedure is also referred to as invers motion.

In the following Eshelby's approach is used for the derivation, where the continuum is generalised to an inhomogeneous body B . The Lagrangian $L = T - W$ of the system is defined as the difference of the kinetic energy

$$T = \hat{T}(\rho_0, v_i) = \frac{1}{2} \rho_0 v_i v_i \quad (7.4)$$

and the strain energy $W = \hat{W}(F_{ij}, X_K)$. Now, the strain energy depends on the deformation gradient F_{ij} and on the position X_K explicitly to consider inhomogeneous materials. Formulating the gradient of the Lagrangian yields

$$\frac{\partial L}{\partial X_K} = \frac{\partial T}{\partial X_K} - \frac{\partial W}{\partial X_K} = \frac{\partial T}{\partial \rho_0} \frac{\partial \rho_0}{\partial X_K} + \frac{\partial T}{\partial v_i} \frac{\partial v_i}{\partial X_K} - \frac{\partial W}{\partial F_{ij}} \frac{\partial F_{ij}}{\partial X_K} - \frac{\partial W}{\partial X_K} \Big|_{\text{expl}} \quad (7.5)$$

Using (7.1) and (7.4), we obtain

$$\frac{\partial T}{\partial \rho_0} = \frac{1}{2} v_i v_i, \quad \frac{\partial T}{\partial v_i} = \rho_0 v_i, \quad \text{and} \quad \frac{\partial W}{\partial F_{ij}} = P_{ij} \quad (7.6)$$

and equation (7.5) can be rewritten as

$$L_{,K} = \frac{1}{2} v_i v_i \rho_{0,K} + \rho_0 v_i v_{i,K} - P_{ij} F_{ij,K} - \frac{\partial W}{\partial X_K} \Big|_{\text{expl}} \quad (7.7)$$

Inserting $v_{i,K} = \dot{F}_{i,K}$, $F_{ij,K} = F_{iK,j}$, the identity $P_{ij} F_{iK,j} = (P_{ij} F_{iK})_{,j} - P_{ij,j} F_{iK}$ and (7.2) yields

$$\begin{aligned} L_{,K} &= \frac{1}{2} v_i v_i \rho_{0,K} + \rho_0 v_i \dot{F}_{iK} - (P_{ij} F_{iK})_{,j} + \underbrace{P_{ij,j}}_{=\rho_0 v_i - f_i} F_{iK} - \frac{\partial W}{\partial X_K} \Big|_{\text{expl}} \\ &\Leftrightarrow -L_{,j} \delta_{Kj} - (P_{ij} F_{iK})_{,j} + \frac{1}{2} v_i v_i \rho_{0,K} - f_i F_{iK} - \frac{\partial W}{\partial X_K} \Big|_{\text{expl}} = -\rho_0 v_i F_{iK} - \rho_0 v_i \dot{F}_{iK} \\ &\Leftrightarrow \underbrace{(-L \delta_{Kj} - P_{ij} F_{iK})_{,j}}_{\Sigma_{Kj}} + \underbrace{\left(\frac{1}{2} v_i v_i \rho_{0,K} - f_i F_{iK} - \frac{\partial W}{\partial X_K} \Big|_{\text{expl}} \right)}_{g_K} = -\rho_0 (v_i F_{iK})_{,j} \end{aligned}$$

The second order tensor Σ_{Kj} in the brackets of the left side is called *energy momentum tensor* and the force g_K is the material force (configurational force), see [9]. Now, a compact equation has been found:

$$\Sigma_{Kj,j} + g_K = -\rho_0 (F_{iK} v_i)_{,j}, \quad (7.8)$$

which has the same structure as the balance of momentum (7.2) and is called *configurational force balance*. A further notation which also can be found in literature is *balance of linear pseudo-momentum*. In the static case, the terms in equation (7.8) are simplified to

$$\Sigma_{Kj,j} + g_K = 0, \quad (7.9)$$

where the energy momentum tensor is

$$\Sigma_{Kj} = W \delta_{Kj} - P_{ij} F_{iK} \quad (7.10)$$

and the configurational force is

$$g_K = -f_i F_{iK} - \left. \frac{\partial W}{\partial X_K} \right|_{\text{expl}}. \quad (7.11)$$

For small deformations, the energy momentum tensor is finally reduced to

$$\Sigma_{kj} = W \delta_{kj} - u_{i,k} \sigma_{ij}. \quad (7.12)$$

In this case, the first component (using $dx_1 = n_1 d\Gamma$) of the material force acting on a crack-tip is related to the J-integral, see the original paper by Rice [1]:

$$J = - \frac{\partial W}{\partial a} = \int_{\Gamma} W dx_1 - u_{i,1} \sigma_{ij} n_j d\Gamma \quad (7.13)$$

where Γ is an arbitrary path surrounding the crack-tip. The interpretation of the J-integral is the energy release rate of the system with respect to a virtual movement δa of the crack-tip along the ligament. The usual way to calculate J is to define a path Γ and solve equation (7.13). The problems we are facing then, is that J is not always path independent, e.g. if mixed mode loading has to be considered. In what follows, an alternative way to determine J consistent with the finite element method is shown.

7.4 Finite Element Formulation

Starting point of the finite element discretization is the weak formulation of the configurational force balance (7.8). To obtain the weak form, we multiply (7.8) by a test function η_K and integrate over B :

$$\begin{aligned} & \int_B (\rho_0 (F_{iK} v_i) + \Sigma_{KJ,J} + g_K) \eta_K dV = \\ & \int_B \underbrace{(\rho_0 F_{iK} v_i)}_{=: -\dot{P}_K} \eta_K + (\Sigma_{KJ} \eta_K)_{,J} - \Sigma_{KJ} \eta_{K,J} + g_K \eta_K dV = 0. \end{aligned}$$

Here, \dot{P}_K is called the pseudo momentum vector. Integrating by parts leads to

$$\int_B -\dot{P}_K \eta_K - \Sigma_{KJ} \eta_{K,J} + g_K \eta_K dV + \int_{\partial B} \Sigma_K N_J \eta_K dA = 0. \quad (7.14)$$

If we consider stationary boundaries, i.e. boundaries which remain fixed, the boundary integral in (7.14) vanishes. Now, the test function is approximated in each element

$$\eta_{K,J} = \sum_I N_{,J}^I \eta_K^I. \quad (7.15)$$

Inserting (7.15) in (7.14) yields

$$\sum_I \eta_K^I \int_B \left\{ -\dot{P}_K N^I - \Sigma_{KJ} N_{,J}^I + g_K N^I \right\} dV = 0. \quad (7.16)$$

Since this equation has to be fulfilled for arbitrary η_K^I , the bracket has to be zero and the discrete material forces are given by

$$G_K^I = \int_B g_K N^I dV = \int_B \dot{P}_K N^I + \Sigma_{KJ} N_{,J}^I dV \quad (7.17)$$

To obtain the total material force G_K^I acting on the node I , the forces G_K^I of all elements adjacent to node I have to be assembled, i.e.

$$G_K^I = \bigcup_{l=1}^{n_e} G_K^I. \quad (7.18)$$

With this formulation, the material forces (and thus the J-integral) can be calculated simply as the physical boundary value is solved: all quantities to compute Σ_{KJ} and \dot{P}_K are already known in every time step.

7.5 Fatigue, Stress Intensity Factor and Crack Growth Rate

Fatigue of a steel structure can be considered as a mechanism of crack growing. Fatigue cracks occur by cyclic load under lower stress condition than allowable stress. During the lifetime of a structure, fatigue cracks propagate mostly in form of subcritical crack growth. For assuring safety of a steel structure, cracks should be detected and monitored in this period of subcritical crack growth. The assessment of a crack can be done by the stress intensity factor $K = \hat{K}(\sigma, a, Y)$. It defines the amplitude of the crack tip singularity and is a function of applied nominal stress σ , crack length a and a geometric function Y . The stress intensity factor can be computed via the J-integral (7.13):

$$J = \frac{K^2}{E'}, \quad (7.19)$$

e.g. numerically by the presented technique. In the two-dimensional case, the modulus of elasticity E' has to be distinguished between plane stress and plane strain:

$$E' = \begin{cases} E & \text{for plane stress} \\ \frac{E}{1-\nu^2} & \text{for plane strain} \end{cases} \quad (7.20)$$

where ν is Poisson's ratio. Fatigue crack growing process is classified to three regions according to the change of fatigue crack growth rate da/dN , where a is the crack length and $N(a)$ is the load cycle. Region I is a state of crack initiation (cracks are not detectable visually). If we detect a crack, we may take our attention to the region II, where crack growing speed increases according to the crack length a . Now, the stress intensity factor K and the crack growth rate da/dN show a relationship of direct proportion, which is known as Paris' equation, see [2]

$$\frac{da}{dN} = C(\Delta K)^m \quad (7.21)$$

where C and m are experimentally determined material constants. Within this region II, crack propagation is called stable crack growth. In region III, crack growth rate quickly increases and the member is about to failure. This is called unstable crack growth. The stress intensity factor at failure is called fracture toughness K_c .

7.6 Application to Durability Analysis

From the theoretical description above, we may suggest a simple way for the durability analysis of a structural part with an initial crack a_0 . As an example, we consider a steel-plate (thickness $t=18\text{mm}$) as sketched in Figure 7.2a. The material constants for steel S235 are taken from standard literature: $C = 5.0 \cdot 10^{-12}$, $m = 3.0$ for Paris' parameter and $J_C = 87\text{N/mm}$ for the critical J-integral. From standard structural analysis, a maximum stress $\max \sigma = 174,8\text{N/mm}^2$ and a cyclic stress $\Delta \sigma = 35\text{N/mm}^2$ are obtained for the structural part under consideration. A section of the finite element model (using a very fine mesh at the crack tip) for computing the J-integral is shown in Figure 7.2b.

In what follows, we give a step-by-step recipe for the evaluation of the structure with respect to fatigue. Please note that this procedure is very general and not restricted to the given example.

In the first step, we compute the J-integral of the structure for different crack lengths and stresses, e.g. via material forces as described in section 7.4. Figure 7.3 shows the results for the considered steel-plate. We chose a crack length variation of $a = 30, 40, 50$ and 60mm over normal stresses from 20N/mm^2 up to 360N/mm^2 . From the maximum stress $\max \sigma$ in the structure together with the material parameter J_C , we obtain the critical crack length a_c . This is the maximum crack length before unstable crack propagation and, thus, failure of the entire structure occurs. In our example, the critical crack length is $a_c = 56\text{mm}$ (by interpolating between the computed curves).

Cycling loading results in minimum and maximum stress

$$\Delta \sigma = \max \sigma - \min \sigma. \quad (7.22)$$

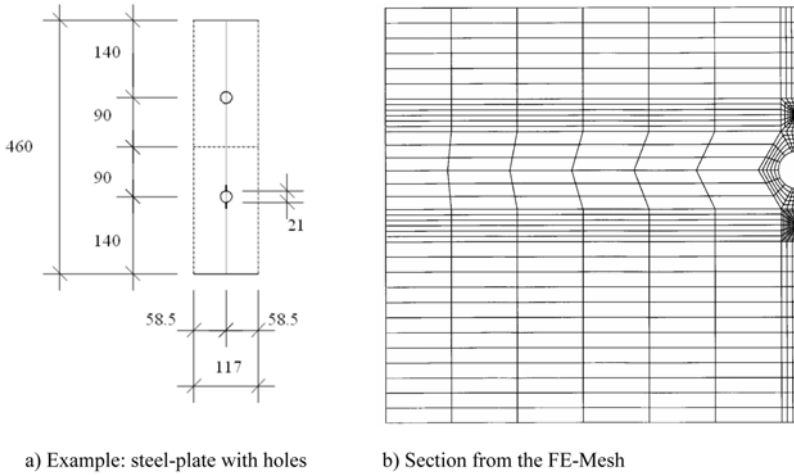


Fig. 7.2 Example of a structure with initial cracks and the corresponding FE model.

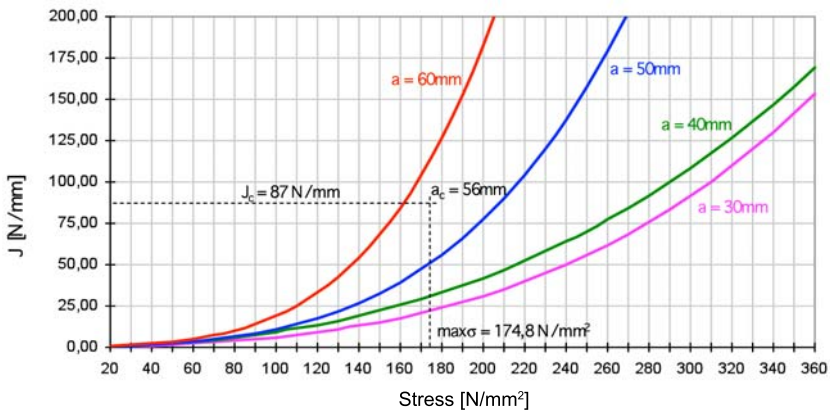


Fig. 7.3 J-integral for different stresses.

In the second step, we therefore calculate the cyclic stress intensity factor ΔK from the J-integral as a function of the crack length a using equation (7.19) and get

$$\Delta K(a) = K(\max \sigma) - K(\min \sigma) = \sqrt{[J(\max \sigma) - J(\min \sigma)] E'}. \quad (7.23)$$

The resulting function for our example is plotted in Figure 7.4 where a least-square-fit has been used for interpolation of the finite element results.

We finally integrate in the third step Paris' equation (7.21)

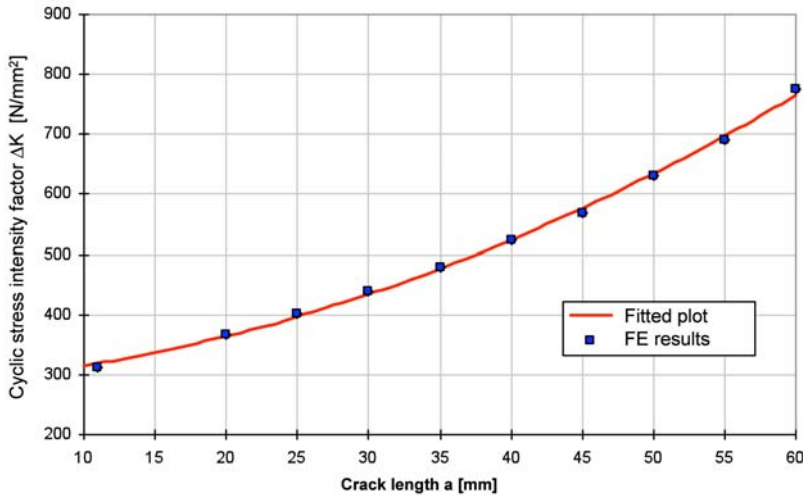


Fig. 7.4 Cyclic stress intensity factor.

$$N(a) = \int \frac{da}{C[\Delta K(a)]^m}, \quad (7.24)$$

e.g. numerically and we obtain the number of cycles before failure as

$$N_c = N(a_c) - N(a_0) \quad (7.25)$$

where a_0 denotes the initial crack length. Figure 7.5 shows the result for the given example. If the crack grows to a length $a > a_0$, the number of load cycles before failure can then be approximated by this diagram as $N_c = N(a_c) - N(a)$.

7.7 Summary

The theory of configurational forces and the corresponding finite element formulation has been presented in the context of non-linear elastic materials under dynamic loading. Using this method, the discrete configurational forces acting on finite element nodes are obtained consistent with the FE-formulation. For crack mode I, the configurational forces are used to compute the J-integral and thus the stress intensity factor is obtained for evaluating a structural part with an initial crack. Furthermore, we have shown how this method can be used in industrial practice for durability analysis of steel structures using Paris' equation. With the presented method of configurational forces, the J-integral is defined not only for mode I but for a general three dimensional stress state. Moreover, inertia effects may also be taken into ac-

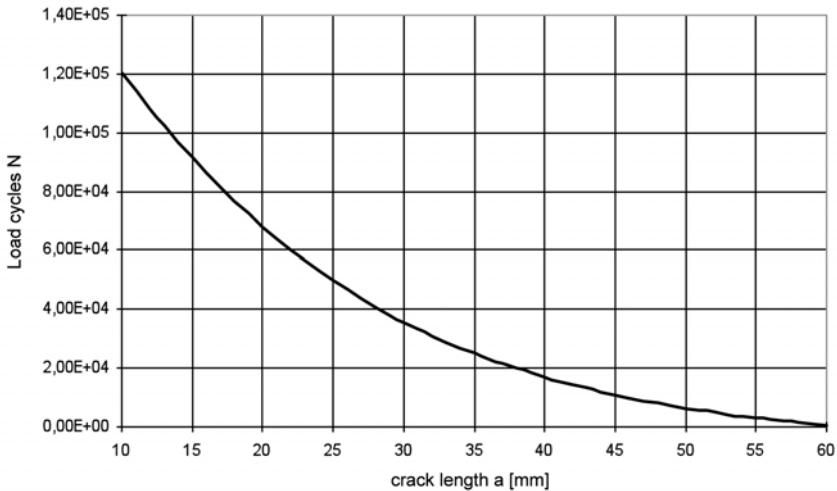


Fig. 7.5 Number of load cycles over crack length.

count due to the fully dynamic formulation. The required experimental setup for using this finding in durability analysis is a topic of further investigation.

References

1. Rice J.R. (1968) A path independent integral and the approximate analysis of strain concentration by notches and cracks. *J. Appl. Mech.*, 35: 379-386.
2. Paris P.C., Erdogan F. (1960) A Critical Analysis of Crack Propagation Laws, *Journal of Basic Engineering*, 85: 528-534.
3. Braun M. (1997) Configurational forces induced by finite-element discretization. *Proc. Estonian Acad. Sci. Phys. Math.*, 46(1/2): 24-31.
4. Steinmann P. (2000) Application of material forces to hyperelastostatic fracture mechanics I: Continuum mechanical setting. *International Journal of Solids and Structures*, 37: 7371-7391.
5. Steinmann P., Ackermann D., Barth F.J. (2001) Application of material forces to hyperelastostatic fracture mechanics II: computational setting. *International Journal of Solids and Structures*, 38: 5509-5526.
6. Mueller R., Kolling S., Gross D. (2002) On configurational forces in the context of the finite element method. *International Journal of Numerical Methods in Engineering*, 53: 1557-1574.
7. Mueller R., Maugin G.A. (2002) On material forces and finite element discretizations. *Computational Mechanics* 29: 52-60.
8. Eshelby J.D. (1951) The force on an elastic singularity. *Phil. Trans. Roy. Soc. A* (244): 87-112.
9. Eshelby J.D. (1970) Energy relations and the energy-momentum tensor in continuum mechanics. In Kanninen M.F. (editor) *Inelastic behaviour of solids*. McGraw Hill. New York.
10. Maugin G.A. (1993) *Material Inhomogeneities in Elasticity*. Chapman & Hall.
11. Gurtin M.E. (2000) *Configurational forces as a basic concept of continuum physics*. Springer Verlag.

12. Kienzler R., Herrmann G. (2000) *Mechanics in material space*. Springer Verlag.
13. Maugin G.A. (2000) Geometry of material space: its consequences in modern computational means. *Technische Mechanik*, 20(2): 95-104.

Part II
Numerical Modeling of Blast and Impact
Phenomena

Chapter 8

The MAX-Analysis: New Computational and Post-Processing Procedures for Vehicle Safety Analysis

David Vinckier

Abstract In vehicle safety analysis there is a need for precise finite element simulations of mine blast and improvised explosive device attacks on armored vehicles to support the design process. Because of the multitude of data that is generated in these simulations – even more so when multiple load cases are analyzed for one vehicle – these computations demand for an intelligent tool for summarization and compression of the simulation data. This paper presents the MAX-analysis, a new set of computational and post-processing tools to summarize all the main quantities of the numerical simulations in just a few images.

8.1 Introduction

After the substantial progress that was made in the last twenty years in crash simulation for the automotive industry, it could be expected that the finite element methods (FEM) would also play an important role in the development of armored vehicles. In fact, since about ten years now, FEM-simulations are used more and more for the development of armored components, fixation systems, armor modules and complete vehicles. However, the crash behaviour in traffic accidents is not the main topic here. The emphasis is rather on the dynamic loading of the vehicle and its occupants as a result of ballistic threats, mines and improvised explosive devices.

The reasons for the need of precise simulation results in the area of armored vehicles are very similar to the ones that pushed the automotive crash simulation: whereas the functionality requirements on the vehicles are getting more diverse, the vehicle weight limits are reached quickly, and the development cost and time frames

David Vinckier
CONDAT Projekt GmbH, Maximilianstrae 28, 85298 Scheyern-Fernhag, Germany, e-mail:
david.vinckier@condat-scheyern.de

make it practically impossible to produce an acceptable design based on experimental knowledge only.

For the ballistic and improvised explosive attacks there exists another argument that shows that simulations are indispensable: even if substantial efforts are made to standardize the load conditions and to minimize the number of these load cases using worst case scenarios, it is not acceptable to limit the analyses to these worst case scenarios only. To be able to define a degree of protection for a vehicle with respect to a specific threat, one has to analyze all relevant shot lines and blast loaded surfaces. This leads to two questions:

- Are the prediction capabilities of the simulation tools sufficient to predict the structural behaviour for all load cases and thereby to define a protection degree for the vehicle?
- How can all these detailed informations be summarized and presented?

With its GSS-package, CONDAT has developed a tool that already answers these questions for the ballistic protection issue. GSS is a simulation program, that was verified in numerous projects and is able to predict vehicle protection degrees for all current ballistic threats with a high level of precision. GSS was used to evaluate degrees of ballistic protection for almost every armored vehicle in the German Bundeswehr.

The computational methods for simulations of mine blast and improvised explosive device (IED) attacks have also reached a very good level, but there is still some work to be done regarding a condensed graphical presentation of the computational results. The reason for this is, that ballistic threats generally interact with the structure in a small localized area, whereas exploding devices typically interact non-locally on much larger surfaces. If for example a shaped charge interaction with an armor module is to be evaluated, then typically only the line of sight properties of the armor would be needed. For a blast IED load case however a complete vehicle section needs to be taken into account to be able to predict the structural response.

In able to summarize the multitude of informations that are generated in these vehicle blast simulations, a series of new computational and post-processing methods were developed. These methods, called 'MAX-analysis' are presented in this paper.

8.2 Prediction Capabilities for Vehicle Mine and IED Blast Simulations

In 1995, CONDAT performed its first finite element simulations of the blast mine loading of an armoured vehicle as part of a specific armor development project. Since then numerous mechanical problems were investigated using numerical tools

for all kinds of light and heavy tracked or wheeled vehicles. In the first phase, the prediction of the local structural deflections was the main goal of the simulations. Now detailed computer aided engineering defines the bulk of the computational activities in this field. Typical themes that are currently being investigated for all kinds of vehicles are:

- the simulation of the local deflections and the computation of the required free deflection spaces,
- the distribution of plastic deformations and the estimation of existing reserves until structural failure,
- the loading level and failure probability of door hinges and locks,
- the loading and dimensioning of screw joints,
- recommendations for the dimensioning of welding joints,
- the simulation of the deformations and vibrations of floors, seating systems and their interaction with the occupants,
- the computation of tibia and lumbar spine forces of the occupant dummies.

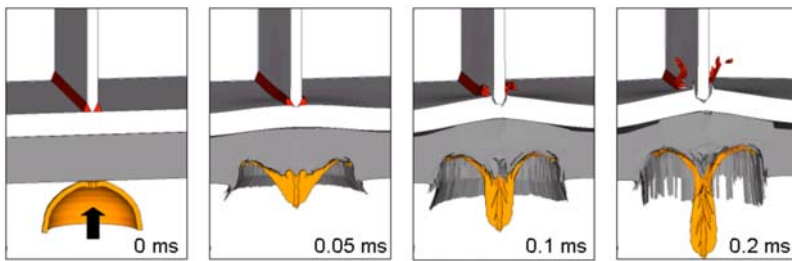


Fig. 8.1 Impact of an explosively formed projectile on a welded structure.

Even if the blast loading often dominates the design of the armor and the vehicle base structure, the effects of fragment and projectile forming mines cannot be neglected. In a recent project, the risk of spalling of welding joints in the vehicle interior due to the impact of an explosively formed projectile was investigated. Figure 8.1 shows the result of a preliminary simulation on a generic vehicle part in preparation of this project.

The essential property of all these investigations is that they are not performed to produce a qualitative impression of the structural dynamics, but rather to provide precise quantitative data, that can directly be input into the vehicle design. This is only possible with a reliable prediction capability tool that is continuously being improved based upon the following key elements:

- powerful modeling and computational capabilities with longtime experience,

- the follow-up of numerous experimental campaigns with generic setups to calibrate the computational tools,
- the continuous actualization and update of material models using laboratory tests and small scale tests,
- the verification of almost all full-scale vehicle computations in the corresponding development or qualification tests.

8.3 The MAX-Analysis: Unification of the Computational Results

The evaluation of the structural behavior of the vehicle is generally done with regard to the probability of injuries for the occupants. If – in a simulation – a structure does not collapse and there is no catastrophic structural failure, then usually the following quantities are used for this evaluation:

1. the dynamic structural deformations: these determine if a contact or impact can take place between the occupant and the vehicle structure,
2. the structural velocities: these quantities have a direct influence on the injury probabilities, if contact occurs between the occupant and the vehicle,
3. the plastic material deformations: for many material types they are a good measure for the risk of structural failure
4. the structural accelerations: they determine the dynamic loads on local fixations and the corresponding devices.

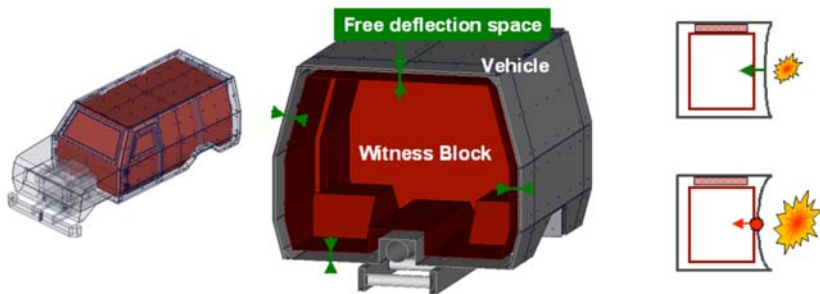


Fig. 8.2 Vehicle model with witness block.

Even if these quantities are dynamic variables, the post-processing can often be limited to their maximum values. The maximum deformations are the best measure for a possible contact between structure and occupant. As another example, the maximum velocities of a floor panel allow a good first estimation of the tibia forces in the occupant dummy. And the maximum plastic deformations, section forces and

accelerations can describe very well the risk for possible material or structural failure.

To evaluate the structural deformations, a so called 'witness block' method is used here, as primarily the deformations relative to the occupants are relevant – and not the global deformations. For that purpose a volume is defined that encloses the available space for the occupants. This volume is called the witness block. Its surface is positioned at a predefined distance (the free deflection space) to the vehicle structure. Wherever the deformed vehicle structure penetrates the witness block, the impact and the contact velocity are registered on the witness block. With this method, the classical image with structural deformations is replaced by an image showing the witness block violations.

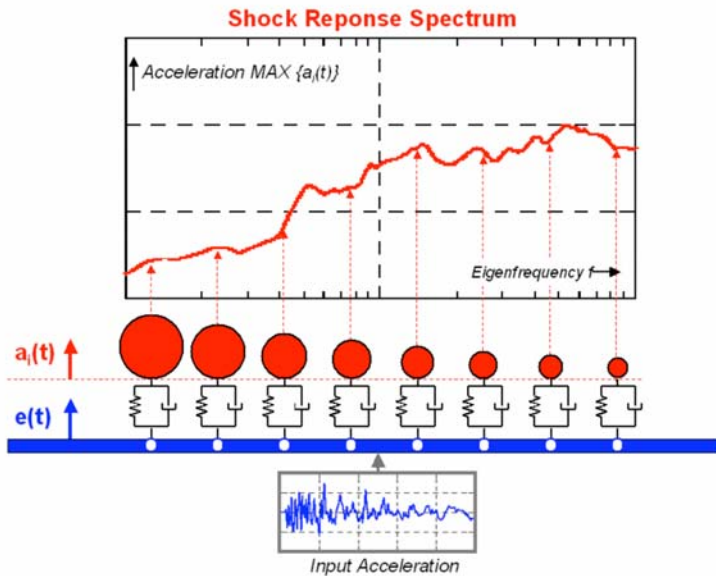


Fig. 8.3 Definition of the response spectrum.

The common procedure for the interpretation of accelerations is through the so called shock response spectra. These spectra provide the maximum output acceleration of a single degree of freedom mass-spring-system as a function of its eigenfrequency, when triggered by an input acceleration (figure 8.3). This means that theoretically, in a simulation, a spectrum can be generated for each nodal point in the model and that for a clearly arranged summary these values need to be compressed once more. The simplest method is to evaluate the spectral values relative to a reference spectrum and to compute the maximum deviation from this reference

spectrum for all frequencies. This then reduces the spectrum to a single value per nodal point. A similar approach can be used to determine the maximum section forces in device fixations as these forces can also be computed from the same single mass-spring-systems. And going one step further, one can then even compute from these maximum forces minum areas for screw fixations.

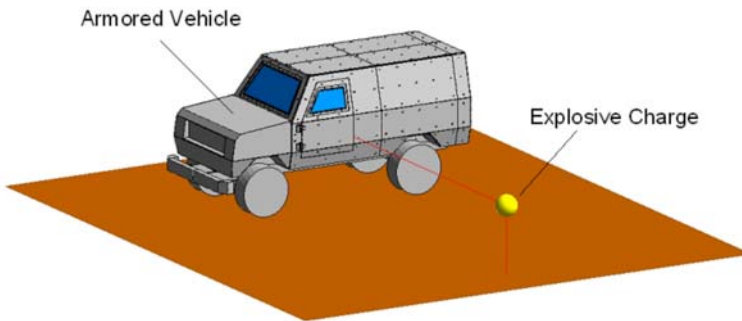


Fig. 8.4 Vehicle model with explosive charge.

Using these MAX-analysis methods, all post-processing values can be summarized in a few images. Figure 8.4 shows a computational model of a generic armored vehicle, that is loaded by a blast IED. Figure 8.5 shows the MAX-analysis results for the main simulation quantities and one position of the IED.

If several load positions must be investigated for the same threat, then all single load MAX-analyses can be compressed to one integrated multi load MAX-analysis as shown in figure 8.6. This also allows to identify the dominating load case as shown in this figure.

8.4 Summary

Detailed full scale vehicle models for vehicle safety analysis nowadays contain up to 1 million elements. A stable time step for the computation of these models with a finite element program with explicit time integration typically varies between 0,5 and 1 μs , sometimes even below 0,5 μs . This means that for the usual simulation time frame of 50 ms one needs up to 105 single time steps and therefore up to $106 \times 105 = 1011$ element states are to be analyzed and evaluated!

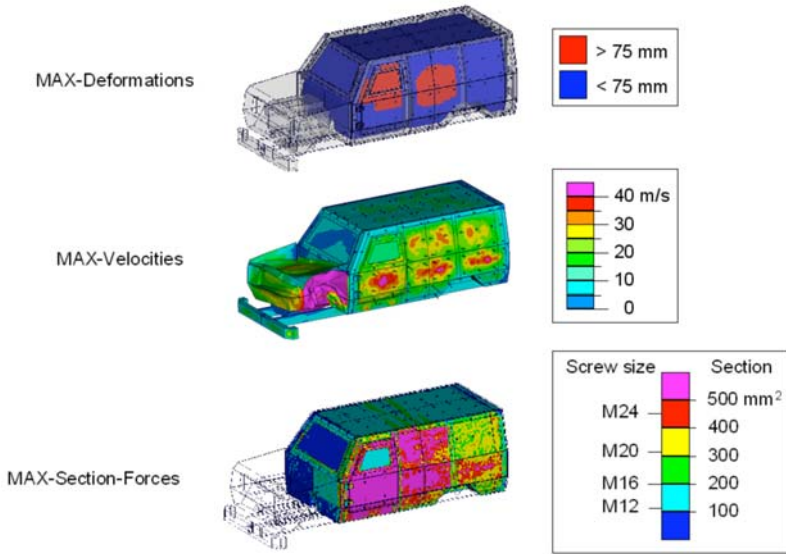


Fig. 8.5 MAX-Analysis of a blast loaded vehicle.

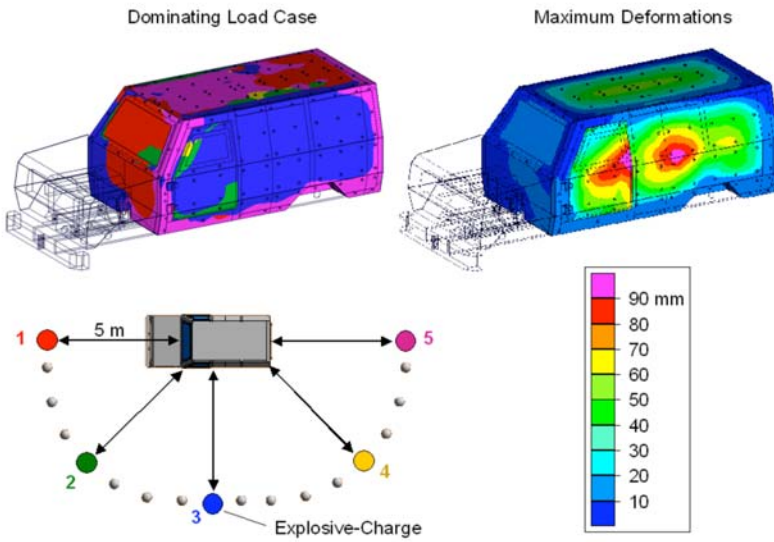


Fig. 8.6 Integrated MAX-deformation analysis for 5 load cases.

In order to handle and process these huge amount of data, new computational and post-processing methods are needed. The MAX-analyses that are presented in this paper are a first step towards an intelligent and transparent visual summary of mine and IED blast vehicle simulations.

These computational development activities are only feasible if full access exists to the programming tools so that the simulation tools can be swiftly updated if needed for the engineering problems of current interest. For its structural dynamics simulations CONDAT uses CONDAT-DYNA3D since more than twenty years. This program was introduced in 1988 by Prof. Thoma, who was in charge of the numerical activities at CONDAT in that period.

Chapter 9

10 Years RHT: A Review of Concrete Modelling and Hydrocode Applications

Werner Riedel

Abstract The RHT concrete model has been developed at Ernst-Mach-Institut 10 years ago. It combines detailed triaxial strength descriptions at moderated strain rates before and beyond damage with non-linear equation of state properties for strong shock waves. The model is readily available to all users of the commercial hydrocode AUTODYN and continuously supported since the year 2000. Over the last decade it has found numerous worldwide applications reflected in publications. They deal with dynamic load cases such as projectile and shaped charge penetration, contact detonation, internal and external blast loading. The key aspects during the development at EMI and the validation, discussion and extended use of the model by various research and development organizations are reviewed in the following.

9.1 Introduction: Dynamic Measurements and Model Development

9.1.1 *The Starting Point of the Developments*

The development of a new concrete model for hydrocodes started at Ernst-Mach-Institut early 1997 with the perspective of the later dissertation by Riedel [13], under the direction of Prof. Dr. Thoma and close support by Prof. Dr. Hiermaier. The initials 'RHT' of this development team later formed the characteristic abbreviation for the model. At that time substantial knowledge on different aspects of the mechanical behavior of concrete was available. Yet, the overlapping disciplines of static strength descriptions, rate dependent strength and shock behavior were not

Werner Riedel
Fraunhofer-Institute for High-Speed-Dynamics, Ernst-Mach-Institute, Eckerstr. 4, 79104, Freiburg, Germany e-mail: riedel@emi.fraunhofer.de

consistently combined to cover with one model approach the range of dynamic applications accessible through hydrocode simulations.

Classical civil engineering models detailed stress-based limit surfaces for failure mainly under uni- and biaxial loads. Measurements and failure surfaces for complete three-dimensional stress states were more seldom, as highly confined conditions only appear statically in very massive constructions with pressures not much above the compressive strength. However, full triaxial stress states were of primary interest for highly dynamic finite element methods, because when compression and release waves become dominant, already relatively slender building components experience high hydrostatic pressures on short timescales. Chen's summarizing work [23] on fully tri-axial stress-based failure surfaces inspired the work towards the RHT model. He described a closed failure surface depending on pressure and stress tri-axiality. Furthermore, he postulated an elastic limit surface inside the failure envelope closed towards high pressures stresses when pores start to crush (see Figure 9.1). The elastic limit surface expanded during hardening towards coincidence with the failure surface.

Detailed stress-strain states beyond the failure envelope, especially residual shear resistance of damaged concrete under triaxial compressions, are normally less relevant for civil engineering analysis. Under dynamic loads such as penetration processes or contact detonation more detailed description of concrete degradation is essential, as the failed material still exhibits resistance and takes kinetic energy during the dynamic event. Holmquist and Johnson [35] were the pioneers in proposing a phenomenological model suitable to cover a wide range of highly dynamic loading scenarios in the hydrocode EPIC. Similar to the widely used Johnson and Cook model for metals, they gave a simple, parametric formulation of the concrete failure surface with decoupled factors for the dependencies on pressure, strain rate and damaged states (9.1). They included a pressure dependent shear resistance surface after partially and total damage of the concrete. This proved to be a key aspect to capture penetration resistance of concrete targets. Deficiencies for a wider applicability of the model turned out to be details of low pressure strength. Their formulation (9.1) did not allow for a consistent fit to tensile, compressive and shear strength (see Figure 9.1) and higher pressure meridians with a single parameter set.

$$f(p, J_2, \dot{\epsilon}) = \sqrt{3J_2} - f'_c (A(1-D) + Bp^{*N}) \left(1 + C \ln \frac{\dot{\epsilon}}{\dot{\epsilon}_0}\right) = 0 \quad (9.1)$$

where

$$D = \sum \frac{\Delta \epsilon_p + \Delta \mu_p}{\epsilon_p^f + \mu_p^f} \quad (9.2)$$

and

$$\epsilon_p^f + \mu_p^f = D_1 (p^* - p_{spall}^*)^{D_2} \geq EFMIN \quad (9.3)$$

Beyond several key aspects of dynamic distortional resistance, Holmquist and Johnson's model also described an important mechanism of concrete behavior towards shock compression: They included a nonlinear equation of state with pore

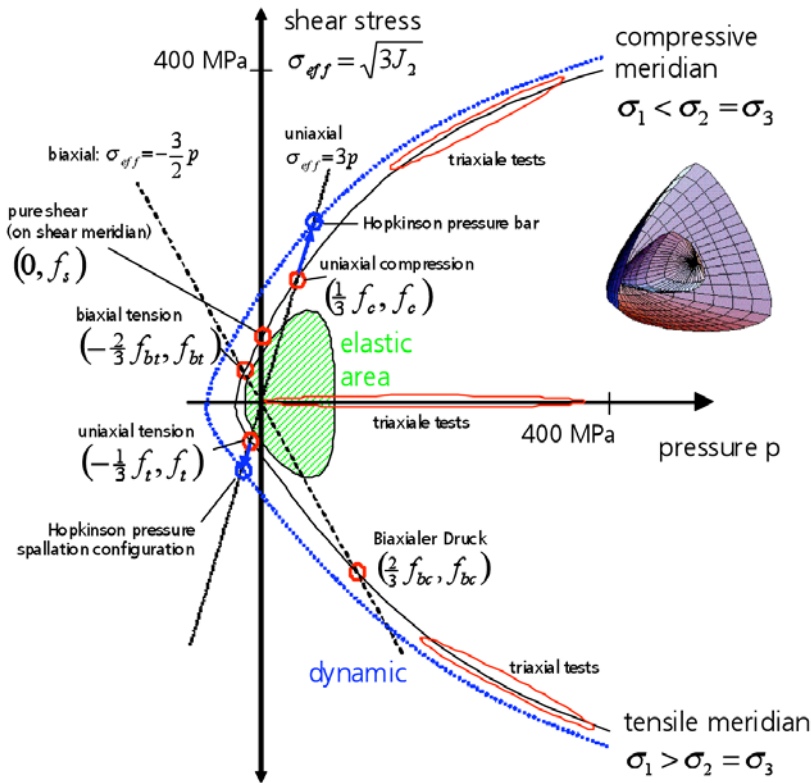


Fig. 9.1 Elastic and failure surfaces based on Chen’s concept [23], with stress points and areas measurable by different static and dynamic loading techniques.

compaction, a process known to dissipate large amounts of energy. Yet, equation of state data for concrete was still in the process of being generated and understood, mainly due to large scale heterogeneity of the material. Grady, Kipp and Chhabildas [31] – [33] adapted two-stage light gas gun projectile and target configurations to measure shock and release conditions on samples large enough to represent almost unscaled conventional strength SAC-5 concrete. The resulting data points from their unique plate impact facility on a two-stage light gas gun are displayed in Figure 9.2, left, using Xs and crossed markers. Contact detonation experiments were developed in the nineties for example at University of Karlsruhe [40] (e.g. data points ‘Ockert 97’ in Figure 9.2, left) and later at the Bundeswehr Technical Center WTD52 [29] to generate Hugoniot data for concrete. This technique allowed to test much larger samples, yet suffered from deficiencies to produce planar and steady shock waves and the difficulty to measure shock pressures directly in the composite. Still, the summary of all data gathered up to that time (see Figure 9.2) clearly indicated strongly nonlinear shock compression behavior of concrete with a marked drop of

shock over particle velocity at pressures between 500 MPa to 2 GPa. But the true reasons for this minimum, whether being porosity, heterogeneity or bond behavior, were not well understood.

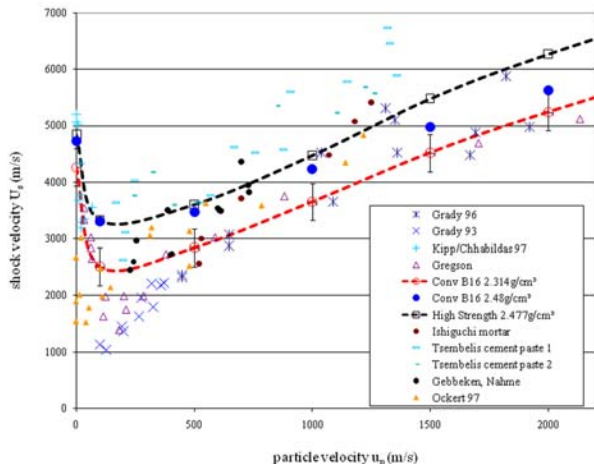


Fig. 9.2 Left: Concrete Hugoniot from literature references and newly derived curves (dashed lines); Right: Mortar sample on sabot for inverse plate impact.

9.1.2 Equation of State for a Large-Scale Heterogeneous Composite

Starting from this state-of-the-art, a different route was undertaken at Ernst-Mach-Institute to provide concrete shock data for pressures across the range of dynamic applications. In the developed mesomechanical method [15] the concrete was decomposed into aggregates larger than 1 mm and the remaining fine-grained mortar between all larger grains (see Figure 9.3). After measuring equation of state properties of the two components separately, hydrocode simulations of the meso-structure were used to derive macroscopic shock data of complete and unscaled concrete.

Inverse plate impact experiments on both components, but specifically with the concrete mortar, were the key experimental method to derive the highly dynamic compression data. The use of Aluminium and Copper witness plates with known material properties during impact of the concrete constituent samples allowed direct derivation of the shock states without further knowledge of its compression behav-

ior. The Rankine-Hugoniot relationships and the known equation of state properties of the impacted witness plate (density $\rho_{witness}$, soundspeed $c_{B,witness}$, slope $S_{witness}$) were used together with the measured free surface velocity u_2 at the initial shock plateau. Equations (9.4)-(9.9) allowed deduction of the shock states σ_h , u_p , U_s , e , ρ_h in the concrete sample [15].

$$\sigma_h = \rho_{witness} c_{B,witness} \left(\frac{1}{2} u_2 \right) + \rho_{witness} S_{witness} \left(\frac{1}{2} u_2 \right)^2 \quad (9.4)$$

$$u_{p,mortar} = v_{imp} - \frac{1}{2} u_2 \quad (9.5)$$

$$U_s = \frac{\sigma_h}{\rho_0 u_p} \quad (9.6)$$

$$e - e_0 = \frac{1}{2} \left(\frac{1}{\rho_0} - \frac{1}{\rho} \right) \sigma_h = \frac{1}{2} u_p^2 \quad (9.7)$$

$$\rho_h (U_s - u_p) = \rho_0 (U_s - u_0) \quad (9.8)$$

$$\varepsilon_h = \frac{u_p}{U_s} \quad (9.9)$$

Low impedance Aluminium witness plates and backings were used around the mortar samples to measure moderate shock amplitudes up to 5 GPa and subsequent release states, which are markedly different due to compaction processes. Shock reverberation of samples between much thicker copper samples of higher impedance provided reflected shock pressures up to 18 GPa. The methodology was developed with Dr. Hartwig Nahme at EMI and used in parallel for composites under space debris impact conditions [24], [41]. From the plate impact tests and additionally confined and unconfined static compression experiments and ultrasonic measurements, detailed dynamic material models were derived for mortar and, also with data from literature, for aggregate.

A direct simulation approach of the mesomechanical structure in a hydrocode was the method of homogenization to derive concrete data from constituents' properties. Therefore a representative sample of concrete was filled with aggregate and mortar matrix. During the implantation of aggregates, sizes were taken from civil engineering sieve lines under statistical distribution of dimensions and locations. Figure 9.3 shows a resulting, visually realistic concrete mesostructure in a hydrocode. To derive shock data, a planar shock (or compression) wave was excited by applying a constant velocity boundary condition to one end of the numerical sample. Lateral dimensions were large enough to describe a representative concrete volume. The lateral boundaries were constrained in normal movement to provide a uniaxial strain compression waves on the macroscopic scale. Figure 9.3, right, shows an example of a moderate elastic-plastic shock wave of 3.2 GPa pressure traveling from left to

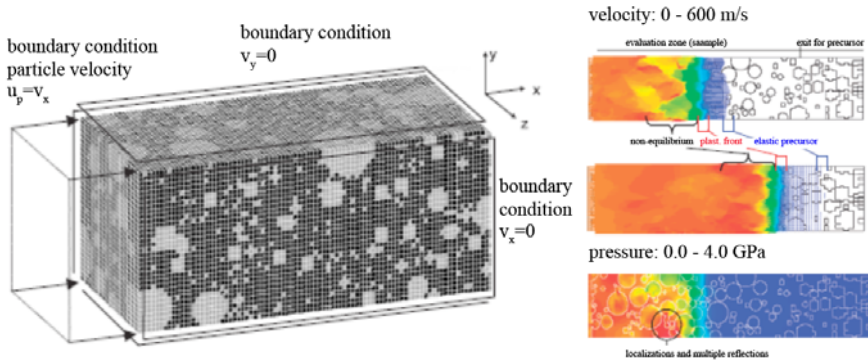


Fig. 9.3 Mesomechanical concrete model to derive the equation of state; Right: Velocity and pressure distributions in a 4.3 GPa planar shock.

right through the heterogeneous sample. The actual transition from mesomechanical states of individual cells to macroscopic properties was achieved through the evaluation of the effective macroscopic wave propagation speed U_s . The compression wave was considered to be arrived when half of the cells of a cross section had reached half the boundary particle velocity u_p .

Varying boundary particle velocities from 1m/s to 3000m/s created compression and shock waves ranging from 10MPa beyond 20 GPa. Interestingly, the characteristic drop of shock versus particle velocity observed in earlier experimental series by Grady and others could be explained in the mesomechanical simulation by the porous compaction properties of the mortar. Alterations of bond strength and bond density on the contrary were shown not to have an effect on the plain strain compression waves [13]. Two different density and distribution mixtures of conventional strength concrete were studied in the original work, high strength concrete has been analyzed in the same complete methodology later [15].

9.1.3 Combining Civil Engineering Knowledge and Shock Physics

The detailed shock properties of concrete then had to be coupled with state-of-the-art knowledge of macroscopic concrete strength. The key requirements for the model development were:

- consistent description from low velocity impacts to highest dynamic loads in shock waves (>10 GPa)
- improved triaxial description compared to the Holmquist and Johnson model, from higher confinements down to lower pressure regime, shear and tension

- rate dependent strength
- description of residual shear resistance of partly and fully damaged concrete under confinement

Despite all the different requirements and phenomena, the complexity of the model should still be user friendly.

$$f(p, \sigma_{eq}, \theta, \dot{\epsilon}) = \sigma_{eq} - Y_{TXC}(p) R_3(\theta) F_{Rate}(\dot{\epsilon}) = 0 \quad (9.10)$$

with

$$p = f(\rho \alpha, e) \quad \text{and} \quad \alpha = 1 + (\alpha_{init} - 1) \left[\frac{p_{comp} - p}{p_{comp} - p_{el}} \right]^N \quad (9.11)$$

The RHT model was developed as a synthesis of existing approaches from different loading regimes. Holmquist and Johnson's basic concepts of rate and pressure dependent failure surface (factors $F_{Rate}(\dot{\epsilon})$ and $Y_{TXC}(p)$ in equation (9.10)), a surface for residual friction resistance and a porous equation of state were taken as a starting point. Also the strain-based, pressure dependent damage evolution law (9.2) was adopted, yet only with respect to deviatoric deformations.

Chen's two surface concept for an initial elastic surface and hardening was additionally introduced with a Willam-Warnke formulation for a Lode angle dependence $R_3(\theta)$ in the deviatoric plane. As in Chen's work, the elastic limit surface was closed towards high hydrodynamic pressures (elliptic a cap function $F_{cap}(p)$ applied to (9.10)). This provided consistency with the variable pore crush pressure of a p-alpha equation of state.

A von Mises potential for plastic flow, neglecting associativity and low pressure shear dilation was used in favor of preserving the classical separation of equation of state and strength properties in hydrocodes.

With this comprehensive phenomenology but modular formulation (9.10) the model was first proposed in 1998 [12], fully developed and discussed until 2000 in the dissertation [13] and summarized again later in [16]. Professor Thoma initiated the integration as a standard model into the commercial hydrocode AUTODYN [42]. The adjustment was concluded in cooperation with Richard Clegg of Century Dynamics Ltd. in 2000 in version 4.1, where it has been continuously supported without further changes as 'RHT concrete'. This step made the model readily available to all users of the commercial hydrocode, forming the basis for the worldwide applications and discussions summarized in the following.

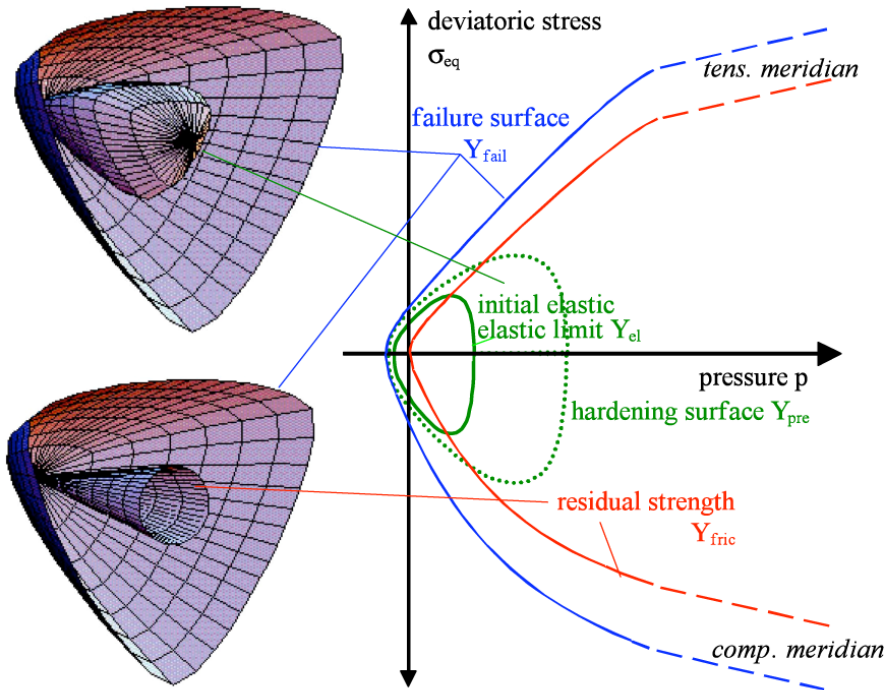


Fig. 9.4 Three RHT limit surfaces of elasticity, ultimate strength and post failure shear resistance depending on pressure, strain rate, triaxial stresses, controlled by porous compaction, hardening and damage evolution.

9.2 Applications in Impact Analysis

9.2.1 Extended Validation and Sensitivity Analysis

The initial validation in [12], [13] simulated the normal impact of a 430kg ogival penetrator ($L=1200\text{mm}$, $D=360\text{mm}$) at 250m/s on a $7.2 \times 7.2 \text{ m}$ and 1.6 m thick reinforced conventional strength concrete target. The simulations were compared to a unique full scale test series at the Bundeswehr Technical Center Meppen WTD91 [46] and 1:4 scaled light gas gun experiments at the Efringen-Kirchen site of Ernst-Mach-Institut. In the simulations, first principal 3D simulations were conducted, but 2D cylindrical symmetric simplification was still extensively used for the normal impact configurations. The rebar was modeled explicitly but simplified in shell layers of equal macroscopic strength and weight for front and rear layers of bending reinforcement. The shear rebar, identified as primary resistance factor close to the ballistic limit in sensitivity analysis, was represented as overlaid connections between front and rear reinforcement of equal strength and weight. For the test

case very close to the perforation limit of the concrete slab, the new model proved to be converging into the range of experimental scatter. Damage extensions were represented reasonably, the effect of scaling proved to be slightly under predicted, possibly an effect of inversed strain rate scaling.

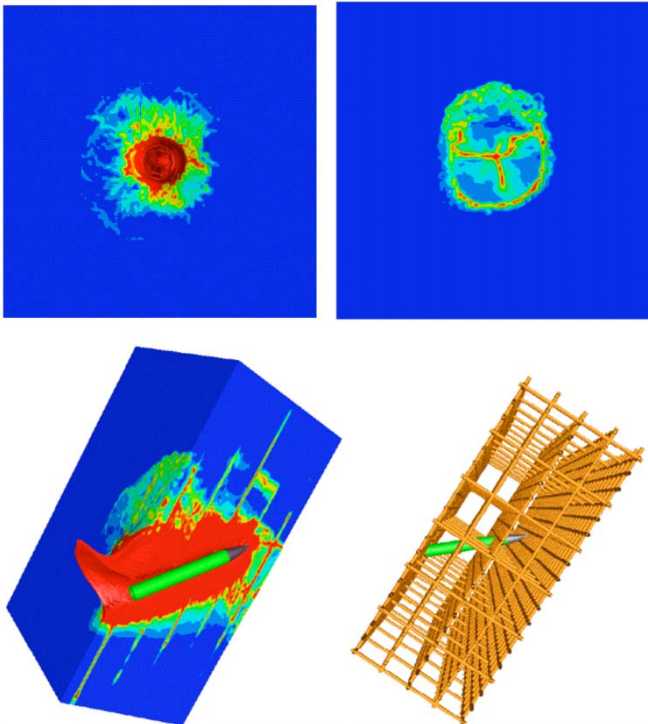


Fig. 9.5 First extensive 3D simulations by FOI including normal and oblique impact and explicit rebar modeling [18].

Håkan Hansson [18], [19] from the Swedish Defense Research Agency FOI first conducted and documented extensive studies with full three-dimensional representation of concrete targets including rebar. He validated the model against deep penetration of 3.6 kg ogival projectiles into unreinforced 48 MPa concrete at 420 m/s. For the normal impact validations he found good correlation between experimental penetration depth of 490 mm and simulations with 529 mm depth, a deviation below 8%. He stated reduced accuracy for perforation cases of plain concrete, dominated by tensile cracking.

His further simulation studies of oblique impacts were the first to include and document explicit rebar modeling using beam elements for every individual rein-

forcement beam (see Figure 9.5). He also analyzed applicability of different types of discretisations, such as Lagrangian mesh based and meshless representations as well as space-fixed Eulerian grids for the concrete target. In parallel, FOI conducted full characterization of a 115 MPa high strength concrete in the complete methodology summarized in chapter 1 with derivation of the concrete equation of state by mesomechanical characterization and simulations [15], triaxial compression experiments at the ERDC-WES up to 500MPa hydrostatic pressure [1] and Hopkinson-Bar experiments to derive the dynamic strength and fracture energy [45]. All the results were condensed to a high strength concrete parameter set for the RHT model.

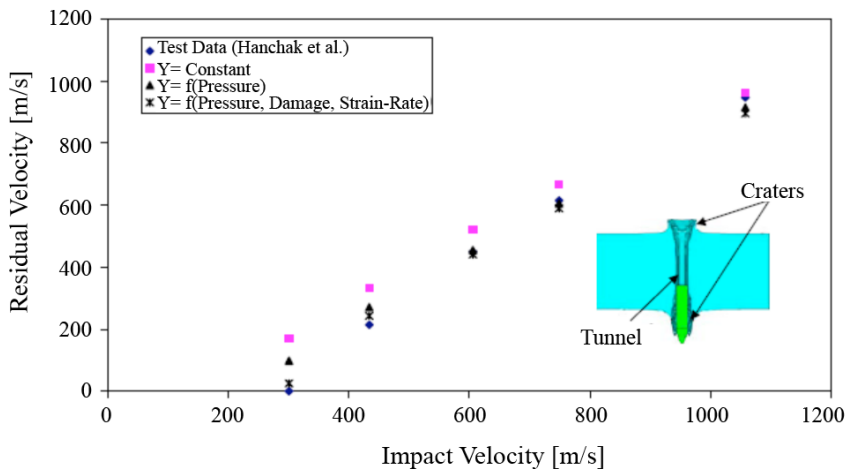


Fig. 9.6 Influence of model complexity on the replication of a R/C ballistic limit curve by Tham, Inst. High Performance Computing Singapore [17].

An investigation of different strength model complexities on the details of the ballistic limit curve has been reported by Tham from the Institute of High Performance Computing at Singapore [17]. He conducted further validation against ballistic limit data from Hanchak et. al. [34] for an ogival steel projectile ($m=0.5\text{kg}$, D 25,4mm) under normal impact between 300 and 1000m/s. He found good correlation with the detailed concrete strength description in the RHT model with respect to perforation velocities and damage extensions (Figure 9.7). Figure 9.6 summarises his sensitivity studies and points out, that perforations well above the ballistic limit are rather insensitive on details of the concrete strength model. Phenomena like pressure dependent failure and strain rate influence become important close to the ballistic limit.

Leppänen [4] at Chalmers University of Technology, Gteborg, Sweden analysed remaining deficiencies of the RHT concrete model. He correctly stated the lack of

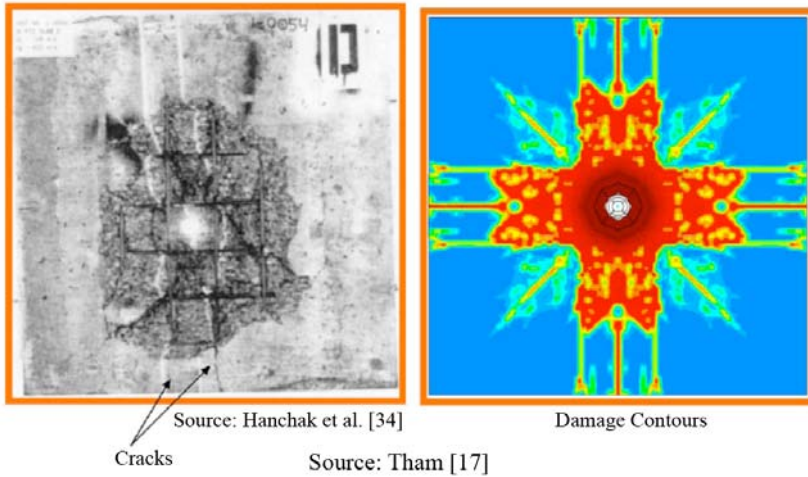


Fig. 9.7 Exit crater comparison for perforation with impact/exit velocity of 749 / 600 m/s [17].

explicit representation of fracture energy and details of the strain rate dependence as potential weak spots in tensile behaviour of unreinforced concrete. He used the test case of spherical steel projectiles impacting around 1900 m/s and 1100m/s on 140mm thick unreinforced concrete ($f_c = 68.9$ MPa) to conduct sensitivity studies on these two phenomena. The conclusion from his analysis was:

- The description of fracture energy strongly influences scabbing and cracking on the rear sides of the target. It has a minor effect on depth of penetration and spalling on the impacted side.
- The shape of the softening curve is less important than the inclusion of the correct amount of fracture energy to be dissipated by cracking.
- The crack zone and width is only moderately influenced by details of the strain rate dependent strength formulation.

Validation with respect to the limit Ricochet angle with detailed modeling of a deformable projectile has recently been conducted by Klein at Ernst-Mach-Institute. He simulated a thin hull 900kg penetrator at impact angles between 30° and 50° to the normal, comparing to earlier full scale tests at WTD91, Meppen and scaled experiments at Ernst-Mach-Institut [20]. Good correlation of deformations in reinforced concrete target and penetrator hull were found and are displayed in Figure 9.10.

The precision in replicating the limit case was necessary to further predict the Ricochet trajectory and velocity and ultimately the location of a possible detonation initiated from a time-controlled fuse (Figure 9.9). A subsequent blast simulation of



Fig. 9.8 200m/s impact footprint and deformed penetrator after a limit Ricochet chase in simulation and experiments at WTD91 and EMI.

the pre-damaged concrete target at relatively close distance was the last step to prove the integral resistance of a heavy shelter structure.

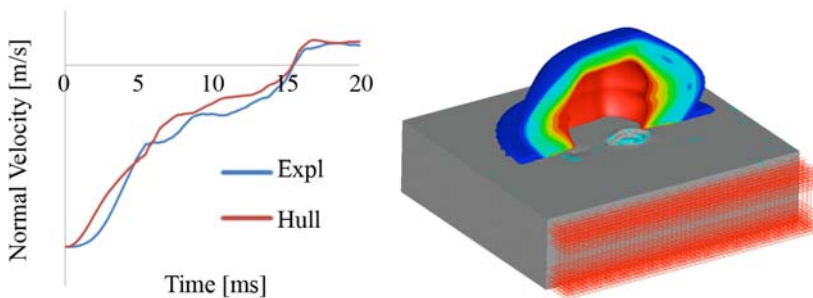


Fig. 9.9 Ricochet and subsequent close detonation on a damaged concrete target with detailed explicit rebar.

9.2.2 Deformable Projectiles and Coupling with Explosions

Joint impact of blast and fragments has been analyzed in a comprehensive study by Leppänen at Chalmers University of Technology at Göteborg, Sweden [5]. The authors placed a fragment charge of 1.3 kg high explosive at 0.6 m distance, accelerating predefined fragments of 4 mm radius at 1650m/s onto concrete blocks of 500 mm thickness.

They studied the joint effect of blast and impact on the damage zone in depth of the concrete both by experimental and numerical studies. In the experimental series the residual strength of the impacted concrete blocks was investigated in sections

subjected to compression and splitting tension tests. They found in simulations and test samples undamaged concrete below the impact zone down to a depth of 150 mm. Beneath that level increased damage was observed by both methods. Their numerical parameter study with and without synergy effects of blast and fragment loading demonstrated that the blast wave does increase the damage in the thick concrete target.

The impact of shaped charge jets has been studied by Berg at Sandia National Laboratories [2]. The simulated penetration depths of 660 mm for a two calibre stand-off lay quite consistently between the hydrodynamic prediction (584 mm) and test with high strength granite (900 mm). One example of their modelling applications is the comparison of damage zone extension for different stand-offs in Figure 9.10.

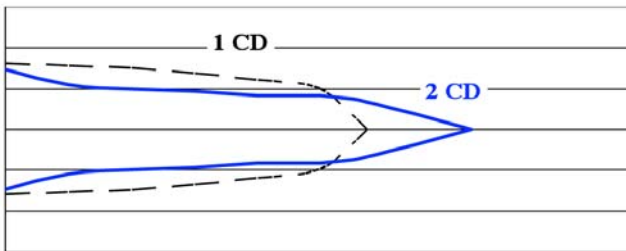


Fig. 9.10 Damage zones for shaped charge penetration into concrete from different caliber stand-offs, simulated at Sandia Nat. Laboratories [2].

9.3 Protecting Critical Infrastructure against Explosion Effects

Protection of infrastructure against explosion effects, such as air blast, contact and internal detonation, is a class of applications for which the RHT model has not been validated during the initial development. However, the consistent description from moderate strain rate effects and low pressure triaxial strength meridians across pore compaction processes up to extremely high pressures in a detailed equation of state promised applicability of the model also to this regime. At Ernst-Mach-Institut and several other research establishments the model has been used analyzed and discussed describing concrete structures under blast and contact detonations. The following chapter will give a condensed review of some key aspects.

A number of different explosion phenomena occurring on a six storey high rise building loaded by 1 ton TNT at 30m distance has recently been studied numerically by Lu et al. [6] from Nanyang Technological University, Singapore. The entire building frame including the basement was modeled by concrete volume elements and explicit rebar beams for storey plates and concrete beams (beams 400x400mm, storey height 3m, height and width above ground 20 x 10m, $f_c=30\text{MPa}$). Body fixed and space fixed hydrocode formulations were coupled to model interactions between building, surrounding gas flow field and soil.

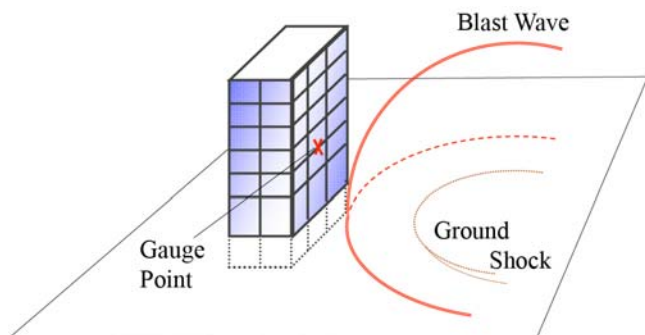


Fig. 9.11 Reinforced concrete frame, blast and ground shock domain for a fully coupled simulation of global and local damage by Lu at Nanyang University, Singapore [6].

The authors implemented their own soil model as a user subroutine. It describes the three phases of water, air and soil particles (indices w , g and s) in an equation of state (9.12) with a continuum damage model for the soil skeleton. Shear strength $f(J_2)$ depending on pressure (I_1) and strain rate is formulated as (9.13).

$$dp - \left(dV - \frac{\partial V_s}{\partial p} dp \right) \left[\left(\frac{\partial V_g}{\partial p_b} + \frac{\partial V_w}{\partial p_p} \right)^{-1} + \frac{\partial p_a}{\partial V_p} + \frac{\partial p_c}{\partial V_p} \right] = 0 \quad (9.12)$$

$$f = \sqrt{J_2} - (\alpha I_1 - k) \left(1 + \beta \ln \left(\frac{\dot{\epsilon}_{eff}}{\dot{\epsilon}_0} \right) \right) = 0 \quad (9.13)$$

The comparison between fully coupled simulations with re-runs only with air-blast and in turn ground shock gave a unique insight into the role and contribution of the different loading regimes. Figure 9.12 displays the simplified response of the second floor ceiling for all three simulation cases. The fully coupled and exclusive air shock analyses are virtually identical for the early peak responses. Decisively

later acts the ground interaction, providing no further critical amplitudes to the structure in the given configuration.

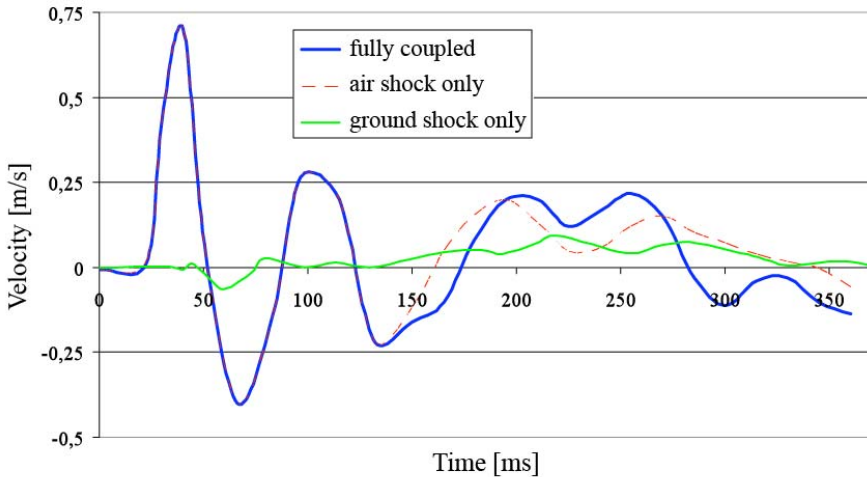


Fig. 9.12 Comparison of fully coupled, isolated air shock and isolated ground shock (left to right): velocity of second floor ceiling. The air shock proves to be dominant loading mechanism [6].

Comparing damage patterns for all three cases and timing of displacement in mid-span of front elements and floor plates, they further illustrated that the response of the complete structure does not alter the response of the most exposed elements. All these phenomena and their specific roles on blast resistance of building are often addressed but are hard to analyze. Therefore the work by Lu is seen as a very enlightening, comprehensive study.

A further interesting work on ground shock of buried reinforced concrete structures has been issued by the same group [7]. They used the same concrete and soil models and discretisations to study a buried side charge at a scaled distance of $2.7 \text{ m/kg}^{1/3}$). They highlighted a number of interesting results on possible assumptions in this case of loading scenarios:

- A 2D plain strain model provides similar concrete damage pattern on the directly affected side wall as a three-dimensional analysis.
- Noticeable differences occur between 2D and 3D in the floor plate accelerations by the shock wave refracted around the corner.
- Comparison with TM-5-1300 engineering formula for free field ground shock peak velocities and accelerations reveals much higher loads in the simulations (58g instead of 6.45g, 1.3m/s instead of 0.31m/s) when the structure is included and its structural response explicitly simulated

- Shock response spectra are evaluated and identify 100 Hz as critical frequencies

Ground shock in the sense of rock fragmentation has been analyzed by Preece [11] at Sandia National Laboratories. For a first qualitative study they modeled rock using the RHT concrete data set and studied fragmentation around explosive filled boreholes with and without pre-split crack behind.

9.3.1 Comparison to Engineering Models and Empirical Formula

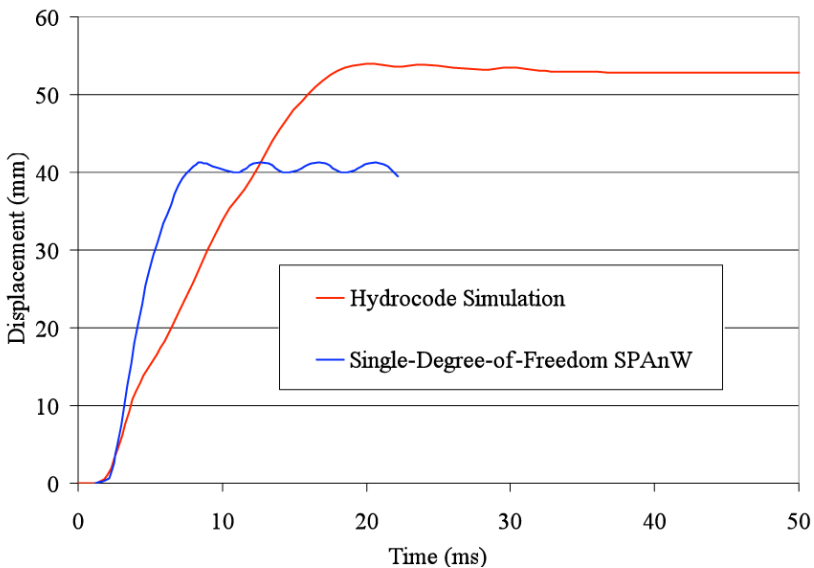


Fig. 9.13 Hydrocode and SDOF simulation of the limit loading of a heavy bunker wall by internal detonation at Sandia [3].

More quantitative validations have been published by Berg and Preece [3] from Sandia National Laboratories while using the model for internal detonation in a heavy concrete shelter. Besides a number of buildings sections predicted purely numerically they also compared a two-way spanned wall to a single-degree-of-freedom model (SPAn32 of US Army Corps of Engineers [43]). The SDOF model predicted a peak velocity $v_{max} = 10.5\text{m/s}$ and a maximum displacement $x_{max} = 42\text{mm}$ at 8 ms, the hydrocode simulated $v_{max} = 5.5\text{m/s}$ and $x_{max} = 54\text{mm}$ at 20 ms

(see also Figure 9.13). Seen the massive structure they found very reasonably agreement of a load case with large shear failure, but not total collapse.

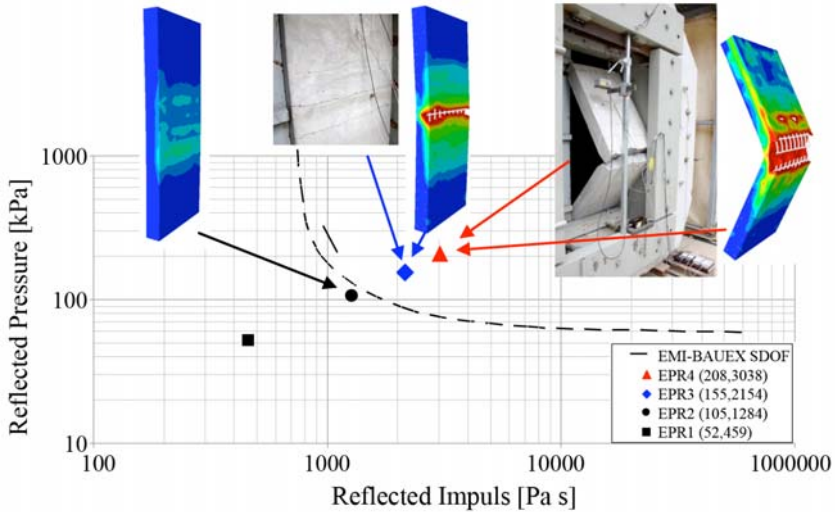


Fig. 9.14 Prediction of blast response and bending failure, compared to shock tube experiments and BAUX-SDOF calculations [14].

A further work by the author (Riedel et al. [14]) compared shock tube test on reinforced concrete panels, to single-degree-of-freedom predictions using EMI-BAUX and hydrocode simulations of concrete with explicit rebar. Good agreement concerning bending failure mechanisms and peak loads has demonstrated in the paper and Figure 9.14. The simplified shock tube samples replicated a typical reinforced concrete wall section ($t=24$ cm, 0.5% tensile reinforcement content) of security relevant office building (see Figure 9.15).

9.3.2 From Power Plant Security to Future High-Rise-Buildings

Riedel et al. [14] also compared experiments, predictions using the empirical engineering tool XPLOSIM [27] and FE simulations with respect to contact detonations (figures 9.16 and 9.17).

Motivation for the higher efforts using detailed FE models and many time steps of explicit time integration is the prediction of more complex scenarios involving the same failure mechanisms. Figure 9.18 shows an application in nuclear security

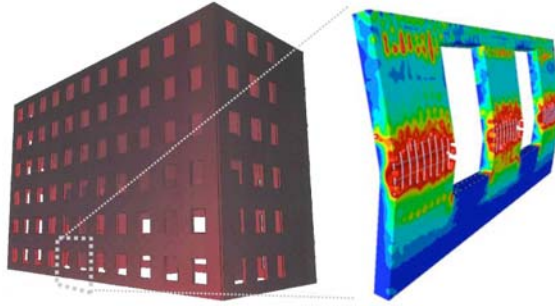


Fig. 9.15 Predictive hydrocode simulation of a security relevant office building under blast, validated by shock tube tests in Figure 9.14.

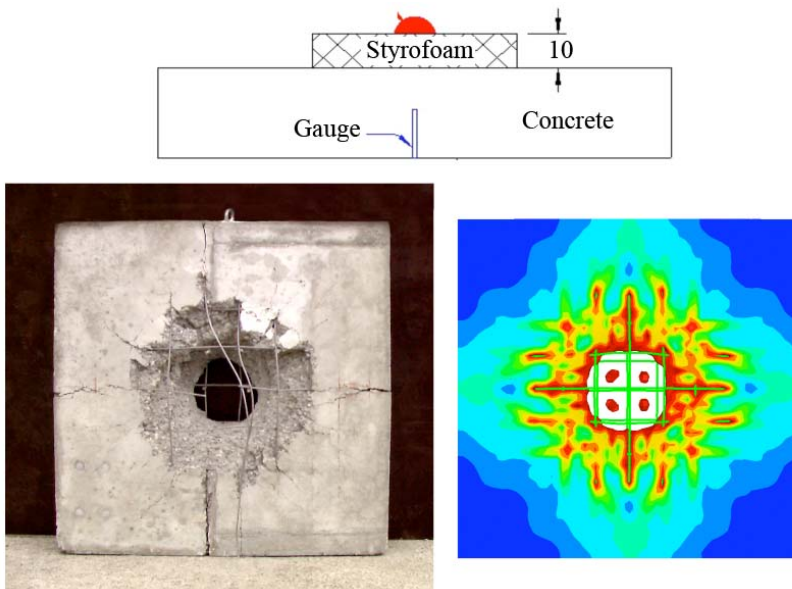


Fig. 9.16 Validation fo hydrocode simulations (right) against experiments (left).

analysis to wall sections composed of different thicknesses and reinforcement degrees.

Aircraft impact was in the past most extensively studied in the context of nuclear security analysis [44]. Hydrocode simulations and single and two degree of freedom models were also established, validated and used for design purposes in this domain. The know-how has recently been reviewed and readapted to the security of high rise buildings. In Germany the civil engineering company Schübler-Plan Consulting Engineers has proposed a concept of a future secure high-rise building

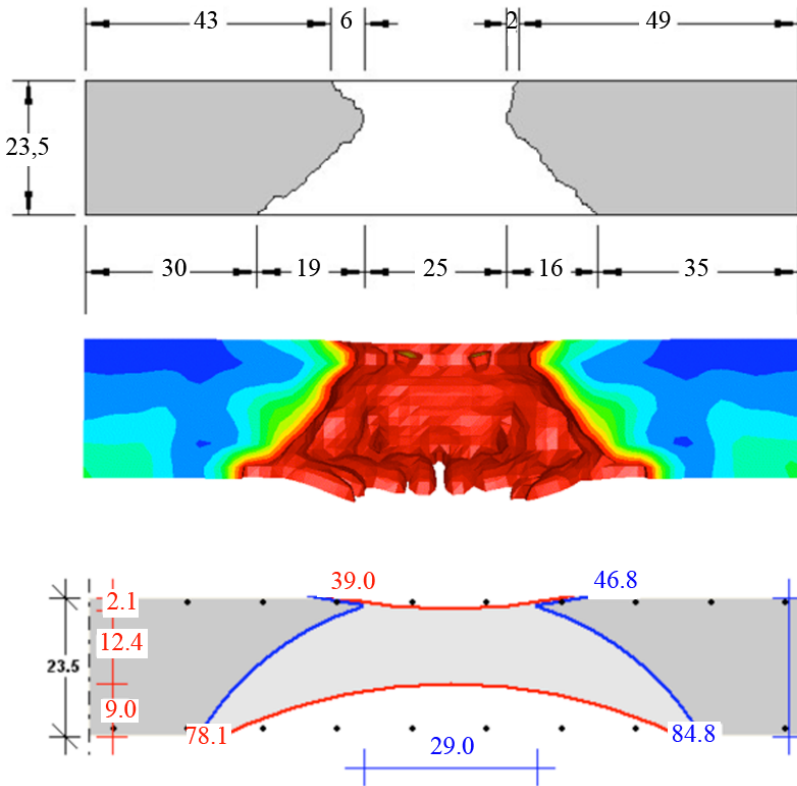


Fig. 9.17 Validation fo hydrocode simulations (middle) against experiments (top) and XPLOSIM [27] engineering tool predictions (lower) in [14].

called 'security scraper' [10]. An ongoing research with the University of Kassel, the principal German competence for ultra-high-performance concretes and Ernst-Mach-Institut deals with the development of a security core, which resists aircraft impact without perforation [9]. Nöldgen [10] showed that SDOF calculations for the dynamics deflection under the momentum of the impact of a complete aircraft provide global bending deflection of the building similar to peak wind gusts. He concluded that penetration resistance against engine impact, with weights up to 6.5 tons for largest civilian airliners, is the critical load case.

As a consequence, he studied in detail the local response of the UHPC high-rise core during the engine impact. Figure 9.19 summarizes the simplification of the engines mass distribution in equivalence to Sugano's analysis [44], leading to a mass spring model simulated by hydrocode (Figure 9.20) and two-degree-of-freedom model. Currently, a best fit of the RHT concrete model to UHPC strength meridians and equation of state properties is used to predict the ballistic limit. A detailed rep-

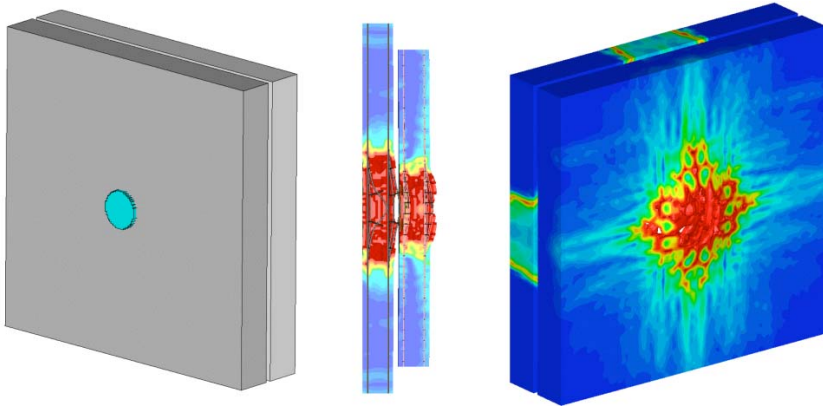


Fig. 9.18 Prediction of intrusion resistance with explosive attacks for nuclear security, courtesy by EnBW AG.

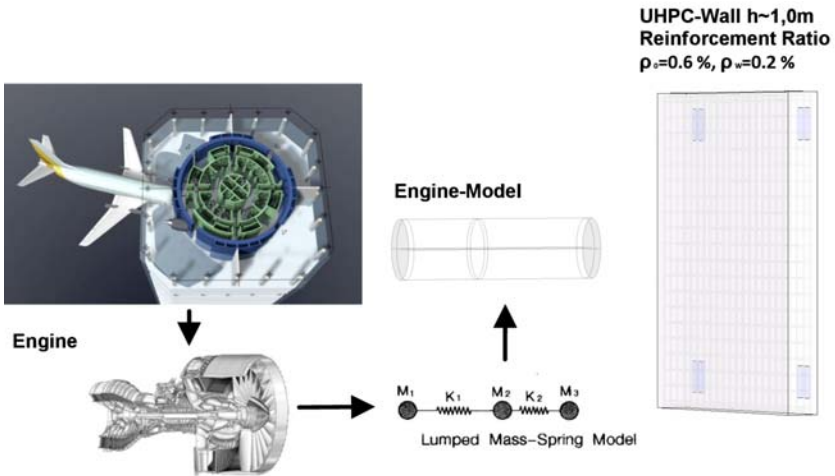


Fig. 9.19 Civilian aircraft impact analysis by Nöldgen, Schüßler-Plan Consulting Engineers [9][10], based on earlier nuclear safety studies [38].

resentation of the significant fracture energy of 1% to 2.5% fiber content is ongoing work. Hopkinson-Bar experiments recently measured dynamic fracture energies of 11000 N/m, which indicate an increase by more than one order of magnitude compared to 380 N/m for conventional concrete without fibers [39].

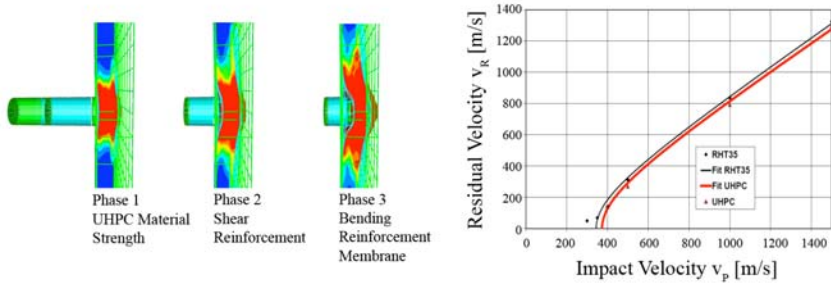


Fig. 9.20 First predictions of failure mechanisms and ballistic limit during aircraft engine on ultra high performance concrete [9].

9.4 Summary and Outlook

One decade after the development and broader entrance to service of the RHT model the understanding and predictive capabilities for the dynamic behavior of concrete have well advanced. The EMI concrete model has contributed to the progress together with other plasticity models as for example by Malvar [37] in the commercial hydrocode LS-Dyna, by Weidlinger Assoc. [38], [25] in the proprietary tool NLFlex or fundamentally different descriptions as by Bazant [21]. During the development at Ernst-Mach-Institut deeper understanding of the equation of state properties of concrete has been built. A number of following developments has been triggered, as the detailed experimental techniques to derive dynamic tensile strength and fracture energy in Hopkinson-Bar spallation tests [45],[39] and the proposition of similar models [30][28].

The RHT model has proven in a number of worldwide applications to successfully link low dynamic strength details to shock physics and to be applicable across the dynamic range of hydrocode simulations. Yet, truly predictive modeling going beyond qualitative agreement with this class of highly non-linear finite-element-methods will always require a significant level of expertise. If this is respected, validation experiments can be reduced and much better predicted prior to the test today.

References

1. Akers S, project progress reports on triaxial test 'swegraphs.ppt' and 'ch2.pdf', US Army Corps of Engineers, ERDC-WES, October 2003.
2. Berg VS, Preece DS, Shaped Charge Induced Concrete Damage Predictions Using RHT Constitutive Modeling, Proceedings International Society of Explosives Engineers, 2004G Volume 2.

3. Berg VS, Preece DS, Reinforced Concrete Structure Failure Mechanisms resulting from Explosive-induced Overpressures, Proceedings International Society of Explosives Engineers, 2004G Volume 2.
4. Leppänen J, Concrete subjected to projectile and fragment impacts: Modelling of crack softening and strain rate dependency in tension, *Int J Imp Eng* 32 (2006) pp1828.
5. Leppänen J, Experiments and numerical analysis of blast and fragment impacts on concrete. *Int J Imp Eng* 31 (2005) 843.
6. Lu Y, Wang Z, Characterization of structural effects from above-ground explosion using coupled numerical simulation, *Computers and Structures* 84 (2006) pp1729.
7. Lu Y, Wang Z, Chong K. A comparative study of buried structure in soil subjected to blast loads using 2D and 3D numerical simulations, *Soil Dynamics and Earthquake Engineering* 25 (2005) pp275.
8. Malvar LJ, Ross CA. Review of strain rate effects for concrete in tension. *ACI Material J* 95/6 (1998) pp735
9. Nöldgen M, Riedel W, Fehling E, Thoma K, Impact on structural Ultra High Performance Concrete (UHPC) elements in high-rise buildings, 2nd Int Symp on Ultra High Performance Concrete, 2008, pp. 759.
10. Nöldgen M, Riedel W, Thoma K, Fehling E, SECURITY SCRAPER - A Comprehensive Concept for Future High-Rise-Buildings, Future Security 3rd Security Research Conference Karlsruhe Sept. 10,11, 2008.
11. Preece D, Chung SH. Blast Induced Rock Fragmentation Prediction using the RHT Constitutive Material for Brittle Materials, Proceedings of the 2gth Annual Symposium on Explosives and Blasting Research, Society of Explosives Engineers, Nashville, TN, 2003.
12. Riedel W, Thoma K, Hiermaier S, Schmolinske E, Penetration of Reinforced Concrete by BETA-B-500, Numerical Analysis using a New Macroscopic Concrete Model for Hydrocodes. Proc. (CD-ROM) 9. Int Symposium on the Interaction of the Effects of Munitions with Structures, Berlin Strausberg (1999) pp315.
13. Riedel W, Beton unter dynamischen Lasten: Meso- und makromechanische Modelle und ihre Parameter, Hrsg.: Fraunhofer-Institut für Kurzzeitdynamik, Ernst-Mach-Institut EMI, Freiburg/Brsg., Fraunhofer IRB Verlag 2004, ISBN 3-8167-6340-5, <http://www.irbdirekt.de/irrbuch/>
14. Riedel W, Mayrhofer C, Customized Calculation Methods for Explosion Effects on Structural Building Components, Proc. Int. Symp. on Structures under Earthquake, Impact and Blast Loading 2008, Ed. Tachinaba, E., Katayama, M., Mukai, Y., Osaka, 2008.
15. Riedel W, Wicklein M, Thoma K, Shock Properties of Conventional and High Strength Concrete, Experimental and Mesomechanical Analysis, *International Journal of Impact Engineering* 35/3 (2008), pp155.
16. Riedel W, Kawai N, Kondo K, Numerical Assessment for Impact Strength Measurements in Concrete Materials, *International Journal of Impact Engineering* 36 (2009), pp283.
17. Tham CY, Reinforced concrete perforation and penetration simulation using AUTODYN-3D, *Finite Element in Analysis and Design*, 41 (2005) pp1401.
18. Hansson H, Penetration in concrete for projectiles with L/D=9, FOI-R-1659-SE, ISSN 1650-1942, Stockholm 2005, www.foi.se
19. Hansson H, Simulation of penetration in normal strength concrete for a projectile with L/D=9. FOI-R-1759-SE, ISSN 1650-1942, Stockholm 2005 www.foi.se
20. Klein H, Untersuchung zur Impakt- und Detonationswirkung einer Sprengbombe auf verschiedene Betonziele, EMI-Bericht I33/08, Freiburg 2009.
21. Bazant ZP, Xiang Y, Prat PC: Microplane Model for Concrete, I: Stress-Strain Boundaries and Finite Strain. *Journal of Engineering Mechanics*, März 1996, S. 245-254.
22. CEB-FIB Model Code 1990. Design Code. Lausanne, Switzerland: Thomas Telford; 1993 pp437.
23. Chen WF, *Plasticity in Reinforced Concrete*. McGraw Hill, New York, 1982. - ISBN 0-07-010687-8.
24. Clegg RA, White DM, Riedel W, Harwick W, Hypervelocity impact damage prediction of composites: Part I – material model and characterisation, *Int J Imp Eng*, 33 (2006) pp190.

25. Daddazio R, Vaughan D, Levine H, Two tools for the evaluation of the effects of blast on buildings Proc. Int. Symp. on Structures under Earthquake, Impact and Blast Loading 2008, Ed. Tachinaba, E., Katayama, M., Mukai, Y., Osaka, 2008.
26. Erkander A, Petterson L, Concrete as a protective barrier against fragment impacts: Fragment impacts on plates made of different concretes (in Swedish), FOA report C 20574-D6(D4), Swedish Defence Research Agency, 1985 pp66.
27. Gebbeken N, Greulich S, Pietzsch A, Landmann, F, (2004) The Engineering-Tool XPLOSIM to Determine the Effects of Explosive Loadings on Reinforced and Fibre Reinforced Concrete Structures, Proc. of 18th Int Symp Military Aspects of Blast and Shock, CD-ROM.
28. Gebbeken N, Greulich S, Pietzsch A, Harmann Th, Modellbildung zur Simulation von Stahlfaserbeton unter hochdynamischer Belastung, Ernst & Sohn , Beton- und Stahlbetonbau 103 (2008), pp398.
29. Gebbeken N, Greulich S, Pietzsch A. Hugoniot properties for concrete determined by full-scaledetonation experiments and flyer-plate-impact tests, Int J Impact Engineering 32 (2006) 2017.
30. Gebbeken N and Ruppert M, A new concrete material model for high dynamic hydrocode simulations", Archive of Applied Mechanics, 70, 463-478, 2000.
31. Grady DE and Furnish MD, Shock and Release Wave Properties of MJ-2 Grout. Sandia National Laboratories Rept., SAND88-1642, Dezember 1988.
32. Grady DE, Impact Compression Properties of Concrete. Proc. 6th Int. Symposium on Interaction of Nonnuclear Munitions with Structures, Panama City, Florida, May 3-7, 1993.
33. Grady DE, Shock and Release Data for SAC-5 Concrete to 25 GPa. Sandia National Laboratories Technical Memorandum - TMDG0595, Oktober 1995.
34. Hanchak SJ, Forrestal MJ, Young ER, Ehrgott JQ, Perforation of concrete slabs with 48 MPa (7 ksi) and 140 MPa (20 ksi) compressive strengths, Int. J. Impact Eng. 12 (1992) pp1.
35. Holmquist TJ, Johnson GR, Cook WH, A computational constitutive model for concrete subjected to large strains, high strain rates, and high pressures. Proc. 14th International Symposium on Ballistics, Québec, 1993, S. 591-600.
36. Langheim H, Stilp A, EMI report V2-86, Ernst-Mach-Institut Freiburg 1986.
37. Malvar LJ, Crawford JE, Wesevich JW, Simons D, A plasticity concrete mode for Dyna 3D, Int J Imp Eng 19 (1997) 847-873
38. Mould JC, Levine HS, A rate-dependent three-invariant softening model for concrete, Studies in Applied Mechanics, Mechanics of Materials and Structures, Voyiadjis et al (Eds), Elsevier, 1994.
39. Millon O, Riedel W, Thoma K, Nöldgen M, Fiber-reinforced ultra-high performance concrete under tensile loads, submitted to Journal de Physique, 2009.
40. Ockert J, Ein Stoffgesetz für die Schockwellenausbreitung in Beton. Dissertation Technische Hochschule Karlsruhe, 1997
41. Riedel W, Nahme H, Thoma K, Equation of State Properties of Modern Composite Materials, Modeling Shock, Release and Spallation, CP706, Shock Compression of Condensed Matter – 2003, 701-704, Ed. M.D. Furnish, Y.M. Gupta, W. Forbes, American Institute of Physics 0-7354-0181-0/04, 2004.
42. N.N., AUTODYN, Theory Manual, Century Dynamics Ltd. Horsham, UK, 2003.
43. N.N., SPAN32 Version 1.2.7.2., Army Engineer District Omaha, CENWO-ED-SH, Protective Design Center, 2001.
44. Sugano T, Tsubota H, Kasai Y, Koshika N, Ohnuma H, von Riesemann WA, Bickel DC and Parks MB, Full-scale aircraft impact test for evaluation of impact force, Nuclear Engineering and Design, 140:373–385, 1993.
45. Schuler H, Hansson H, Fracture behaviour of High Performance Concrete (HPC) investigated with a Hopkinson-Bar, J. Phys. IV France 134 (2006) 1145-1151.
46. Witte, Beschleunigungs-, Dehnungs- und Wegmessung an einer Stahlbetonplatte bei Penetrationsversuchen mit NVA-Munition, 5. und 6. Versuch, WTD91/200 – Nr. 203/98, 1998.

Chapter 10

Numerical Simulations of the Penetration of Glass Using Two Pressure-Dependent Constitutive Models

Sidney Chocron and Charles E. Anderson Jr.

Abstract

10.1 Introduction

Penetration of long gold (Au) rods into borosilicate glass was investigated experimentally as a function of impact velocity [1]. Flash radiography was used to measure the nose position and rod length as a function of time, and high-speed photography was used to measure the position of the failure front as a function of time. It was found that the failure front, which propagates at a speed much faster than the penetrating rod, quickly outdistances the projectile-target interface. Thus, except for the first few moments after impact, the rod presumably penetrates failed glass.

Independently, the responses of initially intact and predamaged borosilicate glass as a function of confinement have been measured. Two methods were used: triaxial compression and confined sleeve. The two characterization methods will be described briefly. The characterization data will then be interpreted using two pressure-dependent constitutive models – Drucker-Prager and Mohr-Coulomb – and constants for the two models derived from the results of the laboratory experiments. Next, numerical simulations of the glass impact experiments, using these two constitutive models, are presented. The numerical results are compared with the exper-

Sidney Chocron

Engineering Dynamics Department, Southwest Research Institute, San Antonio, TX 78250, USA,
e-mail: sidney.chocron@swri.org

Charles E. Anderson Jr.

Engineering Dynamics Department, Southwest Research Institute, San Antonio, TX 78250, USA,
e-mail: canderson@swri.edu

imental data, and conclusions made concerning the applicability of the two constitutive models for representing the penetration response of borosilicate glass.

10.2 Materials

Laboratory characterization tests, using the same type of glass as in the impact experiments, were performed on intact and predamaged samples of borosilicate glass. The brand name of the glass is Borofloat, manufactured by Schott Glass using a float process. X-ray fluorescence analysis performed on the test samples indicates an approximate composition (by weight) of: 80.5% SiO_2 , 12.7% B_2O_3 , 2.5% Al_2O_3 , 3.5% Na_2O , and 0.64% K_2O [2]. Mechanical properties of the intact glass, obtained by ultrasound measurement techniques [2], are: elastic modulus $E = 62.2$ GPa and Poisson's ratio $\nu = 0.20$ [2]. The density (ρ) is 2.23 g/cm^3 .

10.3 Experimental Techniques for Material Characterization

The two laboratory test techniques are briefly described. The two test techniques are complementary since one explores lower pressures (the bomb test) than the other (confined sleeve). The fact that they overlap at confining pressures of 300 or 400 MPa increases the confidence of interpretation of the confined sleeve technique.

10.3.1 'Bomb' Technique

The triaxial compression test is a 'classic' test used to characterize pressure-dependent materials like sands or concrete; for example, see Ref. [3]. A specimen is placed inside a thick-wall steel pressure vessel (the pressure 'bomb'). The pressure bomb is placed in an MTS machine. A steel piston runs from the loading platen of the MTS machine to the specimen through an alumina-loading anvil. A hydraulic fluid, controlled by a pump, is used to load the specimen at different constant fluid pressures. An axial load is applied from the MTS machine. For simplicity, this test will be referred as 'the bomb technique' in the text. Both intact and predamaged samples were tested. The cracks in the predamaged samples were generated by thermal shock as described in Ref. [4].

The equivalent stress for this simple load configuration with cylindrical symmetry is given by:

$$\sigma_{eq} = |\sigma_z - \sigma_r| = \tilde{\sigma}_z - \tilde{\sigma}_r \tag{10.1}$$

where σ_z is the axial load applied through the piston and σ_r is the fluid pressure ($\sigma < 0$ in compression, $\tilde{\sigma} > 0$ in compression). Tests were performed at fluid pressures of 25, 50, 100, 250, and 400 MPa. The nominal strain rate in these tests was 0.001 s^{-1} . The axial strain of the specimen was measured with a calibrated clip gage during the tests.

The results of four typical tests are shown in Fig. 10.1. Tests BF-63 and BF-61 were performed on intact samples at confinement pressures of 250 and 400 MPa, respectively. The dotted lines are straight reference lines that permit determination of when the measurements deviate from linearity. The exact cause of the non-linearity is unknown (perhaps densification?), but this non-linearity is not thought to be related to the propagation of cracks since failure for these samples is 'catastrophic'. Failure occurs suddenly (denoted by the vertical arrows), and after failure, the load carrying stress is zero since the samples 'exploded' in compression.

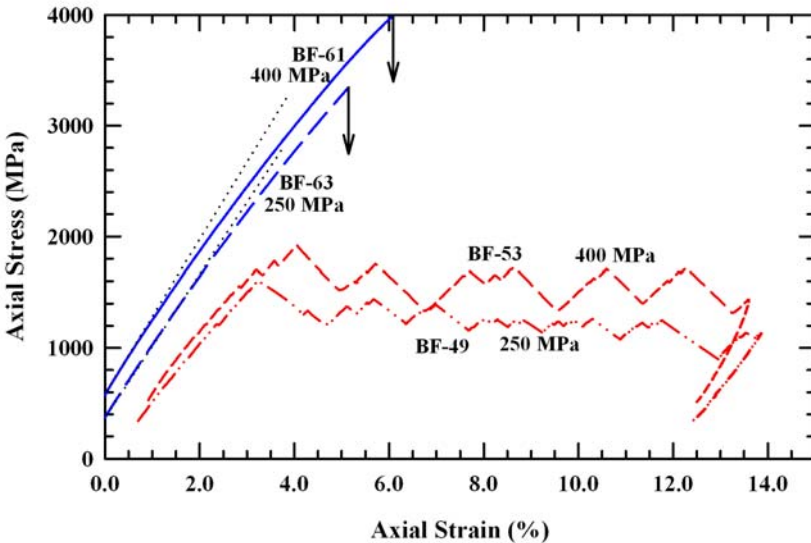


Fig. 10.1 Two intact samples (BF-61 and BF-63) and two predamaged samples (BF-49 and BF-53) tested in the pressure bomb at 250 and 400 MPa nominal confinement pressures.

Failure of predamaged samples is very different, as shown in Fig. 1 for tests BF-49 and BF-53. Upon reaching some maximum axial stress, the load drops, but the specimen still supports a significant amount of load for large strains. The initial drop in load carrying capability (at 2-4% axial strain) results from the formation of a shear plane. The stress-strain curve after this initial failure has a saw-tooth shape,

probably because the failure surfaces of the shear plane slide over each other, occasionally 'catching' and then releasing, creating the saw-tooth pattern. The load that the sample can support after its maximum will be called the 'residual' load. The residual load is not a uniquely defined quantity; instead, the residual load is represented by the 'peaks and valleys' of the sawtooth response.

The maximum confining pressure of ~ 375 - 400 MPa is limited by the hydraulic pump and the seals. Currently, the hydraulic pump cannot sustain pressures above approximately 400 MPa; however, the seals begin to leak profusely above ~ 500 MPa.

10.3.2 'Sleeve' Technique

A second testing technique consists of placing the specimens inside a confinement sleeve. The specimen is inserted into a Vascomax steel sleeve that is honed to fit the specimen. An axial compressive stress is applied to the specimen with an MTS servohydraulic machine by means of tungsten carbide or silicon carbide (SiC-N) platens.

The sleeve technique has also been used in the past to determine pressure dependence of the yield strength. For example, Chen and Ravichandran [5]-[6] characterized ceramics at high strain rates and high pressures by confining them in metallic sleeves. Ma and Ravi-Chandar [7], and Lu and Ravichandran [8] characterized aluminum and a metallic glass at slow strain rates, respectively. More recently, Chen and Luo [9] characterized intact and damaged ceramics under low confinement pressures at high strain rates. A confinement sleeve was also used by Forquin, et al. [10], in combination with numerical simulations, to characterize concrete at high pressures. In general the above references confine the samples at low to moderate pressures (100-300 MPa). In the present work, confinement pressures are significantly higher, on the order of 1 GPa.

An example of the results for a test series with multiple load cycles on a pre-damaged specimen is shown in Fig. 10.2. Jumps in the stress and pressure are apparent during the test, Fig. 10.2(a), and they imply a sudden discontinuity in the pressure applied to the specimen, probably due to internal slippage along a fracture plane. The jumps occur as the axial load is being applied. We believe that the jumps provide fundamental information of how the sample fails as a function of confinement pressure. Consequently, all the jumps recorded in each of the tests (four jumps in the one shown in Fig. 10.2) are placed on an equivalent stress versus hydrostatic pressure graph (the equivalent stress is computed from Eqn. (10.1) once the radial stress is calculated from the hoop strain gage). This technique is explained in detail in Ref. [11]. The right plot in Fig. 10.2 is a summary of the jumps recorded in all the

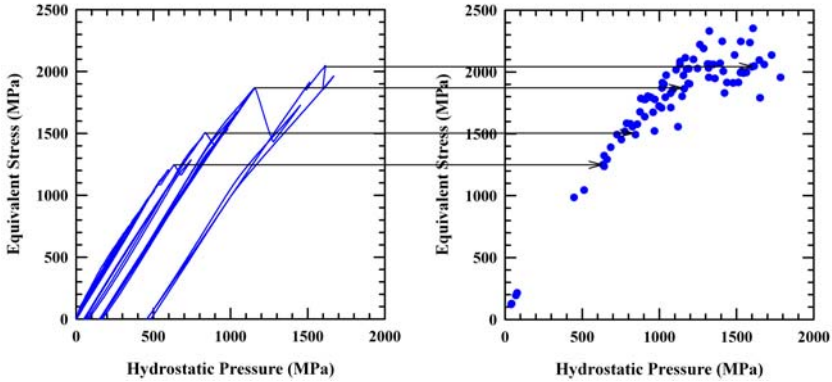


Fig. 10.2 Interpretation of the sleeve tests with predamaged specimens: only the points where sudden jumps occur (left figure, test BF-21) are considered in constructing the constitutive model, right figure.

tests conducted on predamaged samples by the confined sleeve test. It is noted that the hydrostatic pressure is a combination of the confining pressure and the pressure generated by the axial load.

10.4 Constitutive Model Interpretations

As mentioned in the Introduction, the assumption that will be made is that the projectile penetrates failed glass [1]. This is not exactly true at the very beginning of penetration, and details of the transition of intact to failed glass might be important at early times. However, for the range of impact velocities studied here, the failure front propagates at least twice as fast as the rod is penetrating; thus, it would appear that the assumption that the rod penetrates failed material is reasonable. We thus avoid needing a description of how the glass fails. The results of the laboratory experiments are now used to determine constitutive constants for computational material models to describe the strength of failed glass as a function of confinement pressure. A brief description of the models and the model constants is provided in the paragraphs below.

10.4.1 Drucker-Prager Model

The Drucker-Prager (DP) model [12] has the form:

$$Y = \begin{cases} Y_0 + \beta P & P < (Y_{cap} - Y_0) / \beta \\ Y_{cap} & P \geq (Y_{cap} - Y_0) / \beta \end{cases} \quad (10.2)$$

where Y_0 is the zero-pressure strength, β is the slope, P is the hydrostatic pressure (negative of the mean stress), and Y_{cap} is the limiting flow stress. Failure data obtained from tests like the ones shown in Fig. 10.2 were plotted in an equivalent stress versus hydrostatic pressure graph, as shown in Fig. 10.3. The solid triangles indicate predamaged confined tests. The open triangles represent the results of unconfined experiments. The equivalent stress for the confined specimens can be described by a linear function of the hydrostatic pressure. The data in Fig.10.3 suggests that an appropriate Drucker-Prager (DP) model for the predamaged samples can be written as:

$$Y = 0.423 + 1.2P \text{ (units in GPa)} \quad (10.3)$$

A similar procedure was followed to find the DP constants for intact specimens. The constants are shown in Table 10.1 for the two experimental methods. Additionally, the residual strength constants for the bomb tests were obtained from the same test that was used to estimate the predamaged constants. The saw-tooth portion of the data curve after failure was used to determine the 'residual' strength.

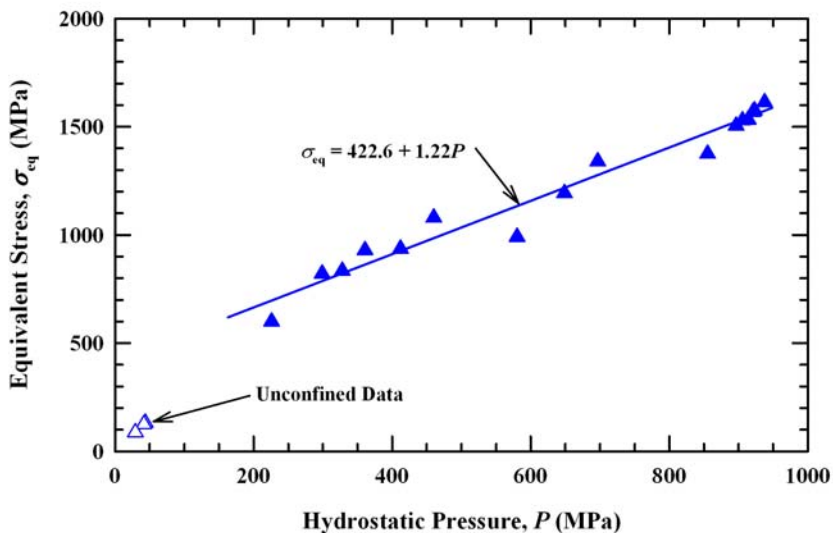


Fig. 10.3 Equivalent stress at failure for predamaged samples tested in the bomb.

It is observed that β , within the uncertainty of the measurements, is the same for the bomb tests and the confined sleeve tests, and is independent of the damage level. However, Y_0 decreases as damage increases. This observation will be important later

as we compare numerical results with penetration data. $\beta = 1.2$ will be used as the slope for the DP model; the influence of Y_0 on the computational predictions will be shown in a parametric study.

Table 10.1 DP parameters for intact and predamaged borosilicate glass.

Specimen	Bomb Test		Sleeve Test	
	Y_0 [GPa]	β	Y_0 [GPa]	β
Intact	1.6	1.2	1.3	1.1
Predamaged	0.42	1.2	0.73	1.0 – 1.3
Residual	0.14	1.1 – 1.2	-	-

Table 10.2 MC parameters obtained for intact and predamaged specimens.

Specimen	μ	Bomb Test	μ	Sleeve Test
		c [GPa]		c [GPa]
Intact	0.6	0.755	0.55	0.58
Predamaged	0.6	0.200	0.61	0.25
Residual	0.63	0.63	-	-

The last parameter required for the DP model is Y_{cap} . Ignoring a few ‘outlier’ points in Fig. 10.2b, the equivalent stress appears to fall between 1.90 GPa and 2.25 GPa, for a nominal value for $Y_{cap} = 2.1 \pm 0.2$ GPa. The data in Fig. 10.2 were obtained for quasi-static loading rates, and loading rates are high in penetration events. A limited number of tests were also performed at high strain rates and the results show that there is no (or negligible) strain-rate effect for borosilicate glass [13]. Bourne, et al. [14], conducted flyer-plate impacts on borosilicate glass and determined the shear strengths of intact and failed borosilicate glass. They found that the failed material has a strength of 1.6 ± 0.5 GPa. The data in Fig. 10.2b and Bourne’s data are consistent within measurement uncertainties, but the data scatter is sufficiently large that it is not particularly helpful in selecting a value for Y_{cap} . Numerical simulations will be used to refine a value for Y_{cap} .

10.4.2 Mohr-Coulomb Model

Predamaged specimens tested in the bomb systematically showed a shear plane at an angle between 55 and 70 degrees. The angle seems to be independent of the confinement pressure applied to the specimen. The DP model is based on the first invariant

of the stress tensor, I_1 , and the second invariant of the stress deviator tensor, J_2 . The flow surface in the π -plane is a circle, and thus, the DP model can never have a characteristic failure angle. Incorporating the third invariant J_3 into the description of failure results in flow surface on the π -plane being a polygon, which then has a characteristic failure angle. The Mohr-Coulomb (MC) model incorporates J_3 , and has a characteristic failure angle independent of the confinement pressure (see Ref. [15]); thus, it was felt that the MC model could be an appropriate candidate for describing the response of glass.

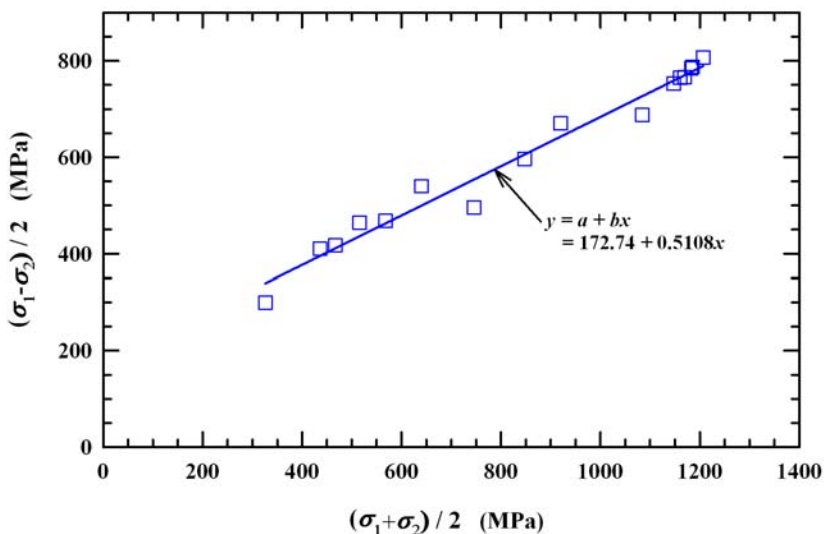


Fig. 10.4 MC failure points for predamaged samples tested in the bomb. σ_1 and σ_3 are the maximum and minimum principal stresses respectively.

The data from the bomb and confined sleeve tests were reanalyzed from the perspective of a MC model; results for the predamaged bomb specimens are displayed in Fig. 10.4. The MC model gives the maximum shear stress, τ , that the glass can support on any plane:

$$\tau = c + \mu \tilde{\sigma}_n \tag{10.4}$$

where c is the cohesion, $\mu \equiv \tan(\Phi)$ is the friction coefficient (Φ is the friction angle), and $\tilde{\sigma}_n$ the normal stress (positive in compression). Letting σ_1 and σ_3 be the maximum and minimum principle stresses, respectively, then $(\sigma_1 + \sigma_3)/2$ is the center of the Mohr circle, and $(\sigma_1 - \sigma_3)/2$ is the radius of the Mohr circle (maximum shear stress). A linear least squares fit of $(\sigma_1 - \sigma_3)/2$ versus $(\sigma_1 + \sigma_3)/2$ was performed on the test data to obtain an intercept and slope, as shown in Fig. 10.4, for the predamaged material: $a = 173$ MPa, $b = 0.51$. The relations between these

regression coefficients and the MC parameters are given by:

$$\Phi = \arcsin(b) \quad \mu = \tan(\Phi) \quad c = a/\cos(\Phi) \quad (10.5)$$

Therefore, for the predamaged samples, a MC model representation can be written as (units in GPa):

$$\tau = 0.21 + 0.6\tilde{\sigma}_n \quad (10.6)$$

Similar analyses were performed for the intact samples, residual strength and the sleeve tests. The constants are presented in Table 10.2.

There is more damage in the predamaged specimens than in the intact specimens. The residual strength measured in the bomb corresponds to a specimen with more damage than for the predamaged specimen. It is remarkable (maybe only a coincidence) that the friction coefficients for intact, predamaged and residual strengths are very similar (≈ 0.6) while the cohesion is severely reduced with increasing damage. This is analogous to what was found for the DP model.

10.5 Numerical Simulation of Penetration

We now apply the two constitutive descriptions to the penetration of glass. Behner, et al. [1], performed long-rod penetration experiments of gold (Au) rods into intact Borofloat 33 glass cylinders with a length of 60 mm and a diameter of 20 mm. The pure Au rods had a diameter of 1 mm and a length of 50 or 70 mm. The experiments were conducted in the reverse ballistics mode where the glass target was launched at the suspended Au rod, which was aligned using a laser. The impact velocity (v_p) was varied over a range of approximately 0.4 to 3.0 km/s. Flash radiographs were used to obtain penetration-time and rod length-time data. The slopes of the linear regression fits to the data provide the penetration (u) and consumption velocities (v_c), respectively, which are plotted in Fig. 10.5 as a function of v_p . High-speed photography was also used to measure the propagation of the failure front in the glass. More details of the experiments are given in Ref. [1].

The nonlinear wave propagation and material response computer program CTH [16] was used to conduct the numerical simulations. CTH contains a wide range of equations of state and viscoplastic models. Although the DP model was resident within CTH, the MC model was not; thus, the MC model needed to be implemented (as described in the Appendix). In addition to the inelastic response of the glass, as represented by either the DP or MC models, the elastic behavior of the damaged material must be modeled. It has been shown that if the material is well confined, a severely cracked sample has elastic constants similar to an intact specimen [17]; thus, the elastic response of failed material is the same as that of the intact material.

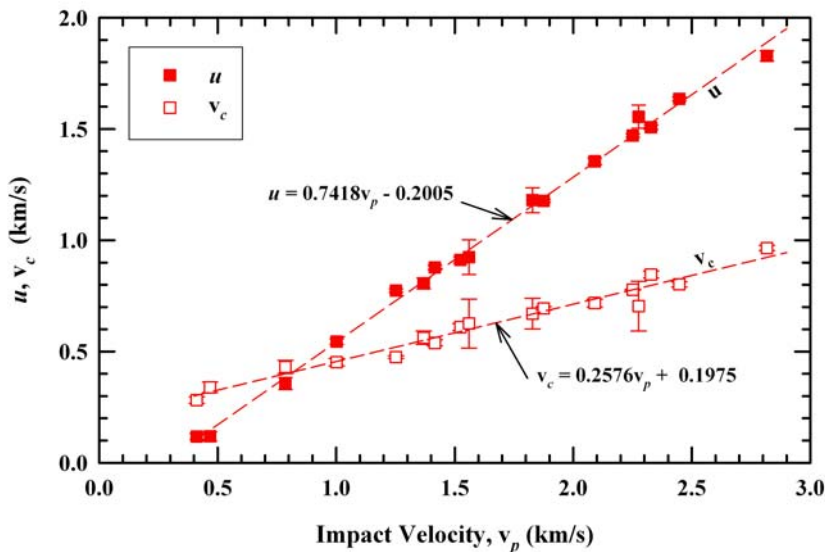


Fig. 10.5 Penetration and consumption velocities vs. impact velocity for borosilicate glass impacted by gold rods (regression lines recalculated to include highest velocity data points [1]).

The Mie-Grneisen equation of state was used to describe the thermodynamic response of the glass and the Au rod. The bulk modulus is 33.23 GPa; it was assumed that the glass had no nonlinear compressibility effects, i.e., $P = \kappa(\rho/\rho_o - 1)$, where κ is the bulk modulus, ρ is the density, and the subscript 'o' refers to the initial density. This is clearly an oversimplification, but it is believed that the penetration velocity would only be marginally affected by the inclusion of nonlinear terms. However, this assumption will be explored in future simulations. The Grneisen coefficient (Γ) was set to 1.0. The Steinberg-Guinan model was used to describe the equation of state and constitutive response of the Au [18], which has a density of 19.3 g/cm³. Seven zones were used to resolve the radius of the projectile (cylindrical symmetry), and this zoning was used throughout the problem.

10.5.1 Drucker-Prager Model

An estimate for Y_{cap} was made from the experimental data in Fig. 10.2, but there was uncertainty in whether the equivalent stress had, in fact, reached a maximum value. Previous work [19] demonstrated that the most important constitutive parameter at high impact velocities is Y_{cap} , i.e., the computational results are fairly insensitive to changes in Y_0 and β at high impact velocities. The highest velocity datum point was not included in the regression fit for u and v_c versus v_p in Ref. [1]. Since we decided

to use the highest velocity point to determine Y_{cap} , the regression analyses for u and v_c were redone, and these are shown in Fig. 10.5. We selected the highest velocity point (2.817 km/s) and conducted a parametric study on the influence of Y_{cap} . Y_{cap} was varied from 1.0 GPa to 2.4 GPa in increments of 0.2 GPa. The results are shown in Fig. 10.6.

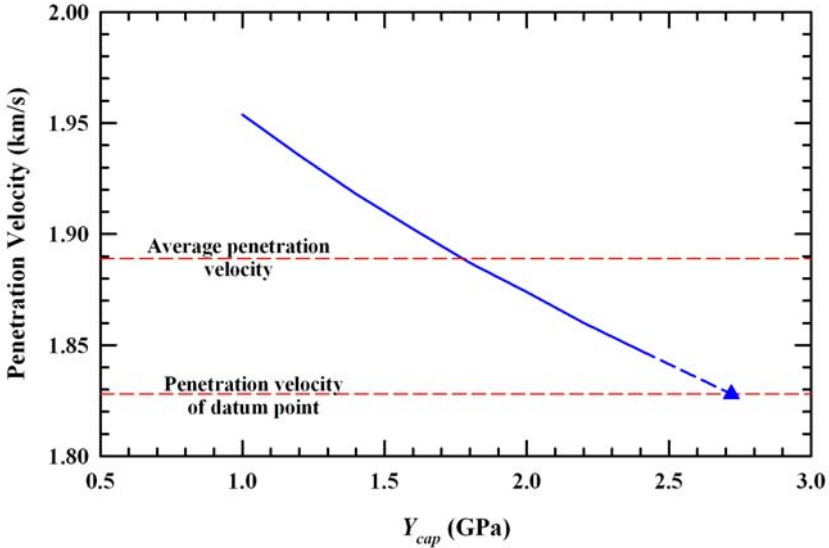


Fig. 10.6 The dependence of the penetration velocity on Y_{cap} .

Two horizontal lines are drawn in Fig. 10.6: one line represents the penetration velocity for the datum point at 2.817 km/s, while the other represents the least-squares fit of u versus v_p (the dashed line in Fig. 10.5). The simulation results were extrapolated to the triangular point to estimate Y_{cap} for a penetration velocity of 1.828 km/s. Note that Y_{cap} must be varied considerably to change the penetration velocity from nominally 1.83 km/s ($Y_{cap} = 2.72$ GPa) to 1.89 km/s ($Y_{cap} = 1.78$ GPa); Y_{cap} must be decreased by 34% to increase the penetration velocity by 3.3%. In spite of this large variation in Y_{cap} , these values are consistent with an interpretation that confining pressures were sufficiently high in the laboratory tests (Fig. 10.2b) that the cap was achieved.

For the next set of simulations, it was decided that the parameters of the constitutive model should be selected to reproduce the average penetration response, which is represented by the dash line in Fig. 10.5. The next set of simulations was conducted over the entire range of impact velocities using Eqn. (10.3) and $Y_{cap} = 1.78$ GPa. Computational results (not shown) fall significantly below the data at impact

velocities less than 1.5 km/s. Examining Table 10.1, it is observed that β is essentially constant (1.2) for the intact, pre-damaged, and residual damaged materials; but that Y_0 decreases with increasing levels of damage. We therefore hypothesize that the glass in front of the penetrator is more highly damaged than in our laboratory experiments, leading to a lower value of Y_0 . Therefore, we conducted a parametric study on Y_0 , with $\beta = 1.2$ and $Y_{cap} = 1.78$ GPa. The impact velocity was incremented in steps of 0.25 km/s, as Y_0 was varied between 0 and 100 MPa. The results are plotted in Fig. 7, where they are compared to the experimental data. The dashed-dot line represents the least-squares regression – as shown in Fig. 10.5 – through the experimental data. It is seen that a value of $25\text{ MPa} \leq Y_0 \leq 50\text{ MPa}$ reproduces the penetration velocity quite well for the lower impact velocities. Y_0 is thus taken as an average of 25 and 50 MPa, i.e., $Y_0 = 38$ MPa.

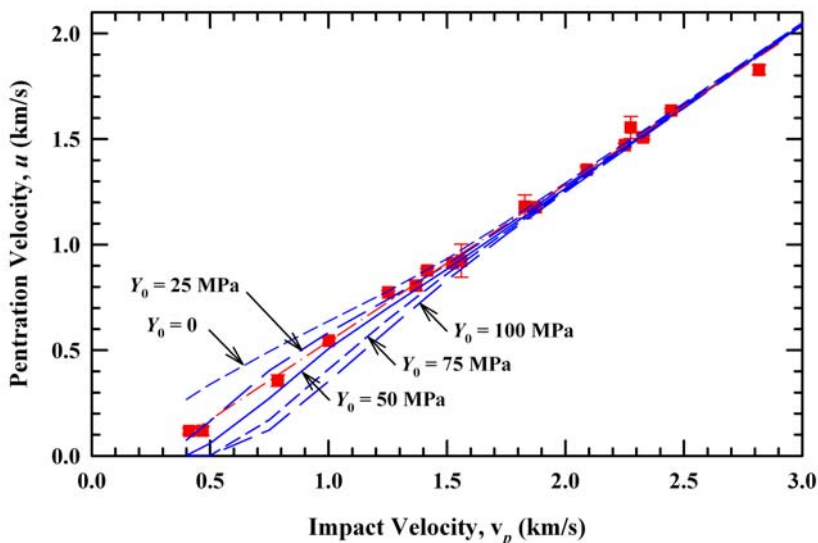


Fig. 10.7 Sensitivity study on Y_0 (with $\beta = 1.2$ and $Y_{cap} = 1.78$ GPa)..

As already indicated, the penetration velocity is not particularly sensitive to changes in Y_{cap} . The simulations indicate that the cap could be between 1.78 GPa and 2.72 GPa (the triangle in Fig. 6); whereas the experimental data indicate that the cap is 2.1 ± 0.2 GPa. We therefore use the experimental data in Fig. 10.2b to provide the estimate for the cap. However, simulations are required to estimate Y_0 for comminuted glass. Thus, for highly damaged borosilicate glass, the applicable DP constants are:

$$Y = \begin{cases} 0.038 + 1.2P & P \leq 1.72 \text{ GPa} \\ 2.1 \text{ GPa} & P > 1.72 \text{ GPa} \end{cases} \quad (10.7)$$

where all units are in GPa.

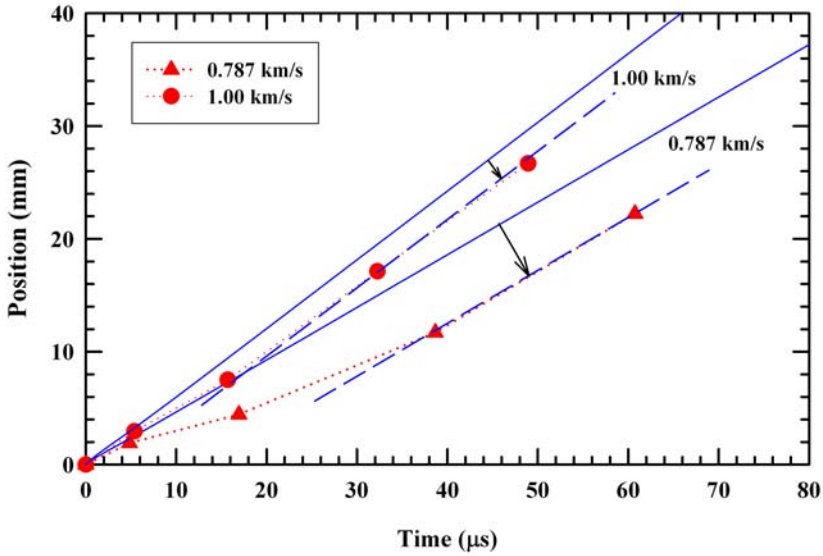


Fig. 10.8 Comparison of the simulation results to position-time data $Y_0 = 25 \text{ MPa}$).

Penetration versus time is nonlinear for the lowest impact velocities [1]. The penetration-time simulation results, using 25 MPa for Y_0 , are compared to the experimental data for the experiments conducted at 0.787 km/s and 1.00 km/s in Fig. 10.8. The experimental data points are linked by the dotted lines. The solid lines are the computational results, and they clearly overpredict the depth of penetration. However, the late time ($> \sim 20 \mu\text{s}$) penetration velocity is captured quite-well by the simulations, as indicated by the dashed lines, which are drawn at the same slopes as the solid lines. There is slight nonlinearity of the penetration-time data at early times for $v_p = 1.2 \text{ km/s}$, but by 1.5 km/s, the penetration-time curves are linear (i.e., constant penetration velocity). Thus, *it is concluded that at the lowest impact velocities, the assumption that the gold rod penetrates only highly damaged glass is not valid; that is, details of the transition from intact to damaged glass are important and cannot be ignored during the early stage of penetration at low impact velocities.*

10.5.2 Mohr-Coulomb Model

As mentioned above, the MC model was implemented into CTH. For the first set of simulations, constitutive parameters very similar to the ones obtained in the bomb tests for predamaged samples were used (a two-parameter model, Equation 10.6). It was found that the penetration velocity was greatly underestimated unless the friction angles and cohesion were greatly reduced. A mesh sensitivity study was conducted, varying the number of zones resolving the projectile radius between 5 (coarse) and 15 (very fine) zones; the simulation results showed very little sensitivity to changes in zoning. Thus, the numerical simulations are numerically resolved.

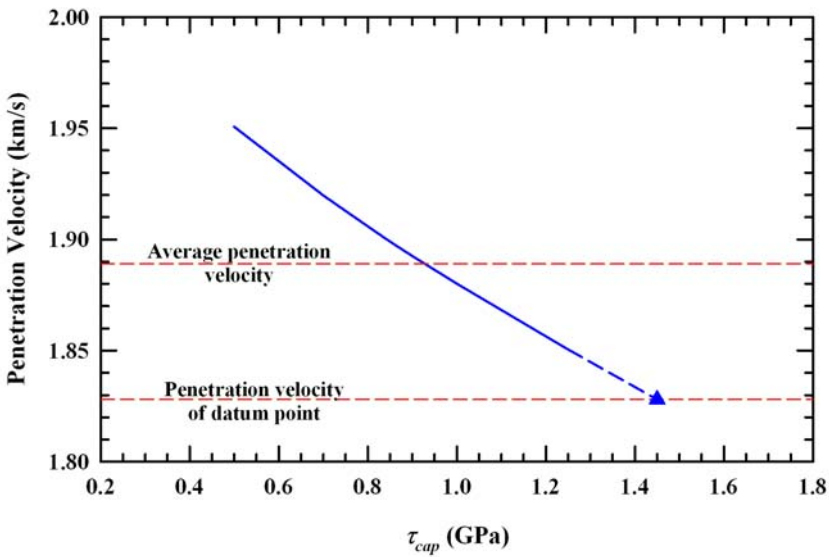


Fig. 10.9 The dependence of the penetration velocity on τ_{cap} .

Therefore, we went to a 3-parameter model by imposing a cap on the shear stress, τ_{cap} . In general, there is not a one-to-one correspondence between DP and MC constitutive parameters. However, for a cylindrical triaxial test where there is radial confinement along with an axial load, then the following equation applies:

$$\tau_{cap} = \frac{Y_{cap}}{2} \quad (10.8)$$

The conditions of cylindrical triaxiality are reasonably reproduced immediately beneath the penetrating projectile, so Eqn. (10.8) should approximately hold. A parametric study on τ_{cap} was conducted, similar to the one that was done for Y_{cap} (Fig. 10.6), using the MC model, at an impact velocity of 2.817 km/s. The results

are shown in Fig. 10.9. We see the same sensitivity between τ_{cap} and the penetration velocity as was shown for Y_{cap} . The results of the parametric study are extrapolated to the penetration velocity of the datum point, represented by the triangle. Again, we elect to model the average penetration response, which from Fig. 10.9 gives a value of $\tau_{cap} = 0.925\text{GPa}$. This is within 4% of the prediction from Eqn. (10.7) using $Y_{cap} = 1.78\text{ GPa}$. Given the accuracy of the simulations (particularly in estimating the penetration velocities), we can state that Eqn. (10.8) provides a relationship between the caps of the DP and MC models.

Next, a parametric study was conducted on the cohesion, c , with $\mu = 0.6$ and $\tau_{cap} = 0.925\text{ GPa}$. Results are shown in Fig. 10.10. The numerical results look essentially identical to the results using the DP model, Fig. 10.7. The cohesion c in the MC model is analogous to Y_0 in the DP model. The fact that numerical simulations need a very small cohesion value to match the ballistic experiments is not seen as a contradiction with the characterization tests. As discussed when the bomb tests were presented, the cohesion decreases with damage. The cohesion of the 'residual-strength' material, see Table 10.2 is already small and, presumably, the material under the projectile is more damaged than the 'residual-strength' material tested in the bomb.

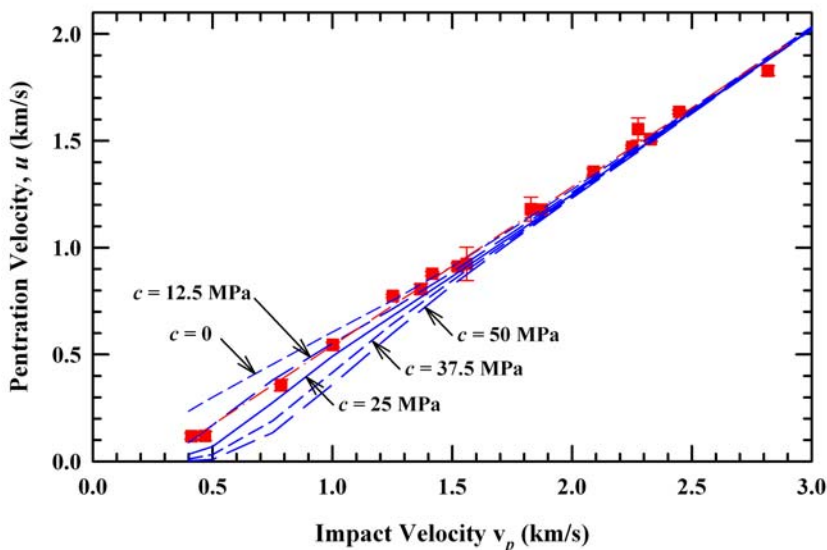


Fig. 10.10 Sensitivity study on c (with $\mu = 0.6$ and $\tau_{cap} = 0.925\text{ GPa}$).

Not shown is a graph for the MC model analogous to Fig. 10.8. The same observations and conclusions hold for the MC model as for the DP model concerning early-time penetration at the lower impact velocities.

Similar to Y_{cap} , it was decided to estimate τ_{cap} from the experimental data instead of taking the value from an 'exact' match of the simulations. Given the above considerations, the three parameter MC model proposed for damaged borosilicate glass is:

$$\begin{cases} \tau = 0.012 + 0.6\tilde{\sigma}_n & \tilde{\sigma}_n \leq 1.65 \text{ GPa} \\ \tau = 1.0 \text{ GPa} & \tilde{\sigma}_n > 1.65 \text{ GPa} \end{cases} \quad (10.9)$$

This model reproduces the characterization experiments (stresses and failure pattern), and the ballistic tests (penetration velocity), albeit the cohesion needs to be increased for the characterization experiments.

10.6 Summary and Conclusions

Numerical simulations of a gold rod penetrating borosilicate glass were conducted using two different pressure-dependent constitutive descriptions – Drucker-Prager (DP) and Mohr-Coulomb (MC) – for the glass. Constants for the two models were derived from laboratory characterization experiments. These laboratory experiments were triaxial compression ('bomb') and confined sleeve tests. The confined sleeve test explores higher pressures than possible with the triaxial test, but the results for the two tests overlap at pressures of about 350 MPa, providing increased confidence in the results.

The slope (β) for the DP model and the friction angle (Φ) for borosilicate glass were determined from the characterization experiments, and were found to be independent of the degree of damage to the glass (intact, predamaged, residual damaged). However, the zero-pressure strength (Y_0) and the cohesion (c) for the DP and MC models, respectively, depended upon the degree of damage, with these parameters decreasing as damage increased.

The confining pressures in the confined sleeve experiments were sufficiently high to achieve a saturation of the load-carrying ability of the damaged glass, i.e., a cap. There was some uncertainty however, because of data scatter, in interpretation of the experimental data. Previous work [19] demonstrated that the cap controls the penetration velocity at high impact velocities so parametric simulations were conducted to investigate the dependence of the penetration velocity on the cap (Y_{cap} and τ_{cap}). The parametric studies here show that the penetration velocity of an Au rod into borosilicate glass is relatively insensitive to quite large variations in the value of the cap. A $\sim 40\%$ increase in the cap resulted in only a $\sim 3\%$ decrease in the penetration velocity. Nevertheless, the value deduced for the cap from numerical simulations was in agreement with the experimental characterization results. Further, it was shown that $\tau_{cap} = Y_{cap}/2$.

It was assumed that the projectile penetrated failed material; thus, details of the transition of intact glass to failed glass were avoided. The rationale for this approach was that the failure front propagates much more rapidly than the projectile penetrates; thus, the projectile penetrates failed material.

Parametric studies were required to deduce the zero-pressure strength (Y_0) and the cohesion (c) for the DP and MC models to reproduce the penetration velocities of the gold rod at the lower impact velocities ($v_p < 1.5\text{km/s}$). The values deduced from the simulations were significantly lower than obtained for the characterization experiments. It was concluded that the material beneath the penetrator is more highly damaged (comminuted) than the damaged glass characterized in the laboratory experiments.

It was also seen that at the lowest impact velocities that the constitutive model underestimates the penetration resistance of the glass at early penetration times; however, the simulations reproduce the later time penetration velocities. This suggests that details of the transition of intact to damage glass are important at the lower impact velocities, and that a more comprehensive glass model (intact, damage initiation, damage propagation) is required in order to model projectile penetration over the full range of impact velocities.

At this point, the DP and MC constitutive models do equally well in predicting the penetration response of a gold rod into damaged borosilicate glass. Two of the three constitutive constants needed for each model were derived from laboratory characterization experiments, but a third parameter – one that appears to be associated with the degree of damage – had to be inferred from matching simulations to ballistic experiments. These observations could potentially simplify a more comprehensive glass model: *damage seems to affect only the zero-pressure intercept (DP model) or cohesion (MC model) of the glass*. A potential advantage of the Mohr-Coulomb model, which may be more relevant for the intact material, is that the MC model provides a characteristic failure angle, whereas for the DP model, damage is isotropic.

Acknowledgements The authors would like to thank Dr. Doug Templeton from RDECOM-TARDEC for his moral and financial support. The authors also thank Dr. James Walker (SwRI) for many helpful technical discussions. We are indebted to Mr. Dennis Orphal (International Research Associates) and Mr. Tim Holmquist (SwRI) for their careful reviews of the manuscript and their constructive suggestions.

Appendix: Implementation of the Mohr-Coulomb Model into CTH

CTH is a nonlinear wave propagation and material response (hydrocode) computer program developed by Sandia National Laboratories [16]. CTH contains a wide range of equations of state and viscoplastic models that can be selected by the user, depending upon the problem. For brittle materials like ceramics or glass, which have a strength that is pressure dependent, the typical choices would be the Johnson-Holmquist [20] Drucker-Prager models. As mentioned earlier, although the DP model can successfully reproduce stress-strain curves obtained in the pressure bomb, it lacks the capability of reproducing a failure pattern like the one observed in the experiments. Since it was not known how important this feature would be when simulating projectile penetration, it was decided to implement the MC model into CTH.

Flow Surface and Implementation

Nayak [21] developed an equation for the MC flow surface that can be very conveniently implemented in hydrocodes:

$$F = \sigma_m \sin \Phi + \bar{\sigma} \cos \theta_0 - \frac{\bar{\sigma}}{\sqrt{3}} \sin \theta_0 \sin \Phi - c \cos \Phi = 0 \quad (10.10)$$

where $\sigma_m = \sigma_{ii}/3$ is the mean stress, $\bar{\sigma}$ is the equivalent stress, and θ_0 is the lode angle defined by:

$$\theta_0 = \frac{1}{3} \arcsin \left(-\frac{3\sqrt{2} J_3}{2 \bar{\sigma}^3} \right) \quad (10.11)$$

J_3 is the third invariant of the stress deviator tensor. CTH uses radial return for most of its viscoplastic models, for example, the von Mises and Drucker-Prager models. That means that the flow rule is non-associative but the return is done in the π -plane and at constant pressure. To circumvent the implementation of the radial return and stress rotations, CTH was modified to use, where possible, algorithms already in CTH. The subroutine implemented calculates F according to Eq. (10.10) for each cell and time step. The algorithm first assumes that the response is completely elastic. If $F < 0$, nothing more needs to be done; but, if $F > 0$, the cell material is yielding and the subroutine computes the radial return scaling factor to bring the deviatoric stress back to MC surface, see Fig. 10.11. It also computes the strength as if it were a von Mises flow surface. This strength is then passed on to CTH so CTH can actually perform the radial return and stress rotations.

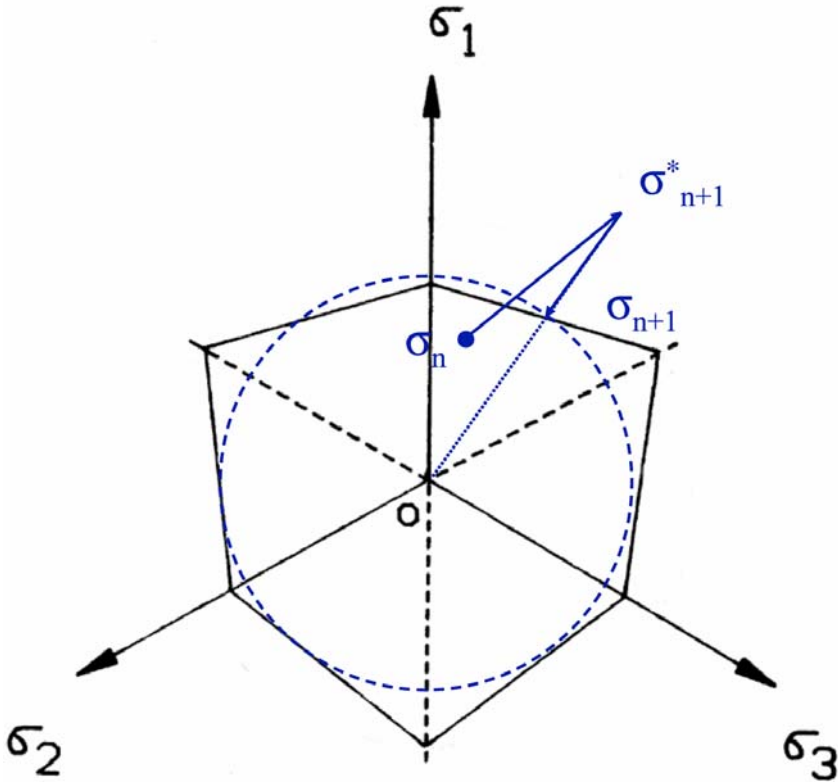


Fig. 10.11 Implementation of Mohr-Coulomb model into CTH.

The parameter m that scales the stress deviators to the flow surface (see, for example, Wilkins [22]) is easy to compute from Eq. (10.11) by just replacing $\bar{\sigma} = m\bar{\sigma}^*$ and $\sigma_m = \sigma_m^*$ where σ^* is a trial stress found assuming that the body is elastic:

$$m = \frac{c \cos \Phi - \sigma_m^* \sin \Phi}{\bar{\sigma}^* \left(\cos \theta_0 - \frac{\sin \theta_0 \sin \Phi}{\sqrt{3}} \right)} \tag{10.12}$$

where, again, c is the cohesion of the MC solid and Φ its friction coefficient.

A shear stress cap τ_{cap} was also implemented in CTH to limit the shear stress the solid can bear. Therefore, the actual MC model that was implemented is:

$$\begin{cases} \tau = c + \tan(\Phi)\sigma_n & \text{when } \tau < \tau_{cap} \\ \tau = \tau_{cap} & \tau \geq \tau_{cap} \end{cases} \tag{10.13}$$

where now the material constants are c , cohesion, $\mu = \tan \Phi$, friction coefficient, and τ_{cap} is the cap. The scaling factor when $\tau_{max} > \bar{\tau}$ is given by:

$$m = \frac{\bar{\tau}}{\bar{\sigma}^* \cos \Phi_0} \quad (10.14)$$

The implementation of the code was thoroughly checked using simple cases where the answer was known analytically, for example, uniaxial strain or uniaxial stress in compression and tension, pure shear, and triaxial compression.

References

1. Behner T, Anderson CE, Orphal DL, Hohler V, Moll M and Templeton DW, (2008), Penetration and failure of lead and borosilicate glass against rod impact. *Int. J. Impact Engng.*, 35:447–456.
2. Patel P and Matoya M, (2005), US Army Research Laboratory, Aberdeen, MD, personal communication.
3. Desai CS and Sirdwardane HJ, (1984), *Constitutive laws for engineering materials with emphasis on geologic materials*. Prentice-Hall, Englewood Cliffs, NJ 07632.
4. Dannemann KA, Chocron S, Nicholls AE and Anderson CE Jr, (2008), Compressive damage development in confined borosilicate glass. *Materials Science and Engineering A - Structures*, 478: 340–350.
5. Chen W and Ravichandran G, (1996), Static and dynamic compressive behavior of aluminum nitride under moderate confinement. *J. Am. Ceram. Soc.*, 79:579–584.
6. Chen W and Ravichandran G, (1997), Dynamic compressive failure of a glass ceramic under lateral confinement. *J. Mech. Phys. Solids*, 45: 1303–1328.
7. Ma Z and Ravi-Chandar K, (2000), Confined compression: A stable homogeneous deformation for constitutive characterization. *Experimental Mechanics*, 40(38): 38–45.
8. Lu J and Ravichandran G, (2003), Pressure-dependent behavior of Zr₄₁Ti₁₃Cu₁₂Ni₁₀Be₂₂.5 bulk metallic glasses. *J. Mater. Res.*, 18: 2039–2049.
9. Chen W and Luo H, (2004), Dynamic compressive responses of intact and damaged ceramics from a single split hopkinson pressure bar experiment. *Experimental Mechanics*, 44(3): 295–299.
10. Forquin P, Árias A and Zaera R, (2006), An experimental method of measuring the confined compression strength of high-performance concretes to analyse their ballistic behaviour. *J. Physique IV*, 134: 629–634.
11. Chocron S, Walker JD, Nicholls AE, Dannemann KA and Anderson CE Jr, (2008), Analytical model of the confined compression test used to characterize brittle materials. *J. Appl. Mech. – Transactions of the ASME*, 75: 021006–1–7.
12. Drucker DC and Prager W, (1952), *Soil Mechanics and plastic analysis of limit design*, Q. *Appl. Math.*, vol. 10, no. 2, 157–175.
13. Chocron S, Dannemann K, Walker J, Nicholls A, Anderson C, (2009), Static and dynamic confined compression of borosilicate glass, to be published in the proceedings of the DYMAT conference, Belgium.
14. Bourne NK, Millet JCF and Field JE, (1999), On the strength of shocked glasses. *Proc. R. Soc. Lond. A*, 455:1275–1282.
15. Nedderman RM, (1992), *Statics and Kinematics of Granular Materials*. Cambridge University Press, The Edinburgh Building, Cambridge CB2 2RU, UK.
16. McGlaun JM, Thompson SL, and Elrick MG, (1990), CTH: A three-dimensional shock wave physics code. *Int. J. Impact Engng.*, 20:351–360.
17. Chocron S, Dannemann KA, Walker JD, Nicholls AE, and Anderson CE Jr, (2007), Constitutive model for damaged borosilicate glass under confinement. *J. Amer. Cer. Soc.*, 90(8):2549–2555.

18. Steinberg DJ, (1996), Equation of state and strength properties of selected materials. UCRL-MA-106439, Change 1, Lawrence Livermore National Laboratory, Livermore, CA.
19. Anderson CE Jr, Chocron S and Behner T, (2009), A constitutive model for in-situ comminuted silicon carbide. *J. Amer. Cer. Soc.*, accepted for publication.
20. Holmquist TJ, Johnson GR, Grady DE, Lopatin CM and Hertel ES Jr, (1995), High strain rate properties and constitutive modeling of glass. *Proc. 15th Int. Symp. on Ballistics*, 237–244, Jerusalem, Israel.
21. Nayak GC and Zienkiewicz OC, (1972), Convenient form of stress invariants for plasticity. *Journal of the Structural Division, Proceedings of the American Society of Civil Engineers*, 98(ST4): 949–954.
22. Wilkins ML, (1999), *Computer Simulation of Dynamic Phenomena*. Springer, 1999.

Chapter 11

On the main mechanisms in ballistic perforation of steel plates at sub-ordnance impact velocities

Tore Børvik, Sumita Dey, Odd Sture Hopperstad and Magnus Langseth

Abstract This review is a summary of earlier published work carried out by CRI-SIMLab during the last decade on the ballistic perforation of steel plates at sub-ordnance impact velocities. The reason for carrying out these studies was twofold. First, we wanted to increase our understanding of the many physical phenomena taking place during structural impact by studying some of the main parameters affecting the ballistic perforation resistance of steel plates in the sub-ordnance velocity regime. Second, we wanted to generate high-precision experimental data for the validation of computational tools to be used in the design of protective structures. The main focus in this summary has been on the experimental part. Since several parameters in the experimental studies are similar, such as the velocity regime, the projectile material and mass, and the target material and geometry, the comparison between the various experimental results are both easier and more reliable. The experimental set-up and the various experimental programmes are first presented in

Tore Børvik

Structural Impact Laboratory (SIMLab), Centre for Research-based Innovation (CRI), Norwegian University of Science and Technology, NO-7491 Trondheim, Norway and Norwegian Defence Estates Agency, Research & Development Department, NO-0103 Oslo, Norway e-mail: tore.Borvik@ntnu.no

Sumita Dey

Structural Impact Laboratory (SIMLab), Centre for Research-based Innovation (CRI), Norwegian University of Science and Technology, NO-7491 Trondheim, Norway and Norwegian Defence Estates Agency, Research & Development Department, NO-0103 Oslo, Norway e-mail: sumita.dey@forsvarsbygg.no

Odd Sture Hopperstad

Structural Impact Laboratory (SIMLab), Centre for Research-based Innovation (CRI) and Department of Structural Engineering, Norwegian University of Science and Technology, Rich. Birke-lands vei 1A, NO-7491 Trondheim, Norway e-mail: odd.hopperstad@ntnu.no

Magnus Langseth

Structural Impact Laboratory (SIMLab), Centre for Research-based Innovation (CRI) and Department of Structural Engineering, Norwegian University of Science and Technology, Rich. Birke-lands vei 1A, NO-7491 Trondheim, Norway e-mail: magnus.langseth@ntnu.no

brief. Then some main experimental results from five different experimental studies are presented and discussed in some detail. A material model used for numerical simulations of the impact event, together with a short description of the material tests and identification of material constants, are described next. Finally, a selection of results from non-linear finite element simulations of the experimental tests is presented, before some concluding remarks are given.

11.1 Introduction

Structural impact problems have become increasingly important for modern industry and society. In design of offshore structures, account is taken for accidental loads such as dropped objects, collisions, explosions and penetration by fragments. Such loads are also pertinent in the design of protective structures in the nuclear and process industry, and in the design of fortification installations for defence purposes. The need for lightweight protection against terrorist attacks and in peacekeeping operations in vulnerable areas of the world is increasing. Also the request for a lighter and more mobile defence has emerged during later years. In the transportation industry, energy absorption and crashworthiness are today critical issues in the design process of vehicles, vessels and aircrafts. Accidental impacts of space debris and meteoroids are still a major concern for the protection of spacecrafts. In addition, many of the problems found in structural impact are relevant to various types of metal forming operations, such as deep drawing, stamping and forging.

This review is a summary of earlier published work carried out by CRI-SIMLab during the last decade on the ballistic perforation of steel plates at sub-ordnance impact velocities ([1]–[22]). The reason for carrying out these studies was twofold. First, we wanted to increase our understanding of the many physical phenomena taking place during structural impact by studying some of the main parameters affecting the ballistic perforation resistance of steel plates in the sub-ordnance velocity regime. Second, we wanted to generate high-precision experimental data for the validation of computational tools to be used in the design of protective structures. No attempts have been done in this study to review and acknowledge the many other available studies on this topic presented in the open literature over the years. It is thus referred to the original papers given in the reference list to find extensive reviews of similar studies.

In this paper, the main focus will be on the experimental work. Since several parameters in the experimental studies are similar, such as the velocity regime, the projectile material and mass, and the target material and geometry, the comparison between the various experimental results are both easier and more reliable. In Section 11.2, the experimental set-up and the various experimental programmes are presented in brief. In Section 11.3, experimental results from five experimental studies are presented and discussed. Section 11.4 presents a material model used for

numerical simulations of the impact event, together with a short description of the material tests and identification of material constants. Section 11.5 gives a selection of results from non-linear finite element simulations of the experimental tests, before some concluding remarks are given in Section 11.6.

11.2 Experimental Studies

11.2.1 Experimental Set-Up

All ballistic tests presented in the following have been carried out in the compressed gas gun shown in Fig. 11.1 [1]. The main components of the gas gun are the 200 bar pressure tank, the purpose-built firing unit for compressed gas, the 10 m long smooth barrel of calibre 50 mm and the 16 m³ closed impact chamber. During testing, the projectile is mounted in a nine-pieced serrated sabot that is stripped by a sabot trap prior to impact. The projectile is launched at striking velocities just below and well above the ballistic limit, i.e. the critical impact velocity of the target configuration. After about 2 m of free flight, the projectile impacts the target. The penetration event is captured by an Ultramac FS 501 ultra-high-speed image converter camera or a Photron Ultima APX-RS digital high-speed video camera. Initial and final velocities are measured by different laser-based optical devices (shown to be accurate to within 1-2 %) and by the high-speed camera systems. More details regarding the experimental set-up and instrumentation used during testing can be found in e.g. Børvik et al. [1][7].

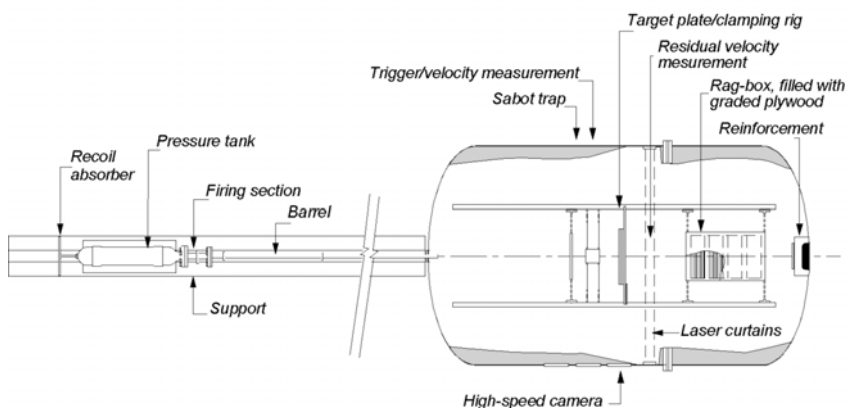


Fig. 11.1 Sketch of compressed gas gun used in the ballistic tests [1].

11.2.2 Projectiles and Targets

Projectiles were manufactured from Arne tool steel with a nominal mass and diameter of 197 g and 20 mm, respectively. In order to keep a constant mass the length of the projectile varied slightly depending on the nose shape. The dimensions of the four different projectiles used in these studies (i.e. blunt, hemispherical, conical and ogival) are given in Fig. 11.2. After machining, they were oil-hardened to a nominal Rockwell C value of about 53. The projectiles were finally measured, painted dead black and equipped with fiducial marks for high-speed camera measurements. Fig. 11.3 (left) shows typical engineering stress-strain curves from quasi-static tensile tests on specimens spark eroded from a projectile after hardening [2].



Fig. 11.2 Geometry and dimensions (in mm) for blunt, hemispherical, conical and ogival nosed projectiles [5] [10].

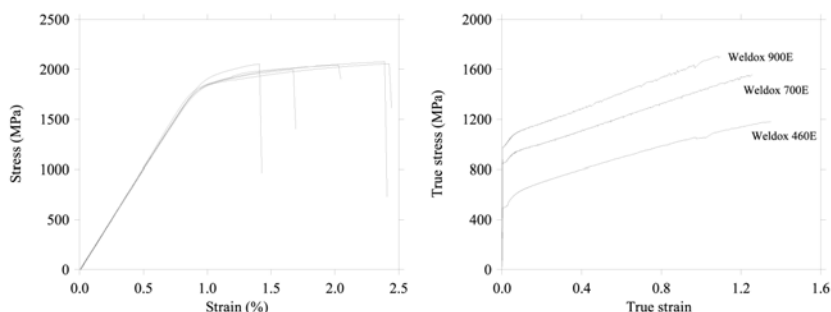


Fig. 11.3 Typical material test data for the hardened projectile (left) and the steel targets (right).

Target plates were made of Weldom 460E, Weldom 700E or Weldom 900E steel from SSAB. Typical true stress-strain curves for the steels are shown in Fig 11.3 (right) [10]. Square plates with dimension 600600 mm² were cut from larger plates, carefully sandblast on both sides and pre-drilled. They were then clamped into a circular frame with diameter 500 mm and tightened with 16 bolts (see Fig. 11.4). To allow high-speed photography during penetration, the frame was equipped with a 150 mm framing window. Initial geometrical imperfections and final target deformations were measured in-situ both before and after each test.

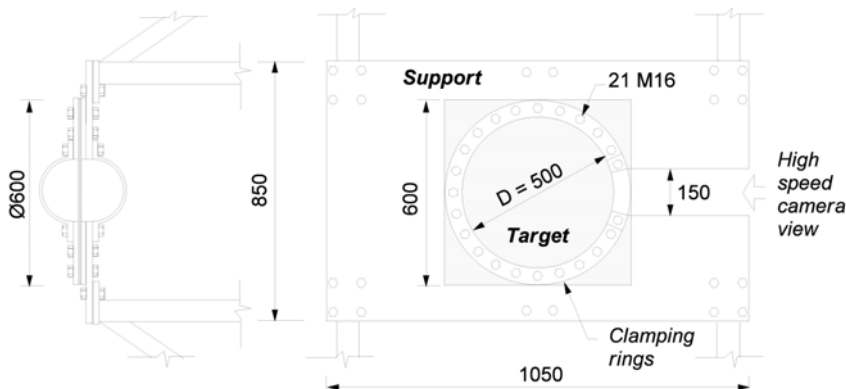


Fig. 11.4 Target plate and clamping frame [7].

11.2.3 Experimental Programs

Five experimental programmes are presented and discussed in the following. The different programmes are outlined in Table 11.1. As mentioned, the primary objectives were to study the main phenomena taking place during structural impact of steel plates in the sub-ordnance velocity regime, and to generate precision test data for computer code validation. Since the impact conditions in the experimental studies are somewhat similar, the comparison between the various experimental results is both easier and more reliable.

Table 11.1 Experimental programmes.

Test Series	Velocity Range	Nose Shape	Target Thickness	Target Material
Effect of projectile impact velocity	150 – 400 m/s	Blunt	12 mm	Weldox 460 E
Effect of target thickness	70 – 500 m/s	Blunt	6 – 30 mm	Weldox 460 E
Effect of projectile nose-shape	150 – 400 m/s	Blunt, hemispherical, conical and ogival	12 mm	Weldox 460 E
Effect of target strength	150 – 400 m/s	Blunt, conical and ogival	12 mm	Weldox 460 E Weldox 700 E Weldox 900 E
Effect of target layering	140 – 380 m/s	Blunt and ogival	12 mm (monolithic) 2 x 6 mm (in contact) 2 x 6 mm (24 mm spacing)	Weldox 700 E

11.3 Experimental Results

11.3.1 Effect of Projectile Impact Velocity

To study the effect of impact velocity during penetration and perforation, 12 mm thick Weldox 460E steel plates were impacted by blunt projectiles (see also Table 1). The details in the study are presented in [1], but some of the most important experimental findings are plotted in Fig. 11.5.

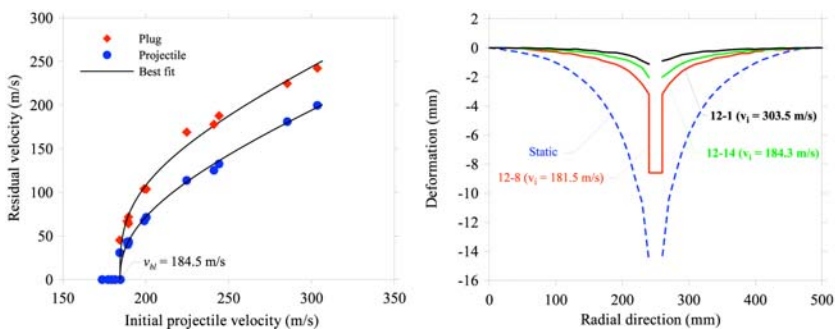


Fig. 11.5 Effect of projectile impact velocity [1].

Here, all parameters in the experimental tests were kept constant except for the projectile impact velocity that varied between 150 and 400 m/s, representing impact velocities just below and well above the ballistic limit velocity of the target plate. From the experimental tests the following main effects are observed:

- All targets failed by localized adiabatic shear banding, pushing a plug with diameter approximately equal to the nose diameter of the projectile out of the target plate. Inside the localized shear bands, and in front of the crack tip, clear proofs of void growth were observed in the scanning electron microscope (see Fig. 11.6).
- A rather distinct jump in residual projectile velocity was seen at the ballistic limit, and the residual velocity was never found really low. The residual velocity of the plug was always found to be higher than that of the projectile. This behaviour was related to multiple impacts between the projectile and plug during perforation and the release of elastic stress waves at failure.
- At the highest impact velocities the energy absorption became constant, indicating that no more energy was absorbed by the projectile-target system as the impact velocity is increased (at least within the limitations of this study).
- Even though the projectiles were hardened, mushrooming took place in the nose at the highest impact velocities. This effect should not be neglected by assuming the projectile as rigid, because considerable energy is absorbed in this deformation mode.

- The permanent target deformation consisted of a combination of localized bulging and global dishing, which decreased from a maximum value at the ballistic limit velocity towards a constant value at higher impact velocities. The deformations under impact generated loading conditions were much more localized than in similar static cases, where the deformation reached out to the boundary.

Some high-speed camera pictures from a typical test in this study can be found in Fig. 11.16 – 11.19.

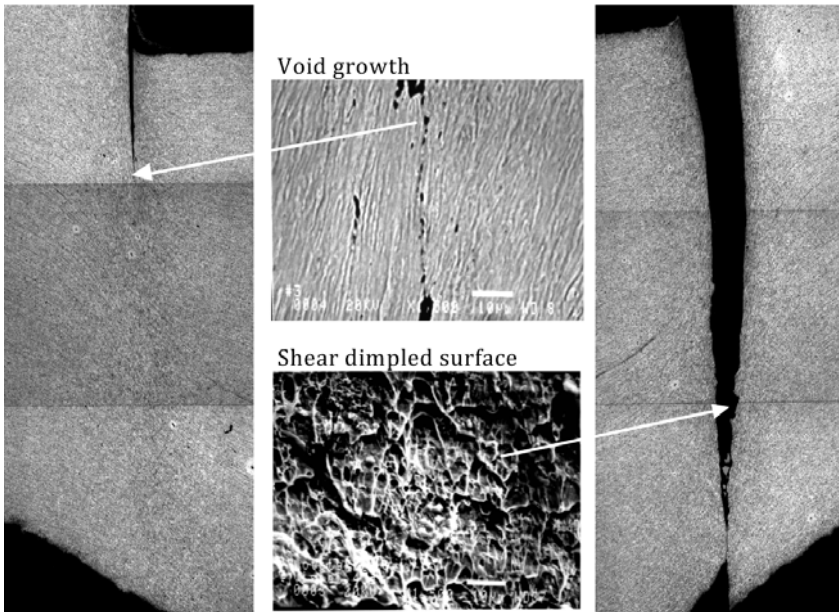


Fig. 11.6 Metallurgical images of the localized shear zone (x32) showing void growth [1] [2].

11.3.2 Effect of Target Thickness

The effect of target thickness was studied by firing blunt projectiles into 6 to 30 mm thick Weldox 460E targets at impact velocities between 70 and 500 m/s. Details from the study can be found in [7], while some of the data are plotted in Fig. 11.7. From these data, the following main conclusions are given:

- A monotonic increase in ballistic limit with target thickness was found. However, a kink in the ballistic limit versus target thickness curve was obtained at a target thickness of about 10 mm (see Fig. 11.7). The change in target response was

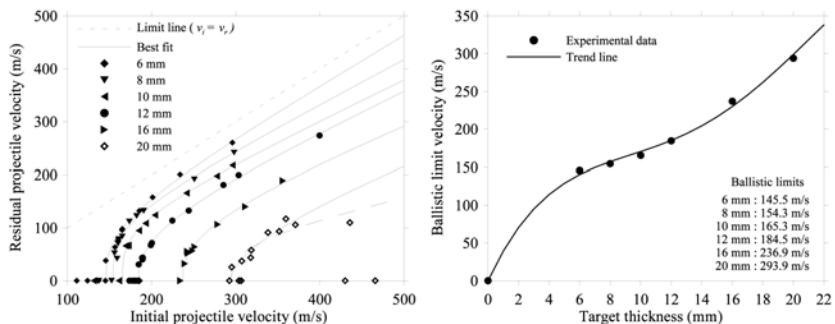


Fig. 11.7 Effect of target thickness – experimental data [7].

related to the observed change in deformation mode with target thickness (Fig. 11.8), from typically thin plate global deformation towards thick plate shear localization. This observation is important in the design of lightweight protective structures.

- Both the jump in residual velocity at the ballistic limit and the slope of the initial versus residual velocity curve were found to decrease with target thickness and projectile impact velocity.
- At thicknesses above 20 mm the projectile fragmented at impact with only limited damage in the target plate, since it failed to establish the through-thickness shear bands required for plugging. This type of behaviour is difficult to capture in finite element simulations (as also will be discussed in Section 11.5).
- The perforation time was found to be fairly constant for all target thicknesses at impact velocities close to the target’s respective ballistic limit.
- While the maximum target deformation was nearly twice the thickness for the thinnest plates, hardly any global deformation could be measured for plates thicker than 16 mm. The projectile deformation on the other hand, increased almost exponentially with target thickness and impact velocity.

The change in deformation mode and projectile break-down at a target thickness above 20 mm are illustrated in Fig. 11.8, while some high-speed camera pictures from typical tests in this study can be found in Fig. 11.16 – 11.19.

11.3.3 Effect of Projectile Nose-Shape

Projectiles with four different nose shapes (blunt, hemispherical, conical and ogival as shown in Fig. 11.2) were used to penetrate 12 mm thick Weldox 460 E steel plates at impact velocities from 150 to 400 m/s (see Table 11.1). Some of the experimental data from this study are plotted in Fig. 9, while the details from the studies are re-

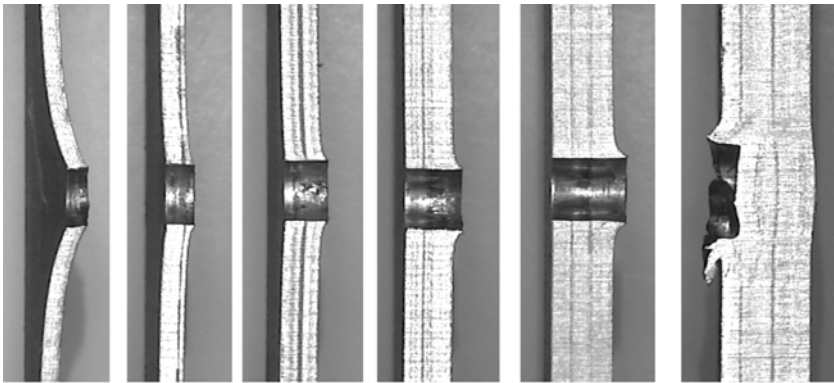


Fig. 11.8 Effect of target thickness – cross-sections of impacted plates [7].

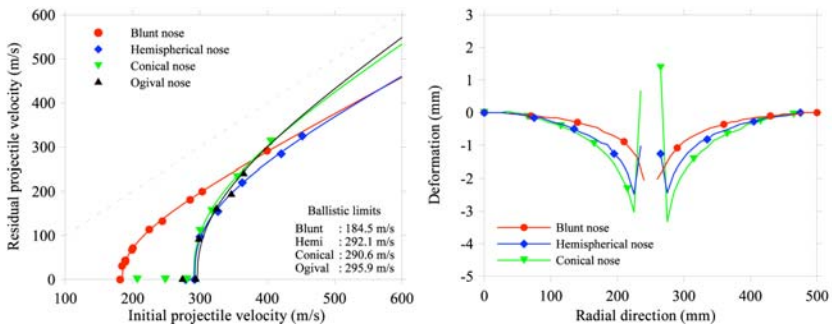


Fig. 11.9 Effect of projectile nose shape – experimental data [5] [10].

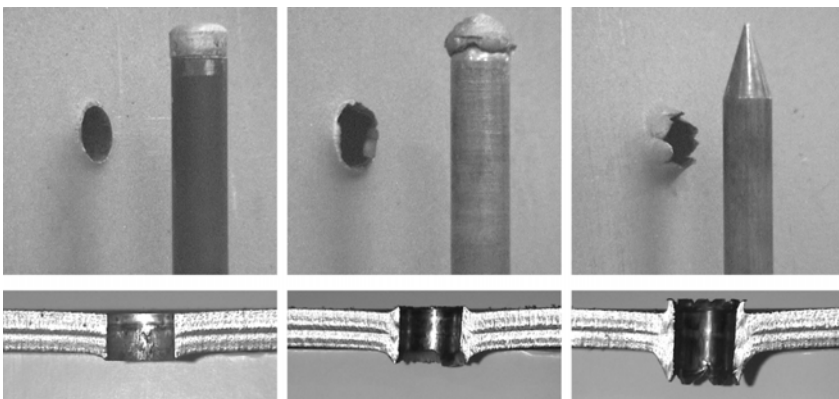


Fig. 11.10 Effect of projectile nose shape – failure modes [5].

ported in [5] and [10]. Based on the obtained results, the following main conclusions can be drawn:

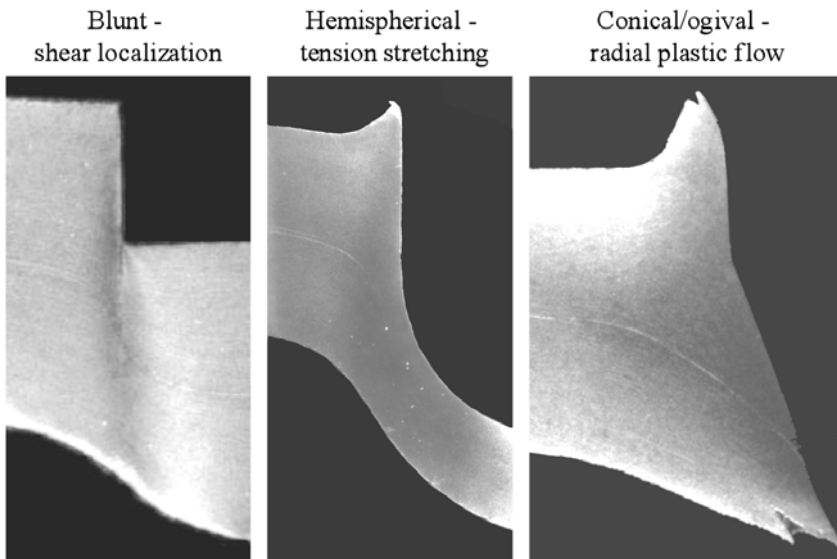


Fig. 11.11 Failure modes as function of projectile nose shape at impact velocities just below the ballistic limit velocity [5].

- Both the ballistic limit velocity and the failure mode of the target plate were severely affected by the nose shape of the projectile. Hemispherical, conical and ogival projectiles gave a similar ballistic limit close to 300 m/s, while the ballistic limit velocity was only about 185 m/s for blunt projectiles.
- Also the initial-residual velocity curves were influenced by the projectile nose shape. For blunt and hemispherical projectiles, the curves seemed to coincide as the impact velocity became high compared to the ballistic limit. The curves for pointed projectiles seemed to exceed the other two at the highest impact velocities and became parallel to the limit line, i.e. the line where the residual velocity is equal to the initial velocity.
- The differences in ballistic limit velocities were attributed to the change in energy absorption and failure mode of the target with projectile nose shape. It appeared that both local and global deformations in the target were largest for pointed projectiles, followed by hemispherical and blunt projectiles in that order.
- Conical and ogival projectiles perforated the target by ductile hole growth, which is controlled by the material's resistance to plastic flow. Hemispherical projectiles caused a localized region of intense tensile strain that finally gave failure due to necking, and a cup-shaped plug was ejected. Blunt projectiles perforated the target by plugging.

- The difference in slope between the various initial-residual velocity curves was most likely due to the difference in projectile deformation during impact. Blunt projectiles deformed (mushroomed) almost exponentially with impact velocity in the actual velocity regime, while pointed projectiles hardly deformed at all. Conical and ogival projectiles required less energy to perforate the target plate than blunt projectiles when the impact velocity was above 440 m/s. For lower impact velocities, the energy consumption was least for blunt projectiles. Plastic deformations also occurred in hemispherical projectiles, but not to the same extent as for the blunt ones.
- From sectioned target plates, it was revealed that sliding frictional effects can be neglected for blunt projectiles. Small frictional effects seemed present for the other projectile nose shapes, and could be accounted for in finite element simulations. However, by including frictional effects in the contact algorithms, predicted ballistic limits will always increase.

The effect of projectile nose shape on the failure modes during penetration and perforation is shown in Fig. 11.10 and Fig. 11.11, while Fig. 11.16 – 11.19 gives high-speed camera pictures from some typical tests.

11.3.4 Effect of Target Strength

Impact tests were performed on 12 mm thick steel plates with blunt, conical and ogival projectiles where the effect of target strength was studied. The target materials were Weldox 460 E, Weldox 700 E and Weldox 900 E (see Table 11.1), where the number indicates the nominal yield stress of the various steels. True stress-strain curves from tensile tests on smooth axisymmetric specimens at quasi-static strain rate and room temperature for the materials are shown in Fig. 11.3 (right), while the details of the experimental program can be found in [10]. Obtained ballistic limit velocities from the experimental study are given in Fig. 11.12. Based on the experimental observations, the following main conclusions are reached:

- In tests using blunt projectiles, the ballistic limit velocity decreased for increasing yield strength, while the opposite trend was found in tests with conical and ogival projectiles.
- Perforation with conical and ogival projectiles caused failure by ductile hole growth in all materials. This failure mode requires more energy when the target strength increases.
- Blunt projectiles caused failure by shear plugging. The decrease in ballistic limit for increasing target strength using blunt projectiles occurred due to the presence of highly localized adiabatic shear bands (4-12 μm) in Weldox 700 E and Weldox 900 E plates, while less localized (i.e. only deformed) adiabatic shear bands (> 100 μm) were found in Weldox 460 E plates.

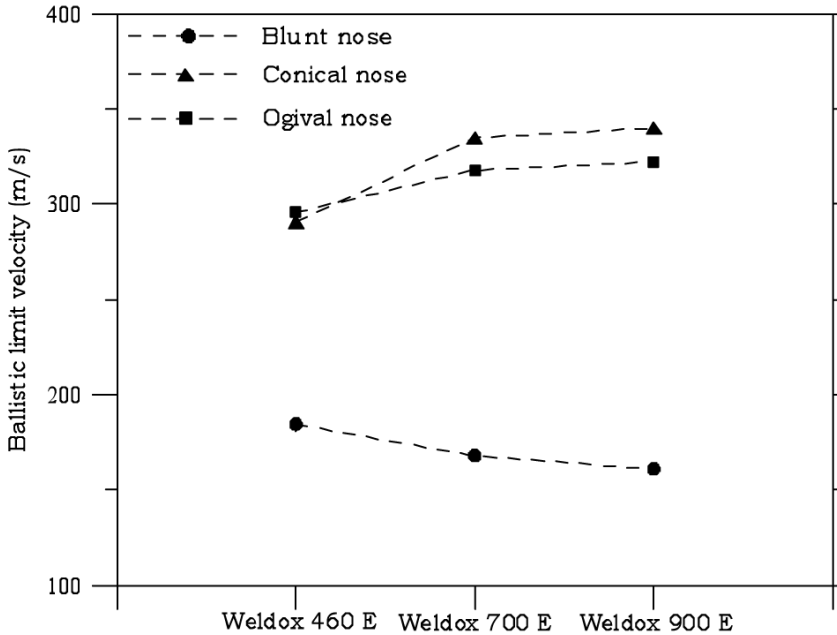


Fig. 11.12 Effect of target strength – ballistic limit velocity versus projectile nose shape and target material [10].

- The ballistic limit velocity of the target was markedly affected by the nose shape of the projectile. Conical and ogival projectiles gave ballistic limit velocities in the order of 300 m/s, while the ballistic limit velocities were well below 200 m/s for blunt projectiles.
- Tests on Weldox 700 E and Weldox 900 E targets with conical projectiles resulted in fragmentation of the projectile nose part during impact, which may have affected the ballistic limit for these two materials. Ogival projectiles did not shatter in any of the tests.
- Although there are large differences in the yield strength of the targets, the difference between the ballistic limits were relatively small for the same projectile nose shape.

Light-microscopy pictures of the localized shear bands as function of target strength are shown in Fig. 11.13. The shear band in Weldox 460E has a width of more than 100 μm and is only deformed, while the shear bands in Weldox 700E and Weldox 900E have widths varying from 8 to 12 μm and 4 to 10 μm , respectively. It should at this point be mentioned that in a later study [15], these shear bands were investigated using SEM and TEM. No proofs of a phase transformation, indicating that the temperature rise due to plastic work reached about 730°C in the shear bands, were found. However, clear proofs of transformed adiabatic shear bands were found in 20 mm thick Weldox 460E targets impacted by blunt projec-

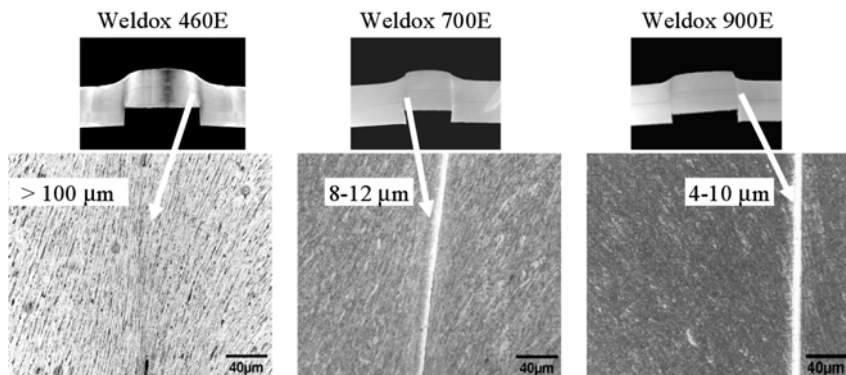


Fig. 11.13 Shear localization as function of target strength [10].

tiles. High-speed camera pictures of some typical tests in this study are given in Fig. 11.16 – 11.19.

11.3.5 Effect of Target Layering

When studying the effect of target thickness (see Section 11.3.2), a kink in the initial-residual velocity curve was observed when the deformation mode changed from thin plate global deformation to thick plate shear localization. This indicates that in a certain thickness range, an increase in target thickness (and consequently weight) only gives a slight increase in perforation resistance. Similarly, when studying the effect of target strength (see Section 11.3.4) it was found that localized shear bands become more distributed as the plate deflects globally. Thus, strongly localized shear bands leading to premature plugging do not occur to the same extent for thinner plates. From findings like these it is reasonable to assume that several thin plates that deform globally will absorb more of the projectile’s kinetic energy during impact than one thick plate. Thus, layered targets of thin plates may seem to be a better energy absorber during ballistic impact than a monolithic target of equal total thickness.

Motivated by these results, the effect of target layering was investigated. In the tests, 12 mm thick target configurations of Weldox 700E were struck by blunt and ogival projectiles and the ballistic limits were determined. The target configurations consisted of 12 mm thick monolithic plates, two 6 mm thick plates in contact (i.e. 2x6 mm) and two 6 mm thick plates spaced with 24 mm of air (i.e. 2x6 + 24 mm). The ballistic perforation resistance of single 6 mm thick plates of Weldox 700 E was

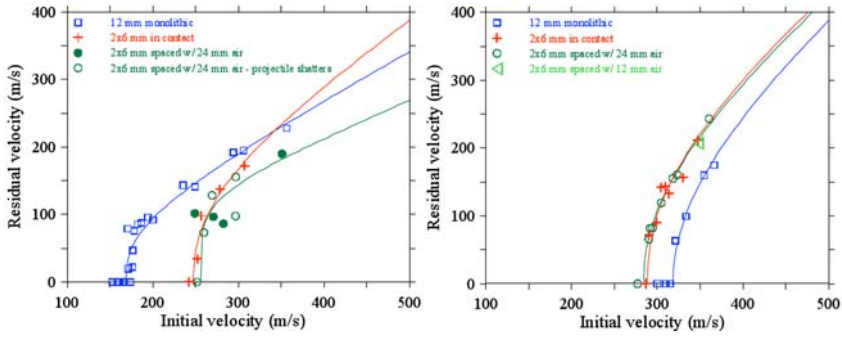


Fig. 11.14 Effect of target layering – blunt projectiles (left) and ogival projectiles (right) [16].

also determined. Test results are reported in [16], while some of the most interesting data are plotted in Fig. 11.14. From this study, the following main effects are found:

- The increase in ballistic limit velocity using monolithic targets and blunt projectiles was only about 20% when increasing the target thickness from 6 to 12 mm.
- By double-layering the target using two 6 mm thick plates in contact, an increase in ballistic limit of nearly 50% was obtained compared to a monolithic target of equal total thickness for blunt projectiles. Similarly, for plates spaced with 24 mm of air an increase in ballistic limit of 40% was obtained. This was caused by a change in deformation and failure mode when moving from a monolithic to a layered target, since the plug from the first plate delays and partly prevents the shear localization in the second plate.
- The increase in ballistic limit for monolithic targets and ogival projectiles was about 60 when increasing the target thickness from 6 to 12 mm.
- By double-layering the target using two 6 mm thick plates, a decrease in ballistic limit of about 10% was obtained both for plates in contact and plates spaced with 24 mm of air compared to a monolithic target of equal total thickness for ogival projectiles. The reason for this is that neither shear nor tensile stresses can be transferred between the layers, so that the resistance of layered targets is expected to be weakened.
- Within the limitations of the study, a main conclusion was that the overall protection level, i.e. the minimum ballistic limit independent of projectile nose shape, seemed to increase significantly by layering the target.

Fig. 11.15 shows pictures of cross-sections of sliced targets at impact velocities close to their respective ballistic limits, revealing the difference in global deformation between the different target configurations. Especially the difference in global deformation between monolithic and layered plates, and between the first and the second plate in the double-layered targets, should be noticed. Some typical high-speed camera images from this study are given in Fig. 11.16 – 11.19.

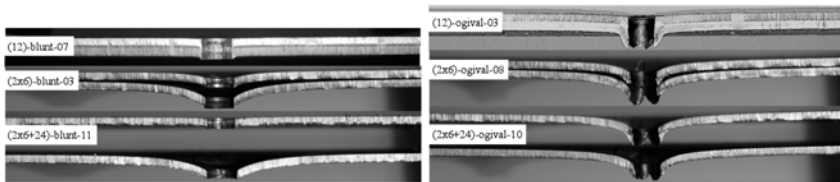
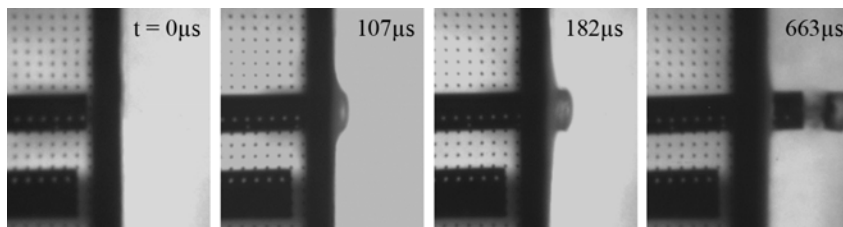
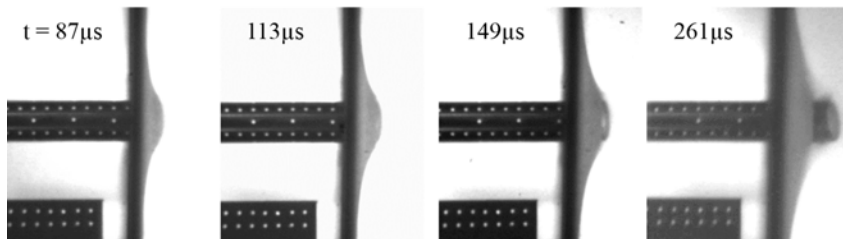


Fig. 11.15 Cross-section of 12 mm thick target configurations (monolithic/layered) perforated by blunt (left) and ogival (right) projectiles at impact velocities close to their ballistic limits [16].

11.3.6 Summary of Experimental Data



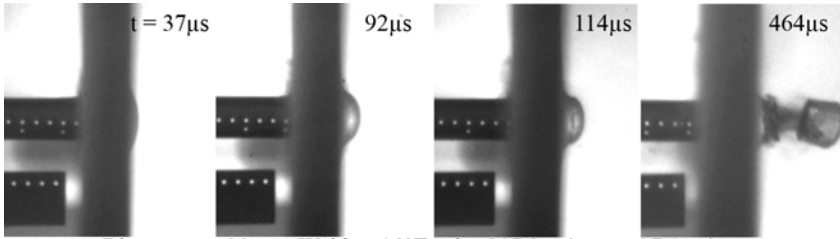
a) Blunt nose - 12 mm Weldox 460E ($v_i = 189.6$ m/s, $v_r = 64.0$ m/s).



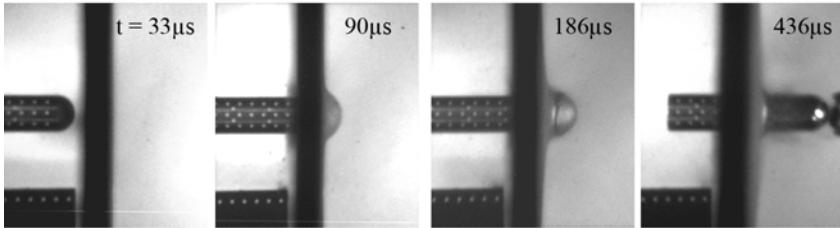
b) Blunt nose - 6 mm Weldox 460E ($v_i = 156.6$ m/s, $v_r = 63.5$ m/s).

Fig. 11.16 Typical high-speed camera images from some of the tests.

Fig. 11.20 gives a comparison between the ballistic limits from all the test series (involving 21 different test configurations), plotted in ascending order. The various configurations are defined in Table 11.2. It is interesting to note that for the lowest ballistic limits, i.e. below 200 m/s, all targets (independent of target material or thickness) are impacted by blunt projectiles, while for the highest ballistic limits, i.e. above 300 m/s, only pointed projectiles are involved.

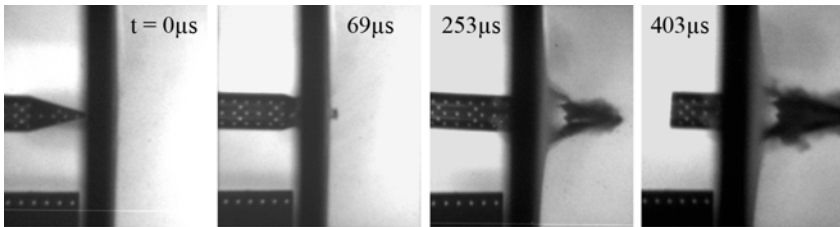


a) Blunt nose - 20 mm Wieldox 460E ($v_i = 307.2 \text{ m/s}$, $v_r = 37.1 \text{ m/s}$).

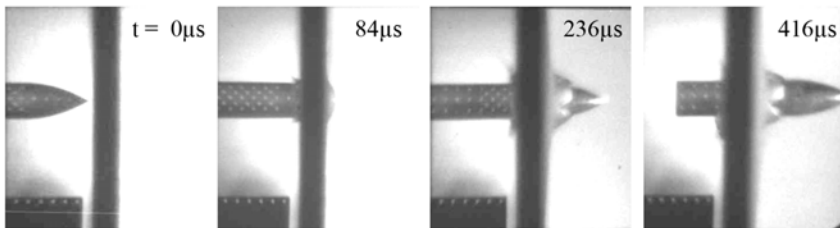


b) Hemispherical nose - 12 mm Wieldox 460E ($v_i = 300.0 \text{ m/s}$, $v_r = 97.2 \text{ m/s}$).

Fig. 11.17 Typical high-speed camera images from some of the tests.



a) Conical nose - 12 mm Wieldox 460E ($v_i = 300.3 \text{ m/s}$, $v_r = 110.3 \text{ m/s}$).



b) Ogival nose - 12 mm Wieldox 700E ($v_i = 321.1 \text{ m/s}$, $v_r = 63.5 \text{ m/s}$).

Fig. 11.18 Typical high-speed camera images from some of the tests.

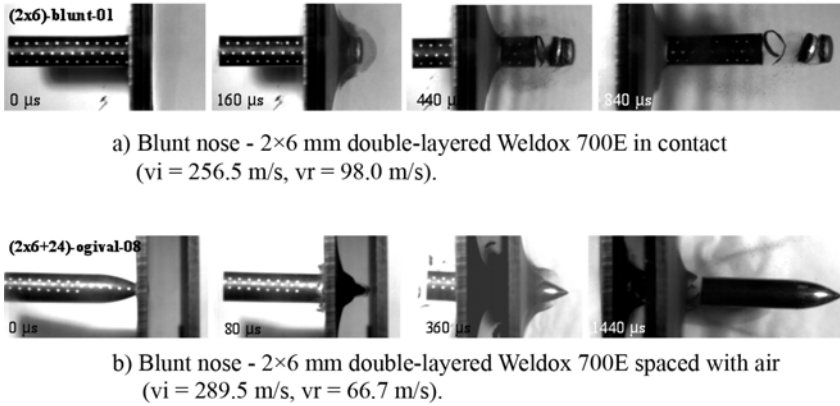


Fig. 11.19 Typical high-speed camera images from some of the tests.

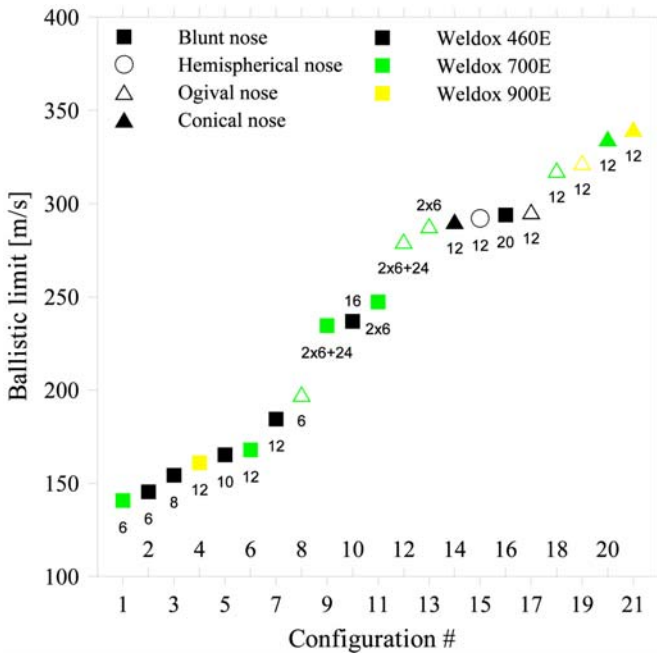


Fig. 11.20 Comparison between ballistic limits from all test series and configurations (see Table 11.2 for the definition of the various target configurations). The number close to each data point gives the thickness of the respective target configuration.

Table 11.2 Ballistic limits from all test series and configurations in ascending order.

Configuration #	Material Type	Yield Stress [MPa]	Thickness [mm]	Nose Shape	Ballistic Limit [m/s]
1	W700E	859	6	Blunt	140.8
2	W460E	499	6	Blunt	145.5
3	W460E	499	8	Blunt	154.3
4	W900E	992	12	Blunt	161.0
5	W460E	499	10	Blunt	165.3
6	W700E	859	12	Blunt	168.0
7	W460E	499	12	Blunt	184.5
8	W700E	859	6	Ogival	198.0
9	W700E	859	2x6+24	Blunt	243.6
10	W460E	499	16	Blunt	236.9
11	W700E	859	2x6	Blunt	247.3
12	W700E	859	2x6+24	Ogival	280.0
13	W700E	859	2x6	Ogival	288.3
14	W460E	499	12	Conical	290.6
15	W460E	499	12	Hemi	292.1
16	W460E	499	20	Blunt	293.9
17	W460E	499	12	Ogival	295.9
18	W700E	859	12	Ogival	318.1
19	W900E	992	12	Ogival	322.2
20	W700E	859	12	Conical	335.0
21	W900E	992	12	Conical	340.1

11.4 Material Modelling, Material Tests and Identification of Material Constants

11.4.1 Constitutive Relation and Fracture Criteria

Ballistic impacts on ductile materials involve contact, large plastic strains, high strain rates, softening due to adiabatic heating, varying stress states and loading histories, strain localization, damage and failure. Thus, the computational material model must be able to take all these effects into account. Further, damage softening may either be uncoupled or coupled with the constitutive equation. In the uncoupled approach, the yield condition, the plastic flow and the strain hardening are assumed to be unaffected by the damage evolution (i.e. the nucleation and growth of voids in ductile materials). On the contrary, damage affects the plastic deformation and may

lead to softening in the final stage before fracture in the coupled approach. In this paper, most simulations shown are carried out assuming uncoupled damage.

A modified version of the well-known Johnson-Cook constitutive relation (or the MJC model in the following to distinguish it from the original model) was used to model the target material. The model is formulated within the framework of thermoelasticity, thermovisco-plasticity and continuum damage mechanics. A detailed description of the model is provided in [4] and only the main equations are given below. By assuming an isotropic (von Mises) material, and by adopting the effective stress concept and the principle of strain equivalence, the equivalent stress σ_{eq} and the accumulated plastic strain rate $\dot{\epsilon}_{eq}$ are defined as [4]

$$\sigma_{eq} = \sqrt{\frac{3}{2} \boldsymbol{\sigma}' : \boldsymbol{\sigma}'} = (1 - \beta D) \tilde{\sigma}_{eq}, \quad \dot{\epsilon}_{eq} = \sqrt{\frac{2}{3} \mathbf{d}^p : \mathbf{d}^p} = \frac{\dot{r}}{(1 - \beta D)} \quad (11.1)$$

where $\boldsymbol{\sigma}'$ is the deviatoric stress tensor, $\tilde{\sigma}_{eq}$ is the damage equivalent stress, \mathbf{d}^p is the plastic deformation rate tensor, \dot{r} is the damage accumulated plastic strain rate, D is the damage variable and β is the damage coupling parameter (i.e. $\beta = 0$ for uncoupled damage and $\beta = 1$ for coupled damage). The equivalent stress is then expressed as

$$\sigma_{eq} = (1 - \beta D) (A + Br^n) (1 + \dot{r}^*)^C (1 - T^{*m}) \quad (11.2)$$

where A , B , n , C and m are material constants. The dimensionless damage plastic strain rate is given by $\dot{r}^* = \frac{\dot{r}}{\dot{\epsilon}_0}$, where $\dot{\epsilon}_0$ is a user-defined reference strain rate. The homologous temperature is defined as $T^* = \frac{T - T_r}{T_m - T_r}$, where T is the absolute temperature, T_r is the room temperature and T_m is the melting temperature. The rate of temperature increase is computed from the energy balance by assuming adiabatic conditions

$$\dot{T} = \chi \frac{\boldsymbol{\sigma} : \mathbf{d}^p}{\rho C_p} = \chi \frac{\sigma_{eq} \dot{\epsilon}_{eq}}{\rho C_p} = \chi \frac{\tilde{\sigma}_{eq} \dot{r}}{\rho C_p} \sigma_{eq} \quad (11.3)$$

where ρ is the material density, C_p is the specific heat and χ is the Taylor-Quinney coefficient that represents the proportion of plastic work converted into heat.

The damage evolution during plastic straining is expressed as

$$\dot{D} = \begin{cases} 0 & \text{for } \epsilon_{eq} \leq \epsilon_d \\ \frac{D_C}{\epsilon_f - \epsilon_d} \dot{\epsilon}_{eq} & \text{for } \epsilon_{eq} > \epsilon_d \end{cases} \quad (11.4)$$

where D_C is the critical damage and ϵ_d is a damage threshold. For simplicity it is assumed in this study that D_C is a material constant and that $\epsilon_d = 0$. The fracture strain is given as

$$\epsilon_f = (D_1 + D_2 \exp(D_3 \boldsymbol{\sigma}^*)) (1 + \dot{\epsilon}_{eq}^*)^{D_4} (1 + D_5 T^*) \quad (11.5)$$

where D_1, \dots, D_5 are material constants determined from material tests, $\sigma^* = \frac{\sigma_H}{\sigma_{eq}}$ is the stress triaxiality ratio where σ_H is the hydrostatic stress, and $\dot{\epsilon}_p^* = \frac{\text{varepsilonpsilon}_{eq}}{\dot{\epsilon}_0}$ is the dimensionless strain rate. Fracture occurs by element erosion (i.e. the stresses in the integration points are set to zero) when the damage of a material element equals the critical damage $D_C \leq 1$. Note that if the damage coupling parameter β in Eq. (11.1) is set equal to zero, $\tilde{\sigma}_{eq} \rightarrow \sigma_{eq}$, $\dot{r} \rightarrow \dot{\epsilon}_{eq}$ and $D_C \rightarrow 1$, and the uncoupled damage formulation (as used in the original JC model) reappears.

Alternatively, for uncoupled damage (i.e. $\beta = 0$ in Eq. (11.2)) failure can be modelled using a fracture criterion proposed by Cockcroft and Latham (CL) where it is assumed that fracture depends on the stresses imposed as well as on the strains developed [14]. The model can be expressed as

$$D = \frac{W}{W_{cr}} = \frac{1}{W_{cr}} \int_0^{\epsilon_f} \langle \sigma_1 \rangle d\epsilon_{eq} \quad (11.6)$$

where W is the Cockcroft-Latham integral, σ_1 is the major principal stress, $\langle \sigma_1 \rangle = \sigma_1$ when $\sigma_1 \geq 0$ and $\langle \sigma_1 \rangle = 0$ when $\sigma_1 < 0$. It is seen that fracture cannot occur in this model when there is no tensile stress operating, which implies that the effect of stress triaxiality on the failure strain is implicitly taken into account. The advantage with the CL failure criterion is that the critical value W_{cr} can be determined from one uniaxial tensile test. Moreover, the model captures some main experimental observation for many steels exposed to impact. From experiments it is seen that for increasing temperature the strength decreases and the ductility increases, while for increasing strain rate the strength increases and the ductility decreases. Thus, W_{cr} remains fairly constant for varying temperature and strain rate. It was shown in Dey et al. [12] that the one-parameter CL model gives equally good results as the five-parameter MJC fracture criterion in LS-DYNA simulations of perforation of steel plates. Also the CL model is coupled with element erosion that erodes the element when reaches its critical value W_{cr} .

In addition to the MJC or the CL fracture criterion, a temperature-based erosion criterion is used in some simulations. The value of the critical temperature is taken as $T_c = 0.9T_m$, which means that the element is eroded when the temperature T in the material reaches 90% of the melting temperature T_m . It is assumed that at these temperatures, the material is so weakened that it does not add much shear resistance to the penetrating projectile. In some simulations a shape-based erosion criterion is also adopted, which erodes the element when the aspect ratio (identified as the ratio between the diagonals in the case of rectangular elements) reaches a critical value of 0.05. This erosion criterion (which is purely numerical) is used to get rid of severely distorted, pathological elements causing time-step drops and error termination [16] [18]. Only a few elements are eroded due to this criterion. The constitutive relation and the various failure criteria are implemented as `*mat107` in LS-DYNA.

It is not recommended to model the projectile as a rigid body, since elastic and plastic deformations that may alter the FE results will take place in the projectile (especially when impacted against hard and/or thick targets, as also discussed in Section 11.3). However, a rather simple constitutive relation for the projectile material is chosen. Due to the shape of the measured stress-strain curves from tensile test specimens taken from hardened projectiles (see Fig. 11.3) it is modelled as a bilinear, elastic-plastic, von Mises material with isotropic hardening (but without strain rate effects and failure/fragmentation) using **mat3* in LS-DYNA, i.e.

$$\sigma = \begin{cases} E \varepsilon & \varepsilon \leq \varepsilon_0 \\ \sigma_0 + E_t(\varepsilon - \varepsilon_0) & \varepsilon > \varepsilon_0 \end{cases} \quad (11.7)$$

where σ_0 is the yield stress, E is Young's modulus and E_t is the tangent modulus.

No additional equation-of-state or artificial bulk viscosity has been introduced in the simulations to treat possible shock waves. Thus, the relation between the pressure p and the volumetric strain ε_V is given by the linear expression $p = K \varepsilon_V$, where K is the bulk modulus. This assumption seems appropriate for weak shocks at impact velocities below 1000 m/s.

11.4.2 Material Data and Model Calibration

A comprehensive material test programme was carried out for Weldox 460 E, Weldox 700 E and Weldox 900 E, where the effects of strain hardening, strain rate hardening, temperature and stress triaxiality on the strength and ductility of the material were studied. Three types of tensile tests were carried out: quasi-static tests with smooth and pre-notched specimens, quasi-static tests at elevated temperatures and dynamic tests over a wide range of strain rates. All specimens were taken parallel to the rolling direction of the plate since the steels were found to be isotropic both in plastic flow and strain to failure. Details from the various material test programmes can be found in e.g. [2]–[3], [8]–[12] and [14]–[15], while some data from the experimental tests are plotted in Fig. 11.21 and Fig. 11.22. Both the equivalent stress and the fracture strain for the steels were found sensitive to stress state, temperature and strain rate.

The modified Johnson-Cook constitutive relation defined in Equation (11.2), the modified Johnson-Cook fracture strain defined in Equation (11.5) and the critical value of the Cockroft-Latham fracture criterion defined in Equation (11.6) were calibrated based on the material test data. Both the constitutive relation and fracture criteria were calibrated by minimising the residuals between model results and corresponding experimental data using the method of least squares. Fig. 11.21 and Fig. 11.22 give a comparison between the material test data and model results for the three steels, while Table 11.3 lists the model constants (based on Dey et al [10]). Even though some deviations are seen, the agreement between test data and model

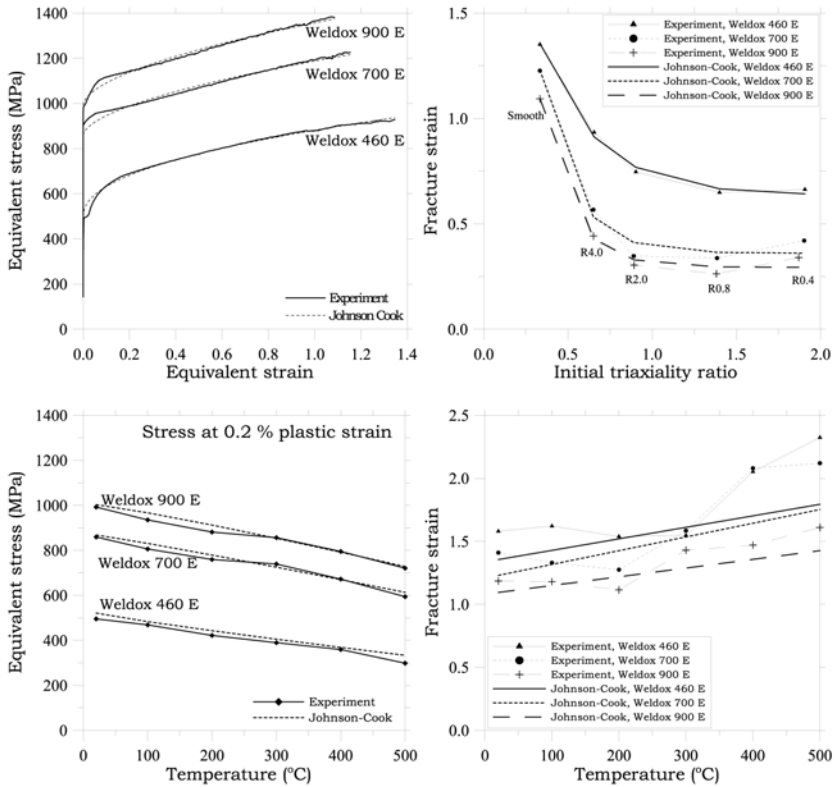


Fig. 11.21 Comparison between data from material tests and model results for Weldox 460 E, Weldox 700 E and Weldox 900 E [10].

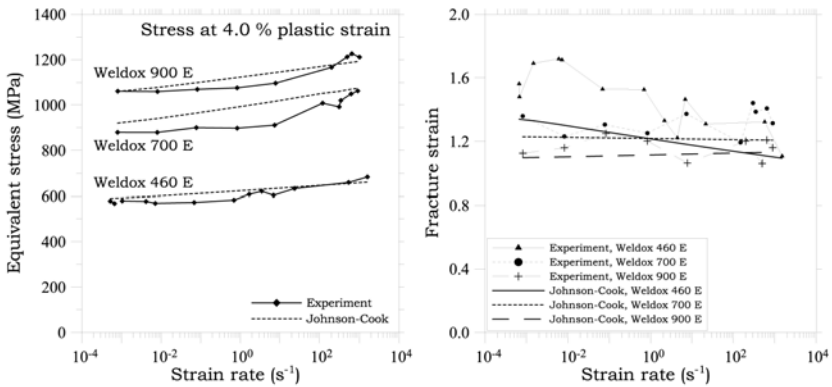


Fig. 11.22 Comparison between data from material tests and model results for Weldox 460 E, Weldox 700 E and Weldox 900 E [10].

Table 11.3 Model constants for the three materials [10].

Material		Weldox 460 E	Weldox 700 E	Weldox 900 E
Yield Stress	A [MPa]	499	859	992
Strain Hardening	B [MPa]	382	329	364
	n [-]	0.458	0.579	0.568
Strain Rate Hardening	C [-]	0.0079	0.0115	0.0087
Temperature Softening	m [-]	0.893	1.071	1.131
MJC Fracture Criterion	D_1 [-]	0.636	0.361	0.294
	D_2 [-]	1.936	4.768	5.149
	D_3 [-]	-2.969	-5.107	-5.583
	D_4 [-]	-0.014	-0.0013	0.0023
	D_5 [-]	1.014	1.333	0.951
CL Fracture Criterion	W_{cr} [MPa]	1219	1424	1510

Table 11.4 Relevant material constants needed in the target’s material model [2].

E	ν	ρ	C_V	χ	α	T_0	T_r	T_m	$\dot{\epsilon}_0$
[GPa]	[-]	[kg/m ³]	[J/kgK]	[-]	[K ⁻¹]	[K]	[K]	[K]	[s ⁻¹]
210	0.33	7850	452	0.9	$1.2 \cdot 10^{-5}$	293	293	1800	$5.0 \cdot 10^{-4}$

Table 11.5 Material constants for hardened projectile [2].

E	ν	ρ	σ_0	E_t
[GPa]	[-]	[kg/m ³]	[MPa]	[MPa]
204	0.33	7850	1900	15000

predictions is in general good. Note that the calibration shown in this study is carried out assuming uncoupled damage, i.e. $\beta = 0$ and $D_C = 1$ in Equations (11.2) and (11.4). Examples of material constants for the materials assuming coupled damage can be found in [2] and [18]. Other relevant material constants that are needed for the target materials in numerical simulations are given in Table 11.4, while model constants for the projectile are presented in Table 11.5.

11.5 Numerical Studies

All experimental studies presented in Sections 11.3 have been analyzed using the explicit solver of the non-linear finite element code LS-DYNA and the material models and constants presented in Section 11.4. In the following, some main conclusions

from these studies will be given in brief, while more details from the various studies can be found in the original papers.

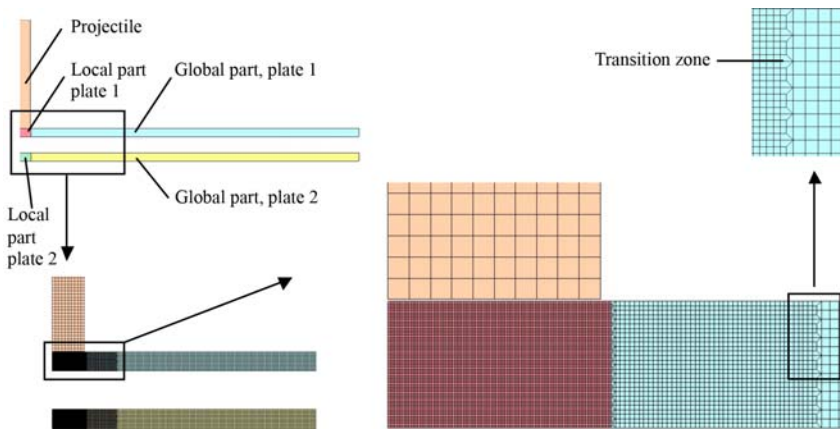


Fig. 11.23 Example of a typical FE mesh used in simulations of a blunt projectile impacting a double-layered target spaced with air (configuration # 9 – see Table 11.2). The coarsening of the mesh towards the boundary using transition elements is also shown for each plate [16].

11.5.1 Numerical Models

The geometry of the finite element models closely resembles the geometry of the various experimental configurations defined in Table 11.2. In a similar way as for the experimental tests, the only variable in each numerical configuration was the impact velocity of the projectile that was varied to exactly determine the ballistic limit of the target based on a number of runs. All targets were assumed axisymmetric with a free span diameter of 500 mm and fully clamped at the support, while the projectiles were modelled with a nominal mass of 197 g and a diameter of 20 mm. The various parts were meshed with 4-node axisymmetric elements with one integration point and stiffness-based hourglass control. A typical element size in the impact region of the target was $100 \times 100 \mu m^2$, while projectiles were modelled using a much coarser mesh. Contact between the various parts during impact was modelled using 2D automatic penalty formulations available in LS-DYNA, normally without frictional effects. Note that simulations involving blunt projectiles were carried out using a fixed element mesh, while simulations involving pointed projectiles needed adaptive rezoning of the mesh to avoid numerical problems [6]. It should finally be mentioned that the finite element models have developed over the years, and may therefore differ between the various numerical studies. In any case, as an example a plot of a typical finite element model of a blunt projectile impacting a double-layered target spaced with air (configuration # 9 – see Table 11.2) is shown in Fig. 11.23.

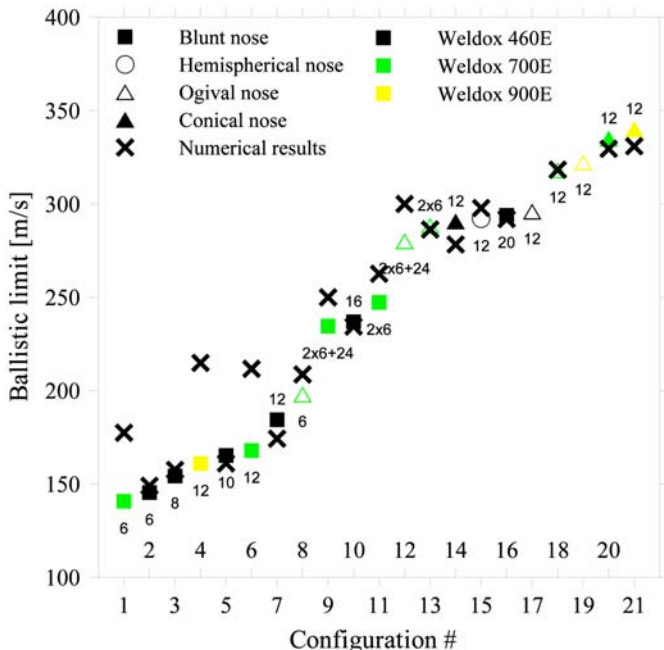


Fig. 11.24 Comparison between numerical and experimental ballistic limits (see Table 11.2 for the definition of the various target configurations), where the number close to each data point gives the thickness of the respective target configuration.

11.5.2 Some Numerical Results

The many details from the various numerical simulations are presented in the original papers given in the reference list. However, Fig. 11.24 gives a direct comparison between the experimentally obtained ballistic limits and the predicted counterparts. In the same way as for Fig. 11.20, the various configurations are defined in Table 11.2. From this plot and the original papers, the following main conclusions can be drawn:

- Very good agreement is in general obtained between the numerical predictions and the experiment results. Thus, finite element simulations using proper material models are able to capture the main physical behaviour during penetration and perforation for a variety of different impact configurations, at least within the limitations of these studies. However, it is important to include the effects of strain hardening, strain rate hardening, thermal softening and stress triaxiality in the numerical models to have reliable results.
- The phenomenological and rather simple modified Johnson-Cook constitutive relation was found to give better results than the physically based and more complex Zerilli-Armstrong model [12], while the five-parameter modified Johnson-

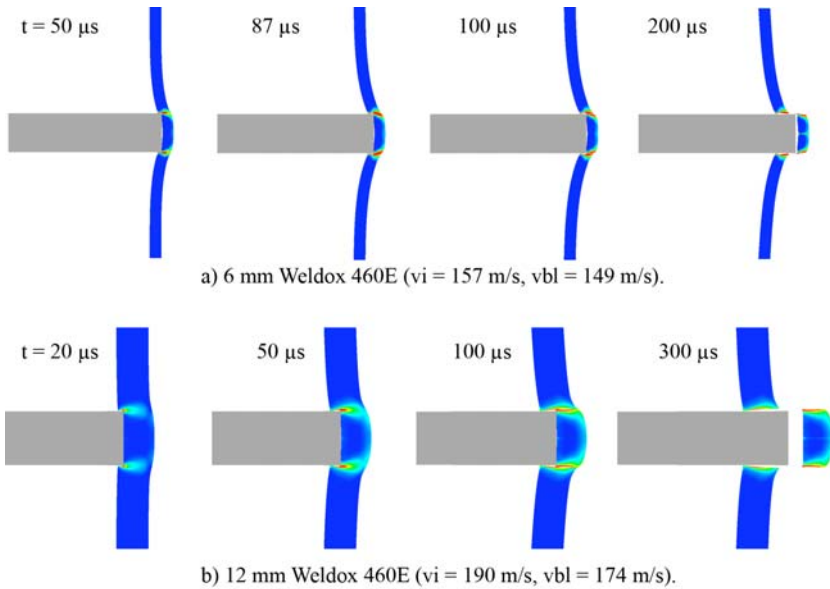


Fig. 11.25 Numerical simulations of the perforation process of Weldox 460E steel plates.

Cook and the one-parameter Cockcroft-Latham failure criteria has proven to give similar results [14].

- The only numerical results that seem to significantly deviate from the experimental data are those involving the highest strength steels and blunt projectiles. The reason for this is the increased shear localization with target strength, as discussed in Section 11.3.4 and shown in Fig. 11.12 and Fig. 11.13. Thus, while the experimental data show a drop in capacity with increasing target strength, the numerical results show the opposite. Until now it has been found difficult to simulate this behaviour correctly regardless of applied material model, but work in progress [21] using a damage-based fracture criterion with quasi-unilateral conditions seems to give promising results.
- On the other hand, as long as the shear localization is diffuse, or when the failure mode is dominated by plastic flow (as in perforation using pointed projectiles), the numerical results are normally close to the experimental data. However, it should be noticed that most numerical predictions of the ballistic limit velocity are non-conservative. Care must therefore be taken when the finite element approach is used in computer-aided design.
- Strong mesh-dependency is found in impacts involving shear localization and plugging for blunt projectiles, while the mesh-size dependency is far less distinct for problems involving pointed nose projectiles. Viscoplasticity and nonlocal damage seem to counteract the problem, but will not remove the mesh-size sensitivity completely. However, for most practical applications the ballistic limit

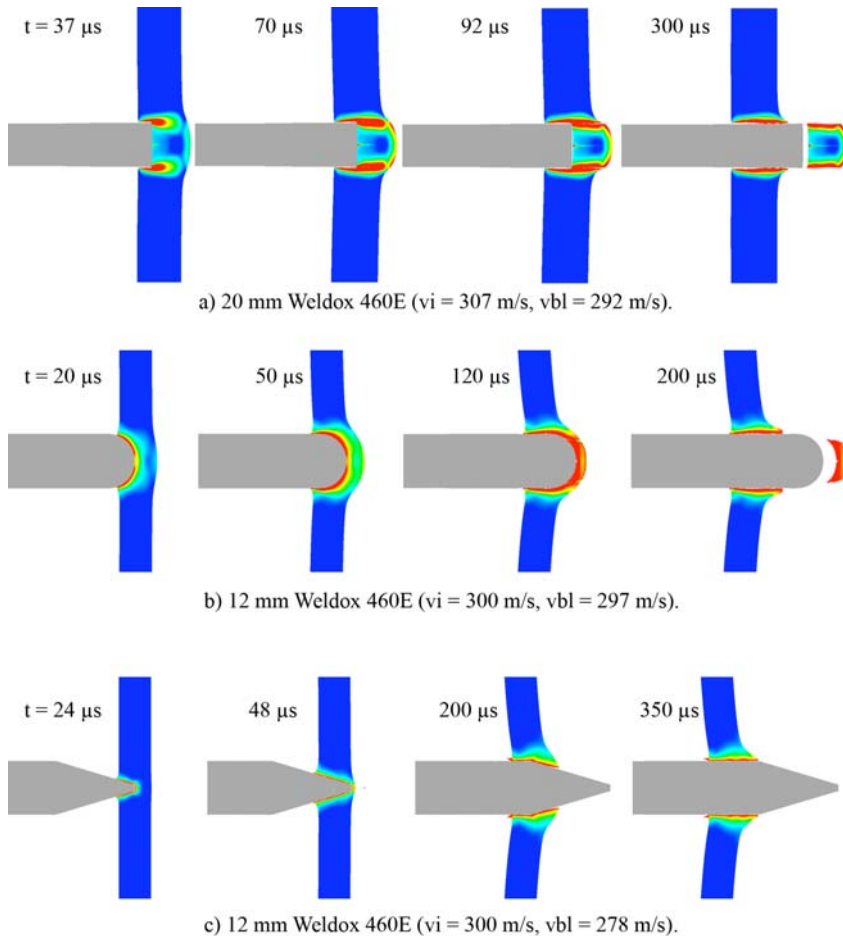


Fig. 11.26 Numerical simulations of the perforation process of Weldox 460E steel plates.

changes slowly with mesh refinement when the element size is sufficiently small. For the most localized shear bands, the physics in the problem makes it unpractical to use an element size at the order of the shear band width, so mesh-size dependency must be expected and accounted for.

- Another problem that is very hard to simulate, is projectile fragmentation during impact. This behaviour is e.g. found during blunt projectile impact of very thick or hard plates. When such failure modes are likely, it seems necessary to change the numerical approach, and element erosion should not be used alone [22].
- It should finally be mentioned that it is obviously not possible to describe petalling and radial cracking using axisymmetric finite element models. For such problems, 3D models using brick elements are required. However, 3D models

of structural impact problems are still a challenge from a computational point of view.

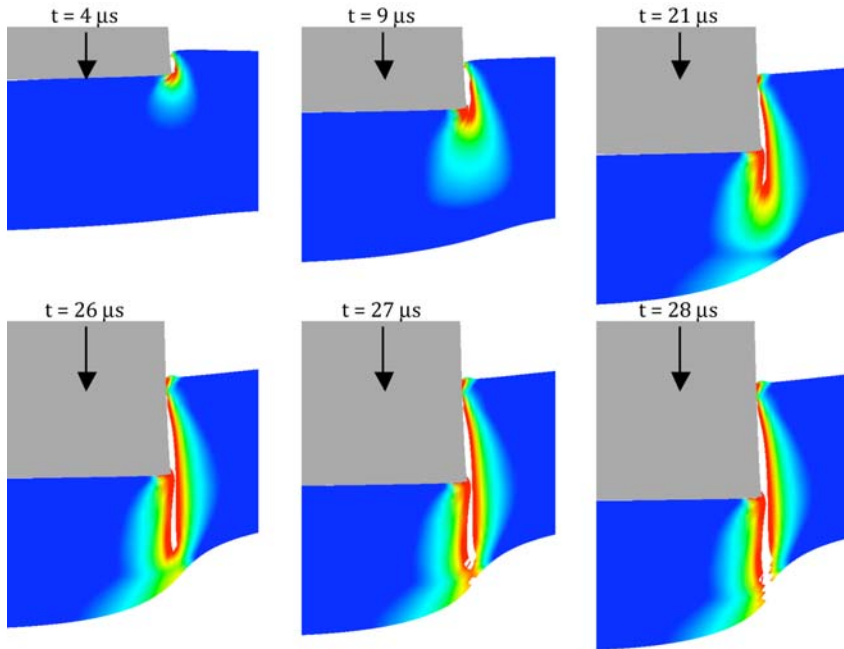


Fig. 11.27 Details of crack propagation and fracture in a 8 mm thick Weldox 460E target plate during impact (plotted as fringes of accumulated plastic strain) [4].

Fig. 11.25 and Fig. 11.26 give some typical plots (as fringes of accumulated plastic strain) from simulations of the perforation process of Weldox 460E plates using various plate thicknesses and projectile nose shapes, while Fig. 11.27 shows the details of the crack propagation and fracture in a 8 mm thick target during impact. Compared to the high-speed camera images in Fig. 11.16 – 11.19, the overall agreement is excellent. Finally, Fig. 11.28 shows plots of the perforation process of double-layered Weldox 700E steel targets spaced with air struck by blunt and ogival projectiles. Also for these configurations, the agreement with the experimental data is good.

11.6 Concluding Remarks

It has been shown that the compressed gas gun is an excellent tool in order to carry out high-precision impact tests in the sub-ordnance velocity regime to study the

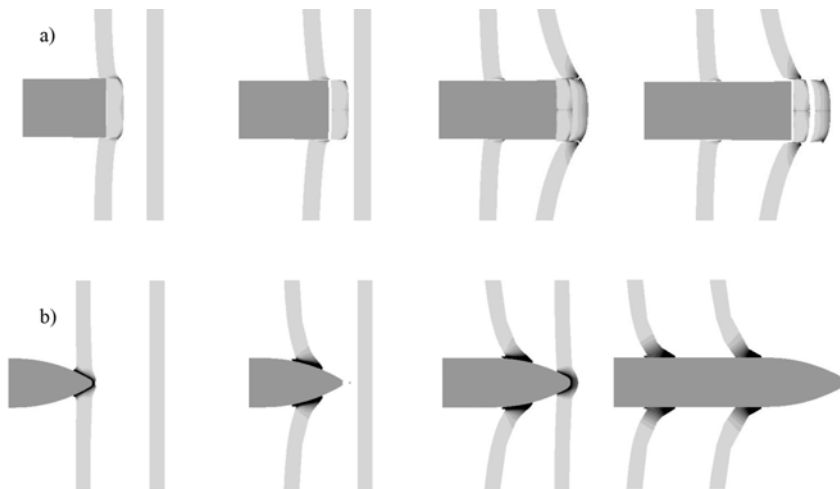


Fig. 11.28 Plots of the perforation process of a 26 mm thick double-layered Weldox 700E steel target a) spaced with 12 mm of air impacted by a blunt projectile and b) spaced with 24 mm of air impacted by an ogival projectile [16].

main mechanisms governing the perforation resistance of high-strength steel target plates. In addition, the experimental results have proven to be suitable for validation of computational methods since both the energy absorption mechanisms and failure mode may easily be changed by varying different impact conditions, such as the projectile nose shape and target thickness.

The LS-DYNA simulations predict with good accuracy the residual projectile velocity and ballistic limit as function of impact velocity, target thickness and projectile nose shape. The numerical models also describe the correct failure modes for varying impact conditions, but rezoning is needed for pointed projectiles [6]. It is also found that simulations with fixed element meshes and rezoning give similar results. However, problems still arise when trying to simulate the drop in ballistic limit with increasing target strength when struck by blunt projectiles [10], even for extremely refined meshes [18] [21], and in situations involving projectile fragmentation during impact of hard and/or thick plates [22].

References

1. Børvik T, Langseth M, Hopperstad OS, Malo KA. Ballistic penetration of steel plates. *International Journal of Impact Engineering* 1999;22(9-10):855-886.
2. Børvik T, Hopperstad OS, Berstad T, Langseth M. A computational model of viscoplasticity and ductile damage for impact and penetration. *European Journal of Mechanics – A/Solids* 2001;20(5): 685-712.

3. Børvik T, Leinum JR, Solberg JK, Hopperstad OS, Langseth M. Observations on shear plug formation in Weldox 460 E steel plates impacted by blunt-nosed projectiles, *International Journal of Impact Engineering* 2001;25(6):553-572.
4. Børvik T, Hopperstad OS, Berstad T, Langseth M. Numerical simulation of plugging failure in ballistic penetration. *International Journal of Solids and Structures* 2001;38(34-35):6241-6264.
5. Børvik T, Langseth M, Hopperstad OS, Malo KA. Perforation of 12 mm thick steel plates by 20 mm diameter projectiles with blunt, hemispherical and conical noses, Part I: Experimental study. *International Journal of Impact Engineering* 2002;27(1):19-35.
6. Børvik T, Hopperstad OS, Berstad T, Langseth M. Perforation of 12 mm thick steel plates by 20 mm diameter projectiles with blunt, hemispherical and conical noses, Part II: Numerical simulations, *International Journal of Impact Engineering* 2002;27(1):37-64.
7. Børvik T, Hopperstad OS, Langseth M, Malo KA. Effect of target thickness in blunt projectile penetration of Weldox 460 E steel plates. *International Journal of Impact Engineering* 2003;28(4):413-464.
8. Hopperstad OS, Børvik T, Langseth M, Labibes K, Albertini C. On the influence of stress triaxiality and strain rate on the behaviour of a structural steel, Part I. Experiments. *European Journal of Mechanics – A/Solids* 2003;22(1):1-13.
9. Børvik T, Hopperstad OS, Berstad T. On the influence of stress triaxiality and strain rate on the behaviour of a structural steel, Part II. Numerical study. *European Journal of Mechanics – A/Solids* 2003;22(1):15-32.
10. Dey S, Børvik T, Hopperstad OS, Leinum JR, Langseth M. The effect of target strength on the perforation of steel plates using three different projectile nose shapes. *International Journal of Impact Engineering* 2004;30(8-9):1005-1038.
11. Børvik T, Hopperstad OS, Dey S, Pizzinato EV, Langseth M, Albertini C. Strength and ductility of Weldox 460 E steel at high strain rates, elevated temperatures and various stress triaxialities. *Engineering Fracture Mechanics* 2005;72(7):1071-1087.
12. Dey S, Børvik T, Hopperstad OS, Langseth M. On the influence of fracture criterion in projectile impact of steel plates. *Computational Materials Science* 2006;38:176-191.
13. Børvik T, Dey S, Clausen AH. A preliminary study on the perforation resistance of high-strength steel plates. *Journal de Physique IV* 2006;134:1053-1059
14. Dey S, Børvik T, Hopperstad OS, Langseth M. On the influence of constitutive relation in projectile impact of steel plates. *International Journal of Impact Engineering* 2007;34:464-486.
15. Solberg JK, Leinum JR, Embury JD, Dey S, Børvik T, Hopperstad OS. Localized shear banding in Weldox steel plates impacted by projectiles. *Mechanics of Materials* 2007;39:865-880.
16. Dey S, Børvik T, Teng X, Wierzbicki T, Hopperstad OS. On the ballistic resistance of double-layered steel plates: An experimental and numerical investigation. *International Journal of Solids and Structures* 2007;44:6701-6723.
17. Teng X, Dey S, Børvik T, Wierzbicki T. Protection performance of double-layered metal shields against projectile impact. *Journal of Mechanics of Materials and Structures* 2007;2(7):1309-1331.
18. Kane A, Børvik T, Hopperstad OS, Langseth M. Finite element analysis of plugging failure in steel plates struck by blunt projectiles. Accepted for publication in *Journal of Applied Mechanics*, 2008.
19. Børvik T, Dey S, Clausen AH. Perforation resistance of five different high-strength steel plates subjected to small-arms projectiles. *International Journal of Impact Engineering* 2009;36:948-964.
20. Dey S, Børvik T, Hopperstad OS. Computer-aided design of double-layered steel plates for ballistic perforation resistance. Submitted for possible journal publication, 2008.
21. Kane A, Børvik T, Hopperstad OS. Numerical study on plugging of steel plates using a thermoelastic-thermoviscoplastic constitutive model and criteria for ductile and shear fracture. Work in progress.

22. Dey S, Børvik T, Xiao X, Hopperstad OS. Computer-aided design of double-layered steel plates for ballistic perforation resistance. Work in progress.

Chapter 12

Dimensioning of concrete walls against small calibre impact including models for deformable penetrators and the scattering of experimental results

Norbert Gebbeken, Tobias Linse, Thomas Hartmann, Martien Teich and Achim Pietzsch

Abstract A new engineering tool for the assessment of impact of small calibre projectiles on concrete targets has been developed. As the experimental data of small calibre impact scatters noticeably, the inclusion of a model that describes the scattering of the results was needed. This is of special interest for the assessment of the safety, the remaining risk and an economical dimensioning of concrete walls. The threat level of ordinary small calibre munition is often overestimated, because the deformation of the projectiles is usually neglected. Hence, two models for deformable projectiles were developed and implemented. One model is for full jacketed projectiles and deduced from experimental data, the second model is for homogenous projectiles and is based on the analysis of data generated by numerical simulations. The key results of the research during the last years and the functionality of the tool are described in this article.

12.1 Introduction

The assessment of the consequences of projectile impact on concrete structures has been studied by scientists for more than a century. In 1910 Pétry (e.g. in [14]) was the first who published an equation with which the penetration depth of munitions can be determined for different materials. Up to today there are at least 20 penetration formulas for different fields of application. To name just a few, the pene-

Norbert Gebbeken

Institute of Engineering Mechanics and Structural Mechanics, University of the German Armed Forces Munich, Werner-Heisenberg-Weg 39, 85577 Neubiberg, Germany e-mail: norbert.gebbeken@unibw.de

Tobias Linse, Thomas Hartmann, Martien Teich and Achim Pietzsch

Institute of Engineering Mechanics and Structural Mechanics, University of the German Armed Forces Munich, Werner-Heisenberg-Weg 39, 85577 Neubiberg, Germany e-mail: tobias.linse@unibw.de

tration formulas from the Army Corps of Engineers (ACE), the National Defense and Research Committee (NDRC), Hughes [13], Fullard [9], CEA-EDF [5], Kar and UKAEA are some of the most famous ones. Li, Kennedy and Yankelevsky reviewed many of these formulas in [14, 16, 28].

These existing penetration formulas were developed for different specific areas of application. Some were deduced for small bullets or small calibre projectiles that are usually much faster than the speed of sound. Others were developed for missiles that are slower but much heavier than small calibre projectiles. Most penetration formulas determine the penetration depth in an infinitely thick half-space. Some equations, like the equation from CEA-EDF, determine the required thickness to prevent perforation. All these equations were established by curve fitting to experimental data. The result of these formulas is always just one single parameter. In most cases this is the penetration depth. To determine the minimum thickness to prevent spalling or perforation, many additional formulas exist. Adeli and Amin [1] collected and compared some of these formulas to experimental data. Often it is not obvious whether the result represents an average level or a dimensioning level. To illustrate this, the result can either be an average penetration depth or a worst case penetration depth. The worst case penetration depth or the required thickness on dimensioning level already include safety factors. Some existing formulas are on the safe side and lead to an inefficient dimensioning of walls - especially for deformable penetrators, as they do not account for the deformation capacity of the projectiles. Often, it is not clear for which area of application the formulas were designed for. If this is not clear there is a risk of misapplication. Last but not least, concrete is a very inhomogeneous material composed of different types and sizes of aggregates. This leads to a noticeable scattering of the impact behaviour. Furthermore, there exist very different types of projectiles, non-deformable solid projectiles or jacketed projectiles which deform during the impact.

As these aspects show, the prediction of the effects of penetration is still complicated, inconvenient and imprecise. Furthermore, the behavior of deformable or jacketed projectiles is not yet fully investigated. A statistical examination, with which it is possible to estimate the remaining risk, and which can be a basis for an economic dimensioning of protective concrete walls is still lacking.

Hence, the focus of research was put on the development and implementation of an algorithm that fulfills all the requirements like accounting for scattering and regarding deformable projectiles, residual velocities, ballistic limits and geometries of damages.

Within this paper, first, the applicability of the mentioned penetration formulas for this project is discussed. After that, the basis of the new penetration algorithm and its derivation are briefly presented. Based on this it is possible to determine penetration depths, residual velocities and minimum thicknesses of concrete walls for non-deformable penetrators. Then, after dealing with non-deformable projectiles, the two models for the deformable penetrators are explained. In a further step, the derivation of the model for the consideration of the scattering of the experimental results is shown. Finally, as the result of the conducted research, the new engineering tool PenSim is presented.

12.2 Penetration and perforation of concrete walls with non-deformable penetrators

A relatively new penetration formula is the penetration formula developed by Forrestal, Altmann, Cargile and Hanchak [8]. This penetration formula is based on an almost analytical approach, the so-called Cavity Expansion Theorie (CET). The CET was originally introduced by Bishop in 1945 [6] and further extended by Goodier [12] in 1965. The advantage of this approach is that only the constant describing the resistance of the concrete has been empirically adjusted to experimental data. The main idea of this approach is to establish an equation that describes the acting force F on the projectile. If the force on the projectile can be appropriately represented, the progress of the deceleration, the velocity and the position of the projectile can be determined by integration with appropriate boundary and transition conditions. Equation (12.1) shows an extended version of Forrestal's approach for the Force F_0 that acts on the projectile. There are three recognisable domains of definition: the cratering phase, the tunneling phase and the breakthrough phase. This formulation was proposed by Sjøel and Teland [21]. They added the breakthrough phase to Forrestal's approach in order to be able to calculate residual velocities, ballistic limits and minimum thicknesses to prevent perforation of the concrete wall.

X_1 is the depth that corresponds to the end of the cratering phase and to the beginning of the tunneling phase. X_2 represents the transition between the tunneling phase and the breakthrough phase. X_3 is either the thickness of the concrete wall or the penetration depth. The notations of the velocities are defined analogously.

$$F = \begin{cases} c \cdot x & 0 < x < X_1 \\ F_0 & X_1 < x < X_2 \\ F_0 \cdot \alpha(x) & X_2 < x < X_3 \end{cases} \quad (12.1)$$

The force F_0 that is acting on the projectile during the tunneling phase is

$$F_0 = \frac{\pi d^2}{4} (S \sigma_c + N \rho v^2) \quad (12.2)$$

with

$$N = \frac{8\psi - 1}{24\psi^2}, \quad \psi = \frac{s}{d}, \quad S = 82.6 \sigma_c^{-0.544} \quad (12.3)$$

c	constant cratering phase	$[-]$
x	x-coordinate of the projectile's nose	$[m]$
N	nose parameter	$[-]$
d	diameter of projectile	$[m]$
σ_c	concrete strength $[Pa]$ for S in $[MPa]$	$[MPa / Pa]$
ρ	concrete density	$[kg/m^3]$
S	material parameter to describe the concrete strength	$[-]$
m	mass of the projectile	$[kg]$
s	radius of the ogive of the projectile	$[m]$
ψ	ratio between radius of the ogive and the diameter	$[-]$
v	impact velocity	$[m/s]$

Forrestal's penetration equation was further extended for blunt projectiles by Lixin [17] and Teland [26]. The material constant S that describes the concrete was adjusted to experimental data for high performance concrete by Sjøøl [20]. Sjøøl and Teland also proposed an extension of Forrestal's formula that allows to determine residual velocities and the minimum thickness to prevent perforation. Forrestal assumed that the target is much thicker than the penetration depth. For this case, the third area of definition is not necessary. With some mathematical manipulations Forrestal's penetration formula

$$X = \frac{2M}{\pi N} \ln \left(1 + \frac{NV_1^2}{SM} \right) + 2 \quad (12.4)$$

with

$$V_1^2 = \frac{V^2 - \frac{\pi}{2}S}{1 + \frac{\pi N}{2M}} \quad (12.5)$$

and the dimensionless parameters

$$X = \frac{x}{d}, \quad V = \sqrt{\frac{m}{d^3 \sigma_c}} \cdot v, \quad M = \frac{m}{d^3 \rho_t} \quad (12.6)$$

can be determined. V_1 is the velocity at the transition between the cratering and the tunneling phase. For reason of clarity, the notation proposed by Sjøøl and Teland is used in this paper. Forrestal used another notation without dimensionless parameters. The complete derivation of Forrestal's equation is explained in [8]. The derivation of the extended version is shown in [21].

The derivation of more universally applicable equations which e.g. also allow the calculation of penetration of thin targets is too extensive to be presented here. The basic ideas are represented in [21] and their realization in [11]. It is assumed that the length of the projectile's nose corresponds to X_1 . In order to get equilibrium of forces between the force that acts on the penetrator and the force of inertia, three equations can be established by applying Newton's second law. With boundary and transition conditions, these equations can be transformed, leading to the following two equations.

$$V_2^2 = V_0^2 - C \left[X_1^2 + 2 \int_{X_1}^{X_2} \alpha X dX \right] \quad (12.7)$$

$$\begin{aligned} \int_{X_2}^{X_3} \alpha dX &= \left[\frac{2M}{\pi N} \ln \left(1 + \frac{NV^2}{SM} \right) \right]_{V_2}^{V_3} \\ &= \frac{2M}{\pi N} \left[\ln \left(1 + \frac{NV_3^2}{SM} \right) - \ln \left(1 + \frac{NV_2^2}{SM} \right) \right] \end{aligned} \quad (12.8)$$

By substituting eq. (12.7) in eq. (12.8) an equation with the two unknown parameters V_3 and X_3 is obtained. For the case of the perforation, X_3 corresponds to the thickness of the concrete wall. In this case the equation has to be solved for V_3 . Then V_3 corresponds to the residual velocity of the projectile. If no perforation occurs, the residual velocity must vanish ($V_3 = 0$) and the equation has to be solved for X_3 .

α is a function that reduces the resistance of the concrete in the vicinity of the wall's rear side. Sjøøl and Teland [21] developed several approaches by using the Mohr-Coulomb material model and the von Mises material model and applying the spherical and cylindrical Cavity Expansion Theorie. Figure 12.1 shows the curves for the different definitions of α . As there is no sufficient experimental data, it is not clear which function approximates reality best. However, as the functions within each CET do not differ extremely, there is no significant variation of the results.

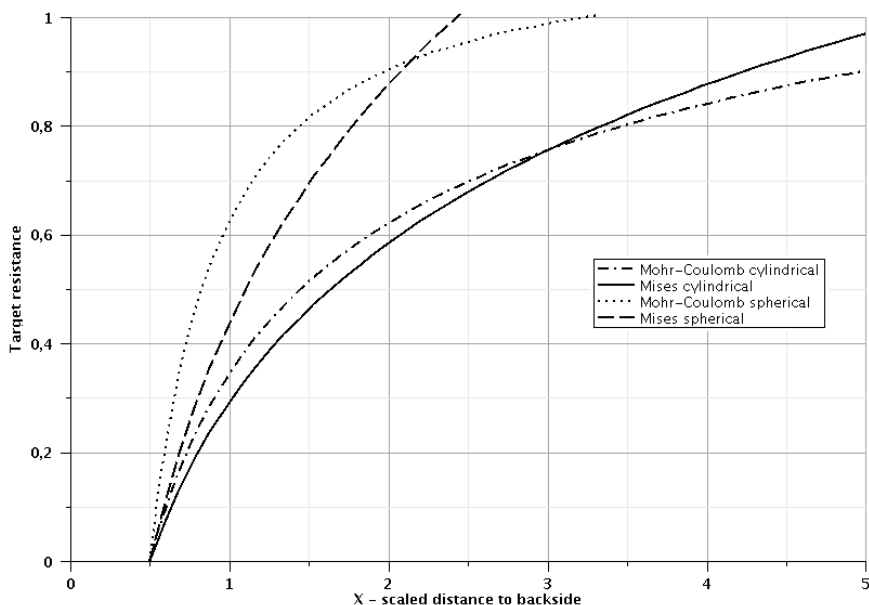


Fig. 12.1 Relative target resistances as functions of distance to backside.

With eq. (12.7) and eq. (12.8) it is possible to determine residual velocities, minimum required thicknesses and ballistic limits. To be able to implement and to solve these equations, three possible cases have to be distinguished:

- The projectile stops in the undamaged region of the concrete wall. This means, the penetration depth is smaller than the thickness of the wall minus the damaged region, that is described with the parameter α .
- The projectile stops in the damaged region.
- The projectile perforates the concrete wall.

As each of these cases requires completely different numerical treatment, it is necessary to elaborate functions that allow the distinction of the different cases prior to computation. To do so, the equivalent thickness X_{equi} of the wall is determined by integration of the function α . Additionally the depth X_α is defined as the penetration depth at which the decay function α starts to affect the material resistance. By comparing the theoretical penetration depth in an infinitely thick wall X_∞ with X_{equi} and X_α the three different cases can then be distinguished (see also [11]), and the appropriate numerical treatment can be applied.

12.3 Deformable projectiles

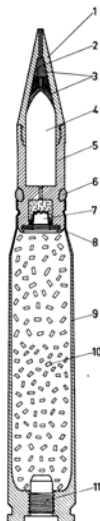
12.3.1 Jacketed projectiles

Ordinary munitions for small calibre weapons are jacketed projectiles. This means the projectile is composed of a soft metal jacket and a core made of either soft or hard metals. Figure 12.2 shows an example for such projectiles. However, the projectiles mostly used for laboratory experiments and, hence, for the derivation of the penetration formulas are usually homogenous projectiles made of steel with a high strength. For the derivation of Forrester's penetration equation such projectiles were used, too. Certainly, non-deformable projectiles represent the worst case for penetration events, but if the penetration depth of standard munition is determined applying Forrester's penetration formula, the penetration depths will be largely overestimated. Table 12.1 compares experimental penetration depths with calculated penetration depths.

Table 12.1 Comparison of experimental penetration depths [15] and calculated penetration depths.

Calibre [mm]	Distance [m]	No. of tests [-]	Penetrator			Core	Concrete strength [MPa]	Penetration depth		Eff. η [-]
			m [g]	V_0 [m/s]	d [mm]			Analyt. [cm]	Exp. [cm]	
5.56 x 45	50	7	4	920	5.56	DC	27.6	15.1	4.0	19.8%
5.56 x 45	50	1	4	920	5.56	SC	27.6	15.1	3.9	20.0%
7.62 x 51	50	MW 4	9.45	820	7.83	SC	24.7	15.8	3.9	18.2%
7.62 x 51	50	MW 2	9.7	844	7.83	HC	24.7	16.9	8.8	42.5%
5.56 x 45	3	MW 3	4	920	5.56	DC	31.8	14.4	4.1	47.3%
5.56 x 45	3	1	4	920	5.56	SC	31.8	14.4	2.5	12.1%
7.62 x 51	3	MW 3	9.45	820	7.83	SC	32.3	14.4	4.0	17.7%
7.62 x 51	3	1	9.7	844	7.83	HC	32.3	15.3	7.0	38.7%
5.56 x 45	100	MW 4	4	920	5.56	DC	24.4	15.8	4.7	22.9%
7.62 x 51	100	MW 4	9.45	820	7.83	SC	24.4	16.2	4.5	20.9%

DC = Double core projectile, SC = Soft core projectile, HC = Hard core projectile



Nr.	Description	Material
1	hull	aluminium alloy
2	device for flash light	MX71-Magnesium
3	filler	polyester resin
4	core	tungsten carbide
5	hull	aluminium alloy
6	ring for conduction	
7	tracer	
8	cap	brass
9	hull for charge	steel
10	charge	
11	igniter	

Fig. 12.2 Cartridge 20 mm x 139 mm DM43.

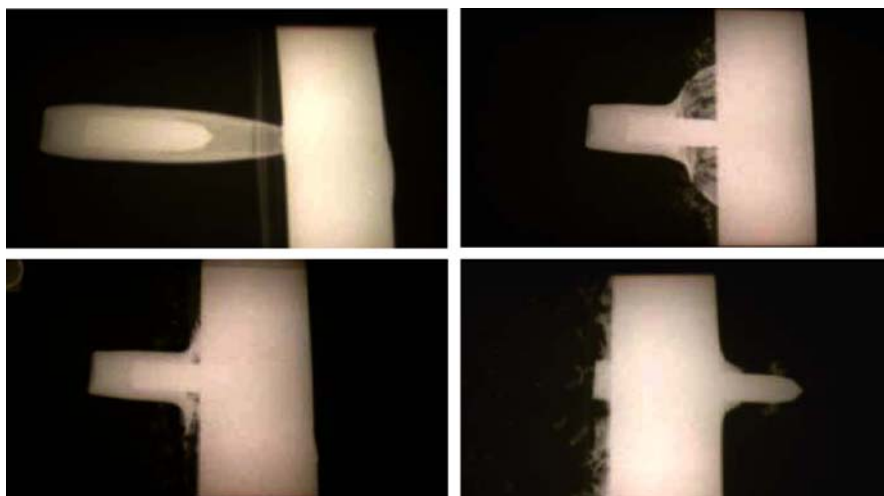


Fig. 12.3 Stripping-off of the hull during impact (from [19]).

The penetration depth of ordinary jacketed munition is significantly smaller than of quasi-rigid penetrators, because the soft jacket is stripped off when the projectile hits the target (figure 12.3). During this process a part of the penetrator’s energy is dissipated. On the one hand the deformation of the hull dissipates energy while on the other hand, due to the increased penetrator diameter, the concrete target shows a higher resistance. That is why more energy is absorbed by the concrete target.

Therefore, one task of this research project was to find a possibility to better assess the penetration depth of ordinary munition. The way chosen to solve this problem was to determine the degree of efficiency of different types of penetrators. For this purpose, experimental data of 139 experiments, mainly from [2, 3, 4, 15], was collected. For each shot, the theoretically necessary velocity to get the right penetration depth with Forrestal’s penetration formula (12.4) was calculated. Knowing the necessary velocity, the necessary kinetic energy E of the projectile can be determined. Then, the degree of efficiency is defined as

$$\eta = \frac{E_{\text{rigidbody projectile}}}{E_{\text{real projectile}}} \quad (12.9)$$

Similar to table 12.1, table 12.2 provides further data on the degrees of efficiency for different projectiles. Details on the experimental setups can be found in the given references.

Table 12.2 Degree of efficiency for different types of munitions determined from experimental data.

Type of Munition	Reference	Core	Efficiency η
5.56 x 45 mm	[15]	DC	26.6 %
5.56 x 45 mm	[15]	SC	16.1 %
7.62 x 51 mm	[15]	SC	19.0 %
7.62 x 51 mm	[27]	SC	18.7 %
7.62 x 51 mm	[15]	HC	41.2%
7.62 x 51 mm	[27]	HC	24.8 %
7.62 x 51 Smk	[3]	HC	52.1 %
7.62 x 51 Smk	[2]	HC	27.9 %
7.62 x 54R B32	[4]	HC	55.5 %
7.62 x 54R B32	[4]	HC	21.3 %
7.62 x 54R B32	[3]	HC	61.7 %
20 x 139 mm DM43A1	[3]	HC	78.1 %

For the rapid assessment of the threat level for different types of projectiles, a classification is needed. Hard core projectiles have a degree of efficiency between 21.3 % and 78.1 %. Hard core projectiles with a larger diameter have a higher degree of efficiency. The reason for this is the higher mass fraction of the core in larger projectiles. Soft core projectiles show a degree of efficiency of just about 20 %, whereas with a degree of efficiency of about 30 % double core projectiles are slightly better.

Due to the large set of data on which the values are based, for unknown projectiles we suggest the degrees of efficiencies outlined in table 12.3. However, as these values are solely determined from experiments with munition used by the German Armed Forces, they must be used carefully.

Table 12.3 Degree of efficiency for different types of munitions.

Typ of core	Degree of efficiency	Remark
Soft Core	20%	
Double Core	30%	
Hard Core	55%	if $d < 7$ mm
	55% - 80 %	linear interpolation
	80%	if $d \geq 12$ mm

12.3.2 Homogenous deformable projectiles

As the model for jacketed projectiles (see section 12.3.1) is not suitable for homogenous deformable projectiles, a second model was developed in order to assess the effects of these penetrators, too.

Besides the impact velocity, the stresses in the projectile depend on various parameters: the projectile diameter, the shape of the nose, and the material densities of target and projectile materials.

All projectiles, even projectiles made of high strength materials like tungsten carbide, deform if a certain impact velocity is exceeded. This limit is called the "limit of non-deformable penetration" and the corresponding velocity is called the "critical velocity". Certainly, the deformation of a projectile made of lead will differ significantly from a projectile made of tungsten carbide. Chen [7] described the transition from non deformable penetration to deformable penetration. He showed that if the critical velocity is exceeded the penetration depth decreases significantly because of the deformation of the penetrator. For deformable penetration or hydrodynamic penetration several models exist. The first model for hydrodynamic penetration was derived by Birkhoff in 1948. A more sophisticated model is the model of Alkesevskii and Tate which was published in 1966 and which was extended by Jones, Gillis and Foster. Tate refined his model in 1986 [23, 24]. In 1991 Luk and Piekutowski and in 1992 Cinnamon, Jones, House and Wilson published further models [18]. Teland summarised these models and some of the derivations in [25].

A major shortcoming of all these models is that they are rather complicated and that it is often not clear for which kind of penetration they can be applied. Furthermore, with the transition from non-deformable to deformable penetrators, it was not possible to integrate one of these models into the concept of the new engineering tool. Hence, a complete new approach was pursued.

The idea was to find a methodology to describe the penetrator's shape after the impact depending on the material properties and the impact velocity. Knowing the penetrator geometry after deformation, the penetration process can be approximately described applying the already explained algorithm for rigid body projectiles (section 12.2).

Chen [7] showed that the critical velocity v_c at which deformable penetration occurs can be determined by

$$v_c = \sqrt{\frac{2 \cdot (Y_P - R_T)}{\rho_T}} \quad (12.10)$$

with

Y_P	yield strength of the material of the penetrator,
R_T	yield strength of the material of the target,
ρ	density of the target material.

With eq. (12.10), it is possible to estimate at which velocity deformation starts to occur. This expression, however, does not consider the projectile's nose shape. Furthermore, there is no formulation describing the projectile's shape and diameter after the impact. These necessary descriptions were determined by a large number of simulations (more than 200) with the Hydrocode Autodyn. In order to verify the results of the simulations, extensive numerical studies were conducted and summarised in [10].

For the determination of the necessary functions that describe the penetrator diameter after impact, several computations have been carried out where the material strengths, the projectile diameter, the impact velocity and the nose shape were varied and their influence on the penetrator's deformation was investigated. For each simulation, the shape and the diameter of the penetrator after the impact was determined. Based on these data, new relationships could be established. Figure 12.4 shows the results of the simulations conducted to extend eq. (12.10) for ogive nose projectiles. In the figure the numerically determined diameters after impact are plotted as a function of the impact velocity and the material strength of the penetrator. The numerical studies show that an ogive nose projectile begins to deform significantly later than blunt projectiles, and the critical velocity for ogive nosed penetrators is about 100 % higher.

Introducing the constant Φ for the nose shape in eq. (12.10) yields

$$v_c = \Phi \cdot \sqrt{\frac{2 \cdot (Y_P - R_T)}{\rho_T}} \quad (12.11)$$

and

$$\Phi = 2 - N, \quad (12.12)$$

where N is the penetrator nose parameter from eq. (12.3).

As soon as the projectile nose begins to deform, the diameter of the penetrator increases significantly. In figure 12.4 the measured deformation factors Δ , which describe the deformed/undeformed diameter ratio, are plotted. Thus, a deformation factor of $\Delta = 2$ means that the diameter after impact is twice the diameter before the impact.

To describe the deformation, the following relation is proposed:

$$\Delta = \begin{cases} 1 & \frac{v}{v_c} < 0.8 \\ 2.5 \frac{v}{v_c} - 1 & 0.8 < \frac{v}{v_c} < 1.2 \\ 2 & \frac{v}{v_c} > 1.2 \end{cases} \quad (12.13)$$

The results of the simulations also showed good agreement for the blunt projectiles (cf. [11]) and by applying eqs. (12.11), (12.12) and (12.13), all numerical results can be well reproduced. Furthermore, even a comparison with experimental data from jacketed projectiles with soft cores - which can be approximated as homogenous deformable penetrators - shows good agreement. Hence, this model can be considered as suitable to assess whether penetrators of certain materials will be deformed during a specific impact process. Generally, a direct comparison of this theoretical deformation and data gained from experiments with deformable projectiles would be of great interest. However, there is no sufficient data available at the moment.

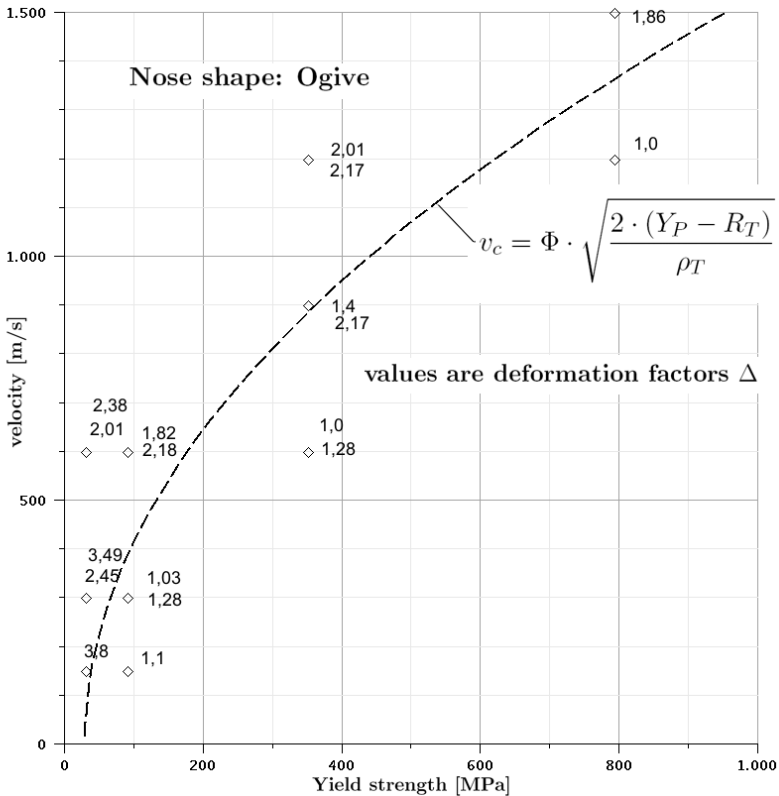


Fig. 12.4 Deformation factors for different impact velocities and yield strengths and critical velocity for different yield strengths.

12.4 Scattering of experimental data

It is a well-known fact that most experimental data scatter in a certain range. Especially due to the inhomogeneity of concrete the results of experiments with small calibre penetrators scatter noticeable. Höcherl and Kunz [15] studied the penetration depth of hard core munition fired from the German assault rifle G36 in concrete targets. Table 12.4 shows the penetration depths measured in seven experiments. The mean value of the experiments is 40 mm, the maximum value is 60 mm and the minimum value is 32 mm. This shows that the deviation of the mean value is not negligible. In the development of a model for the design of concrete walls against impact the scattering has to be considered.

Table 12.4 Comparison of experimental penetration depths [15].

Shot number	5-1	5-2	5-3	5-4	5-5	5-6	5-7
Penetration depth [mm]	60	31,5	45	40	32	34	37

As concrete is a composite of aggregates and cement paste, it is a highly inhomogeneous material. In particular for small penetrators this is of special importance. Due to the inhomogeneity of the concrete the forces acting on the penetrator are not evenly distributed and lead to a deviation from the firing direction. That is probably one of the reasons why Forrester's constant for the material resistance S does not represent the resistance of the concrete satisfactorily for large penetrators. An approach that as well accounts for the diameter of the penetrator as for the mean diameter of the aggregates might deliver a better description for S . However, such a description does not exist yet.

Another reason for the scattering of experimental results are the yaw and impact angle of the projectiles.

For setting up a broad statistical study, it would be necessary to have a large number of shots with different penetrators and different penetrator velocities and different concrete compositions. To gather information how the experiments are performed and its influence on the results, it might also be interesting to have the experiments performed by several experimental laboratories.

However, as such a statistical database does not exist, it is not possible to evaluate the significance and scattering of all important parameters. A number of seven repetitions must unfortunately already be considered as high. Nevertheless, to quantify the scattering it is reasonable to calculate the deviation of the experimental data from the prediction of the theoretical model. This approach has the advantage that a single frequency distribution of the deviation of all experiments with different projectile velocities, masses, nose shapes, diameters and different concrete strengths can be obtained.

Figure 12.5 shows a comparison of calculated (theoretical) and experimental data. The data depicted in the figure was taken from experimental results from Sjøel,

Forrestal and Bergmann for non-deformable projectiles with a diameter less than 25 mm (details in [11]).

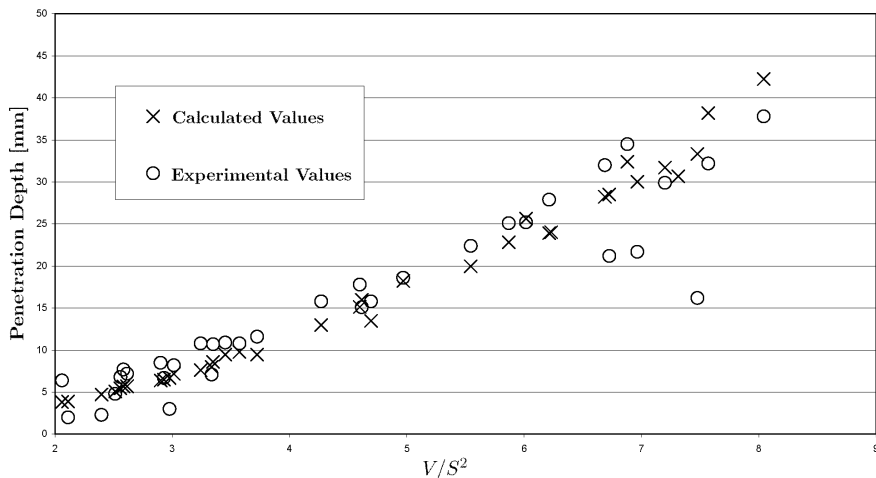


Fig. 12.5 Comparison of experimental data from Sjøøl [22] and calculated penetration depths.

For 86 experimentally determined penetration depths the theoretically necessary impact velocity was calculated using equation (12.4). This velocity was then compared to the experimental impact velocity. As the criterion to describe the variation of the results the kinetic energy was chosen. Sorting the experiments by their variation of the energy the empiric distribution function for the deviation of the impact energy is obtained (top of figure 12.6).

The lower chart in figure 12.6 shows the empiric cumulative distribution function, which is obtained by integration of the empiric distribution function. On the axis of abscissas the variation of the energy and on the ordinate the cumulated probability is plotted. With this function it is possible to determine the level of confidence and to calculate the necessary additional projectile energy to obtain a desired safety margin.

The table 12.5 shows the necessary factors for the impact energies for some probabilities of occurrence. These factors can be interpreted as safety factors. If the probability of perforation of a concrete wall should be less than 5 % the design value of the penetrator’s energy must be increased by a factor of 1.45.

This approach enables the user to get information on the confidence level of the predicted results. This is of special interest for an economic dimensioning of walls and the assessment of risk for existing walls.

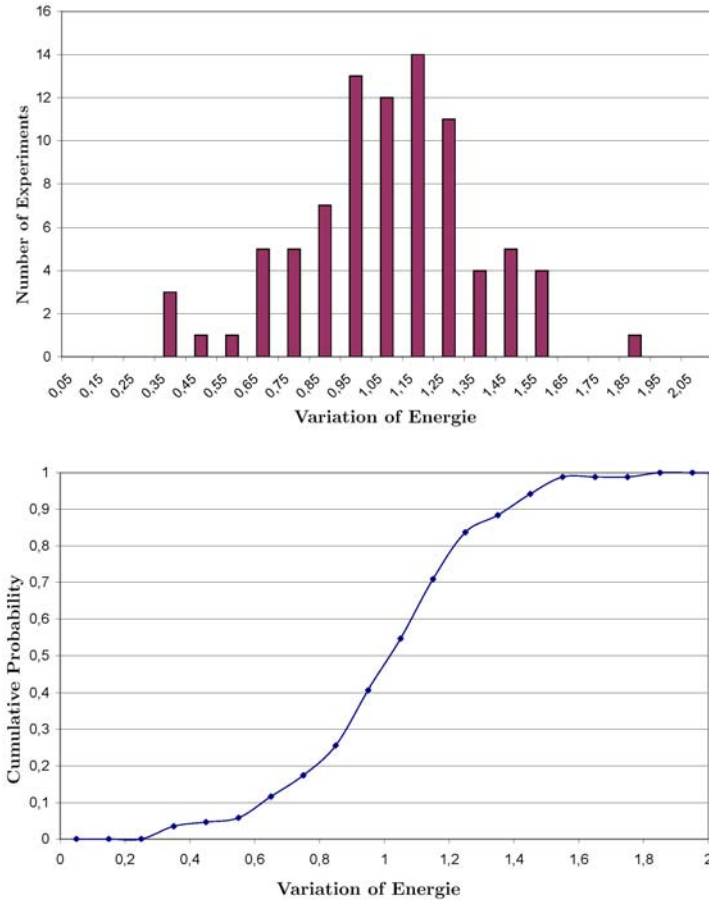


Fig. 12.6 Empiric distribution and cumulative distribution function for penetrators with a diameter smaller than 25 mm.

Table 12.5 Increase factors for the impact energy considering different safety levels.

Certainty	Increase factor for impact energy
0,7	1,15
0,8	1,2
0,9	1,38
0,95	1,45
0,99	1,8

12.5 The new software-tool PenSim

The aim of this research project was to develop an engineering tool that is easy to use, has clear ranges of application, and delivers more information about deformable penetrators than existing tools. The above mentioned and briefly described results of this research project have been implemented. Many more studies were necessary that are not presented in this paper, e.g. studies to describe the geometry of the damages. All results of this research project, the complete algorithm and the verification of its results are described in detail in [11].

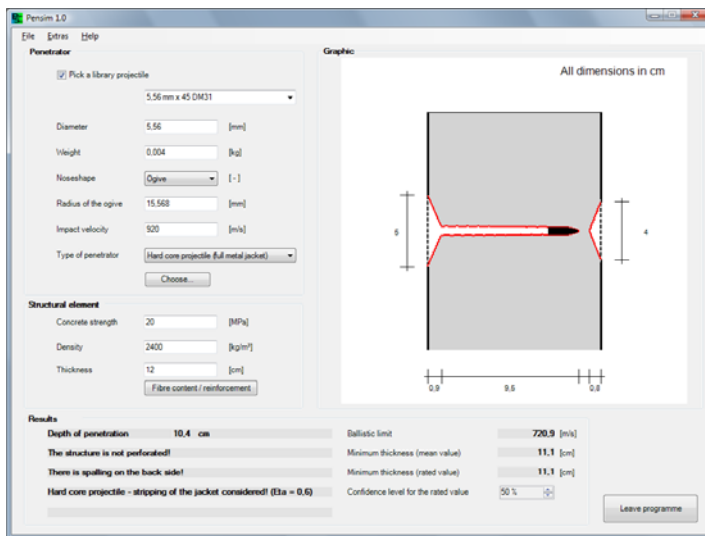


Fig. 12.7 Graphical user interface of PenSim - Input and Result Window.

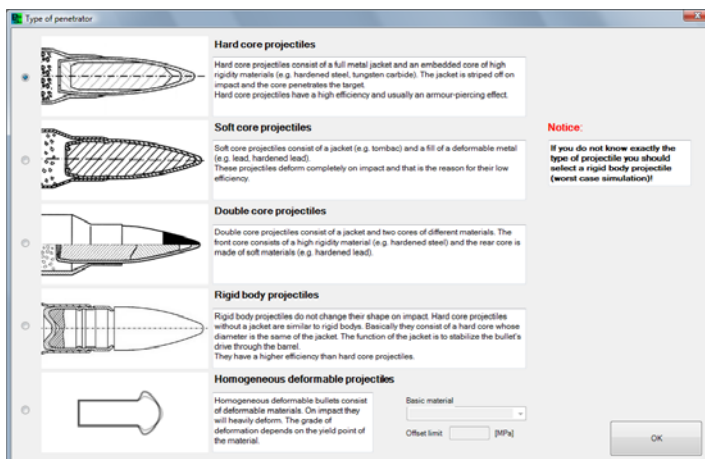


Fig. 12.8 Graphical user interface of PenSim - Selection of the typ of projectile.

Figure 12.7 shows the Graphical user interface (GUI) where the necessary data that characterises the projectile and the concrete wall can be entered. On the right hand side of the depicted program window the results of the computation are displayed graphically. In figure 12.8, the different types of projectiles are illustrated for the program input. Additionally, different penetrators can be stored in a library for convenience. Further can be mentioned that the GUI is available in German, English and French.

Acknowledgements The authors would like to express their gratitude to Mr. Dipl.-Ing. Landmann of the Wehrtechnische Dienststelle 52 (WTD 52) and OTL Heckersbruch of the Streitkräfteamt (SKA) for the support, the technical discussions, and the financing of the project. Furthermore, the authors appreciate the help of Prof. J. Höcherl (University of the Federal Armed Forces) providing experimental data and contributing to the numerous fruitful discussions.

References

1. Adeli H and Amin AM, (1985), Local effects of impactors on concrete structures, *Nuclear Engineering and Design*, 88:301–317.
2. Barwich, (1992), Neues Material: SIFCON Vergleichende Waffenwirkungsversuche an Zielstrukturen aus Stahlbeton, Stahlfaserbeton und SIFCON, WTD-Nr.:91-100/014/94, Wehrtechnische Dienststelle für Waffen und Munition WTD 91, Meppen.
3. Barwich, (1995), Hochfester Beton (HFB) Waffenwirkungsversuche an Zielstrukturen aus hochfestem Beton, WTD-Nr.: 91-100/013/96, Wehrtechnische Dienststelle für Waffen und Munition WTD 91, Meppen.
4. Barwich, (2000), Hochfester Beton (HFB) Waffenwirkungsversuche an Zielstrukturen aus hochfestem Beton, WTD Nr. 91-100/002/2000 E / K44I / T0356 / M5169, Wehrtechnische Dienststelle für Waffen und Munition WTD 91, Meppen.
5. Berriaud C, Sokolovsky A, Gueraud R, Dulac J, Labrot R, (1978), Comportement local des enceintes en beton sous l'impact d'un projectile rigide, *Nuclear Engineering and Design*, 45:457–469.
6. Bishop R, Hill R, Mott N, (1945), The theory of indentation and hardness tests, *The proceedings of the physical society*, 57 - Part 3:147–159.
7. Chen XW, Q.M. L, (2004), Transition from Nondeformable Projectile Penetration to Semi-hydrodynamic Penetration, *Journal of Engineering Mechanics ASCE*, 123–127.
8. Forrestal M, Altman B, Cargile J, Hanchak S, (1994), An empirical equation for penetration depth of ogive-nose projectiles into concrete targets, *International Journal of Impact Engineering* 15(4):395–405.
9. Fullard K, Baum MR, (1991), The assessment of impact on nuclear power plant structures in the United Kingdom, *Nuclear Engineering and Design*, 130:113–120.
10. Gebbeken N, Greulich S, Linse T, Teich M, (2007), Simulations of Projectile Impact on Concrete Structures, 12th International Symposium on Interaction of the Effects of Munitions with Structures ISIEMS Orlando USA.
11. Gebbeken N, Linse T, (2008), Entwicklung eines Engineering Tools zur Ermittlung der Schutzwirkung von betonartigen Bauteilen gegen kleinkalibrige Penetratoren - Abschlussbericht 20.12.08, Universität der Bundeswehr München, Lehrstuhl für Statik, (classified).
12. Goodier JN, (1965), On the mechanics of indentation and ratering in solid targets strain-hardening metal by impact of hard and soft spheres, *AIAA proceedings of the seventh symposium on hypervelocity impact III*.
13. Hughes G, (1984), Hard missile impact on reinforced concrete, *Nuclear Engineering and Design*, 77(1):23–35.

14. Kennedy RP, (1976), A review of procedures for the analysis and design of concrete structures to resist missile impact effects, *Nuclear Engineering and Design*, 37(2):183–203.
15. Kunz J, (2004), *Versuchsbeschüsse von Baustrukturen*, Universität der Bundeswehr München, Fachbereich für Maschinenbau, Wissenschaftliche Einrichtung für Waffentechnik, Prof. Dipl.-Ing. Johann Höcherl.
16. Li Q, Reid s, Wen h, Telford A, (2005), Local impact effects of hard missiles on concrete targets, *International Journal of Impact Engineering* 32(1-4):224–284.
17. Lixin Q, Yunbin Y, Tong L, (2000), A semi-analytical model for truncated-ogive-nose projectiles penetration into semi-infinite concrete targets, *International Journal of Impact Engineering* 24(9):947–955.
18. Luk VK, Piekutowski AJ, (1991), An analytical model on penetration of eroding long rods into metallic targets, *International Journal of Impact Engineering* 11(3):323–340.
19. Moxnes JF, Friis EK, Froyland O, (2005), Experimental and Numerical Study of the Penetration of Tungsten Carbide Into Steel Targets During High Rates of Strain, 22nd International Symposium on Ballistics, Vancouver BC, Canada.
20. Sjol H, Teland JA, (2000), Prediction of concrete penetration using Forrestal's formula, Norwegian Defence Research Establishment.
21. Sjol H, Teland JA, (2001), Perforation of concrete Targets, Norwegian Defence Research Establishment FFI/Rapport-2001/05786.
22. Sjol H, Teland JA, Kladheim O, (2002), Penetration into concrete - analysis of small scale experiments with 12 mm projectiles, Norwegian Defence Research Establishment.
23. Tate A, (1986), Long rod penetration models - Part I. A flow field model for high speed long rod penetration, *International Journal of mechanical sciences* 28:535 – 548.
24. Tate A, (1986), Long rod penetration models - Part II. Extensions to the hydrodynamic theory of penetration, *International Journal of mechanical sciences* 28:599–612.
25. Teland JA, (1999), A Review of analytical penetration mechanics, Norwegian Defence Research Establishment, FFI/Rapport-99/01264.
26. Teland JA, Sjol H, (2000), Penetration into Concrete by truncated projectiles, Norwegian Defence Research Establishment.
27. N.N., WTD91, (1970), Erprobungsstelle 91 der Bundeswehr, Erprobungsabschlussbericht Teil II, Ermittlung der Eindringtiefen von kleinkalibrigen Geschossen und Handgranaten in Mauerwerk, Beton und Sand, E/P 45 G/00019/00538 vom 28.9.70, Erprobungsstelle 91 der Bundeswehr.
28. Yankelevsky DZ, (1997), Local response of concrete slabs to low velocity missile impact, *International Journal of Impact Engineering* 19(4):331–343.

Chapter 13

Numerical Analysis of Fluiddynamic Instabilities and Pressure Fluctuations in the Near Field of a Detonation

Arno Klomfass

Abstract The near field of a blast wave generated by the detonation of a centrally ignited, spherical TNT charge is investigated via numerical simulation. The study focuses on the effects of the Rayleigh-Taylor and the Richtmyer-Meshkov instabilities on fluctuations in the pressure field. The numerical simulations are performed with a finite volume multi-fluid ALE-method on globally adapted grids, which stretch with the expanding blast wave. The paper describes the details of the applied methods and gives a survey on the results obtained.

13.1 Introduction

The detonation of a High Explosive (HE) produces mainly gaseous products in a state of high pressure (typically some 100 kbars) and high density (comparable to the density of the unreacted HE). The expansion of the product gas drives a strong shock wave in the surrounding air. This is illustrated in figure 13.1 for a spherical detonation of 1 kg TNT. The expansion of the product gas starts when the detonation wave reaches the outer surface of the charge at a time about $8 \mu\text{s}$ after initiation at its center. At that instance the primary and secondary shock waves are generated by refraction of the detonation wave at the interface between product gas and ambient air. The expansion of the product gas starts with about 7000 m/s and comes to a rest after about 1 ms when the cloud of product gas reaches a first maximum at a radius of about 0.85 m. The primary shock front propagates outward and continuously separates from the cloud of product gas; its propagation velocity asymptotically approaches the ambient sound speed. The secondary wave initially propagates towards the center of the sphere against the outward directed flow of expanding product gas. After about 1.3 ms the wave is reflected at the center; it reaches the surface of the

Arno Klomfass
Fraunhofer Ernst-Mach-Institut, Eckerstr.4, 79104 Freiburg, Germany, e-mail: klomfass@emi.fhg.de

product gas at about 2.4 ms. There it is refracted into the outward propagating secondary shock and the inward propagating tertiary wave. This again is reflected at the center at about 4.2 ms and leaves the cloud of product gas at about 5.6 ms ¹

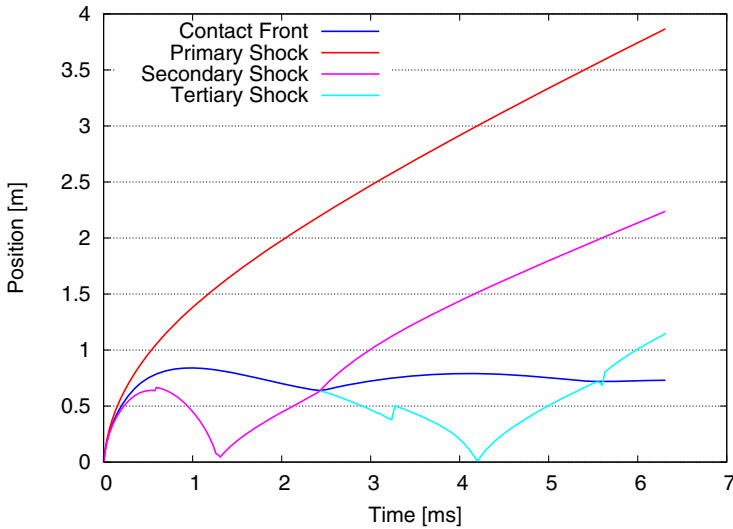


Fig. 13.1 Trajectories of the fluid interface and the primary shock and trajectories of subsequent waves as computed with EMI Flow Solver APOLLO.

During the expansion of the product gas perturbations arise at the interface between product gas and air. Their amplitudes quickly grow and the initially spherical surface of the product gas evolves into an irregular shape resembling a cauliflower, c.f. figure 13.2. This process is caused by the Rayleigh-Taylor (RT) and Richtmyer-Meshkov (RM) instabilities. Both concern the motion of an interface between two fluids of different densities. The RTI occurs when a fluid of higher density is accelerated into a fluid of lesser density. This situation occurs upon the initial expansion of the product gas. The RMI occurs when an interface between fluids of different densities is impulsively accelerated. Such a situation exists when the detonation front and later the secondary shock pass the surface of the product gas.

For further insight the figure 13.3 (left) shows the evolution of the density ratio and the impedance ratio, respectively, between air and product gas at the fluid interface during the expansion process. Prior to the generation of the primary shock front, the density and the impedance of the ambient air are negligible in comparison to the conditions of the product gas and also the unreacted HE. Upon compression and heating by the primary shock wave however, the impedance of the air

¹ The amplitudes of the secondary wave and the tertiary wave are relatively small; it is therefore difficult to identify their exact positions in the numerical solution. The visible jumps in the shown trajectories result from this difficulty.

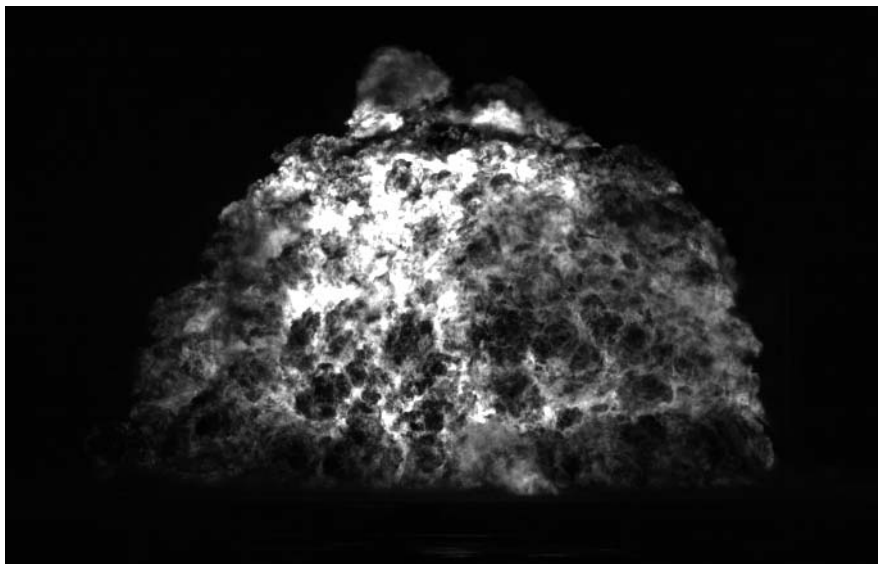


Fig. 13.2 Image obtained with a high speed camera, showing the rough, cauliflower-like surface of the cloud of product gas.

becomes comparable to the condition of the product gas at the fluid interface (ratio value about 0.3). The density ratio however remains small (about 0.1) throughout the expansion process. The assimilation of the impedances is responsible for the generation of the secondary and tertiary waves by refraction. The dissimilarity of the densities enables the enduring affect of the instabilities.

The static pressure and the velocity are constant across the fluid interface at any time. Due to the different densities the dynamic pressure $p_{dyn} = \rho \mathbf{v}^2/2$ however differs on both sides of the interface. Figure 13.3 (right) shows the evolution of the ratio between the dynamic and the static pressure individually for both air and product gas at the interface during the expansion process. It can be recognized that the dynamic pressure in the product gas is clearly larger than the static pressure almost throughout the entire expansion process. In the air, the dynamic pressure at the interface rapidly falls below the static pressure. Pressure measurements, which contain a dynamic part (e.g. the total pressure or the reflected pressure), will provide different values depending on whether the measurement position is inside or outside of the product gas. The irregular surface of the cloud of detonation products thus directly inflicts spatial and temporal fluctuations of such pressure measurements in the near field.

If the detonation occurs close to the ground or near a large solid object, the situation becomes more complex. The primary shock is reflected back into the expanding cloud of product gas; the cloud itself is deflected laterally on the object surface. The

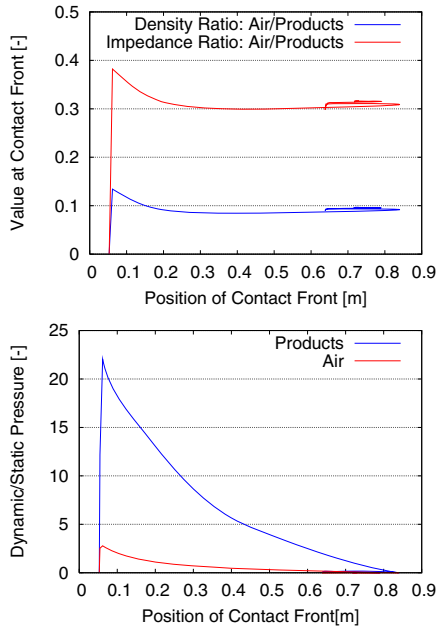


Fig. 13.3 Ratios of density and impedance between air and product gas at the fluid interface during the expansion of the product gas (left); ratio of dynamic pressure to static pressure for air and product gas at the fluid interface during the expansion of the product gas (right) as calculated with APOLLO.

interaction of the reflected shock with the product gas and the primary shock leads to strongly inhomogeneous pressure distributions in distinct regions.

The work described in this paper aims to clarify the processes in the near field of a detonation and their effects on the pressure fields through specifically tailored numerical simulations.

While standard hydro-code simulations provide useful results for most detonation- and blast problems, they are typically performed with moderate spatial resolutions which are not sufficient for an adequate capturing of the instabilities. The capturing of the instabilities is indeed a demanding task, as it requires an accurate multi-fluid algorithm and a high spatial resolution.

An efficient approach for the simulation is the application of a globally adapted grid, which stretches with the expanding blast wave and thus ensures an adequate spatial resolution throughout the expansion process. Furthermore, the relative motion between the fluid and the co-expanding grid becomes small on the average. Thereby the effects of numerical diffusion are decreased by this approach.

The paper describes the numerical method applied in this study and presents the results for two cases: spherical free field detonations of 1kg TNT in air and the detonation of 1 kg TNT at a height of 0.2 m above ground. Since diffusion, heat conduction and viscosity are neglected in the applied physical model, the obtained

results are invariant against changes in length scale. The results can thus be scaled to other charge sizes.

13.2 Physical Models

The conservation equations for time dependent flows of compressible fluids provide the basic model for the subject matter. As a simplifying approximation the fluids are considered inviscid, non-heat conducting and non-diffusive, i.e. the two different fluids (air and product gas) do not mix on the molecular level in this model. Applied to a material volume V_m , the conservation equations can be written as:

$$\begin{aligned} \frac{D}{Dt} \int_{V_m} \mathbf{U} dV &= \oint_{A_m} \mathbf{L} \mathbf{n} dA \\ \mathbf{U} &= (1, \rho, \rho \mathbf{v}, \rho e^{tot})^T, \quad \mathbf{L} = (\mathbf{v}, 0, -p \mathbf{I}, p \mathbf{v})^T, \quad e^{tot} = e + \frac{1}{2} \mathbf{v} \mathbf{v}, \end{aligned} \quad (13.1)$$

where \mathbf{n} is the outward pointing normal vector to the surface A_m of the material volume and I is the unit tensor. The geometric conservation law which describes the rate of change of the volume has been added to the system of equations in a consistent way (first equation in the system). The above equations can be re-formulated for control volumes V , which arbitrarily move relative to both the fluid and laboratory space by using Reynolds transport theorem. The following ALE (Arbitrary Lagrange Euler) formulation of the equations is then obtained:

$$\frac{d}{dt} \int_V \mathbf{U} dV + \oint_A \mathbf{U} (\mathbf{v} - \mathbf{v}_A) \mathbf{n} dA = \oint_{A_m} \mathbf{L} \mathbf{n} dA. \quad (13.2)$$

Here d/dt denotes the time derivative with respect to the control volume V , the surface of which moves with the velocity field \mathbf{v}_A .

For the numerical solution on arbitrarily moving grids the equations have to be extended to mixed material volumes. The method applied here follows a volume-of-fluid methodology in the most general form, where a full set of conservative variables \mathbf{U}_α is assigned to each fluid $\alpha = 1, N$. For a control volume which contains multiple fluids the extended conservation equations are:

$$\frac{d}{dt} \int_V f_\alpha \mathbf{U}_\alpha dV + \oint_A f_\alpha \mathbf{U}_\alpha (\mathbf{v}_\alpha - \mathbf{v}_A) \mathbf{n} dA = \phi_\alpha \oint_{A_m} \mathbf{L} \mathbf{n} dA + \int_{V_m} \mathbf{S}_\alpha dV. \quad (13.3)$$

The factor f_α is a scalar field, which describes the spatial distribution of the fluids. It assumes values of either one or zero depending on the presence ($f_\alpha = 1$) or absence ($f_\alpha = 0$) of fluid α at a point in space. The volume integral over f_α - as in the first term on the left side of (13.3) - thus renders the partial volume V_α of fluid α in the mixed material volume. The surface integral over f_α (as in the second term on the left hand side) renders the partial surface area A_α covered by the fluid.

Note, that the surface integral on the right hand side gives the total rates of change of volume, mass, momentum and energy for the mixed material volume. The factor ϕ_α is the diagonal matrix of the partitioning factors. They control, which fractions of the total rates of change act on the different fluids within the mixed volume. The elements of ϕ_α are therefore defined as:

$$\phi_\alpha = \text{diag} \left(\frac{\delta V_\alpha}{\delta V}, \frac{\delta M_\alpha v_{\alpha,x}}{\delta M v_x}, \dots, \frac{\delta M_\alpha v_{\alpha,z}}{\delta M v_z}, 0, \frac{\delta E_\alpha^{\text{tot}}}{E^{\text{tot}}} \right). \quad (13.4)$$

In the above relation, quantities without subscript α denote the total values of the mixed volume (sum over all fluids). The source term S_α describe the internal transfer and equilibration processes among the fluids within the mixed volume.

By summing the equations over the individual fluids the original conservation equations are recovered, provided that $\sum \phi_\alpha = \mathbf{I}$ and $\sum S_\alpha = 0$. Hence, the above equations inherently obey fluid-wise and global conservation.

The conservation equations are closed by equations of state for each fluid. For the present purpose we use an ideal gas equation of state for air and a JWL equation of state for TNT.

Additional closures are required for the partitioning factors and source terms. As a model for the derivation of the first factor in (13.4) a volume of mixed material under isentropic compression is considered. As we refer to a material volume and no chemical reactions occur between the fluids, the mass fractions $X_\alpha = M_\alpha/M$ are constant. With $Y_\alpha = V_\alpha/V$ denoting volume fractions and $a = (\partial p/\partial \rho)_s^{1/2}$ denoting the sound speed the following relations can be derived:

$$\frac{\delta V_\alpha}{\delta V} = Y_\alpha \frac{\rho a^2}{\rho_\alpha a_\alpha^2} \quad \text{with} \quad a = \left(\sum_\alpha \frac{\rho Y_\alpha}{\rho_\alpha a_\alpha^2} \right)^{-\frac{1}{2}} \quad \text{and} \quad \rho = \sum_\alpha \rho_\alpha Y_\alpha. \quad (13.5)$$

As each fluid in a mixed volume has individual density and energy, the pressures of the fluids will generally differ from each other. Using the above expression, an average pressure can be defined as:

$$p = \sum_\alpha p_\alpha \frac{\delta V_\alpha}{\delta V}. \quad (13.6)$$

By this definition the fluid with the larger compressibility dominates the average pressure more than the stiffer fluid.

The partitioning of the change of momentum is calculated under the assumption that all fluids in the mixed volume experience the same acceleration. This assumption leads to the partitioning factors for momentum components being equal to the mass fractions. The average velocity within the mixed volume is also calculated by mass weighting.

$$\frac{\delta M_\alpha v_{\alpha,i}}{\delta M v_i} = X_\alpha, \quad \mathbf{v} = \sum_\alpha X_\alpha \mathbf{v}_\alpha. \quad (13.7)$$

Finally, the partitioning of the change of total energy of the mixed volume must be derived. As $E_{\alpha}^{tot} = E_{\alpha}^{int} + E_{\alpha}^{kin}$ we first consider the partitioning factors of the kinetic and internal energies separately. Under the assumption that the individual fluid pressures and fluid velocities are about equal to the respective average values, the partitioning factors for the energies become:

$$\frac{\delta E_{\alpha}^{int}}{\delta E^{int}} = \frac{\delta V_{\alpha}}{\delta V}, \quad \frac{\delta E_{\alpha}^{kin}}{\delta E^{kin}} = X_{\alpha}. \quad (13.8)$$

With these factors, the partitioning of the change of total energy can be calculated according to

$$\frac{\delta E_{\alpha}^{tot}}{\delta E^{tot}} = \frac{\delta V_{\alpha}}{\delta V} \frac{dE^{int}}{dE^{tot}} + X_{\alpha} \frac{dE^{kin}}{dE^{tot}}. \quad (13.9)$$

For the evaluation of this expression, the actual change rates of the internal energy and the kinetic energy of the mixed material volume are determined as in the conservation equations:

$$dE^{tot} = - \oint_{A_m} p \mathbf{v} \mathbf{n} dA, \quad dE^{kin} = - \mathbf{v} \oint_{A_m} p \mathbf{I} \mathbf{n} dA, \quad dE^{int} = dE^{tot} - dE^{kin}. \quad (13.10)$$

With these relations the partitioning factors are completely defined. The source terms S_{α} are all zero in the current model with the exception of the momentum exchange between the fluids in a mixed volume. For this part we assume that the velocity component normal to the fluid interface within the volume is equilibrated instantaneously. Research on adequate models for the equilibration processes is continuing and a detailed discussion will therefore be postponed.

13.3 Numerical Methods

For the numerical solution of the extended conservation equations an explicit finite volume scheme on block structured grids is used.

In this scheme the time integration of the discretized equations is performed with an operator split. In a first step a Lagrangian update is calculated (neglect the second term on the left hand side of equation 13.3) and in a subsequent second step the remapping to the arbitrarily moving and deforming grid cell is performed (evaluate the second term on the left hand side of equation 13.3).

In the first step the fluxes \mathbf{L} which depend on the pressure and the material velocity on the cell surfaces are obtained from an approximate solution of a Riemann problem via a HLL-type solver. For the evaluation of the Riemann problem any mixed cells are homogenized by using the average values of pressure, velocity, density and sound speed as defined above.

The second step covers the convection of the fluids relative to the moving and deforming grid. In this step, the fluxes $f_{\alpha} U_{\alpha} (\mathbf{v}_{\alpha} - \mathbf{v}_A)$ are calculated via a donor-cell method. The treatment of mixed cells in the second step requires the determination

of the partial surface areas $A_{\alpha,i}$ covered by the individual fluids for each cell surface i . For this evaluation we use an approximate relation for the fraction g of a cell surface covered by a fluid α :

$$A_{\alpha,i} := \oint_{A_i} f_\alpha dA \approx A_i g(Y_\alpha, \mathbf{n}_i \mathbf{n}_\alpha) \quad \text{with} \quad \mathbf{n}_\alpha = \frac{\text{grad}(Y_\alpha)}{|\text{grad}(Y_\alpha)|}. \quad (13.11)$$

The function g depends on the volume fraction Y_α of fluid α in the donor cell and the orientation of the fluid interface in the donor cell towards the considered cell surface. Assuming a locally planar fluid interface this orientation is expressed through the scalar product $\mathbf{n}_i \mathbf{n}_\alpha$ where \mathbf{n}_i is the normal vector to the cell surface and \mathbf{n}_α the normal vector to the fluid interface. The normal to the fluid interface is obtained from the local gradient of the volume fraction, which is numerically approximated by a central difference. The relation $g(Y_\alpha, \mathbf{n}_i \mathbf{n}_\alpha)$ was determined empirically and is incorporated in the code in tabular form. Figure 13.4 shows an isoline representation of this relation.

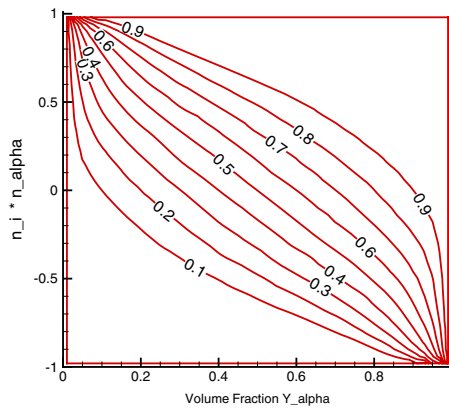


Fig. 13.4 Graphical representation of the preferential transport function.

The properties of the function g can be explained by considering some particular cases. If the gradient vector is pointing normally to a considered cell surface ($\mathbf{n}_i \mathbf{n}_\alpha = 1$), the covered fraction of the cell surface is one; if the gradient is pointing in opposite direction ($\mathbf{n}_i \mathbf{n}_\alpha = -1$) the covered fraction is zero. In case the gradient is parallel to a cell surface ($\mathbf{n}_i \mathbf{n}_\alpha = 0$), the covered area fraction is directly proportional to the volume fraction. The function establishes what is called a preferential or non-diffusive transport.

Both flux steps, the Lagrangian and the remap step, are carried out with higher order accuracy by using a MUSCL-type scheme, which is here based on a tri-linear reconstruction of the conservative variables. Within mixed cells, the order of ac-

curacy is reduced to one. Finally, it should be mentioned, that the actual process of detonation is modeled via a programmed burn algorithm, which adds a specific amount of internal energy to the unburned TNT material as a function of space, time and prescribed detonation velocity. This is a standard procedure as applied in most hydro-codes.

13.4 Computational Methodology

The numerical method described above is implemented in the APOLLO flow solver of the institute. This code is parallelized by domain decomposition and permits simulations with large grids on a Linux cluster. For the presented 3D case we used up to 65 processors and a total grid size of about 18 million cells. The 2D cases were run on 25 processors with total grid size up to about 1 million cells.

In all presented cases the detonation of 1 kg TNT (a sphere with radius 5.27 cm) in air at standard conditions was studied. The spherical body of TNT was ignited at its center at $t=0$.

To obtain a reference solution with perfectly spherical symmetry a 1D simulation with very high resolution was carried out. The same perfectly symmetrical 1D solution at the time immediately after the detonation front reaches the surface of the TNT sphere ($t \approx 8 \mu\text{s}$) was also used as initial condition for the 2D and 3D simulations.

For the investigated free field detonation, the initial dimensions of the computational grid were $x, y \in [0, 0.2 \text{ m}]$ in the 2D case and $x, y, z \in [0, 0.2 \text{ m}]$ in the 3D case, with the center of explosion at $x=y=z=0$, such that a 90 degree section of the initially spherical configuration is considered in the simulation. The 2D grid was wedge shaped with an opening angle of 10 degrees along both x-axis and y-axis and had one cell in thickness-direction. The initial resolution of the grids was varied in different simulations between 0.8 mm and 0.2 mm for the 2D cases. The 3D case was run with an initial resolution of 0.8 mm only. In the course of the computation the grid is stretched according to a prescribed velocity-time profile, such that the blast front is contained within the computational domain up to a radius of about 2 m reached at about $t=2 \text{ ms}$. The grid motion is then stopped and the blast front leaves the domain through extrapolation boundary conditions. Note that the cloud of detonation gases has reached its maximum expansion in the free field case at a time of about $t=1 \text{ ms}$.

For the simulation of the detonation above ground the initial grid dimension was $x \in [0, 0.3 \text{ m}]$ (radial direction) and $y \in [0, 0.4 \text{ m}]$ (height direction). Here only a 2D simulation with axial symmetry was performed. The center of explosion was located at $x=0 \text{ m}$ and $y=0.2 \text{ m}$. The initial grid resolution was 0.4 mm. The grid is stretched within 2 ms to dimensions $x \in [0, 2.6 \text{ m}]$, $y \in [0, 3.5 \text{ m}]$.

As a stimulus for the onset of the instabilities a pre-defined perturbation field was overlaid onto the initial perfectly symmetrical velocity field. This perturbation field was defined by

$$v(r, \beta, \delta) = v(r) (1 + \xi f(\beta, \delta) d(\beta, \delta)), \quad (13.12)$$

where β and δ are angular coordinates with respect to the center of the charge and $v(r)$ is the radial velocity component. The function $f \in [-1, 1]$ describes a sinusoidal distribution with the smallest possible wavelength that can be resolved on the given grid (four cells per period). In the 3D case the function f describes an even distribution of dimples (similar to a golf ball), again with the smallest possible wavelength for the given grid. The function $d \in [0, 1]$ describes a smooth angular variation of the amplitudes, such that the overlaid perturbations become small in the x, y and z -direction through the center of the charge and large in the diagonal direction. The motivation is explained in the following. The instabilities would in fact also occur without the overlaid perturbations, as the inherent perturbations resulting from the Cartesian grid suffice for their triggering. However, the grid-inherent perturbations exhibit an anisotropic behavior, as the sphere surface has different orientations towards the cell surfaces at different positions in the grid. This leads to the undesired effect that the instabilities start to grow at different rates in different directions from the center of the sphere: in the direction where the fluid interface is parallel to cell surfaces the initiation is faster than in the diagonal direction. The additionally overlaid perturbations were intended to overrule this effect. A remaining anisotropy however can especially be recognized in the simulations for the detonation above ground.

13.5 Results 1D, 2D and 3D Free Field

The following figure 13.5 shows a comparison of blast parameters obtained from 1D simulations with the empirical fits given in [1]. The comparison documents the basic accuracy of the model. The figure 13.1 shown in the introduction has also been obtained from the same 1D solution.

Figure 13.6 shows density fields obtained from the 2D computations with different resolutions. Overlaid is the contour of the fluid interfaces. The plots were taken at times of about $t=0.92$ ms, which corresponds to the time when the cloud of detonation gas first reaches its maximum expansion. Figure 13.7 shows an image from the 3D computation taken at the same time. For comparison with the 2D results two diagonal planar slices were extracted from the 3D fields.

It can be seen that the protuberances are less regular in the 3D calculation than in the 2D calculation with identical resolution. Furthermore it can be recognized in the 2D simulations, that the lengths of the protuberances become smaller as the resolution is increased, while at the same time their number increases. In figure 13.8 a comparison of the calculated time dependent volume of product gas is shown in terms of the time dependent radius of an equivalent sphere. It can be seen, that the oscillation of the cloud volume is less pronounced in the 2D and 3D cases than in the 1D reference computation. With increasing resolution however, the amplitude of oscillation increases slightly towards the 1D solution.

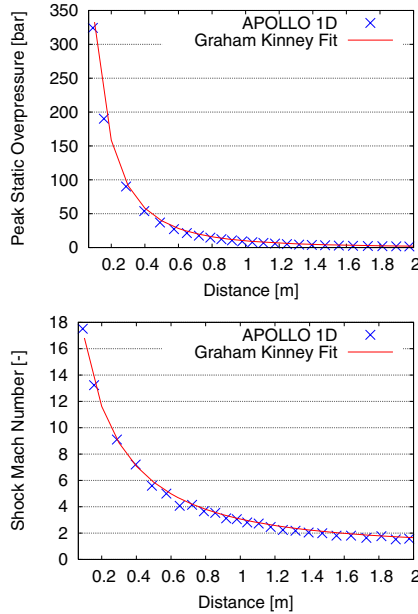


Fig. 13.5 Comparison of calculated blast parameters (1D spherical) with empirical fits from [1].

In figure 13.9 and 13.10 some selected time curves of the static and total pressure at different positions are presented for the 2D simulations with the highest initial resolution (0.2mm). The curves in each plot were taken at the same radius but at different angular positions, which were selected arbitrarily. Notable deviations from spherical symmetry due to the fluid dynamic instability are recognized at the fluid interface and also at the blast front.

Figures 13.11 and 13.12 provide an overview of the variations of static and total overpressure amplitudes and impulses obtained from the simulations with different resolutions. These results can be summarized as follows:

- The static overpressure amplitudes exhibit significant variations in a zone of scaled distances between about 0.2 and 0.7 $\text{m/kg}^{1/3}$, with maximum variations of about $\pm 10\%$ to $\pm 15\%$ at a scaled distance of about 0.4 - 0.5 $\text{m/kg}^{1/3}$. The variation grows with increasing grid resolution.
- The total overpressure amplitudes show similar variations in the same range of scaled distances. The variation however decreases with increasing grid resolution.
- The impulses exhibit a corresponding tendency; the maximum variations reach about 7% - 8%.

13.6 Results 2D Above-Ground Detonation

For the above ground detonation of the spherical charge the blast field can be subdivided into two distinct zones with time dependent extent: a zone above and a zone below the wave, which is reflected off the ground. In the first zone undisturbed free field conditions prevail and thus the findings of the preceding section apply to this zone. The second zone would ideally (if no instabilities would occur) be axially symmetric. An analysis of the effects of the instabilities will thus require 3D simulations. The 2D axially symmetric simulations carried out so far thus focus only on the effects of the reflected wave on the blast field.

Figure 13.13 shows some selected total pressure fields which illustrated the evolution of the blast field. In these plots one can also observe the numerically caused anisotropic initiation and growth of the instabilities, which could for this calculation not be prevented by the overlaid initial perturbations.

Some details of the occurring wave interactions are explained with figure 13.14. In a central zone the reflected wave propagates upward against the flow of expanding product gas; this part of the wave (A) is almost planar and parallel to the ground. In the zone of shock heated air between the primary blast front and the product gas the wave velocity is larger than in the product gas. The part (B) of the reflected wave thus runs upward with a higher velocity than part (A) of the reflected wave. The wave (B) is refracted at both the blast front and the fluid interface. At the intersection points of wave (B) with these surfaces new waves (C,E) are created. The superposition with the primary blast front leads to an outward inclination of the primary blast front (C). This again leads to a further reflection on the ground, (D). Similarly, the wave (E) interacts with the part (A) of the reflected wave.

In these zones of wave interactions and refractions a spatially and timely strongly inhomogeneous pressure distribution already prevails. The fluid dynamic instabilities lead to additional fluctuations.

Figure 13.13 provides an overview of the spatial distribution of blast parameters. Displayed are the maximum amplitudes and impulses of the static and the total overpressure as occur in the simulated time interval between 0 and 4 ms. Note that the displayed range of values is truncated at the maximum value: white regions thus indicate any values above the referenced value. The plots clearly indicate zones where the superposition of the primary and the reflected wave lead to increased pressure amplitudes and impulses. Especially at the boundaries of these regions large gradients of these blast parameters occur. Measurements taken in the vicinity of these boundaries will thus sensitively depend on the position. Furthermore, the zone boundaries can be affected by the fluid dynamic instabilities. Repeatability of measurements can be very poor in the vicinity of these boundaries.

13.7 Conclusions

The presented simulations indicate that the fluid dynamic instabilities can indeed lead to fluctuations of the pressure in the near field of a detonation. For the investigated case of a 1 kg TNT detonation in free field a zone extending from 0.2 to about 0.7 m was identified where significant fluctuations of both the local peak values and the impulses of the total pressure and the static pressure occur. The extent of this zone obeys the usual scaling laws. At positions beyond the specified zone pressure fluctuations might still occur, but do not affect the peak values or impulses any more.

The evolution of the unstable fluid interface shows a fractal behavior, with a large spectrum of length scales. The simulations therefore depend strongly on the grid resolution such that convergence is difficult both to measure and to achieve. For this reason the reliability of the results concerning the strength of the fluctuations is still questionable. Further investigations on the grid convergence and the influence of distinct modeling parameters are necessary to clarify this aspect.

The blast field generated by a detonation above ground is dominated by the reflected wave and its interaction with the expanding product gas and the primary blast front. Due to these interactions distinct zones exist in the spatial distributions of peak pressures and impulses. The position and extent of these zones could be identified by the performed 2D simulations. At the boundaries of these zones very strong gradients of the blast parameters occur. In the vicinity of these boundaries the values of the blast parameters therefore depend sensitively on positions and repeatability of measurements might thus be very poor. In addition, the position of these zones might be affected by the fluid dynamic instabilities. In order to clarify this aspect 3D simulations are necessary, which have not been carried out yet.

References

1. Kinney, G. F., Graham, K.J.E.. Explosive Shocks in Air, Springer (1985)

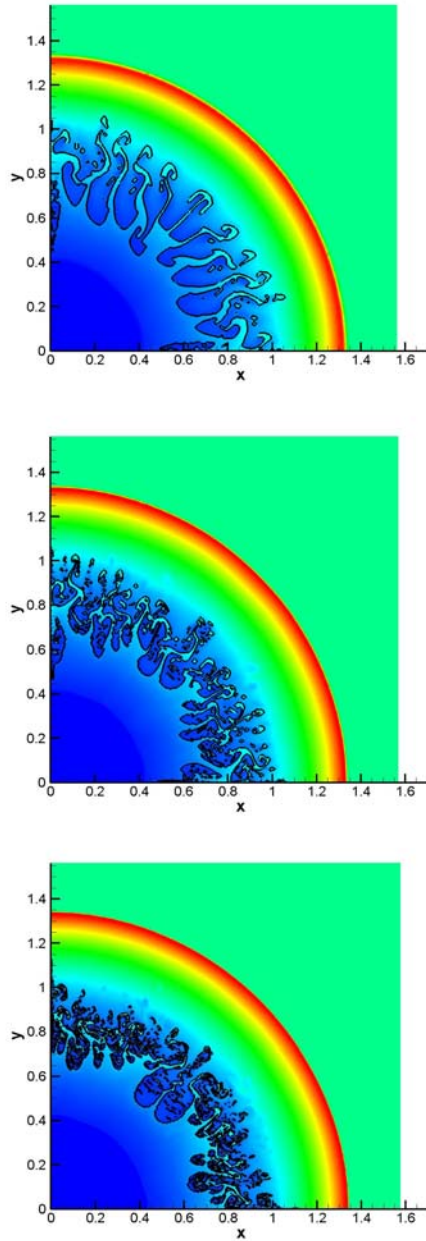


Fig. 13.6 Density fields from 2D simulations with initial resolutions of 0.8 mm, 0.4 mm and 0.2 mm (top to bottom) at time $t = 0.92$ ms.

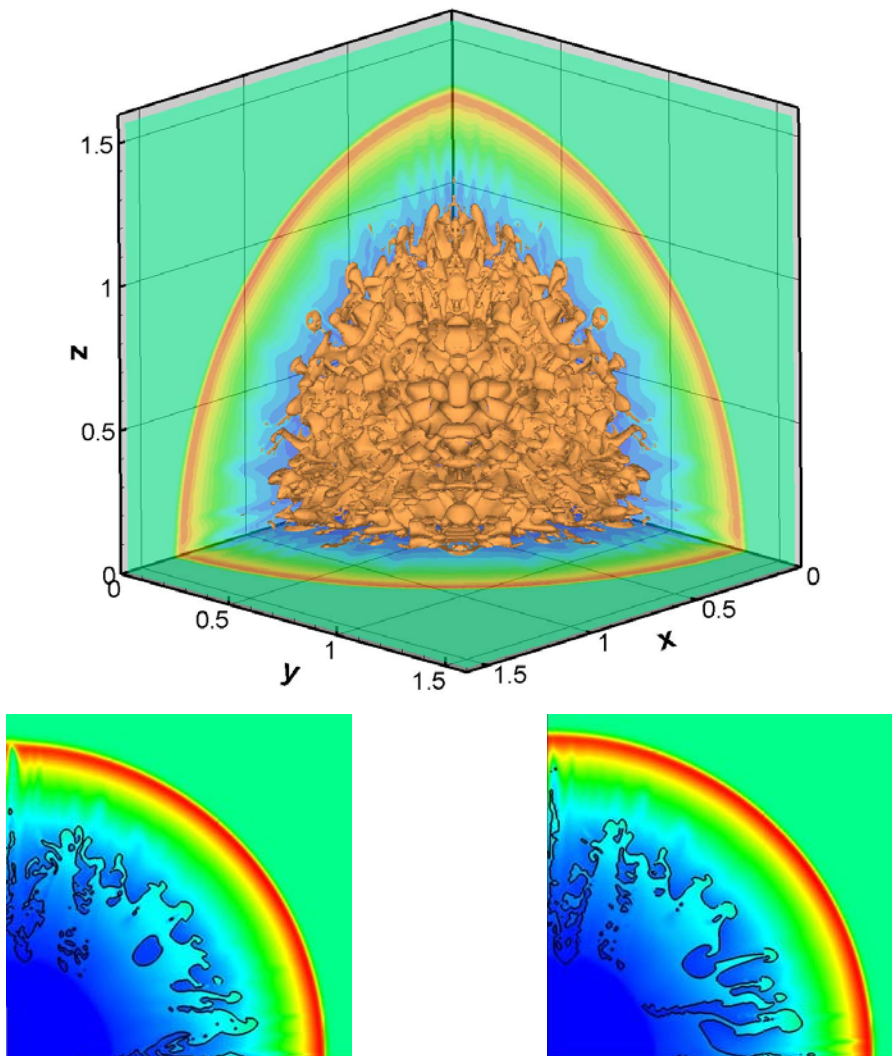


Fig. 13.7 Image obtained from the 3D simulation with initial resolution 0.8 mm at time 0.92 ms (top) and two diagonal slices extracted from the same 3D simulation - compare with 2D result with same resolution (top of figure 14.7).

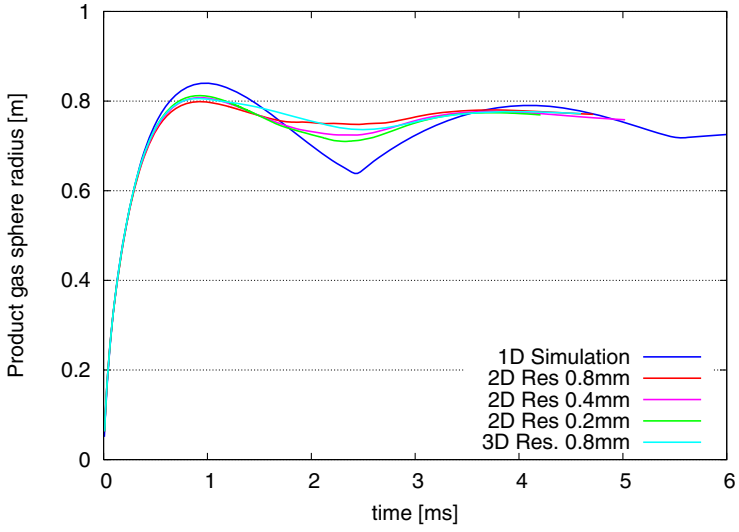


Fig. 13.8 Radius of the (equivalent) sphere of detonation gases from 1D, 2D and 3D simulations.

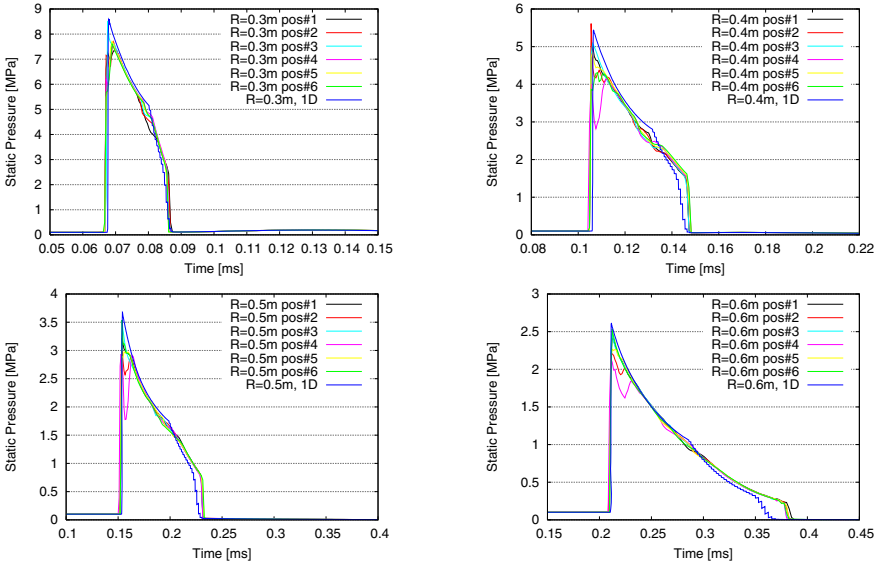


Fig. 13.9 Selected records of static pressures at different distances as obtained by 2D simulation with initial resolution of 0.2 mm.

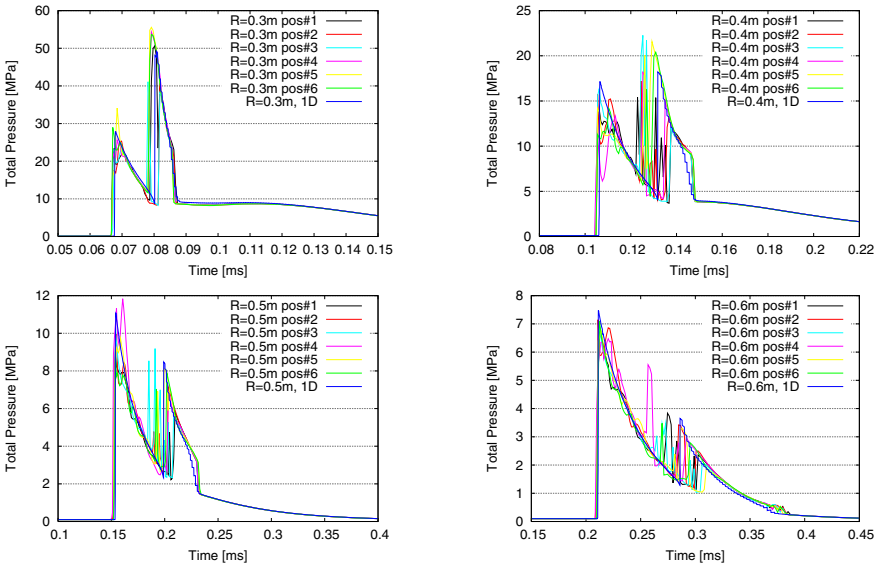


Fig. 13.10 Selected records of total pressures at different distances as obtained by 2D simulation with initial resolution of 0.2 mm.

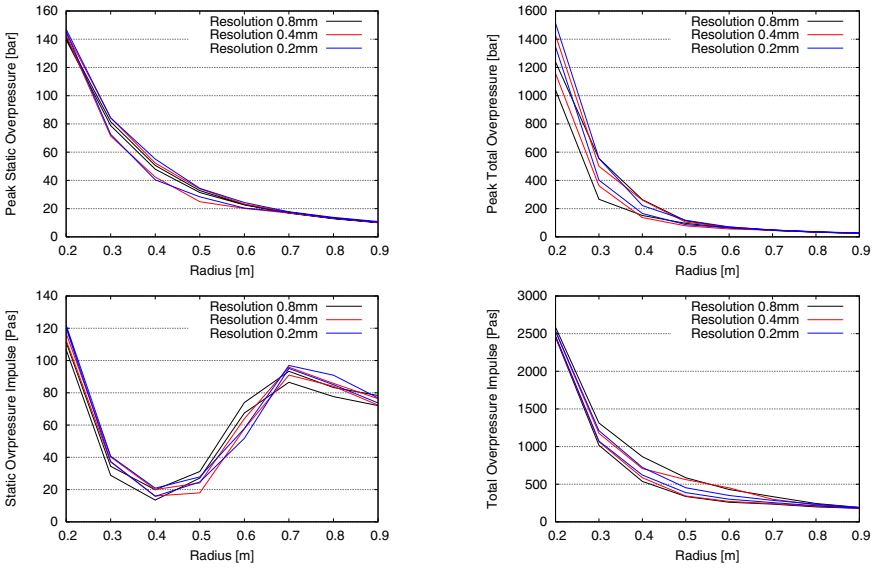


Fig. 13.11 Upper and lower bounds of static and total overpressure amplitudes and impulses obtained in the 2D simulations with different grid resolutions.

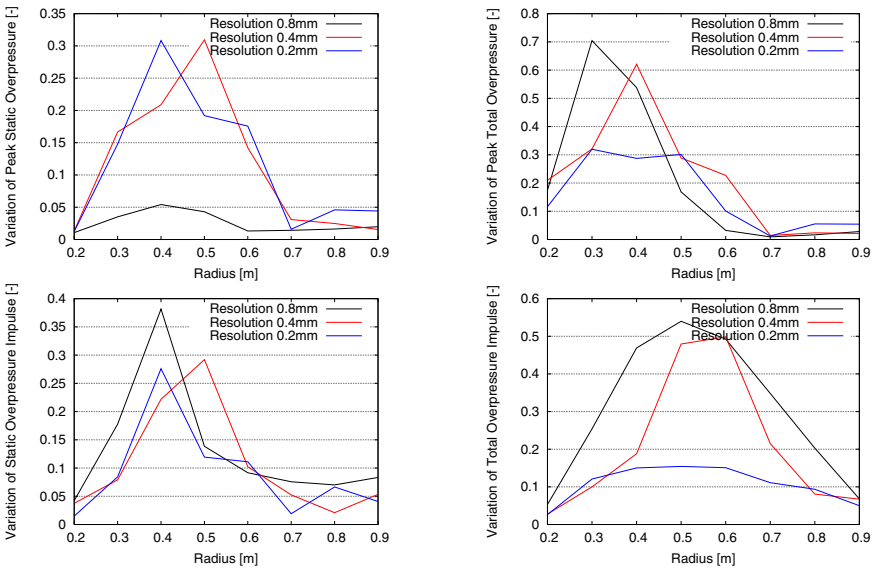


Fig. 13.12 Variations (upper minus lower bound divided by average) of static and total overpressure amplitudes and impulses obtained in the 2D simulations with different grid resolutions.

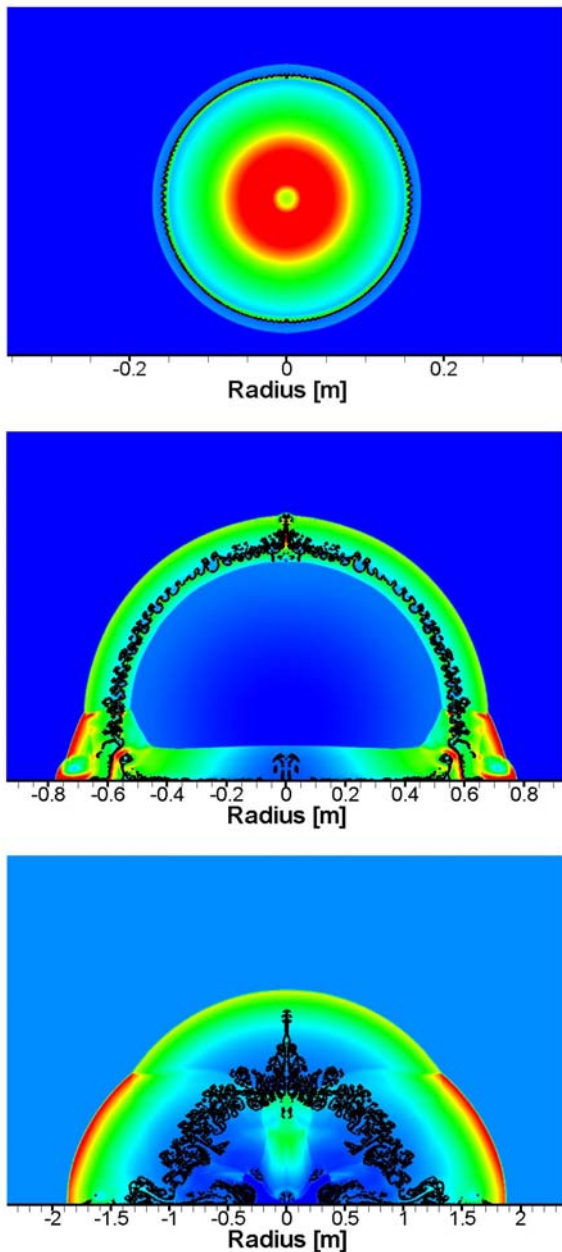


Fig. 13.13 Sequence of total pressure fields for the detonation of 1kg TNT at 0.2 m (center of charge) above ground. Times from top to bottom: 0.03 ms, 0.26 ms, 1.3 ms

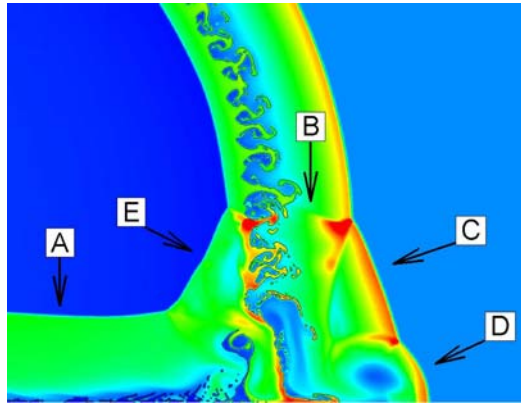


Fig. 13.14 Details of the wave interaction processes as explained in the text.

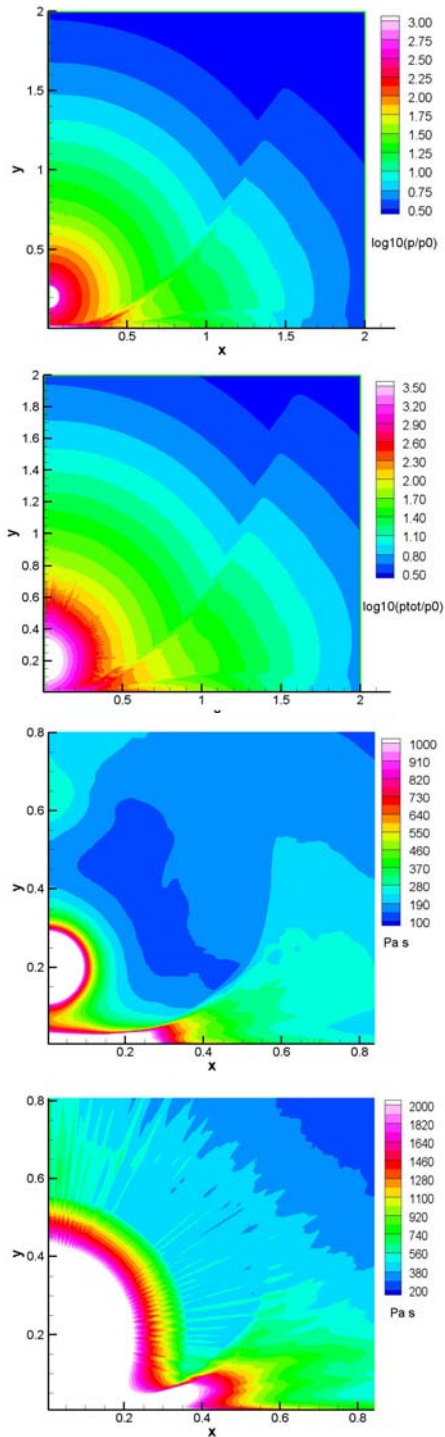


Fig. 13.15 Spatial distribution of amplitudes (above) and impulses (below) of static (left) and total overpressures (right) as recorded in the simulations.

Chapter 14

Numerical Simulation of Muzzle Exit and Separation Process for Sabot–Guided Projectiles at $M > 1$

Jörn van Keuk and Arno Klomfass

Abstract Coupled fluid–structure simulations of muzzle exit and separation process for sabot–guided sub–caliber projectiles in supersonic flight are presented. In order to guarantee a separation without significant perturbations for the projectile aspects of both aerodynamics and structure loading have to be considered. Such simulations require sophisticated methods for fluid–structure interaction. A particular challenge results from the significant relative motion of sabot, projectile and muzzle. A two stage strategy based on a switch from an earth–based to a moving coordinate system is proposed. By this means, an investigation of the complete physical process for the separation including interactions with the barrel and the high pressure gas is possible. The AUTODYN software extended by in–house developed user–subroutines is applied for the simulations. Results for high–strength sabots of caliber 40 mm and different muzzle velocities are presented and compared with corresponding experimental data.

14.1 Introduction

The muzzle exit and separation process of sabot–guided projectiles include several physical processes that influence the exterior ballistic flight of the projectile downstream from the muzzle [2]. Barrel oscillations can cause non–symmetric interactions between the barrel and the projectile. Additionally, the high–pressure gas leaves the muzzle exit at a high Mach number leading to a significant incident flow from reverse for a short time. Both effects can perturb the flight trajectory due to

Jörn van Keuk

Ernst-Mach-Institute, Eckerstr. 4, 79104 Freiburg, Germany, e-mail: keuk@emi.fhg.de

Arno Klomfass

Ernst-Mach-Institute, Eckerstr. 4, 79104 Freiburg, Germany, e-mail: klomfass@emi.fhg.de

asymmetries. Finally, for sub-caliber projectiles the separation process from the sabot starts directly behind the muzzle exit.

In order to guarantee a muzzle exit and separation without significant perturbations of the projectile the sabot has to be designed appropriately regarding both aspects of aerodynamics and structural loading. Additionally, lowest possible weight is desired for the sabot since it represents a parasitic mass. Therefore, the applicability of light-weighted materials e.g. Magnesium or Magnesium-Lithium alloys is subject of recent research work in this field [3, 4].

14.2 Technical Specifications / Experimental Setup

The applicability of light-weighted materials for sabots of sub-caliber projectiles is investigated experimentally at the German-French Research Institute [3, 4]. The experimental configuration consists of a long rod made of tungsten surrounded by a 4-part-sabot for the guidance inside the barrel (see Fig. 14.1).



Fig. 14.1 Penetrator / sabot model [3, 4].

Different materials e.g. Magnesium, Magnesium-Lithium alloys, are investigated for the sabot. The characteristic dimensions of the configuration and the experimental conditions are listed in the following tables (see Tab.14.1,14.2).

Table 14.1 Technical specifications for the projectile / sabot configuration

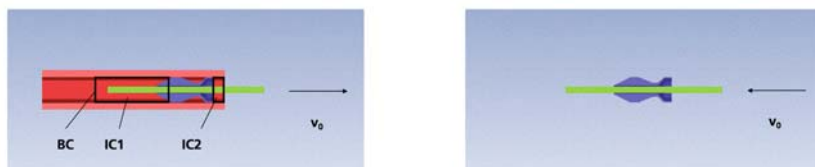
Projectile caliber	10 mm
Projectile length	200 mm
Sabot caliber	40 mm

Table 14.2 Experimental Conditions [3, 4]

	Shot A [3]	Shot B [4]
Sabot material density [g/cm^3]	1.78 (Mg)	1.52 (Mg Al3 Li9)
Propellant Mass [kg]	0.38	0.4
Max. Gas Pressure [MPa]	341.2	380.3
Muzzle Velocity [m/s]	1510.0	1633.0
Acceleration [m/s^2]	794008.0	897000.0

14.3 Numerical Solution Method

The numerical solution method presented in this paper is based on a switch from an earth-based coordinate system to a moving coordinate system at a distinct time during the solution process. Initially, the physical phenomena near the muzzle exit are simulated using an earth-based coordinate system (Phase A). By this means, the interactions between the barrel and the projectile as well as the incident flow from reverse can be explicitly simulated. At a sufficient distance downstream from the barrel the computation is stopped and the coordinate system is switched. Hence, the second part of the simulation can be reduced to the close vicinity of the projectile and the sabot (Phase B). Following this approach the required computational cost can be reduced to a reasonable amount and nevertheless all essential physical effects of the process can be captured. For a schematic of this method see Fig. 14.2.

**Fig. 14.2** Numerical solution method (switch of coordinate system).

For the simulations shown in this paper the commercial code AUTODYN [1] was used as basis. The method proposed demands an explicit modification of the standard solution procedure in this code to allow the switch of the coordinate system. This was done via appropriate, in-house developed user-subroutines.

Since the gas modelling in AUTODYN is confined to air as a perfect gas, it is not possible to do interior ballistics computations with this code. For that reason the computation is started inside the barrel close to the muzzle exit. The effects of

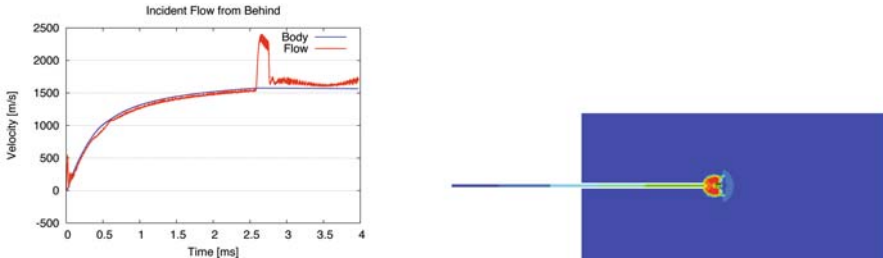


Fig. 14.3 Axis-symmetric computation of the firing process for a cylindrical body.

the high-pressure gas as well as the compressed air directly ahead of the projectile are considered via appropriate initial and boundary conditions (IC1, IC2, BC in Fig. 14.2).

In order to obtain proper data for the initial and boundary conditions a preliminary investigation was carried out for the firing process of a simple, cylindrical body. Here, the AUTODYN code was used in its 2D axis-symmetric option. The results for the flow phenomena at the muzzle exit are shown in Fig. 14.3. Additionally, a comparison of the body velocity and the flow velocity close to the back of the projectile (distance 10mm) is plotted. Both figures show the significant incident flow from reverse for $\sim 0.2\text{ms}$ that was already mentioned above.

14.4 Simulation Results / Comparison with Experiments

Numerical simulations of muzzle exit and separation process for a sabot-guided penetrator were carried out for different sabot materials and firing conditions using the method described above. Corresponding technical specifications are given in Tab.14.1 and 14.2. The experimental results obtained at the German-French Research Institute [3, 4] were used for validation purposes.

The sequence of the proposed method in principle can be understood from Fig. 14.4. On the left hand side of the figure a snapshot of the separation process and the computed velocity field including the muzzle exit and high pressure gas from the earth-based view (Phase A) is plotted. The right hand side of the figure shows the phenomena for a later time step after the coordinate switch to a moving observer.

Fig. 14.5-14.7 show a comparison of computed results for the relative position of penetrator and sabot with photographs from the experiments for Shot B. The camera positions downstream from the barrel in the experiment define distinct time levels in the simulation after the coordinate switch. The overall agreement of simulation and experiment is satisfactory for the method proposed in this work (simulation of phases A and B). The kinematics of separation was qualitative correctly predicted

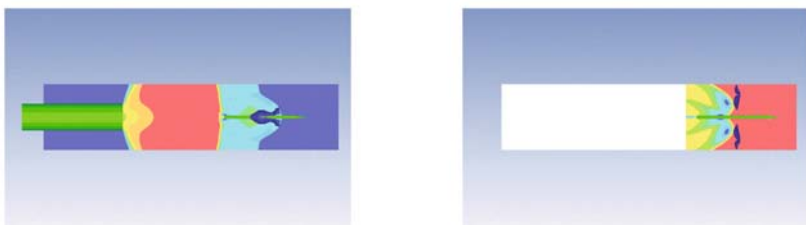


Fig. 14.4 Computed velocity fields during phases A and B.

and even the time dependence of the process is acceptably captured. For the purpose of comparison additional simulations were carried out using a simpler approach of computing only Phase B. The muzzle exit was neglected in these simulations and an instantaneous inflow for long rod and sabot was chosen as the initial condition in this case. The consequence is a worse resolution of the temporal behavior of the process due to the neglect of the physical effects at the muzzle exit as can be seen in Fig. 14.6.

In Fig. 14.8-14.10 the corresponding comparison for Shot A is depicted. The qualitative agreement concerning the kinematics of separation is again satisfactory, but the temporal behavior of the process shows stronger discrepancies, whereby the proposed method of computing Phase A and B again performs better. A possible reason is the penetrator pike in this case that was not taken into account in the simulations.

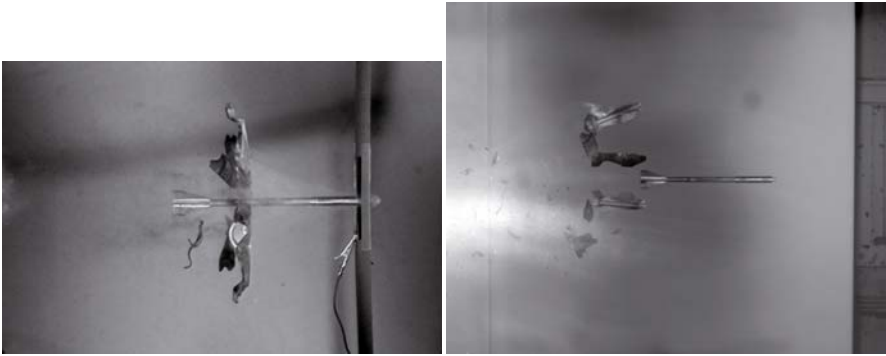


Fig. 14.5 Photographs from the experiments for Shot B [4].



Fig. 14.6 Numerical simulation of phase B for Shot B [5].



Fig. 14.7 Numerical simulation of phase A and B for Shot B [5].

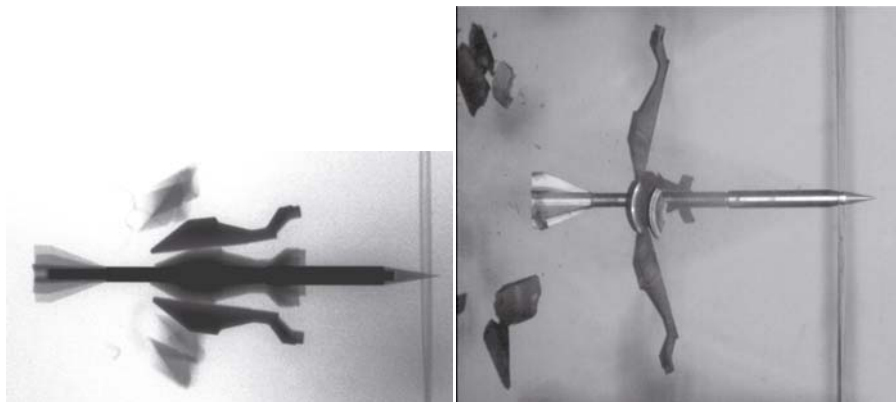


Fig. 14.8 Photographs from the experiments for Shot A [3].

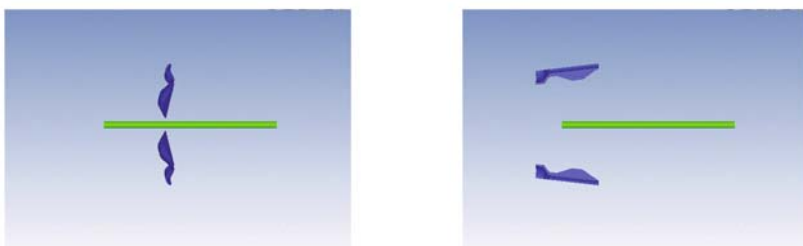


Fig. 14.9 Numerical simulation of phase B for Shot A [5].



Fig. 14.10 Numerical simulation of phase A and B for Shot A [5].

Finally, in Fig. 14.11 the computed Mises stresses for two target points located at the "bottleneck" of the sabot are shown. Again, the importance of considering the muzzle exit is obvious, that leads to significantly stronger mechanical loadings during the first – critical – part of the process. These higher stresses are caused by the strong incident flow from reverse that cannot be captured by the simpler approach of only simulating Phase B.

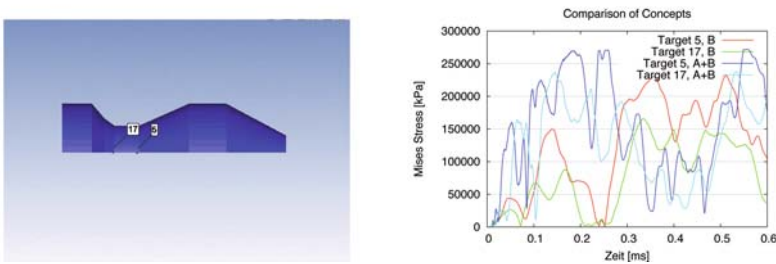


Fig. 14.11 Comparison of computed Mises stresses for different concepts.

14.5 Conclusions / Future Work

Numerical simulations of muzzle exit and separation process for sabot-guided projectiles have been presented. A two stage strategy based on a switch of the coordinate system was proposed as solution procedure. Initially, an earth-based coordinate system is preferred in order to resolve the complicated flow situation and interactions at the muzzle exit. At a sufficient distance downstream from the barrel the computation is stopped and restarted using a moving coordinate system.

Results were compared to corresponding experimental investigations showing an overall good agreement regarding the kinematics of separation. The necessity of explicitly taking into account physical effects of the muzzle exit was demonstrated.

As an essential result of the simulations penetrator / sabot undergo a significant inflow from reverse directly behind the muzzle exit. This situation leads to a critical mechanical loading for the sabot structure during this phase.

Subject of future work will be an improvement of initial and boundary conditions in order to increase the temporal accuracy of the numerical results. Additionally, the sensitivity of the results with respect to the sabot material model will be investigated.

References

1. AUTODYNTM: Interactive Non-Linear Dynamic Analysis Software. Theory Manual, Revision 4.3, Century Dynamics Inc.
2. Klingenberg, G., Heimerl, J. M.: Gun Muzzle Blast and Flash. Progress in Astronautics and Aeronautics. **139** (1991)
3. Schirm, V., Lach, E.: Konstruktion und Erprobung eines Treibkäfigs aus einem hochfesten Werkstoff auf Magnesium-Basis. ISL-Report RV 223/2005, German-French Research Institute (2005)
4. Schirm, V., Lach, E.: Erprobung einer hochfesten Magnesium-Lithium-Aluminium-Legierung als Werkstoff für einen Treibkäfig im Kaliber 40 mm. ISL-Report RV 239/2008, German-French Research Institute (2008)
5. van Keuk, J., Klomfass, A.: Numerical Simulation of Muzzle Exit and Separation Process for Sabot-Guided Projectiles at $M > 1$. Proceedings 24th International Symposium on Ballistics. New Orleans (2008)

Chapter 15

Numerical Analysis of the Supercavitating Flow about blunt Bodies

Arno Klomfass and Manfred Salk

Abstract The paper presents a physical model and a numerical method which are suitable for a detailed analysis of compressible supercavitating flows. The numerical method solves a 3D finite-volume approximation of the conservation equations for an inviscid fluid with two phases in local equilibrium using a two-step explicit time integration scheme. The applied equation of state is based upon the IAPWS formulation which is incorporated in the solver in tabular form. The validity of the method and the model are evaluated by comparison with available experimental data for cavity shapes and drag coefficients of blunt bodies. Features of steady state flow fields are discussed, with special respect to the effects of compressibility.

15.1 Introduction

The flow field about a body travelling with high velocity in water is dominated by a phase transition from liquid to gaseous state. This phase transition occurs when the fluid pressure is locally reduced to the saturation pressure. At 20°C the saturation pressure of water is about 20 mbar such that a phase transition in a flow with that temperature and a free stream static pressure of 1 bar can occur at flow velocities above about 10 m/s. At such low velocities the phase transition exhibits itself in the appearance of small vapor bubbles in the low pressure region of the flow field. At significantly higher velocities a closed gaseous cavity is formed, into which the body -apart from its bow- may be fully embedded, c.f. fig.15.1. This regime, called supercavitation, is of specific interest for high speed underwater body motion, as the viscous drag becomes negligible within the cavity. General aspects of interest

Arno Klomfass
Fraunhofer EMI, Eckerstr.4, 79104 Freiburg, Germany, e-mail: klomfass@emi.fhg.de

Manfred Salk
Fraunhofer EMI, Eckerstr.4, 79104 Freiburg, Germany, e-mail: salk@emi.fhg.de

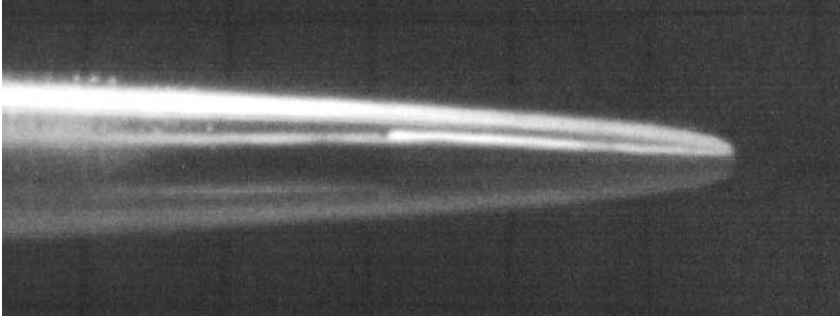


Fig. 15.1 Slender body in supercavitating flight, experiment EMI, 2004

are the forces and moments that act on a body in supercavitating flow, the shapes of cavities, and the strength of the shock waves generated in the water. Numerous investigations were carried out with respect to these issues over the past decades. Most of them focused on steady state flows over discs and cones. For the cavity shape behind a disc Savchenko proposed the following relations, see e.g. [2]:

$$\begin{aligned}
 R_c(x)/R_n &= \sqrt{3.659 + 0.847(x/R_n - 2) - 0.23\sigma(x/R_n - 2)^2}, & x/R_n > 2.0 \\
 R_c(x)/R_n &= (1 + 3x/R_n)^{1/3}, & x/R_n < 2.
 \end{aligned}
 \tag{15.1}$$

where R_n is the radius of the disc, and $\sigma = 2(p_\infty - p_c)/\rho v_\infty^2$ is the cavitation number, which relates the difference of free stream ambient pressure and pressure inside the cavity to the dynamic pressure of the flow. On the basis of the potential flow theory, Brennen, [3], as well as Garabedian, c.f. [2], obtained numerical solutions for the cavity shapes and the drag coefficients for blunt bodies in incompressible supercavitating flows. The values typically reported in literature for discs and spheres at $\sigma \rightarrow 0$ are 0.82 and 0.32, respectively. The influence of compressibility is rarely addressed in literature as water with an ambient sound speed of about 1450 m/s may well be assumed incompressible up to velocities of several hundred m/s. Current theoretical and numerical treatment of supercavitation is mainly based on the full set of conservation equations. There, models of local thermodynamic equilibrium and thermodynamic non-equilibrium can be distinguished. Under the assumption of local equilibrium a unique two-phase equation of state (EOS) suffices for the description of the two-phase fluid. A variety of approximations and combinations of liquid state EOS and gaseous state EOS are found in literature for this case. In the non-equilibrium case the two phases are treated as individual fluids that are governed through finite rate evaporation and condensation processes.

15.2 Physical Models

15.2.1 Conservation Equations

The physical model applied in this work is the full set of conservation equations for an inviscid, non heat-conducting, compressible fluid in local thermodynamic equilibrium. The effects of viscosity are small for the considered high velocity flows over blunt bodies: with an ambient viscosity of 0.001 kg/ms Reynolds numbers are typically in excess of 10^6 for the considered flows. Furthermore, due to the small compressibility of the liquid the heating is moderate even at high velocities and the effects of heat-conduction are thus negligible. The EoS, $p = p(\rho, e)$, is thus the only fluid specific model required for the closure of the system of equations.

For the numerical solution the conservation equations are here applied in integral form to an arbitrarily moving and deforming control volume. This so-called ALE-formulation allows to solve the equations on time dependent grids and thus to simulate flows around accelerated bodies. It also forms a suitable basis for the two-step integration scheme described in section 15.3.

$$\frac{d}{dt} \int_V \mathbf{U} dV = \oint_S (\mathbf{L} + \mathbf{K}) \mathbf{n} dS, \quad (15.2)$$

$$\mathbf{U} = (1, \rho, \rho \mathbf{v}, \rho e^{tot})^T, \quad \mathbf{L} = (\mathbf{v}, 0, -p\mathbf{I}, -p\mathbf{v})^T, \quad \mathbf{K} = \mathbf{U}(\mathbf{w} - \mathbf{v}).$$

In the above equations \mathbf{U} contains the set of conservative variables, where \mathbf{v} denotes the material velocity. The column matrices \mathbf{L} and \mathbf{K} denote the Lagrangian and the convective flux densities, respectively, that act on the control volume's surface S , with outward directed normal unit vector \mathbf{n} . The prescribed velocity field \mathbf{w} governs the time dependent motion of the control volume surface (i.e. the grid motion in the numerical integration). For a consistent numerical approximation, the conservation equations for mass, momentum and density are augmented by the so-called geometrical conservation law for the size of the control volume, which forms the first of the equations comprised in the above system (15.2). The system is subject to boundary and initial conditions.

15.2.2 Equation of State

The EoS of a pure substance covers the three phases solid, liquid and gas. The different phases can in certain regions coexist, as e.g. within the vapor region (mixture of liquid and gas). An equation of state, that covers the liquid-, the gas- and the vapor regions must be non-linear in density or volume, as these quantities attain non-unique values within the vapor region (for a given pressure and temperature below the critical point any density between the corresponding boiling and condensation points can exist in thermodynamic equilibrium). A simple model pertaining

to this feature is the van der Waals equation of state, which is however too simple for use in quantitative investigations. On the other side numerous elaborate models with high accuracy exist, that are either computationally too expensive for usage in CFD or simply have the wrong set of independent variables (e.g. p,T) that makes them unsuitable for CFD calculations based on conservative variables.

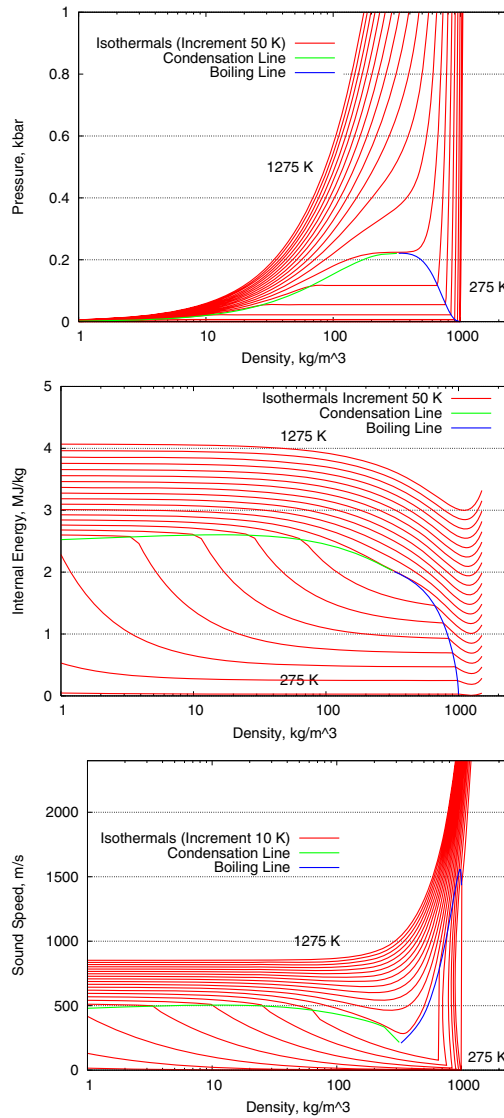


Fig. 15.2 Isotherms of pressure, specific energy and sound speed of pure water according to the IAPWS model

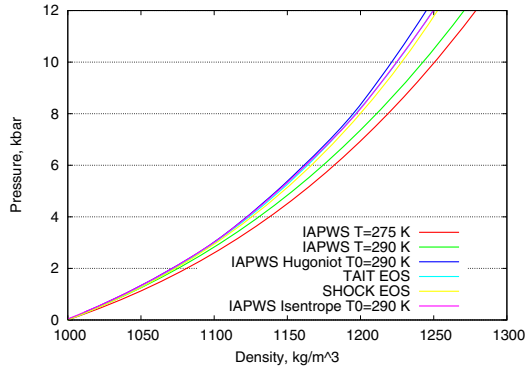


Fig. 15.3 Comparison of selected pressure curves with other models

The EOS initially used in the current work was based on the models of an ideal gas, a liquid with linear density- and temperature-dependent pressure and the Clausius-Clapeyron-relation for the vapor pressure. This model was however limited to temperatures sufficiently below the critical point, as the two independent models for liquid and gas do not coalesce at and above the critical point. For an extended range of application a suitable model was found in the *IAPWS formulation for scientific use*, which covers temperatures and pressures up to 1273K and about 1GPa. It is available as a collection of FORTRAN routines (e.g. from www.ruhr-uni-bochum.de/thermo/), with a variety of combinations of dependent and independent state variables, [1]. As the codes are not efficient enough for direct usage in CFD calculations a tabular representation and suitable interpolation procedures are used instead. Figure 15.2 gives an overview for several thermodynamic properties; in figure 15.3 a comparison with the Tait EOS for liquid water and the so-called Shock-EOS is given. The latter assumes a linear relation $D = a_0 + sV$ between material velocity V and shock velocity D . These models are defined as

$$p^{(Tait)} = \frac{\rho_0 a_0^2}{n} \left(\left(\frac{\rho}{\rho_0} \right)^n - 1 \right), \quad p^{(shock)} = \rho_0 a_0^2 \frac{\varepsilon}{(1 - s\varepsilon)^2}, \quad \varepsilon = 1 - \frac{\rho_0}{\rho}, \quad (15.3)$$

with $n = 7.15, s = 1.9, a_0 = 1450m/s, \rho_0 = 1000kg/m^3$. Both agree well with the Hugoniot and the Isentrope, which were numerically integrated from the IAPWS model.

15.3 Numerical Method

The numerical method applied in this work is a spatially three dimensional finite-volume scheme with explicit time integration, that works with cell-centered conservative variables on block structured body-fitted hexaeder grids. It is implemented in

the institute's APOLLO code. In order to treat the strongly non-linear equation of state in a robust manner, the original one-step integration scheme of APOLLO has been modified into a two-step scheme, where the first step produces a Lagrangian update and the second step treats the convection process. With superscript k indicating an initial time level, $*$ the Lagrangian status at $t + \Delta t$ and $k + 1$ the final status at the new time level, the integration steps can be written as

$$(\mathbf{UV})^{k+1} = (\mathbf{UV})^* + \Delta t \sum \mathbf{K}^* \mathbf{n}^k S^k, \quad (\mathbf{UV})^* = (\mathbf{UV})^k + \Delta t \sum \mathbf{L}^k \mathbf{n}^k S^k. \quad (15.4)$$

An acoustic Riemann solver is applied in the first step for the calculation of the velocity, pressure and power at the material interface used in \mathbf{L} . The subsequent re-mapping from the Lagrangian updated cells onto the actual grid cells at the new time step $k + 1$ is achieved with a donor cell method for the calculation of \mathbf{K} . Both fluxes, \mathbf{L} and \mathbf{K} , are approximated to higher order accuracy by employing a MUSCL-type extrapolation of the conservative cell-averaged quantities.

15.4 Steady State Flow Fields

In the following, selected results for a disc, a sphere and different cones at zero angle of attack are presented. All considered bodies had base radii of 0.5 cm and were embedded centrally in grids of size 40x40 cm, with a resolution of about 0.25 mm in the vicinity of the body. In circumferential direction the grids covered an angular section of 14 degree with one computational cell. Free field conditions were 1 bar ambient pressure and 293 K. In the flow fields shown below the cavity shapes according to (15.1) and the streamline emanating from the disc edge are added to the plots.

The streamlines coincide well with the cavity surfaces, which suggests that the steady state cavity surface is a contact surface with no mass transported across it. The cavity obtained from the numerical solution for $V_\infty = 1000 \text{ m/s}$ agrees in the upstream part with Savchenko's formula for incompressible flow; the deviation observed further downstream is attributed to the closeness of the grid boundary, which affects the numerical solution increasingly as $M \rightarrow 0$. At 2300 m/s the cavity is clearly narrower within the whole downstream range due to the effect of compressibility.

From the entirety of results, the approximation (15.5) was derived, which describes the influences of Mach number and body shape on the cavity radius $R_c(x)$. Here δ denotes the half angle of a conical cavitator, R_n the (base) radius of the body, $R_{c,ref}$ refers to the disc at $M = 0$, e.g. as given by relation (15.1).

$$\frac{R_c(x) - R_n}{R_{c,ref}(x) - R_n} = f_{shape} \sqrt{1 - 0.13M^2}, \quad f_{cone} = 1 - \frac{0.16}{\tan(\delta)}, \quad f_{sphere} = 0.69. \quad (15.5)$$

The following figures show the drag coefficients for different Mach numbers and body shapes together with available literature data. Using a formula suggested by Guzevin for $M \rightarrow 0$, c.f. [2], the drag coefficient of a conical cavitator can be estimated as

$$C_D(M, \delta) = \frac{1}{2} + 1.81 \left(\frac{\delta}{\pi} - \frac{1}{4} \right) - 2 \left(\frac{\delta}{\pi} - \frac{1}{4} \right)^2 + 0.15 M . \quad (15.6)$$

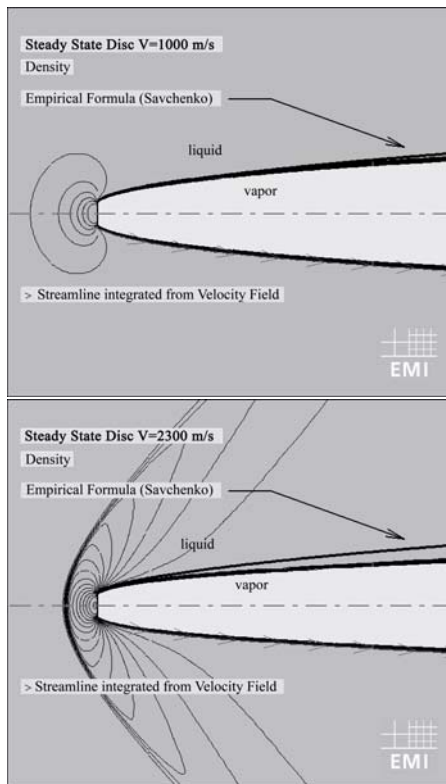


Fig. 15.4 Calculated steady state flow fields (isodensity lines) about a disc at 1000 m/s and 2300 m/s.

15.5 Summary

The presented results provided an extended view into compressible supercavitating flows. The suggested models and methods were confirmed by comparison with

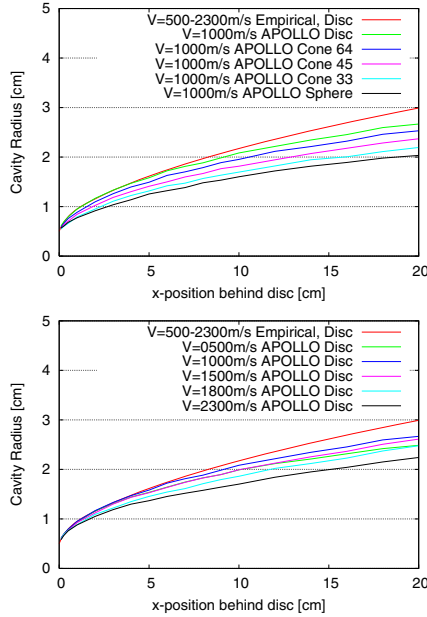


Fig. 15.5 Summary of cavity shapes for different Mach numbers and body geometries.

available data from literature. This holds also for the results obtained for transient flows, which could not be included in the present paper due to limited space. Current investigations focus on the flight behavior of slender bodies, which are inherently meta-stable in supercavitating flows. Figure 15.7 shows, as an example, a still from a free flight simulation, where the fluid dynamic equations are solved on a moving grid simultaneously with the rigid body equations of motion.

References

1. Wagner W., Pruss A. (2002) The IAPWS Formulation 1995 for the Thermodynamic Properties of Ordinary Water Substance for General and Scientific Use. *Journal of Physical and Chemical Reference Data*, AIP, Vol.31, No.2, pp.387-535
2. N.N., RTO Lecture Series EN-010 / AVT-058, Supercavitating Flows.(2002)
3. Brennen C., A numerical solution of axisymmetric cavity flows. *Journal of Fluid Mechanics* (1969), Vol.37, IV, pp.671-688.

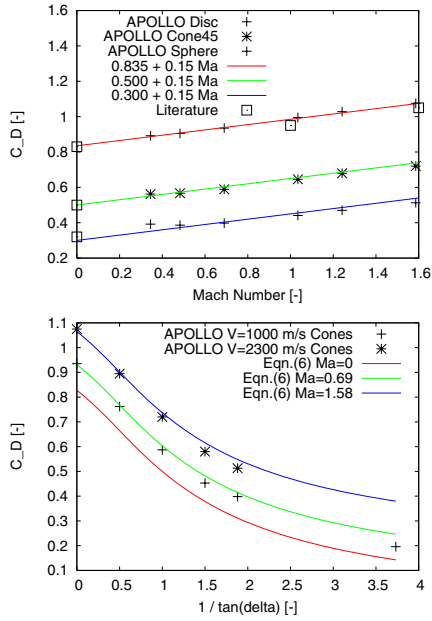


Fig. 15.6 Drag coefficients for different Mach numbers and body geometries.

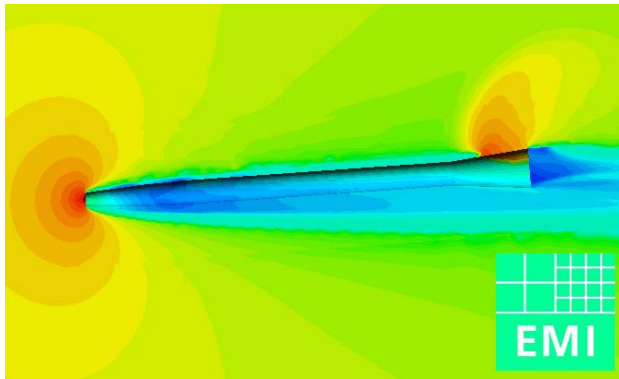


Fig. 15.7 Instantaneous pressure field during tail-cavity interaction in a free flight simulation

Chapter 16

Numerical Analysis Method for the RC Structures Subjected to Aircraft Impact and HE Detonation

Masahide Katayama and Masaharu Itoh

Abstract This paper proposes and demonstrates a numerical simulation method suitable to analyze the local damage and dynamic response of the structures composed of the reinforced concrete (RC) and/or the geological materials subjected to the severe impulsive loading by the aircraft impact and the high explosive detonation. After the brief description about the numerical simulation method, the former part of this work attests that the present method has an enough accuracy to simulate the dynamic behavior of the RC structures subjected to the impulsive loading, through the comparison of the numerical analysis results with those of reference experiments. In the latter part of this work, three-dimensional numerical simulation results are investigated which were performed by using the basically the same analysis method as applied in the former part, but for much more complicated physical system. Through the discussion on the numerical simulation results the effectiveness of the present method is demonstrated from the viewpoint of the high-velocity impact safety, the explosion safety, and the structural integrity evaluation.

16.1 Introduction

Recently the serious hazards have increased such that terrorists attack various public buildings and structures by using high explosives (HE). At the same time, another type of hazards cannot be ignored, i.e. the hazards caused by the industrial accidents in use of the energetic materials like reactive gas mixtures as well as high explosives. Since these hazards are not small-size problems, it is indispensable to discuss as

Masahide Katayama
Impact Dynamics Team, ITOCHU Techno-Solutions, 2-5, Kasumigaseki 3-chome, Chiyoda-ku,
Tokyo 100-6080, Japan e-mail: masahide.katayama@ctc-g.co.jp

Masaharu Itoh
Impact Dynamics Team, ITOCHU Techno-Solutions, 2-5, Kasumigaseki 3-chome, Chiyoda-ku,
Tokyo 100-6080, Japan e-mail: masaharu.itoh@ctc-g.co.jp

interactions between the energetic materials and the constructional structures. However, these problems consist of highly non-linear and complex physical systems so that numerical analyses for such problems, especially in the three-dimensional model, can never have been solved until around a decade ago except for a few huge computer systems in the world. Both hardware and software are now available in order to solve some of such difficult problems, not to say sufficient.

From another viewpoint, an accident previously considered hypothetical became real when the hijacked Boeing 767 passenger jet crashed into the North Tower of the New York World Trade Center on 11th September, 2001. The possibilities of aircraft impacts against infrastructures have been investigated mainly in nuclear industries since 80's [1, 2, 3]. However, the aircrafts discussed in these studies were not commercial jetliners but military jet fighters such as an F-4 Phantom.

In the meantime, the concrete and geological materials indicate complicated behaviors in the compressive and the tensile region, especially when subjected to the severe impact or impulsive loading. Therefore, a number of material properties are necessary to describe such highly nonlinear and dynamic phenomena. On the other hand, it is general that only the limited properties are measured in the usual material test of these materials, i.e. limited to density, elastic moduli and static compressive strength. So it is of great use, if the present scheme provides us the recommended values of the dynamic material properties based on the correlation between the static compressive strength and the other properties. The author and others have proposed and improved such constitutive and failure models for over ten years [4, 5], and K. Thoma et al. also have been developed their own model for the concrete referred to as the RHT model [6].

In this paper we proposes and demonstrates a numerical simulation method by using these two material models suitable to analyze the local damage and dynamic response of the structures composed of the reinforced concrete (RC) and/or the geological materials subjected to impulsive loading by the aircraft impacts and the HE detonations.

16.2 Analytical Method

16.2.1 Analysis Code

A multiple solver type hydrocode: AUTODYN [7, 8] is used for the numerical simulation conventional, Godunov-type and FCT (Flux-Corrected Transport)], the ALE (Arbitrary Lagrangian-Eulerian), the SPH (Smoothed Particle Hydrodynamics), the shell and the beam solvers, moreover the interactions among these solvers can be taken into account in a problem. These solvers are compared and investigated in

order to clarify what solver is the most suitable and efficient to model the individual part of the present problem: the concrete, the reinforcement, the soil/sand, the air and the HE, etc. The three-dimensional calculation for such complex physical system is very heavy even for the current advanced computers. The modeling method for the actual problems is proposed from the practical viewpoint that we persist in using not so expensive but easily obtainable and easily usable computers.

16.2.2 Material Models

The material model in AUTODYN consists of two parts: i) the equation of state (E.O.S.) describes the relationship among pressure (p), density (ρ) and internal energy (e) as indicated by Eq. (16.1), and ii) the material strength model does the constitutive relation including the failure model, as many hydrocodes do.

$$p = F(\rho, e) . \quad (16.1)$$

In the low-velocity structural analyses, the Young's modulus (E) and the Poisson ratio (ν) are used for the solid materials. And the bulk modulus (K) is derived by Eq. (16.2), so that the usage of E and ν is just equivalent to that of K .

$$K = \frac{E}{3(1-2\nu)} \quad (16.2)$$

Considering that the definition of the bulk modulus is given by Eq. (16.3), this can be recognized as using the simplest EOS, i.e. the proportional (linear) E.O.S. to the density and neglecting the energy term,

$$p = -K \frac{dV}{V_{ref}} = K \left(\frac{\rho}{\rho_{ref}} - 1 \right) \quad (16.3)$$

where V is the volume and subscript 'ref' denotes reference variable.

In this study, we applied the linear E.O.S. sometimes to the concrete in the interests of simplicity, and did all the times to the beam and shell elements, because the change of density cannot be taken into account in these elements. The porous E.O.S. was applied sometimes to the concrete and all the times to the soil, but we leave out its detailed descriptions because limitations of space here.

The numerical erosion model is not exactly a physical material model, but it is very useful to model the cratering and spalling (scabbing) of the solid materials, as well as the scattering of the liquid materials in the Lagrangian frame of reference. During the subsequent calculations, some of the Lagrangian elements can become grossly distorted and, unless some remedial action is taken, can seriously impair the

progress of the calculation. Therefore, procedures have been incorporated into AUTODYN to remove such Lagrangian elements from the calculation, if a pre-defined strain exceeds a specified limit. When an element is removed from the calculation process in this way the mass within the element can either be discarded or distributed to the corner nodes of the element. If the mass is retained, conservation of inertia and spatial continuity of inertia are maintained. However the compressive strength and internal energy of the material within the element are lost whether or not the mass is retained.

In AUTOYDN, Lagrangian grids can impact and slide along any Lagrangian surface, at the same time, this surface can be dynamically redefined as the surface changes through the numerical erosion. Erosion is a technique wherein Lagrangian elements are transformed into free mass points not connected to the original element. These free nodes can optionally further interact with other bodies or the original body from which they were eroded. This feature allows the study of impact interaction problems including deep penetrations in the low to hypervelocity range using a Lagrangian technique.

16.2.2.1 Concrete

We adopted two-parameter Drucker-Prager criterion instead of the four- or five-parameter failure surface used by Han and Chu in the static non-uniform hardening plasticity model [9]. In this paper we show the numerical results only on a relatively high-velocity ($> 100m/s$) impact problem as a concrete structure. However, we demonstrated and verified in other opportunity that the present material model (referred to as DYCAP model) is also applicable to the lower velocity impact problems of the concrete [5].

To describe dynamic behavior of fragile material such as concrete is complicated because it shows highly nonlinear behaviour and its multi-axial behaviour is hard to be measured by the experiment. Many constitutive equations of concrete were proposed until now, but the only few ones can predict dynamic behaviour of concrete in the multi-axial stress state, and the applicable region are often very limited. We are concerned with two constitutive equations that can be applicable to the multi-axial stress state. One is Drucker-Prager's equation that shows good results in the region of high strain rate. Another is Han & Chen's non-uniform hardening plasticity model that can be applied to the region of low strain rate. We combined both equations together to establish a new constitutive model (DYCAP), introducing strain rate dependency and strain hardening to this. In this model yield surface is described by:

$$f = \sigma_y - s(k_{0c}, k_{0t}, p) \sigma_y^d = 0 \quad (16.4)$$

where σ_y is yield stress, σ_y^d is the ultimate stress surface that is Drucker-Prager's criterion, s is the shape factor that describes non-uniform hardening behaviour, p is hydrostatic pressure, k_{0c} is the hardening parameter for compression, and k_{0t} is the hardening parameter for tension.

To incorporate the strain rate effect, the dynamic compressive strength \hat{f}'_c and the dynamic tensile strength \hat{f}'_t proposed by Yamaguchi et al.[10] are introduced to the Drucker-Prager's equation as shown in Eq. (16.5) and (16.6).

$$\hat{f}'_c(\dot{\epsilon}) = \left[1.021 - 0.05076 \log \dot{\epsilon} + 0.2583 (\log \dot{\epsilon})^2 \right] f'_c \tag{16.5}$$

$$\hat{f}'_t(\dot{\epsilon}) = \left[0.8267 - 0.02987 \log \dot{\epsilon} + 0.04379 (\log \dot{\epsilon})^2 \right] f'_t \tag{16.6}$$

where $\dot{\epsilon}$ is strain rate $\dot{\epsilon} = \sqrt{(2/3) \dot{\epsilon}_{ij} \dot{\epsilon}_{ij}}$ and strain rate tensor $\dot{\epsilon}_{ij}$.

The strain hardening effect is incorporated by use of the shape factor s , which is a function of hardening factors: k_{0c} and k_{0t} . The shape factor s is defined in the three different regions in the same manner as Chen's method [11], that is in the tensile region, I the transitional region, and in the compression region. The detailed equation is found in the literature by Itoh et al. [4]. The typical relation between yield stress and pressure in the DYCAP model is shown in Fig. 16.1 . The curve is arranged by ϵ_t/ϵ_t^d where ϵ_t is the largest tensile strain in its history and ϵ_t^d is the dynamic ultimate tensile strain.

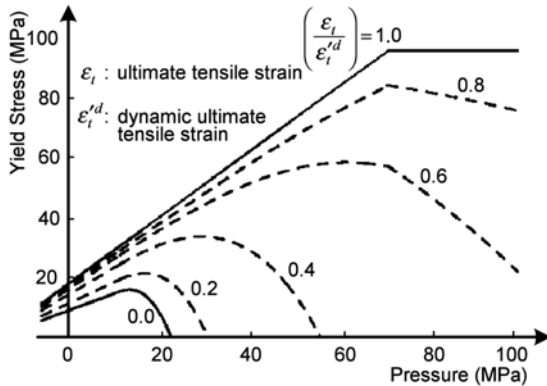


Fig. 16.1 Typical relation between yield stress and pressure in the DYCAP model.

16.2.2.2 High explosives (HE)

We applied the JWL equation of state to the HE proposed by Lee et al. [12], and using programmed 'on-time burning' model assuming the ideal stationary detonation. The equation of state is shown in Eq. (16.7), and the detonation properties and the parameters of the JWL equation for many high explosives have been compiled by Dobratz et al. for a couple of decades [13].

$$p = A_{JWL} \left(1 - \frac{\omega\eta}{R_1}\right) \exp\left(-\frac{R_1}{\eta}\right) + B_{JWL} \left(1 - \frac{\omega\eta}{R_2}\right) \exp\left(-\frac{R_2}{\eta}\right) + \omega\eta\rho_{ref}e \quad (16.7)$$

where $\eta = \rho/\rho_{ref}$ and A_{JWL} , B_{JWL} , R_1 , R_2 , ω are the material properties of the HE. In the handbook [13], the other important variables like the detonation velocity (V_{det}) and the initial internal energy (e_0) are also included. The constitutive model of the HE is neglected, namely assumed to be hydrodynamic.

16.2.2.3 Ductile materials

It has been known that a linear relationship between the shock velocity (U_s) and the particle velocity (u_p), as shown by Eq. (16.8), can adequately represent the Hugniot relation for many condensed materials which impact at velocities less than the threshold for shock-induced vaporization.

$$U_s = c_0 + s_1 u_p \quad (16.8)$$

where c_0 and s_1 are experimentally determined material constants and c_0 denotes the bulk sound velocity. Then the following Mie-Grüneisen form of the shock Hugniot E.O.S. is derived by assuming Grüneisen Γ as shown in the Eq. (16.10) of [14]:

$$p = p_{ref}(\rho) + \rho\Gamma \{e(\rho) - e_{ref}(\rho)\} \quad (16.9)$$

$$\Gamma \equiv \frac{1}{\rho} \left(\frac{\partial p}{\partial e} \right)_\rho \quad (16.10)$$

This equation of state is not only recognized to be applicable for a wide variety of solid and liquid materials, but also the material data of the E.O.S. for many materials are published by not a few research organizations [15].

In the Johnson-Cook constitutive model applied mainly to ductile materials, the yield stress (Y) is estimated by the function of strain (ϵ), strain rate ($\dot{\epsilon}$) and homologous temperature (T^*) defined by Eq. (16.12).

$$Y = (A_{J-C} + B_{J-C}\epsilon^n)(1 + C_{J-C}\ln\dot{\epsilon}^*)(1 - T^{*m}) \quad (16.11)$$

where $\dot{\epsilon}^* = \dot{\epsilon}/\dot{\epsilon}_0$ is the dimensionless plastic strain rate for $\dot{\epsilon}_0 = 1.0s^{-1}$,

$$T^* \equiv \frac{T - T_{room}}{T_{melt} - T_{room}} \quad (16.12)$$

and T_{room} and T_{melt} are the room temperature and melting temperature, respectively. The variables: A_{J-C} , B_{J-C} , C_{J-C} , m and n are determined by an experimental procedure [12]. However, the thermal term is neglected for the beam and shell solvers, because no volume changes, consequently no temperature changes, of the elements are calculated in these solvers.

16.3 Numerical Analyses

16.3.1 Missile Impact on RC Structure (2D)

16.3.1.1 Numerical analysis models

In order to verify the present material model of the concrete, we carried out a number of numerical analyses [4] to simulate an experimental test program conducted by Muto et al. [2]. The main purpose of the reference test is to investigate the local damage of the reinforced concrete structure caused by the accidental aircraft impact on the nuclear related protective structures. The test program consists of three scale models for F-4 Phantom fighter: 1/7.5-, 1/2.5- and full-scale models. Two types of projectiles, i.e. rigid and deformable, were adopted to model the engine part of the aircraft in the experiment.

Although the target RC structures are square in the experiment, two-dimensional axisymmetric model was used in the numerical analysis so that the targets may be assumed to be the circular plates with the equivalent sectional areas. The parts of concrete material were modeled by the Lagrangian frame of the reference, shell elements were applied to the reinforcement and the thin parts of the 1/7.5-scale deformable missile as shown in Fig. 16.2. Therefore, the reinforcement was also modeled by the thin circular plate with the equivalent mass. It should be noted that the bending moment was taken into account for the shell elements in the missile, while was ignored for the shell element modeling the reinforcement, i.e. was assumed to be membrane. Each lower half indicates the numerical mesh used in the calculation in Fig. 16.2. The concrete plate was constrained at the radial end to both the axial and radial directions. To the interface between the missile and the RC structure, the slide/impact interactive boundary condition without friction was applied, and all the elements in the concrete, missile and reinforcement were also enabled

to interact with the elements that exist in the same component after subjected to a serious deformation. The capabilities of the interaction and the numerical erosion triggered by the maximum geometric strain enable us to simulate the complicated deformation processes. For Lagrangian elements the erosion strains 100 to 500 % were used, while the erosion strains equivalent to the ultimate physical (material) strains were applied for shell and beam elements, because there do not occur any bulk deformations in the case of these two- or one-dimensional elements.

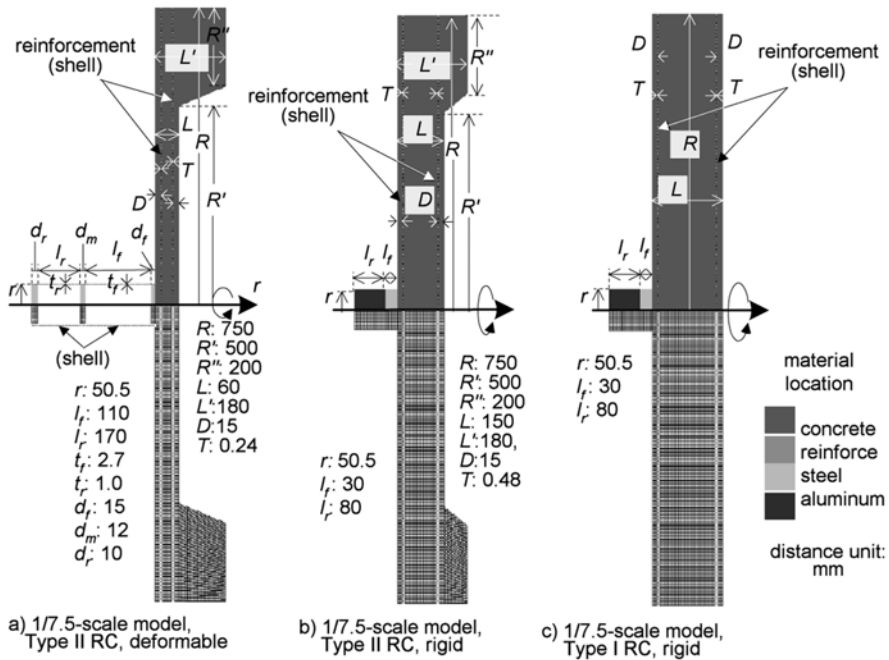


Fig. 16.2 Geometrical models and numerical meshes in the analysis.

16.3.1.2 Numerical results

Only the results of the 1/7.5-scale model are discussed in this paper, and the cases and results in both the experiment and the numerical analysis are summarized in Fig. 16.3, 16.4 and Table 16.1 for the selected 1/7.5 model tests reported in the references [2]. Both results are compared in their residual velocities of the projectiles, in the vertical/horizontal/average diameters of the front craters and rear scabbing of the target plates, and in the overall damage status of the target plates. The numerical results can be considered to simulate the overall deformations of the reinforced con-

crete panels, because the present numerical results nearly predict both the cratering in the front side and the scabbing (spalling) in the rear side.

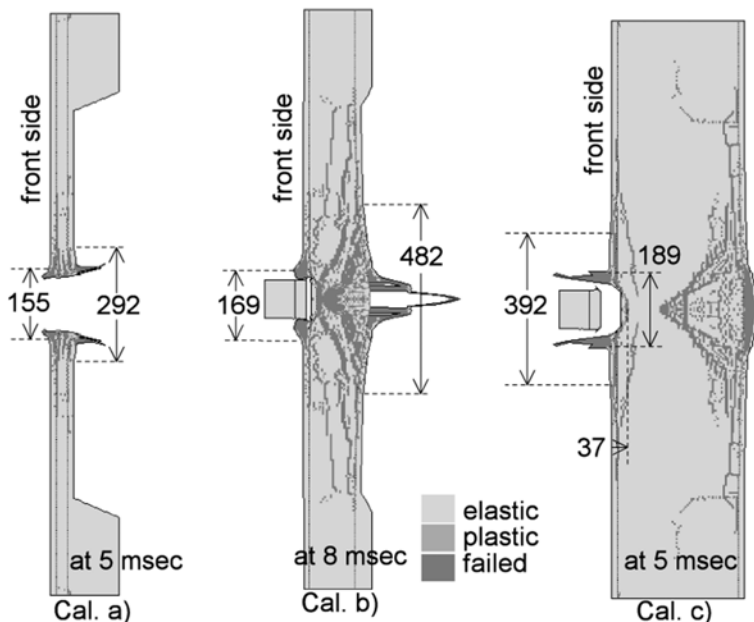


Fig. 16.3 Numerical results for the 1/7.5-scale model cases.

Table 16.1 Conditions and results of the 1/7.5 model comparing between the calculations (C) and the experiments(E).

ID	C/E	T* (mm)	V _{imp} ** (m/s)	V _{res} *** (m/s)	Projectile	Front Diameter			Depth (mm)	Rear Diameter			Status
						ver. (mm)	hor. (mm)	av. (mm)		ver. (mm)	hor. (mm)	av. (mm)	
a)	C	60	194	138	deformable	-	-	155	-	-	-	292	perforated
1-1	E	60	194	143	deformable	178	171	175	-	420	335	378	perforated
b)	C	150	143	-1.94	rigid	-	-	169	32.3	-	-	482	scabbing
1-3	E	150	143	N/A	rigid	155	185	170	N/A	590	440	515	scabbing
c)	C	350	198	-11.8	rigid	-	-	189	37	-	-	-	perforated
1-8	E	350	198	N/A	rigid	320	302	311	42	-	-	-	perforated

*: Thickness
ver.: vertical

**: Impact Velocity
hor.:horizontal

***: Residual Velocity
av.:average

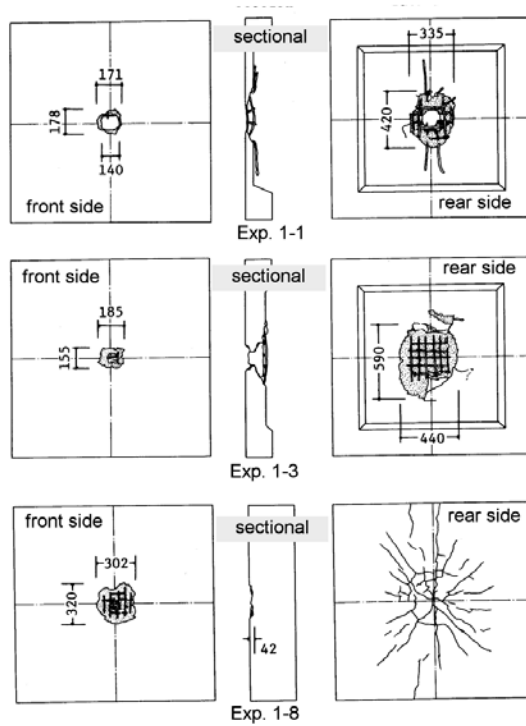


Fig. 16.4 Experimental results for the 1/7.5-scale model cases.

16.3.2 HE Detonations On and Near the RC Slab (2D & 3D)

16.3.2.1 Analysis models

The effects of the detonation on RC slabs have been investigated experimentally, when the HE is placed and detonated on the surface of the RC slab [17, 18, 19, 20]. Some numerical studies on the damage of the RC slabs subjected to the contact HE detonation have also conducted over the comparison with the experimental results [17, 21, 22]. However, almost all numerical analyses are carried out by two-dimensional models until recently. The reason of such a limitation seems to have come from both the computational hardware and software capabilities as they were, when those studies were conducted.

In the experiment by Kraus et al. [17], the RC slab has the dimensions 2.0 2.0 0.3 m with a concrete compressive strength of 44 to 48 MPa, and has a percentage of reinforcement of 42 kg/m². The cubic high explosive is placed in the center of and directly on the slab. The used HE is PETN with a mass of 1.0 kg and the

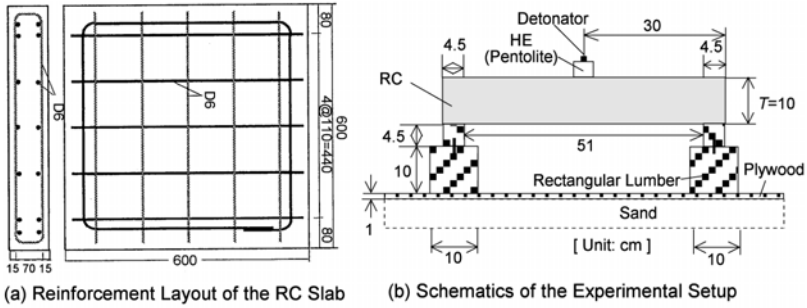


Fig. 16.5 Configuration of the HE detonation test on the RC slab by Tanaka et al.

density of 1.5 g/cm³. In the calculation, the concrete, reinforcement and HE were modeled by the Lagrangian element. Next, Fig. 16.5 depicts the configuration of one of a series of HE detonation tests on the RC slab conducted by Tanaka et al. [19]. We performed a three-dimensional calculation to simulate this experimental condition. In this calculation, the concrete and HE were modeled by the Lagrangian element with the numerical erosion capability, while the reinforcement was done by the beam element, by using finer numerical discretization than the previous calculation. The numerical grids used in the present calculation are indicated in Fig. 16.6.

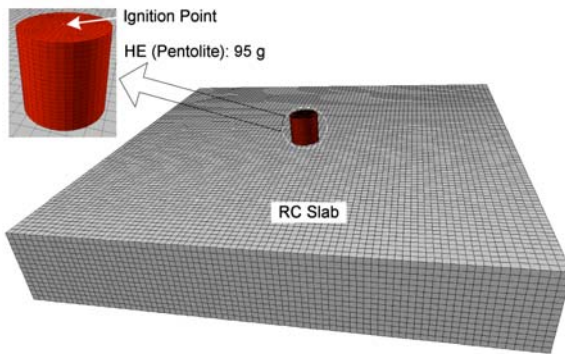


Fig. 16.6 Three-dimensional numerical grids to simulate the HE detonation test on RC slab by Tanaka et al.

The compressive strength of the concrete measured 28-day later is 56 MPa, and the reinforcement has the yield strength of 300 MPa and the tensile strength of 419 MPa. The cylindrical HE with a diameter of 41.8 mm is placed in the center of and directly on the slab. The HE is the pentolite with a mass of 95 g.

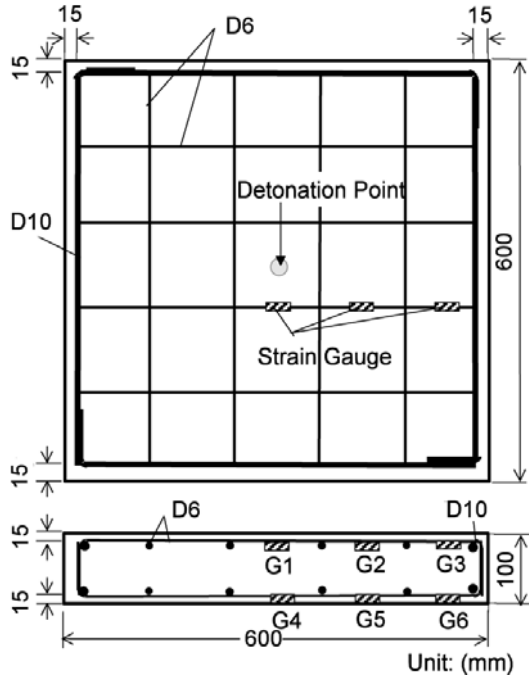


Fig. 16.7 Reinforcement Layout of the the RC slab by Morishita et al.

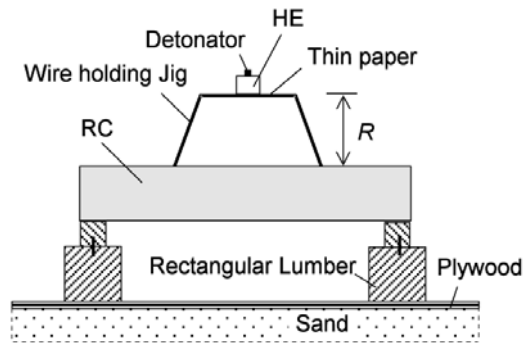


Fig. 16.8 Setup of the Experiments by Morishita et al.

Thirdly, Morishita et al. conducted another type of HE detonation tests near the RC slab, in which the HE are placed in the center of RC slabs but at the position standoff from the surface of RC slab [20]. Figures 16.7 and 16.8 indicate the configuration for the tests. It should be noted that the alignment of the reinforcements is different from the above mentioned contact explosion experiment, especially that there are no reinforcements at the center of the RC slab. We also performed two numerical simulations for this type of experiment: with the standoffs of 100 mm and 50 mm. In these calculations, the concrete was modeled by the Lagrangian element with the numerical erosion capability, the reinforcement was done by the beam element, as they were modeled in the contact explosion calculation. However, the HE was modeled by the Eulerian frame of reference, and the atmosphere was taken into account by the same numerical grid that the HE was modeled.

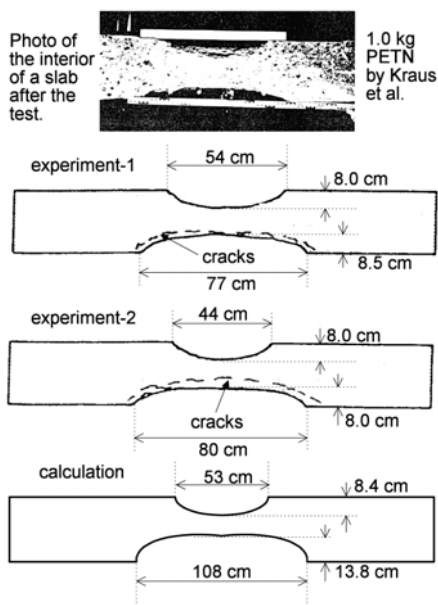


Fig. 16.9 Comparison of the present 3-D calculation with the experimental results by Kraus et al.

The main parts of these numerical simulations were carried out in the three-dimensional model, after a preliminary axisymmetric two-dimensional calculation to simulate the pentolite detonation and its propagation process in the atmosphere with the initial pressure of 101.3 kPa. The preliminary calculation was carried out by using the multiple-material Eulerian solver. Then, the two-dimensional distribution of the physical properties of the pentolite products and air at the final stage was

remapped to the three-dimensional analysis model as an initial condition. All the pentolite products are assumed to be in the gas phase at this moment.

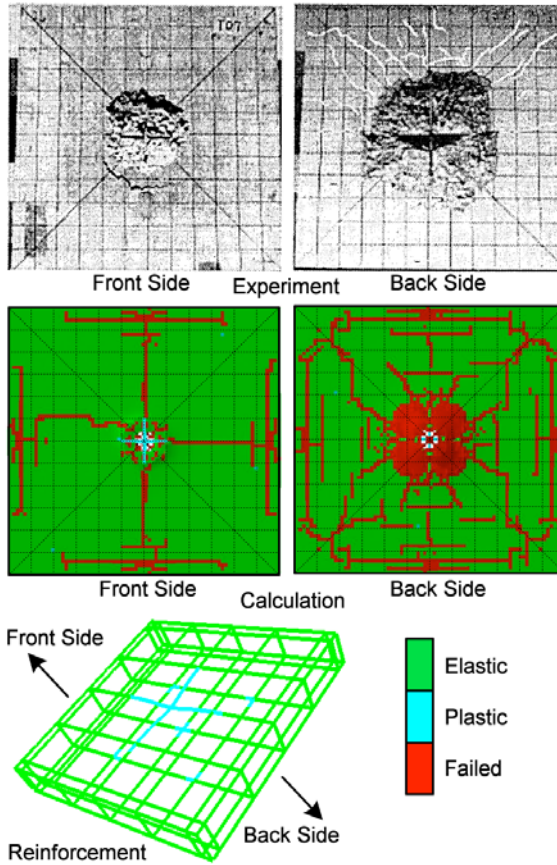


Fig. 16.10 Comparison of the 3-D calculation of the HE detonation on RC slab with the experimental results by Tanaka et al.

In the three-dimensional calculation we applied FCT-Euler solver to the gas materials (pentolite products and air), because this solver is suitable to model the shock in the gas and is much faster than the multiple-material Eulerian solver. The Euler-Lagrange interactive boundary condition was applied to the front surfaces of the RC slab. In order to attain this motivation, the E.O.S. for the pentolite was switched from the JWL equation to the ideal gas equation (as shown in Eq. (13)) as well as the air, and the pentolite products were assumed to have the same ratio of specific

heat (γ) of 1.4 just same as the air, because the third term of the JWLEOS is equivalent to the ideal gas EOS, after perfectly burned.

$$p = (\gamma - 1)\rho e \quad (16.13)$$

16.3.2.2 Numerical results

First, Fig. 16.9 shows the schematic comparison of the three-dimensional calculation, which was performed in 1997 by the authors, with the experimental results conducted by Kraus et al. This three-dimensional calculation was carried out by using relatively coarse numerical discretization in today's environment, so that the deformed slab obtained by the calculation does not have so smoothed outline. The schematic deformation in Fig. 16.9 only represents the typical parameters: i.e. the diameters and depths of front and rear craters.

Secondly, Fig. 16.10 shows the comparison of the damage of the RC slab between the calculation and the experiment in the front and back sides for the Tanaka's experiment. The calculational result seems to evaluate the crater diameters in both sides a little bit smaller than the experiment, but the overall damage of the RC slab in the calculation indicates a fairly good agreement with the experiment. Especially, the calculation successfully simulates the exposure of the reinforcement in the front side and the pattern of the crack extension in the back side.

The lower figure depicts the damage and deformation of the reinforcement in a three-dimensional bird's-eye view by removing the concrete grid. Thirdly, Fig. 16.11 depicts the remapping procedure from two-dimensional model to three-dimensional one for the Morishita's experiment: the upper contours show the pressure distributions and the lower ones do the density distributions. There appear no material boundaries in the three-dimensional contours, because we assumed that pentolite products in gas phase and air are the same material.

The comparison between the experimental and calculational results of the stand-off explosion is shown in Fig. 16.12. Only very shallow craters are observed on the front side in both experimental and calculational results of the 100-mm-standoff case, whereas obvious craters appear in the 50-mm-standoff case. Calculational results successfully simulate the spalling and cracking behaviours on the back side as well as the damages in the central cross section, in comparison with the corresponding photos in the experiment for the 50-mm-standoff case, especially these results might be characterized by the crack patterns both along the reinforcements and in the radial directions. All the beam elements modeling reinforcements seem to remain in the elastic state, differently from the result of contact explosion.

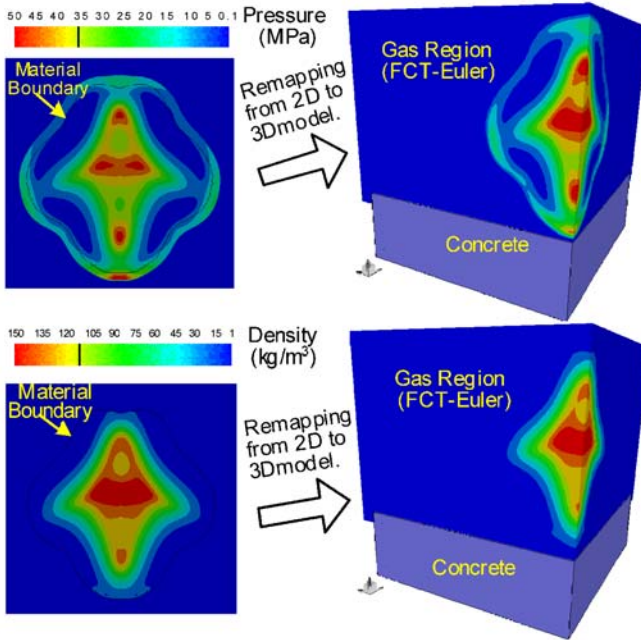


Fig. 16.11 Remapping procedure from 2D/multiple-material Euler to 3D/FCT-Euler model.

16.3.3 F-4 Phantom Crashing on a RC Wall (3D)

16.3.3.1 Analysis Model

Next reference experiment was performed by Sandia National Laboratories on the terms of the contract with the Muto Institute of Structural Mechanics, Inc. in Japan [2, 3]. This experiment is situated as a full-scale model one of a series of impact tests mentioned in the section 16.3.1. The experiment yielded an extensive set of response data, of which we focus on the following main measurements,

- 1) Crushing behaviour of the F-4 Phantom,
- 2) Impact force loaded on the RC target structure,
- 3) Damage on the concrete.

Recommendations for future studies are also presented to improve the accuracy of the proposed model. Before describing the numerical simulation we briefly summarize the impact test. The primary purpose of the test was aimed at determining the impact force as a function of time when an F-4 Phantom impacts onto a massive, essentially rigid, reinforced concrete. Figure 16.13 is the instantaneous photograph of the impact.

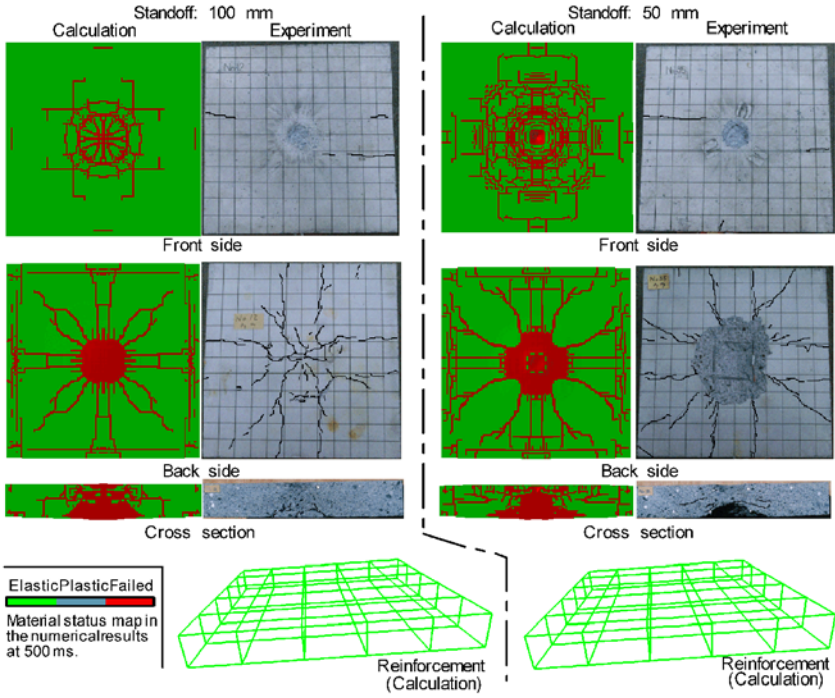


Fig. 16.12 Comparison of the 3-D calculation of the HE detonation on RC slab with the experimental results by Morishita et al.



Fig. 16.13 The instantaneous photograph of the F-4 impacting the target (Courtesy of Sandia National Laboratories).

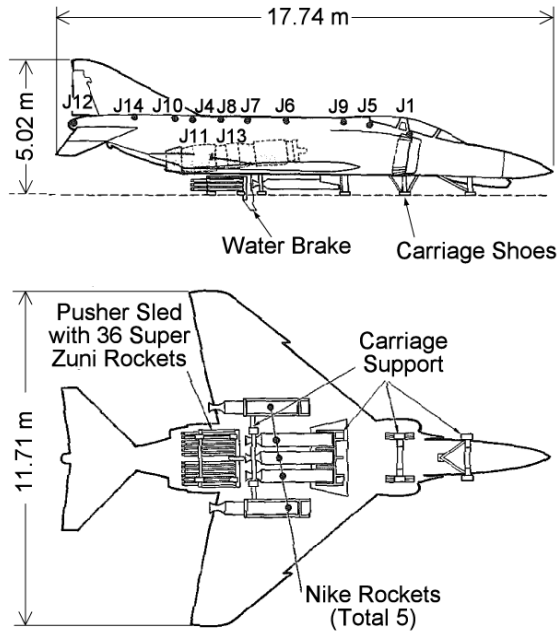


Fig. 16.14 Test configuration of F-4 Phantom [16].

The test configuration of the F-4 is shown in Fig. 16.14. The front and the main landing gears were removed. Instead a sled with a carriage structure was attached on the under surface of the aircraft. The sled was mounted on two rails of 600 meter long which guided the F-4, accelerated by rockets, to the target. The impact speed was adjusted to 215 m/s. Note that the shape and layout of the fuel tanks were not available, when this project started in 2004.

The total impact weight was 19 tones comprising 12.7 tones of the F-4, 1.5 tones of the sled and the carriage, 4.8 tones of water which is used to simulate the weight of fuel. The weight specification is listed in Table 16.2. The target was a rectangular block of reinforced concrete 7 meter square and 3.66 meter thick which weighs 469 tones (i.e. approximately 25 times heavier than the F-4). It was placed on an air-bearing platform which enabled almost free movement in the direction of impact. The geometry of the fuselage of the F-4 Phantom is created first by the general-purpose mesh generation computer program TrueGrid [23]. Then the obtained geometry is imported into the finite element model of the AUTODYN as shown in the left-hand side of Fig. 16.15. The size of the F-4 is adjusted to fit to the configurations shown in Fig. 16.14.

Table 16.2 Specification of the impact weight.

Components	Test (t)	Simulation (t)
Fuselage and Wings, etc.	9.2	9.3
Engines	3.5	3.4
Water	4.8	4.8
Rocket and Sled	1.5	–
(Total)	19.0	17.5

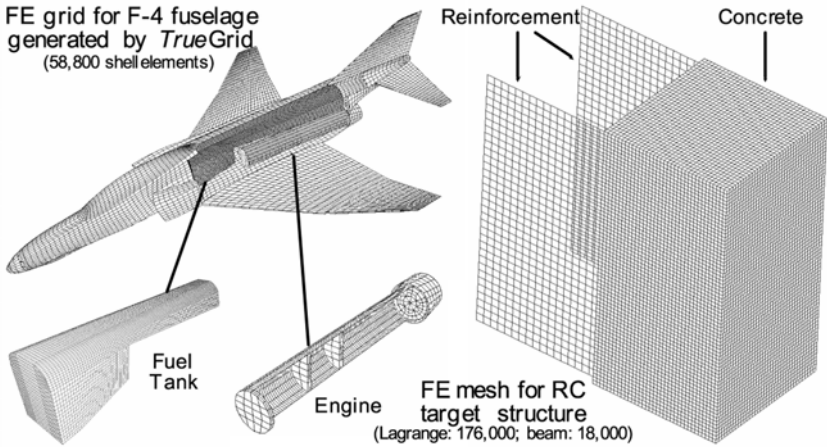


Fig. 16.15 Geometrical models of the F-4 Phantom and the RC target structure.

Because of the severe impact loading condition a constitutive model for the material of the aircraft is required to consider the strain hardening and the strain rate effects. The Johnson-Cook model [24] was adopted and the material properties of the 2024-T351 aluminium were taken from the material library of AUTODYN. The material properties of Glass-Epoxy for the windshield were also taken from the same library. Most components of the aircraft were modeled by shell elements except the engines and the water inside the fuel tanks. They were discretized by solid elements. We adopted the simple model for the engine which was designed for and used by the separate impact test [2] as shown in the lower middle of Fig. 16.15 because the actual GE-J79 engine is too complicated to consider. The material properties of the engine were also taken from the same reference.

As mentioned above the shape and layout of the fuel tanks were not provided in the test report, we refer to [25] in order to place it inside the fuselage in the improved model carried out in 2005. The lower left-hand side of Fig. 16.15 shows the mesh of the tank in which water is filled with. The surface nodes of the water were rigidly joined with the corresponding ones of the tank. The following material properties were used for the water: density of kg/m^3 , bulk modulus of 2.25 GPa and spall strength of -2.5 MPa.

We adopted a numerical method to scale the density of the aluminium which is increased by four times that of the actual one. Without this technique the thickness of the fuselage and the wings should be specified as 16 mm in order to match the weight of 9.2 tones. We assume that a reasonable thickness is about one fourth of it. Hence the density is scaled up in order to save the computer time to improve the Courant condition.

The concrete wall is divided uniformly as shown in the right-hand side of Fig. 16.15. Each element is approximately a cube of 0.1 meter. In order to represent the material nonlinearity of the concrete we adopt the RHT [6] model which has the following specific features like pressure hardening, strain hardening, strain rate hardening and damage with tensile crack softening. The properties are taken from the material library of the AUTODYN and calibrated with the compressive strength of 23.5 MPa.

Also shown in Fig. 16.15 are the reinforcing bars which are modeled by beam elements. The ratio of reinforcement of the test is 0.4 %. The same ratio is applied to the model. The following material properties of the steel [16] are used: Young's modulus of 206 GPa, Poisson's ratio of 0.3, yield strength of 490 MPa, ultimate strength of 740 MPa and ultimate strain of 0.19.

In the test, it was observed that each wing tip and a portion of tail were sheared off due to the impact, and the other parts were completely destroyed. Pieces of the aircraft and lumps of crushed engines were found in the wide area. A sequence of images recorded by high speed cameras at the test site displayed that the main wings were severed by the edges of the target.

16.3.3.2 Numerical results

Figure 16.16 shows the deformed mesh configurations after impact. The aircraft collapses from the front section as if it impacts into a rigid wall. Most of the finite elements are numerically eroded because of large deformations. Only remained are the pieces of the fuselage, the portions of the tail wings, the thickened parts of the

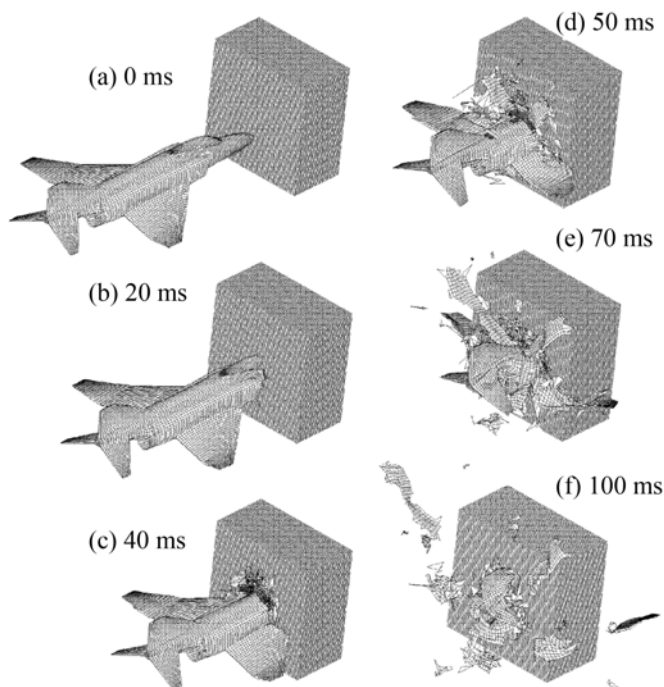


Fig. 16.16 Sequence of the impact and deformation of F-4 and RC structure.

engines (Fig. 16.17(c)) and the tip of main wings. These results reproduce successfully the crushing behaviour of the aircraft observed in the test.

The impact force histories obtained by the test and by two sorts of simulation are compared in Fig. 16.18. The case not modeling the fuel tanks (old one) underestimates the impact force, as well as its peak shifts to the right-hand side. On the other hand, the case modeling the fuel tanks (new one) simulates the impact force history by the experiment fairly well in the shape, magnitude and timing. This agreement is brought about by the feature of the numerical model, namely, the mass distributions of the engines and water are approximately reproduced, and the sum of the weight of these components amounts to almost half the weight of the aircraft, neglecting the differences caused by not modeling the rockets, sled, etc. Note that the head of fuel tanks is located before that of the engine, and that this fact causes the appearance of the peak of the impact force in the new model. The impact force of the calculation is evaluated by differentiating the momentum response of the whole RC structure by time. The obtained transient curve is then shifted 8 ms to the origin (left) in order to compare its peaks with the test ones.

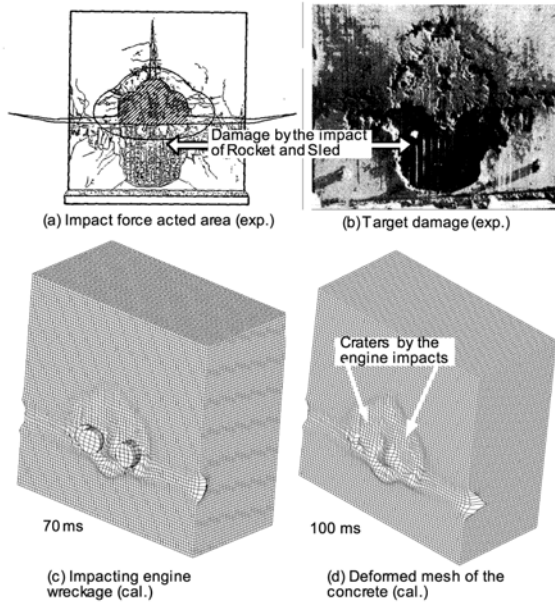


Fig. 16.17 The Damage aspect on the RC structure by the calculation (cal.) and the experiment (exp.).

The impact of the engines caused craters like two 'eyes' [2]. The formation of the craters are illustrated by (c) and (d) of Fig. 16.17. The crater depth (60 mm) reported in the experiment is slightly shallower than that obtained in the calculation (65 mm). The impact of the fuselage inflicted only minor damage on the target to form a shallow dent on the surface in both the experiment and the calculation. The distinct shape like a flattened 'pear' is formed similarly in both results. The impact of the rockets and sled caused major damage to the concrete in the lower part. But this cannot be reproduced by the calculation justifiably, as they were not taken into account in the present calculation.

16.3.4 Boeing 747 Jet Impacting on Thick Concrete Walls (3D)

16.3.4.1 Analysis models

The objective of this work is to numerically assess the damage of the wall caused by the impact of the B747 which is almost 15 times heavier than the F-4. All the components of the jetliner in our numerical model, namely, the fuselage, the wings and the engines were modeled by shell elements. The five different types of targets were assumed to be reinforced or non-reinforced concrete walls with three differ-

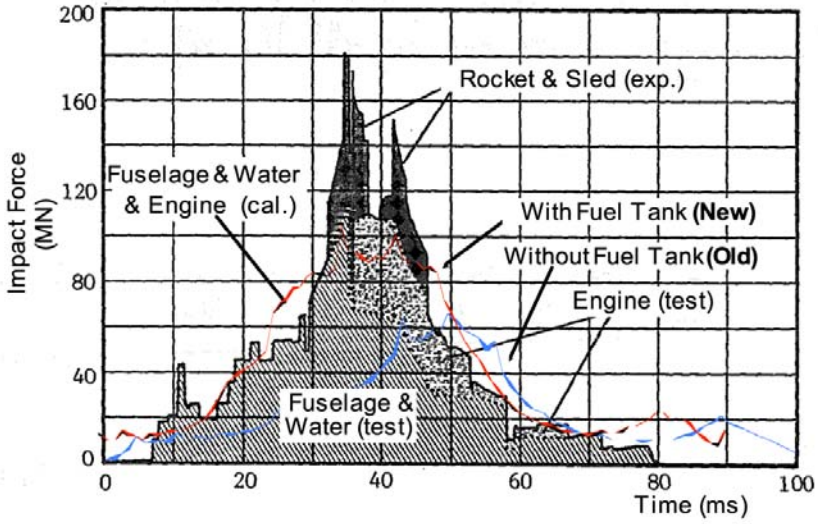


Fig. 16.18 The impact force histories loaded to the RC structure by the calculation (cal.) and the experiment (exp.).

ent thicknesses, additionally a rigid wall case was also carried out. The impacts between these elements were taken into account by using a contact capability. An eroding slide-line capability was utilized to prevent mesh tangling.

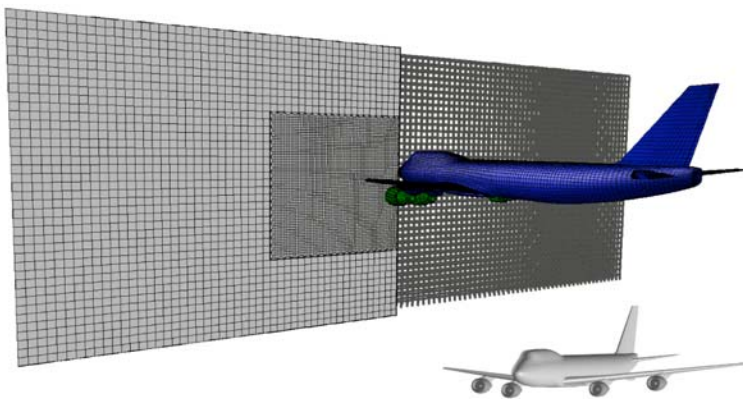


Fig. 16.19 Geometrical grid and model of B747 and RC wall in the calculation.

The shell solver was applied to the jetliner, the hexahedral solid solver to the concrete wall, and the beam solver to the reinforcement by using AUTODYN-3D. The geometry of the jetliner is created as a first step by using TrueGrid in a similar way of the F-4 Phantom model. Then the obtained geometry was imported into the AUTODYN finite element model as shown in Fig. 16.19. The overall length is 70.5 m and the wing span is 64.0 m. The thickness of the shell elements was adjusted so that the numerical model was consistent with the actual Boeing 747 [[26]. The total mass of the jetliner is thus 3.4105 kg (340 t) including four engines and the fuel. The impact velocity of the jetliner was assumed to be 83.3 m/s (300 km/h) which slightly exceeds the landing speed of about 77.8 m/s (280 km/h). Because of the intense impact loading condition, a constitutive model for the material of the jetliner is required to take into consideration both the strain hardening and strain rate effects. The Johnson-Cook model is adopted and the material properties of the 2024-T351 aluminum are taken from a reference [16].

Table 16.3 Numerical analysis cases.

Case Name	Wall Thickness	Reinforcement
CASE-1	1 m	0.8%
CASE-2	2 m	0.8%
CASE-3	2 m	None
CASE-4	3 m	0.8%
CASE-5	3 m	None
CASE-6	Rigid	–

Six cases of numerical analyses were carried out for different types of targets as shown in Table 16.3. All the concrete targets have rectangular shapes with the same 150 m width and 60 m height. As indicated in the left-hand side of Fig. 16.19 for the CASE-4, fine meshes were assigned to the central region where the impact loading is concentrated while coarse meshes were used for the surrounding region. The fine region has a face of 60 m \times 30 m and a thickness of 3 m which consists of 1206015 meshes. The size of one solid element is then 0.5 m \times 0.5 m \times 0.2 m. The surrounding region was divided uniformly into rectangular solid elements. Each element has a size of 1.5 m \times 1.5 m \times 0.2 m. The concrete wall has 186,000 solid elements totally.

In order to represent the material nonlinearity of the concrete we adopted the RHT [6] model which has the following specific features like pressure hardening, strain hardening, strain rate hardening and damage with tensile crack softening. The material properties calibrated with the compressive strength of 35 MPa were taken from the material library of AUTODYN. The bottom of the wall was rigidly fixed, while no boundary condition was applied to the other five surfaces.

The right-hand side of Fig. 16.19 also depicts the double-reinforced arrangement. The number of longitudinal rebars is 99 and that of lateral ones is 39. They are placed 0.4 meter inside the front surface of the wall. The same number of bars is put along the back surface. The ration of the reinforcement is corresponding to 0.8 percent. The following material properties were used for the reinforcement: density of 7.8103 kg/m³; bulk modulus of 1.71105 MPa; shear modulus of 7.88105 MPa; yield stress of 2.15102 MPa; fracture strain of 0.19.

16.3.4.2 Numerical results

Figure 16.20 summarizes the overview on the numerical results of the present study for five different target walls except for CASE-6, while each assumption for the impactor (jetliner) is the same. The calculations of CASE-1 through CASE-5 were carried out up to 1 s and CASE-6 was done up to 0.6 s. The figures of (a-1) through (c-1) depict the deformations or damages estimated to the jetliners and the concrete walls in the impact side and the back side, for the CASE-1 through CASE-3 respectively, as well as the figures of (d-1) through (f-1) do in the impact side and from the upper viewpoint, for the CASE-4 through CASE-6 respectively. The graphs of (a-2) through (f-2) indicate the energy balance histories by each material for the CASE-1 through CASE-6 respectively. 'Body' means all the material of the Jumbo jet except for engines; 'Eng.' does all the material in the four engines; 'Con.' does all the concrete material; 'R-F' does all the reinforcement steel. On the other hand, 'Int.' stands for the internal (distortional) energy and 'Kin.' does the kinetic energy.

In every case the buckling occurs in the nose of the fuselage, and it is subjected to serious deformation. However, outstanding crashes on four engines are observed only in the CASE-1 (1 m thickness; with the reinforcement). On the contrary, every jetliner except for CASE-1 drops its main wings in the tip, like birds do when they flap. No significant deformations can be observed behind the main wings in every case.

Comparing among Fig. 16.20 (a-1) through (f-1), we can know that the concrete wall are perforated completely in the cases of CASE-1 and CASE-3 (2 m thickness; without the reinforcement). Especially, in the case of CASE-1, the both front and rear reinforcements are broken and cut in the vicinity of the impact surface. The rear reinforcements of CASE-2 seem to survive, but they are not supportable in any sense, actually some of them are known to be fractured by an additional output separately done. And outstanding spalling (scabbing) can be observed in the back side of the concrete wall of CASE-2. Slight dents or multiple shallow craters are formed around the impact area on the front side, whereas no significant deformations can be observed on the back side, for both the CASE-4 and CASE-5 that have the same thickness of 3 m.

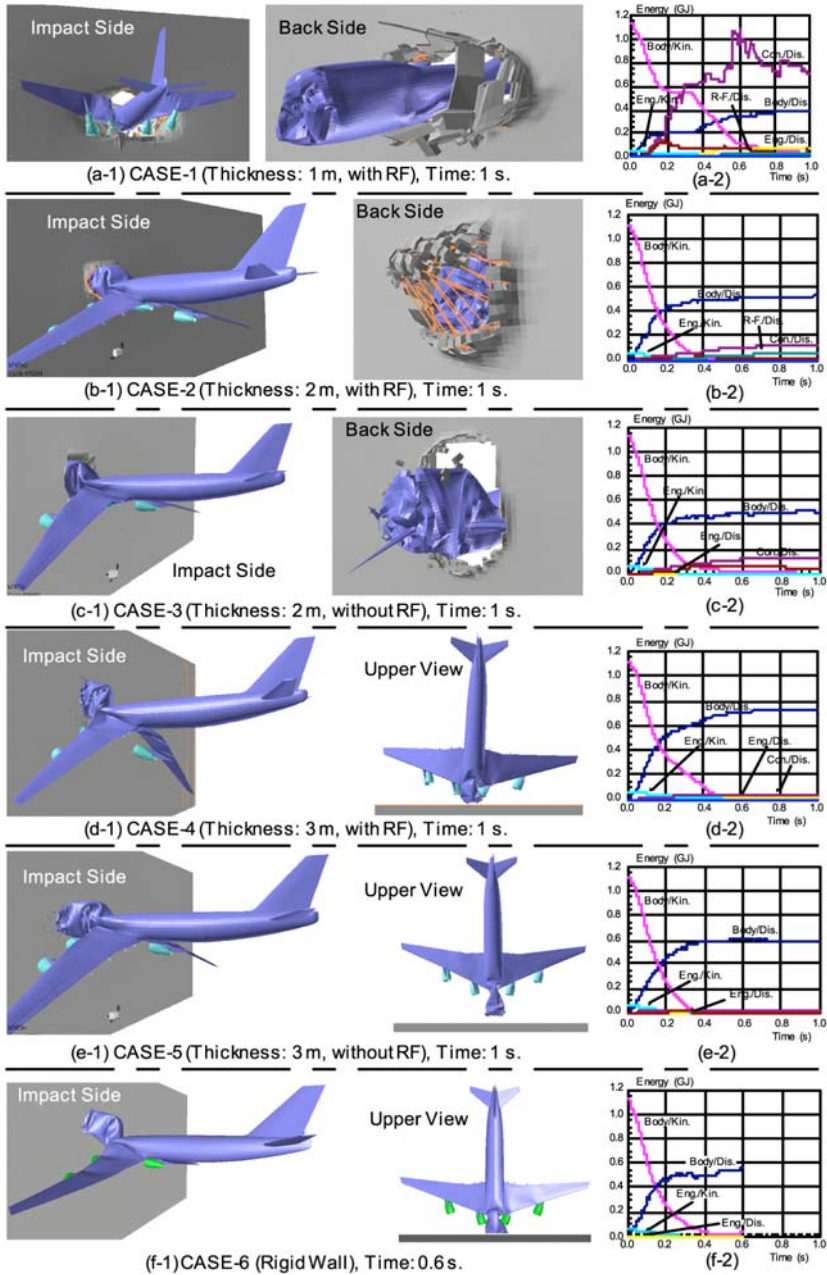


Fig. 16.20 Overview of the numerical results for five different concrete targets.

By the comparison among six graphs shown in Fig. 16.20 (a-2) through (f-2), the history of the kinetic energy of the jetliner of CASE-1, 'Body (Kin.)', is apparently different from the other cases: it indicates two-step decrease curve. This history tells us that the nose of the jetliner perforated the concrete wall at about 0.15 s, and that the four engines impacted on the wall again in order after about 0.3 s. And, it takes over 0.8 s for the jetliner of CASE-1 to be decelerated sufficiently, while the jetliners of other cases are stopped or rebounded within 0.5 s. However, since the internal energy of the concrete of the CASE-1 shows extraordinary increase, the calculated fact that the increase of the internal energy of the jet ('Body') is less than the other cases can be recognized to be caused by some numerical energy error. That the total energy of the system decreases less than the initial amount (the kinetic energies of 'Body' and 'Eng.')

 in the CASE-2 through the CASE-6 can be explained by the numerical erosion of the elements.

From the comparisons between the CASE-2 and the CASE-3, and between the CASE-4 and the CASE-5, any significant differences cannot be found, and this fact is coincident with the former comparisons of the deformations and damages investigated by (b-1) through (e-1). Although the histories of the energies for the CASE-4 and the CASE-5 differ from each other a little, there seem not to be any convictive reasons, and it might be amplified by the asymmetry of the jets caused by a minute numerical error.

Note that the elapsed computer time required to execute the CASE-6 was 1/15th less than CASE-1, although the phenomenon time of the former case is 40 % shorter than that of the latter case. We can see that most parts of the computing time of these models were exhausted for the concrete walls.

16.3.5 HE Detonation in Tunnel Structure with Inner Steel Liner (3D)

16.3.5.1 Analysis models

Here, we shall suppose a HE detonation problem in the concrete tunnel structure with the inner steel liner, as shown in Fig. 16.21. The spherical HE is suspended in the atmosphere and is ignited in the center of the charge. The concrete structure is built on the soil, the one end of the tunnel is closed and the other end is open. The structure has the vertical part with the height of 2 m and is embedded as a basis in the soil to the depth of 1 m. The thin steel liner covers on the inner surface of the tunnel without constraint to the concrete wall, but the inner surface of the closed end of the concrete structure is bare. The high explosive is spherical TNT with a mass of 1000 kg (1 t) and a diameter of 1.06 m.

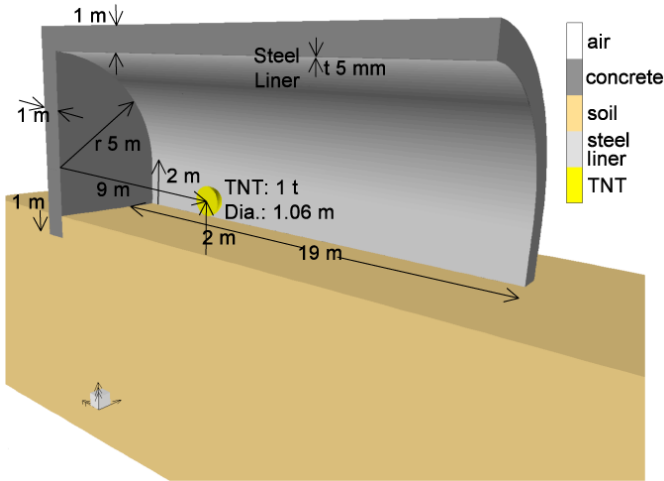


Fig. 16.21 Initial analysis model of the HE explosion in the tunnel vault structure with a inner steel liner.

The main part of the numerical simulation was carried out in the three-dimensional model, after a preliminary one-dimensional calculation, similarly in the case of the standoff explosion analysis described in the Sec. 16.3.2. The preliminary calculation was carried out by using the multiple-material Eulerian solver for spherical TNT. Then, the one-dimensional distribution of the physical properties of the TNT products and air at the final stage was remapped to the three-dimensional analysis model as an initial condition. All the TNT products are assumed to be in the gas phase at this moment.

Fig. 16.22 depicts the one-dimensional calculation by the wedge-shaped grid, and the remapping procedure from one-dimensional model to three-dimensional one by showing the pressure distributions in both models.

The concrete and soil were modeled by the Lagrangian solver, the steel liner was done by the shell solver of AUTODYN. The effect of reinforcements was taken into account by the equivalent and homogeneous material model applied to Lagrangian elements modeling the concrete. The interactive boundary condition with the free slide was applied to the interfaces between the concrete and the liner, and between the concrete and the soil. The Euler-Lagrange interactive boundary condition was done to all the surfaces of the concrete, soil and liner faced to the air. The FCT-Euler grid was defined 1 m below the soil surface in order to take account of the subsequent deformation of the soil. The flow-out boundary condition was applied to all the surfaces of the FCT-Euler grid except for those in the soil, and the transmit

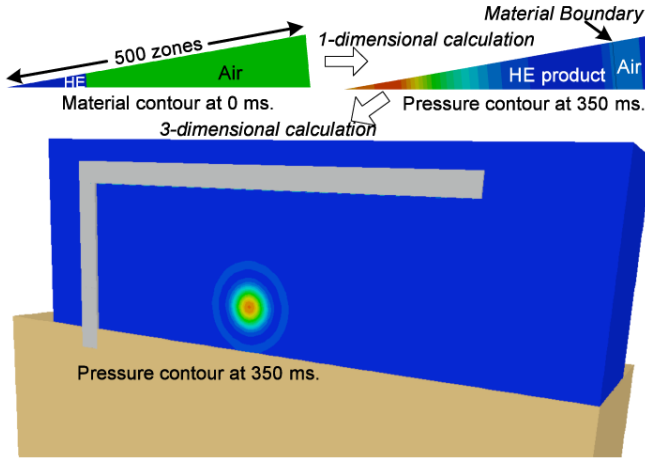


Fig. 16.22 Remapping procedure from 1D/multiple-material Euler to 3D/FCT-Euler model.

boundary condition was applied to all the surfaces except for the ground surface, as to avoid unphysical reflections of the pressure wave.

The FCT-Euler method is much faster than the Godunov type multiple-material Eulerian solver, however the method has the limitation of the applicability only to the analysis of gas dynamics.

16.3.5.2 Numerical results

Figure 16.23 shows the pressure distribution in the gas region, at the same time, it shows the material status map in the structural material region at 3 ms on the vertical cross-sectional surface in the axial direction. We can see that the reflection of the shock wave in the air occurs just after its first impact onto the inner surface of the tunnel, and the reflection estimates the high pressure region over 4 MPa, consequently the rise of the pressure on the inner surface of the tunnel causes spall failure (scabbing) in the vicinity of the outer surface of it. The soil was evaluated to be failed in wider region than the concrete at this moment. This fact might be because the HE is located nearer from the soil and the soil has a weaker tensile strength than the reinforced concrete. However, there can be observed no significant deformations or displacements in the structural materials at 3 ms. It takes much more time for light gases to deform the heavy structures significantly, due to their inertia.

The material status maps of the bird’s-eye view depict the aspects of the damage only in the structural material regions at 75 ms, as shown in Fig. 16.24. The inner steel liner is shifted and plotted to the right-hand side so that the material status of the inner surface of the concrete may be observed clearly as well as that of the steel

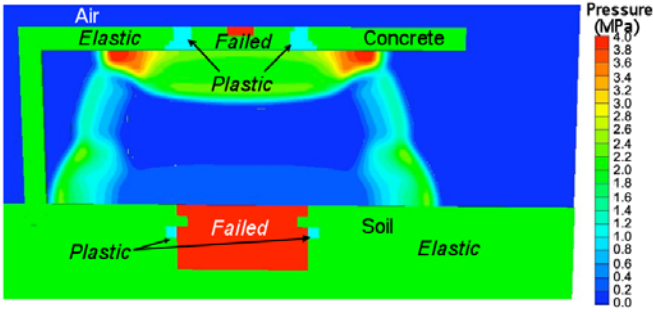


Fig. 16.23 Overview of the numerical results for HE explosion in the tunnel: Pressure in gas, material status in structural components at 3 ms.

liner at the same time. We can see a deformation pattern in the left-hand side part of the steel liner like the deep drawing of the plastic sheet metal forming, and almost all region of the steel liner is judged to be plastic at this moment. The concrete structure has several failed lines in the axial direction and is also characterized to have a number of cracks in circumferential direction near the source of explosion. It indicates serious deformation and displacement at this moment. The failed region in the soil has expanded much wider than at 3 ms, the maximum vertical displacement of the soil surface is 0.23 m deep according to the calculational results at 75 ms.

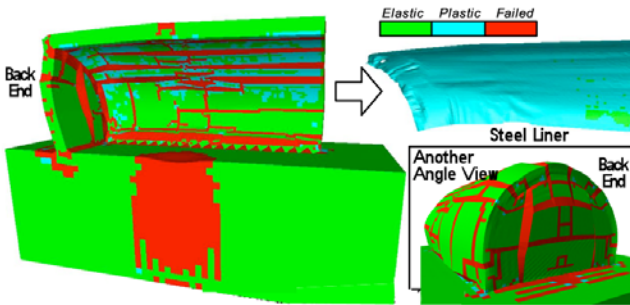


Fig. 16.24 Overview of the numerical results for HE explosion in the tunnel: Material status in structural components at 75 ms.

Another bird's-eye view enables us to comprehend the outer aspect of the deformation and damage of the concrete structure, and the aspect of the damage of the soil surface, as shown in the lower right corner of Fig.16.24. This figure was created to project mirror symmetric elements, as the three-dimensional calculation was performed for only half the system.

16.4 Conclusions

We have demonstrated the availability and effectivity of our proposed three-dimensional numerical simulation method by AUTODYN in order to solve the impact loading and subsequent effect on the concrete and geological material to the severe impulsive loading by the aircraft impact and HE detonation, after the comparison of the results obtained by using same numerical method with basically simplified experimental tests, whereas including an actual test like the F-4 Phantom impact test. All of the calculations in this paper were carried out by using usual personal computers, so that we can say that the current hardware and software for the impact analysis to the complex physical system provide us useful solutions and expressions to understand the phenomena. However, at the same time, we do still have serious problems as shown below:

- 1) Requirement for the computer memory (hardware): even 10^6 times of the current memory is not sufficient always, e.g. the assessment of the blast effect at the far-away positions and high-velocity impact of the vehicles against to more complex structures.
- 2) Requirement for the computing speed (hardware): for the large-scale and the complicated interaction problem.
- 3) Requirement for the automatic mesh refinement (AMR) technique to trace the shock front precisely without dulling (software): even in the very large-scale problem.

We expect that more remarkable progress in both hardware and software will be made in the future.

Acknowledgements The author gratefully acknowledge my colleagues in ITOCHU Techno-Solutions Corporation, especially Dr. Shigeyuki TAMURA for his contribution to the 2-D aircraft impact analyses, and Mr. Toshio OHTA and Dr. Robert RAINSBERGER (XYZ Scientific Applications Inc.) for their efforts to build 3-D geometrical models for the aircraft impact analyses. He also thanks all the contributors to the references [27, 28, 29].

References

1. Zorn NF, et al.: A probabilistic approach for evaluation of load time history of an aircraft impact. Proc. 6th SMiRT Conf., Paris, 1–6 (1981)
2. Muto, K., et al.: Experimental studies on local damage of reinforced concrete structures by the impact deformable missiles part 1–4. Trans. 10th SMiRT, Vol. J, Anaheim, US, 257–299 (1989)
3. Sugano T, Tsubota H, Kasai Y, Koshika N, Ohnuma H, von Riesenmann WA, Bickel DC and Parks MB, Full-scale aircraft impact test for evaluation of impact force, Nuclear Engineering and Design, 140:373–385, 1993.

4. Itoh M, Katayama M, Mitake S, Niwa N, Beppu, M, Ishikawa N, Numerical study on impulsive local damage of reinforced concrete structures by a sophisticated constitutive and failure model. SUSI VI, Cambridge, UK, 569–578 (2000)
5. Tamura, S., Katayama, M., Itoh, M., Mitake, S., Harada, K., Beppu, M., Ishikawa, N.: Numerical study on the local damage of reinforced concrete column caused by a vertical impact load. Proc. of 4th ISIE, Kumamoto, Japan, 737–742 (2001)
6. Riedel, W., Thoma, K., Hiermaier, S., Schmolinske, E.: Penetration of reinforced concrete by BETA-B-500, numerical analysis using a new macroscopic concrete model for hydrocodes, Proc. 9th ISIEMS, Berlin, Germany (1999)
7. Birnbaum, N.K., Cowler, M.S., Itoh, M., Katayama, M., Obata, H.: AUTODYN – An interactive non-linear dynamic analysis program for microcomputer through supercomputers. Trans. 9th SMiRT, Vol. B, Lausanne, Swiss, 401–406 (1987)
8. Quan, X., et al.: Numerical simulation of structural deformation under shock and impact loads using a coupled multi-solver approach. 5th SILOS, Hunan, China (2003)
9. Han, J., Chen, W.F.: A nonuniform hardening plasticity model for concrete materials, *Mechanics of Materials*. 4(4), 283–302 (1985)
10. Yamaguchi, H., Fujimoto, K., Nomura, S.: Stress-strain relationship for concrete under high tri-axial compression part2 rapid loading (in Japanese). Trans. Archit. Inst. Japan, 396: 50–59 (1989)
11. Chen, W.F.: Theory of Concrete Plasticity. In: Constitutive equations for engineering materials Volume 2: Plasticity and Modeling. Elsevier, Amsterdam, pp. 840–849 (1994)
12. Lee, E.L., Hornig, H.C., Kury, J.W.: Adiabatic expansion of high explosive detonation products. UCRL-50422, Lawrence Livermore Nat'l Lab., (1968)
13. Dobratz, B.M., Crawford, P.C. : LLNL explosives handbook: properties of chemical explosives and explosive simulants, UCRL-52997-Chg.2, Lawrence Livermore Nat'l Lab. (1985)
14. McQueen, R.G., Marsh, S.P., Taylor, J.W., Fritz, J.N., Carter, W.J.: The equation of state of solids from shock wave studies. In: R., Kinslow (ed.), *High-Velocity Impact Phenomena*, pp. 294–299, Academic Press, New York (1970)
15. Marsh, S.P., et al.: LASL Shock Hugoniot Data. University of California Press, California (1980); Kohn, B.J.: Compilation of Hugoniot equations of state. AFWL-TR-69-38, Air Force Weapons Lab. (1969); Trunin, R.F.: *Shock Compression of Condensed Materials*. Cambridge University Press, Cambridge (1998); etc.
16. Johnson, G.R., Cook, W.H.: A constitutive model and data for metals subjected to large strains, high strain rates and high temperatures. Proc. 7th ISB, The Hague, The Netherlands, 541–547 (1983)
17. Kraus, D., Roetzer, J., Thoma, K.: The Interaction of High Explosive Detonations with Concrete Structures. EURO-C, Innsbruck, Austria (1994)
18. Morishita, S., Tanaka, H., Ito, T., Yamaguchi, H.: Damage of reinforced concrete slabs subjected to contact detonations (in Japanese). *Struct. Eng. (Jpn. Soc. Civ. Eng.)*, 46 (A), 1787–1797 (2000)
19. Tanaka, H., Tsuji, M.: Effects of reinforcing on damage of reinforced concrete slabs subjected to explosive loading (in Japanese). *Concr. Res. Technol. (Jpn. Concr. Inst.)*, 14 (1), 1–11 (2003)
20. Morishita, S., Tanaka, H., Ito, T.: Study on the Damage due to contact detonations (Part2) (in Japanese). Tec. Rep. 6735, Tec. R& D Inst., Jpn. Def. Agency (2000)
21. Kraus, D., Roetzer, J., Thoma, K.: Effect of high explosive detonations on concrete structures. *Nuc. Eng. Des.*, 150 (2-3), 309–314 (1994)
22. Eible, J., Ockert, J.: Response of concrete structures to shock loading. 7th ISIEMS, Berlin, Germany, 31–38 (1995)
23. TrueGrid User Manual Version 2.1, XYZ Scientific Applications, California (2001)
24. Johnson, G.R., Cook, W.H.: A constitutive model and data for materials subjected to large strain, high strain rates, and high temperatures. Proc. ISB, 541–547 (1983)
25. Famous airplanes of the world (in Japanese), 23, Bunrin-do, Tokyo, (1972)
26. The Boeing Company Web., Boeing 747 Family: Technical, <http://www.boeing.com/commercial/747family/technical.html>.

27. M. Katayama, M. Itoh, S. Tamura, M. Beppu, T. Ohno, 'Numerical Analysis Method for the RC and Geological Structures Subjected to Extreme Loading by Energetic Materials', *International Journal of Impact Engineering*, Vol.34, Issue 9, pp.1546–1561, Sep. 2007.
28. Katayama, M., Itoh, M., Rainsberger, R.: Numerical Simulation of Jumbo Jet Impacting on Thick Concrete Walls – Effects of Reinforcement and Wall Thickness. 2nd Asian Conference on High Pressure Research (ACHPR-2), Nara, Japan (2004)
29. Itoh, M., Katayama, M., R. Rainsberge: Computer simulation of an F-4 Phantom crashing into a reinforced concrete wall. 2nd Int. Conf. Comp. Ballistics, Cordoba, Spain, 207–217 (2005)

Chapter 17

Groundshock Displacements – Experiment and Simulation

Eliahu Racah

Abstract A basic work on groundshock experimental measurement and numerical modeling and simulation is described. The work includes measurement of groundshocks caused by an above ground FAE explosion, soil data collection and interpretation and numerical simulation. An anti-minelfield 'Carpet' system charge was initiated above ground in order to form a FAE cloud detonated on ground surface. Tri-axial seismograms were measured at different ranges.

Reproduction of these measurements in a numerical simulation requires the knowledge of soil properties such as density, elastic moduli, compressibility and strength envelope. In order to determine these properties, soil density measurements, a refraction survey, direct shear tests and pressiometer tests at various ground depths were performed. The soil properties were used in MSC.Dytran numerical simulation. The DYMAT14 soil and crushable foam material model was used to model the soil. At ranges equal to and greater than 30 m the maximum radial and vertical displacements show a very good agreement (less than 0.05 mm difference) between experimental and numerical results. At shorter ranges the experimental results are jumpy and much higher than the numerical results. It is assumed that in the experiment, the close range sensors, being attached to the ground surface by 10 cm long pegs, were released by the explosion effect.

The results of this work show a numerical prediction capability of long range groundshock effects. No soil properties calibration was needed in order to fit numerical and experimental results. Further work is needed to get reliable measurements and numerical validation of groundshocks at close ranges, especially groundshocks caused by buried HE detonations coupled with large crater formation.

Eliahu Racah

RAFAEL Advanced Defense Systems, MANOR Advanced Defense Technologies Division, P.O. Box 2250 (770), Haifa 31021, Israel e-mail: racahe@rafael.co.il

17.1 Introduction

A comprehensive survey of analytical approaches to groundshocks is given in Smith and Hetherington [1]. These approaches constitute the base for groundshock calculation in the popular weapons effects calculation program ConWep¹.

The analytical approaches might give reasonable estimates of ground displacements for engineering design of buried structures, based on simplifying assumptions specified in design manuals like TM-5-855-1 [2]. Estimates of derived quantities like velocities and accelerations are not to be trusted and in order to get a more accurate wave mechanics history a numerical hydrodynamic simulation is needed.

Using numerical simulations for groundshock analysis is easier said than done. Besides the obvious problem of soil properties varying from site to site, there are no well proven models to represent soils stressed by dynamic loadings and there are no well established methods to determine soil properties needed for such models. As will be shown here, even the measurement of groundshock velocity and displacement near an explosion is not an easy task.

The work presented here represents an effort to overcome these problems.

17.2 Experiment

17.2.1 Experimental Setup

The soil at the test site is sandy silt containing some limestone rock fragments. Ground surface is made of approximately 30 cm thick layer of cemented sandy silt.

A fuel-air explosive (FAE) cloud, formed by an anti-minefield 'Carpet' system charge, was detonated on ground surface using two CH6 HE charges, on two opposite sides².

The ground surface velocities and displacements were measured³ using seismic recording gauges of type GEOSONICS SSU2000DK and INSTANTEL MINIMATE PLUS. In the former gauges the sensor (geophone) is connected to the recorder via a 3 m long cable while in latter gauges the sensor is inside the recorder

¹ ConWep: Conventional Weapons Effects Program, Prepared by D.W. Hyde, US Army Waterways Experimental Station, Vicksburg, Mississippi, 2007

² Experiment performed by RAFAEL/MANOR

³ Measurements made by the Geophysical Institute of Israel

box. The geophones (designed to measure earthquakes and not explosions) were attached to the ground surface by 10 cm long pegs.

In order to protect the recorders from explosion effects they were put inside covered bottomless steel boxes, which in their turn, were placed in a dug hole (Figure 17.1). Some of the external geophones were placed on the bottom of the holes but most of them were placed outside the hole, 3 m away. Measurements were taken at 10, 20, 30, 40 and 80 m range.



Fig. 17.1 Protection steel box (uncovered) in a dug hole.

Pressure gauges to measure FAE blast were also placed in the test arena at 5 and 15 m range.

17.2.2 Experimental results

Typical graphs of tri-axial ground particle velocity and displacement vs time are shown in Figure 17.2. The displacements are calculated by integration of the measured velocities. As there is no indication of positive and negative directions, only the magnitudes should be considered. The transversal displacement shown is caused by the interaction of detonation waves in the FAE cloud due to the two detonators.

At all ranges, the geophones placed inside the holes behaved erratically while the geophones placed 3 m away gave reasonable results. It seems that the disturbed soil in the holes prevented firm attachment of the geophone pegs to the ground.

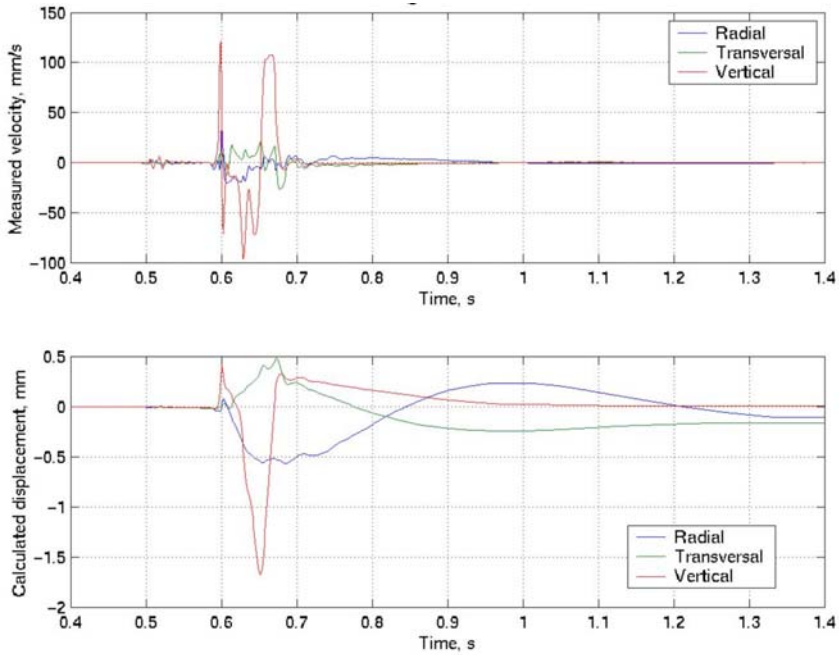


Fig. 17.2 Typical seismic gauge measurements (20 m range).

The maximum ground displacements acquired by the seismic gauges that seemed to work properly are shown in Table 17.1.

Table 17.1 Maximum experimental displacements.

Range [m]	Radial Displacement [mm]	Transversal Displacement [mm]	Vertical Displacement [mm]
10	2	2	> 27
20	0.6	0.5	1.7
30	0.19	0.06	0.21
40	0.14	0.12	0.17
80	0.05	0.02	0.07

17.3 MSC.DYTRAN DYMMAT14 Material Model

The experiment was reproduced by a numerical simulation using MSC.Dytran [3]. The DYMAT14 material model [4] was used to model the soil. The DYMAT14 model is for materials exhibiting compressible plasticity; that is, their behavior is pressure dependent. It can be used to model aspects of the behavior of a wide range of materials that contain voids and crush or compact under pressure. Examples include soils, foams, concrete, metallic honeycombs and wood.

The material model uses isotropic plasticity theory and the response of the material to deviatoric (shear) loading and hydrostatic (pressure) loading is completely uncoupled.

17.3.1 Deviatoric Behavior

The yield surface in principal stress space is a surface of revolution centered about the hydrostatic pressure line. It is defined by $\Phi_S(J_2, p) = 0$

$$\Phi_S(J_2, p) = J_2 - (B_0 + B_1 p + B_2 p^2) \quad (17.1)$$

where p is the pressure, J_2 is the second invariant of the stress deviation tensor S_{ij} :

$$J_2 = \frac{1}{2} S_{ij} S_{ij} \quad (17.2)$$

The coefficients B_0 , B_1 and B_2 can be related to the user-defined constants A_0 and A_1 according to:

$$B_0 = \frac{1}{3} A_0^2; \quad B_1 = \frac{2}{3} A_0 A_1; \quad B_2 = \frac{1}{3} A_1^2 \quad (17.3)$$

The yield surface is cylindrical when A_1 is zero and it has a shape as shown in Figure 17.3 when A_1 is non zero.

The yield stress σ_y can be expressed in terms of the coefficients A_0 and A_1 . The yield stress is defined as:

$$\sigma_y = \sqrt{\frac{3}{2} J_2} \quad \text{where} \quad J_2 = \{J_2 | \Phi_S(J_2, p) = 0\} \quad (17.4)$$

Thus,

$$\sigma_y = \sqrt{3(B_0 + B_1 p + B_2 p^2)} = A_0 + A_1 p \quad (17.5)$$

The cut-off pressure value is calculated as the intersection point of the yield surface with the hydrostat.

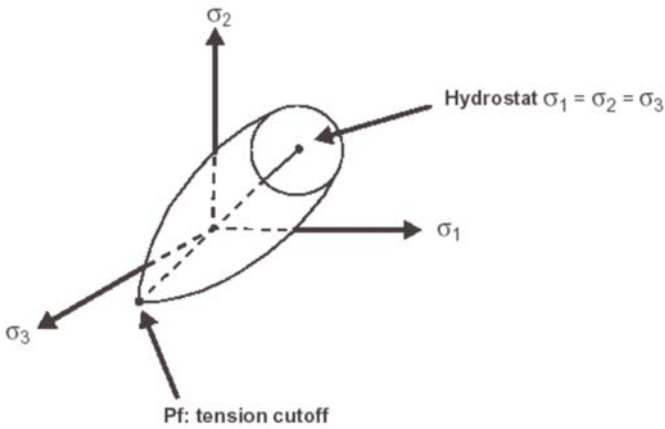


Fig. 17.3 Yield surface with hydrostat.

The open end of the cylinder, cone or paraboloid points into compression and is capped by a plane that is normal to the hydrostat. There is no strain hardening on the yield surface, so the relationship between deviatoric stress σ' and deviatoric strain ϵ' is elastic perfectly plastic as shown in Figure 17.4. The elastic behavior is governed by the shear modulus G .

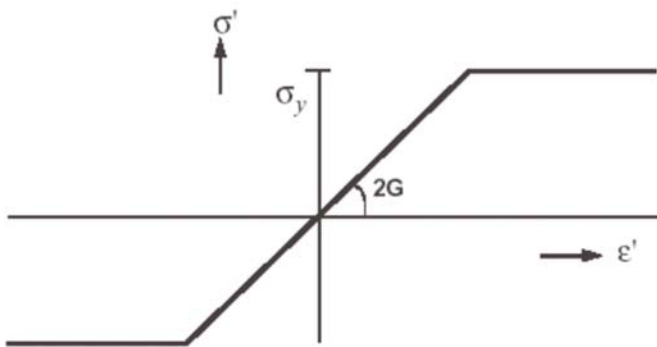


Fig. 17.4 Stress-strain curve.

17.3.2 Hydrostatic Behavior

The hydrostatic component of the loading causes volumetric yielding. This means that the cap on the open end of the yield surface moves along the hydrostat as volumetric yielding occurs. The relationship between hydrostatic pressure and volumetric strain can be of any shape (Figure 17.5).

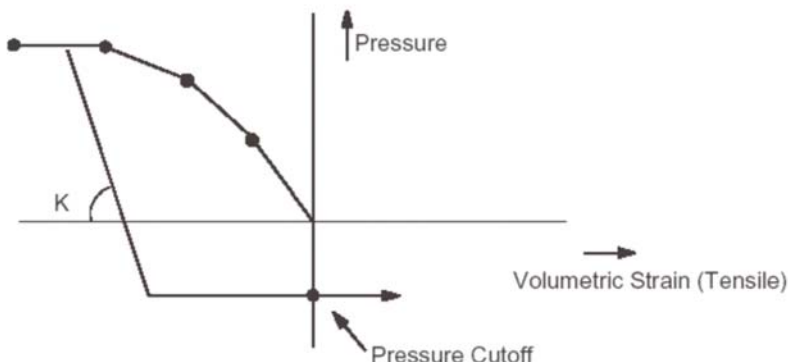


Fig. 17.5 Volumetric yielding.

The curve is defined in terms of the crush factor, $1 - V/V_0$, where V is the current volume and V_0 the initial volume. It is a number between 0 and 1 where 0 indicates no crush and 1 indicates that the material is completely crushed and has 0 volume.

The material unloads elastically from any point on the curve with bulk modulus K . A failure pressure cutoff is specified (Figure 17.6). If the pressure falls below the failure pressure, the element fails and cannot carry tensile loading for the remainder of the analysis. It can still carry compressive loading.

17.4 Soil Data

Soil data had to be collected and interpreted in order to use them in DYMAT14 material model.

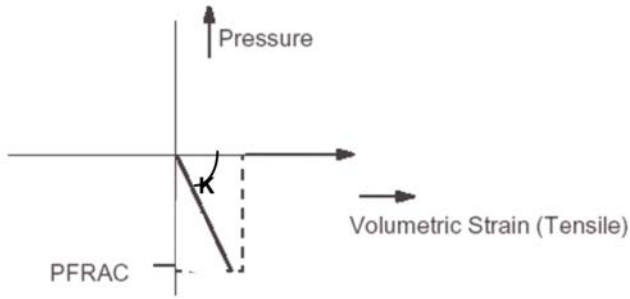


Fig. 17.6 Failure pressure cutoff.

17.4.1 Density

A test pit was dug *in situ*⁴ and disturbed specimens were taken from various depths, up to 7.5 m, in order to measure the density and moisture content using the 'Sand Cone' method (Figure 17.7). The soil density was found to be 2010 kg/m^3 except for the 30 cm surface layer where it was found to be 1660 kg/m^3 . The solid matrix density was found to be 2700 kg/m^3 in the main soil body and 2790 kg/m^3 in the surface layer.



Fig. 17.7 Sampling field density (Sand Cone): sampling (left) and hole volume measurement using a given density sand (right).

⁴ Geotechnical investigation made by the Building and Infrastructure Testing Laboratory, Technion Research and Development Foundation

17.4.2 Refraction Survey and Elastic Moduli

The pressure and shear wave velocities and the bulk and shear moduli in the ground different layers, found by a refraction survey of the test site⁵, are shown in Table 17.2.

Table 17.2 Ground wave velocities and elastic moduli.

Depth [m]	Pressure Wave Velocity [m/s]	Shear Wave Velocity [m/s]	Bulk Modulus [MPa]	Shear Modulus [MPa]
0 – 0.3	710	300	627	149
0.3 – 10	1230	690	1762	957
> 10	1520	800	2955	1286

The wave velocities were measured using seismic recording gauges (see Experimental Setup section above) and the energy sources were a falling hammer for pressure waves and a lateral impact pendulum for shear waves (Figure 17.8).



Fig. 17.8 Refraction survey: pressure waves (left) and shear waves (right).

The shear modulus was calculated using the relation

$$G = \rho v_s^2 \quad (17.6)$$

where v_s is the propagation velocity of shear waves. The bulk modulus was calculated using the relation

$$K = \frac{2G(1 + \nu)}{3(1 - 2\nu)} \quad (17.7)$$

where ν is the Poisson ratio which was calculated using the relation

⁵ Seismic refraction survey made by the Geophysical Institute of Israel

$$v = \frac{(v_p/v_s)^2 - 2}{2(v_p/v_s)^2 - 2} \quad (17.8)$$

where v_p is the propagation velocity of pressure waves.

17.4.3 Pressiometer Tests and Volumetric Crush

Pressiometer tests measure soil volumetric changes vs hydraulic pressure applied in a deep test borehole drilled in the site (Figure 17.9). The test results⁴ are represented by the linear volumetric crush curve

$$p = K^* \left(1 - \frac{V}{V_0} \right) \quad (17.9)$$

where K^* is an engineering bulk modulus equal to 66.5 [MPa].



12 m deep test borehole



Hydraulic pressure device



Pressure and volumetric change gauges

Fig. 17.9 Pressiometer test.

17.4.4 Direct Shear Tests and Yield Surface

Soil cohesion strength, c , and angle of friction, ϕ , were measured⁴ by direct shear tests using a double shear box instrument (Figure 17.10). The yield surface (eq. (17.5)) coefficients A_0 and A_1 were calculated by the following equations ([5], [6]):

$$A_0 = \frac{6c \cos \phi}{3 - \sin \phi} \tag{17.10}$$

$$A_1 = \frac{6 \sin \phi}{3 - \sin \phi} \tag{17.11}$$

The numerical values are given in table 17.3.

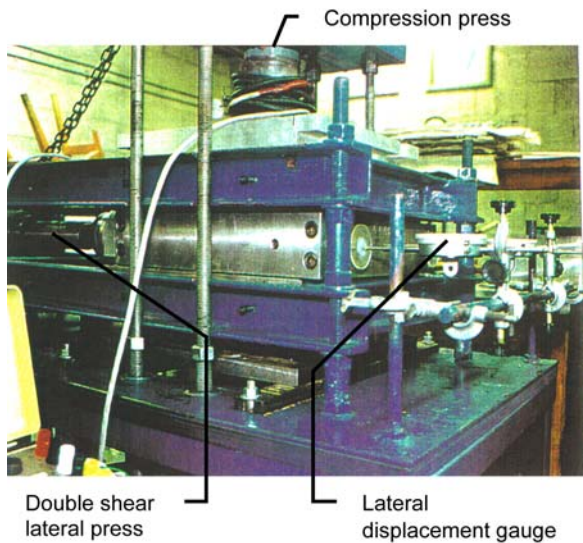


Fig. 17.10 Direct shear test.

Table 17.3 Yield surface coefficients.

Depth [m]	Cohesion Strength [MPa]	Angle of Friction [°]	A_0 [MPa]	A_1 [-]
0 – 0.3	0.04	38	0.08	1.55
> 0.3	0.12	58	0.18	2.36

17.5 Simulation

17.5.1 Simulation Setup

The simulation setup is shown in Figure 17.11. Two orthogonal vertical symmetry planes are used. The detonation of the FAE cloud in air is modeled using an Eulerian mesh while the ground is modeled using a Lagrangian mesh. The two meshes, representing a quarter space of 150X150X95 m, are coupled.

The Eulerian mesh contains 100,352 cells. Cell size in the FAE cloud region is 0.2 m and it is growing from there in all directions. The Lagrangian mesh contains 81,536 cells. Cell size in the FAE cloud region is 0.2 m in the horizontal directions and 0.15 m in the vertical direction, and it is growing from there in all directions.

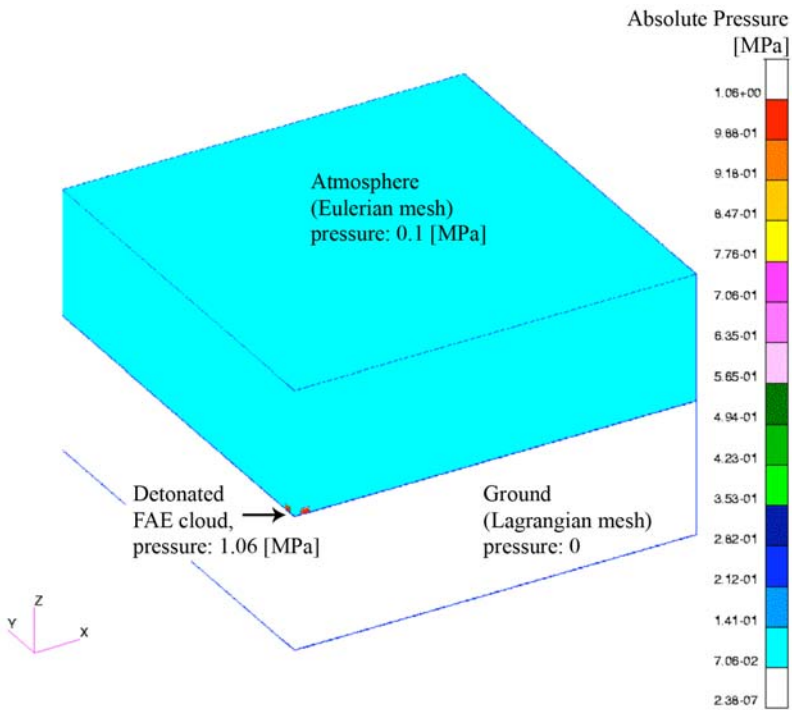


Fig. 17.11 Simulation Setup.

Air is modeled as an ideal gas having atmospheric pressure. The toroidal fully detonated FAE cloud is modeled as an ideal gas with a pressure of 1.06 MPa. This is about half the real detonation pressure achieved by detonating the cloud at the lo-

cation of the detonators. The latter method was avoided in order to allow the ground Lagrangian mesh to adjust itself to the air atmospheric pressure. As a result, no transversal waves were produced in the simulation.

The ground three layers are shown in Figure 17.12. The calculated sound speed for each layer is identical to the sound speed found experimentally (Table 17.2).

17.5.2 Simulation Results and Discussion

Simulation results showed that plastic deformation of the ground was confined to the FAE cloud region. Outside this relatively small region the ground waves are in the elastic range (see Figure 17.13).

Figure 17.14 shows a characteristic comparison between graphs obtained in the experiment and graphs calculated by the simulation.

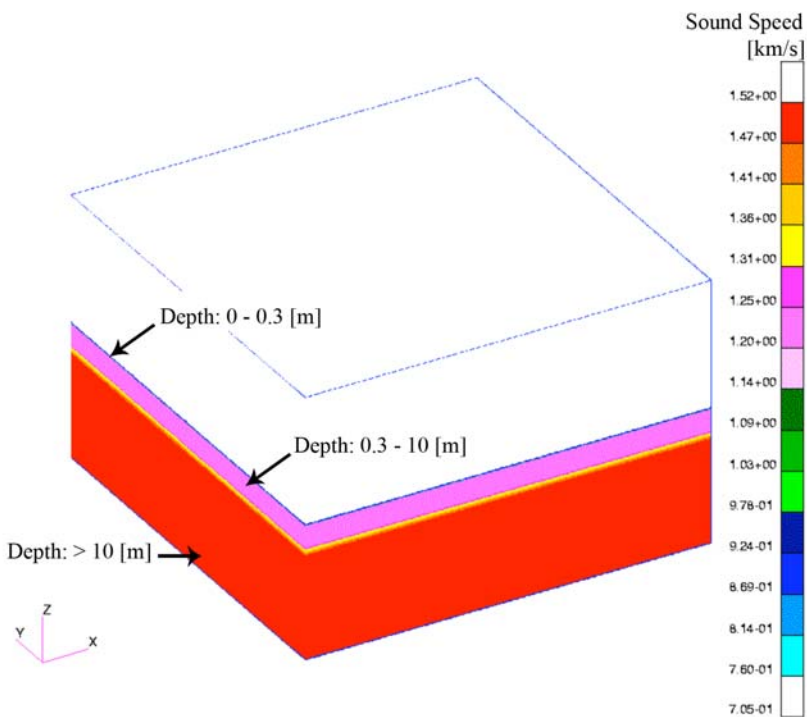


Fig. 17.12 Ground Layers.

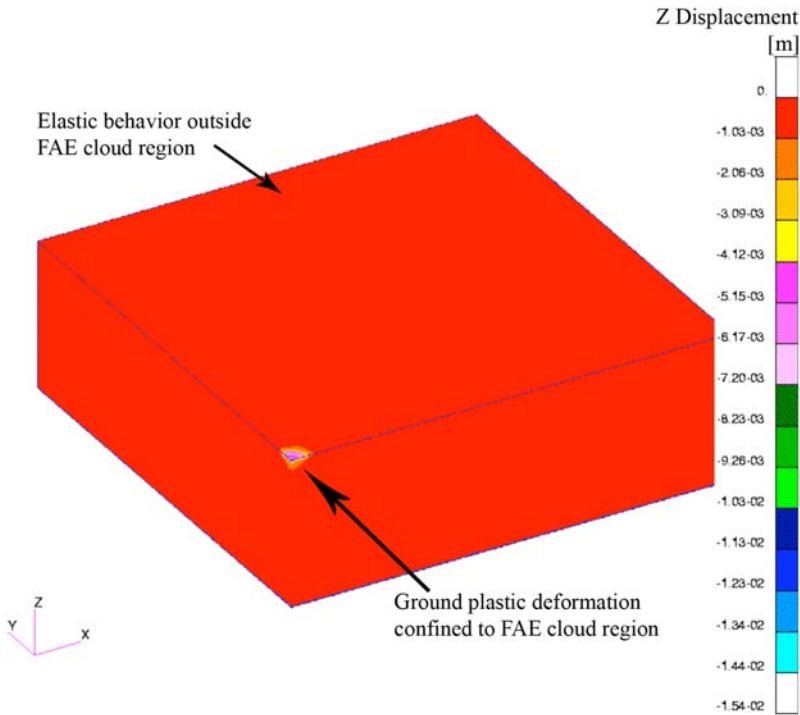


Fig. 17.13 Vertical displacement after 500 ms.

The following points are worth noting in Figure 17.14.

- The vertical directions in the experimental graphs are plotted upside down.
- The vertical displacement reference line was lowered by 0.14 mm due to the simulation delay in adjusting the ground pressure to the atmospheric pressure.
- The experimental graphs are sampled every millisecond while the calculation step in the simulation is at least ten fold shorter. This partly explains the relative noisiness of the simulation graphs.
- The simulation model doesn't include an attenuation mechanism that can represent the inter-granular friction in real soils. Therefore, the simulation is invalid beyond 100 ms from the first large oscillation.

Considering all the above reservations, it can be seen in Figure 17.14 that the first displacement oscillations in both experimental and simulation graphs are very similar, both qualitatively and quantitatively.

Maximum ground displacements obtained in the experiment and the simulation are compared in Figure 17.15. It can be seen that at ranges of 30 m and above, the maximum radial and vertical displacements show a similar behavior of moderate gradient, in both experiment and simulation, with a quantitative difference of less

than 0.05 mm. At ranges shorter than 30 m, the calculated graphs behave moderately as in the longer ranges while the experimental graphs rise to order of magnitude higher values.

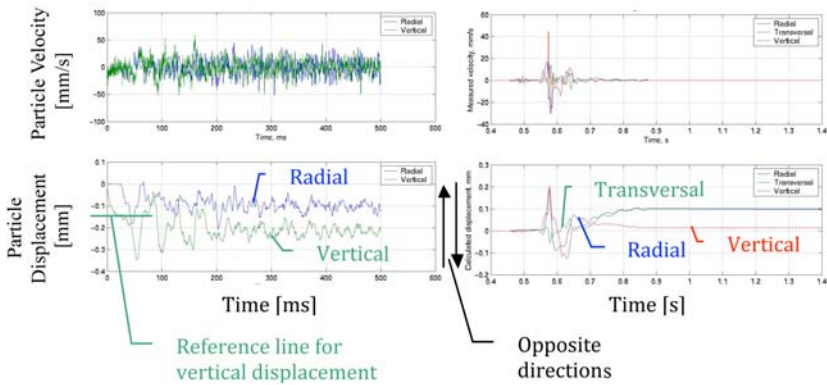


Fig. 17.14 Comparison between experiment (right) and simulation (left) at 30 m range.

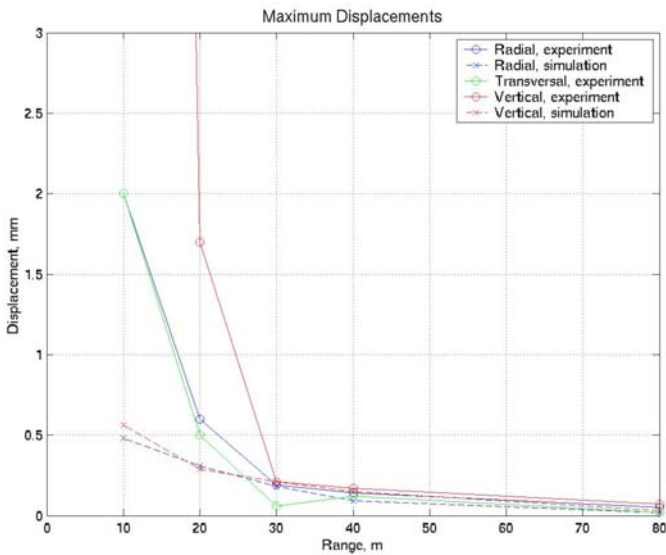


Fig. 17.15 Maximum ground displacements.

There is no physical explanation to this rise in the experimental graphs but to assume that the geophones 10 cm long pegs were too short for attaching them firmly to the ground at short ranges. This resulted in a jumpy movement, independent of the ground movement.

17.6 Conclusion

A capability of long range measurement and numerical prediction of groundshocks was developed and proved, showing very good accuracy. Soil properties measurement methods used didn't require any calibration to fit numerical and experimental results.

Further work is needed to get reliable measurements and numerical validation of groundshocks at close ranges, especially groundshocks caused by buried HE detonations coupled with large crater formation.

Acknowledgements The author is indebted to all the many people who took part in this work, the list of which is too long to be written here. Special thanks are due to Mr. Eitan Abudi of RAFAEL/MANOR, Dr. Uri Friezlander of the Geophysical Institute of Israel and Mr. Eran David of David Consultants.

References

1. Smith PD, Hetherington JG, Blast and Ballistic Loading of Structures, Butterworth-Heinemann, Oxford, England, 1994
2. Fundamentals of Protective Design for Conventional Weapons, US Army Technical Manual No. 855-1, Headquarters, Department of the Army, Washington DC, 1986
3. MSC.Dytran User's Guide, Version 2002, MSC.Software Corporation, Santa Ana, CA, November 2001
4. MSC.Dytran Theory Manual, Version 2002, MSC.Software Corporation, Santa Ana, CA, November 2001
5. Dr. Alexander Puzrin, Faculty of Civil Engineering, Technion IIT, Haifa, Israel, personal communication
6. Desai CS, Siriwardane HJ, Constitutive Laws for Engineering Materials, Prentice-Hall, Inc., Englewood Cliffs, NJ, 1984.

Part III
Numerical Simulation of Hypervelocity
Impact Effects

Chapter 18

Hypervelocity Impact Induced Shock Waves and Related Equations of State

Stefan Hiermaier

18.1 Introduction

Precondition for stable shock wave propagation is a convex Equation of State (EoS) in terms of pressure and volume. The first mathematical proof for the existence and dependence of shock waves on that non-linearity was derived by Bethe [1]. In this introductory chapter, a more phenomenological approach to derive conditions for shock wave formation will be given along with some examples for Equations of State used in hydrocodes.

The other contributions in this third part of the book deal with the phenomena observed during hypervelocity impact (HVI) on space vehicle structures and on geological materials. A well known general problem in the simulation of shock waves related to the numerical discretization is the formation of unphysical oscillations. Apart from specific shock related types of discretizations, e.g. Godunov methods, any other existing type can be adjusted via the so-called artificial viscosity addressed in the related chapter 19 of this part of the book. The specific need for meshfree discretizations which, in addition, allow for the simulation of HVI-related fragment cloud formation is reflected in the review chapter 20 on Smooth Particle Hydrodynamics (SPH). The chapters 21 and 22 deal with the analytical and numerical methodologies for risk analyses on space vehicles related to hypervelocity impact. The final chapter 23 deals with the numerical simulation of cratering processes resulting from both meteorite impact and nuclear explosions.

Stefan Hiermaier

Fraunhofer-Institute für Kurzzeitdynamik, Ernst-Mach-Institute, Eckerstr. 4, 79104, Freiburg, Germany e-mail: hiermaier@emi.fraunhofer.de

18.2 Shock Wave Formation and the Necessity of Adequate Equations of State

18.2.1 Wave Dispersion due to Nonlinear Compressive Material Characteristics

The origin of shock waves experienced in gaseous media upon the transit of supersonic objects was identified as the superposition of waves emitted from the object (Doppler [2], Mach and Salcher [3]). Obviously, another physical reason must be present when shock waves are initiated under impact loads in solid matter. Experience shows that external dynamic compressive loads, e.g. initiated by impact or blast, can possibly cause very strong waves with extremely short rise times inside solid bodies. Again, superposition of different wave components is responsible for the steepening of the wave front and ultimately leading to shock waves. However, the corresponding wave superposition now takes place as a consequence of a specific type of *dispersion*, i.e. a change of sound speed with increasing pressure level. This type of dispersion arises in media with nonlinear compressive behaviour and it is a precondition for the shock formation in these media.

Physical reason for the mentioned type of dispersion is the relation between wave speed c and density ρ or volume V , respectively. Basically, the adiabatic speed of sound c in an arbitrary medium is defined by:

$$c^2 = \left. \frac{\partial p}{\partial \rho} \right|_s = \left. \frac{\partial p}{\partial V} \right|_s \frac{\partial V}{\partial \rho} \Big|_s = \left. \frac{\partial p}{\partial V} \right|_s \frac{\partial (\rho^{-1})}{\partial \rho} \Big|_s = \frac{-1}{\rho^2} \left. \frac{\partial p}{\partial V} \right|_s \quad (18.1)$$

Thus, the wave propagation speed c is proportional to the square root of the pressure-volume gradient. In other words, compression of a material with a nonlinear compressive characteristic, e.g. as illustrated in figure 18.1, results in strongly varying wave speeds depending on the compression state. Starting the compression from an initial condition described by volume V_0 , density ρ_0 and pressure $p_0 = 0$ an elastic pressure wave will travel into the material at a speed of

$$c_0 = \frac{1}{\rho_0^2} \sqrt{- \left. \frac{\partial p}{\partial V} \right|_0}. \quad (18.2)$$

As the material is further compressed into the plastic regime, we find a major change in the slope of the governing $p - V$ -characteristic. Consequently, related pressure waves are now propagating slower. From state $p_2 - V_2$ onwards, however, the slope is increasing again and, thus, leading to faster wave speeds.

The related processes of a steepening wave front, ultimately forming a shock wave, is illustrated in figure 18.2. A dynamically applied load $F(t)$ initiates pressure waves in a material with a nonlinear pressure-volume characteristic $p(V)$. That

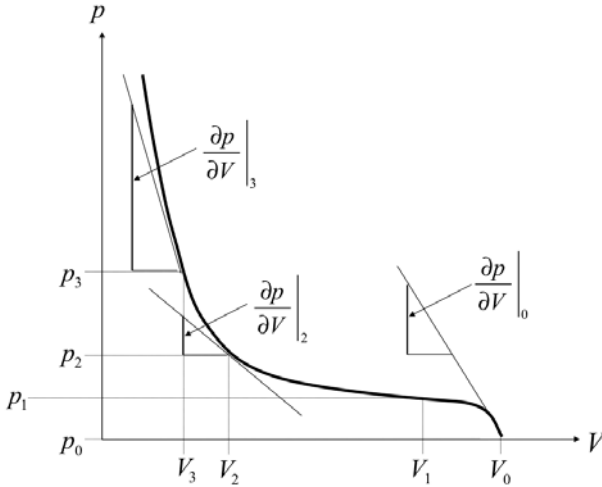


Fig. 18.1 Nonlinear compressive $p - V$ -characteristic of a material.

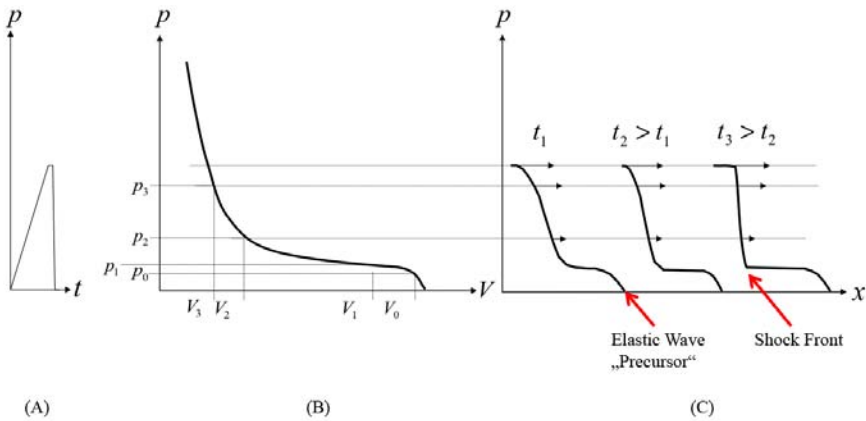


Fig. 18.2 Shock wave formation due to dispersion: (A) Imposed load history. (B) Nonlinear compressive material behaviour. (C) Propagation of elastic and plastic wave components in the loaded material.

nonlinearity leads to differences in the propagation speed of individual wave packages according to their pressure amplitude:

- Initially, elastic wave packages propagate at the elastic wave speed c_0 , already defined in equation 18.2.

- Wave packages originating from pressure levels around p_1 propagate much slower, causing the elastic wave components to run ahead as a so-called 'precursor'.
- From pressure levels equal or higher than p_2 onwards, the related wave packages propagate at ever increasing speeds.
- The increased wave speed leads to a steepening plastic wave front since wave packages resulting from higher pressure levels overtake others resulting from earlier initiated low-pressure states.
- Ultimately, a shock wave is formed.

In the light of these phenomenological observations and with a mathematical description for the slopes in the $p - V$ diagram of Figure 18.1, conditions for the formation of shock waves can be formulated as:

$$\frac{\partial p}{\partial V} < 0 \quad \text{and} \quad (18.3)$$

$$\frac{\partial^2 p}{\partial V^2} > 0 \quad (18.4)$$

18.2.2 Requirements to an EoS with Respect to Shock Formation

Obviously, the compression curve $p(V)$ can only cover an isothermal part of the thermodynamic conditions that a solid material may undergo under dynamic deformations. Therefore, criteria for the driving dispersion effect need to be found with respect to the shape of the *state surfaces* $p(V, e)$. Whether dispersion occurs or not, depends on the shape of the state surfaces and thus on the Equation of State describing it. A first generalized thermodynamic description of conditions for a stable shock wave propagation in media with an arbitrary Equation of State was established in 1942 by Hans Bethe [1]. Investigating the behaviour of pressure, internal energy, volume and entropy for various classes of solid, liquid and gaseous matter, Bethe established two conditions for the existence and one for the stability of shock waves. The two sufficient criteria for its existence are:

$$\left. \frac{\partial^2 p}{\partial V^2} \right|_S > 0 \quad (18.5)$$

and

$$\Gamma = V \left. \frac{\partial p}{\partial e} \right|_V > -2 \quad (18.6)$$

where Γ denotes the Grüneisen parameter. In addition, Bethe found the inequality

$$\left. \frac{\partial p}{\partial V} \right|_e < 0 \quad (18.7)$$

as criterion for a shock wave to be stable against break-up .

With respect to an isothermal case reflected in a compression curve, the intuitively derived equations (18.3) and (18.4), are equivalent with conditions (18.5) and (18.7).

How do the conditions (18.5) - (18.7) relate to the mentioned type of dispersion? There is a single thermodynamic parameter \mathcal{G} called *fundamental derivative*¹ that describes the link uniquely:

$$\mathcal{G} = -\frac{1}{2} V \frac{\frac{\partial^3 e}{\partial V^3} \Big|_S}{\frac{\partial^2 e}{\partial V^2} \Big|_S} = -\frac{1}{2} V \frac{\frac{\partial^2 p}{\partial V^2} \Big|_S}{\frac{\partial p}{\partial V} \Big|_S} \quad (18.8)$$

Using the sound speed c in the medium ahead of a shock wave defined by:

$$c^2 = -V^2 \frac{\partial p}{\partial V} \Big|_S \quad (18.9)$$

the fundamental derivative

$$\mathcal{G} = \frac{V^3}{2c^2} \frac{\partial^2 p}{\partial V^2} \Big|_S = 1 + \frac{\rho}{c} \frac{\partial c}{\partial \rho} \Big|_S \quad (18.10)$$

quantifies more obviously the rate of change in sound speed with density as well as the curvature of isentropes in the $p - V$ plane and, thus, links the dispersion to the convex shape of the Equation of State.

18.3 Equations of State for the Simulations of Shock Processes

18.3.1 Complete versus Incomplete Equations of State

Basically, any formulation of hydrostatic pressure p depending on density ρ and specific internal energy e , or equivalently on volume V and temperature T , defines an Equation of State (EoS):

$$p = p(\rho, e) = p(V, T) = p(V, e) \quad (18.11)$$

However, (18.11) does not cover heat conduction and other effects that would require temperature. Equations of State of that kind are therefore often called *incomplete EoS*. Complete formulations, on the other hand, take into account temperature

¹ The fundamental derivative, also known as *Duhem parameter* was introduced by Thompson [5]

T and specific entropy s and are therefore formulated using the specific Helmholtz free energy ψ as:

$$\psi(V, T) = e - T s \quad (18.12)$$

From the Gibbs fundamental equation

$$dE = dQ - dW \leq T dS - p dV \quad (18.13)$$

and for the reversible limit case we find:

$$de = T ds - p dV \quad (18.14)$$

and thus

$$p(V, T) = -\frac{\partial \psi}{\partial V} \quad (18.15)$$

and

$$s(V, T) = -\frac{\partial \psi}{\partial T} \quad (18.16)$$

for a complete Equation of State. Generally, the applications addressed in the context of this book are not affected by heat conduction effects and, thus, incomplete Equations of State can be used. For detailed derivations of complete EoS, interested readers may be referred to Menikoff [23] to find examples of Helmholtz free energies and derived equations of state. As an example for complete Equations of State, porous materials will be described with the Menikoff-Kober EoS in section 18.3.3.

An exceptional impact processes that demands for the application of complete Equations of State is given in case of large meteorite impacts on geological structures. The term 'large' indicates meteorite sizes of one to ten kilometers in diameter. The huge dimensions of both impactor, i.e. the meteorite, and target, i.e. for example earth, extends the time interval between shock initiation and arrival of the first release wave to several seconds. Under such conditions, we find combinations of extremely high shock pressures between 10 and 100 [GPa] with shock pressure durations in the regime of seconds. Hence, heat conduction processes find enough time to take place in the Hugoniot states. This makes the formulation of complete Equations of State inevitable.

Geologist investigating the cratering processes during large meteorite impact by numerical simulation use and improve related complete Equations of State, e.g. the ANEOS equation developed by Thompson et al. [24]. An important adjustment of ANEOS – originally limited to monatomic gases – to realistic cratering processes was recently provided by Melosh [25].

18.3.2 Mie-Grüneisen Shock EoS

A very often found incomplete nonlinear EoS is the Mie-Grüneisen, or, Shock EoS. It uses the experimentally derived Hugoniot pressures and energies (p_H, e_H) as reference states together with the Grüneisen assumption

$$\Gamma = V \left. \frac{\partial p}{\partial e} \right|_V \quad (18.17)$$

to calculate pressures p from given volume V and specific internal energy e as²:

$$p(V, e) = p_H - \frac{\Gamma(V)}{V} (e - e_H) \quad (18.18)$$

An important part of the experimental derivation of the Hugoniot states is the description of a relation between shock velocities v_S and particle velocities v_1 . For example, a linear type of such a relation

$$v_S = c_0 + S v_1 \quad (18.19)$$

using the two parameters c_0 and S leads to a description of the Hugoniot states by

$$p_H = p_0 + \rho_0 c_0^2 \frac{\eta}{(1 - S \eta)^2} \quad (18.20)$$

$$e_H = e_0 + \frac{\eta}{\rho_0} p_H - \frac{\eta^2}{2} \frac{c_0^2}{(1 - S \eta)^2} \quad (18.21)$$

with

$$\eta = 1 - \frac{\rho_0}{\rho} \quad (18.22)$$

Hence, besides the Hugoniot condition that can be experimentally characterized using $v_S - v_1$ data of the material, the Grüneisen Γ is needed as final parameter to establish the Equation of State. Some further thermodynamical relations can be useful to identify data for the Grüneisen parameter:

$$\Gamma = V \left. \frac{\partial p}{\partial e} \right|_V = \frac{V}{c_V} \left. \frac{\partial p}{\partial T} \right|_V = -\frac{V}{c_V} \left. \frac{\partial p}{\partial V} \right|_T \left. \frac{\partial V}{\partial T} \right|_P = -\frac{V}{c_P} \left. \frac{\partial p}{\partial V} \right|_S \left. \frac{\partial V}{\partial T} \right|_P \quad (18.23)$$

with the specific heats at constant volume and pressure c_V and c_P , respectively. In that context, Meyers [7] points out that the term $\left. \frac{1}{V} \frac{\partial V}{\partial T} \right|_P$ is equal to the volumetric thermal expansion 3α and that $-\left. \frac{1}{V} \frac{\partial V}{\partial P} \right|_T$ represents the isothermal compressibility K . Thus, Γ can be expressed by

² See Hiermaier [6] for a detailed introduction to the theories leading to the Mie-Grüneisen EoS.

$$\Gamma = V \frac{3\alpha}{c_V K} \quad (18.24)$$

Further ways to calculate the Grüneisen constant were developed by Slater [8] or Dugdale and MacDonald [9]. Detailed discussions on the related theories are to be found in Rice et al. [10] and, more recently, including a new own method in Nagayama et al. [11].

To estimate the accuracy and limitations of the Mie-Grüneisen EoS (18.18), it can alternatively be understood as isochoric extrapolation off the shock Hugoniot formulated as Taylor series developed around the Hugoniot pressure p_H :

$$p(V, e) = p_H - \left(\frac{\partial p}{\partial e} \right)_V (e - e_H) + \dots \approx p_H - \frac{\Gamma}{V} (e - e_H) \quad (18.25)$$

Equation (18.25) explains the assumption needed to establish the Mie-Grüneisen EoS and, thus, helps to assess the quality and limitations of it. Basically, it is a first order approximation of the state surface in the neighbourhood of the measured Hugoniot curve along an isochoric path. Another important limitation of the Mie-Grüneisen EoS is that it is not capable of phase changes.

18.3.3 Equations of State for Porous Materials

There is a wide spectrum of materials with an inherent porosity which may be either intentionally inserted or present to a certain unavoidable minimum due to production reasons. Examples for deliberately produced porosity are cellular materials used to provide thermal, acoustic or shock damping effects with a particular structural stiffness at low specific weight. Others, e.g. polymers, concrete or energetic materials, dispose of some level of porosity that is not always desirable and needs to be reflected in material characterization.

Dynamic deformation behaviour of porous and granular materials is most often investigated regarding two particular aspects:

- The energy dissipation effect of porous materials like polymeric and metallic foams or concrete is one focus. Propagation of acoustic as well as shock waves is damped through irreversible deformation of cells. Kinetic energy of impact and crash processes, ranging from low velocity head impact to hypervelocity impact of micro-meteoroids on space vehicle structures, is transformed into plastic strain and failure. The porosity and the stiffness of the matrix material determine the stress level at which the structure deforms and, thus, for example the deceleration of an impacting body.

- Insensitivity as well as the detonation characteristics of plastic bonded energetic materials is influenced by the porosity. Here, the shock velocities and the strain localization due to the porous nature are of interest.

Energetic materials are not topic of this book. Readers interested in the dynamic deformation behaviour of explosives are for example referred to Davison et al. [12].

Characteristic Deformation Phases in Porous Materials

The complexity in modelling porosity under shock loading conditions arises from the unusual compaction behaviour of porous materials including distinct variations in the materials' stiffnesses in three phases:

- Typically, a first deformation phase of porous materials can be described as *elastic compression* of the matrix material. The stiffness is defined by the properties of the matrix material.
- Depending on the type of the matrix material, it is followed by a second phase of *failure and collapse of pores* which can occur as ductile plastic deformation or as brittle fragmentation and includes stability aspects on the scale of the pore wall dimensions. Characteristic for the macroscopic aspect of this deformation stadium is very little stiffness and subsequent deformation at a more or less constant stress level. Hyperelastic matrix materials do not show this phase.
- A third and final deformation stadium, called *compaction phase*, is observed when the pores are all compressed. The stiffness changes again drastically towards the matrix material's elastic-plastic compressive properties.

If the sound speed in the matrix material is c_M and c_P is the sound speed of the porous material, the bulk modulus K_P of the porous material in the first elastic compaction phase can be described via the sound speeds:

$$K_P = \rho \frac{dp}{d\rho} = \rho c_P^2 \quad (18.26)$$

In the third phase, the bulk modulus corresponds to the bulk modulus of the matrix material.

The transition between phase one and three can be described in terms of the material properties of the matrix material using a porosity parameter α :

$$\alpha = \frac{\rho_M}{\rho} = \frac{V}{V_M} \quad (18.27)$$

that relates the matrix and, thus, fully compacted density ρ_M to the current density ρ of the porous material. Often, the inverse of α is used to relate the specific volume of the matrix material V_M at zero pressure to the current specific volume of the porous material. In the context of the following section we will denote that alternative measure of porosity by ϕ :

$$\phi = \frac{V_M}{V} = \frac{\rho}{\rho_M} = \alpha^{-1} \quad (18.28)$$

The choice of ϕ over α was motivated through the use of specific volumes and the preferred variation of ϕ between zero for a non-existing matrix, i.e. a vacuum, and unity for a fully dense material. A preference that seems indeed more convenient than the variation from infinity to unity.

With the porosity of the undeformed material $\alpha_P = \rho_M/\rho_P$ the current sound speed at an arbitrary compression state can be described through:

$$c = c_P + (c_M - c_P) \left(\frac{\alpha - \alpha_P}{1 - \alpha_P} \right) \quad (18.29)$$

and, thus, the current stiffness of the partly compacted material accordingly.

Influence of Porosity on the Hugoniot State

A characteristic phenomenon observed when porous materials are shock loaded is the convex shape of the $v_S - v_1$ curves and the related deflection of the Hugoniot curve:

Porosity in solids leads to a typical decrease in the observed shock velocity v_S with increasing v_1 for low particle velocities. It is the dispersive nature of the propagated stress waves in the regime just above the compressive strength of porous materials that leads to the observed phenomenon. At a certain v_1 value the shock velocity shows a minimum and starts to rise again with convergence to the slope of the solid materials $v_S - v_1$ characteristic. Riedel and Kawai [13] investigated the phenomenon in mortar by experimental and numerical means. Their proposed stress gauge instrumentation along with the theoretical distinctions of stress waves proposed by Fowles and Williams [14] seems to be a promising methodology for a better understanding of shock waves in inhomogeneous materials.

A porous material with very reproducible mechanical properties is achieved when a matrix is filled with hollow spheres. As an example for that kind of cellular material, epoxy resin filled with glass micro-spheres was investigated by Weirick [15]. Figure 18.3 compares the findings of Weirick with the $v_S - v_1$ characteristic of mortar reported by Riedel [16]. Hugoniot pressures of the micro-sphere filled epoxy material and of the energetic material PBX-9407 as listed in Marsh [17] are given in Figure 18.4. The graphs reflect the aforementioned characteristics of shock loaded porous materials.

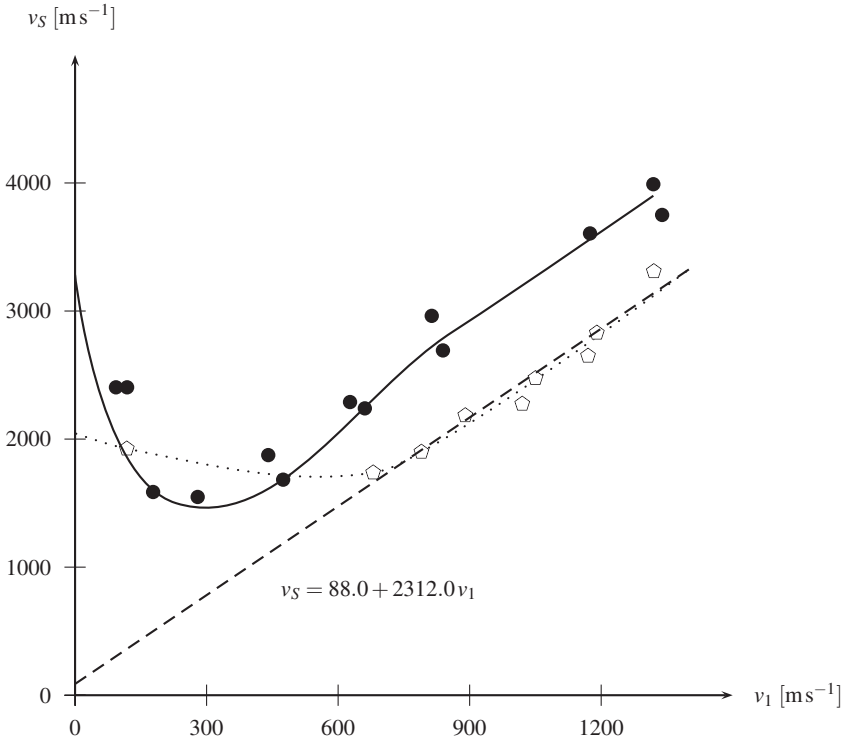


Fig. 18.3 Shock-particle velocity results for Epoxy resin (dashed line) and Epoxy filled to 42 volume percent with glass micro-balloons (◇) both investigated by Weirick [15] compared to mortar data (●) provided by Riedel [16].

Herrmann’s $p - \alpha$ Equation of State

Deformation behaviour of porous materials has long been a topic of scientific investigations. First comprehensive description of shock loaded porous materials including a formulation for a related Equation of State were derived more than forty years ago. A first formulation of an EOS was proposed by Herrmann [18]. In order to relate the porous materials’ EOS to the one of the solid matrix material, Herrmann invented a porosity and energy dependent formulation, called $p - \alpha$ Equation of State:

$$p = p\left(\frac{V}{\alpha}, e\right) = p(\phi V, e) \tag{18.30}$$

The distinction of (18.30) to other equations of state is the porosity in the argument of the pressure function. Thus, any existing EOS can be used to replace the volume dependency by the V/α -dependency.

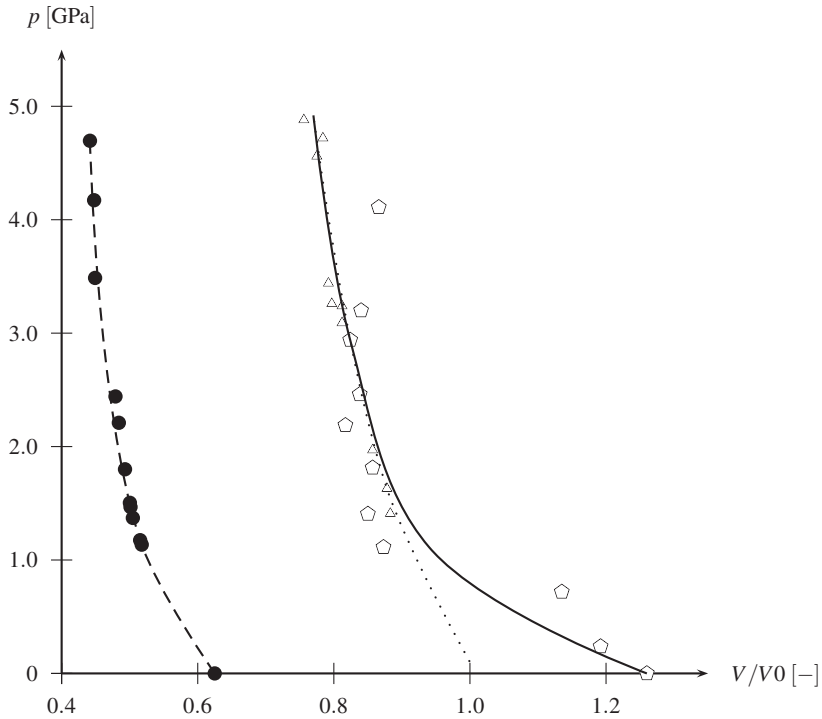


Fig. 18.4 Hugoniot states for pure Epoxy resin (\triangle , dotted), Epoxy filled to 42 volume percent with glass microspheres (\diamond , solid) both Weirick [15]), and PBX-9407 (\bullet , dashed) according to data from Marsh [17].

Equation (18.30) was adjusted by Carrol and Holt [19] to average the pressure in the matrix material over the total porous volume:

$$p = \frac{1}{\alpha} p\left(\frac{V}{\alpha}, e\right) = \phi p(\phi V, e) \tag{18.31}$$

The porosity is now a thermodynamic state variable depending on pressure and internal energy:

$$\alpha = \alpha(p, e) \tag{18.32}$$

where the energy dependence is mostly not formulated explicitly due to the lack of data. This gap is usually closed to a sufficient degree of accuracy through an implicit energy dependence carried in the Hugoniot reference curve referred to in the solid materials EOS. This approach is valid as long as no additional energy source terms are in the porous material. Swegle [20] points out that an important advantage of (18.31) over (18.30) is that it avoids unphysically larger bulk sound speeds in the

porous material than in the matrix material.

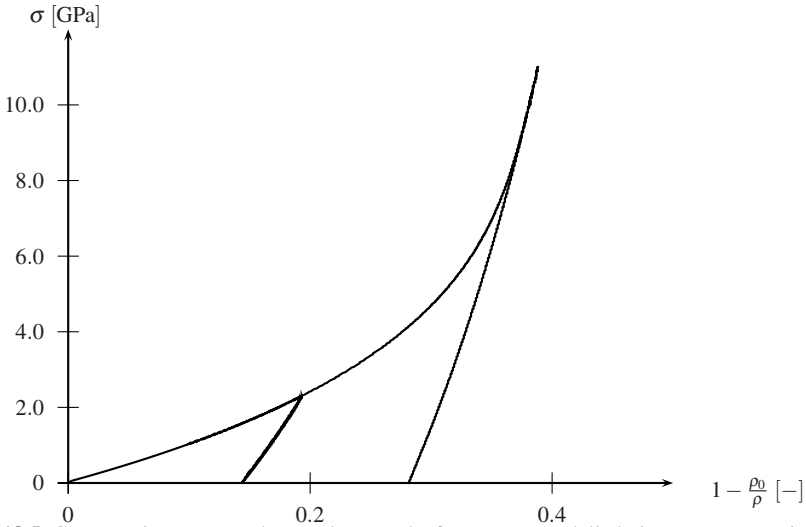


Fig. 18.5 Compression curve and two release paths for cement modelled via a $p - \alpha$ Equation of State (Data courtesy of Riedel [16]).

A possible description of the porosity parameter, amongst various other formulations, was proposed by Butcher and Karnes [21] for porous iron:

$$\alpha = 1 + (\alpha_p - 1) \left(\frac{p_C - p}{p_C - p_e} \right)^n \tag{18.33}$$

with a parameter n set to $n = 2$ in [21]. The pressure at initial pore collapse p_e and pressure at the beginning of the compaction phase, denoted by p_C , are further parameters to be defined experimentally. The implicit coupling of pressure, volume, internal energy and porosity demands for an iterative solution of the equations in numerical implementations.

Wünnemann et al. [26] recently proposed the so-called $\epsilon - \alpha$ -model implemented in the iSALE code as an extension to the $p - \alpha$ Equation of State for porous geological materials under hypervelocity impact.

Menikoff-Kober Porous Equation of State

A thermodynamically consistent formulation of a complete Equation of State for porous materials was introduced by Menikoff and Kober [22] via a decomposition

of the Helmholtz potential into a contribution from the pure solid material ψ_s and potential energy ψ_p associated with the porosity:

$$\psi(V, T, \phi) = \psi_s(\phi V, T) + \psi_p(\phi) \quad (18.34)$$

where the porosity is here described via the solid volume fraction $\phi = V_M/V = \rho/\rho_M = \alpha^{-1}$. Alternatively to (18.33), compaction laws for porous materials can also be formulated using ϕ , a parameter p_c denoting the pressure at full compaction, i.e. closure of all pores, and an initial porosity $1 - \phi_0$:

$$\phi_{eq}(pV) = 1 - (1 - \phi_0) e^{-\frac{pV - p_0V_0}{p_cV_0}} \quad (18.35)$$

To find the porosity ϕ_{eq} of an equilibrium state, Menikoff and Kober minimize the free energy (18.34) to get:

$$pV - \phi_{eq} \frac{d\psi_p}{d\phi}(\phi_{eq}) = 0 \quad (18.36)$$

which needs to be solved simultaneously with the equation for equilibrium pressure p_{eq} that is defined according to (18.15) as:

$$p_{eq}(V, e) = -\phi_{eq} \frac{\partial \psi(V_s, e_s)}{\partial V} \quad (18.37)$$

where $V_s = \phi_{eq}V$ and $e_s = e - \psi_p(\phi_{eq})$ are the specific volume and internal energy of the pure solid. Menikoff and Kober point out that equation (18.37) equals the $p - \alpha$ equation, except for the thermodynamically requested distinction between specific internal energy e of the porous material and the one of the solid matrix e_s .

Menikoff [23] uses the matrix material's adiabatic exponent $\gamma_s = \rho_s c_s^2 / P_s$ to describe the ratio of equilibrium and matrix sound speed as:

$$\left(\frac{c_{eq}}{c_s}\right)^2 = 1 - \left(\frac{\gamma_s - 1}{\gamma_s}\right)^2 \frac{c_s^2}{c_s^2 + \phi_{eq}^2 \frac{d^2\psi_p}{d\phi^2}(\phi_{eq})} \quad (18.38)$$

and, thus, to quantify the decrease in sound speed with increasing porosity. Two further interesting quantities for porous materials formulated in [23] are the Grüneisen parameter:

$$\Gamma = \left(\frac{p_{eq}V + \phi_{eq}^2 \frac{d^2\psi_p}{d\phi^2}}{c_s^2 + \phi_{eq}^2 \frac{d^2\psi_p}{d\phi^2}}\right) \Gamma_s \quad (18.39)$$

and the related specific heat at constant volume:

$$C_V = \left(\frac{\phi_{eq}^2 \frac{d^2 \psi_p}{d\phi^2} + \phi_{eq} \frac{d\psi_p}{d\phi}}{\phi_{eq}^2 \frac{d^2 \psi_p}{d\phi^2} + c_s^2 - \Gamma_s^2 C_{V_s} T_s} \right) \frac{\Gamma_s}{\Gamma} C_{V_s} \quad (18.40)$$

References

1. Bethe HA, (1942), On the Theory of Shock Waves for an Arbitrary Equation of State. In: Johnson J, Cheret R (eds.), (1998), *Classic Papers in Shock Compression Science*, Springer, New York.
2. Doppler CA, (1848), Über den Einfluß der Bewegung des Fortpflanzungsmittels auf die Erscheinung der Äther-, Luft- und Wasserwellen, *Abhandlung der Königlich Böhmisches Gesellschaft der Wissenschaften in Prag* 5 [V]: 293–306.
3. Mach E, Salcher P, (1887), Photographische Fixierung der durch Projectile in der Luft eigeleiteten Vorgänge, *Sitzungsbericht, Akad. Wiss. Wien* 95 (IIa): 764–780.
4. Duhem P, (1909), Sur la Propagation des Ondes de Choc au Sein des Fluides, *Zeitschrift für Physikalische Chemie* 69: 169–186
5. Thompson PA, (1971), A Fundamental Derivative in Gas Dynamics, *Physics of Fluids* 14: 1843–1849
6. Hiermaier S, (2008), *Structures Under Crash and Impact*, Springer, New York.
7. Meyers MA, (1994), *Dynamic Behavior of Materials*, John Wiley - Interscience Publication, New York.
8. Slater JC, (1939), *Introduction to Chemical Physics*. McGraw-Hill, New York.
9. Dugdale JS, MacDonald DKC, (1953), The Thermal Expansion of Solids, *Physical Review* 89: 832–834.
10. Rice MH, McQueen RG, Walsh JM, (1958), Compression of Solids by Strong Shock Waves. In: Seitz F, Turnbull D (eds), *Solid State Physics*, Volume 6, Academic Press Inc., Publishers, New York and London.
11. Nagayama K, Mori Y, (1994), Simple Method of Calculating Grüneisen Parameter Based on the Shock Hugoniot Data for Solids, *J. Phys. Soc. Jap.* 63: 4070–4077.
12. Davison L, Horie Y, Shahinpoor M, (1997), *High-Pressure Shock Compression of Solids IV - Response of Highly Porous Solids to Shock Loading*, Springer, New York.
13. Riedel W, Kawai N, (2007), Numerical Simulation of Mortar Strength Measurements at Highest Strain Rates, *Proceedings to the 2007 International Symposium on Interaction of the Effects of Munitions with Structures, ISIEMS-07, Orlando, FL*.
14. Fowles R, Williams RF, (1970), Plane Stress Wave Propagation in Solids, *Journal of Applied Physics* 41: 360–363.
15. Weirick LJ, (1992), Shock Characterization of Epoxy-42 Volume Percent Glass Microballoons. In: Meyers MA, Murr LE, Staudhammer KP (eds.), *Shock Wave and High Strain Rate Phenomena in Materials*, Marcel Dekker, Inc., New York.
16. Riedel W, (2000), *Beton unter dynamischen Lasten. Meso- und makromechanische Modelle und ihre Parameter*, Doctoral Thesis, Fraunhofer Institute for High Speed Dynamics, Ernst-Mach-Institute, Issue 5 of the scientific series Thoma K, Hiermaier S (eds), *ε - Forschungsergebnisse aus der Kurzzeitdynamik*. ISBN: 3-8167-6340-5.
17. Marsh SP (ed), (1980), *LASL Shock Hugoniot Data*, University of California Press, Berkeley and Los Angeles, CA.
18. Herrmann W (1969), Constitutive Equation for the Dynamic Compaction of Ductile Porous Materials, *Journal of Applied Physics* 40: 2490–2499.
19. Carrol M, Holt AC, (1972), Suggested Modification of the P-α Model for Porous Materials, *Journal of Applied Physics* 43: 759–761.
20. Swegle JW, (1980), Constitutive Equation for Porous Materials with Strength, *Journal of Applied Physics* 51: 2574–2580.

21. Butcher BM, Karnes CH, (1968), Sandia Labs. Research Report SC-RR-67-3040, Sandia Laboratory, Albuquerque, NM.
22. Menikoff R, Kober E, (2000), Equation of State and Hugoniot Locus for Porous Materials: P- α Model Revisited. In: Furnish MD, Chhabildas LC, Hixson RS (eds.), Shock Compression of Condensed Matter - 1999. American Institute of Physics.
23. Menikoff R, (2007), Empirical Equations of State for Solids. In: Horie Y (ed), Shock Wave Science and Technology Reference Library, Vol. 2, Solids I, Springer, Berlin, Heidelberg.
24. Thompson SL, Lauson HS, (1972), Improvements in the Chart D radiation-hydrodynamic CODE III: Revised analytic equations of state, Sandia National Laboratory, Albuquerque, NM.
25. Melosh HJ, (2000), A New and Improved Equation of State for Impact Computations, Lunar and Planetary Science XXXI: # 1903.
26. Wünnemann K, Collins GS, Melosh HJ, (2006), A strain-based porosity model for use in hydrocode simulations of impacts and implications for transient crater growth in porous targets, Icarus 180, 514–527.

Chapter 19

Artificial Viscosity Methods for Modelling Shock Wave Propagation

James Campbell and Rade Vignjevic

Abstract The paper gives an overview of the artificial viscosity method widely used today to allow the simulation of problems containing shock waves. The development of the most common basic form of the viscosity term is summarised and its behaviour is illustrated through simulations of a 1D piston problem. Test problems that are commonly used to test different viscosity formulations are then discussed to further illustrate the method. Finally other shock viscosity forms such as edge and tensor viscosities are briefly discussed.

19.1 Introduction

The requirement to model shock wave propagation has been around since the earliest days of hydrocodes, with finite difference simulations used at Los Alamos during the Manhattan project in order to study the behaviour of shock waves. An understanding of shock propagation was critical for the design of the atomic bomb.

A shock wave has a thickness of the order of a few molecular mean free paths. This is a very small dimension, much smaller than the typical length scale considered in continuum mechanics simulations. It is completely impractical to consider modelling a macroscopic problem with a mesh size small enough to resolve this. The result is that a shock represents a discontinuity in the solution, a surface over which there is a jump in velocity, pressure, density and energy.

James Campbell

Cranfield University, School of Engineering - Applied Mechanics, Cranfield, Bedford, UK, e-mail: j.campbell@cranfield.ac.uk

Rade Vignjevic

Cranfield University, School of Engineering - Applied Mechanics, Cranfield, Bedford, UK, e-mail: v.rade@cranfield.ac.uk

One possible approach is to treat the shock as a interface between two regions of the flow. In this approach the Hugoniot equations along with the material's Equation of State (EOS) can be used to solve for the jump in solution variables across the shock. These values are then applied as boundary conditions to the two regions of flow. This approach can be used in one dimensional simulations, but in two- or three- dimensional simulations it is impractical as the shock represents a moving interface of potentially complex shape. Tracking this potentially arbitrary boundary accurately, and applying the necessary jump conditions over the interface represents a complex numerical and algorithmic challenge.

Two well established methods exist today for the treatment of shocks within numerical simulations:

- Artificial viscosity
- Godunov's method

The artificial viscosity concept, developed by von Neumann and Richtmyer [1], allowed the first practical numerical simulations of problems containing strong shocks. The concept involves the introduction into the numerical scheme of a viscosity like term that acts to spread the thickness of any shock wave over several mesh cells. As the shock no longer represents a discontinuity in the solution, standard numerical methods can be used to simulate the shock propagation. This approach has proved to be simple and robust, accounting for its continuing use today. The drawbacks of the method is that it can introduce an unacceptable degree of mesh sensitivity into the solution and there is a trade-off between shock thickness and degree of oscillation behind the shock.

Godunov's method [2] and the class of numerical methods developed from it represent an entirely different approach. In summary Godunov's method assumes that all solution variables within a cell are constant at the start of a step, with discontinuities occurring at the edges of a cell treated through the solution of a Riemann problem. This approach allows the shocks in the solution to be physically and naturally treated. The drawback is the high numerical cost of solving the Riemann problem. This has required the use of approximate Riemann solvers which introduce further approximations into the numerical method. Even approximate solutions of the Riemann problem remain expensive when complex equations of state are required, which has effectively limited the common application of the methods to fluid mechanics simulations. In addition, like the artificial viscosity method, it introduces mesh sensitivity into the solution. Further information on Godunov's method and Riemann solvers can be found in Toro [3].

19.2 The Von Neumann - Richtmyer viscosity

The governing equations of Lagrangian hydrodynamics are the momentum (19.1), the energy (19.2) and the continuity (19.3) equations:

$$\rho \frac{d\mathbf{v}}{dt} = \nabla \cdot \boldsymbol{\sigma} , \quad (19.1)$$

$$\rho \frac{de}{dt} = \boldsymbol{\sigma} : \mathbf{D} , \quad (19.2)$$

$$\frac{d\rho}{dt} = -\rho \nabla \cdot \mathbf{v} \quad (19.3)$$

where ρ is density, $\boldsymbol{\sigma}$ is the stress tensor, \mathbf{v} is the velocity vector, e is the specific internal energy. \mathbf{D} is the rate-of-deformation tensor defined as the skew symmetric part of \mathbf{L} , the velocity gradient tensor:

$$\mathbf{L} = (\nabla \mathbf{v})^T \quad \text{and} \quad \mathbf{D} = \frac{1}{2}(\mathbf{L} + \mathbf{L}^T) \quad (19.4)$$

The approach taken by Von Neumann and Richtmyer [1] for one dimensional shock wave calculations was to modify the momentum and energy equations by adding a dissipative, viscosity like, term q to the stress tensor. Introducing this term into the governing equation acts to smear out the shock so as to produce a thickness of the order of the resolution length of the computational mesh. A particular feature of this approach is that the term is added to the equations throughout the computational domain, not just where a shock is present, removing the need to track shocks. As the dissipative term is added for purely mathematical reasons, it can be any function that satisfies the following constraints [1]:

1. The modified conservation equations (19.1-19.3) must possess solutions without discontinuities.
2. The thickness of a shock must everywhere be of the order of the resolution length of the mesh, independent of the strength of the shock.
3. The dissipative term must be negligible outside of the shock wave.
4. The Hugoniot equations must hold when all other dimensions are large compared to the shock thickness.

The expression proposed by Von Neumann and Richtmyer for their viscosity is written for the one-dimensional case as

$$q = -\rho(c\Delta x)^2 \frac{\partial v}{\partial x} \left| \frac{\partial v}{\partial x} \right| , \quad (19.5)$$

where c is a dimensionless constant. The viscous term q is then included in the solution by replacing the stress, $\boldsymbol{\sigma}$, in the governing equations by $(\boldsymbol{\sigma} - q\mathbf{I})$. This term is quadratic in the velocity gradient and is positive in compression and negative in tension. As the viscosity term is not required in expansion it is common to set $q = 0$ when $\frac{\partial v}{\partial x} > 0$.

The Von Neumann-Richtmyer q shown in equation (19.5) does work effectively, and with a value of c of the order of 2 will spread a shock over three to five mesh cells [4]. Its disadvantage is that any oscillation that does occur behind the shock is only slowly damped out and lowering the value of c to reduce the thickness of the shock results in an overshoot that produces oscillation. To address this problem

Landshoff [5] proposed an expression for q that was linear in the velocity gradient. This term vanishes less rapidly behind a shock front and so rapidly damps out the oscillation, but as the term is smaller in the shock front itself much larger overshoots occur. Landshoff recommended that the two terms be combined to produce a q that combines the best features of each:

$$q = -\rho c_L \Delta x a \left| \frac{\partial v}{\partial x} \right| - \rho c_Q (\Delta x)^2 \frac{\partial v}{\partial x} \left| \frac{\partial v}{\partial x} \right|, \quad (19.6)$$

where a is the local speed of sound and c_L and c_Q are dimensionless constants that multiply the linear and quadratic terms respectively. This basic form of viscosity proved effective and is still widely used today.

Extending the one-dimensional form of the viscosity (19.6) to two or three dimensions requires appropriate definitions of the velocity gradient and the characteristic length. It is common to follow the original idea of Von Neumann and Richtmyer [1] by replacing the velocity gradient term with the trace of the rate-of-deformation tensor:

$$\begin{aligned} q &= -\rho c_L l a \dot{D}_{kk} - \rho c_Q l^2 \dot{D}_{kk}^2 & \text{if } \dot{D}_{kk} < 0 \\ q &= 0 & \text{if } \dot{D}_{kk} \geq 0 \end{aligned} \quad (19.7)$$

The definition of the characteristic grid length, l , is not so simple. Ideally the characteristic length used would be the element thickness in the shock propagation direction, but calculating this for all elements every step is difficult and costly. The usual approximation used in three dimensions is the cube root of the volume, $\sqrt[3]{V}$, and in two dimensions the square root of the area, \sqrt{A} . These values are simple and quick to calculate and provide a good estimate of the critical length provided the aspect ratios of the elements are close to one. As the element aspect ratio becomes poor the use of these estimates leads to increasing unphysical behaviour and even numerical problems.

19.2.1 Demonstration

The behaviour of the von Neuman-Richtmyer viscosity will now be illustrated through simulations of a 1D piston problem. In this problem a box with an initial length of 1 is filled with a cold perfect gas with $\gamma = 5/3$ and initial density $\rho_0 = 1.0$. The right hand end of the box is fixed, while the left hand end is a piston that moves into the box with a fixed velocity of 1.0. A shock of infinite strength ($P_0 = 0$) is generated by the piston motion and moves into the gas ahead of the piston, figure 19.1.

An exact solution to this problem can be obtained using the Hugoniot relations that connect the state ahead of the shock with the state behind:

$$v_s = \frac{(v_1 - v_0)\rho_1}{\rho_1 - \rho_0}, \quad (19.8)$$

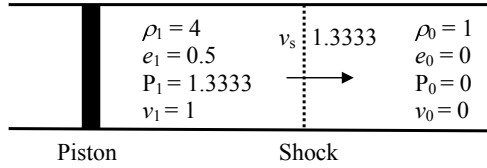


Fig. 19.1 Diagram of the 1D piston problem, showing the state of the gas ahead and behind the shock.

$$P_1 - P_0 = \rho_0 v_s (v_1 - v_0), \tag{19.9}$$

$$e_1 - e_0 = \frac{P_1 + P_0}{2} \left(\frac{1}{\rho_0} - \frac{1}{\rho_1} \right). \tag{19.10}$$

These equations link the density, ρ , pressure, P , specific internal energy, e , and particle velocity, v , across a shock travelling with velocity v_s . The state ahead of the shock is denoted with subscript 0 and behind the shock with subscript 1.

To calculate the exact solution for this problem a fourth equation is required, the perfect gas equation of state:

$$P = (\gamma - 1)\rho e. \tag{19.11}$$

These equations can now be solved explicitly to derive an expression for the pressure jump across the shock in terms of the conditions ahead of the shock and the change in particle velocity across the shock:

$$P_1 = P_0 + \rho_0 \frac{(\gamma + 1)}{4} (\Delta \mathbf{v})^2 + \rho_0 |\Delta \mathbf{v}| \sqrt{\left(\frac{\gamma + 1}{4} \right)^2 (\Delta \mathbf{v})^2 + a_0^2}, \tag{19.12}$$

where a is the local speed of sound given by

$$a = \sqrt{\frac{\gamma P}{\rho}} \tag{19.13}$$

The conditions ahead and behind the shock and the shock speed are given in 19.1.

Figures 19.2 to 19.6 show results from several simulations of this problem with varying c_L and c_Q . All the simulations were performed using the DYNA Lagrangian hydrocode [6], using the standard form of viscosity given by equation (19.7). The model consists of 100 elements along the length of the box. Eight node hexahedral continuum elements were used, along with symmetry boundary conditions to enforce a state of uni-axial strain. All the elements are perfect cubes at the start of the problem so $l = \sqrt[3]{V}$ is a good measurement of the critical length. All the results are shown as plots of element pressure vs. element coordinate at time $t = 0.7$. At this point the piston coordinate 0.7 and the shock coordinate is 0.93.

The first simulation, figure 19.2, shows a result using the quadratic term only with a small coefficient ($c_L = 0.0$ and $c_Q = 0.5$). The overshoot and oscillation behind

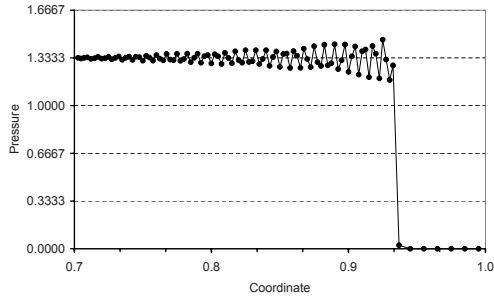


Fig. 19.2 Pressure profile for piston problem at time $t = 0.7$, with $c_L = 0.0$ and $c_Q = 0.5$.

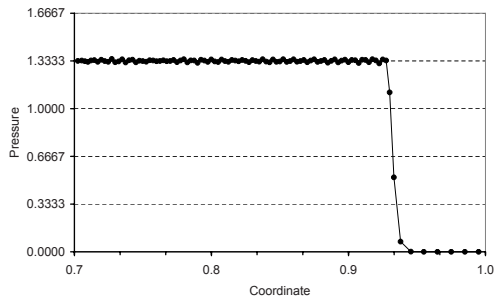


Fig. 19.3 Pressure profile for piston problem at time $t = 0.7$, with $c_L = 0.0$ and $c_Q = 2.0$.

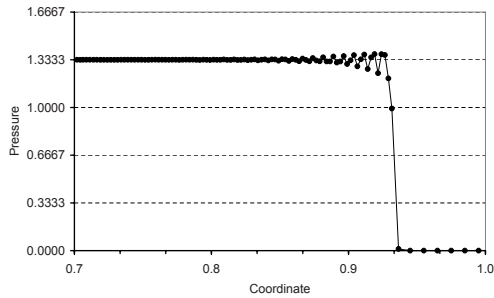


Fig. 19.4 Pressure profile for piston problem at time $t = 0.7$, with $c_L = 0.1$ and $c_Q = 0.5$.

the shock can be clearly seen and is only slowly damped. In a practical analysis the level of noise in this solution would not be acceptable. Increasing the value of the quadratic coefficient reduces the level of overshoot and hence the oscillation as can be seen in figure 19.3 ($c_L = 0.0$ and $c_Q = 2.0$). Here the solution behind the shock is good, but at the cost of a wider shock front. The effect of introducing the linear term is to more rapidly damp out the oscillations behind the shock as can be seen in figure 19.4 ($c_L = 0.1$ and $c_Q = 0.5$). Here even a fairly small value for the

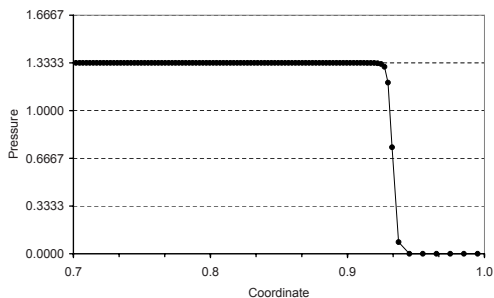


Fig. 19.5 Pressure profile for piston problem at time $t = 0.7$, with $c_L = 1.0$ and $c_Q = 0.5$.

linear coefficient results in a much more rapid damping behind the shock with only a small increase in the width. Increasing the linear coefficient eventually results in a monotonic profile with no overshoot behind the shock but again at the cost of a wider front, figure 19.5.

Today, in a 1D calculation like this, the width of the shock front is not a problem as the computational cost of each simulation is negligible and a high spatial resolution can be used. In 3D models it is still desirable to keep the width of the shock as small as practical as increasing the spatial resolution can easily result in models that are too computationally expensive to use.

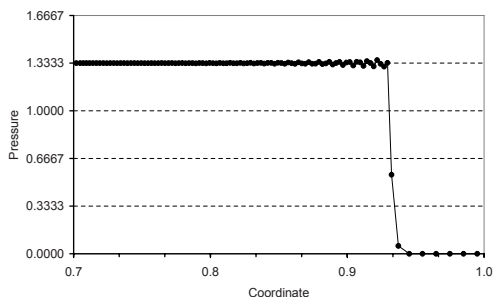


Fig. 19.6 Pressure profile for piston problem at time $t = 0.7$, with $c_L = 0.06$ and $c_Q = 1.5$.

There is a further and more serious problem with artificial viscosity that must be considered when selecting the values of the two coefficients. This problem was studied by Noh who called it shockless Q heating [7]. The viscosity term is non-zero everywhere where compression occurs and this leads to error in the solution where the assumption that the dissipative term is negligible outside the shock wave does not hold. Due to this error, as the linear term is larger than the quadratic term when \dot{D}_{kk} is small, it is common to keep the value of the linear coefficient small. The default values used in the DYNA code are $c_L = 0.06$ and $c_Q = 1.5$ [6], experience has shown that these values provide a reasonable balance between shock thickness and

oscillation behind the shock for many cases. Results for the piston problem using these coefficients are shown in figure 19.6. The value of the quadratic coefficient results in a reasonably sharp shock front with a small overshoot and small linear term damps out the oscillation behind the shock.

19.2.2 Wall Heating

This is an error that occurs on shock formation, for example at the start of the piston problem. It manifests in the solution as region where the density is underestimated and the internal energy overestimated. While this problem has been known and studied since the early days of shock computations, the now common name wall heating comes from the study by Noh [7]. He showed that this error is unavoidable as it is present in the solution of the governing differential equations containing a q term. The presence of this error is often ignored as often it only affects the solution in a small region and does not threaten the overall stability of the calculation. However in some particular applications, such as when the shock is generated at the centre of convergent geometry, the error can be significant and so solutions have been proposed, an example is the artificial heat flux term developed by Noh [7] to smear out this error. This error is still investigated; see for example Rider [8] for a more recent study.

19.3 Test problems for shock viscosity formulations

Since its original development many different forms for the artificial viscosity term have been proposed. The motivation has included improving the solution near the shock and in particular reducing the mesh sensitivity introduced when the original 1-D formulation has been extended to 2- and 3- dimensions. In principle any problem involving shock propagation can be used to investigate the properties of a shock viscosity, but one result of the continued development has been the emergence of certain test problems that are more commonly used to test or illustrate different formulations. Three problems will now be considered in more detail: the Sod shock tube [9], the Noh problem [7] and the Saltzman piston problem [11]. Other test problems that are used include the Sedov blast wave [10], uniform compression [7] and the Coggeshall adiabatic compression problem [10].

19.3.1 Sod shock tube

In addition to the piston problem used previously another commonly used 1D problem is the Sod shock tube problem, named after Gary Sod who used this prob-

lem to investigate the performance of several numerical methods [9]. This problem consists of two regions of perfect gas with different initial densities and pressures, figure 19.7. In both regions the gas is initially at rest. The solution consists of a rarefaction wave that travels to the left, a contact discontinuity and a shock that travels to the right. In both regions the ratio of specific heats is $\gamma = 1.4$. It is common to take the initial position of the contact discontinuity as $x = 0.5$. The exact solution for this problem at $t = 0.25$ is shown in figure 19.8. As with the piston problem this can be used to investigate the effect of the viscosity formulation on the shock front, but in addition the viscosity should not affect the solution at the contact discontinuity or in the rarefaction wave.

Left	Right
$\rho_L = 1.0$	$\rho_R = 0.125$
$P_L = 1.0$	$P_R = 0.1$
$v_L = 0.0$	$v_R = 0.0$

Fig. 19.7 Initial conditions of the Sod shock tube problem.

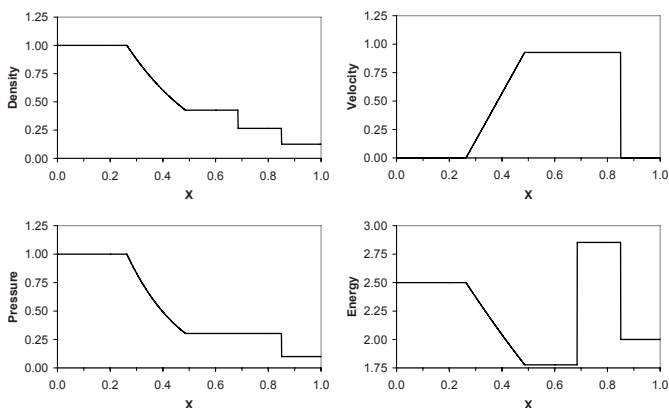


Fig. 19.8 Exact solution for Sod shock tube problem showing density, velocity, pressure and energy at time $t = 0.25$.

The Sod shock tube problem is an example of a 1D Riemann problem for the Euler equations which are commonly used for testing fluid dynamics codes [3].

19.3.2 Noh generic constant velocity shock

This problem, usually just called the Noh problem, has become a widely used test for hydrocodes since it was first described by Noh [7]. While it is a 1D problem there are three variants, one in planar geometry, one in axi-symmetric geometry and the final in spherically symmetric geometry. In all three cases the problem consists of a region of cold ideal gas, $\gamma = 5/3$, with $\rho_0 = 1.0$ and $P_0 = 0.0$. The initial velocity $v_0 = -1.0$ everywhere. In all three cases the shock speed is $v_s = 1/3$, and all have constant post-shock conditions.

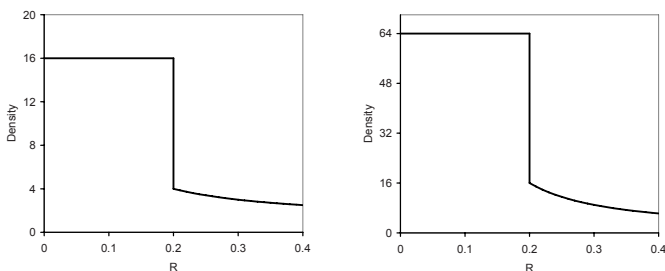


Fig. 19.9 The exact solution for density at $t = 0.6$ for Noh's axi-symmetric problem (left) and spherical problem (right).

The planar version is identical to the piston problem considered previously; the change is that is in a frame of reference where the piston is at rest. Exact results for the density at $t = 0.2$ is shown in figure 19.9 for the axi-symmetric and spherical cases. In both of these cases there is a region of uniform compression ahead of the shock, and especially with the spherical case the shockless Q heating error can be seen in this region.

Noh originally developed these problems to investigate the wall heating error. An example of the wall heating error can be seen in figure 19.10, showing results for the axi-symmetric problem calculated on a polar mesh. The effect of wall heating can be seen in the significant under-estimate of the density near the point of convergence in the numerical solution. The results shown use the edge viscosity formulation developed by Caramana [10].

Another application of the Noh problem is to investigate the effect of mesh sensitivity when the shock propagates through a non-uniform mesh. The example shown in figure 19.10 used a polar mesh where the element edges are aligned with the flow and the mesh reflects the symmetry of the flow. For practical reasons it is rare to achieve this and using a rectangular mesh where all elements are initially square for the Noh problem can be used to investigate the consequences.

Figure 19.11 shows the results from a DYNA simulation of the axi-symmetric Noh problem. The elements are initially uniform cubes with symmetry boundary conditions used to enforce plane strain. The simulation used the standard viscosity

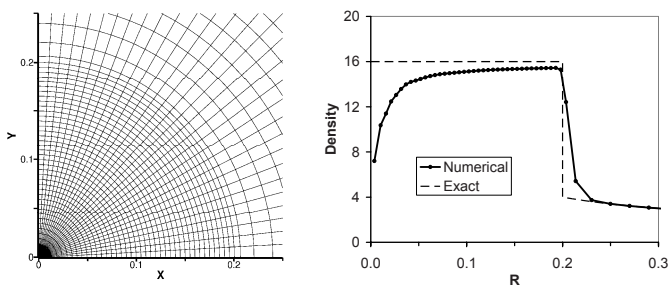


Fig. 19.10 Example axi-symmetric Noh problem results on a polar mesh (left) showing the density error due to wall heating (right). Solution time $t = 0.2$.

(19.7) with the default values for the viscosity coefficients. The mesh sensitivity of the solution can be seen in both the mesh plot, especially along the 45 degree line, and in the scatter of the density results. The Noh problem does represent a tough problem for shock codes as it involves an infinitely strong shock and hence the level of mesh sensitivity is severe, but it must be understood that mesh sensitivity is present in all simulations that use the artificial viscosity method to capture the shock behaviour.

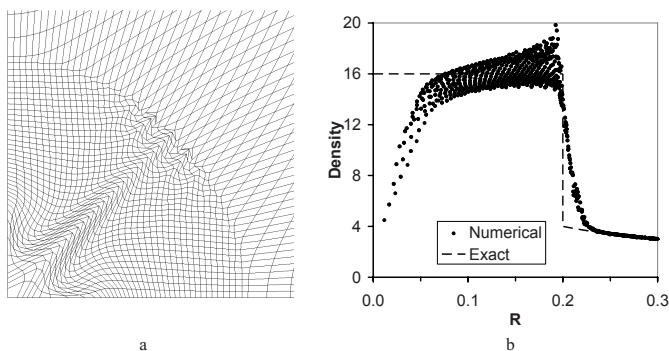


Fig. 19.11 Simulation results for the axi-symmetric Noh problem on a Cartesian mesh using the Von Neumann - Richtmyer viscosity at solution time $t = 0.2$. (a) Final mesh. (b) Plot of element density vs. radius for all elements.

19.3.3 Saltzman piston

The Saltzman piston problem [11] is a problem that has been widely used to test shock viscosities [10, 11, 12, 13, 14]. It tests the ability of a code to propagate a

one dimensional shock through a two dimensional mesh. The initial conditions and analytical solution are identical to the piston problem considered earlier, however the initial mesh is different, figure 12. The mesh fills a rectangular domain that is 1.0 long by 0.1 high with 100 elements along the long edge and 10 elements along the short edge. The initial x coordinate of each node is defined in terms of their logical coordinates i and j as

$$x(i, j) = (i - 1)dx + (11 - j) \sin\left(\frac{\pi(i - 1)}{100}\right)dy, \quad (19.14)$$

where $dx = dy = 0.01$. The result of this is a distorted mesh, figure 19.12, although all elements have an aspect ratio close to one.



Fig. 19.12 Initial mesh for Saltzman piston problem

The standard viscosity is unable to preserve the one-dimensional solution, with the distortion of the mesh behind the shock clear in figure 19.13.

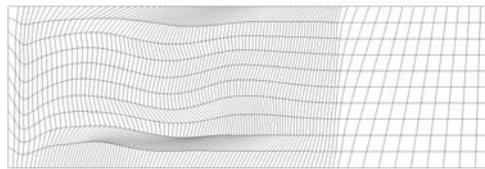


Fig. 19.13 Mesh at $t = 0.7$ for the Saltzman piston problem using the default DYNA viscosity.

However, the numerical solution remains a reasonable approximation to the analytical solution. Two variants of the Saltzman piston have been proposed, both alter the height of the rectangular domain leaving all other parameters unchanged. By

altering the initial element aspect ratio both represent a tougher challenge for a viscosity than the standard test. In the first variant the height of the domain is increased by a factor of 100. This variant was originally proposed by Margolin [11] to investigate how very high aspect ratio elements affect the solution. The standard viscosity does not perform well on this problem [12] as the characteristic length calculated from the element volume is much larger than the thickness of the element in the shock direction. In the second variant the height of the domain is reduced by a factor of 4. This variant was originally proposed by Campbell and Shashkov [14] to investigate how a moderate element aspect ratio affects the solution and to provide a greater degree of discrimination between viscosity forms. A further option with the Saltzman piston problem is to run the calculation past time $t = 0.75$. At this time the shock reaches the fixed end of the piston and is reflected. The reflected shock now propagates through mesh that has been distorted by the initial shock. Again this provides a greater challenge to the analysis code.

19.4 Alternative forms of artificial viscosity

The problems and errors resulting from the use of artificial viscosity have led to the development of many different forms with varying properties. This section will briefly discuss two basic forms: the edge centred and the tensor viscosities, illustrating each with an example.

All forms of viscosity should satisfy the four conditions set out by Von Neumann and Richtmyer, see section 19.2 of this paper. More recently Caramana et al. [10] specified five additional properties that an artificial viscosity should possess, these are

1. Dissipativity: The artificial viscosity must only act to decrease kinetic energy.
2. Galilean invariance: The viscosity should vanish smoothly as the velocity field becomes constant.
3. Self-similar motion invariance: The viscosity should vanish for uniform contraction and rigid rotation.
4. Wave-front invariance: The viscosity should have no effect along a wave front of constant phase, on a grid aligned with the shock wave.
5. Viscous force continuity: The viscous force should go to zero continuously as compression vanishes and remain zero for expansion.

A viscosity that satisfies these conditions will not suffer from the shockless Q heating error and should show reduced mesh sensitivity over the standard form.

19.4.1 Edge centred viscosity

In an edge centred viscosity the viscosity force is calculated at an element edge rather than centred within an element. The strength of this approach is that the uncertainty over the choice of characteristic length in higher dimensions is removed, the length of the edge is now the natural choice. Each element edge connects two nodes and the forces resulting from the viscosity are directly applied to them. These forces should be applied in the direction of the relative velocity of the two nodes, not along the line joining them. This change significantly improves the results and according to Margolin [11] is known as the Barton fix.

The viscosity developed by Caramana et al. [10] is an example of a modern edge viscosity that includes limiter terms. It is based on an alternative to equation (19.6) that was investigated by Wilkins [4] who attributed it to Kurapatenko [15].

$$q_{Kur} = \rho \left\{ c_2 \frac{(\gamma+1)}{4} |\Delta \mathbf{v}| + \sqrt{c_2^2 \left(\frac{\gamma+1}{4} \right)^2 (\Delta \mathbf{v})^2 + c_1^2 c_s^2} \right\} |\Delta \mathbf{v}| \quad (19.15)$$

where c_1 and c_2 are non-dimensional constants, γ is the ratio of specific heats and $\Delta \mathbf{v} = \frac{\partial \mathbf{v}}{\partial x} \Delta x$. This expression was derived from the pressure jump across a shock in an ideal gas. Wilkins shows that when simulating an ideal gas, using this viscosity removes the overshoot behind a shock.

In two dimensions the viscosity force for edge k of element e , that connects two nodes b and c , is

$$\mathbf{f}_k = \begin{cases} (1 - \psi_k) q_{Kur} (\widehat{\Delta \mathbf{v}}_k \cdot \mathbf{s}_c^e) \widehat{\Delta \mathbf{v}}_k & \text{if } (\Delta \mathbf{v}_k \cdot \mathbf{s}_c^e) < 0 \\ 0 & \text{if } (\Delta \mathbf{v}_k \cdot \mathbf{s}_c^e) \geq 0. \end{cases} \quad (19.16)$$

\mathbf{f}_k then contributes to the total force at points b and c . Vector \mathbf{s}_c^e is a unit vector in the direction normal to the line connecting the mid-point of edge k to the centre of element e . The velocity difference for the edge is $\Delta \mathbf{v}_k = \mathbf{v}_b - \mathbf{v}_c$, and $\widehat{\Delta \mathbf{v}}_k$ is the unit vector in the direction of this velocity difference. For the edge the density and sound speed are

$$\rho_k = \frac{2\rho_b\rho_c}{\rho_b + \rho_c}, \quad c_{s,k} = \min(c_{s,b}, c_{s,c}). \quad (19.17)$$

The density and sound speed at a node is the volume weighted average of the surrounding elements. The function ψ_k is defined as

$$\psi_k = \max[0, \min(0.5(r_{l,k} + r_{r,k}), 2r_{l,k}, 2r_{r,k}, 1)], \quad (19.18)$$

$$r_{r,k} = \frac{\Delta \mathbf{v}_{k+1} \cdot \widehat{\Delta \mathbf{v}}_k}{\Delta \mathbf{x}_{k+1} \cdot \widehat{\Delta \mathbf{x}}_k} \bigg/ \frac{|\Delta \mathbf{v}_k|}{|\Delta \mathbf{x}_k|}, \quad r_{l,k} = \frac{\Delta \mathbf{v}_{k-1} \cdot \widehat{\Delta \mathbf{v}}_k}{\Delta \mathbf{x}_{k-1} \cdot \widehat{\Delta \mathbf{x}}_k} \bigg/ \frac{|\Delta \mathbf{v}_k|}{|\Delta \mathbf{x}_k|}. \quad (19.19)$$

Subscripts l and r refer to the left and right edges respectively. The left edge is found by considering all other edges that connect to node b and selecting the edge that forms the largest angle with edge k . The right edge is found in the same manner by considering edges that connect to node c .

The term ψ can be considered as a multi-dimensional form of a one dimensional TVD advection limiter. It acts to switch off the viscosity when the second derivative of the velocity field is zero and ensures that the viscosity satisfies the conditions of self-similar motion invariance and wave front invariance.

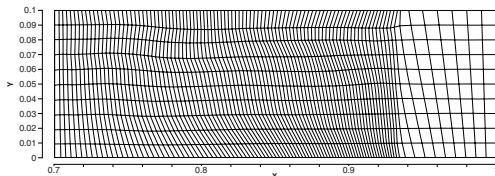


Fig. 19.14 Mesh at $t = 0.7$ for the Saltzman piston problem using the Caramana edge viscosity.

Results for the Saltzman piston problem using the Caramana edge viscosity are shown in figure 19.14, and shows a smoother solution than that obtained using the standard form, figure 19.13.

19.4.2 Tensor viscosity

In a tensor viscosity the scalar q term is replaced by a tensor \mathbf{Q} . The potential benefit of this change is that the effect of the viscosity can be directionally dependent, like an edge viscosity, while still being element centred. In addition there is no requirement that \mathbf{Q} be symmetric, and a nonsymmetric viscosity can remove mode conversion [11]. This means that for a shear flow in which all velocities are parallel, the viscous force will only act in the velocity direction. With a symmetric tensor viscosity the force would have a component perpendicular to the velocity direction.

The tensor viscosity developed by Campbell and Shashkov [14] is an example of a modern tensor viscosity that includes limiter terms. It assumes a form similar to physical viscosity, but based on \mathbf{L} rather than \mathbf{D} and so is not symmetric:

$$\mathbf{Q} = \mu \mathbf{L}^T. \tag{19.20}$$

μ is a scalar coefficient defined as

$$\mu = (1 - \psi)\rho \left\{ c_2 \frac{(\gamma + 1)}{4} |\Delta \mathbf{v}| + \sqrt{c_2^2 \left(\frac{\gamma + 1}{4} \right)^2 (\Delta \mathbf{v})^2 + c_1^2 c_s^2} \right\} l \tag{19.21}$$

where ψ is a limiter function similar to the function used in the Caramana edge viscosity although using the value of Δv in four directions rather than two.

Results for the Saltzman piston problem using this tensor viscosity are shown in figure 19.14, again showing a smoother solution than that obtained using the standard form. It should be noted that both the Caramana edge viscosity and this tensor viscosity are formulated within the framework of mimetic finite difference methods although there is no reason why they could not be extended to other numerical approaches.

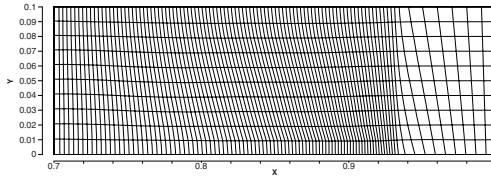


Fig. 19.15 Mesh at $t = 0.7$ for the Saltzman piston problem using the Campbell and Shashkov tensor viscosity.

19.5 Summary

This paper discusses the artificial viscosity method for the simulation of shock waves that is widely used today, especially for solid mechanics applications. The behaviour of the most widely available form of artificial viscosity is illustrated through a set of examples covering test problems that are commonly used to test different viscosity formulations. Finally other shock viscosity forms such as edge and tensor viscosities are briefly discussed.

References

1. Von Neumann J., Richtmyer R.D. (1950) A method for the calculation of hydrodynamic shocks. *J. Appl. Phys.* **21**, 232-237.
2. Godunov S. K. (1959) A difference scheme for numerical computation of discontinuous solutions of equations in fluid dynamics. *Mat. Sb.* **47**, 271-306.
3. Toro E.F. (1999) *Riemann Solvers and Numerical Methods for Fluid Dynamics*. Springer-Verlag Berlin Heidelberg
4. Wilkins M.L. (1980) Use of artificial viscosity in multidimensional fluid dynamic calculations. *J. Comput. Phys.* **36**, 281-303.
5. Landshoff R. (1955) *A numerical method for treating fluid flow in the presence of shocks*. LA-1930, Los Alamos National Laboratory.
6. Lin J.I. (2004) *DYNA3D: A nonlinear, explicit, three-dimensional finite element code for solid and structural mechanics*. UCRL-MA-107254, Lawrence Livermore National Laboratory.

7. Noh W.F. (1987) Errors for calculations of strong shocks using an artificial viscosity and an artificial heat flux. *J. Comput. Phys.* **72**, 78-120.
8. Rider W.J. (2000) Revisiting wall heating. *J. Comput. Phys.* **162**, 395-410.
9. Sod G.A. (1978) A survey of several finite difference methods for systems of nonlinear hyperbolic conservation laws. *J. Comput. Phys.* **27**, 1-31.
10. Caramana E.J., Shashkov M.J., Whalen P.P. (1998) Formulations of artificial viscosity for multi-dimensional shock wave computations. *J. Comput. Phys.* **144**, 70-97.
11. Margolin L.G. (1988) *A centered artificial viscosity for cells with large aspect ratios*. UCRL-53882, Lawrence Livermore National Laboratory.
12. Benson D.J. (1991) A new two-dimensional flux-limited shock viscosity for impact calculations. *Comput. Methods Appl. Mech. Engrg.* **93**, 39-95.
13. Benson D.J., Schoenfeld S. (1993) A total variation diminishing shock viscosity. *Comput. Mech.* **11**, 107-121.
14. Campbell J.C., Shashkov M.J. (2001) A tensor viscosity using a mimetic finite difference algorithm. *J. Comput. Phys.* **172**, 739-765.
15. Kurapatenko V.F. (1967) *In: Difference methods for solutions of problems of mathematical physics, I (Editor: N.N. Janenko)*. Amer. Math. Soc., Providence, R.I., p. 116.

Chapter 20

Review of Development of the Smooth Particle Hydrodynamics (SPH) Method

Rade Vignjevic and James Campbell

Abstract The paper gives an overview of developments of the SPH method. Especial attention is given to the main shortcomings of the original form of the method namely consistency, tensile instability and zero energy modes. A derivation of an example of a correction necessary to assure first order consistency is given. The origin of the tensile instability and a few proposed solutions to this problem are described. Similar consideration is given with respect to the zero energy modes typical for the collocational SPH method.

20.1 Introduction

This paper discusses the development of the Smooth Particle Hydrodynamics (SPH) method in its original form, which is based on the updated Lagrangian formalism. SPH is a relatively new numerical technique for the approximate integration of partial differential equations.

It is a meshless Lagrangian method that uses a pseudo-particle interpolation method to compute smooth field variables. Each pseudo-particle has a mass, Lagrangian position, Lagrangian velocity, and internal energy; other quantities are derived by interpolation or from constitutive relations. The pseudo-particles move with the velocity of the continuum, but are not associated with a grid and consequently do not have fixed connectivity.

Rade Vignjevic

Cranfield University, School of Engineering - Applied Mechanics, Cranfield, Bedford, UK, e-mail: v.rade@cranfield.ac.uk

James Campbell

Cranfield University, School of Engineering - Applied Mechanics, Cranfield, Bedford, UK, e-mail: J.Campbell@cranfield.ac.uk

The advantage of the meshless approach is its ability to solve problems that cannot be solved effectively using other numerical techniques. It does not suffer from the mesh distortion problems that limit Lagrangian approaches based on a structured mesh when simulating large deformations. As it is a Lagrangian method it naturally tracks material history information, such as damage, without the diffusion that typically occurs in Eulerian approaches due to advection.

Gingold and Monaghan [18] and Lucy [42] initially developed SPH in 1977 for the simulation of astrophysics problems. Their breakthrough was a method for the calculation of derivatives that did not require a structured computational mesh. Review papers by Benz [10] and Monaghan [45] cover the early development of SPH.

From the early days of SPH the importance of the smoothing kernel function as the essential feature of the SPH scheme was recognised. The Gaussian and the cubic B spline kernel functions are the most widely used, see Monaghan and Lattanzio [47]. However, most practical work relies on monotone splines which, when used with small supports, allow for more accurate numerical solutions and higher numerical efficiency according to Balsara [4]. Liu et al. [39] among a number of other researchers demonstrated that in general, regardless of the choice of kernel function, the SPH method is not even zero-order consistent. This is a consequence of the fact that the accuracy of the kernel interpolation depends on the distribution of the interpolation points within the kernel support. This effect is especially pronounced in the vicinity of boundaries, where the kernel support extends beyond the domain of the problem considered and consequently becomes incomplete Liu et al. [40].

Libersky and Petchek [36] extended SPH to work with the full stress tensor in 2D. This addition allowed SPH to be used in problems where material strength is important. The development of SPH with strength of materials continued with its extension to 3D by Libersky [37]. Applications of SPH to model solids, i.e. materials with strength, further highlighted shortcomings in the basic method: consistency, tensile instability, zero energy modes, treatment of contact and artificial viscosity. These shortcomings were discussed in detail in the first comprehensive analyses of the SPH method by Sweigle [68] and Wen [83]. The problems of consistency and accuracy, identified by Belytschko [5], were addressed by Randles and Libersky [59], Vignjevic and Campbell [76] and a number of other researchers. This resulted in a normalised first order consistent version of the SPH method with improved accuracy. The attempts to ensure first order consistency in SPH resulted in the emergence of a number of variants of the SPH method, such as Element Free Galerkin Method (EFGM) Belytschko [7], Kongauz [33], Reproducing Kernel Particle Method (RKPM) Liu [40][41], Moving Least Square Particle Hydrodynamics (MLSPH) Dilts [16], Meshless Local Petrov Galerkin Method (MLPG) Atluri and Zhu [1]. These methods allow the restoration of consistency of any order by means of a correction function. It has been shown by Dilts [16] and independently by Atluri et al. [2] that the approximations based on corrected kernels are identical to moving least square approximations.

A comprehensive stability analysis of particle methods in general by Belytschko [8], Xiao and Belytschko [84], and independently by Randles [59] who worked specifically on the SPH method provided improved understanding of the methods analysed and confirmed the conclusions from Swegle's initial study. Randles unique analysis, which included space and time discretisation, showed that SPH can be stabilised by precise choice of time step size and a predictor corrector type of time integration. Rabczuk et al. [58] demonstrated that if used within a total Lagrangian framework SPH does not exhibit tensile instability.

Tensile instability in SPH manifests as a non-physical motion of particles which form clusters. This was first observed in materials loaded in tension (negative stress), however the instability can develop under compressive loading, see Swegle [68]. In simulations of solids this instability may result in non-physical numerical fragmentation.

Another unconventional solution to tensile instability and the zero energy mode instability problems was first proposed by Dyka [17] in which the stresses are calculated at locations other than the SPH particles (non-collocational SPH). The results achieved in 1D were encouraging but a rigorous stability analysis was not performed. A 2D version of this approach was investigated by Vignjevic and Campbell [76], based on the normalised version of SPH. This investigation showed that extension to 2D was possible, although general boundary condition treatment and simulation of large deformations would require further research.

Monaghan [51] showed how the instability can be removed by using an artificial stress which in the case of fluids is an artificial pressure. When used in simulation of solids this artificial, in other words non-physical, stress may result in an unrealistic material strength and therefore has to be used with caution.

In spite of these developments, the crucial issue of convergence in a rigorous mathematical sense and the links with conservation have not been well understood. Encouraging preliminary steps in this direction have already been made by Moussa and Vila [54], who proved convergence of their meshless scheme for non-linear scalar conservation laws; see also Moussa [53]. This theoretical result appears to be the first of its kind in the context of meshless methods. Furthermore, Moussa and Vila, proposed an interesting new way to stabilise normalised SPH and allow for treatment of boundary conditions by using approximate Riemann solvers and up-winding, an approach usually associated with finite volume shock-capturing schemes of the Godunov type. This work developed a strong following including: Parshikov et al. [55] who also use a Riemann solver to calculate the numerical flux between pairs of interacting particles; Cha and Whitworth [14], who have applied the Riemann solver of van Leer [72][73] to isothermal hydrodynamics; and Inutsuka [26] who proposed an interesting but fairly complex approach to obtain second-order accurate SPH in 1D.

The improvements in accuracy and stability achieved by kernel re-normalisation or correction do not come for free; now it is necessary to treat the essential boundary conditions in a rigorous way. The approximations in SPH do not have the property of strict interpolants, so that in general they are not equal to the particle value of the dependent variable, i.e. $u^h(\mathbf{x}_j) = \sum_I \phi_I(\mathbf{x}_j) u_I \neq u_j$. Consequently it does not suffice to impose zero values at the boundary positions to enforce homogeneous boundary conditions. Another issue with this approach is that in conventional SPH the boundary is diffuse. In the case of normalised SPH particles do lie on the domain boundary which is in this case precisely defined.

The treatment of boundary conditions and contact could be and was neglected in the conventional SPH method. If the imposition of the free surface boundary condition (stress free condition) is simply ignored, then conventional SPH behaves in an approximately correct manner, giving zero pressure for fluids and zero surface stresses for solids, because of the deficiency of particles at the boundary. This is the reason why conventional SPH gives physically reasonable results at free surfaces. Contact between bodies in conventional SPH is treated by smoothing over all particles neighbouring the contact interface, regardless of material types in contact (for instance contact between a solid body and a fluid). Although simple this approach can give physically incorrect results, such as tensile forces between the bodies in contact.

Campbell et al. [13] made an early attempt to introduce a more systematic treatment of boundary condition by re-considering the original kernel integral estimates and taking into account the boundary conditions through residual terms in the integral by parts. Very interesting work on boundary conditions in SPH is due to Takeda et al. [70], who applied SPH to a variety of viscous flows.

A similar approach has also been used to a limited extent by Randles [59] with the ghost particles added to accomplish a reflected symmetrical surface boundary condition. Belytschko, Lu and Gu [7] imposed the essential boundary conditions by the use of Lagrange multipliers leading to an awkward structure of the linear algebraic equations, which are not positive definite. Krongauz and Belytschko [32] proposed a simpler technique for the treatment of the essential boundary conditions in meshless methods, by employing a string of finite elements along the essential boundaries. This allowed for the boundary conditions to be treated accurately, but reintroduced the shortcomings inherent to structured meshes.

Randles et al. [59][60] were first to propose a more general treatment of boundary conditions based on an extension of the ghost particle method. In their approach the boundary is considered to be a surface one half of the local smoothing length away from the so-called boundary particles. A boundary condition is applied to a field variable by assigning the same boundary value of the variable to all ghost par-

ticles. A constraint is imposed on the boundary by interpolating it smoothly between the specified boundary particle value and the calculated values on the interior particles. This serves to communicate to the interior particles the effect of the specific boundary condition. There are two main difficulties in this:

- Definition of the boundary (surface normal at the vertices).
- Communication of the boundary value of a dependent variable from the boundary to internal particles.

A penalty contact algorithm for SPH was developed by Campbell and Vignjevic [12]. This algorithm was tested on normalised SPH in combination with the Randles approach for treatment of free surfaces. The contact algorithm considered only particle-particle interactions, and allowed contact and separation to be correctly simulated. However tests showed that when this approach is used zero-energy modes are often excited. Further development of this contact algorithm for the treatment of contact problems involving frictionless sliding and separation under large deformations was achieved by the contact conditions through the use a contact potential for particles in contact, see Vignjevic et al. [78]. Inter-penetration is checked as a part of the neighbourhood search. In conventional SPH contact conditions are enforced on the boundary layer, $2h$ thick, while in the case of the normalized SPH, contact conditions are enforced for the particles lying on the contact surface.

In a number of engineering applications it is beneficial to discretise only certain parts of the domain with particles and the rest with finite elements. The main reasons for this is to take advantage of the strengths of both methods, which include significantly better numerical efficiency of the finite element (FE) method, and in SPH modelling arbitrary crack propagation, large deformations and adaptive refinement of the discretisation.

One of the first coupling procedures for FE-SPH coupling was proposed by Ataway et al. [3]. They developed a penalty based approach for modelling of fluid-structure interactions where the fluid was discretised with particles and the structure was modelled with finite elements. A similar approach was proposed by Johnson [28] and Johnson et al. [29]. In addition to the contact algorithm, they developed a tied interface where SPH particles are fixed to FE nodes. This allows for a continuous coupling of the SPH and the FE domains. Sauer [64] proposed an SPH-FE coupling by extending the SPH domain onto the FE mesh. Different possibilities for exchanging forces between FE nodes and particles were shown, and the approach was used for adaptive conversion of elements into particles. The main difference with most other coupling methods is the use of a strong-form coupling. This approach was successfully applied to a number of impact problems, see Sauer et al. [65][66] and Hiermaier et al. [21][22]. Using a variation of the contact algorithm they developed for SPH, De Vuyst and Vignjevic [15] coupled Cranfield University SPH code with Lawrence Livermore National Laboratory DYNA3D.

Coupling algorithms developed for other meshless techniques can be applied for use with SPH. Among many recently proposed techniques a selected few are mentioned below. A mixed hierarchical approximation based on meshless methods and FE, proposed by Huerta et al. [23][24], remove the discontinuities in the derivative across the interior boundaries when coupling FE and the element-free Galerkin method (EFG). Belytschko and Xiao [9] proposed the 'bridging domain coupling method' which uses Lagrange multipliers over a domain where FE and particle discretisations overlap. They applied this approach to multi-scale simulations for coupling continua with molecular dynamics. Another method for atomic and continua scale bridging was proposed by Wagner and Liu [82] and Kadowaki and Liu [31]. By matching dynamic impedances of different discretisation domains spurious wave reflection is prevented in this approach.

A comprehensive overview of techniques for coupling of a range of meshless methods with FE with examples is given in Li and Liu [38].

20.2 Basic Formulation

The spatial discretisation of the state variables is provided by a set of points. Instead of a grid, SPH uses kernel interpolation to approximate the field variables at any point in a domain. For instance, an estimate of the value of a function $f(\mathbf{x})$ at the location \mathbf{x} is given in a continuous form by an integral of the product of the function and a kernel (weighting) function $W(|\mathbf{x} - \mathbf{x}'|, h)$:

$$\langle f(\mathbf{x}) \rangle = \int_{\Omega} f(\mathbf{x}') W(|\mathbf{x} - \mathbf{x}'|, h) d\mathbf{x}' \quad (20.1)$$

Where: the angle brackets $\langle \ \rangle$ denote a kernel approximation, h is a parameter that defines the size of the kernel support known as the smoothing length and \mathbf{x}' is the new independent variable.

The kernel function usually has the following properties:

- Compact support, which means that it is zero everywhere but on a finite domain, in conventional SPH this domain is taken to be all points within twice the smoothing length, h , of the centre:

$$|\mathbf{x} - \mathbf{x}'| \geq 2h \quad (20.2)$$

- Normalised

$$\int_{\Omega} W(|\mathbf{x} - \mathbf{x}'|, h) d\mathbf{x}' = 1 \quad (20.3)$$

These requirements, formulated by Lucy [42], ensure that the kernel function reduces to the Dirac delta function when h tends to zero:

$$\lim_{h \rightarrow 0} W(|\mathbf{x} - \mathbf{x}'|, h) = \delta(|\mathbf{x} - \mathbf{x}'|, h) \quad (20.4)$$

And therefore, it follows that:

$$\lim_{h \rightarrow 0} \langle f(\mathbf{x}) \rangle = f(\mathbf{x}) \quad (20.5)$$

If the function $f(\mathbf{x})$ is only known at N discrete points, the integral of equation 20.1 can be approximated by a summation:

$$\begin{aligned} f_I = f(\mathbf{x}_I) &\approx \langle f(\mathbf{x}_I) \rangle = \int_{\Omega} f(\mathbf{x}') W(|\mathbf{x} - \mathbf{x}'|, h) d\mathbf{x}' \\ &\approx \sum_{J=1}^N \frac{m_J}{\rho_J} f(\mathbf{x}_J) W(|\mathbf{x}_I - \mathbf{x}_J|, h) \end{aligned} \quad (20.6)$$

In the above equation, the subscript I and J denote particle number, m_J and ρ_J the mass and the density of particle J , N the number of neighbours of particle I (number of particles that interact with particle I , i.e. the support of the kernel), $\frac{m_J}{\rho_J}$ is the volume associated to the point or particle J and $W_{IJ} = W(|\mathbf{x}_I - \mathbf{x}_J|, h)$.

In SPH literature, the term particles is misleading as in fact these particles have to be thought of as interpolation points rather than mass elements.

Equation (20.6) constitutes the basis of the SPH method. The value of a variable at a particle, denoted by superscript I , is calculated by summing the contributions from a set of neighbouring particles (Figure 20.1), denoted by superscript J , for which the kernel function is not zero:

$$\langle f(\mathbf{x}_I) \rangle = \sum_J \frac{m_J}{\rho_J} f(\mathbf{x}_J) W(|\mathbf{x}_I - \mathbf{x}_J|, h) \quad (20.7)$$

20.3 Conservation Equations

The conservation equations in the Lagrangian framework are given by:

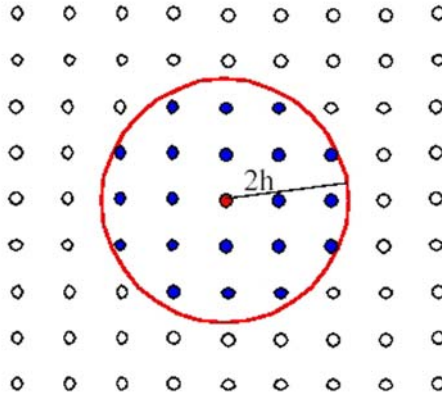


Fig. 20.1 Set of neighbouring particles.

$$\frac{D\rho}{Dt} = -\rho \nabla \cdot \mathbf{v} \tag{20.8}$$

$$\frac{D\mathbf{v}}{Dt} = \frac{1}{\rho} \nabla \cdot \boldsymbol{\sigma} \tag{20.9}$$

or

$$\frac{D\mathbf{v}}{Dt} = \nabla \cdot \left(\frac{\boldsymbol{\sigma}}{\rho} \right) + \frac{\boldsymbol{\sigma}}{\rho^2} \cdot \nabla \rho \tag{20.10}$$

$$\frac{DE}{Dt} = \frac{1}{\rho} \boldsymbol{\sigma} : \nabla \mathbf{v} \tag{20.11}$$

or

$$\frac{DE}{Dt} = \frac{1}{\rho^2} \boldsymbol{\sigma} : \nabla(\rho \mathbf{v}) - \frac{\boldsymbol{\sigma} \cdot \mathbf{v}}{\rho^2} \cdot \nabla \rho \tag{20.12}$$

where $\frac{D}{Dt}$ is the material time derivative and $\mathbf{v} = \dot{\mathbf{x}}$.

Equations (20.10) and (20.12) are the forms proposed by Monaghan [46]. Kernel interpolation allows the derivation of the basic SPH form of these conservation equations as follows:

$$\left\langle \frac{D\rho(\mathbf{x})}{Dt} \right\rangle = \int_{\Omega} \rho(\mathbf{x}') \nabla \cdot \mathbf{v}(\mathbf{x}') W(|\mathbf{x} - \mathbf{x}'|, h) d\mathbf{x}' \quad (20.13)$$

$$\begin{aligned} \left\langle \frac{D\mathbf{v}(\mathbf{x})}{Dt} \right\rangle &= \int_{\Omega} \nabla \cdot \left(\frac{\boldsymbol{\sigma}(\mathbf{x}')}{\rho(\mathbf{x}')} \right) W(|\mathbf{x} - \mathbf{x}'|, h) d\mathbf{x}' \\ &\quad + \int_{\Omega} \frac{\boldsymbol{\sigma}(\mathbf{x}')}{\rho(\mathbf{x}')^2} \cdot \nabla \rho(\mathbf{x}') W(|\mathbf{x} - \mathbf{x}'|, h) d\mathbf{x}' \end{aligned} \quad (20.14)$$

$$\begin{aligned} \left\langle \frac{DE(\mathbf{x})}{Dt} \right\rangle &= \int_{\Omega} \frac{\boldsymbol{\sigma}(\mathbf{x}')}{\rho(\mathbf{x}')^2} : \nabla (\rho(\mathbf{x}') \mathbf{v}(\mathbf{x}')) W(|\mathbf{x} - \mathbf{x}'|, h) d\mathbf{x}' \\ &\quad - \int_{\Omega} \frac{\boldsymbol{\sigma}(\mathbf{x}') \cdot \mathbf{v}(\mathbf{x}')}{\rho(\mathbf{x}')^2} \cdot \nabla \rho(\mathbf{x}') W(|\mathbf{x} - \mathbf{x}'|, h) d\mathbf{x}' \end{aligned} \quad (20.15)$$

All of the above equations contain integrals of the form:

$$\int_{\Omega} W(|\mathbf{x} - \mathbf{x}'|, h) f(\mathbf{x}') \frac{\partial g(\mathbf{x}')}{\partial \mathbf{x}'} d\mathbf{x}' \quad (20.16)$$

Using a Taylor series expansion at point $\mathbf{x}' = \mathbf{x}$, it follows:

$$\begin{aligned} &\int_{\Omega} W(|\mathbf{x} - \mathbf{x}'|, h) f(\mathbf{x}') \frac{\partial g(\mathbf{x}')}{\partial \mathbf{x}'} d\mathbf{x}' \\ &= \int_{\Omega} \left\{ f(\mathbf{x}) \frac{\partial g(\mathbf{x})}{\partial \mathbf{x}} + (\mathbf{x} - \mathbf{x}') \frac{d}{d\mathbf{x}} \left(f(\mathbf{x}) \frac{\partial g(\mathbf{x})}{\partial \mathbf{x}} \right) + \dots \right\} W(|\mathbf{x} - \mathbf{x}'|, h) d\mathbf{x}' \end{aligned} \quad (20.17)$$

As W is an even function, the terms containing odd powers of $\mathbf{x}' - \mathbf{x}$ vanish. Neglecting second and higher order terms, which is consistent with the overall order of the method, gives:

$$\begin{aligned} &\int_{\Omega} W(|\mathbf{x} - \mathbf{x}'|, h) f(\mathbf{x}') \frac{\partial g(\mathbf{x}')}{\partial \mathbf{x}'} d\mathbf{x}' \\ &= f(\mathbf{x}) \frac{\partial g(\mathbf{x})}{\partial \mathbf{x}} \int_{\Omega} W(|\mathbf{x} - \mathbf{x}'|, h) d\mathbf{x}' = f(\mathbf{x}) \frac{\partial g(\mathbf{x})}{\partial \mathbf{x}} \end{aligned} \quad (20.18)$$

Substituting $\left\langle \frac{\partial g(\mathbf{x})}{\partial \mathbf{x}} \right\rangle$ for $\frac{\partial g(\mathbf{x})}{\partial \mathbf{x}}$ gives:

$$f(\mathbf{x}) \frac{\partial g(\mathbf{x})}{\partial \mathbf{x}} = f(\mathbf{x}) \int_{\Omega} \mathbf{W}(|\mathbf{x} - \mathbf{x}'|, \mathbf{h}) \frac{\partial \mathbf{g}(\mathbf{x}')}{\partial \mathbf{x}'} d\mathbf{x}' \quad (20.19)$$

Using the last relation in equations (20.13), (20.14) and (20.15) yields

$$\left\langle \frac{D\rho(\mathbf{x})}{Dt} \right\rangle = -\rho(\mathbf{x}) \int_{\Omega} W(|\mathbf{x} - \mathbf{x}'|, h) \nabla \cdot \mathbf{v}(\mathbf{x}') d\mathbf{x}' \quad (20.20)$$

$$\begin{aligned} \left\langle \frac{D\mathbf{v}(\mathbf{x})}{Dt} \right\rangle &= \int_{\Omega} W(|\mathbf{x} - \mathbf{x}'|, h) \nabla \cdot \left(\frac{\boldsymbol{\sigma}(\mathbf{x}')}{\rho(\mathbf{x}')} \right) d\mathbf{x}' \\ &\quad + \frac{\boldsymbol{\sigma}(\mathbf{x})}{\rho(\mathbf{x})^2} \int_{\Omega} W(|\mathbf{x} - \mathbf{x}'|, h) \nabla \rho(\mathbf{x}') d\mathbf{x}' \end{aligned} \quad (20.21)$$

$$\begin{aligned} \left\langle \frac{DE(\mathbf{x})}{Dt} \right\rangle &= \frac{\boldsymbol{\sigma}(\mathbf{x})}{\rho(\mathbf{x})^2} \int_{\Omega} W(|\mathbf{x} - \mathbf{x}'|, h) \nabla (\rho(\mathbf{x}') \mathbf{v}(\mathbf{x}')) d\mathbf{x}' \\ &\quad - \frac{\boldsymbol{\sigma}(\mathbf{x}) \cdot \mathbf{v}(\mathbf{x})}{\rho(\mathbf{x})^2} \int_{\Omega} W(|\mathbf{x} - \mathbf{x}'|, h) \nabla \rho(\mathbf{x}') d\mathbf{x}' \end{aligned} \quad (20.22)$$

Note that all equations include kernel approximations of spatial derivatives:

$$\langle \nabla f(\mathbf{x}) \rangle = \int_{\Omega} \nabla f(\mathbf{x}') W(|\mathbf{x} - \mathbf{x}'|, h) d\mathbf{x}' \quad (20.23)$$

Integrating by parts gives:

$$\begin{aligned} \langle \nabla f(\mathbf{x}) \rangle &= \int_{\Omega} \nabla (W(|\mathbf{x} - \mathbf{x}'|, h) f(\mathbf{x}')) d\mathbf{x}' \\ &\quad - \int_{\Omega} f(\mathbf{x}') \nabla W(|\mathbf{x} - \mathbf{x}'|, h) d\mathbf{x}' \end{aligned} \quad (20.24)$$

Using Green's theorem, the first term of the right hand side can be rewritten as:

$$\int_{\Omega} \nabla (f(\mathbf{x}') W(|\mathbf{x} - \mathbf{x}'|, h)) d\mathbf{x}' = \int_S f(\mathbf{x}') W(|\mathbf{x} - \mathbf{x}'|, h) \mathbf{n} dS = 0 \quad (20.25)$$

The surface integral is zero if the domain of integration is larger than the compact support of W or if the field variable assumes zero value on the boundary of the body (free surface). If none of these conditions are satisfied, modifications should be made to account for boundary conditions.

One should observe that in Equations (20.20), (20.21) and (20.22) the spatial derivatives of the field variables are substituted by the derivatives of the kernel function giving:

$$\left\langle \frac{D\rho(\mathbf{x})}{Dt} \right\rangle = \rho(\mathbf{x}) \int_{\Omega} \mathbf{v}(\mathbf{x}') \nabla W(|\mathbf{x} - \mathbf{x}'|, h) d\mathbf{x}' \quad (20.26)$$

$$\begin{aligned} \left\langle \frac{D\mathbf{v}(\mathbf{x})}{Dt} \right\rangle &= - \int_{\Omega} \frac{\sigma(\mathbf{x}')}{\rho(\mathbf{x}')} \nabla W(|\mathbf{x} - \mathbf{x}'|, h) d\mathbf{x}' \\ &\quad - \frac{\sigma(\mathbf{x})}{\rho(\mathbf{x})^2} \int_{\Omega} \rho(\mathbf{x}') \nabla W(|\mathbf{x} - \mathbf{x}'|, h) d\mathbf{x}' \end{aligned} \quad (20.27)$$

$$\begin{aligned} \left\langle \frac{DE(\mathbf{x})}{Dt} \right\rangle &= - \frac{\sigma(\mathbf{x})}{\rho(\mathbf{x})^2} \int_{\Omega} \rho(\mathbf{x}') \mathbf{v}(\mathbf{x}') \nabla W(|\mathbf{x} - \mathbf{x}'|, h) d\mathbf{x}' \\ &\quad + \frac{\sigma(\mathbf{x}) \mathbf{v}(\mathbf{x})}{\rho(\mathbf{x})^2} \int_{\Omega} \rho(\mathbf{x}') \nabla W(|\mathbf{x} - \mathbf{x}'|, h) d\mathbf{x}' \end{aligned} \quad (20.28)$$

The final step is to convert the continuous volume integrals to sums over discrete interpolation points. Finally, after a few algebraic manipulations to improve the consistency between all equations, the most common form of the SPH discretised conservation equations are obtained:

$$\left\langle \frac{D\rho_I}{Dt} \right\rangle = \rho_I \sum_{j=1}^N \frac{m_j}{\rho_j} (\mathbf{v}_j - \mathbf{v}_I) \nabla W(|\mathbf{x}_I - \mathbf{x}_j|, h) \quad (20.29)$$

$$\left\langle \frac{D\mathbf{v}_I}{Dt} \right\rangle = - \sum_{j=1}^N m_j \left(\frac{\sigma_j}{\rho_j^2} + \frac{\sigma_I}{\rho_I^2} \right) \nabla W(|\mathbf{x}_I - \mathbf{x}_j|, h) \quad (20.30)$$

$$\left\langle \frac{DE_I}{Dt} \right\rangle = - \frac{\sigma_I}{\rho_I} \sum_{j=1}^N m_j (\mathbf{v}_j - \mathbf{v}_I) \nabla W(|\mathbf{x}_I - \mathbf{x}_j|, h) \quad (20.31)$$

20.4 Kernel Function

To complete the discretisation one has to define the kernel function. Numerous possibilities exist, and a large number of kernel function types are discussed in literature, ranging from polynomial to Gaussian. The most common is the B-spline kernel that was proposed by Monaghan [46]:

$$W(v, h) = \frac{C}{h^D} \begin{cases} \left(1 - \frac{3}{2}v^2 + \frac{3}{4}v^3\right) & v < 1 \\ \frac{1}{4}(2-v)^3 & 1 \leq v \leq 2 \\ 0 & \text{otherwise} \end{cases} \quad (20.32)$$

where $v = \frac{|\mathbf{x} - \mathbf{x}'|}{h}$, D is the number of dimensions of the problem (i.e. 1, 2 or 3) and C is the scaling factor which depends on the number of dimensions and ensures that the consistency conditions 2 and 3 are satisfied:

$$C = \begin{cases} \frac{2}{3} & D = 1 \\ \frac{10}{7\pi} & D = 2 \\ \frac{1}{\pi} & D = 3 \end{cases} \quad (20.33)$$

The derivatives of the kernel function have the following property $\frac{\partial W(|\mathbf{x} - \mathbf{x}'|, h)}{\partial x'_k} = -\frac{\partial W(|\mathbf{x} - \mathbf{x}'|, h)}{\partial x_k}$. It is important not to forget the dimensionality of the kernel function W . For instance, in one dimension, W has dimension of length⁻¹ and the dimension of $\frac{\partial W}{\partial x}$ is thus length⁻². The mass, m , should be interpreted as mass per unit area, with the cross-sectional area equal to one.

20.5 Variable Smoothing Length

If large deformations occur, particles can move apart. In the case of conventional (Eulerian) SPH, if the smoothing length remains constant, the particle spacing can become so large that particles will no longer interact. On the other hand, in compression, the number of neighbour particles within the support can become large, which can significantly slow down the calculation. In order to avoid these problems, Gingold and Monaghan [18] suggested that it would be preferable to allow h for any particle to be related to its density according to

$$h = G \left(\frac{m}{\rho} \right)^{\frac{1}{n}} \quad (20.34)$$

where n is the number of dimensions and G is a constant approximately $G \approx 1.3$. Benz [10] proposed the use of a variable smoothing length with the intent of maintaining a healthy neighbourhood as the continuum deforms. His equation for the evolution of h is:

$$h = h_0 \left(\frac{\rho_0}{\rho} \right)^{\frac{1}{n}} \quad (20.35)$$

where h_0 and ρ_0 are initial smoothing length and density and n is the number of dimensions of the problem. Another frequently used equation for the evolution of h based on conservation of mass is:

$$\frac{dh}{dt} = \frac{1}{n} h \nabla \cdot \mathbf{v} \quad (20.36)$$

According to Monaghan [52] and Price and Monaghan [57], h should be determined from the summation equations so that it is consistent with the density obtained from the summation, i.e. $\rho_I = \sum_J m_J W(|\mathbf{x}_I - \mathbf{x}_J|, h_I)$, where ρ_I is estimated from the SPH summation.

It is important to observe that the methods for variation of h described above are empirical in nature. The evolution of h if treated rigorously should be coupled and consistent with the discretised form of the conservation equations. A rigorously derived Eulerian SPH with a variable smoothing length requires further research and is still outstanding.

20.6 Neighbour Search

In the SPH method the interpolation points move with the continuum and as a consequence the neighbours of a particle are not fixed. This implies that the SPH kernel approximation of any field variable at a particle I requires as a first step a search for the neighbouring particles J that are within the kernel support of particle I .

Therefore, the neighbour search is an important and CPU-time consuming step in an SPH computation. Based on the distance between the interpolation points the neighbour search routine must list the particles that are inside the neighbourhood of each particle at each time step. A direct search between every particle is particularly inefficient, requiring a time proportional to N^2 , where N is the total number of particles.

A bucket sort algorithm is more efficient. In this method, an underlying grid of cells of size $2h_{\text{MAX}}$ is generated and the particles are sorted according to the box, within a background grid, in which they are located (Figure 20.2). The total extent of the grid is defined to contain all particles and is updated as the problem evolves. Then for each particle, the neighbours are searched among the particles contained in the same box and its neighbouring boxes. This allows the computational time to be cut down to a time proportional to $N \log N$, Monaghan and Lattanzio [47].

Each particle I carries the information about the box that currently contains the particle. Then, to determine the neighbour list of the particle a search is performed over all particles contained in the same box and its neighbouring boxes. This results in a search over three boxes in 1D, nine boxes in 2D and 27 boxes in 3D.

Good algorithm design can minimise the computational cost of the search. For example the coordinates of each particle can also be stored in an integer format which reduces the time for data access. The integer coordinates x_{int}^I are computed from the particle position vector x_I as:

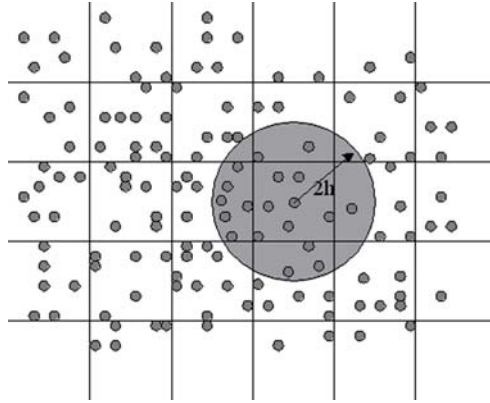


Fig. 20.2 Bucket sort and neighbour search.

$$x_{\text{int}}^I = \text{floor} \left(\frac{N_{\text{SUB}}}{2h_{\text{MAX}}} x^I \right) \quad (20.37)$$

Where N_{SUB} is the number of box subdivisions, typically $N_{\text{SUB}} = 1000$.

20.7 SPH Shortcomings

As mentioned in the introduction, the basic SPH method has been shown to have several problems:

- Consistency
- Tensile instability
- Zero-energy modes

20.7.1 Consistency

The SPH method even in its continuous form is inconsistent within $2h$ of the domain boundaries due to kernel support incompleteness. In its discrete form the method loses its O^{th} -order consistency not only in the vicinity of boundaries but also over the rest of the domain if particles have an irregular distribution. Meglicki [43] showed that node disorder results in a systematic error. Therefore a proper SPH grid should be as regular as possible and not contain large discrepancies in particle spacing in order to perform an accurate simulation.

First-order consistency of the method can be achieved in two ways. Firstly, by correcting the kernel function, and secondly, by correcting the discrete form of the convolution integral of the SPH interpolation. Johnson [30] uses the former correction procedure and proposed the Normalised Smoothing Function. Vignjevic [76] also implemented a kernel normalisation and correction to lead to a Corrected Normalised Smooth Particle Hydrodynamics (CNSPH) method which is first-order consistent. The full derivation of this correction is given below. In SPH methods based on a corrected kernel, it is no longer possible to ignore boundary conditions. In basic SPH, free surface boundary conditions are not imposed and are simply ignored as variables tends to zero at boundaries because of the deficiency of neighbour particles.

20.7.1.1 Derivation of Normalised Corrected Gradient SPH formula

Starting from the conventional SPH method of Gingold and Monaghan, which is not even zero-order consistent, a number of researchers worked on the development of a first-order consistent form of SPH. The result of this effort at Cranfield was named Normalised Corrected SPH (NCSPH) and the same term is used in this text for any other similar version of the method.

The approximation of fields using a NCSPH interpolation has been published by Randles and Libersky [60], Vignjevic [76], Bonet [11]. Bonet used properties of the integrals of motion (linear and angular momentum) to derive Normalisation and Gradient Correction for kernel interpolation. This approach lacks generality and does not provide the insight into the origin and the nature of the problem. A full derivation of the correction, proposed by Vignjevic [76], is given below. The derivation is based on the homogeneity and isotropy of space. These are properties of space, which have as a consequence conservation of linear and angular momentum, see Landau [34]. The mixed correction insures that homogeneity and isotropy of space are preserved in the process of spatial discretisation.

An interpolation technique should not affect the homogeneity of space. One way of demonstrating this is to prove that the interpolation of the solution space itself is invariant with respect to translational transformation, in other words independent of a translation of the coordinate axes. In order to express this statement mathematically one can start by writing the general expression for the SPH interpolation of a vector field:

$$\langle \mathbf{F}(\mathbf{x}_I) \rangle = \sum_J \frac{m_J}{\rho_J} \mathbf{F}(\mathbf{x}_J) W(|\mathbf{x}_I - \mathbf{x}_J|, h) \quad (20.38)$$

If the field to be interpolated is the solution space then $\mathbf{F} = \mathbf{x}$ and Equation (20.38) becomes:

$$\langle \mathbf{x} \rangle = \sum_J \frac{m_J}{\rho_J} \mathbf{x}_J W(|\mathbf{x}_I - \mathbf{x}_J|, h) \quad (20.39)$$

In a different, translated coordinate system, this equation is:

$$\langle \mathbf{x}' \rangle |_{\mathbf{x}'=\mathbf{x}'_I} = \sum_J \frac{m_J}{\rho_J} \mathbf{x}'_J W(|\mathbf{x}'_I - \mathbf{x}'_J|, h) \quad (20.40)$$

Where \mathbf{x}' is the coordinate vector in the new coordinate system. If the translation vector by which the origin of the coordinate system was moved is defined as $\Delta \mathbf{x}$ then the relationship between \mathbf{x} and \mathbf{x}' is:

$$\mathbf{x}' = \mathbf{x} - \Delta \mathbf{x} \quad (20.41)$$

If the interpolated coordinates of a point are independent of the translation of coordinate axes then the following should hold:

$$\langle \mathbf{x}' \rangle = \langle \mathbf{x} \rangle - \Delta \mathbf{x} \quad (20.42)$$

By substituting Equation (20.42) into Equation (20.41) for both \mathbf{x}_I and \mathbf{x}_J one obtains:

$$\langle \mathbf{x}' \rangle = \sum_J \frac{m_J}{\rho_J} \mathbf{x}_J W(|\mathbf{x}_I - \mathbf{x}_J|, h) - \sum_J \frac{m_J}{\rho_J} \Delta \mathbf{x} W(|\mathbf{x}_I - \mathbf{x}_J|, h) \quad (20.43)$$

or

$$\langle \mathbf{x}' \rangle = \langle \mathbf{x} \rangle - \Delta \mathbf{x} \sum_J \frac{m_J}{\rho_J} W(|\mathbf{x}_I - \mathbf{x}_J|, h) \quad (20.44)$$

By comparison of Equation (20.44) and Equation (20.42) it is clear that the discretised space will only be homogeneous if the following condition is satisfied:

$$\sum_J \frac{m_J}{\rho_J} W(|\mathbf{x}_I - \mathbf{x}_J|, h) = 1 \quad (20.45)$$

Similarly, an interpolation technique should not affect isotropy of space. One way of demonstrating this is to prove that the interpolation of the solution space itself is independent of a rotation of the coordinate axes. The same holds for the SPH approximation. The change in coordinates due to a rotation of the coordinate axes is:

$$\mathbf{x}' = \mathbf{C} \cdot \mathbf{x} \quad (20.46)$$

where \mathbf{C} is the rotation transformation tensor. For small rotations this can also be stated as:

$$\mathbf{x}' = \mathbf{x} - \Delta \phi \times \mathbf{x} \quad (20.47)$$

where $\Delta \phi$ is an infinitesimal rotation vector.

If one wants to ensure that the SPH approximation does maintain the fact that space is isotropic then the approximation has to satisfy the following condition:

$$\langle \mathbf{x}' \rangle \equiv \langle \mathbf{C} \cdot \mathbf{x} \rangle = \mathbf{C} \cdot \langle \mathbf{x} \rangle \quad (20.48)$$

or

$$\langle \mathbf{C} \rangle = \mathbf{C} \quad (20.49)$$

In other words the rotation matrix has to be approximated exactly. To consider this condition one can start by rewriting

$$\begin{aligned} \mathbf{x}' &= \mathbf{x} - \Delta\phi \times \mathbf{x} \\ &= \mathbf{x} - \nabla(\Delta\phi \times \mathbf{x}) \cdot \mathbf{x} \\ &= \mathbf{x} - \phi^{\mathbf{x}} \mathbf{x} \\ &= (\mathbf{I} - \phi^{\mathbf{x}}) \cdot \mathbf{x} \end{aligned} \quad (20.50)$$

where $\phi^{\mathbf{x}}$ is a skew-symmetric dyadic:

$$\phi^{\mathbf{x}} = \begin{bmatrix} 0 & -\Delta\phi_z \mathbf{e}_1 \mathbf{e}_2 & \Delta\phi_y \mathbf{e}_1 \mathbf{e}_3 \\ \Delta\phi_z \mathbf{e}_2 \mathbf{e}_1 & 0 & -\Delta\phi_x \mathbf{e}_2 \mathbf{e}_3 \\ -\Delta\phi_y \mathbf{e}_3 \mathbf{e}_1 & \Delta\phi_x \mathbf{e}_3 \mathbf{e}_2 & 0 \end{bmatrix} \quad (20.51)$$

For small rotations, the rotation transformation tensor is given by:

$$\mathbf{C} = \mathbf{I} - \phi^{\mathbf{x}} \quad (20.52)$$

The approximation of the rotated coordinates is:

$$\langle \mathbf{x}' \rangle \equiv \langle \mathbf{C} \mathbf{x} \rangle = \langle \mathbf{C} \rangle \langle \mathbf{x} \rangle = \langle \mathbf{I} - \phi^{\mathbf{x}} \rangle \langle \mathbf{x} \rangle \quad (20.53)$$

This means that the requirement on the interpolation is:

$$\mathbf{I} - \phi^{\mathbf{x}} = \langle \mathbf{I} - \phi^{\mathbf{x}} \rangle \quad (20.54)$$

or

$$\phi^{\mathbf{x}} = \langle \phi^{\mathbf{x}} \rangle \quad (20.55)$$

Expanding this expression leads to:

$$\begin{aligned} \langle \phi^{\mathbf{x}} \rangle &= \sum_J \frac{m_J}{\rho_J} \Delta\phi \times \mathbf{x}_J \nabla W(\mathbf{x}_I - \mathbf{x}_J, h) \\ &= \sum_J \frac{m_J}{\rho_J} (\phi^{\mathbf{x}} \mathbf{x}_J) \nabla W(\mathbf{x}_I - \mathbf{x}_J, h) \\ &= \phi^{\mathbf{x}} \sum_J \frac{m_J}{\rho_J} \mathbf{x}_J \otimes \nabla W(\mathbf{x}_I - \mathbf{x}_J, h) \end{aligned} \quad (20.56)$$

Therefore to preserve space isotropy, i.e. $\phi^{\mathbf{x}} = \langle \phi^{\mathbf{x}} \rangle$ the following condition has to be satisfied.

$$\sum_{J=1}^{nbr} \frac{m_J}{\rho_J} \mathbf{x}_J \otimes \nabla W(\mathbf{x}_I - \mathbf{x}_J, h) = \mathbf{I} \quad (20.57)$$

The form of the normalised kernel function and the approximation of the first order derivatives which provides first-order consistency is given in Table 20.1. below.

Table 20.1 Corrected forms of the kernel function and its gradient.

	Space Homogeneity	Space Anisotropy
Condition which has to be satisfied	$\sum_{J=1}^{nbr} \frac{m_J}{\rho_J} W(\mathbf{x}_I - \mathbf{x}_J, h) = 1$	$\sum_{J=1}^{nbr} \frac{m_J}{\rho_J} \mathbf{x}_J \otimes \nabla W(\mathbf{x}_I - \mathbf{x}_J, h) = \mathbf{I}$
Normalised -		
Corrected form	$\tilde{W}_{IJ} = \frac{W(\mathbf{x}_I - \mathbf{x}_J, h)}{\sum_{J=1}^{nbr} \frac{m_J}{\rho_J} W(\mathbf{x}_I - \mathbf{x}_J, h)}$	$\tilde{\nabla} \tilde{W}_{IJ} = \nabla \tilde{W}_{IJ} \left(\sum_{J=1}^{nbr} \frac{m_J}{\rho_J} \mathbf{x}_J \otimes \nabla \tilde{W}_{IJ} \right)^{-1}$

Using the NCSPH approximations the conservation equations assume the following form:

$$\left\langle \frac{D\rho_I}{Dt} \right\rangle = \rho_I \sum_{J=1}^{nbr} \frac{m_J}{\rho_J} (\mathbf{v}_J - \mathbf{v}_I) \cdot \tilde{\nabla} \tilde{W}_{IJ} \tag{20.58}$$

$$\left\langle \frac{D\mathbf{v}_I}{Dt} \right\rangle = - \sum_{J=1}^{nbr} m_J \left(\frac{\sigma_I}{\rho_I^2} + \frac{\sigma_J}{\rho_J^2} \right) \cdot \tilde{\nabla} \tilde{W}_{IJ} \tag{20.59}$$

$$\left\langle \frac{DE}{Dt} \right\rangle = - \frac{\sigma_I}{\rho_I^2} \sum_{J=1}^{nbr} m_J (\mathbf{v}_J - \mathbf{v}_I) \cdot \tilde{\nabla} \tilde{W}_{IJ} \tag{20.60}$$

20.7.2 Tensile Instability

A Von Neumann stability analysis of the SPH method was conducted by Swegle et al. [68] and Balsara [4] separately. These revealed that the SPH method suffers from a tensile instability. This instability manifests itself as a clustering of the particles, which resembles fracture and fragmentation, but is in fact a numerical artefact, see Figure 20.3 below.

Swegle concluded that the instability doesn't result from the numerical time integration algorithm, but rather from an effective stress resulting from a non-physical negative modulus being produced by the interaction between the constitutive relation and the kernel interpolation. In other words the kernel interpolation used in spatial discretisation changes the nature of the original partial differential equations. These changes in the effective stress amplify, rather than reduce, perturbations in the strain. From Swegle's stability analysis it emerged that the criterion for stability was that:

$$W'' \sigma > 0 \tag{20.61}$$

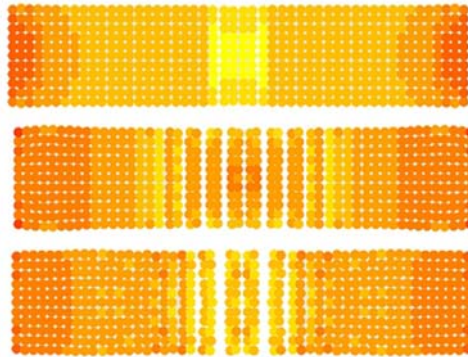


Fig. 20.3 Typical collocated Eulerian SPH behaviour under tension. Although the linear elastic model was used for this simulation (i.e. no fracture is included in the constitutive model), unphysical fracture of the 2-D specimen occurs as a consequence of numerical instability in areas of high tensile stresses.

where W'' is the second derivative of W with respect to its argument and σ is the stress, negative in compression and positive in tension. A stability analysis leading to the stability condition (20.61) is given at the end of this section.

This criterion states that instability can also occur in compression, not only in tension. Indeed, if the slope of the derivative of the kernel function is positive, the method is unstable in tension and stable in compression and if the slope is negative, it is unstable in compression and stable in tension.

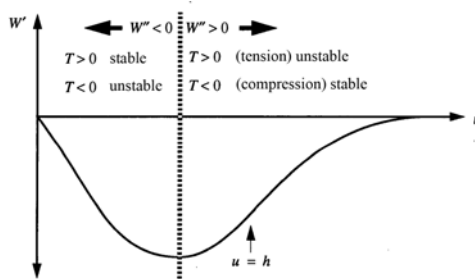


Fig. 20.4 Stability regimes for the B-spline kernel function (Swegle, 1994).

The fact that this instability manifests itself most often in tension can be explained. Figure 20.4 shows the stability regime for the B-spline kernel function. The minimum of the derivative is situated at $u = 2/3h$. In standard configurations, the smoothing length is 1.2 to 1.3 times the particle spacing. Thus, standard con-

figurations are unstable in tension. This explains why this unstable phenomenon is generally observed in tension and hence its misleading name 'tensile instability'.

In order to remedy this problem several solutions have been proposed. Guenther [19] and Wen et al. [83] proposed a solution known as Conservative Smoothing. Randles and Libersky [58] proposed adding dissipative terms, an approach related to conservative smoothing. Dyka and Ingel [17] proposed an original solution by using a non collocated discretisation of stress and velocity points. At one set of points the stresses are evaluated, while the momentum equation is calculated at another set of points. The 'stress' points are equivalent to the Gauss quadrature points in FE, the other set of points is equivalent to the element nodes. This approach was extended to two dimensions, in combination with kernel normalisation, by Vignjevic and Campbell [76]. Other solutions were proposed, for instance see Monaghan [52] who proposes the addition of an artificial force to stabilise the computation. Recently Randles and Libersky [60] combined MLS interpolation with the stress and velocity point approach. They called this approach the Dual Particle Dynamics method.

The conservative smoothing and the artificial repulsive forces methods have limited applicability and have to be used with caution because they may affect the strength of material being modelled. At present, the most promising approach is non-collocational spatial discretisation. This problem is the focus of attention for a number of researchers working on meshless methods.

20.7.2.1 Stability analysis of conventional (Eulerian) SPH

For the analysis of the SPH momentum equation in current configuration, the following 1-D SPH momentum equation with nodal integration is considered:

$$m_I \ddot{u}_I = - \sum_{J \in S} V_J W'_I(x_I - x_J, h) \sigma_J \quad (20.62)$$

Where: V_J is the current volume of particle J , σ_J is the Cauchy stress of particle J and $W'_I(x_I - x_J, h) = \left. \frac{\partial W_I(x_I - x', h)}{\partial x} \right|_{x' = x_J}$. In order to introduce the displacement perturbation on the right hand side of (20.62), the current volume V_J was expressed in terms of the initial particle mass and density as:

$$V_J = \left. \frac{m}{\rho} \right|_J \quad (20.63)$$

where the current density in (20.63) was defined as

$$\rho = J^{-1} \rho_0 \quad (20.64)$$

The substitution of equation (20.64) and equation (20.63) into equation (20.62) and using the fact that in 1D $J = F$, yields:

$$m_I \ddot{u}_I = - \sum_{J \in S} \frac{m_J}{\rho_0} W'_I(x_I - x_J, h) F_J \sigma_J \quad (20.65)$$

In equation (20.65), the deformation gradient is expressed with respect to the current configuration, hence:

$$F_J = \left. \frac{\partial x}{\partial X} \right|_J = \left. \frac{\partial u}{\partial X} \right|_J + 1 = \left. \frac{\partial u}{\partial x} \frac{\partial x}{\partial X} \right|_J + 1 = \frac{1}{1 - \left. \frac{\partial u}{\partial x} \right|_J} \quad (20.66)$$

Equation (20.65) is linearised using perturbations $\bar{u} = u + \bar{u}$, $\bar{x} = x + \bar{x}$, $\bar{F} = F + \bar{F}$ and $\bar{\sigma} = \sigma + \bar{\sigma}$ as follows:

$$m_I \ddot{\bar{u}}_I = - \sum_{J \in S} \frac{m_J}{\rho_0} W'_I(\bar{x}_I - \bar{x}_J, h) \bar{F}_J \bar{\sigma}_J \quad (20.67)$$

$$m_I \ddot{\bar{u}}_I = - \sum_{J \in S} \frac{m_J}{\rho_0} W'_I(\bar{x}_I - \bar{x}_J, h) (\sigma + \bar{\sigma}) (F + \bar{F}) \quad (20.68)$$

which yields

$$m_I \ddot{\bar{u}}_I = - \sum_{J \in S} \frac{m_J}{\rho_0} W'_I(\bar{x}_I - \bar{x}_J, h) (\sigma_J F_J + \sigma_J \bar{F}_J + \bar{\sigma}_J F_J) \quad (20.69)$$

in (20.69) the product $\bar{\sigma} \bar{F}$ was neglected.

When perturbations $\bar{x} = x + \bar{x}$ are introduced, the smoothing function values change as:

$$W(\bar{x}_I - \bar{x}_J, h) = W((x_I + \bar{x}_I) - (x_J + \bar{x}_J), h) \quad (20.70)$$

with $\bar{x}_I = u_I$ and $\bar{x}_J = u_J$ equation (20.70) can be rewritten as

$$W((x_I + \bar{x}_I) - (x_J + \bar{x}_J), h) = W((x_I - x_J) + (u_I - u_J), h) \quad (20.71)$$

Taylor series expansion yields:

$$W(\bar{x}_I - \bar{x}_J, h) = W(x_I - x_J, h) + \Delta x W'(x_I - x_J, h) \quad (20.72)$$

where $\Delta x = u_I - u_J$. Similarly, the derivative of the kernel function in equation (20.72) can be approximated as:

$$W'(\bar{x}_I - \bar{x}_J, h) = W'(x_I - x_J, h) + \Delta x W''(x_I - x_J, h) \quad (20.73)$$

Hence

$$\begin{aligned} W'(\bar{x}_I - \bar{x}_J, h) - W'(x_I - x_J, h) &= (\bar{u}_I - \bar{u}_J) W''(x_I - x_J, h) \\ &= \bar{W}'(x_I - x_J, h) \end{aligned} \quad (20.74)$$

Subtracting equation (20.62) from (20.69) yields:

$$\begin{aligned}
 m_I \ddot{u}_I &= - \sum_{J \in S} \frac{m_J}{\rho_{0J}} W'_I(\bar{x}_I - \bar{x}_J, h) (\sigma_J F_J + \sigma_J \tilde{F}_J + \tilde{\sigma}_J F_J) \\
 &\quad + \sum_{J \in S} \frac{m_J}{\rho_{0J}} W_I(x_I - x_J, h) \sigma_J F_J
 \end{aligned}
 \tag{20.75}$$

Equation (20.75) after rearranging becomes:

$$\begin{aligned}
 m_I \ddot{u}_I &= \sum_{J \in S} \frac{m_J}{\rho_{0J}} (-W'_I(\bar{x}_I - \bar{x}_J, h) + W_I(x_I - x_J, h)) \sigma_J F_J \\
 &\quad - \sum_{J \in S} \frac{m_J}{\rho_{0J}} W'_I(\bar{x}_I - \bar{x}_J, h) (\sigma_J \tilde{F}_J + \tilde{\sigma}_J F_J)
 \end{aligned}
 \tag{20.76}$$

And after substituting equation (20.74) into (20.76) one gets:

$$\begin{aligned}
 m_I \ddot{u}_I &= - \sum_{J \in S} \frac{m_J}{\rho_{0J}} [(\tilde{W}'_I(\bar{x}_I - \bar{x}_J, h)) \sigma_J F_J \\
 &\quad + W'_I(\bar{x}_I - \bar{x}_J, h) (\sigma_J \tilde{F}_J + \tilde{\sigma}_J F_J)]
 \end{aligned}
 \tag{20.77}$$

To perform the Von Neumann stability analysis a Fourier form of perturbation was substituted into the linearised momentum equation

$$\tilde{u} = u_0 e^{i(\omega t + \kappa X)}
 \tag{20.78}$$

where κ is wave number and ω is frequency.

The resulting dispersion relation for the current configuration is expressed as follows, the reader is referred to Randles et al. [60, 61] and Rabczuk et al. [58] for a detailed explanation:

$$\begin{aligned}
 \omega^2 &= \frac{\bar{C}^{\sigma\tau}}{\rho} \left[\sum_{J \in S} W'(j\Delta x) \sin(\kappa \Delta x) \right]^2 \\
 &\quad - \frac{\sigma}{\rho} \left\{ \sum_{J \in S} W''(j\Delta x) [1 - \cos(\kappa j\Delta x)] - \left[\sum_{J \in S} W'(j\Delta x) \sin(\kappa j\Delta x) \right]^2 \right\}
 \end{aligned}
 \tag{20.79}$$

Upon inspection of equation (20.79) it is immediately clear that the three terms contained herein yield three different conditions for stability:

- 1) When the material is unstable, in other words when $\bar{C}^{\sigma\tau}$ vanishes, which corresponds to the material instability of the continuum ($\bar{\omega}^2 = \frac{\bar{C}^{\sigma\tau}}{\rho_0}$, $\bar{C} \leq 0$, equation (3.63), Reveles [63]). This implies (20.79) could have two possible solutions: $\omega = \pm i\sqrt{\bar{x}}$, the negative solution would yield Condition 2 outlined below.
- 2) At the cut-off wave number $\kappa = \frac{\pi}{\Delta x}$, $j = -1$, this is the onset of stability for the particle equations in current configuration for an equally spaced particle ar-

rangement. In this case, the first term in the right hand side of equation (20.79) vanishes. Again, two possible solutions exist: $\omega = \pm i\sqrt{x}$, the negative solution would yield Condition 2.

- 3) When $\sigma > 0$ and $\bar{C}^{\sigma\tau} \neq 0$, which is the tensile instability identified by Sweigle. The second term inside the brackets on the right hand side is always positive, hence, if only $\frac{\bar{C}^{\sigma\tau}}{\rho} \left[\sum_{j \in S} W'(j\Delta x) \sin(\kappa \Delta x) \right]^2$ and $\left(\sum_{j \in S} W'(j\Delta x) \sin(\kappa j\Delta x) \right)^2$ existed, the particle equation would be unconditionally stable (i.e. the only possible solution for ω is a positive real). However, if $\sum_{j \in S} W''(j\Delta x) [1 - \cos(\kappa j\Delta x)]$ is sufficiently positive and $\sigma > 0$, the product of what is in brackets in equation (20.79) and σ would yield a negative value, hence $\omega = \pm i\sqrt{x}$ and again, the negative solution would yield Condition 2. This condition is given by Sweigle et al. [68][69] as $\sigma W'' > 0$ which defines the onset of tensile instability of the SPH equations with nodal integration.

Note that stability condition 1) is desirable as it represents the stability of continuum equations. Conditions 2) and 3) are the result of the type of discretisation carried out in SPH. From this analysis it is clear why some special smoothing functions can reduce or eliminate the tensile instability altogether: as long as the smoothing function is carefully selected, the second derivative might yield a negative value which can restore stability in the particle equation. For the cubic spline, (widely employed for SPH approximations) the value of the second derivative of the smoothing function at a distance $u = 2/3$ (Figure 20.4), from particle I is positive. Therefore, the onset of tensile instability is defined by $\sigma W'' > 0$ Sweigle [68].

The stability analysis of the Eulerian SPH equations, presented above, has revealed that the stability of the system is governed by three terms: a material stability term, which is desirable since this term is also present in the continuum equations, and two more terms which are the result of the type of discretisation carried out, namely the spurious singular mode term and the tensile instability term.

An effective illustration of the distortion of material instability by the spatial discretisation, for the case of a hyperelastic material, is given in Figure 20.5 taken from [58]. The domains of material stability for the Lagrangian kernel, an Eulerian kernel and that of the governing partial differential equation, i.e. the momentum equation are clearly identified. The stable domains are defined in the space of the two principal stretches, λ_1 and λ_2 .

20.7.3 Zero-Energy Modes

Zero-energy modes are a problem that is not unique to particle methods. These spurious modes, which correspond to modes of deformation characterised by a pattern

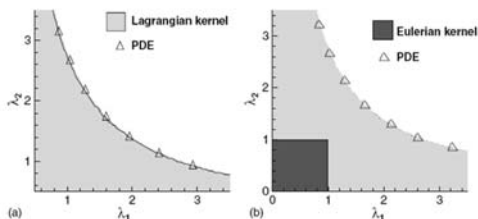


Fig. 20.5 (a) Stable domain for MLS particle method with stress point integration and Lagrangian kernel compared to the stable domain for the PDE; (b) Stable domains of MLS particle methods for stress point integration with Eulerian and Lagrangian kernel for hyperelastic material; dashed and solid lines bound the stable domains for Lagrangian and Eulerian kernels, respectively [58].

of nodal displacement that produces zero strain energy, can also be found in the finite difference and finite element methods.

Swegle [68] was first to show that SPH suffers from zero energy modes. These modes arise from the nodal integration. The fundamental cause is that all field variables and their derivatives are calculated at the same locations (particle positions), which makes the SPH method collocational. For instance, for a 1D oscillatory velocity field, illustrated in Figure 20.6, the kernel approximation would give negligible velocity gradients and consequently stresses at the particles. These modes of deformation are not resisted and can be easily excited by rapid impulsive loading. Another explanation can be found in the origin of the kernel approximation. As the kernel approximation, which is the basis of SPH, is an interpolation of a set of discrete data, a constant field, can be approximated with a sinusoidal curve/surface if the order of the interpolation is high enough.

If one approximates the derivative of the velocity field shown in Figure 20.5 with a central difference formula:

$$\left. \frac{dv}{dx} \right|_{x=x_i} = \frac{f(v_{i+1}) - f(v_{i-1})}{x_{i+1} - x_{i-1}} = 0 \tag{20.80}$$

at all sampling points. Hence this mode can not be detected, and can grow unresisted in other words this mode could grow to a level where it dominates the solution.

Zero energy or spurious modes are characterised by a pattern of nodal displacement that is not rigid body motion but still produces zero strain energy.

One of the key ideas to reduce spurious oscillations is to compute derivatives away from the particles where kernel functions have zero derivatives. Randles [60] proposed a stress point method. Two sets of points are created for the domain discretisation, one carries velocity, and another carries stress. The velocity gradient

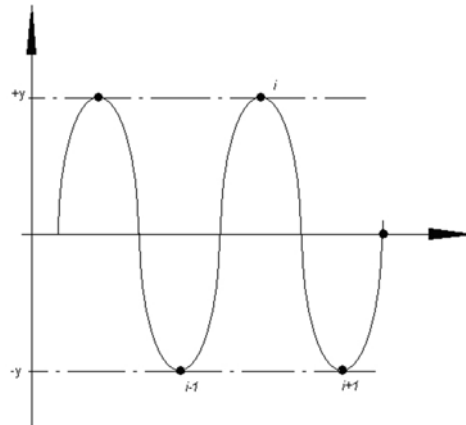


Fig. 20.6 Velocity field that corresponds to a zero energy mode of deformation.

and stress are computed on stress points, while stress divergence is sampled at the velocity points using stress point neighbours. According to Swegle et al. [68][69], these spurious modes can be eliminated by replacing the strain measure by a non-local approximation based on gradient approach. Beissel [5] proposed another way to stabilise nodal integration, the least square stabilisation method.

20.8 Summary

The paper gives an overview of the development of the SPH method. Especial attention is given to the main shortcomings of the original form of the method namely consistency, tensile instability and zero energy modes. These are important to understand as the SPH method is increasingly used in engineering analysis, and without an understanding of the method inappropriate conclusions may be drawn from numerical results.

The paper covers

- A discussion of the kernel interpolation that forms the basis of the SPH spatial interpolation method. In kernel interpolation the variable at a particle is calculated from summing the contribution from all neighbouring particles. The use of a differentiable kernel function allows the spatial gradient of the variable to be approximated.
- An overview of the conventional SPH forms of the conservation equations of Lagrangian continuum mechanics. It should be noted that in these forms the bound-

ary is diffuse and not clearly defined, which is important to understand when modelling solids or liquids.

- A summary of the kernel function, varying smoothing length and neighbour search algorithm that are commonly used in SPH implementations.
- An example of the derivation of a correction necessary to insure first-order consistency is given. The conventional SPH method is not first order consistent and is not even zero-order consistent except in the special case when particles are evenly distributed.
- The introduction of corrected SPH requires boundary conditions to be treated rigorously. In the conventional SPH method the deficiency in neighbour particles at the boundary of the domain leads to an error in the interpolation that allows free surfaces to be approximately treated.
- A summary of a stability analysis of SPH is presented and used to explain the so called tensile instability problem. This problem is relevant for solid mechanics simulations where the instability can lead to fracture occurring and preventing accurate analysis of problems involving material fracture. A few proposed solutions to this problem are described. Similar consideration is given with respect to the zero energy modes typical for the collocational SPH method.

This paper provides an overview of the key aspects of the SPH method and discusses issues that any user of the method should be aware of.

References

1. Atluri S., Zhu T. (2000) A new meshless local Petrov Galerkin (MLPG) approach in computational mechanics, *Computational Mechanics*, Vol 22, pp 117-127
2. Atluri S., H. G. Kim, J. Y. Cho, (2000), A critical assessment of the truly meshless local Petrov Galerkin (MLPG) and local boundary integral equation (LBIE), *Computational Mechanics*, Vol 24, pp 348-372
3. Attaway S. W., Heinstejn M.W., and Swegle J.W. (1994) Coupling of smooth particle hydrodynamics with the finite element method. *Nuclear Engineering and Design*, 150:199–205.
4. Balsara D.S., Von Neumann stability analysis of smoothed particle hydrodynamics – Suggestions for optimal algorithms, *J. Comput. Phys.*, 121 (1995), 357–372.
5. Beissel, S. and Belytschko T. (1996). Nodal integration of the element-free Galerkin method. *Computational Methods Applied Mechanical Engineering*, Vol. 139 , pp. 49-71.
6. Belytschko T., Krongauz Y., Organ D., Fleming M., Krysl P. (1996) Meshless Methods: An overview and recent developments *Computer methods in applied mechanics and engineering*, 139:3–47.
7. Belytschko T., Y.Y. Lu, and L. Gu. (1994) Element-free Galerkin methods. *International Journal for Numerical methods in Engineering*, 37:229–256, 1994.
8. Belytschko T., Xiao S. (2002), 'Stability Analysis of Particle Methods with Corrected Derivatives', <http://www.tam.northwestern.edu/xiaop/stable.html>
9. Belytschko T, Xiao SP. (2004), A bridging domain method for coupling continua with molecular dynamics. *Computer Methods in Applied Mechanics and Engineering*; 193: pp. 1645-1669.
10. Benz, W. (1990). Smooth particle hydrodynamics: a review. In J.R. Buchler, editor, *The Numerical Modelling of Nonlinear Stellar Pulsations*, pp. 269-288. Kluwer Academic Publishers. Cited in: Campbell J. (1998). *Lagrangian hydrocode modelling of hypervelocity impact on spacecraft*. PhD thesis, Cranfield University

11. Bonet J. and Kulasegaram S. (1999). Correction and stabilization of smooth particle hydrodynamics methods with application in metal forming simulation. *International Journal of Numerical Methods Engineering*, Vol. 47, pp. 1189-1214.
12. Campbell J., Vignjevic R., Libersky L., (2000), A Contact Algorithm for Smoothed Particle Hydrodynamics, *Computer Methods in Applied Mechanics and Engineering*, Vol. 184/1, pp 49-65, March 2000.
13. Campbell P. M., (1989), Some new algorithms for boundary value problems in smooth particle hydrodynamics. Technical Report DNA-TR-88-286, Mission Research Corporation.
14. Cha S. H. and Whitworth A.P., (2003), Implementations and tests of Godunov-type particle hydrodynamics, *Mon. Not. R. Astron. Soc.*, 340 pp. 73-90
15. De Vuyst T., Vignjevic R. and Campbell J. (2005), Modelling of Fluid-Structure Impact Problems using a Coupled SPH-FE solver, *Journal of Impact Engineering*, Volume 31, Issue 8, pp. 1054-1064
16. Dilts G. A., (1997), Moving -least squares-particle hydrodynamics I, consistency and stability. *International Journal for Numerical Methods in Engineering*, 44, pp. 1115-55
17. Dyka C. T., Ingel R.P., (1995), An approach for tension instability in smoothed particle hydrodynamics (SPH). *Computers and Structures*, 57(4), pp. 573-580
18. Gingold, R.A. and Monaghan, J.J. (1977). Smoothed particle hydrodynamics: theory and application to non-spherical stars. *Monthly Notices Royal Astronomical Society*, Vol. 181, pp. 375-389.
19. Guenther C., Hicks D.L., Swegle J.W. (1994). Conservative smoothing versus artificial viscosity. Technical Report SAND94-1853.
20. Harten A., P. D. Lax P. D.. and van Leer B., (1983). On upstream differencing and Godunov-type schemes for hyperbolic conservation laws, *SIAM Review*, V 25, no 1, pp 35 -61.
21. Hiermaier S., Peter J., Sauer M., Thoma K. (2001): Coupled FE-Particle Codes Applied to Material Characterization and Crash Simulation. *European Conference on Computational Mechanics (ECCM)*, Krakau, Polen, 26.-29.06..
22. Hiermaier S. and Sauer M., (2003), Adaptive FE-Meshfree Modelling for impacts of liquid filled vessels on thin walled structures. *Proceedings of IMECE'03, ASME International Mechanical Engineering Congress and Exposition*, Washington DC, paper IMECE2003-44189
23. Huerta A, Fernandez-Mendez S., (2000), Enrichment and coupling of the finite element and meshless method, *International Journal for Numerical Methods in Engineering*; 48: pp. 1615-1636.
24. Huerta A, Fernandez-Mendez S, Liu WK., (2004), A comparison of two formulations to blend finite elements and meshfree methods. *Computer Methods in Applied Mechanics and Engineering*; 193 (12-14): pp. 1105-1117
25. Hughes T. J. R. (1987). *The finite element method*, Prentice Hall.
26. Inutsuka S.-I., Reformulation of smoothed particle hydrodynamics with Riemann solver, *J. Comput. Phys.*, 179 (2002), pp. 238-267
27. Johnson, G.R., Petersen, E.H. and Stryk, R.A. (1993). Incorporation of an SPH option in the EPIC code for a wide range of high velocity impact computations. *International Journal of Impact Engineering*, Vol. 14, pp. 385-394.
28. Johnson, G.R. (1994). Linking of Lagrangian particle methods to standard finite element methods for high velocity impact computations *Nuclear Engineering and Design*, Vol. 150, pp. 265-274.
29. Johnson G. R. and S.R. Beissel. (1996a). Normalised smoothing functions for SPH impact computations. *International Journal for Numerical Methods in Engineering*, 39:2725-2741.
30. Johnson, G.R., Stryk, R.A. and Beissel, S.R. (1996b). SPH for high velocity impact computations. *Computer Methods in Applied Mechanics and Engineering*, Vol. 139, pp. 347-373.
31. Kadowaki H, Liu WK., (2005), A multiscale approach for the micropolar continuum model. *Computer Modeling in Engineering and Sciences*; 7(3): pp. 269-282.
32. Krongauz Y., Belytschko T. (1997). Enforcement of essential boundary conditions in measles approximations using finite elements. Submitted to *International Journal for Numerical Methods in Engineering*.

33. Krongauz Y., Belytschko T. (1997). Consistent pseudo derivatives in meshless methods Computer methods in applied mechanics and engineering, 146:371–386.
34. Landau L. D. Lifshitz E.M. (1960). Mechanics, Course of Theoretical Physics, V 1, Pergamon Press
35. Lattanzio J. C., J.J. Monaghan, H. Pongracic, P. Schwarz. (1996). Controlling penetration. SIAM, Journal for Scientific and Statistic Computation, V 7, No 2, pp 591–598.
36. Libersky, L.D. and Petschek, A.G., (1990), Smooth particle hydrodynamics with strength of materials. Advances in the Free Lagrange Method, Lecture Notes in Physics, Vol. 395, pp. 248-257.
37. Libersky L.D., Petschek A.G., Carney T.C., Hipp J.R. and Allahdadi F.A., (1993), High Strain Lagrangian Hydrodynamics: A Three-Dimensional SPH Code for Dynamic Material Response, Journal of Computational Physics, Vol. 109, Issue 1, November, pp. 67-75.
38. Li S, Liu WK., (2004), Meshfree Particle Methods. Springer: Berlin
39. Liu M. B., Liu G. R. and Lam K. Y., (2003), Constructing smoothing functions in smoothed particle hydrodynamics with applications, J. Comp. Appl. Math, 155, 263-284
40. Liu W. K., Jun S. and Zhang Y. F., (1995), Reproducing kernel particle methods, Int. J. Num. Meth. Engrng., 20, pp. 1081-1106
41. Liu W. L., Jun Li S, Adee J. and Belytschko T., (1995), Reproducing kernel particle methods for structural dynamics, International Journal for Numerical Methods in Engineering, 38: pp. 1655-1679
42. Lucy, L.B., (1977), A numerical approach to the testing of fusion process. Astronomical journal, Vol. 88, pp. 1013-1024
43. Meglicki Z., Analysis and Application of Smoothed Particle Magneto-Hydrodynamics, PhD thesis, Australian National University
44. Mitchell A. R. and Griffiths D. F., (1980), The finite difference method in partial differential equations, John Wiley
45. Monaghan J.J., (1982), Why particle methods work, SIAM Journal on Scientific and Statistical Computing, 3(4): pp. 422-433
46. Monaghan J.J. and Gingold R.A., (1983), Shock simulation by the particle method SPH, Journal of Computational Physics, Vol. 52, pp. 374-389
47. Monaghan J.J. and Lattanzio J.C., (1985), A refined particle method for astrophysical problems. Astronomy and Astrophysics, Vol. 149, Issue 1, pp. 135-143
48. Monaghan J.J., Pongracic H., (1985), Artificial viscosity for particle methods. Applied Numerical Mathematics, 1: pp. 187-194
49. Monaghan J.J., (1989), On the problem of penetration in particle methods. Journal of Computational Physics, 82:, pp. 1-15
50. Monaghan J.J., (1992), Smoothed Particle Hydrodynamics. Annual Review of Astronomy and Astrophysics, 30: pp. 543-574
51. Monaghan, J.J., (2000), SPH without a Tensile Instability. Journal of Computational Physics, Vol. 159, pp. 290-311
52. Monaghan J., (2002), SPH compressible turbulence Mon. Not. R. Astron. Soc. 335, pp. 843-52
53. Moussa B., (2000), Meshless Particle methods: Recent developments for non-linear conservation laws in bounded domain, in Godunov Methods: Theory and Applications, E. F. Toro (Editor), Kluwer Academic/Plenum Publishers
54. Moussa B., J. P. Vila, (2000), Convergence of the SPH method for scalar nonlinear conservation laws, SIAM Journal of Numerical Analysis, Vol 37 number 3, pp 863-887.
55. Parshikov A. N., Medin S. A., Loukashenko I. I. and Milekhin V. A., (2000), Improvements in SPH method by means of inter-particle contact algorithm and analysis of perforation tests at moderate projectile velocities, Int. J. Impact Engng., 24 pp 779-796
56. Petschek A. G. and Libersky, L. D., (1993), Cylindrical smoothed particle hydrodynamics. Journal of Computational Physics, Vol. 109, pp. 76-83.
57. Price J. and Monaghan J., (2004), Smoothed particle magneto-hydrodynamics: II. Variational principles and variable smoothing length terms, Mon. Not. R. Astron. Soc. 348, pp. 139-52

58. Rabczuk T, Belytschko T, Xiao SP., (2004), Stable particle methods based on Lagrangian kernels. *Computer Methods in Applied Mechanics and Engineering*; 193: pp. 1035-1063
59. Randles P. W. and Libersky L. D., (1996), Smoothed particle hydrodynamics: Some recent improvements and applications, *Computer methods in applied mechanics and engineering*, 139, pp. 375-408.
60. Randles, P.W., Libersky, L.D. and Petschek, A.G., (1999), On neighbors, derivatives, and viscosity in particle codes, in: *Proceedings of ECCM Conference, Munich, Germany*
61. Randles, P.W., Libersky, L.D., (2000), Normalised SPH with stress points, *Int. Journal Numerical Methods in Engineering*, Vol. 48, pp. 1445-1462
62. Resnyansky, A. D., (2002), DYNA-modelling of the high-velocity impact problems with a split-element algorithm, *International Journal of Impact Engineering*, Vol. 27, Issue 7, pp. 709-727.
63. Reveles J., (2006), Development of a Total Lagrangian SPH Code for the Simulation of Solids Under Dynamic Loading, PhD Thesis, Cranfield University
64. Sauer M., (2000), Adaptive Kopplung des netzfreien SPH-Verfahrens mit finiten Elementen zur Berechnung von Impaktvorgaengen. Dissertation, Universitaet der Bundeswehr Muenchen, Institut fuer Mechanik und Statik
65. Sauer M., Hiermaier S., Scheffer U. (2001): Modeling Penetration Events using FE/MLSPH Adaptive Coupling. Intern. Symp. on the Interaction of the Effects of Munitions with Structures (10th ISIEMS), San Diego, California, USA, 07.-11.06.
66. Sauer, M., Hiermaier, S., Thoma, K., (2002): Modelling the Continuum/Discrete Transition Using Adaptive Meshfree Methods, *Proceedings of the Fifth World Congress on Computational Mechanics (WCCM V)*, July 7-12, 2002, Vienna, Austria.
67. Stryk R. A., Johnson G.R. and Beissel S.R., (1996), SPH for high velocity impact computations. *Computer methods in applied mechanics and engineering*, 139, pp. 347-373
68. Swegle, J.W., Attaway, S.W., Heinstejn, M.W., Mello, F.J. and Hicks, D.L., (1994), An analysis of smooth particle hydrodynamics, Sandia Report SAND93-2513.
69. Swegle J, (2000) Conservation of momentum and tensile instability in particle methods, Sandia Report 2000-1223
70. Takeda H. T., S. M. Miyama, M. Sekiya. (1994). Numerical simulation of viscous flow by smooth particle hydrodynamics, *Progress of Theoretical Physics*, 92 pp 939-960.
71. Van der Vegt L.J. J. W., Van der Ven H. and Boelens O. J., (1995), Discontinuous Galerkin methods for partial differential equations, in *Godunov Methods: Theory and Applications*.
72. Van Leer B., (1979), Towards the ultimate conservative difference scheme, *J. Comput. Phys.*, 32 pp. 101-136
73. Van Leer B., (2006), Upwind and high-resolution methods for compressible flow: From donor cell to residual-distribution schemes, *Commun. Comput. Phys.*, 1, pp. 192-206
74. Vila J. P., On particle weighted methods and smooth particle hydrodynamics, *Math. Models Methods Appl. Sci.*, 9 (1999) 2, pp. 161-209
75. Vignjevic R., De Vuyst T., Campbell J., (2000), Modelling of Spall in an Anisotropic Aluminium Alloy, *Journal of Space Debris*, Volume 2, Number 4, pp. 225-232
76. Vignjevic R., Campbell J., Libersky L., (2000), A Treatment of Zero Energy Modes in the Smoothed Particle Hydrodynamics Method, *Computer Methods in Applied Mechanics and Engineering*, Vol. 184/1, pp. 67-85
77. Vignjevic R., De Vuyst T., Campbell J., (2002a), The use of a homogeneous repulsive force for contact treatment in SPH, *Fifth World Congress on Computational Mechanics, Vienna, Austria, July 7-12*
78. Vignjevic R., Hughes K. and Taylor E.A., (2002b), Finite element modelling of failure of a multi-material target due to high velocity space debris impacts. *Space Debris*, Vol. 2, pp. 41-50.
79. Vignjevic R., De Vuyst T., Gourma M., (2001), Interpolation Techniques in Meshless Methods, *Computer Modelling in Engineering and Science Journal*, V 2, No. 3, pp 319-337
80. Vignjevic R.; Reveles J., Campbell J., (2006a), SPH in a Total Lagrangian Formalism, *Computer Methods in Applied Mechanics and Engineering*, Vol. 14, No. 3, pp. 181-198,

81. Vignjevic R.; De Vuyst T.; and Campbell J., (2006b), A Frictionless Contact Algorithm for Meshless Methods , A Frictionless Contact Algorithm for Meshless Methods, Computer Methods in Applied Mechanics and Engineering, Vol. 13, No. 1, pp. 35-48,
82. Wagner GJ, Liu WK. (2001), Hierarchical enrichment for bridging scales and meshfree boundary conditions. International Journal for Numerical Methods in Engineering; 50: pp. 507-524.
83. Wen Y., Hicks D.L. and Swegle, J.W. (1994), Stabilising SPH with conservative smoothing. Technical Report SAND94-1932
84. Xiao SP, Belytschko T. (2005) Material stability analysis of particle methods. Advances in Computational Mathematics; 23: pp. 171-190

Chapter 21

Assessing the Resiliency of Composite Structural Systems and Materials Used in Earth-Orbiting Spacecraft to Hypervelocity Projectile Impact

William P. Schonberg

Abstract Spacecraft that are launched to operate in Earth orbit are susceptible to impacts by meteoroids and pieces of orbital debris (MOD). The effect of a MOD particle impact on a spacecraft depends on where the impact occurs, the size, composition, and speed of the impacting object, the function of the impacted system. In order to perform a risk analysis for a particular spacecraft under a specific mission profile, it is important to know whether or not the impacting particle (or its remnants) will exit the rear of an impacted spacecraft wall. A variety of different ballistic limit equations (BLEs) have been developed for many different types of structural wall configurations. BLEs can be used to optimize the design of spacecraft wall parameters so that the resulting configuration is able to withstand the anticipated variety of on-orbit high-speed impact scenarios. While the level of effort exerted in studying the response of metallic multi-wall systems to high speed particle impact is quite substantial, the extent of the effort to study composite material and composite structural systems under similar impact conditions has been much more limited. This paper presents an overview of the activities performed to assess the resiliency of composite structures and materials under high speed projectile impact. The activities reviewed will be those that have been aimed at increasing the level of protection afforded to spacecraft operating in the MOD environment, and more specifically, on those activities performed to mitigate the mechanical and structural effects of an MOD impact.

21.1 Introduction

Spacecraft that are launched to operate in Earth orbit are susceptible to impacts by meteoroids and pieces of orbital debris (MOD). These impacts can occur at ex-

William P. Schonberg

Civil, Architectural, and Environmental Engineering Department Missouri University of Science & Technology, Rolla, Missouri 65409, USA e-mail: wschon@mst.edu

tremely high speeds and can damage flight- and mission-critical systems. As a result, spacecraft designers must be aware of the response of various spacecraft components and structural elements under high speed impact loading conditions. Precautions must be taken to ensure that a spacecraft's operation and functional units are not compromised when it is (inevitably) struck by an orbital debris particle or by a meteoroid.

Of course, the effect of a MOD particle impact on a spacecraft depends on where the impact occurs, the size, composition, and speed of the impacting object, the function of the impacted system, etc. The result of such an impact can be minimal (a small hole or crater on a remote non-functional spacecraft surface), or it can degrade a functional spacecraft component (overlapping pits on a mirror or telescope lens), or it can compromise spacecraft functionality, even to the point of loss of life (a perforated ISS module).

The traditional approach to mitigating damage that would be caused by such impacts consists of placing one or more 'bumper' shields small distances away from the primary load-bearing 'inner wall' of the spacecraft. Behind the inner wall of such a multi-wall system, as in the case of the International Space Station, for example, are located the equipment racks, crew quarters, science experiment hardware, etc. This concept was first proposed in 1947 as a means of mitigating the potentially hazardous effects of meteoroids and, within the last three decades, orbital debris. This 'bumper' derives its effectiveness by shattering the projectile and converting it from a discrete concentrated mass to a wide-angle spray of much smaller particles, some of which could even be in a molten or gaseous state.

However, most satellites launched into Earth orbit, and even some manned spacecraft (such as the Space Shuttle), are constructed with honeycomb sandwich panels as their primary structural load bearing elements without a bumper shield because design, cost, and / or mission constraints prevent the inclusion of a protective shield. In these cases, the load-bearing honeycomb sandwich panels (HC/SPs) also serve as the protection systems for the spacecraft components that are located behind them, such as electronics, avionics, fuel cells, pressure vessels, etc.

In order to perform a risk analysis for a particular spacecraft under a specific mission profile, it is important to know whether or not the impacting particle (or its remnants) will exit the rear of a spacecraft wall system, whether it is a 'Whipple-type' multi-wall system or a 'single' HC/SP wall. This issue, that is, whether or not the ballistic limit of a spacecraft wall system will be exceeded under a given set of impact conditions, has been studied extensively over the last five decades by many investigators. A variety of different ballistic limit equations (BLEs) have been developed for many different types of structural wall configurations. For an overview of the various efforts performed in the areas of BLE development spacecraft protec-

tion against damage caused by MOD impacts from the late 1950s through the early 2000s, the reader is referred to [1].

In general, BLEs define the threshold particle size that will cause perforation of the rear wall of a structural wall system as a function of variables known to affect the ballistic limit, namely, impact velocity and angle, particle density and shape, and component wall thicknesses and material properties. These ballistic limit equations are typically drawn as ballistic limit curves (BLCs) that are lines of demarcation between regions of rear-wall perforation and no perforation for a given spacecraft wall system under consideration. Once developed, BLEs and BLCs can be used to optimize the design of spacecraft wall parameters so that the resulting configuration is able to withstand the anticipated variety of on-orbit high-speed impact scenarios. By understanding the debris environment size and velocity distributions that are expected to impact a spacecraft, spacecraft shielding and designs, as well as their associated BLEs, can also be tailored to meet spacecraft risk requirements while minimizing weights.

NASA and ESA continue to develop BLEs for their structural configurations of interest. The majority of the NASA and early ESA efforts have been directed towards developing BLEs for dual-wall systems such as those that can be found on the International Space Station. The high-speed impact testing that provided the data for these BLEs typically used spherical aluminum projectiles fired in light gas guns at impact velocities between 3 and 7 km/s. This data was fitted with scaled single-wall equations below 3 km/s, and with theoretical momentum-based or energy-based penetration relationships above 7 km/s to obtain three-part BLEs that cover the full impact velocity range of interest, that is, from approx. 0.5 to 16 km/s. It is important to note that the empirical nature of these BLEs subjects them to potential inaccuracy, particularly when applied to spacecraft wall configurations that have not been well tested.

NASA has encoded their BLEs in Bumper II, the software application tool it uses to perform MOD risk assessments. The original Bumper tool was developed in the mid-1980s for the Space Station Freedom Program. Bumper was upgraded to Bumper II in 1991, and separate versions of Bumper II are used now for Space Shuttle, Space Station, Constellation Program risk assessments. Reference [2] presents an overview of the development of Bumper II, including the underlying advances in high-speed impact response prediction for multi-wall structures from the mid-1960s through the mid-2000s.

Similarly, the BLEs developed by ESA reside in that agency's risk assessment tool ESABASE. Like Bumper II, it is a 3-D numerical analysis tool for evaluation of MOD environments, impact probabilities and resulting damage effects. It is based on the latest MOD environment models and particle/wall interaction models, and provides impact probabilities and resulting damage effects for user specified spacecraft geometry and mission parameters. ESABASE, as does Bumper II,

merges MOD environments, failure criteria, and damage predictions to produce risk estimates for specified levels of crew, mission, or vehicle loss.

21.2 Historical Overview

A review of the literature reveals that while the level of effort exerted in studying the response of metallic (mostly aluminum) multi-wall systems to high speed particle impact is quite substantial, the extent of the effort to study composite material and composite structural systems such as HC/SP panels under similar impact conditions has been much more limited. The two main information sources for this subject are the proceedings of the International Ballistics Symposia (published by the host organization) and the proceedings of the Hypervelocity Impact Symposia (published by the International Journal of Impact Engineering). An overview of the papers presented at these venues on the subject of high speed impact of composite materials and HC/SPs is shown in Fig. 21.1. Also shown in Fig. 21.1 is an accounting of papers on this topic appearing in other venues and journals. As can be seen in Fig. 21.1, interest in this area of research is rapidly increasing, especially since the 1990s.

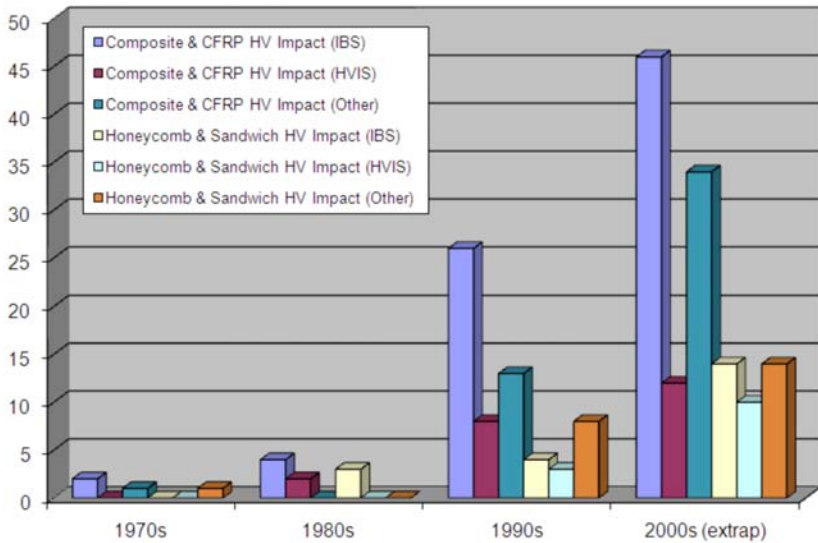


Fig. 21.1 Number of Papers on Composite and HC/SP HVI.

The objective of this paper is to present an overview of the activities performed by the scientific and engineering communities to assess the resiliency of composite

structures and materials under high speed impact. Specifically, in this paper we focus on composite materials subjected to hypervelocity impact, that is, impact speeds on the order of 2 km/s and higher. This study of composite materials under these loading conditions is a relatively new field of scientific and engineering study, as opposed to the study of composite materials under low velocity impact. There is also a phenomenological demarcation between impact regimes. At 'hypervelocity', the impacting materials behave, for all practical purposes, as fluids. That is, material densities, equations of state, and the principles of shock physics govern the impact and recovery processes; considerations of material strength, elasticity, and even plasticity are second-order effects, and enter the response analysis primarily in the later stages of such impact events. At 'low velocity' the opposite is true: response is governed primarily by material strength considerations.

The activities reviewed in this paper are those that have been aimed at understanding and increasing the level of protection afforded by such systems to satellites and spacecraft operating in the MOD environment, and more specifically, on those activities performed to mitigate the mechanical and structural effects of an MOD impact. These effects include primarily the penetration and perforation of spacecraft systems and subsystems. Since the results and papers presented at the IBS typically deal with ordnance-type impacts involving armor/anti-armor engagements, the subject matter of these papers, as well as others concerned with ordnance-type impacts, is outside of the scope of the current review activity.

21.3 Composite Material Panels

21.3.1 HVI Response Characterization

Early studies performed in the 1960s, 1970s, and 1980s stemmed from the realization that earth-orbiting spacecraft and their components are exposed to ultra-high speed impacts by meteoroids; orbital debris was not yet considered a problem (see, e.g., [3]-[6]). Serious attention began to be paid to the problem of very high speed impact of composite materials in the 1980s (see, e.g., [7, 8]) for a number of reasons.

- Manufacturing costs became more reasonable and construction protocols more standard. This allowed composite materials to be considered for use in an increasing number of spacecraft applications. Space station trusses [9], robotic arms and booms [10, 11], fuel tanks and pressure vessels [12] were all designed to be made from some form of composite material.
- Orbital debris rose to the forefront as perhaps the most serious spacecraft design consideration. Since the average impact velocity of a debris particle was as much as a factor of 5 lower than that of a meteoroid, it was thought that the high

strength of composite materials might be able to play a larger role in lowering the damage potential of on-orbit impacts by orbital debris particles.

- LDEF post-retrieval symposia also provided many opportunities for scientists and engineers to comment on impact damage morphologies in the composite material portions of the retrieved satellite (see, e.g., [13]-[16]).

Most of the early HVI studies were performed to characterize the tendency of an impacted composite material panel to degrade through delaminations within the laminate at locations not readily apparent through visual inspection. This characteristic of composite materials makes repairing whatever damage might have occurred exceedingly difficult, which is in stark contrast to our ability to see and repair damage to metallic panels. For example, a simple cratering event in a composite material panel will also cause delaminations to occur over distances many times the crater diameter away from the impact site. However, whatever crater damage is observed in a metallic panel constitutes all or nearly all of the damage sustained by the panel; whatever additional internal damage may exist is minimal and is in the immediate vicinity of the original crater itself. It was, therefore, very important to characterize this damage propagation characteristic of composite materials [17]-[21]. Residual strength of impact composite material panels was concern [22], as was the synergism between HVI damage and atomic oxygen erosion [23].

Some studies also tried to see if mathematical models currently used to approximate the HVI response of metals could also be applied (and if so, with what level of accuracy) in the modeling of the response of composite materials to HVI loadings. Yew and Kendrick [8], Sil'vestrov [24] and Homae [25] found that they could, for example, if the impacted composite plates were 'relatively thick' and if the response characteristic of interest was a 'global' quantity like a hole diameter or a penetration depth. More recently sophisticated numerical and analytical modeling techniques have been developed (see, e.g., [26]-[29]) that have allowed HVI loadings of composite materials to be analyzed by hydrocodes such as Autodyn.

Other response characterization studies were aimed at suggesting improvements in laminate construction (e.g. braiding as opposed to filament winding [30] that would increase those materials' resistance HVI damage. One positive response characteristic that was noted early on was that composite materials produce much less impact ejecta than did metals under the same impact conditions. Furthermore, whatever ejecta are produced by an HVI on a composite material is much less dense than the corresponding metallic ejecta [31]. These properties are important in space applications where there is a desire to not only not pollute further the orbital environment with more solid particulates, but also to not create particles that can strike other exposed spacecraft components as they are ejected from the impact site. Of course, composite material configurations are getting more and more sophisticated – several recent studies have explore the HVI of CFRP sandwiched in between two layers of Kevlar [32, 33].

21.3.2 Use in MOD Protection Systems

As is the HVI response characteristics of composite materials began to be established, attention quickly turned to their use as part of perforation resistant structural systems on the international space station. Work in this area proceeded fairly sequentially, with first consideration being given to using composite materials as outer bumpers in dual-wall systems, then as inner bumpers in multi-wall systems, and then finally as the innermost walls in multi-wall systems. The following sections discuss some of the highlights of the work performed by the HVI community in assessing the effectiveness of composite materials as part of a perforation-resistant structural wall system.

Composite Outer Bumpers

The response of dual-wall systems with Kevlar and graphite/epoxy (Gr/Ep) outer bumpers was compared against that of equal-weight all-aluminum dual-wall systems in the late 1980s by Schonberg [34]. The aluminum bumpers were more effective in spreading out the debris created by the initial impact on the bumper than were the Kevlar bumpers. Apparently the interaction of the shock waves in the projectile and the Kevlar bumpers prevented complete break-up of the projectiles, which decreased the dispersion of debris cloud fragments, thereby increasing the likelihood of pressure wall perforation. However, the pressure wall damage areas in dual-wall systems with Gr/Ep bumpers more wide-spread than those in equivalent systems with Kevlar bumpers. Pressure wall perforations in Gr/Ep systems consisted of several small holes, not one large hole as in the Kevlar systems. From these results, it was concluded that using a laminated composite as the outer bumper in a dual-wall system does not offer any protection advantage as compared to the protection level provided by an all-aluminum dual-wall system.

These results were supported by Christiansen [9], who performed an in-depth study in the early 1980s to evaluate the effectiveness of metallic, composite, and ceramic materials as MOD shields. Christiansen found that while Gr/Ep alone did not shield as well as did aluminum, it had some potential to enhance MOD protection levels when used as the second bumper in a double-bumper system with an aluminum outer bumper. The use of composite materials as inner bumpers is discussed in the next section.

The 1990s saw an increase in the number of studies performed using composite materials (either CFRP or metal-matrix) and/or ceramic materials as outer bumpers in dual-and multi-wall systems. Porous fillers as part of all-aluminum multi-wall systems were also considered [35, 36]. In nearly all of the studies, the results showed that the composite material bumpers fared at best only marginally better in terms of ballistic limit of the dual-wall systems than their equivalent monolith aluminum

counterparts (see, e.g. [37]-[40]). However, there were some differences in bumper hole sizes, fragmentation of the impacting projectile, debris cloud composition and motion/spread between the dual-wall systems with composite and with aluminum bumpers.

Composite Inner Bumpers

The response of triple-wall systems with Kevlar and Spectra inner bumpers was compared against that of all-metallic triple-wall systems [41]. In nearly all the Kevlar inner bumper tests the Kevlar panels were not perforated, whereas their aluminum counterparts sustained large holes. In the Spectra tests, both the Spectra and aluminum inner bumpers were perforated. However, the pressure walls in the Spectra systems sustained little or no damage, while those in corresponding all-aluminum systems were usually perforated. These results demonstrate that using a composite material as the inner bumper does increase the protection afforded to a spacecraft against damage caused by MOD impacts. In a recent study, Katz [42] developed an analytical model to study the energy absorption mechanisms that come into play when composite materials such as those considered by Schonberg in [41] are struck by projectiles travelling at hypervelocities.

Other multi-wall shielding concepts involving composite materials as the inner bumper(s) that have been tested under HVI loading conditions were a Nextel multi-shock shield [43]-[46], a mesh double-bumper shield [44, 47, 48], a hybrid Nextel/aluminum multi-shock shield [49], a double-bumper shield using with a GLARE inner bumper [50], an all-mesh multi-bumper shield [51], and a so-called 'stuffed Whipple shield' in which a layer of Kevlar and Nextel cloth blankets is placed between the bumper and pressure wall of a traditional all-aluminum Whipple-type system [52, 53].

As summarized by Schonberg in [1], the results of the various test programs performed showed that multi-wall systems involving composite material bumpers, especially those made of Nextel as in the stuffed Whipple shield, in combination with aluminum bumpers produced less damaging secondary debris or ejecta, were

- more efficient in converting the projectile's kinetic energy into internal thermal energy,
- less sensitive to projectile shape,
- less sensitive to the obliquity of the impacting projectile,

and resulted in less cumulative damage to the pressure wall of the multi-wall system when compared with traditional Whipple-type all-aluminum single-bumper systems (see also [54]). In addition, such multi-wall systems were found to provide better

protection against more hazardous non-spherical projectiles when compared to the protection level offered by all-aluminum systems [55].

Regarding the performance of the stuffed Whipple shield, while the test results in Ref. [52] showed that such a system provides a large increase in the ballistic limit over corresponding unenhanced systems, test results obtained in the late 1990s have shown that a perforation of a stuffed shield system, if it occurs, could be catastrophic from a cracking standpoint [56]. As such, the marked increase in ballistic limit that comes from using a Nextel/Kevlar blanket instead of the more traditional MLI blanket must be balanced in a risk assessment calculation with possible increases in crew vulnerability as a result of increased post-perforation air leak rates [57, 58]. Initial results indicate that when all catastrophic failure modes are considered, catastrophic loss appears to possibly be more likely for weaker shields than for the more robust stuffed Whipple shield.

Composite Pressure Walls

In the mid-1990s, a study was performed to compare the response of dual-wall systems with Gr/Ep pressure walls against that of equal-weight all-aluminum dual-wall systems [59]. The results showed there are several advantages of using Gr/Ep as a pressure wall material: (1) it eliminates severe cracking and petalling sustained by aluminum walls in systems impacted by large projectiles; (2) its ballistic performance is superior to that of aluminum for impact velocities above 5.5 km/s; and (3) patching a hole in a perforated Gr/Ep panel, even if it were larger than in an aluminum panel, would be relatively easy since the Gr/Ep remains non-deformed and the patch can be, e.g., adhesively bonded. Repairing a perforated aluminum wall would be a more difficult procedure since the aluminum would likely be cracked and petalled. On-orbit repair of perforated aluminum panels would therefore require cutting and welding tools that are EVA compatible, while the repair of perforated Gr/Ep panels would not.

In a recent numerical study, Ito and Sekine [60] found that the ballistic limit of a dual-wall system with an aluminum bumper and a Gr/Ep pressure wall can be increased if a thin aluminum plate were to be bonded on the 'top' surface of the Gr/EP pressure wall. However, despite their apparent potential for use as the innermost wall in perforation resistant structures, it appears that other issues, such as ease of construction and manufacturability, continue to prevent composite materials from being considered for and used in this capacity.

21.4 Honeycomb Sandwich Panels

Most satellites launched into Earth orbit are constructed with honeycomb sandwich panels (HC/SPs) as their primary structural load bearing elements. A typical honeycomb sandwich panel is shown in Figure 21.2.



Fig. 21.2 Generic Honeycomb Sandwich Panel with Aluminum Facesheets.

Behind such panels are located spacecraft components that are appropriate for the particular spacecraft or satellite mission and function (e.g. electronics, avionics, fuel cells, pressure vessels, etc.). In order to be able to perform a risk analysis for a particular satellite under a specific mission profile, it is important to know more than just whether or not the satellite will be struck by a meteoroid or an orbital debris (MOD) particle. It is equally important to know, in the event of such an impact, whether or not the impacting particle (or its remnants) will exit the rear of the HC/SP (i.e. whether or not the ballistic limit of the HC/SP will be exceeded) and, if so, where the debris created in such an impact will land and what internal components it will strike. In this section, we discuss the work that has been performed by various researchers in the hypervelocity impact community to address these two issues.

21.4.1 Early Work – The 1960s and 70s

Perhaps the first study performed involving HC/SPs being struck by very high speed projectiles examined the effectiveness of aluminum honeycomb shields in preventing meteoroid damage to liquid-filled spacecraft tanks [61]. Much like the monolithic shields proposed by Whipple, HC shields were found to shatter impacting projectiles and scatter impact debris over a wide area of the protected tanks. The spacing between the HC material and the tank was found to have a significant effect on the damage levels sustained by the tanks. This led the authors to conclude that the effectiveness of the HC shield material to protect against meteoroid impact was inconclusive. This uncertainty in the effectiveness of HC shields was reinforced by

a subsequent study that explored the channeling effect associated with impacts on HC/SPs [62]. By subjecting a HC/SP mock-up to high speed impacts, this study concluded that '[do] indeed have the ability to channel debris against the second sheet' in a multi-wall configuration. Following these two studies, interest in using HC/SPs as meteoroid shields for spacecraft being developed and flown in the 1960s, 70s, and 80s understandably declined.

In an effort to study the channel effect noted by early investigations, Jex, Miller, and McKay subjected dual-wall systems without and without HC filler to high speed impact [63]. Much to everyone's surprise, they found that 'the HC structure had a better predictive capability than the same structure without honeycomb when ballistic limits were compared.' They suggested the reason for this was that the secondary fragmentation and energy loss associated with the initial impact debris fragments hitting HC walls as that debris travelled through the HC more than overcompensated for any channeling effects. However, by the time the results of this study were made, monolithic shielding had already become the preferred configuration for protecting spacecraft against meteoroid impacts.

21.4.2 The 1980s and 90s

High speed impact testing of HCSPs experienced a rebirth in the late 1980s and early 1990s when an increasing number of satellites were being designed with HCSPs as the main load-bearing structural elements and subsequently subjected to potential impacts by man-made debris in earth orbit. The question naturally arose as to how well these satellites would fare if such an impact were to occur. In an early study that attempted to answer this question for the (then) newly developed RADARSAT [64], it was found that yes indeed an orbital debris particle impact on certain critical satellite components would bring the survivability down to an unacceptably low level. As a result of the results obtained, '[a] number of modifications considered practical in terms of weight, volume, and cost were implemented to improve protection of the more critical units.' In another satellite impact study, the results of eighteen (18) tests that were performed (1) to determine the ballistic limits of typical AXAF HC/SPs, and (2) to quantify the extent of damage to underlying AXAF components in the event of an HC/SP perforation are presented and discussed in a fair amount of detail [65, 66].

HC/SPs were also considered briefly as possible bumpers in early space station wall impact studies (see, e.g., [67]). However, the thrust of this particular study, for example, was not so much the HC/SPs or their protected systems, but rather the exterior space station components in the vicinity of an impact that could be affected by ricocheting secondary debris. No significant difference between the ricochet par-

ticle generation ability of HC/SPs and that of monolithic bumpers was noted by the authors.

Other spacecraft components either protected by or made with HC/SPs that were tested under hypervelocity loading conditions include Ni-H battery cells [68] and metallic thermal protection systems [69]. The tests involving Ni-H batteries showed that for all of the test conditions investigated, the battery cells responded 'in a benign manner ... [they] simply vented their hydrogen gas and some electrolyte following a perforation, but did not burst or generate any large debris fragments.' The authors found that while a 'hypervelocity impact on a Ni/H₂ cell used in space would result in the loss of functionality of the battery of which it was part of [sic], but would not result in a catastrophic failure that would cascade to other cells or nearby hardware.' Unfortunately, with respect to the metallic TPS study, although the paper discusses the results of some high speed impact tests performed in support of the development of a 'superalloy honeycomb TPS concept' for the Reusable Launch Vehicle, those results are not actually presented. Hence, it is difficult to assess the validity of the claims made regarding such a TPS construction as being an 'attractive, viable candidate for the RLV.'

Towards the end of the 1990s, a series of studies was performed in Europe to 'determine ways to improve the tolerance of unmanned spacecraft to hypervelocity impacts by the use of shielding with minimal additional cost, mass and volume,' and, by assessing the orbital debris and meteoroid threat for two (then) new satellites, METOP and ERS-2, 'demonstrate the benefits of [that] new shielding.' [70]-[78] The work performed considered single as well as double-layer HC/SPs, and the use of multi-layer insulation blankets, either on its own or with a HC/SP. The studies concluded that double-layer honeycomb shielding, combined with a secondary shielding of internal components, wiring, etc, is a cost- and mass-effective way in which to enhance the robustness of a spacecraft operating in the meteoroid and orbital debris environment.

The studies performed to develop cost-effective debris shields also compared the response of dual-wall systems with HC panels against that of similar monolithic all-aluminum systems. They found that because of its internal construction, an impacted HC panel is able to absorb a significant portion of the energy associated with the debris created by the original impact. As such, spacecraft protected by HC panels would be expected to fare better in the M/OD environment from a protection perspective than would comparable all-aluminum systems. These conclusions were confirmed by other investigators as well (see, e.g., [79, 80]).

21.4.3 Recent Work

Testing in support of the METOP and ERS-2 study was performed at the Fraunhofer Ernst-Mach-Institute, where work was also underway to understand the response of other typical satellite and/or spacecraft wall systems: Rosetta, EnviSat, GOCE, BeppoSax, RADARSAT2, and the ATV [81]-[90]. These studies again confirmed that 'sandwich panels have a better tolerance to hypervelocity impacts than monolithic structures,' and that placing a blanket of MLI 'in front of the sandwich panels contributes significantly to the overall protection performance' of those panels. Detailed numerical models of HC/SPs have also recently been developed to support the tests being performed [91]. Information gleaned from numerical analyses of HC/SPs under hypervelocity impact provides additional insights into the response of such structures, and can be used to tailor a particular HC/SP design to enhance its impact performance.

Most recently, over one hundred impact tests were performed at Fraunhofer EMI to assess the vulnerability of a variety of representative spacecraft components (e.g. fuel pipes, heat pipes, pressure vessels, electronics boxes, harnesses, and batteries) to simulated MOD impacts [92]-[94]. Post-impact functionality of these components was studied and compared and against required minimums. In the end, the authors were able to provide recommendations for general spacecraft design considerations with regard to the elements they test as well as an assessment of the consequences on spacecraft operation of various possible damage levels. In addition, the study showed that the particle diameters that would lead to equipment or component failure are several times those required to perforate the structural walls of the spacecraft only.

Another outcome of the spacecraft component vulnerability study was a new BLE that could be applied to various structural configurations, including single wall systems, dual-wall systems, multi-wall systems with HC/SPs, batteries, e-boxes, harnesses, etc. [95, 96]. To assess how well these BLEs performed in terms of predicting perforation (P) or non-perforation (NP) of HC/SP systems with aluminum and composite facesheets, an exercise was undertaken to compare the P / NP predictions of the equations in [95] and in [96] against actual P/NP occurrences as found in the data from the experimental investigations discussed in this section [97]. It was found that these BLEs are fairly conservative: they successfully predicted HC/SP perforation in nearly all of the tests that resulted in perforation, while allowing approximately half of the non-perforating tests to be incorrectly labeled as tests with a perforation. This indicates the likelihood that use of these BLEs in design applications could result in overly robust shielding hardware. The reader is also referred to Reference [98] for additional details regarding the work performed on numerical simulation of HC/SPs under MOD impact loads.

In addition to knowing whether or not the impacting particle (or its remnants) will exit the rear of the HC/SP, it is equally important to know, if indeed the ballistic

limit of the HC/SP has been exceeded, where the debris created in such an impact will land and what internal components it will strike. To help address this issue, a system of empirical equations that can be used to predict the trajectories and spread of the debris clouds that exit the rear facesheet following a high speed perforating impact of a HC/SP was recently developed [99]. The equations developed in this study incorporate the following features:

- presence (or the lack thereof) and composition of a multi-layer thermal insulation (MLI) blanket on the exterior of the HC/SP;
- material composition of the HC/SP facesheets (either aluminum or a carbon-fiber-reinforced polymer, or CFRP);
- facesheet thicknesses and overall HC/SP thickness;
- HC core properties (core size, wall thickness, and material); and,
- projectile diameter, material, impact velocity, and trajectory obliquity.

Empirical equations were also developed to predict the dimensions of the holes in the front and rear HC/SP facesheets. These hole dimension equations can be used to calculate the amount of mass in a debris cloud if the HC/SP is perforated by a high speed impact. The trajectory angles can then be used to determine where this mass will travel and what spacecraft components will be impacted, and the spread angles equations will determine the extent of the footprint made by this mass on any encountered surface. All of this information can then be fed into a risk assessment code to calculate the probability of spacecraft failure under a prescribed set of impact conditions.

21.5 Conclusions

This paper has presented an overview of the work performed by the scientific and engineering communities to assess the resiliency of composite structures and materials under high speed impact. The activities reviewed are those that have been aimed at understanding and increasing the level of protection afforded by such systems to satellites and spacecraft operating in the MOD environment, and more specifically, on those activities performed to mitigate the potentially deleterious mechanical and structural effects of an MOD impact. It was found that

- using a laminated composite as the outer bumper in a dual-wall system does not offer any protection advantage as compared to the protection level provided by an all-aluminum dual-wall system;
- using a composite material as the inner bumper does increase the protection afforded to a spacecraft against damage caused by MOD impacts; and,
- there are several advantages of using a laminate composite as the pressure or innermost wall material of a multi-wall system, including the elimination of the

severe cracking and petaling that would be sustained by aluminum walls in systems impacted by large projectiles.

The study of HC/SPs under HVI loadings is an on-going research area, with most of the activities focusing on determining whether or not, in the event of a very high speed impact, the impacting particle (or its remnants) will exit the rear of the HC/SP (i.e. whether or not the ballistic limit of the HC/SP will be exceeded) and, if so, where the debris created in such an impact will land and what internal components it will strike. The development of numerical models that simulate such impacts on HC/SPs with increased fidelity is providing scientists and engineers much-needed information that can ultimately be used to develop resilient satellites and spacecraft systems.

Acknowledgements The author is grateful for the support provided by the Humboldt Foundation through a Fraunhofer-Bessel Research Award that enabled some of the studies whose results were discussed in this paper.

References

1. Schonberg WP (2001). Protecting Spacecraft Against Meteoroid/Orbital Debris Impact Damage: An Overview. *Space Debris*, 1:195-210.
2. Schonberg WP (2008). The Development of Ballistic Limit Equations for Dual-Wall Spacecraft Shielding: A Concise History and Suggestions for Future Development, Proceedings of the 49th AIAA/ASME/ASCE/AHS Structures, Structural Dynamics, and Materials Conference, AIAA Paper No. 2008-1966, Chicago, IL.
3. Williams JG, Goodman GP (1965). Structural and Materials Investigation of a 1/8-Scale-Model Space Structure of Toroidal Configuration and Filamentary Construction. NASA TN-D-2652, Washington, DC.
4. McMillan AR (1966). Hypervelocity Impacts into Stainless-Steel Tubes Armored with Reinforced Beryllium. NASA TN-D-3512, Washington, DC.
5. Cour-Palais BG (1969). Meteoroid Protection by Multiwall Structures. Proceedings of the 1969 Hypervelocity Impact Conference, Cincinnati, Ohio.
6. Williams JG (1971). High-Velocity-Impact Tests Conducted with Polyethylene Terephthalate Projectiles and Flexible Composite Wall Panels. NASA TN-D-6135, Washington, DC.
7. Cour-Palais BG (1987). Hypervelocity Impact in Metals, Glass and Composites. *International Journal of Impact Engineering*, 5:221-237.
8. Yew CH, Kendrick RB (1987). A Study of Damage in Composite Panels Produced by Hypervelocity Impact. *International Journal of Impact Engineering*, 5:729-738.
9. Christiansen EL (1987). Evaluation of Space Station Meteoroid/Debris Shielding Materials. Report No. 87-163, Eagle Engineering Inc, Texas.
10. Tennyson RC, Shortliffe GD (1997). Hypervelocity Impact Tests on Composite Boom Structures for Space Robot Applications. *Canadian Aeronautics and Space Journal*, 43(3), 195-202.
11. Tennyson RC, Shortliffe GD (1997). MOD Impact Damage on Composite Materials in Space. Proceedings of the 7th International Symposium on Materials in a Space Environment, Toulouse, France, p. 485-492. ESA SP, Noordwijk, Netherlands.
12. Salome R, et al (2001). High Pressure Composite Tank Behavior under a Hypervelocity Impact. In: Proceedings of the Third European Conference on Space Debris, H. Sawaya-Lacoste, ed. ESA SP-473, 2:621-627, Noordwijk, Netherlands.

13. Finckenor M (1992). Meteoroid/Space Debris Impacts on MSFC LDEF Experiments. LDEF: 69 Months in Space. First Post-Retrieval Symposium, Part 1, 435-442. NASA Langley Research Center.
14. Tennyson RC (1992). Additional Results on Space Environmental Effects on Polymer Matrix Composites: Experiment A0180. LDEF Materials Workshop 1991, Part 2, 571-592, NASA Langley Research Center.
15. Tennyson RC, et al (1992). Proposed Test Program and Data Base for LDEF Polymer Matrix Composites. LDEF Materials Workshop 1991, Part 2, 593-600, NASA Langley Research Center.
16. Roybal R (1995). A New Technique for Ground Simulation of Hypervelocity Debris , LDEF: 69 Months in Space. Third Post-Retrieval Symposium, Part 3, 1379-1388, NASA Langley Research Center.
17. Lamontange C, et al (1999). Normal and Oblique Hypervelocity Impacts on Carbon Fiber/Peek Composites. *International Journal of Impact Engineering*, 23:519-532.
18. Tennyson RC, Lamontange C (2000). Hypervelocity Impact Damage to Composites. *Composites Part A*, 31:785-794.
19. Tennyson RC, Lamontange C (2000). High-Velocity Impact Damage to Polymer Matrix Composites. In: *Impact Behavior of Fiber-Reinforced Composite Materials and Structures*, S. R. Reid and G. Zhou, eds., 280-299, Woodhead Publishing Ltd., England.
20. Lamontange C, Manuelpillai GN, et al (2001). Projectile Density, Impact Angle and Energy Effects on Hypervelocity Impact Damage to Carbon Fiber/Peek Composites. *International Journal of Impact Engineering*, 26:381-398.
21. Daigo K, et al (2004). Hypervelocity Impact Studies on Composite Material. Paper No. IAC-04-IAA.5.12P.03, Proceedings of the 55th Congress of the International Astronautical Federation, Vancouver, Canada.
22. Unda J, et al (1994). Residual Strength of CFRP Tubes Subjected to Hypervelocity Debris Impact. Paper No. IAF-94-I.5.212, Proceedings of the 45th Congress of the International Astronautical Federation, Jerusalem, Israel.
23. Verker R, et al (2007). Residual Stress Effect on Degradation of Polyimide under Simulated Hypervelocity Space Debris and Atomic Oxygen. *Polymer*, 48:19-24.
24. Sil'vestrov VV, et al (1995). Hypervelocity Impact on Laminate Composite Panels. *International Journal of Impact Engineering*, 17:751-762.
25. Homae T, et al (2006). Hypervelocity Planar Plate Impact Experiments of Aramid Fiber-reinforced Plastics. *Journal of Reinforced Plastics and Composites*, 25(11):1215-1221.
26. Clegg RA, White DM, et al (2006). Hypervelocity Impact Damage Prediction in Composites. Part I - Material Model and Characterization. *International Journal of Impact Engineering*, 33:190-200.
27. Riedel W, Nahme H, et al (2006). Hypervelocity Impact Damage Prediction in Composites. Part II - Experimental Investigations and Simulations. *International Journal of Impact Engineering*, 33:670-680.
28. Cheng WL, Langlie S, et al (2003). Hypervelocity Impact of Thick Composites. *International Journal of Impact Engineering*, 29:167-184.
29. Lee M (2003). Hypervelocity Impact into Oblique Ceramic/Metal Composite Systems. *International Journal of Impact Engineering*, 29:417-424.
30. Munjal AK, et al (1990). Impact Damage Evaluation of Graphite/Epoxy Composite Materials for Space Applications. Proceedings of the 22nd International SAMPE Technical Conference, 1200-1207, Boston, Massachusetts.
31. Tennyson RC, Manuelpillai G (1994). Prediction of Space Hypervelocity Impact Damage in Composite Materials. Proceedings of the 8th CASI Conference on Astronautics, Ottawa, Canada, 441-450.
32. White DM, Taylor EA, et al (2003). Numerical Simulation and Experimental Characterization of Direct Hypervelocity Impact on a Spacecraft Hybrid Carbon Fiber/Kevlar Composite Structure. *International Journal of Impact Engineering*, 29:779-790.

33. Grujicic M, et al. (2006). Hypervelocity Impact Resistance of Reinforced Carbon–Carbon/Carbon–Foam Thermal Protection Systems. *Applied Surface Science*, 252:5035–5050.
34. Schonberg WP (1990). Hypervelocity Impact Response of Spaced Composite Material Structures. *International Journal of Impact Engineering*, 10:509–523.
35. Li Y, et al (2004). Energy-Absorption Performance of Porous Materials in Sandwich Composites under Hypervelocity Impact Loading. *Composite Structures*, 64:71–78.
36. Colombo P, et al (2003). Effect of Hypervelocity Impact on Microcellular Ceramic Foams from a Pre-ceramic Polymer. *Advanced Engineering Materials*, 5(11):802–805.
37. Robinson JH, Nolen AM (1995). An Investigation of Metal Matrix Composites as Shields for Hypervelocity Orbital Debris Impacts. *International Journal of Impact Engineering*, 17: 685–696.
38. Sil'vestrov VV, et al (1999). Protective Properties of Shields of Ceramic/Aluminum Composite for Hypervelocity Impact. *Combustion, Explosion, and Shock Waves*, 35(3):7.
39. Sil'vestrov VV, Plastinin AN, et al (1999). An Investigation of Ceramic/Aluminum Composites as Shields for Hypervelocity Impacts. *International Journal of Impact Engineering*, 23:859–867.
40. Tamura H, Mutou Y (2005). Quantitative Analysis of Debris Clouds from SiC-Fiber-Reinforced Silicon Nitride Bumpers. *International Journal of Impact Engineering*, 31:1192–1207.
41. Schonberg WP, Walker EJ (1991). Use of Composite Materials in Multi-Wall Structures to Prevent Perforation by Hypervelocity Projectiles. *Composite Structures*, 19:15–40.
42. Katz S, et al (2008). Response of Composite Materials to Hypervelocity Impact. *International Journal of Impact Engineering*, 35:1606–1611.
43. Cour-Palais BG, Crews JL (1990) A Multi-Shock Concept for Spacecraft Shielding. *International Journal of Impact Engineering*, 10:135–146.
44. Boslough MB, Chhabildas LC, et al (1993). Hypervelocity Testing of Advanced Shielding Concepts for Spacecraft Against Impacts to 10 km/s. *International Journal of Impact Engineering*, 1993, 14:95–106.
45. Cour-Palais BG, Piekutowski AJ, et al (1993). Analysis of the UDRI Tests on Nextel Multi-Shock Shields. *International Journal of Impact Engineering*, 14:193–204.
46. Thompson LE, Johnson MS (1993). Response of Woven Ceramic Bumpers to Hypervelocity Impacts. *International Journal of Impact Engineering*, 14:739–749.
47. Christiansen EL, Kerr JH (1993). Mesh Double-Bumper Shield: A Low-Weight Alternative for Spacecraft Meteoroid and Orbital Debris Protection. *International Journal of Impact Engineering*, 14:169–180.
48. Horz F, Cintala MJ (1993). Impact Experiments into Multiple-Mesh Targets: Concept Development of a Lightweight Collisional Bumper, NASA-TM-104764, Johnson Space Center, Houston, Texas.
49. Christiansen EL. (1993). Design and Performance Equations for Advanced Meteoroid and Debris Shields. *International Journal of Impact Engineering*, 14:145–156.
50. Lambert M, Schneider E (1995). Shielding Against Space Debris. A Comparison Between Different Shields: The Effect of Materials on their Performances. *International Journal of Impact Engineering*, 17:477–485.
51. Horz F, Cintala MJ, et al (1995) Multiple-Mesh Bumpers: A Feasibility Study. *International Journal of Impact Engineering*, 17:431–442.
52. Christiansen EL, Crews JL, et al (1995). Enhanced Meteoroid and Orbital Debris Shielding. *International Journal of Impact Engineering*, 17:217–228.
53. Destefanis R, Faraud M (1997). Testing of Advanced Materials for High Resistance Debris Shielding. *International Journal of Impact Engineering*, 20:209–222.
54. Munjal AK (1998). Minimizing Hypervelocity Micrometeoroid Impact Damage to Composite Space Structures. Paper No. III.4, Proceedings of the 1998 Leonid Meteoroid Storm and Satellite Threat Conference, The Aerospace Corporation, Los Angeles, California.
55. Christiansen EL, Kerr JH (1997). Projectile Shape Effects on Shielding Performance at 7 km/s and 11 km/s. *International Journal of Impact Engineering*, 20:165–172.

56. Schonberg WP, Williamsen JE (1997). Empirical Hole Size and Crack Length Models for Dual-Wall Systems Under Hypervelocity Projectile Impact. *International Journal of Impact Engineering*, 20:711-722.
57. Schonberg WP, Williamsen JE (1999). Modeling Damage in Spacecraft Impacted by Orbital Debris Particles. *Journal of Astronautical Sciences*, 47:103-115.
58. Williamsen JE, Evans HA, Schonberg WP (1999). Effect of Multi-Wall System Composition on Survivability for Spacecraft Impacted by Orbital Debris. *Space Debris*, 1(1):37-43.
59. Schonberg WP, Walker EJ (1994). Hypervelocity Impact of Dual-Wall Structures with Graphite/Epoxy Inner Walls. *Composites Engineering*, 4(10):1045-1054.
60. Ito R, Sekine H (2006). Ballistic Limits of GR/EP and Hybrid Composite Rear Walls Protected by a Debris Shield. *International Journal of the Society of Materials Engineering for Resources*, 13(2):118-122.
61. Anon (1964). Effectiveness of Aluminum Honeycomb Shields in Preventing Meteoroid Damage to Liquid-Filled Spacecraft Tanks, NASA CR-65261, Johnson Space Center, Houston, Texas.
62. Sennett RE, Lathrop BL (1968). The Effects of Hypervelocity Impact on Honeycomb Structures. Paper No. 68-314, Proceedings of the 9th AIAA Structures, Structural Dynamics, and Materials Conference, Palm Springs, California.
63. Jex DW, Miller AM, McKay CA (1970). The Characteristics of Penetration for a Double-Sheet Structure with Honeycomb, NASA TM-X-53974, Marshall Space Flight Center, Huntsville, Alabama.
64. Terrillon F, Warren HR, Yelle MJ (1991). Orbital Debris Shielding Design of the RadarSat Spacecraft. Paper No. IAF-91-283, Proceedings of the 42nd International Astronautical Congress, Canada.
65. Frost CL, Rodriguez PI (1997). AXAF Hypervelocity Impact Test Results Proceedings of the 2nd European Conference on Space Debris, W. Flury, ed., ESA SP-393, 423-428, Noordwijk, The Netherlands.
66. Sanchez GA, Kerr JH (1996). Advanced X-Ray Astrophysics (AXAF) Meteoroid and Orbital Debris (M/OD) Test Report, Report No. JSC-27354, Johnson Space Center, Houston, Texas.
67. Shephard GLY, Scheer SA (1993). Secondary Debris Impact Damage and Environment Study. *International Journal of Impact Engineering*, 14:671-682.
68. Frate DT, Nagra HK (1996). Hypervelocity Impact Testing of Nickel-Hydrogen Battery Cells. AIAA Paper No. 96-4292, Proceedings of the 1996 AIAA Space Programs and Technologies Conference, Huntsville, Alabama (also NASA TM-107325).
69. Blosser ML (1997). Development of Metallic Thermal Protection Systems for the Reusable Launch Vehicle. Proceedings of the Space Technology and Applications International Forum, Albuquerque, New Mexico.
70. Taylor EA, et al (1997). Hypervelocity Impact on Spacecraft Carbon Fiber Reinforced Plastic / Aluminum Honeycomb. Proceedings of the Institution of Mechanical Engineers (UK), 211(G):355-363.
71. Taylor EA, Herbert MK, Kay L (1997). Hypervelocity Impact on Carbon Fiber Reinforced Plastic (CFRP) / Aluminum Honeycomb at Normal and Oblique Angles. Proceedings of the 2nd European Conference on Space Debris, W. Flury, ed., ESA SP-393, 429-434, Noordwijk, The Netherlands.
72. Herbert MK, Taylor EA (1998). Hypervelocity Impact Response of Honeycomb: Shielding Performance and Spacecraft Subsystem Design Issues. Proceedings of the Hypervelocity Impact Shielding Workshop, H. Fair, ed., Institute for Advanced Technologies, Austin, Texas.
73. Taylor EA (1998). Cost Effective Debris Shields for Unmanned Spacecraft. Proceedings of the Hypervelocity Impact Shielding Workshop, H. Fair, ed., Institute for Advanced Technologies, Austin, Texas.
74. Taylor EA, et al (1999). Hypervelocity Impact on Carbon Fiber Reinforced Plastic / Aluminum Honeycomb: Comparison with Whipple Bumper Shields. *International Journal of Impact Engineering*, 23:863-893.
75. Schäfer F (1999). Impact Tests on Metop Sandwich Panels with MLI, EMI Report E-05/99, Ernst Mach Institute, Freiburg, Germany.

76. Turner RG, Taylor EA (2000). Cost Effective Debris Shields For Unmanned Spacecraft, Final Report, ESA Contract No. 12378/97/NL, Matra Marconi Space.
77. Turner RG, Taylor EA, et al (2001). Cost Effective Debris Shields for Unmanned Spacecraft. *International Journal of Impact Engineering*, 26:785-796.
78. Taylor EA, et al (2003). Hypervelocity Impact on Spacecraft Honeycomb; Hydrocode Simulation and Damage Laws. *International Journal of Impact Engineering*, 29:691-702.
79. Sibeaud JM, Prieur C, Puillet C (2005). Hypervelocity Impact on Honeycomb Target Structures. Proceedings of the 4th European Conference on Space Debris, W. Flury, ed., ESA SP-587, Noordwijk, The Netherlands.
80. Sibeaud JM, Thame L, Puillet C (2008). Hypervelocity Impact on Honeycomb Target Structures: Experiments and Modeling *International Journal of Impact Engineering*, 35(12):1799-1807.
81. Schäfer F, Schneider E (1996). Hypervelocity Impacts on CFRP, EMI Report CFRP-01, Ernst Mach Institute, Freiburg, Germany.
82. Lambert M (1997). Hypervelocity Impacts and Damage Laws. *Advances in Space Research*, 19(2):369-378.
83. Schäfer F (1999). Impact Tests on Rosetta Sandwich Panels with MLI, EMI Report E-02/99, Ernst Mach Institute, Freiburg, Germany.
84. Schäfer F (1999). Impact Tests on ATV Sandwich Panels, EMI Report E-11/99, Ernst Mach Institute, Freiburg, Germany.
85. Lambert M, Schäfer F, Geyer T (2001). Impact Damage on Sandwich Panels and Multi-Layer Insulation. *International Journal of Impact Engineering*, 21:369-380.
86. Ryan S, Riedel W, Schäfer F (2004). Numerical Study of Hypervelocity Space Debris Impacts on CFRP/Al Honeycomb Spacecraft Structures. Paper No. IAC-04-W.1.02, Proceedings of the 55th International Astronautical Congress, Vancouver, Canada.
87. Schäfer F, Schneider E, Lambert M (2004). Review of Ballistic Limit Equations for CFRP Structure Walls of Satellites. Proceedings of the 5th International Symposium on Environmental Testing for Space Programs, ESA SP-558, Noordwijk, The Netherlands.
88. Schäfer F, et al (2005). Hypervelocity Impact Testing of CFRP/AL Honeycomb Satellite Structures. Proceedings of the 4th European Conference on Space Debris, W. Flury, ed., ESA SP-587.
89. Schäfer F (2005). Composite Materials Impact Damage Analysis, EMI Report I-83-05, Ernst Mach Institute, Freiburg, Germany.
90. Ryan S, Schäfer F, Riedel W (2006). Numerical Simulation of Hypervelocity Impact on CFRP/Al HC/SP Spacecraft Structures Causing Penetration and Fragment Ejection. *International Journal of Impact Engineering*, 33:703-712.
91. Wicklein M (2006). Carbon Fiber Material Models for Hypervelocity Impact Simulations: Testing, EMI Report No. I-73/06, Ernst Mach Institute, Freiburg, Germany.
92. Putzar R, Schäfer F, et al (2005). Vulnerability of Shielded Fuel Pipes and Heat Pipes to Hypervelocity Impacts. Proceedings of the 4th European Conference on Space Debris, W. Flury, ed., ESA SP-587, Noordwijk, The Netherlands.
93. Putzar R, Schäfer F, et al (2005). Vulnerability of Spacecraft Electronic Boxes to Hypervelocity Impacts. Paper No. IAC-05-B.6.4.02, Proceedings of the 56th International Astronautical Congress, Fukuoka, Japan.
94. Schäfer F, Putzar R (2006). Vulnerability of Spacecraft Equipment to Space Debris and Meteoroid Impacts, EMI Report I-15-06, Ernst Mach Institute, Freiburg, Germany.
95. Schäfer F, Ryan S, et al (2008). Ballistic Limit Equation for Equipment Placed Behind Satellite Structure Walls. *International Journal of Impact Engineering*, 35:1784-1791.
96. Ryan S, Schäfer F, et al (2007). A Ballistic Limit Equation for Hypervelocity Impacts on Composite Honeycomb Sandwich Panel Satellite Structures. *Advances in Space Research*, 41(7):1152-1166.
97. Schonberg WP, Schäfer F, Putzar R (2009). Effectiveness of HC/SP Ballistic Limit Equations in Predicting Perforation / Non-Perforation Response. *Journal of Spacecraft and Rockets*, submitted for publication consideration.

98. Ryan, S (2009). Numerical Simulation in Micrometeoroid and Orbital Debris Risk Assessment. In Predictive Modeling of Dynamic Processes: A Tribute to Klaus Thoma, ed. S. Hiermaier, Springer, Berlin Germany.
99. Schonberg WP, Schäfer F, Putzar R (2009). Hypervelocity Impact Response of Honeycomb Sandwich Panels, *Acta Astronautica*, submitted for publication consideration.

Chapter 22

Numerical Simulation in Micrometeoroid and Orbital Debris Risk Assessment

Shannon Ryan

Abstract The threat of micrometeoroid and orbital debris (MMOD) impacts on space vehicles is assessed in terms of the probability of an impactor penetrating the spacecraft hull, and the probability of a penetrating impact resulting in catastrophic failure. These values are calculated in risk analysis codes which combine spacecraft geometry, debris environment models, and equations that define the penetration limits of the spacecraft outer structure (called ballistic limit equations, or BLEs). To characterize the performance of spacecraft structures under impact of MMOD particles at hypervelocity, experimental facilities such as two-stage light gas guns are commonly used. However, these facilities are only capable of reproducing approximately 40% of expected in-orbit impact conditions. As a result, numerical techniques are ideally suited for application in this field. The use of numerical hydrocodes in MMOD risk assessment is, historically, very limited. However, as code maturity continues to develop, their application becomes increasingly accepted. Within this chapter three examples are presented in which numerical hydrocodes were used in tandem with experimental testing for MMOD risk assessments. Beginning with the most simplistic application, i.e. derivation of perforation limits, the examples extend to the propagation of impact-induced dynamic disturbances through complex satellite structures.

22.1 Introduction

There are few engineering applications that lend themselves to numerical analysis more naturally than the impact of micrometeoroid and orbital debris (MMOD) particles on spacecraft hardware at hypervelocity. For a spacecraft in Low Earth Orbit (LEO), orbital debris encounter velocities range from 1 km/s to 15 km/s, with an av-

Shannon Ryan
USRA Lunar and Planetary Institute / NASA Johnson Space Center, USA e-mail: shannon.j.ryan@nasa.gov

erage of approximately 9 km/s. Encounter velocities with meteoroid particles range from 11 km/s to 72 km/s, with an average of approximately 20 km/s. Experimental facilities, such as two-stage light gas guns, are capable of accelerating particles to maximum velocities of approximately 9 km/s, allowing the reproduction of only 40% of on-orbit impact conditions in LEO. For the remainder, numerical techniques are required.

MMOD risk assessment is performed with a geometric spacecraft model, orbit profile, and planned mission duration. Meteoroid and orbital debris flux models such as NASA’s Meteoroid Engineering Model (MEM) [1] and Orbital Debris Engineering Model (ORDEM2000) [2] are used to predict the MMOD impact flux relevant for the spacecraft geometry and orbital profile. Environment models such as MEM and ORDEM2000 provide information on debris flux in terms of threat direction and velocity distribution. These are used together with penetration-limit equations called Ballistic Limit Equations, or BLEs, to determine the critical debris particle that will cause failure of the spacecraft MMOD shield or critical component, and provide probabilities of its impact. This process is performed within MMOD risk analysis software, such as NASA’s BUMPER-II, a functional overview of which is provided in Fig. 22.1.

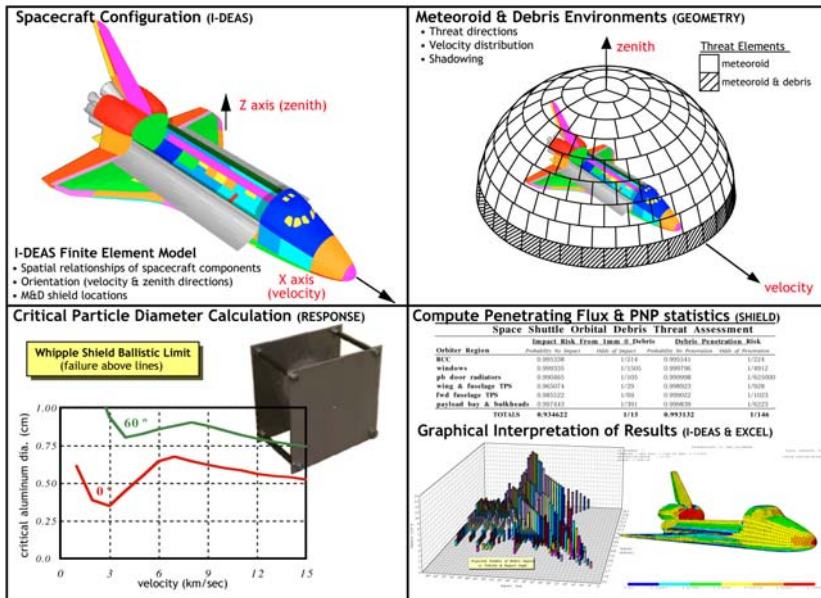


Fig. 22.1 Functional overview of NASA’s BUMPER-II Meteoroid and Orbital Debris Risk Assessment Tool.

BLEs used in risk assessment software are generally based on analytical considerations but use experimental data to empirically anchor the expressions at the highest obtainable impact velocities (see e.g. [3] [4]). For the most common types of spacecraft MMOD shielding configurations i.e. dual-wall configuration referred to as a Whipple shield, the penetration equations are divided into three regimes: low velocity, transition (or shatter), and hypervelocity. The limits of these regimes are defined by the physical processes that occur during impact of the projectile upon the front component of the multi-wall shield, known as a bumper. Upon impact, compressive waves propagate into both the projectile and bumper plate. At free boundaries these waves are reflected as rarefaction waves, or tensile release waves. In the low velocity regime, pressures generated during impact are insufficient to induce failure of the projectile because the amplitude of the rarefaction wave does not exceed the tensile fracture strength of the projectile material. With increasing projectile velocities, the amplitude of compressive shockwaves generated in both impacting bodies increases until fragmentation of the projectile occurs. This indicates the beginning of the transition or shatter impact regime. As impact velocities are further increased, the projectile is fragmented into smaller and more finely dispersed fragments. In the low and intermediate velocity regimes, failure of the shield rear wall is cratering and spallation from individual fragment impacts. The hypervelocity regime is defined at the point at which the rear wall failure mechanism changes from a cratering type of failure to that of an impulsive failure, where the impacting debris cloud acts as a blast load. For aluminum-on-aluminum impacts, transition from the low-shatter regime and shatter-hypervelocity regime occurs at ~ 3 and 7 km/s, respectively. The low-shatter regime transition velocity has been shown to depend on the ratio of projectile diameter to bumper thickness (see e.g. [5]).

In the hypervelocity regime, penetration limits do not scale optimally (i.e. with projectile momentum) as a result of impact obliquity and non-spherical projectile effects. Rather, they are scaled at a rate above the cube root of impactor kinetic energy to account for solid projectile/bumper fragments amongst the debris impacting upon the shield rear wall or pressure hull [6]. For intermediate impact velocities, linear interpolation between the regime velocity limits is commonly used. The majority of HVI data used to empirically adjust and validate shielding ballistic limit equations has investigated the performance of traditional all-aluminum Whipple shield structures impacted by spherical aluminum particle at velocities between 6.0 - 7.0 km/s (e.g. [7][8][9]). Thus, validation of these equations is primarily performed in a regime with very little analytical basis.

In general, there exist a small number of BLEs for common shield configurations such as single wall, Whipple shield, stuffed Whipple shield, etc. that have been validated from test data on a baseline shield and a number of variations. For instance, development of a ballistic limit equation for a Nextel/Kevlar stuffed Whipple shield in [10] used 26 tests performed on seven variations of the shield using three different bumper thicknesses, seven different stuffing configurations, two different rear

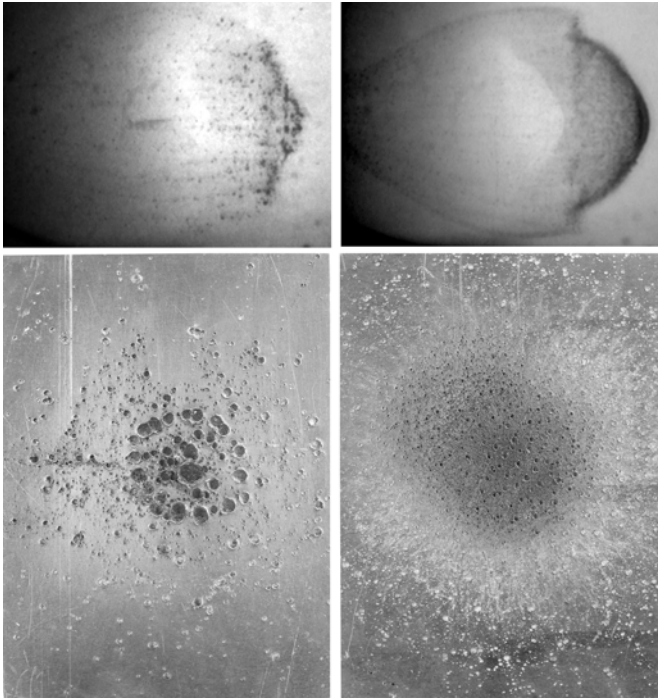


Fig. 22.2 Fragment clouds (top) and resulting impact damages (bottom) in thick aluminum plates for two impact tests on thin Al-plates in the transition velocity regime (left: 4.8 km/s; right: 6.7 km/s).

wall thicknesses, with constant spacing. Unfortunately, MMOD shielding configurations on flight hardware vary extensively, depending on perceived risk, design requirements (i.e. weight, spacing), launch vehicle capacity, etc. On the International Space Station (ISS), there are hundreds of different MMOD shields that vary by material, configuration, mass, thickness, and volume. Extensive impact testing and derivation of validated ballistic limit equations for each shielding configuration would be prohibitively expensive and time consuming. Therefore, these shields are commonly grouped into rough shield categories such as the stuffed Whipple. Generally such grouping is reasonable as the baseline equations are applicable for multiple configurations, however, the variation within these groups can often exceed the validated range of the equations. For instance, a sandwich panel shield with an aluminum open-cell foam core may be considered as a stuffed Whipple shield in which the areal weight of the foam core is considered the shield 'stuffing'. Clearly the damage mechanisms and failure processes in an open-cell foam sandwich panel would be expected to vary greatly from those in a stuffed Whipple shield, and therefore the application of this equation should be considered highly questionable. In addition to grouping of widely different shield types into empirical equations with

limited validity, hybrid ballistic limit equations which are a combination of baseline BLEs, are regularly applied. With hybrid BLEs the penetration limits of an ablative heat shield bonded to a support structure of aluminum honeycomb sandwich panel may be approximated, for instance, by a summation of the critical diameters of the individual ablator and sandwich panel. Again, such application of empirical equations is questionable yet is often considered necessary due to economic and time restraints. This is an area ripe for the use of numerical tools.

For velocities above those obtainable in laboratory experiments, the ballistic limit of a given structure is scaled in current penetration equations proportionally to impactor kinetic energy raised to the one-third power, i.e. $t_w \propto KE^{1/3}$. This approach is consistent with NASA practice [11]. Schmidt et al. [12] investigated the use of alternate materials to simulate the response of aluminum shields for impact velocities up to 18 km/s in order to assess the validity of kinetic energy scaling. They considered cadmium as a surrogate material as it melts and vaporizes at much lower specific energies than aluminum. The similarity between aluminum-on-aluminum and cadmium-on-cadmium impacts was evaluated for complete projectile melt. The authors theorized that if complete melt of an aluminum projectile impacting on an aluminum plate occurs at a velocity of 7 km/s, the same condition for cadmium on cadmium impact will occur at ~ 2.25 km/s (i.e. velocity scaling factor of 3.1). When failure of a multi-wall shield is caused by specific impulse loading of the completely molten debris cloud, dimensional analysis shows cadmium as a superior surrogate than other known materials due to similarity requirements of velocity, debris cloud momentum, ratio of specific heats, and bumper strength. Zinc provides a slightly better match for the similarity requirements; however, its velocity scaling is lower than that of cadmium (2.1 vs 3.1). For cadmium impact tests up to a scaled velocity of 18 km/s, the perforation limits of the simulated aluminum Whipple shield were found to increase in the hypervelocity regime as a result of vaporization of the debris cloud (see Fig. 22.3). Although the scaled cadmium impact tests provided similar perforation limits to aluminum shields, the mechanism of failure was not always reproduced. Thus, while cadmium provides good agreement for the dimensional analysis-derived similarity requirements, some conditions such as load rate and peak stress that are directly related to impact velocity cannot be scaled. Christiansen et al. [13] investigated the validity of cadmium scaling for a number of aluminum Whipple shield configurations and impact conditions and found that the ballistic limit of a shield varied by up to 25% between the baseline aluminum and scaled cadmium tests. The authors concluded that the velocity scaling factor of 3.1 derived by Schmidt et al. is not constant, but likely varies as a function of shield parameters and impact conditions.

A number of researchers have applied numerical techniques to investigate the behavior of MMOD shields at velocities above current experimental limits (e.g. [14][15]). The results of these numerical studies have shown, in general, agreement with the cadmium scaling experiments (i.e. increased ballistic performance at velocities above 8-11 km/s for Al-on-Al impacts). However, it should be noted that

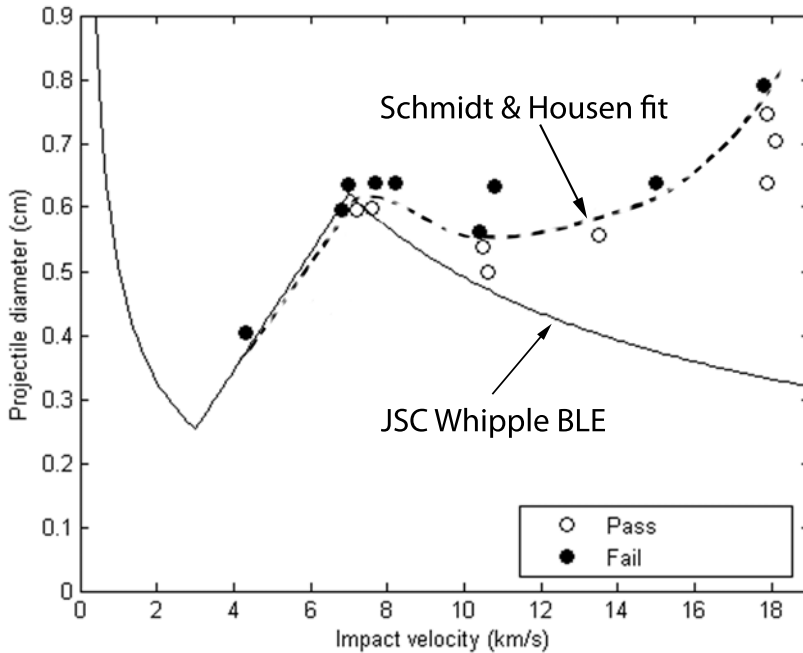


Fig. 22.3 Scaled ballistic limit curve for an aluminum Whipple shield developed from Cadmium scaling impact tests up to velocities of 18 km/s (from [12]).

the modeling approach used in a number of the simulations casts some doubt over their predicted results. For instance, validation of the numerical model in [14] was performed via comparison with experimental damages at lower impact velocities (7.2 km/s). The Shock (Mie-Grüneisen), Tillotson, and SESAME Equations of State (EOS) were all used to simulate impact damage, with the Shock EOS providing the most comparable result. However, this EOS does not model phase change. Thus, at the higher impact velocities in which projectile vaporization is expected to cause an upturn in the ballistic limit curve, material behavior is not accurately reproduced.

The maturity of predictive numerical tools, along with modern computing power, has reached such a point that their application in micrometeoroid and debris risk assessment for space vehicles is currently underutilized. Although test data will always be required for validation of numerical curves, there is a significant capacity for application of simulation tools in support of experimental evaluations. In this chapter, we will examine three applications for which numerical tools have already been applied with a degree of success, and discuss the strengths and weaknesses of these applications.

22.2 Ballistic Limit Simulation of a Representative Satellite Structure Wall

Sandwich panels with aluminum honeycomb cores and carbon fiber reinforced plastic facesheets (CFRP/Al HC SP) are amongst the most commonly used structures onboard satellites today. Their high strength, high stiffness, low weight, and low thermal expansion make them ideal for such applications. However, until recently, knowledge of the performance of these structures under impact from hypervelocity MMOD particles was relatively unknown. To remedy this, an extensive study was performed at Fraunhofer Ernst-Mach-Institute (EMI) under European Space Agency (ESA) contract to investigate the impact performance and damage mechanisms in CFRP under hypervelocity impact (see [16]). In this study, six CFRP/Al HC SPs representative of satellite structure walls were subject to extensive hypervelocity impact testing. For characterization of the sandwich panel ballistic limits, 27 impact tests were performed over a variety of impact velocities and angles and with varying projectile diameters. The same structure walls were used in an additional 67 impact tests which evaluated the lethality of fragments ejected within the simulated satellite interior onto critical components such as electronic boxes, cable harnesses, batteries, etc.

Recent developments [17] in the modeling of fiber-reinforced composite materials allow orthotropic constitutive behavior, non-linear equation of state, orthotropic non-linear hardening, and individual material plane interactive failure initiation criteria to be described. This represents a significant improvement over existing hydrocode capabilities in reproducing the behavior of anisotropic composite materials during HVI. Although developed and validated for use with high-strength aramid fiber composites, its application to structural composites (i.e. CFRP) was proven in preliminary investigations.

With the new capabilities in composite material modeling, in addition to the impact experiment database, numerical simulation of hypervelocity impact on composite materials appears to have reached a level of maturity such that its application in vehicle design and analysis is reasonable. With this in mind, a number of numerical simulations were performed using the commercial hydrocode ANSYS AUTODYN 3D [18] to evaluate the ballistic limit of a sandwich panel structure with an aluminum honeycomb core and CFRP facesheets.

22.2.1 Target Definition

The CFRP/Al HC sandwich panel from ESA's ENVISAT satellite was selected for the numerical investigation, an overview of which is given in Fig. 22.4.

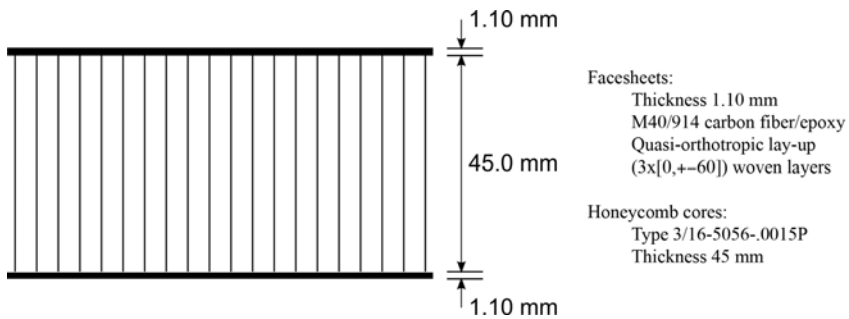


Fig. 22.4 Details of the ENVISAT CFRP/Al HC SP.

A preliminary material data set for the CFRP composite laminate in use on the ENVISAT satellite (M40/914) is provided in [17] for application with the advanced orthotropic composite material model. The material data is based on limited experimental characterization of similar materials. Application of this data set in [17] and [19] has shown accurate phenomenological reproduction of the material behavior under hypervelocity impact. Details of the numerical setup are given in [19].

22.2.2 Experimental Validation of the Numerical Simulation

Validation of numerical models is generally performed via comparison with experimental results. In this case, simulations are performed to characterize the failure limits of the ENVISAT CFRP/Al HC SP, and as such, validation of the model is performed through comparison of experimental damage extension and failure thresholds. As with any experiment, HVI testing is subject to a degree of scatter. Thus, for validation of the numerical model, it is imperative to first quantify this effect. In Fig. 22.5, two nominally identical CFRP/Al HC SP structures subject to nominally identical impacts are shown. Although front facesheet damages are similar, variation in rear facesheet damage extension (both clear hole diameter and surface spallation) exceed 100%. The differences in rear facesheet damage extension may be due to variation in the target parameters, manufacturing flaws in the target materials, experimental facility operation, or numerous other reasons. For impacts on HC core sandwich panels in which the projectile is smaller than the HC cell diam-

eter, an additional source of experimental scatter is the non-homogenous nature of the honeycomb. The impact location of the projectile relative to the hexagonal cells can affect projectile fragmentation and dispersion, as shown in Fig. 22.6. An investigation of this effect found that impact location (relative to the honeycomb cells) does not affect the gross result of the impact simulation (i.e. perforation or no perforation). However, the mass, dispersion, and lethality of perforating fragments was significantly affected.

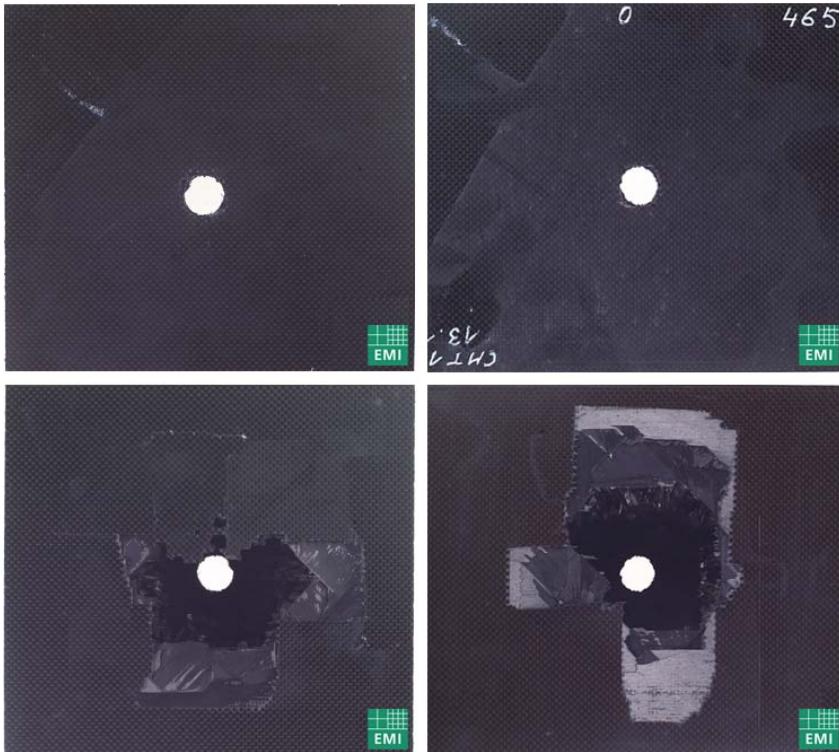


Fig. 22.5 Facesheet damage experimental scatter for EMI experiment 4633 (left): $d_p = 5.0$ mm, $V = 6.75$ km/s, $\alpha = 0^\circ$; and 4653 (right): $d_p = 5.0$ mm, $V = 6.69$ km/s, $\alpha = 0^\circ$. Top: front facesheet damage; bottom: rear facesheet damage.

For validation of the ENVISAT numerical model, three impact experiments were simulated. An overview of the impact conditions, damage, and result (i.e. perforation (P), detached spallation (SP) or no perforation (NP)) is given in Table 22.1. Of the three experiments, only one of the three simulations predicted the correct result, however, in all simulations a detached spallation result was obtained. Given the thickness (1.10 mm) and brittle nature of the CFRP material, the margin between a

perforated and non-perforated result is expected to be within the experimental scatter bounds. As such, a detached spallation test result is highly unlikely.

Table 22.1 Validation for the ENVISAT CFRP/Al HC sandwich panel numerical model.

Analysis Type	EMI test no.	Velocity [km/s]	Projectile diameter [cm]	Impact angle [°]	Result [P/SP/NP]
Exp	2285	6.30	1.10	0	SP
Sim	–	6.30	1.10	0	SP
Exp	2287	5.30	1.10	0	P
Sim	–	6.30	1.10	0	SP
Exp	2295	6.60	0.90	0	NP
Sim	–	6.60	0.90	0	SP

22.2.3 Simulation Results

The ENVISAT model was used to perform an additional 25 ballistic limit simulations over a range of impact velocities at normal incidence. The simulation parameters and results can be seen in Fig. 22.7. For simulations providing a detached spall result, the total mass of spall fragments was recorded, and is indicated in Fig. 22.7 by the marker size. Including the three validation cases, a total of 28 simulations were performed, for which twelve detached spall and nine no perforation results were obtained. The large number of spallation results suggests that the numerical model was not able to correctly reproduce the progression of damage states through incipient spallation, spall ejection, and perforation of the sandwich panel rear facesheet. To assess the accuracy of the numerical simulations, the results can be compared to ballistic limit equation predictions.

BLEs define the limits of structural perforation in terms of impactor mass, velocity and angle. They are commonly expressed as a ballistic limit curve, which demarcates between impact conditions causing structural perforation and no perforation in projectile diameter-velocity space. A ballistic limit equation for triple wall structures incorporating CFRP/Al HC SPs has been defined in [20] from 55 hypervelocity impact experiments on six space-representative CFRP/Al HC SP structures. Modified for application with dual-wall targets, the ballistic limit equation is expressed in the low velocity regime ($V/\cos\theta \leq V_{LV}$), as :

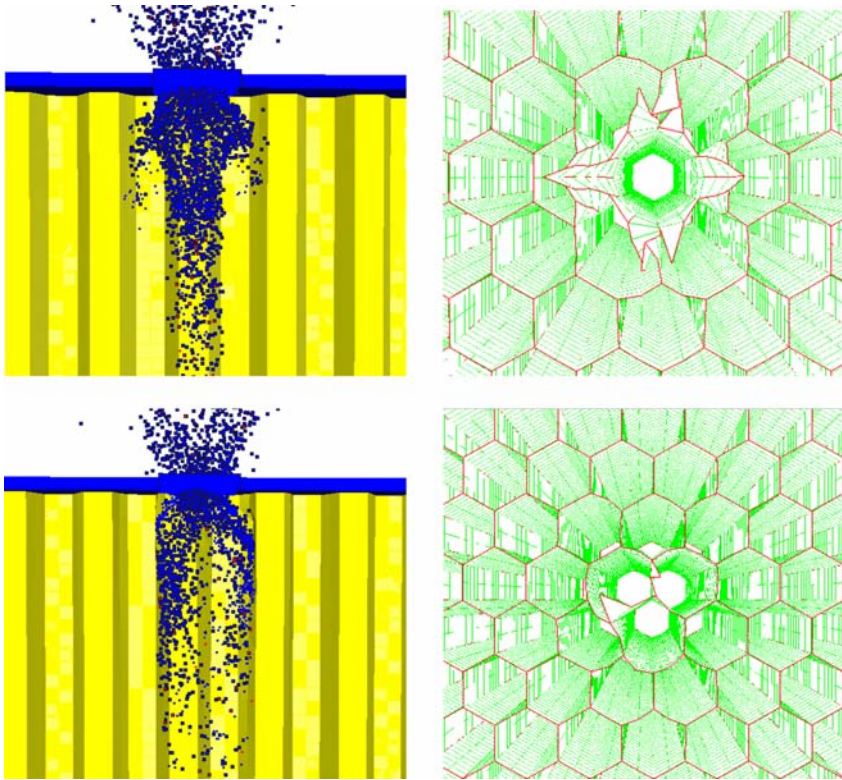


Fig. 22.6 The effect of honeycomb cell impact location on fragment channelling within a sandwich panel honeycomb core (1.1 mm Al-sphere at 6.3 km/s, normal incidence). Upper: impact within a cell; Lower: impact upon a 3-wall junction.

$$d_c(V) = \left[\frac{t_w / K_{3S} \cdot (\sigma_{ref} / 40)^{1/2} + t_b}{0.6 \cdot (\cos \theta)^{4/3} \cdot \rho_p^{1/2} \cdot V^{2/3}} \right]^{18/19} \tag{22.1}$$

In the shatter regime ($V_{LV} < V / \cos \theta < V_{HV}$) linear interpolation is used:

$$d_c(V) = d_c(V_{LV}) + \frac{d_c(V_{HV}) - d_c(V_{LV})}{V_{HV} - V_{LV}} \cdot (V - V_{LV}) \tag{22.2}$$

In the hypervelocity regime ($V / \cos \theta \geq V_{HV}$):

$$d_c(V) = \frac{1.155 \cdot S^{1/3} \cdot t_w \cdot (\sigma_{ref} / 70)^{1/3}}{K_{3D}^{2/3} \cdot \rho_p^{1/3} \cdot \rho_{ref}^{1/9} \cdot V^{2/3} \cdot \cos \theta^{4/3}} \tag{22.3}$$

The constants used in Equations (22.1)-(22.3) are defined in Table 22.2. The ballistic limit curve of the ENVISAT CFRP/Al HC SP is shown in Fig. 22.7 along

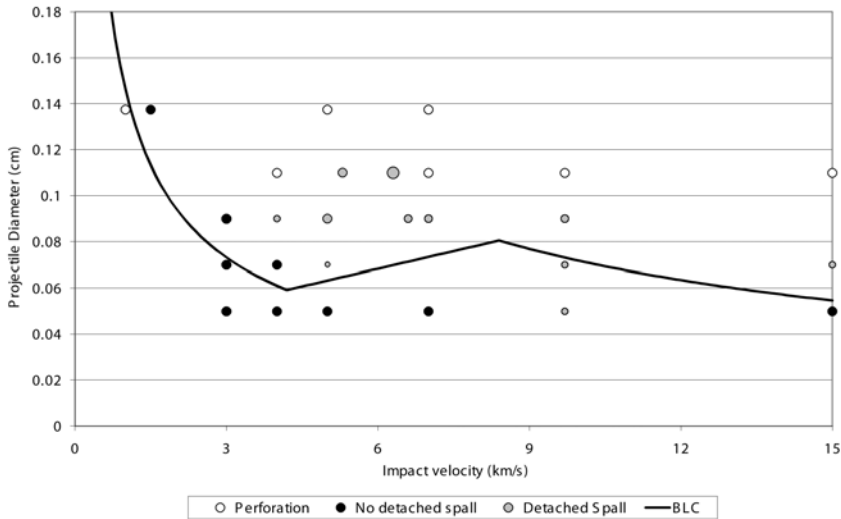


Fig. 22.7 Ballistic limit curve and numerical simulation results for the ENVISAT CFRP/AL HC SP (larger spall market indicates higher spall mass).

with the simulation results. Of the 28 simulations, 22 (79%) agreed with the empirical equation predictions (detached spallation is considered failure). Across the range of impact conditions simulated, the numerical model generally provides consistent results in terms of increasing rear facesheet damage with increasing impact energy. The exception to this is the two simulations at low velocity, which show that a 1.375 mm sphere will perforate the structure at 1.0 km/s, while at an increased velocity of 1.5 km/s there is no damage to the structure rear surface. The simulation results mimic the shape of the ballistic limit curve, although the gain in shielding performance in the intermediate impact velocity regime (due to increasing projectile fragmentation) does not appear to be as significant as that predicted by the BLE.

22.3 Simulation of Hypervelocity Impact on a Representative Satellite Structure Wall Causing Penetration and Fragment Ejection

For manned spacecraft such as the Space Shuttle Orbiter and International Space Station (ISS), the risk of mission failure due to impact is calculated in terms of the probability of perforation of the pressure hull, and the probability of catastrophic failure resulting from perforation (e.g. perforation of a critical flight component, module unzipping, etc.). For unmanned spacecraft, calculating mission risk based

Table 22.2 List of constants for use in the SRL ballistic limit equation for CFRP/Al HC SPs.

Constant	Description	Unit	Value
ρ_{ref}	Density of reference Al-alloy (Al 2024-T81)	[g/cm ³]	2.78
σ_{ref}	0.2% yield strength of reference Al-alloy (Al 2024-T81)	[ksi]	59.5
t_b	Front facesheet equivalent Al-alloy thickness	[cm]	$t_{b,CFRP} \cdot \frac{\rho_{b,CFRP}}{\rho_{ref}} + \frac{AD_{MLL}}{\rho_{ref}}$
t_w	Rear facesheet equivalent Al-alloy thickness	[cm]	$t_{w,CFRP} \cdot \frac{\rho_{w,CFRP}}{\rho_{ref}}$
K_{3S}	Ballistic fit factor	–	1.1
K_{3D}	Hypervelocity fit factor	–	0.40
V_{LV}	Low-intermediate regime transition velocity	[km/s]	4.2
V_{HV}	Intermediate-hypervelocity regime transition velocity	[km/s]	8.4

on penetration of the spacecraft structure wall fails to take into account the lack of vehicle pressurization, and the intrinsic shielding of internal components. As such, penetration-based risk assessments may be inherently conservative for unmanned and un-pressurized vehicles. Putzar et al. [21] evaluated the vulnerability of satellite components to MMOD impact, identifying critical components and failure thresholds for both shielded and unshielded equipment such as batteries, electronic boxes, fuel pipes, etc. The authors found that by considering failure to occur when penetration of the satellite wall led to either temporary or permanent failure of critical mission components instead of merely penetration of the spacecraft outer wall, mission MMOD failure probabilities could be significantly reduced.

The study by Putzar et al. looked at failure of components shielded behind aluminum bumper plates, aluminum honeycomb sandwich panels, and multi-layer insulation (MLI). For spacecraft utilizing CFRP/Al HC SP structure walls, the vulnerability of internal components varies from those reviewed by Putzar et al. given the minimal penetration lethality of CFRP fragments. CFRP ejecta causes minimal mechanical damage to internal components, however the slow moving debris forms a conductive cloud that can lead to arc discharges and current leakage from unshielded electronic components. To investigate the behavior of penetrating CFRP fragment clouds, a number of numerical simulations were performed for conditions leading to perforation of a CFRP/Al HC SP structure wall and ejection of material within a satellite interior.

22.3.1 Target Definition

For simulation of impacts leading to penetration and ejection of fragments within a satellite body the RADARSAT-2 +/-Z platform CFRP/Al HC SP structure was selected. Details of the panel are shown in Fig. 22.8. In the absence of material data, a procedure defined in [22] that applies a number of common composite mechanics and shock physics theories along with general material properties to derive a complete preliminary material data set for use with the advanced orthotropic composite material model was applied. The derived RADARSAT material data set used in the simulations can be found in [22]. Details of the numerical setup are found in [23].

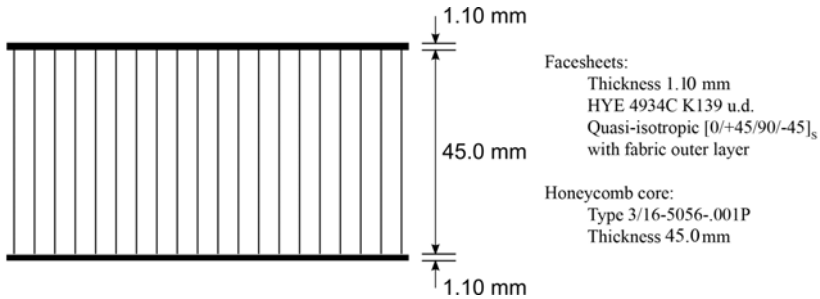


Fig. 22.8 Details of the RADARSAT-2 +/-Z platform CFRP/Al HC SP.

22.3.2 Experimental Validation of the Numerical Simulation

For validation of the numerical model, three hypervelocity impact experiments on the RADARSAT CFRP/Al HC SP leading to perforation and fragment ejection were simulated. Validity of the numerical model was assessed via damage measurements in the front and rear facesheets of the sandwich panel (d_h , D_{SP}), dispersion of fragments both within the honeycomb core (d_{hc}) and following perforation of the sandwich panel (β), and damage extension on the simulated internal component (D_{DUST} , D_{WP99}). Definition of damage measurements is provided in Fig. 22.9.

For conventional metallic targets, measurement of fragment cloud dispersion angles and witness plate (satellite interior) damage is relatively straightforward, as shown in Fig. 22.10. However, for impacts on CFRP/Al HC SP structures, these become more difficult, as shown in Fig. 22.10. Initially, the expansion angle of the perforating debris cloud is effectively hemispherical (i.e. $\beta_{ext} \cong 180^\circ$). At latter stages, a high density zone of the fragment cloud can be observed, however this fails to capture all debris fragments.

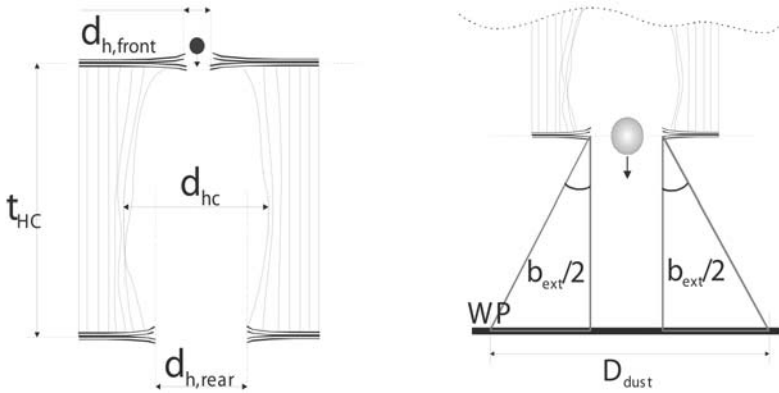


Fig. 22.9 Definition of sandwich panel damage measurements for assessing the validity of the RADARSAT numerical model.

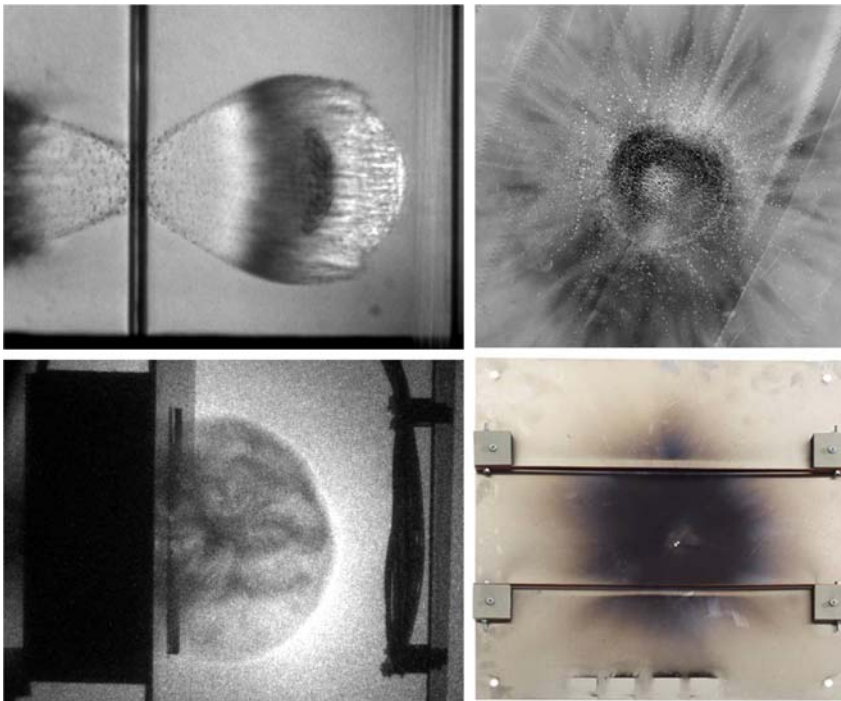


Fig. 22.10 Measurement of fragment cloud dispersion angle and witness plate damaged area for conventional aluminum targets (top) and CFRP/Al HC SPs (bottom).

Definition of fragment dispersion angles using witness plate damage is also more difficult for CFRP/Al HC SPs than traditional metallic targets. As previously men-

tioned, individual delaminated carbon fibers cause very little mechanical damage. Indeed, charred CFRP deposits can simply be wiped off the surface of experimental witness plates without any apparent damage to the structure. The difficulties in defining fragment ejecta angles and witness plate damage extension are also applicable to the numerical model. In Fig. 22.11 a series of images are shown that demonstrate the numerical propagation of perforating fragments. In the numerical model, each individual finite element that passes through virtual membrane is propagated to the location of the internal component (witness plate). The same question arises of how (and when) the limits of the fragment cloud should be defined. Characteristics of the fragment cloud dispersion are similar to those shown in Fig. 22.10: initially, the fragment cloud shows a near hemispherical dispersion angle; at a later time, the fragment cloud has separated into high- and low-density zones, the dispersion angle of which varies significantly. Again, measurement of the deposit/damage area is subject to interpretation. No standardized levels exist for measuring the fragment cloud ejecta angle in either numerical simulations or experiments looking at ejection of charred CFRP fragments. It is possible with experimental images to define a generic spectral limit that relates the amount of light transmitted through the fragment ejecta to the cloud density. A technique that defines the fragment ejecta angle based on cloud density is also possible for measurement of the numerical simulation. However, in the simulations, the limit of the smallest fragment in the ejecta cloud is limited to the grid discretization. Thus, the density of the fragment cloud in the numerical simulation is only, at best, approximate given the small and fine distribution of the ejected CFRP fragments. Furthermore, a comparison between the two approximate methods is expected to be highly unreliable given the approximate nature of the measurement techniques.

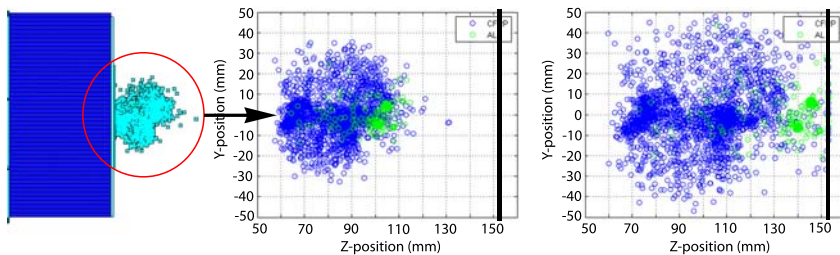


Fig. 22.11 Numerical fragment cloud expansion following perforation of a CFRP/Al HC SP.

Details of the three impact experiments used for validation of the RADARSAT numerical model are provided in Table 22.3. Damage measurements from both the experimental and numerical structures are provided in Table 22.4. In general it can be noted that an increase in the projectile diameter corresponds to an increase in the inaccuracy of the numerical model damage values. For normal impact of a 3.0 mm projectile at high velocity (S1), the simulated damage measurements agree rea-

Table 22.3 Details of validation experiments (prefix E) and simulations (prefix S) used for validation of the RADARSAT numerical model.

Test no.	EMI exp.	Velocity [km/s]	Projectile diameter [cm]	Impact angle [°]
E1	4635	6.64	3.00	0
S1	n/a	6.70	3.108	0
E2	4671	2.60	4.00	0
S2	n/a	2.50	3.955	0
E3	4633	6.71	5.00	0
S3	n/a	6.70	5.085	0

sonably well with the experiment (30% with the exception of D_{WP99}). An increase in the projectile size to 4.0 mm (S2) results in significant (~200%) over-prediction of the damage measurements for both sandwich panel facesheets and WP deposits. Following a further increase in the projectile diameter to 5.0 mm (S3), the deviation of the simulation damage values from the experimental measurements was even more pronounced: front surface measurements were over-predicted by up to 600% while rear surface measurements were under-predicted by up to 230%. The front facesheet in the numerical model showed extensive delamination, which is a phenomenon not observed in the experiments, leading to over-prediction of the front facesheet damage extension in the numerical simulations. One possible cause is that the through-thickness tensile strength of the laminate, a property approximated by the quasi-static transverse tensile strength of a unidirectional ply, is under-estimated. Nonetheless, the front facesheet damage extension is not expected to significantly affect the behavior of fragments perforating the sandwich panel rear facesheet.

Table 22.4 Experimental and numerical simulation damage measurements for the three RADARSAT CFRP/Al H CSP validation cases.

Test no.	Front facesheet		Rear facesheet		Witness plate		
	d_h [mm]	D_{sp} [mm]	d_h [mm]	D_{sp} [mm]	D_{WP99} [mm]	D_{DUST} [mm]	β_{ext} [°]
E1	8.4x8.8	11x10	5.8x6.4	15x10	49x49	113x110	55.6
S1	8.1x8.4	39x48	8.4x4.2	11x12	0x0	96x75	43.2
E2	7.8x8.2	9x12	4.5x5.4	15x19	33x13	50x54	26.5
S2	17.3x18.1	20x25	12.2x11.4	18x13	44x28	104x102	49.0
E3	11.3x11.7	14x14	53.6x38.8	73x52	72x73	137x153	52.6
S3	27.5x33.0	102x108	11.7x12.4	22x27	79x67	146x108	59.8

22.3.3 Simulation Results

In addition to the validation cases, seven numerical simulations were performed to investigate impacts leading to penetration of the RADARSAT CFRP/Al HC SP and ejection of fragments within the satellite interior. The simulations were performed over a range of impact velocities (2.50-10.0 km/s) and impact angles (0/45/60°). The results of the numerical simulations are summarized in Table 22.5. For S7, S8 and S10, the front facesheets were excessively delaminated and as such damage measurements are not provided. The results of the numerical simulations can be used to develop trends in the behavior of the fragment cloud within the satellite interior. For instance, under normal impact the dispersion of fragments following penetration of the sandwich panel increases with increasing impact velocity. This trend has also been observed in experiments [16]. Under oblique impact, however, an increase in impact velocity results in a decrease in the diameter of the witness plate deposited area, shown in Table 22.5.

Table 22.5 Results of the RADARSAT CFRP/Al HC SP numerical simulations causing penetration and fragment.

Test no.	V [km/s]	d_p [mm]	α [°]	$d_{h,front}$ [mm]	$D_{SP,front}$ [mm]	$d_{h,rear}$ [mm]	$D_{SP,rear}$ [mm]	D_{WP99} [mm]	$D_{DUST,WP}$ [mm]	β [°]
S4	10.00	3.955	0	23.8x30.8	79x91	9.9x10.7	22x20	62x44	144x132	65.1
S5	2.50	3.1075	0	11.8x12.8	19x22	10.4x6.4	13x12	25x13	90x65	38.1
S6	2.50	3.955	45	15.9x12.9	26x23	9.8x5.4	22x12	50x16	127x77	50.5
S7	10.00	3.955	45	–	–	14.3x5.2	20x13	35x19	96x71	40.5
S8	6.70	3.955	60	–	–	4.3x4.3	41x29	14x12	110x75	47.6
S9	2.50	3.955	60	18.0x8.4	34x34	11.4x4.3	11x9	42x4	123x85	51.4
S10	10.00	3.955	60	–	–	14.0x9.8	28x31	0x0	113x58	40.4

In Fig. 22.12, witness plate deposits for three numerical simulations are shown. The simulations were all performed at 60° with a 4.0 mm Al-sphere projectile. With increasing impact velocity, the diameter of the deposited area is shown to clearly decrease. However, rather than a decrease in total fragment mass, the concentration of ejecta along the shot axis (0,0) is increased. A possible explanation for this is that under increasing impact velocity, the facesheet fragments are more effectively channeled within the honeycomb cells about the shot axis. Thus, following perforation of the rear facesheet, the fragments have a lower expansion angle. There is no recognizable trend in rear facesheet damage extension for increasing impact velocity at oblique incidence.

In Fig. 22.13 the mechanical damage potential of fragments impacting the aluminum witness plate are shown for three impact angles: 0° /45° /60°. Mechanical

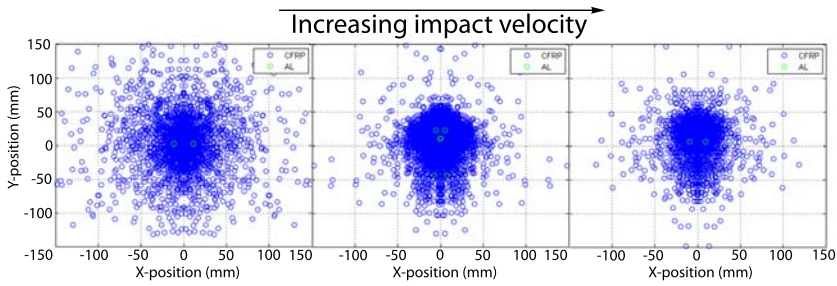


Fig. 22.12 The effect of increasing velocity on WP deposits for oblique (60°) impact. From left to right: 2.5/6.7/10.0 km/s.

damage is plotted as kinetic energy of aluminum fragments, following the assumption that CFRP fibers induce minimal mechanical damage. The figure shows that an increase in impact angle results in a decreased witness plate damage, which agrees with the experimental findings.

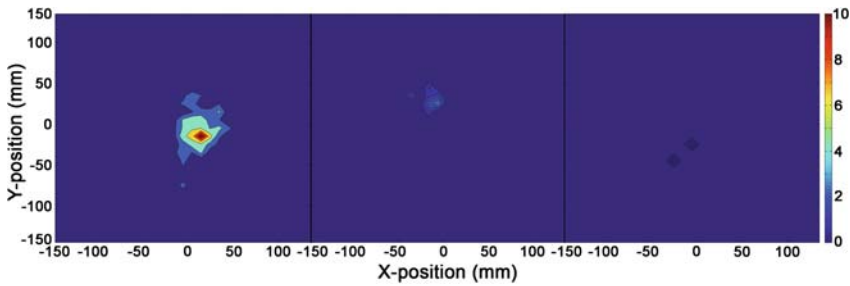


Fig. 22.13 Contours of aluminum fragment kinetic energy in units of [J] for impact on an aluminum WP (4.0 mm Al-sphere at 10 km/s). From left to right: 0° / 45° / 60° .

22.4 Numerical Simulation of Impact Induced Disturbances in Satellite Structures

The previous studies have evaluated the application of predictive numerical tools for the calculation of mission risk in terms of penetration-based failure of the spacecraft hull and failure of critical interior components. The next generation of European satellites will employ ultra-high sensitivity equipment that require platform stability orders of magnitude higher than those of previous missions. For such science missions, degradation of measurement accuracy due to a noisy dynamic back-

ground would result in mission failure equal to, albeit less spectacularly, MMOD-penetration based catastrophic failure. Regular impact of micro-sized debris particles can induce transient disturbances in satellite structures which, given the platform stability required, are capable of propagating throughout the satellite structure to areas of critical stability such as measurement devices.

The Global Astrometric Interferometer for Astrophysics (GAIA) will operate in a Lissajous orbit about the Earth-Sun L2 point, at which the primary debris environment consists of natural, micro-sized particles traveling at velocities over 20 km/s. As such, in-orbit impact conditions cannot be reproduced in laboratory experiments, and numerical simulations are required to characterize the transient structural response. Structural finite element analysis (FEA) codes are the preferred engineering tool for investigating the response of structures under static and dynamic loading. However, considering that there are three orders of magnitude variance between the dimensions of the satellite and common impactor (m vs μm), simulation of the entire satellite structure is not feasible in terms of the required computational time and cost. Furthermore, structural analysis codes are not suited for simulation of such extreme high loading-rate events. Considering the impact process, a high amplitude shock wave is initially generated at the impact location, causing plastic deformation (e.g. cratering) in the front surface of the target. As the shock wave propagates into the surrounding structure, this plastic wave is rapidly damped out, evolving into an elastic wave. Hydrocodes can be utilized to model the local structure during the impact event for which the evolution of disturbance waves in the structural panel can be characterized. Outside of the zone of plastic deformation, the elastic waveform can be approximated by an analytical function that can then be used as a load-input to a structural FE model of the entire satellite.

22.4.1 Target Definition

A CFRP panel representative of those used onboard the GAIA service module (SVM) and payload module (PLM) was selected for simulation (details in Fig. 22.8). In the absence of experimentally-characterized material data, properties were theoretically approximated using a procedure defined in [24]. Details of the numerical setup can be found in [25].

22.4.2 Experimental Validation of the Numerical Simulation

Validation of the numerical model was performed via comparison of the experimentally measured impact-induced disturbance waveform propagating in the sandwich

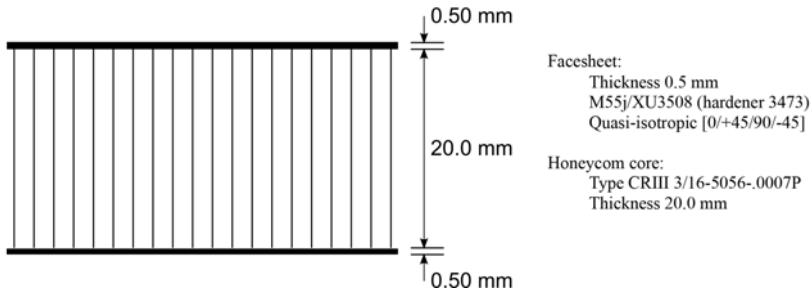


Fig. 22.14 Details of the GAIA CFRP/Al HC SP.

panel rear facesheet. A Polytec Laser Vibrometer (LV) measurement that provides an effectively massless measurement device was used in the experiments. Initial validation experiments were performed on a 2 mm thick Al 7075-T6 plate, impacted by a 2.0 mm Al-sphere at 5.3 km/s (normal incidence). The disturbance waveforms (numerical and experimental) were measured 150 mm from the impact site, and are shown in Fig. 22.15. The waveforms can be separated into three distinct phases corresponding to different wave types: longitudinal, shear and flexural. The longitudinal wave has the highest velocity and is represented in the acceleration signal by the initial pulse. The flexural wave has the highest amplitude, lowest frequency, and lowest propagation velocity (arrives at the sensor at $\sim 48 \mu\text{s}$ after impact). Based on wave type propagation speeds it is considered that the signal between the longitudinal and flexural waveforms represents the shear wave, however this remains unclear. All three experimental waveform types are well reproduced well by the numerical simulation.

Numerical disturbance waveforms in the CFRP laminates (facesheets) were also simulated for comparison with experimental signals, see Fig. 22.16. Although the longitudinal arrival time and directional dependency of the wave propagation were reproduced correctly, significant discrepancies are noted in all three constituent waveform types in the disturbance signal and in no way can the simulation be considered predictive. The inability of the numerical model to accurately reproduce the numerical waveform highlights current limitations in material modeling for shock wave propagation in anisotropic solids. A better method is required to handle the shock wave physical assumptions in both experimental parameter derivation and numerical equation of state formulation and stress tensor decomposition. For instance, experimental derivation of anisotropic solid equation of state parameters is performed with planar flyer plate impact experiments assuming a hydrostatic stress condition. Although valid for isotropic materials, for anisotropic solids this is clearly inadequate because of directional stress dependencies.

The facesheet model was carried over for validation of the honeycomb sandwich panel model described in the previous section. A comparison between the numerical

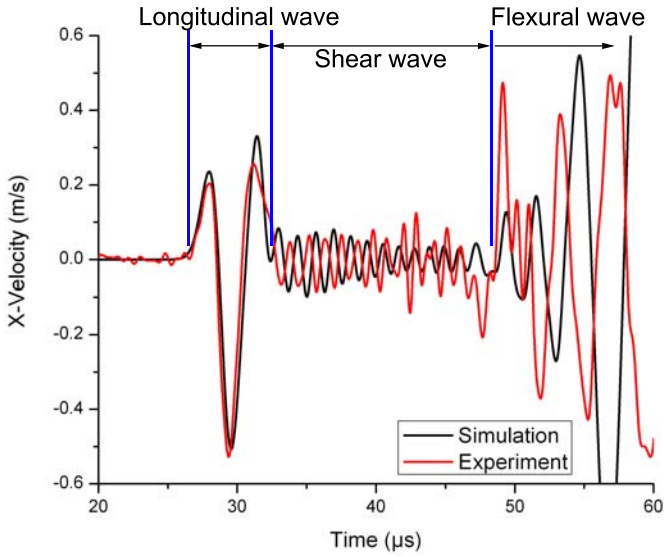


Fig. 22.15 Comparison of experimental and numerical disturbance waveform in a 2 mm thick Al 7075-T6 plate measured 150 mm from impact of 2.0 mm Al-sphere at 5.3 km/s (0°).

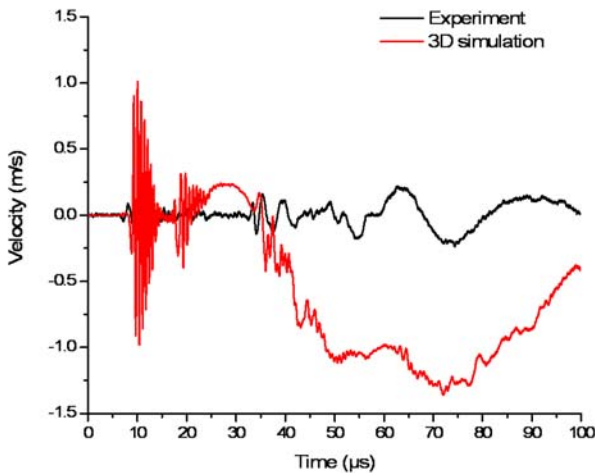


Fig. 22.16 Comparison of experimental and numerical disturbance waveform in a 0.8 mm thick CFRP facesheet measured 150 mm from impact of 0.8 mm Al-sphere at 4.9 km/s (0°).

and experimental waveforms is made in Fig. 22.17. Although the facesheet numerical model was unable to predict the disturbance waveform with any degree of ac-

curacy, the sandwich panel model is shown to reasonably simulate a number of key waveform characteristics. The longitudinal wave amplitude and arrival time are well reproduced, in addition to the flexural wave arrival time, amplitude, and frequency. Furthermore the shear wave trends ($\sim 10\text{-}30\ \mu\text{s}$) after impact are reproduced to a reasonable degree. The primary difference in the two waveforms is the $-x$ velocity section of the flexural waveform predicted in the numerical model. Although the CFRP facesheet model was unable to reasonably simulate the disturbance signal, the quality of the sandwich panel numerical signal is quite good. The reasoning for this is that the honeycomb core acts to stiffen the structure in an isotropic manner, making the anisotropic CFRP response less prominent.

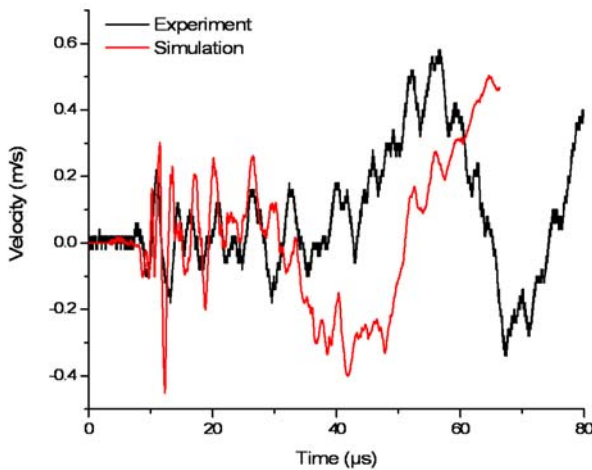


Fig. 22.17 Comparison of experimental and numerical disturbance waveform in a CFRP/Al HC SP measured 150 mm from impact of 1.5 mm Al-sphere at 5.69 km/s (0°).

22.4.3 Simulation Results

A series of 14 simulations were performed to characterize shock wave propagation through CFRP/Al HC SP structures, details of which are given in Table 6.

In order to be approximated by an empirical function, the disturbance waveform must be simplified. The longitudinal waveform was found to rapidly dissipate with propagation distance. Additionally, characterization of the disturbance waveform is

Table 22.6 Hypervelocity impact-induced disturbance simulation details.

	Proj. diameter [mm]	Proj. mass [mg]	Velocity [km/s]	Momentum [g m/s]
1	0.05	1.83×10^{-4}	4.9	8.980×10^{-4}
2	0.05	1.83×10^{-4}	10.0	1.833×10^{-3}
3	0.2	0.012	4.9	0.058
4	0.2	0.012	10.0	0.117
5	0.4	0.094	4.9	0.460
6	0.4	0.094	6.0	0.559
7	0.4	0.094	10.0	0.938
8	0.4	0.094	20.0	1.863
9	0.6	0.317	16.0	5.031
10	0.7	0.503	20.0	9.986
11	0.8	0.751	4.9	3.652
12	0.8	0.751	10.0	7.453
13	0.8	0.751	17.5	13.042
14	0.8	0.751	20.0	14.905

made for input in structural codes with a maximum valid frequency range of ~ 500 kHz (longitudinal waveform frequency in CFRP was measured at ~ 1 MHz). As such, a 500 kHz low-pass filter is applied to the numerical signal prior to characterization. Considering the rapid decay of the longitudinal waveform and the frequency filtering, it is apparent that the flexural waveform is the key signal feature. For approximation of the flexural waveform, a polynomial-exponential decay function is applied:

$$V(t) = A(t - t_0)^2 e^{-\beta(t - t_0)} \quad (22.4)$$

where V is out-of-plane velocity (m/s), t is the time after impact (μ s), t_0 is the arrival time of the disturbance signal at the measurement gauge (μ s), and A and β are constants.

Equation (22.4) defines a state initially at rest (for $t < t_0$, the equation is not valid). Upon arrival of the transient signal ($t = t_0$), there is an initial acceleration in the direction of the projectile velocity vector (V). The disturbance velocity reaches a maximum as the projectile either perforates or is halted by the CFRP facesheet, following which it asymptotes to zero (i.e. rest). To characterize evolution of the disturbance waveform as it propagates from the impact site, a series of disturbance measurements are simplified using Equation (22.4) (an example of which is shown in Fig. 22.18). The constants of the polynomial-exponential decay fits can then be characterized in terms of distance from the impact site, an example of which is shown in Fig. 22.18 for constant A .

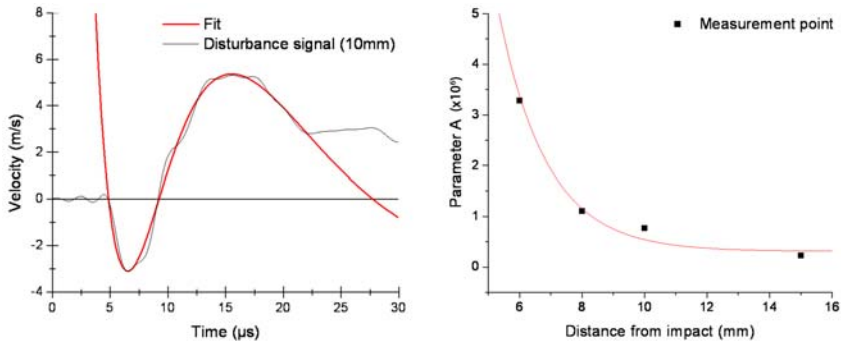


Fig. 22.18 Characterization of the disturbance waveform. Left: Fitting the polynomial-exponential decay function to the filtered signal; Right: Characterizing the constant A in terms of distance from the impact site (impact of a 0.6 mm Al-sphere at 16 km/s (0°)).

Once the waveform evolution has been characterized, extrapolation of the constants to the excitation origin can be performed from which the original elastic excitation pulse is determined (shown in Fig. 22.19 for impact of a 0.6 mm Al-sphere at 16 km/s). The excitation origin is defined on the front facesheet as the extension of plastic damage, which is determined from extrapolation of the signal arrival time t_0 , while the rear facesheet excitation origin is dependent on expansion of projectile and front facesheet fragments within the honeycomb core. For the simulations considered, fragments were channeled within 2 honeycomb core cells (shown in Fig. 22.19). As such, the extension of the rear facesheet excitation zone is set equal to twice the honeycomb cell diameter.

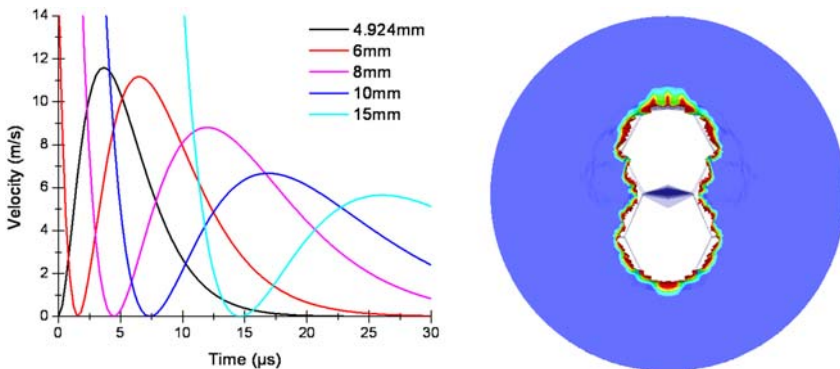


Fig. 22.19 Extrapolation of the simplified disturbance curves to the excitation origin defined as a cylinder with diameter equal to twice the diameter of HC cells.

A general excitation function can be defined that incorporates the effects of projectile diameter and impact velocity on the impact-induced disturbance in terms of impactor momentum. For application as an excitation load within a structural code, the function is defined as force with respect to time, where mass is equal to the front or rear facesheet excitation origin, and acceleration is the time derivative of Equation (22.4).

$$F(t) = m \cdot a(t) \tag{22.5}$$

$$a(t) = 2Ate^{-\beta t} - At^2\beta e^{-\beta t} \tag{22.6}$$

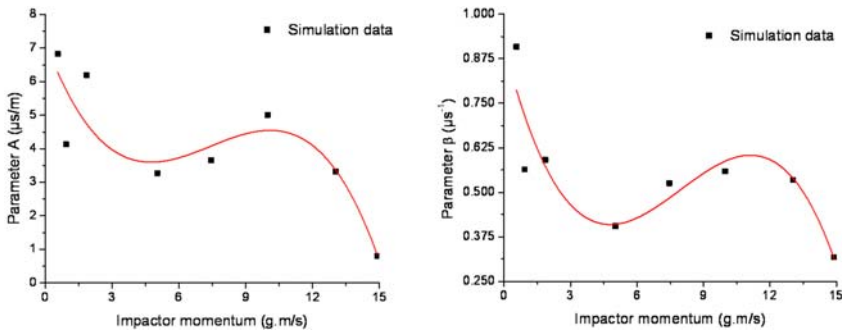


Fig. 22.20 Characterization of generalized excitation function constants for the sandwich panel rear facesheet.

The constants in Equation (22.6) are characterized at the excitation origin in terms of impactor momentum. For impacts that penetrate the front facesheet, impact disturbances propagate in both the front and rear facesheets, however, only the facesheet with the greatest amplitude excitation is considered. In Fig. 22.20, characterization of the constants in Equation (22.6) is made for the rear facesheet. Initially, particles with low momentum are unable to penetrate the sandwich panel front facesheet and, therefore, all momentum transfer is made to the front facesheet. As the projectile momentum is increased, excitation of the front facesheet also increases until the facesheet is penetrated. Upon penetration of the front facesheet, the fragment cloud propagates through the honeycomb core and impacts upon the rear facesheet. The momentum of the perforated fragments is low at the penetration threshold, and as such the majority of momentum transfer continues to occur in the front facesheet. As the degree of perforation increases, the front facesheet demonstrates an increasing 'punch-out' type perforation, and the distribution of momentum transferred to the sandwich panel becomes rear facesheet dominated. As the rear facesheet perforation threshold is reached and exceeded, similar behavior is expected. The cubic shape of the fit curves for the constants A and β in Fig. 22.20

describe this transition for the rear facesheet (i.e. reaching and exceeding a level of 'significant perforation').

Table 22.7 Excitation function equation constants (front and rear facesheet).

Front facesheet	Rear facesheet
$m = 0.0382 \times 10^{-3} \text{ kg}$	$m = 0.0860 \times 10^{-3} \text{ kg}$
$A = 39.49 - 32.55 \times 0.68P_p$	$A = 7.19 - 1.79P_p + 0.278P_p^2 - 0.0125P_p^3$
$\beta = 2.73 - 0.85P_p + 0.22P_p^2$	$\beta = 0.91 - 0.25P_p + 0.037P_p^2 - 0.0015P_p^3$

The constants of the excitation function for the GAIA CFRP/Al HC SP are defined in Table 22.7 for both the front and rear facesheets. In Fig. 22.21, the peak force described by the excitation functions is plotted in terms of impactor momentum. The front facesheet function is valid for impactor momentum less than 2.64 g.m/s, representing the condition of significant perforation in the front facesheet. For larger momentum projectiles, the rear facesheet excitation function should be applied. Ideally, there is a smooth transition between the peak force defined by the two functions, however in this case, it is considered that in the 2.64-4.5 g.m/s range, the equations provide a conservative approximation.

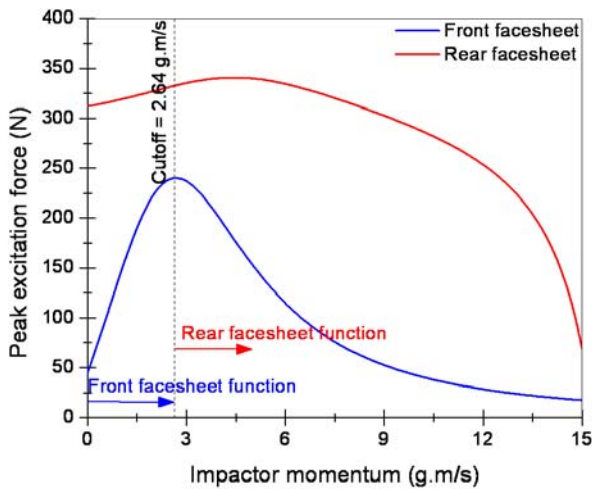


Fig. 22.21 Generalized excitation function peak force in terms of impactor momentum.

In [27] the excitation function was applied to four points on the GAIA satellite finite element model: two points on the service module and two points on the payload module (telescope). For the four impact points considered, line of sight deviation of the telescope was evaluated in terms of the mission requirements. It was determined that for daily impacts, disturbances will not affect telescope measurements. However, impact of larger projectiles (e.g. 1 per year size impactors) as far removed as the service module are capable of propagating through the satellite platform and inducing line of sight deviations on the payload module (telescope) that exceed specifications. It was concluded that the GAIA mission should expect re-configuration from preliminary design due to HVI impacts degrading measurement performance.

22.5 Discussion and Summary

Structures exposed to the space environment are subject to regular impact of micrometeoroid and orbital debris (MMOD) particles travelling at velocities between 1-72 km/s. The threat of these impacts on mission safety must be evaluated for all manned flights prior to launch. This is a task performed using software tools that incorporate debris environment models, spacecraft geometry models, and penetration limit equations (ballistic limit equations). These equations are based on analytical considerations, and use hypervelocity test data to empirically anchor them at the limit of experimentally obtainable impact velocities (currently around 7-8 km/s). Although a subject of research for over 40 years, the complexity of material behavior and damage mechanisms at such high loading rates has thus far prevented the derivation of analytically sound ballistic limit equations. As such, development of penetration limit equations for new shielding configurations is performed by modifying existing BLEs for similar structures, and performing a minimal number of validation tests when time and money permits. In a worst-case scenario, shields that cover limited surface area and are not subject to high debris flux can have ballistic limit equations assigned that were validated for configurations with little resemblance to the new configuration.

In this chapter, three investigations applying numerical tools in MMOD risk assessment have been discussed. These studies have evaluated and tested the application and accuracy of numerical tools to MMOD risk assessment for common satellite structures (CFRP/Al HC SP). Numerical simulations investigating the failure limits of satellite structures, the ejection of fragments within satellite interiors, and the propagation of impact-induced disturbances throughout high stiffness satellite platforms have been performed. Validation of the numerical predictions with experimental measurements have identified a number of short-comings in equation of state definition and stress tensor decomposition for anisotropic materials models, however the models have, for the most part, shown to provide qualitatively accurate

reproduction of experimental phenomena. The findings have led to, for example, the recommendation of preliminary satellite platform design reconfiguration [27].

Although the application of numerical tools in MMOD risk assessment is increasing (as demonstrated by the three examples presented), they remain largely underutilized. Ideally, numerical codes could be used during vehicle preliminary design to evaluate different shielding concepts and perform parametric studies to optimize subsequent impact testing. Furthermore, the simulations could be applied to provide a stronger engineering basis to the extrapolation of damage equations to velocities above experimentally obtainable limits. In theory, such numerical studies would permit significant savings in development time and expense as well as provide a more optimally designed shield with well validated failure limits. In practice however, shielding configurations often outpace the capability of numerical codes. For instance, a numerically driven shielding development may be feasible for monolithic metallic single or dual wall configurations today, however for new materials or structures such as honeycomb sandwich panels or metallic foams the time associated with material model development and implementation required for accurate simulations can exceed by an order of magnitude, that of an experimental study. For instance, the non-linear orthotropic material model used in the three studies discussed in this chapter was developed for high-strength composites under ESA contract over four years, and required an additional two year extension for application to high stiffness composites. The conclusion of the study represented a large step forward in the state-of-the-art, yet numerical simulations at the conclusion of the study were still only capable of reproducing gross experimental results (i.e. perforation or no perforation) 66% of the time. Thus, application of numerical tools is still limited by the maturity of advanced material models and the difficulty of modeling complex structures such as foams, fabrics, etc. Despite the difficulties, the large number of configurations, particularly for composite materials, and limitations of experimental facilities means that numerical tools must play an active and integral role in MMOD risk assessment.

References

1. Jones, J.: Meteoroid Engineering Model – Final Report. University of Western Ontario, London, NASA SEE/CR-2004-400 (2004)
2. Liou, J.-C., Matney, M., Anz-Meador, P., Kessler, D., Jansen, M., Theall, J.: The New NASA Orbital Debris Engineering Model ORDEM2000. Lockheed Martin Space Operations, Houston, NASA TP-2002-210780 (2002)
3. Cour-Palais, B.: Hypervelocity Impact Investigations and Meteoroid Shielding Experience Related to Apollo and Skylab. *Orbital Debris*, 247-275 (1982)
4. Christiansen, E., Kerr, J.: Ballistic Limit Equations for Spacecraft Shielding. *International Journal of Impact Engineering* 26, 93-104 (2001)
5. Piekutowski, A.: Fragmentation-Initiation Threshold for Spheres Impacting at Hypervelocity. *International Journal of Impact Engineering* 29, 563-574 (2003)

6. Cour-Palais, B.: Meteoroid Protection by Multiwall Structures. AIAA Hypervelocity Impact Conference, Cincinnati (1969)
7. Christiansen, E.: Meteoroid/Debris Shielding. NASA Johnson Space Center, Houston, NASA TP-2003-120788 (2003)
8. McMillan A.: Experimental Investigations of Simulated Meteoroid Damage to Various Spacecraft Structures, General Motors Corporation, Santa Barbara, NASA CR-915 (1968)
9. Schonberg, W., Copper, D.: Repeatability and Uncertainty Analyses of NASA/MSFC Light Gas Gun Test Data. University of Alabama, Huntsville, NASA CR-192496 (1993)
10. Christiansen, E., Crews, J., Williamsen, J., Robinson, J., Nolen, A.: Enhanced Meteoroid and Orbital Debris Shielding 17, 217-228 (1995)
11. Frost, V.: Meteoroid Damage Assessment – NASA Space Vehicle Design Criteria (Structures). Aerospace Corporation, Langley, NASA SP-8042 (1970)
12. Schmidt, R., Housen, K.: Cadmium Simulation of Orbital-Debris Shield Performance to Scaled Velocities of 18 km/s. *Journal of Spacecraft and Rockets* 31(5), 866-877 (1994)
13. Christiansen, E., Crews, J., Kerr, J., Cour-Palais, B., Cykowski, E.: Testing the Validity of Cadmium Scaling. *International Journal of Impact Engineering* 17, 205-215 (1995)
14. Palmieri, D., Faraud, M., Destefanis, R., Marchetti, M.: Whipple Shield Ballistic Limit at Impact Velocities Higher Than 7 km/s. *Int. J. of Impact Engineering* 26, 579-590 (2001)
15. Kerr, J., Fahrenthold, E.: Three Dimensional Hypervelocity Impact Simulation for Orbital Debris Shield Design. *International Journal of Impact Engineering* 20, 479-489 (1997)
16. Schaefer, F., Ryan, S., Destefanis, R., Rott, M., Mandeville, J.: Composite Materials Impact Damage Analysis – Final Report. FhG EMI, Freiburg, Report No. I-69/05 (2005)
17. Riedel, W., Nahme, H., White, D., Clegg, R.: Advanced Material Model for Hypervelocity Impact Simulations (ADAMMO), FhG EMI, Freiburg, ESA CR(P) 4397 (2003)
18. Anon.: ANSYS AUTODYN User Manual – Version 11.0, Century Dynamics Inc., Concord (2007)
19. Ryan, S., Riedel, W., Schaefer, F.: Numerical Study of Hypervelocity Space Debris Impacts on CFRP/Al Honeycomb Spacecraft Structures. 55th IAC, Vancouver (2004)
20. Ryan, S., Schaefer, F., Lambert, M.: A Ballistic Limit Equation for Hypervelocity Impacts on CFRP/Al HC Satellite Structures 41, 1152-1166 (2008)
21. Putzar, R., Schaefer, F., Romberg, O., Stokes, H., Heine, A., Zimmermann, J.: Vulnerability of Spacecraft Equipment to Space Debris and Meteoroid Impacts – Final Report. Fraunhofer Ernst-Mach-Institut (EMI), Freiburg, Report No. I-15/06 (2006)
22. Ryan, S., Riedel, W.: Preliminary Theoretical Material Characterization for Numerical Modelling of Composite Structures. 56th IAC, Fukuoka, IAC-05-C2.5.10 (2005)
23. Ryan, S., Schaefer, F., Riedel, W.: Numerical Simulation of Hypervelocity Impact on CFRP/Al HC SP Spacecraft Structures Causing Penetration and Fragment Ejection. *International Journal of Impact Engineering* 33(1-2), 703-712 (2006)
24. Ryan, S., Wicklein, M., Mouritz, A., Riedel, W., Schaefer, F., Thoma, K.: Theoretical Prediction of Dynamic Composite Material Properties for Hypervelocity Impact Simulations. *Int. Journal of Impact Engineering* (2009)
25. Ryan, S., Schaefer, F., Guyot, M., Hiermaier, S., Lambert, M.: Characterizing the Transient Reponse of CFRP/Al HC Spacecraft Structures Induced by Space Debris Impact at Hypervelocity. *International Journal of Impact Engineering* 35, 1756-1763 (2008)
26. Ryan, S.: Hypervelocity Impact Induced Disturbances on Composite Sandwich Panel Spacecraft Structures. *Forschungsergebnisse aus der Kurzezeitdynamik – No. 15*, Fraunhofer Institut fuer Kurzezeitdynamik, Freiburg, ISBN 978-3-8167-7522-5 (2008)
27. Vergniaud, J., Guyot, M., Lambert, M., Schaefer, F., Ryan, S., Hiermaier, S., Taylor, E.: Structural Vibrations Induced by HVI – Application to the GAIA Spacecraft. *International Journal of Impact Engineering* 35, 1836-1843 (2008)

Chapter 23

Numerical Modeling of Crater Formation by Meteorite Impact and Nuclear Explosion

Charles L. Mader

Abstract The NOBEL code for modeling compressible fluid dynamics is used to model the formation of the Arizona meteor crater by a 50 meter diameter iron asteroid impacting basalt at 12 kilometers/second. The code is also used to model the crater generated by the SEDAN 104 kiloton nuclear explosion. To reproduce the observed crater sizes it is necessary to include the properties of pulverized rock created by the shocking and rarefaction of the rock.

23.1 The NOBEL Code

The U.S. Department of Energy's Accelerated Strategic Computing Initiative (ASCI) during 2000 to 2005 resulted in major advances in computer technology and in methods for improving the numerical resolution of compressible reactive hydrodynamic calculations.

In NOBEL, the three-dimensional partial differential equations for compressible flow are solved by a high resolution differencing scheme using an adaptive grid technique described in [1]. The solution technique uses Continuous Adaptive Mesh Refinement (CAMR). The decision to refine the grid is made cell-by-cell continuous throughout the calculation. The computing is concentrated on the region of the problem which require high resolution.

Refinement occurs when gradients in physical properties (density, pressure, temperature, material constitution) exceed defined limits, down to a specified minimum cell size for each material. With the computational power concentrated on the re-

Charles L. Mader
Mader Consulting Co., Honolulu, HI 96825-2860, USA e-mail: MCCOHI@aol.com

gions of the problem which require higher resolution, very large computational volumes and substantial differences in scale can be simulated.

The code can describe one-dimensional slab or spherical geometry, two-dimensional slab or cylindrical geometry, and three-dimensional Cartesian geometry.

The code incorporates multiple material equations of state (analytical or SESAME tabular). Every cell can in principle contain a mixture of all the materials in a problem assuming that they are in pressure and temperature equilibrium. The assumption of temperature equilibrium is inappropriate for mixed cells with interfaces between different materials. The errors increase with increasing density differences. The problem is minimized by using fine numerical resolution at interfaces. The amount of mass in mixed cells is kept small resulting in small errors being introduced by the temperature equilibrium assumption. The strength is treated using the Hooke's Law, Von Mises yield model described in [1].

A variety of boundary conditions is available, the most important being reflective boundary walls, reflective internal boundaries, and "freeze regions" which allow specific inflows and unrestricted outflows of material.

Very important for cavity generation and collapse is the capability to initialize and describe gravity correctly, which is included in the code. The initial density and initial pressure changing with depth or altitude is correctly included.

The code was developed for general applications to run on a wide variety of computers from desktop PC's (Windows, Linux and Apple Macintosh) to the latest MMP or SMP supercomputers. The code has operated on different super computers, the oldest being the ASCI Red teraflop system installed at Sandia National Laboratory in 1996 to the Roadrunner petaflop computer installed at Los Alamos National Laboratory in 2008.

The code has all the techniques for modeling reactive flow and detonation chemistry and physics described in [1]. It has been used to model Richtmyer-Meshkov and shock induced instabilities. Also modeled using Nobel is the 1958 Lituya Bay impact landslide generated 485 meter high tsunami, the water cavities generated by projectiles and explosions and resulting water waves, the 1883 Krakatoa hydrodynamic volcanic explosion and resulting tsunami, shaped charge jet formation and penetration, detonation wave propagation and failure, corner turning, desensitization by preshocking, explosive performance and applications such as cylinder tests, underwater explosions, denting of metal plates, Mach and regular shock and detonation wave interactions and the problems associated with explosive hazards from accidental initiation. The K-T impact 65 million years ago at Chicxulub by a 10 kilometer diameter granite asteroid moving 15 kilometers/second has been modeled using RAGE which is a version of NOBEL with radiation. These applications of the NOBEL code are described in [1] and [2].

23.2 Modeling the Arizona Meteor Crater

The Arizona Barringer meteor crater was generated about 50,000 years ago by an iron asteroid about 50 meters in diameter and impacted the earth at about 12 kilometers/second. A picture of the crater is shown in Figure 23.1. A sketch of the crater is shown in Figure 23.2. The crater is 1.2 kilometers in diameter, currently 175 feet deep with a 50 meter high rim. In addition there is about 250 meters of rubble below the current bottom of the crater making the initial asteroid generated crater about 500 meters deep from the top of the rim. The impacted rock was basalt.

The rim of the crater was generated by the rock ejecta folding over the crater rim as shown in Figure 23.3. The 640 kilogram iron-nickel fragment found near the crater is shown in Figure 23.4.



Fig. 23.1 The Arizona Barringer meteor crater.

The impact of a 50 meter diameter iron asteroid moving at 12 kilometer/second with Basalt was modeled using NOBEL. The equation of state used for iron was the Sesame table number 4270. The iron shock Hugoniot was described by the shock velocity U_S and particle velocity U_P fit $U_S = 0.458 + 1.49U_P$ where the velocity units are centimeters/microsecond. The initial iron density is 7.896 grams/cc.

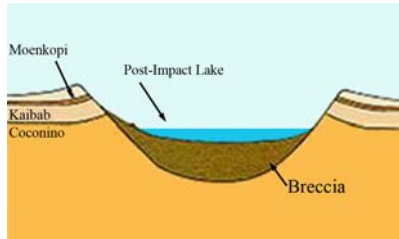


Fig. 23.2 Sketch of the geometry of the Arizona meteor crater.

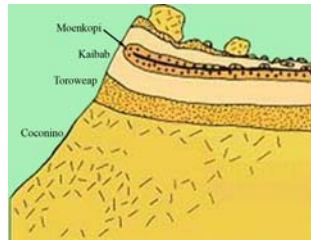


Fig. 23.3 Sketch of the geometry of the folded rim of Arizona meteor crater.



Fig. 23.4 A 640 kilogram iron-nickel meteorite fragment found near the Arizona Barringer crater.

The equation of state used for Basalt was the Sesame table number 7530. The shear modulus used was 0.25 and the yield was 0.02 kilobar. Gravity was included in the calculation.

The geometry of the calculation was cylindrical with 0.5 kilometer of air above 2.0 kilometers of Basalt. Calculations were performed for a 50 meter and a 25 meter mesh. The calculations were performed using personal computers.

If the Basalt is modeled as a fluid with a yield of 0.0 kilobar, the density profiles at various times are shown in Figure 23.5. After the cavity has been created, it collapses and forms a jet that then falls back and forms waves just as does a rock projected into water.

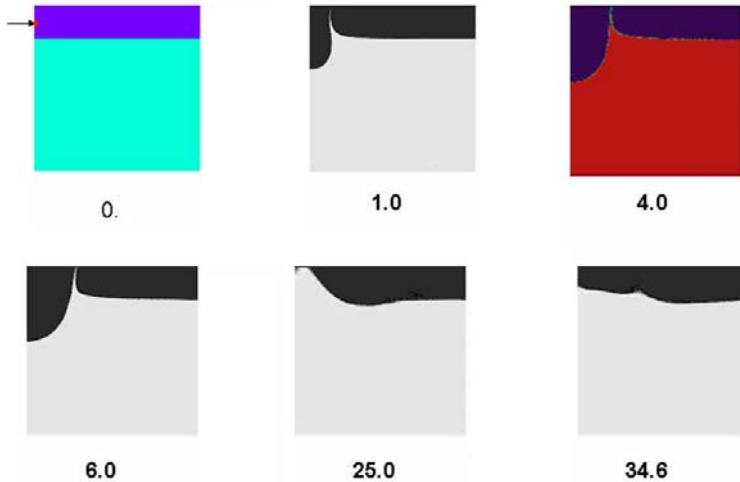


Fig. 23.5 The density plots for a 50 meter diameter iron asteroid impacting Basalt modeled as a fluid with a yield of zero. The basalt is 2 kilometers high and 2.5 kilometers wide in cylindrical geometry with the axis on the left side of the figures. The time is shown in seconds. The initial position of the asteroid is shown by the arrow next to the red sphere in the first frame.

If the basalt has a yield of 0.05 kilobar the final crater diameter is too small and if the yield is 0.01 kilobar the crater is too large. A yield of 0.02 kilobar results in a crater about the diameter of the crater and permits a rebound from the maximum depth to about the final depth of the Arizona meteor crater. The density plots at various times are shown in Figure 23.6.

The small yield for the basalt is a result of the basalt being initially shocked and melted and then rarefied to form a pulverized material with not much strength. The term for the process is the basalt has been 'fluidized'. The yield required to describe the basalt behavior represents the fluidized rock. In the SEDAN crater modeling that process is represented by an initially large yield and after the cavity is generated and fluidization has occurred the crater rebound is described by a smaller yield for the fluidized rock.

The final crater geometry for Basalt with a yield of 0.02 kilobar for calculations with an initial mesh of 50 x 50 cells and initial cell sizes of 50 and 25 meters are shown in Figure 23.7.

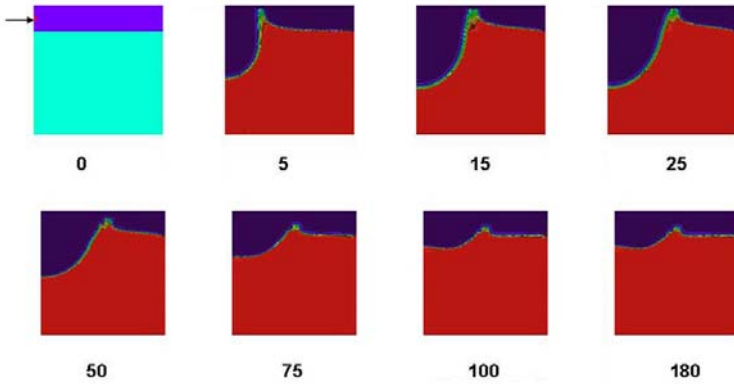


Fig. 23.6 The density plots for a 50 meter diameter iron asteroid impacting Basalt modeled with a yield of 0.02 kilobar. The basalt is 2 kilometers high and 2.5 kilometers wide in cylindrical geometry with the axis on the left side of the figures. The time is shown in seconds. The initial position of the asteroid is shown by the arrow next to the red sphere in the first frame.

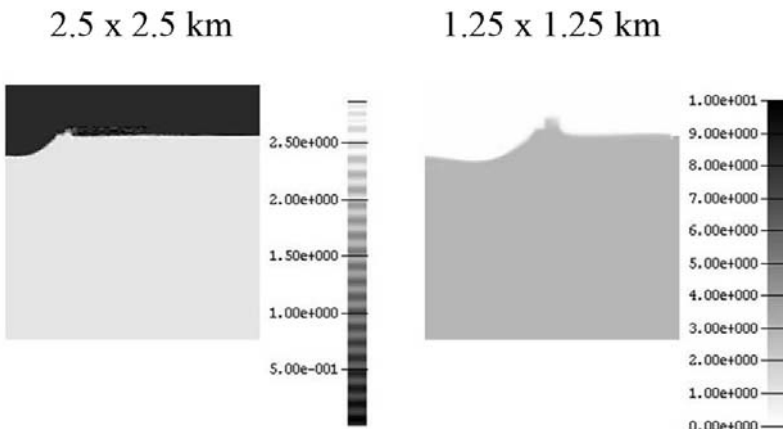


Fig. 23.7 The final crater geometry for Basalt with a yield of 0.02 kilobar for calculations with an initial mesh of 50 x 50 cells and initial cell sizes of 50 and 25 meters.

23.3 Modeling the SEDAN Crater Created by a Nuclear Explosion

The SEDAN nuclear test was performed July 6, 1962 as part of the Plowshare series of tests designed to develop earth evacuating techniques using the energy from

nuclear explosions that resulted in low levels of residual radioactivity. The major application was believed to be for the creation of a sea level channel to replace the Panama canal.

The nuclear explosive device was buried 194 meters deep in the Nevada Tuff rock. The energy of the explosion was equivalent to 104 kilotons of TNT. The height of the dome before breach was 90 meters which occurred 3 seconds after the explosion. The final crater diameter was 360 meters, the final crater depth was 97 meters. After the explosion, drilling determined that the maximum depth of melt was 246 meters. The final crater dimensions are shown in Figure 8 and the crater is shown in Figure 9. The explosion moved 12 million tons of earth. The Richter magnitude of the event was 4.75.

The explosion is shown in Figure 10 about 10 seconds after the dome breach. The picture is taken from a film of the explosion that is available at www.mccohi/crater/sedanshot.mpeg.

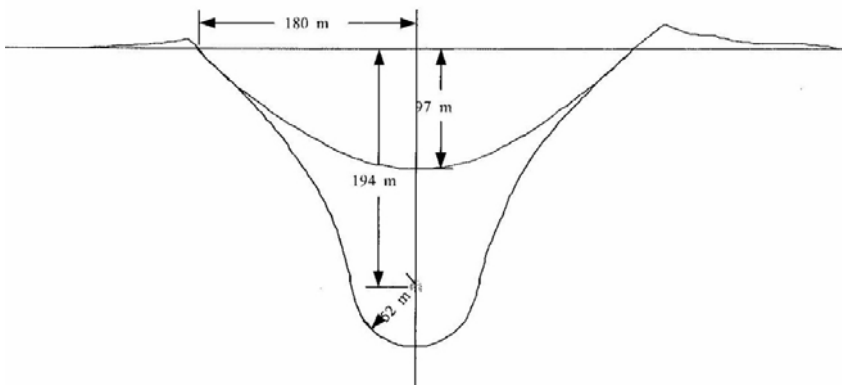


Fig. 23.8 The crater geometry. The nuclear explosive was located 194 meters below the surface. The final crater was 180 meters in radius and 97 meters deep with a melt zone shown by the outer line with a maximum depth of 246 meters.

The NOBEL model for the SEDAN nuclear explosion was modeled by a 30 meter diameter water sphere at 194 meter depth in Tuff with an initial energy of 104 kilotons or 4.353×10^{23} ergs. The Nevada test site Tuff has been extensively characterized and the Sesame table number 7111 was used for modeling its equation of state. The Tuff shock Hugoniot was described by the shock velocity U_S and particle velocity U_P fit $U_S = 0.199 + 1.22U_P$ where the velocity units are in centimeters/microsecond. The initial Tuff density was 1.39 grams/cc. The shear modulus was 0.25 megabar. The Tuff yield was 0.1 kilobar for the first 2.5 seconds which is approximately the time of maximum cavity size. The yield was then lowered to 0.004 kilobar to account for the lower strength of pulverized Tuff that has been



Fig. 23.9 The SEDAN crater in 1963 and 2003 with Los Alamos National Laboratory Scientists on viewing platform. Author is second from right.

shocked and rarefied or 'fluidized'. Bingham first introduced the concept in his book 'Fluidity and Plasticity' [3]. The concept and book was suggested by Dr. Bill Van Dorn during our current efforts to model craters on the moon and their rings and mascons.

Calculations for Tuff without strength (a yield of 0.0) results in a cavity diameter that is more than twice too large. If the Tuff initially has a yield of 0.1 kilobar and then lowered to 0.003 kilobar the cavity diameter is about as observed but there is too much cavity collapse. The final cavity depth is smaller than observed.

As shown in Figure 23.9 the SEDAN crater is not exactly spherical and as shown in Figure 23.10 the ejecta pattern was very irregular. The NOBEL numerical model assumes that the SEDAN event can be modeled with cylindrical symmetry which



Fig. 23.10 A frame from a film taken of the nuclear explosion after the dome breach. The film is available at www.mccoehi.com/crater/sedanshot.mpeg.

is only a first approximation of the actual complicated nature of the Tuff which has significant density and composition inhomogenities.

The cylindrical geometry of the calculation was modeled by an initial mesh of 32 meters square and 32 x 64 cells or 1 kilometer radius and 2 kilometers high with 1 kilometer of air and 1 kilometer of Tuff. The calculations included gravity and were performed using personal computers.

If the Tuff is modeled with a yield of 0.1 kilobar for the first 2.5 seconds and then the yield is lowered to 0.004 kilobar, the resulting density profiles are shown in Figure 23.11. The SEDAN crater dimensions are reproduced by the calculation.

The final cavity density profiles for a pulverized Tuff yield of 0.004 kilobar are shown in Figures 12. The 0.004 yield results in a cavity similar to that of the SEDAN nuclear explosion.

23.4 Conclusions

The NOBEL code for modeling compressible fluid dynamics was used to model the formation of the Arizona Barringer crater by a 50 meter diameter iron asteroid impacting at 12 kilometers/second. The strength of the basalt required to reproduce the final crater dimensions had to be small (0.02 kilobar yield) because the basalt was shocked and pulverized. Most of the ejecta was propelled outside the crater as

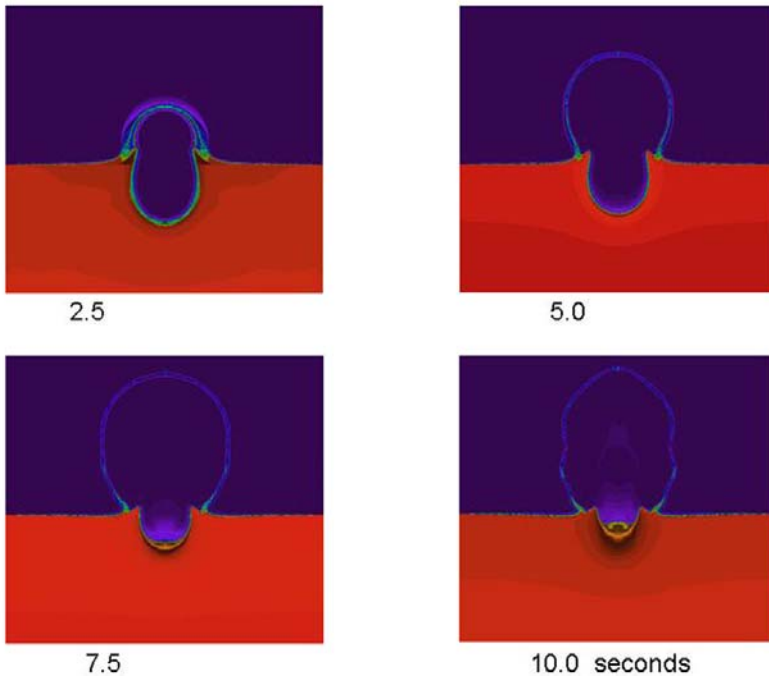


Fig. 23.11 The SEDAN crater formation by a 104 kiloton nuclear explosive with a Tuff yield of 0.1 kilobars for the first 2.5 seconds, which is at about at the time of maximum cavity generation and then lowered to 0.004 kilobars to account for the lower strength of the pulverized Tuff that has been 'fluidized'.

was a significant amount of the iron asteroid with only a small amount falling back into the final crater.

The SEDAN crater created in Nevada Tuff by a 105 kiloton nuclear explosion buried 194 meters deep was modeled. To reproduce the crater dimensions the initial yield of the Tuff was 0.1 kilobar for 2.5 seconds when the crater was at maximum size and then the yield was reduced to 0.004 kilobar to model the pulverized or 'fluidized' Tuff.

PowerPoint presentations and the AVI and MPEG movies of the NOBEL modeling of the Arizona Meteorite crater and SEDAN nuclear explosion generated crater are available at www.mccohi.com/crater/crater.htm.

This modeling of craters is part of a program to calibrate crater modeling for our study (with Dr. Van Dorn) of the multi-ringed lunar maria and underlying mascons - the so called 'Lunar Tsunamis' because they are similar to frozen tsunami waves.

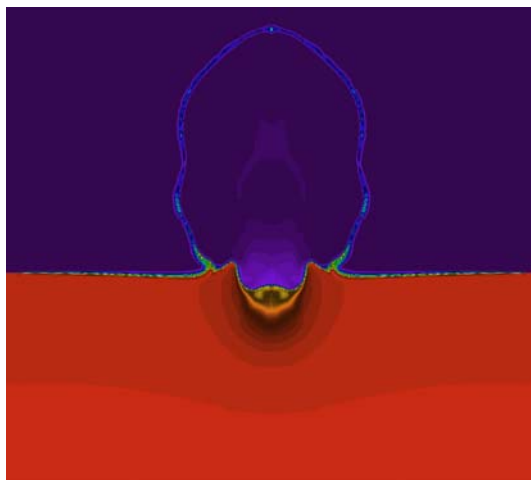


Fig. 23.12 The density profile of the SEDAN crater modeled including 'fluidization'.

References

1. Mader, Charles L. : Numerical Modeling of Explosives and Propellants, CD-ROM. CRC Press (2008).
2. Mader, Charles L. : Numerical Modeling of Water Waves, 2008 DVD, CRC Press (2004).
3. Bingham, Eugene C. : Fluidity and Plasticity, McGraw Hill (1922).

Index

- ALE formulation, 243
- Artificial viscosity, 350
 - Caramana requirements, 361
 - Edge centred viscosity, 362
 - Kurapatenko, 362
 - Noh problem, 358
 - Piston problem, 352
 - Saltzman piston, 359
 - Sod shock tube, 356
 - Tensor viscosity, 363
 - von Neumann Richtmyer, 350
 - Wall heating, 356
- Ballistic limit equations, 399
- Barlat constitutive model, 71
- Bulk tensile test, 91
- Columbia accident, 35
- Concrete
 - Elastic surface, 144
 - Failure surface, 144
 - Hugoniot data, 145
 - Mesomechanical model, 148
- Configurational forces, 124
 - Eshelby, 124
 - Gurtin, 124
 - Maugin, 124
- Conservation equations
 - Lagrangean, 373
 - SPH, 374
- Coupon test, 92
- Crack opening
 - Benzeggagh-Kenane criterion, 96
- Crashworthiness simulation, 70
- Damage model
 - Effective stress concept, 82
- GISSMO, 75
- Initiation, 96
- Isotropic, 97
- Derivative
 - fundamental, 337
- Dispersion, 334
- Double Cantilever Beam test (DCB), 93
- Energy release rate
 - Mode-I, 97
 - Mode-II, 97
- Equation of State, 337
 - complete, 337
 - Herrmann $p - \alpha$, 343
 - JWL, 286
 - Menikoff-Kober, 346
 - Mie-Grüneisen, 339
 - porous, 340
 - Shock EoS, 339
- Foam
 - Columbia accident, 35
 - Crash loaded, 30
 - Damage model, 19
 - Impact test, 23
 - Leg impact, 17
 - Plasticity model, 112
- Forming Intensity, 79
- Forming limit curve (FLC), 44, 77
- Forming simulation, 70
- Fundamental derivative, 337
- Gurson model, 72
- Herrmann $p - \alpha$ EOS, 343
- Hill's energy functional, 28
- Hydrocode

- components, 3
 - solution cycle, 6
- Hydrocodes
 - marching solution, 5
- Hypervelocity Impact
 - Ballistic limit equations, 399
 - CFRP, 117
 - Composite material panels, 401
 - Honeycomb sandwich panels, 406
 - Risk analysis, 398
- IED simulation, 137
- Instabilities
 - Rayleigh-Taylor, 239
 - Richtmyer-Meshkov, 239
- J-Integral, 126
- Lemaitre effective stress concept, 76
- Material model
 - Barlat, 71
 - Cohesive zone, 90, 94
 - Drucker-Prager, 171
 - Forming limit curve, 44
 - Fu-Chang, 11
 - Gurson, 72
 - Holmquist-Johnson-Cook, 144
 - Johnson-Cook, 98
 - Mohr-Coulomb, 174
 - RHT concrete, 143
 - Riedel-Hiermaier-Thoma RHT, 143
 - Tvergaard Needleman, 72
- Material test
 - Bulk tensile, 91
 - Confinement sleeve technique, 170
 - Coupon, 92
 - DCB, 93
 - End-notched flexure (ENF), 94
 - T-Peel, 92
 - Triaxial compression, 168
- Mesomechanical model
 - Concrete, 148
- $p - \alpha$ Equation of State, 343
- Plastic volume increase, 72
- Plasticity model, 108
 - Aluminum honeycomb, 114
 - CFRP, 117
 - Chen, 109
 - Constant volume, 108
 - Hill, 110
 - von Mises, 110
- Porous material, 341
- Rayleigh-Taylor instabilities, 239
- RHT model, 143
 - Limit surfaces, 150
- Richtmyer-Meshkov instabilities, 239
- Shock wave, 334
 - conditions for its formation, 336
 - existence, 336
 - Formation, 334
 - stability, 336
- Smooth Particle Hydrodynamics, 367
 - (In-)Consistency, 380
 - B-spline kernel, 377
 - Conservation equations, 374
 - Kernel estimate, 372
 - Neighbour search, 379
 - Smoothing Length, 378
 - Stability analysis, 386
 - Tensile Instability, 384
 - Zero energy modes, 389
- State surfaces, 336
- Vehicle safety analysis, 135
- Void nucleation, 72
- von Mises equivalent stress, 78
- Wave propagation codes, 3